ESHID-602963

RECEIVED
MAR 28 2018
NMED
Hazardous Waste Bureau

Los Alamos
NATIONAL LABORATORY
EST. 1943

Associate Directorate for Environmental Management
P.O. Box 1663, MS M992
Los Alamos, New Mexico 87545
(505) 606-2337

EM-LA

Environmental Management
P. O. Box 1663, MS M984
Los Alamos, New Mexico 87545
(505) 665-5658/FAX (505) 606-2132

Date: MAR 28 2018
Refer To: ADEM-18-0007
LAUR: 18-21326

John Kieling, Bureau Chief
Hazardous Waste Bureau
New Mexico Environment Department
2905 Rodeo Park Drive East, Building 1
Santa Fe, NM 87505-6303

Subject: Compendium of Technical Reports Related to the Deep Groundwater Investigation for the RDX Project at Los Alamos National Laboratory

Dear Mr. Kieling:

Enclosed please find two hard copies with electronic files of the Compendium of Technical Reports Related to the Deep Groundwater Investigation for the RDX Project at Los Alamos National Laboratory. A pre-submission review meeting was held between Los Alamos National Security, LLC, and the New Mexico Environment Department (NMED) on September 6, 2017. The submittal of this compendium of reports fulfills submittal of Milestone #2 in the Fiscal Year 2018 Appendix B of the 2016 Compliance Order on Consent between NMED and Department of Energy.

If you have any questions, please contact Steve Paris at (505) 606-0915 (smparis@lanl.gov) or Cheryl Rodriguez at (505) 665-5330 (cheryl.rodriguez@em.doe.gov).

Sincerely,

Enrique Torres, Program Director
Environmental Remediation Program
Los Alamos National Laboratory

Sincerely,

David S. Rhodes, Director
Office of Quality and Regulatory Compliance
Environmental Management
Los Alamos Field Office

ET/DR/SP:sm

Enclosures: Compendium of Technical Reports Related to the Deep Groundwater Investigation for the RDX Project at Los Alamos National Laboratory (EP2018-0006)

Cy: (w/enc.)
Cheryl Rodriguez, DOE-EM-LA
Steve Paris, ADEM ER Program
Tim Goering, ADEM ER Program
Gilles Bussod, EES-14

Cy: (w/electronic att.)
Laurie King, EPA Region 6, Dallas, TX
Raymond Martinez, San Ildefonso Pueblo
Dino Chavarria, Santa Clara Pueblo
Steve Yanicak, NMED-DOE-OB, MS M894
emla.docs@em.doe.gov
Public Reading Room (EPRR)
PRS Database
ADESH Records

Cy: (w/o enc./date-stamped letter emailed)
lasomailbox@nnsa.doe.gov
Peter Maggiore, DOE-NA-LA
David Rhodes, DOE-EM-LA
Enrique Torres, ADEM ER Program
Randy Erickson, ADEM ER Program
Jocelyn Buckley, ADESH-EPC-CP
Mike Saladen, ADESH-EPC-CP
Benjamine Roberts, ADESH-EPC-DO
William Mairson, ADESH-EPC-DO/PADOPS
Craig Leasure, PADOPS

LA-UR-18-21326
March 2018
EP2018-0006

Compendium of Technical Reports Related to the Deep Groundwater Investigation for the RDX Project at Los Alamos National Laboratory

Los Alamos
NATIONAL LABORATORY
EST. 1943

Prepared by the Associate Directorate for Environmental Management

EP2018-0006

Compendium of Technical Reports Related to the Deep Groundwater Investigation for the RDX Project at Los Alamos National Laboratory

March 2018

Responsible project manager:

Printed Name	Signature	Title	Organization	Date
Steve Paris		Project Manager	Environmental Remediation Program	3/22/2018

Responsible LANS representative:

Printed Name	Signature	Title	Organization	Date
Randall Erickson		Associate Director	Associate Directorate for Environmental Management	3/22/18

Responsible DOE-EM-LA representative:

Printed Name	Signature	Title	Organization	Date
David S. Rhodes		Office Director	Quality and Regulatory Compliance	3-27-2018

CONTENTS

Figures

Attachments

Attachment 5	Biostimulation and Microbial Community Profiling Reveal Insights on RDX Transformation in Groundwater
Attachment 6	Characterization of the Microbial Population and RDX Degradation in Groundwater at Technical Area 16
Attachment 7	RDX Degradation in Sediments Treated Both Chemically and with Biostimulant Amendments
Attachment 8	Hydrogeology and Model Calibration for Contaminant Fate and Transport at Technical Area 16
Attachment 9	2017 Status Report: Tracer Tests at Consolidated Unit 16-021(c)-99, Technical Area 16

Acronyms and Abbreviations

3-D	three-dimensional
CME	corrective measures evaluation
DNX	hexahydro-1,3-dinitro-5-nitro-1,3,5-triazine
DOE	Department of Energy (U.S.)
GWIP	groundwater investigation work plan
HE	high explosives
HGCM	hydrogeochemical conceptual model
HMX	octahydro-1,3,5,7-tetranitro-1,3,5,7-tetrazocine
IR	investigation report
LANL	Los Alamos National Laboratory
LANS	Los Alamos National Security, LLC
LPZ	lower perched zones
MBR	mountain-block recharge
MFR	mountain-front recharge
MNX	hexahydro-1-nitroso-3,5-dinitro-1,3,5-triazine
NMED	New Mexico Environment Department
NOD	notice of disapproval
RDX	hexahydro-1,3,5-trinitro-1,3,5-triazine
SWSC	Sanitary Wastewater Systems Consolidation Spring
SZ	saturated zone
TA	technical area
TNX	2,4,6-trinitroxylene
TNT	2,4,6-trinitrotoluene
VZ	vadose zone

1.0 INTRODUCTION

This document presents a compendium of technical reports on studies related to the contamination of groundwater by RDX (hexahydro-1,3,5-trinitro-1,3,5-triazine) for the RDX Project at Los Alamos National Laboratory (LANL or the Laboratory). The technical reports presented in this document summarize the results of recent studies on the hydrology, geology, and geochemistry of Technical Area 16 (TA-16), conducted in the period from 2015 to 2018 to support the deep groundwater investigation of RDX contamination at the site (Figure 1.0-1). A summary of the groundwater models developed for the deep groundwater investigation is also included, along with some of the preliminary modeling results.

Although RDX is the primary contaminant discussed throughout this document, other high explosives (HE) contaminants are present in Cañon de Valle, including HMX (octahydro-1,3,5,7-tetranitro-1,3,5,7-tetrazocine); TNT (2,4,6-trinitrotoluene), and barium (LANL 2003, 085531). However, RDX is the primary focus of these studies because of its relative mobility and because it exceeds the New Mexico Environment Department (NMED) tap water screening level of 7.02 µg/L in deep perched-intermediate groundwater and in the regional aquifer. Barium exceeds the NMED Water Quality Control Commission groundwater standard of 1000 µg/L in alluvial groundwater and is present in high concentrations in sediments within Cañon de Valle, but barium is not present at elevated concentrations in deep perched and regional groundwaters.

This document consists of two parts. Section 1.0 provides the background and context for the compendium. Section 2.0 summarizes the highlights of each compendium report, included as Attachments 1 through 9.

Figure 1.0-1 shows the location of TA-16 with respect to Laboratory TAs and surrounding landholdings. Figure 1.0-2 shows the deep perched-intermediate zone and regional aquifer monitoring well network and water table contours, respectively, in the vicinity of Consolidated Unit 16-021(c)-99. Figure 1.0-3 shows the conceptual hydrogeologic east-west cross-section for Cañon de Valle in the vicinity of the 260 Outfall at TA-16.

1.1 Background

The U.S. Department of Energy (DOE) and Los Alamos National Security, LLC, (LANS) submitted the “Corrective Measures Evaluation Report for Intermediate and Regional Groundwater” (CME) (LANL 2007, 098734) to NMED in August 2007. The CME recommended a remediation strategy for monitored natural attenuation in the intermediate and regional groundwater, with possible pump and treat actions to reduce HE contaminant concentrations in groundwater. NMED subsequently issued a notice of disapproval (NOD) for the CME in April 2008 (NMED 2008, 101311). In the NOD, NMED required the Laboratory to conduct additional characterization to assess the extent of contamination in perched-intermediate groundwater and in the regional aquifer, and to further evaluate the feasibility of the remedial alternatives proposed in the CME based on their assessment that insufficient information was available to determine whether the Laboratory’s proposed actions were appropriate and protective.

Specifically, NMED requested in the NOD that the Laboratory develop a supplemental investigation work plan (SIWP) to

1. characterize the extent of the contaminant plume in the intermediate zone
2. characterize the extent of contaminant plume in the regional aquifer
3. characterize the hydrogeologic properties in the regional aquifer

4. characterize the hydrogeologic and hydrogeochemical properties in the intermediate zone
5. determine HE degradation rates
6. provide recommendations for additional monitoring wells
7. provide recommendations for the replacement of monitoring wells unsuitable for the well network
8. collect site-specific data for use in evaluating the feasibility of remedy implementation for remedial alternatives
9. propose actions to reduce uncertainties associated with the conceptual model, including uncertainties related to infiltration rates, groundwater travel times, and the contaminant source

In response to NMED's 2008 NOD, the Laboratory developed the "Supplemental Investigation Work Plan for Intermediate and Regional Groundwater at Consolidated Unit 16-021(c)-99" (LANL 2008, 103165). In this document, the Laboratory proposed additional characterization activities to address uncertainties in the hydrogeologic conceptual model at TA-16. These activities included installing additional perched-intermediate and regional groundwater monitoring wells, performing additional groundwater monitoring, and conducting single-well aquifer tests to further characterize hydraulics of the perched-intermediate and the regional aquifer. To address hydrogeologic uncertainties, subsequent work plans were submitted, proposing multiwell aquifer tests and cross-hole tracer tests (LANL 2012, 210352; LANL 2015, 600535; LANL 2015, 600686).

In 2012, the Laboratory conducted an evaluation of the TA-16 well network to (1) evaluate its adequacy to support the selection of corrective action alternatives for a future CME, (2) support ongoing investigations in the area, and (3) detect potential contaminants upgradient of water supply wells (LANL 2012, 213573). The network evaluation resulted in recommendations to (1) convert several multiscreen wells to improve their reliability, (2) install a monitoring well in the perched-intermediate zone north of Cañon de Valle, and (3) install two additional monitoring wells in the regional aquifer to characterize contaminant flow paths and to monitor for contaminants. NMED approved the TA-16 well network evaluation with modifications in June 2012 (NMED 2012, 520747).

Activities subsequently completed in accordance with these work plans include the following:

- conducting an electrical resistivity geophysical survey to map the electrical structure of the vadose zone (VZ) in the vicinity of Cañon de Valle (LANL 2014, 259157);
- installation and monitoring of perched-intermediate monitoring wells R-25b, R-25c (dry), R-47i, R-63i, CdV-9-1(i), and CdV-16-4ip;
- installation and monitoring of regional monitoring wells R-48, R-58, and R-68;
- reconfiguration of wells CdV-R-37-2 and CdV-R-15-3 from Westbay sampling systems to single-screened wells with purgeable sampling systems;
- conducting short-duration aquifer tests in new monitoring wells;
- conducting extended duration aquifer tests at CdV-16-4ip in 2011 and 2014;
- deploying groundwater tracers in perched-intermediate well CdV-9-1(i) with two piezometers, and in monitoring wells R-25b and CdV-16-1(i), and performing subsequent sampling for tracers in monitoring wells near tracer-injection points (LANL 2017, 602161); and
- conducting extended-duration (30-d) cross-hole aquifer tests using CdV-9-1(i), CdV-16-4ip, and CdV-16-1(i) as pumping locations and monitoring the effects in surrounding wells in 2016, in accordance with the "Work Plan for Intermediate Groundwater System Characterization" (LANL 2015, 600535). The Laboratory submitted a report on these tests in 2017 (LANL 2017, 602288).

On September 6, 2016, DOE and LANS submitted the "Groundwater Investigation Work Plan for Consolidated Unit 16-021(c)-99, Including Drilling Work Plans for Wells R-68 and R-69" (GIWP) (LANL 2016, 601779) to address uncertainties related to increasing concentrations of RDX observed in monitoring well R-18, completed in the regional aquifer north of Cañon de Valle. The GIWP recommended installing up to two monitoring wells completed in the regional aquifer.

The first well, R-68, was completed in early 2017 (LANL 2017, 602539). The need for a second well, R-69, was to be assessed based on the data collected from R-68. Information gained from the drilling and sampling of R-68 was evaluated in a summary report for R-68 (LANL 2017, 602539), providing the basis for a recommendation to drill the additional monitoring well R-69. Monitoring well R-69 is planned for installation in calendar year 2018.

The characterization activities discussed above have associated work plans, completion reports, and various technical reports documenting these activities and the data from these activities. However, other studies have also been conducted to address questions initially posed in the 2008 NOD (NMED 2008, 101311) regarding the nature and extent of contamination and data collection to be used to evaluate potential corrective actions for RDX in the VZ and groundwater. Data from some of these studies have not been provided to NMED. This compendium of technical reports was developed as a vehicle to provide these additional data to NMED to complete the administrative record. Many of these studies were completed recently, and others are still in progress.

The overall objectives of the studies discussed in this compendium are to provide additional data to address some of the data gaps identified by NMED in the 2008 NOD (NMED 2008, 101311). Specific data gaps addressed include (1) the nature of the contaminant source, (2) the nature and extent of contamination, (3) additional details on the conceptual model including the hydrogeology, infiltration, and recharge factors controlling the degradation of RDX, (4) potential technologies for the remediation of RDX, and (5) a summary of the groundwater models to be used to evaluate contaminant fate and transport and potential corrective actions in the future.

Groundwater flow and transport models to be used to evaluate contaminant fate and transport and potential site-specific corrective actions are presented in this compendium. Data from these compendium studies support the groundwater investigation report (IR), planned for submission to NMED in March 2019. This IR will summarize the hydrogeologic conceptual model and will address the remaining data gaps related to the deep groundwater CME identified by NMED in the NOD (NMED 2008, 101311). The IR will include the results of a groundwater risk assessment that will evaluate the potential impacts of transport of the RDX inventory in the VZ to the regional aquifer.

1.2 Objectives for Each Compendium Study

The objectives for each compendium study are summarized below.

Attachment 1: 2017 Update of the RDX Inventory Report

The objective of this study is to present an updated estimate of the mass of RDX in the subsurface environment in the vicinity and downgradient of the 260 Outfall in Cañon de Valle. This estimate was developed based on the latest characterization results from recently installed monitoring wells and boreholes in TA-16 and TA-9. Although a similar analysis was conducted in 2005, this 2017 update uses recent data from a substantially larger set of monitoring wells and boreholes and addresses the reduction of the near-surface contamination at the 260 Outfall as a result of the 2009–2010 "Summary Report for the Corrective Measures Implementation at Consolidated Unit 16-021(c)-99" (LANL 2010, 108868). The mass of RDX was estimated for (1) the near-surface soils and sediments around the 260 Outfall and in Cañon de Valle, (2) the underlying VZ beneath the outfall and Cañon de Valle, (3) the VZ beneath the mesa discharge to Sanitary Wastewater Systems Consolidation (SWSC) and Burning Ground Springs, and (4) the deep perched-intermediate groundwater and the regional aquifer. This refined estimate of RDX inventory in each of the zones will be used for the planned groundwater risk assessment section of the IR to evaluate the potential effects of RDX on the regional aquifer. This information will also be useful for assessing potential corrective actions, should a CME be required.

Attachment 2: Geology of Technical Area 16 and Vicinity, Los Alamos National Laboratory

This report describes the recent geologic investigations undertaken to support the investigation of RDX-contaminated groundwater in the vicinity of TA-16. This study focused on gathering and evaluating new information on geologic contacts, internal bedding features, and structural controls for the study area, based on data collected during the drilling of monitoring wells and boreholes over the last decade. The data are used to update the sitewide geologic model that provides the framework for groundwater flow and transport models for the RDX deep groundwater investigation (Attachment 8). The data also update the hydrogeochemical conceptual model for the study area (Attachment 3). Groundwater recharge pathways are controlled by stratigraphic units, internal bedding features, structural controls, faults and fracture zones, and the hydraulic properties of the geologic strata. An accurate understanding of these elements is necessary to understand contaminant migration to groundwater and to model contaminant fate and transport.

Attachment 3: A Refined Hydrogeochemical Conceptual Model for the RDX Project

Six different studies using isotope data, geochemistry, and field measurements were conducted to update the hydrogeochemical conceptual model (HGCM) for the RDX study area. These studies are summarized in Attachment 3 and include (1) a factoral analysis of the geochemical signatures of waters from different hydrostratigraphic units, used to evaluate recharge and flow pathways, (2) a review of concentration-discharge relationships used to evaluate contaminant residence times in the near-surface environment, (3) a study of infiltration along Cañon de Valle to assess deep mountain-block recharge (MBR), (4) a review of stable isotope and temperature data to evaluate recharge sources, (5) a study of postfire water chemistry data to determine if fire-induced changes can be used as a tracer, and (6) the analysis of mountain block and local recharge using a simple mixing-model approach and geochemical modeling. These studies have significantly improved our understanding of the HGCM for the area and indicate that MBR has a profound influence on the concentrations of contaminants in perched-intermediate and regional aquifers. The updated HGCM provides the framework for the groundwater flow and contaminant transport models presented in Attachment 8 and allows more accurate simulations of RDX concentrations in the perched-intermediate zone and the regional aquifer.

Attachment 4: Fate and Transport of Hexahydro-1,3,5-trinitro-1,3,5-triazine (RDX) and its Degradation Products in Sedimentary and Volcanic Rocks, Los Alamos, New Mexico

The objective of this study is to better understand the extent of adsorption/desorption and transport of RDX and its degradation products in the deep perched-intermediate and regional aquifers at TA-16. This report summarizes the results of laboratory batch and column studies conducted to measure contaminant retardation factors and partitioning coefficients (K_d) for RDX and its degradation products. These parameters are site specific and are highly influenced by the underlying lithology and geochemical conditions. They are best determined using laboratory measurements on water and sediments obtained from the site and not derived from the literature on other sites. The data collected during this study will be used as input parameters to RDX fate and transport models in the groundwater risk assessment study. The planned IR will evaluate the impacts of the RDX inventory transport on the regional aquifer. The results will inform the site conceptual model (HGCM; see Attachment 3) and provide transport parameters for RDX and its degradation products at TA-16.

Attachment 5: Biostimulation and Microbial Community Profiling Reveal Insights on RDX Transformation in Groundwater

The objective of this study is to assess the potential for RDX natural biodegradation in groundwater at TA-16. This report summarizes (1) the characterization of the microbiome in the perched-intermediate zone and the regional aquifers and (2) the response of the microbial population to biostimulation under varying geochemical conditions. Microbial activity can accelerate the biodegradation of RDX and has been documented to be an important control on the spread of RDX contamination. However, the ability of microbes to degrade RDX is tied to the specific biogeochemical conditions of the site and the ability of the native microbes to utilize RDX as a food source. The data collected from this work indicate that the microbial populations in the perched-intermediate and the regional aquifer are very diverse and contain microbes from genera known to degrade RDX. The study also presents biostimulation studies that establish the conditions that are conducive to RDX biodegradation. The data from this study improve our understanding of the biogeochemical conditions in the perched-intermediate zone and the regional aquifers, and the potential of biostimulation as a remedial alternative, and will feed into the IR. The data will be used to evaluate potential corrective actions for RDX in groundwater, if a CME is required.

Attachment 6: Characterization of the Microbial Population and RDX Degradation in Groundwater at Technical Area 16

The objective of this study is to evaluate (1) the microbiome in the alluvial groundwater and the perched-intermediate and the regional aquifers at TA-16 and (2) the parameters that control RDX degradation in groundwater. The study revealed a diverse microbial population at all locations tested and identified microbes that may potentially degrade RDX under appropriate redox conditions. Environmental parameters controlling RDX degradation in TA-16 groundwater were also evaluated. Data from this study provide insight on RDX biodegradation in groundwater at TA-16 and will be used during the evaluation of the fate and transport of RDX from the alluvial groundwater to deeper perched-intermediate and regional aquifer groundwater in the groundwater risk assessment for the IR.

Attachment 7: RDX Degradation in Sediments Treated Both Chemically and with Biostimulant Amendments

The objective of this study is to evaluate the potential of chemical and biological treatment technologies that could be used to stimulate RDX degradation under TA-16 site-specific conditions. The report summarizes the results of exploratory laboratory experiments conducted in batch and column modes to characterize the rate of RDX degradation under conditions representative of the TA-16 site. Experiments were conducted to explore the feasibility of utilizing chemical additives (sodium dithionite, potassium permanganate, and/or carbonate/bicarbonate), and biostimulants (using molasses and safflower oil) as possible in situ treatment technologies. These data will be useful as initial screening options during consideration of potential treatment technologies, should corrective action be required.

Attachment 8: Hydrogeology and Model Calibration for Contaminant Fate and Transport at Technical Area 16

The objective of this report is to summarize the groundwater flow and transport models developed to evaluate fate and transport of RDX. This attachment presents a calibrated three-dimensional (3-D) VZ/saturated zone (SZ) model that incorporates the results of the recent geologic characterization discussed in Attachment 2 and the updated geologic framework model. This model may be used for the groundwater risk assessment to simulate the transport of the RDX subsurface inventory (Attachment 1) to the regional aquifer. An analytical 3-D VZ/SZ “pipe-and-disk” model is also presented, along with preliminary results from this model. Other modeling capabilities that could be used to evaluate potential corrective action alternatives are also discussed. In addition, this report presents a discussion of a novel machine-learning data analysis technique to explore mixing scenarios for various groundwater source types. This technique was used to assess possible sources for RDX in perched intermediate groundwater and the regional aquifer.

Attachment 9: 2017 Status Report: Tracer Tests at Consolidated Unit 16-021(c)-99, Technical Area 16

The overarching objective for the tracer tests being conducted at TA-16 is to test the hydraulic connectivity of the various hydrogeologic strata at TA-16. The tracer test results provide an improved understanding of (1) local hydraulic gradients and groundwater velocities/fluxes within the perched-intermediate zone; (2) lateral advective travel times and associated hydrologic parameters within the Otowi Member of the Bandelier Tuff Formation and the Puye Formation; and (3) vertical advective travel times between perched zones and the regional aquifer (LANL 2012, 210352; NMED 2012, 210098). This report updates and summarizes the monitoring results of these tracer tests, initiated in November 2015, through December 2017. The tracer test results will feed into the groundwater IR, and should help to improve our conceptual model for contaminant transport between zones.

2.0 KEY FINDINGS FROM EACH COMPENDIUM STUDY

This section summarizes key findings from each of the compendium reports presented in Attachments 1 through 9, highlighting the results of recent studies on the hydrology, geology, and geochemistry that were conducted to support the deep groundwater investigation of RDX at TA-16.

2.1 Attachment 1: 2017 Update of the RDX Inventory Report

There are limited data on the amounts of contaminated discharge released from the 260 Outfall into Cañon de Valle between 1950 and 1996, when the outfall was decommissioned. Furthermore, the relative composition of the HE used at the facility varied over time (particularly with regard to relative percent of RDX, HMX, and TNT in the effluent), adding additional uncertainty to the assessment of the contaminant inventory in the subsurface. The subsurface environment (e.g., geologic structure and composition, fluid flow pathways, and hydrologic and hydrochemical fluid properties of natural and contaminated groundwater) is highly heterogeneous and complex, which is not conducive to deterministic estimates for the mass of RDX present in the subsurface.

In 2005, a preliminary assessment of the subsurface inventory of RDX in the vicinity of Cañon de Valle (Gard and Newman 2005, 093651) estimated the mass of RDX from RDX concentrations in seven subsurface zones. Based on this study, the total estimated mass of RDX in the underlying VZ and groundwater ranged from 1520 to 23,334 kg, with approximately 40% to 61% of the inventory located in deep perched-intermediate and regional groundwater.

Considerable additional characterization has been conducted since 2005, with new monitoring wells completed in perched-intermediate and regional aquifers. These new monitoring wells provided the current spatial distribution of RDX in groundwater at TA-16 and in perched zones encountered during drilling.

In addition, the surface corrective measures implementation activities conducted at the 260 Outfall in 2009 and 2010 (LANL 2010, 108868) removed an estimated 6 kg of RDX from the holding pond area and likely immobilized a significant mass of RDX in the subsurface through injection grouting of the underlying surge bed. However, the mass of immobilized RDX was not estimated in this study.

In 2016 and 2017, the estimated RDX inventory in the subsurface was reevaluated based on RDX concentrations measured in groundwater samples from monitoring wells and borehole screening data, including data from new wells completed in perched-intermediate zones and in the regional aquifer. Attachment 1 presents these results for the contaminant source inventory. The updated evaluation estimates mass of RDX in the subsurface ranges from 1533 to 3608 kg, with approximately 19% to 52% of the inventory in deep perched and regional groundwater.

The revised estimates of the RDX inventory in the subsurface environment indicate the following.

- The total mass of RDX in the subsurface environment is approximately 85% less than originally estimated in the 2005 study.
- Most of the RDX in groundwater resides within the deep perched-intermediate zone.
- The updated inventory assessment indicates there is less RDX in the perched-intermediate and regional aquifer groundwater than originally estimated in 2005.

Overall, the updated reevaluation of the RDX mass represents a substantial improvement in our understanding of the RDX contaminant distribution within the subsurface environment and is consistent with the site conceptual model, as well as our model predictions on the transport of RDX from surface and near-surface sources to deeper aquifers. The lower mass of RDX in the updated inventory assessment reflects a better constrained data set to develop inventory estimates, with more wells providing RDX data from the perched-intermediate zones and the regional aquifer, as well as RDX data derived from screening samples collected in the VZ during drilling. This significantly improved data set has resulted in a more accurate estimate of the RDX mass distribution in the VZ and the groundwater system.

2.2 Attachment 2: Geology of Technical Area 16 and Vicinity, Los Alamos National Laboratory

Attachment 2 summarizes the regional geologic setting of the RDX investigation area and provides descriptions of the stratigraphic units and structural features that make up the site. Major uncertainties in the site conceptual model for TA-16 include recharge pathways for HE-contaminated groundwater through the VZ and the areal extent of deep perched groundwater near Cañon de Valle, which is present in both the Otowi Member of the Bandelier Tuff and in the Puye Formation. Because bedding features have the potential to influence groundwater pathways and flow directions, this work addresses uncertainties in the site geologic model by documenting the dips of geologic contacts and internal bedding features for rocks that make up the VZ. New data and interpretations presented in this report augment the sitewide geologic model that is currently used to assess hydrogeologic site conditions. Stratigraphic and structural data presented in this report provide a geologic framework for developing site conceptual models and are critical information for planning groundwater remediation strategies.

Stratigraphic contacts were examined and updated using multiple lines of evidence, including binocular microscope examination of borehole cuttings, lithologic examinations of cores, chemical fingerprinting of pumices, and analysis of geophysical logs. Updated contacts were used to make cross-well correlations, to generate structure contour maps showing the bedding orientations and dips of units, and to locate and measure displacements of faults. Internal bedding and orientation features observed within the Otowi Member were correlated between wells.

Infiltration pathways in the upper VZ are dominated by strongly welded ash-flow tuffs of Tshirege units Qbt 3 and Qbt 2. Because these tuffs are characterized by low porosity and low permeability, groundwater accumulation and movement are probably controlled by a combination of horizontal fracture flow along partings and porous flow in sandy pyroclastic surge deposits. Bedding orientations suggest groundwater flow may be diverted towards the east and southeast. Vertical pathways through the tuffs probably occur where horizontal flows intersect abundant fractures and faults.

Tshirege units Qbt 1v and Qbt 1g, Cerro Toledo Formation, Otowi Member, and Guaje Pumice Bed are highly porous and variably stratified deposits. Vertical, gravity-driven moisture flow through these rocks is likely to be diverted laterally at bedding contacts, particularly in the Cerro Toledo Formation, lower part of the Otowi Member, and Guaje Pumice Bed. Bedding orientations favor diversion of moisture flow towards the east and southeast in these units. Flow directions for perched groundwater in the lower Otowi Member are likely to be towards the southeast based on the orientation of potential perching horizons. These gradients support the interpretations for flow directions inferred from the water table map for the upper deep perched zone. Although fractures are less common than in the overlying welded tuffs, they may provide vertical pathways through saturated portions of the lower Otowi Member.

2.3 Attachment 3: A Refined Hydrogeochemical Conceptual Model for the RDX Project

Attachment 3 presents a series of analyses that update the HGCM of the area. The analyses presented in this attachment provide valuable insight into the relative importance of three primary recharge mechanisms that control infiltration along the Pajarito Plateau and profoundly influence contaminant concentrations in the deeper perched-intermediate and regional aquifers. These infiltration mechanisms include (1) MBR, which consists of diffuse subsurface recharge over the mountain block that percolates through the rock and flows laterally as groundwater into the basin, (2) mountain-front recharge (MFR), which consists of mountain overland flow that infiltrates at the mountain front, and (3) in the context of the TA-16 area, recharge that occurs downstream of perennial springs in Cañon de Valle and the 260 Outfall at TA-16 (Figure 1.0-3). MBR is the principal uncontaminated deep groundwater source for the perched-intermediate and regional aquifers. The local recharge is modified by HE and postfire contaminants from the TA-16 area and diluted by perennial springs, snowmelt runoff and episodic flooding in the Cañon de Valle. At TA-16 this local recharge is the principal source of alluvial aquifers and to a lesser extent, the perched-intermediate groundwaters, and more rarely, the top of the regional aquifer. The relative contributions of recharge sources are discussed in more detail in the summaries of sections 3.0 and 6.0 below.

Section 1.0 presents a statistical analysis of aqueous elemental and stable isotope chemistry data from six SZs, including surface water, alluvial groundwater, springs, deep upper and lower perched-intermediate zones, and the regional aquifer. The statistical characterization of the geochemistry of these hydrologic zones suggests that a combination of water-rock interactions along different flow pathways and recharge sources from provenances outside the site area contribute to the evolution of the hydrologically distinct zones at TA-16. Using the factor analysis results, specific analytes were used to test for statistically significant differences between zones.

The results show that the groundwater zones, spatially recognized as part of the TA-16 conceptual model for many years, are also geochemically distinct. These zones include the regional aquifer, the upper and lower perched-intermediate zones, several springs, and the alluvial aquifer. Differences in the geochemistry of these zones reflect rock-water interactions along flow paths through different lithologic units as well as contaminant contributions from some pathways. Lithium and chloride were found to be very good indicators of long, deep flow paths where statistically significant differences were found between the regional and perched-intermediate zones and shallower zones.

Section 2.0 discusses concentration-discharge relationships for springs and streams from the TA-16 area that exhibit strongly correlated temporal variations between discharge and dissolved species in the near-surface hydrologic system. These are associated with seasonal storms, snowmelt, flooding events and drought. Though RDX from TA-16 springs and stream water exhibits a chemostatic behavior that could result in higher contaminant residence times in the subsurface, this contaminant is also a redox-sensitive species prone to (1) dilution and transport in periods of increased runoff and flooding from seasonal storms and snowmelt and (2) photodegradation at the surface during periods of drought.

Section 3.0 is a water balance analysis from historical data derived from Cañon de Valle springs and stream-gauging measurements along upper and lower Cañon de Valle. In terms of the water balance, three recharge mechanisms are typically recognized: (1) MBR, or pristine, uncontaminated recharge over the mountain block that percolates vertically and laterally through the rock and flows into deeper perched-intermediate and regional aquifers, (2) MFR, which consists of mountain overland flow (generally streamflow) that infiltrates at the mountain front, and (3) local TA-16 recharge that includes perennial spring discharges, outfalls, snowmelt, and episodic flooding.

The data support the concept that subvertical fracture zones observed in Cañon de Valle are likely a significant source of local and MFR from the surface to the perched-intermediate and regional groundwater. Snowmelt appears to be a significant source of MFR, and the fracture pathways are an important component of the watershed flow system, with major implications for the transport of RDX to intermediate and regional aquifers.

Spring groundwater, shallow bedrock mesa saturation, perched-intermediate zones, and the deeper regional aquifer are largely recharged by infiltration from the mountain block, including surface water in the upper Cañon de Valle. MFR infiltration occurs in part at the canyon bottom via fault zone fractures, and is subsequently diverted laterally at different depths along high-permeability horizons (e.g., partings and surge beds). Downstream of the Pajarito Fault system, local recharge occurs episodically into the alluvial aquifer system at TA-16. Conversely, surface water from higher elevations upstream of TA-16 percolates deeper in the subsurface as MBR to the lower perched-intermediate and regional aquifers.

Section 4.0 is on isotope hydrology, and establishes the connection between the six water-saturated components of the TA-16 hydrologic system presented above. Shallow zones (i.e., surface water, springs and the alluvial aquifer) are hydrologically connected and respond to seasonal variations in local recharge, MFR, and MBR via surface flow and infiltration. As evidenced by young, contaminated recharge to the regional aquifer, the impact of stream flow on the perched-intermediate zone and regional aquifers is localized and limited to the perennial reach of Cañon de Valle. Recharge to deeper aquifers occurs from two sources, intermittent and continuous. The intermittent source is from MFR caused by large episodic flooding events, via subvertical fracture/fault zones that crop out at the canyon bottom of Cañon de Valle and serve as fast pathways to deeper aquifers. The deeper continuous source is due to MBR to the deeper perched-intermediate and regional aquifers.

Section 5.0 documents how large postfire and snowmelt flooding events produce traceable changes in the calcium concentrations (Ca) and alkalinity ($CaCO_3$) of infiltrating waters. Snowmelt signatures affect the shallower groundwater system, whereas postfire signatures are found in shallow and deep wells. The presence of increased Ca in the deepest regional well (R-25, screen 4) demonstrates the existence of a very fast pathway (3-mo travel time) between Cañon de Valle bottom surface and the regional aquifer associated with localized subvertical fracture networks or the Pajarito fault zone.

Section 6.0 estimates from mixing models indicate that regardless of the geochemical composition or contaminant concentrations of the local recharge endmember, MBR is a major component in both the perched-intermediate (>40%) and regional (>90%) aquifers. Findings of high proportions of uncontaminated MBR have favorable implications for the long-term fate of RDX, particularly in the regional aquifer. The high proportions of MBR in the perched-intermediate zone will help buffer concentrations over time, and the very high proportions in the regional system will help moderate concentrations both vertically and laterally.

2.4 Attachment 4: Fate and Transport of Hexahydro-1,3,5-trinitro-1,3,5-triazine (RDX) and its Degradation Products in Sedimentary and Volcanic Rocks, Los Alamos New Mexico

In order to better understand the physiochemical interactions that dictate the transport of RDX and its degradation products in perched-intermediate groundwater at TA-16, experimental batch and column tests on RDX and its degradation products were carried out using oxic groundwater compositions representative of the perched-intermediate zone. The tests were conducted on rocks and minerals from the Bandelier Tuff and the Puye Formation. Within laboratory experimental times of 2–7 d, the volcanic and sedimentary lithologies that represent the contaminated VZ in the vicinity of TA-16 show no capacity to delay RDX or its derivatives' transport, and no substantial abiotic degradation of RDX was observed.

2.5 Attachment 5: Biostimulation and Microbial Community Profiling Reveal Insights on RDX Transformation in Groundwater

In spite of a nonreducing subsurface environment characterized by the presence of nitrate anions (NO_3^-), sulfate (SO_4^{2-}), dissolved oxygen, and a paucity of soluble nutrients, the bacterial diversity measured in groundwater samples from the TA-16 perched-intermediate aquifer is significant. Experimental biostimulation results presented in Attachment 5 suggest that bio-engineered remediation of subsurface contaminants at TA-16 may be feasible if the natural physiochemical environment can be modified to induce anoxic environments that are more favorable for RDX degradation. Introduction of a carbon source can transform the geochemical conditions in the subsurface to strict anaerobic aquifer conditions maintained by well injection and biostimulation.

2.6 Attachment 6: Characterization of the Microbial Population and RDX Degradation in Groundwater at Technical Area 16

A microbial survey of different aquifers at TA-16 presented in Attachment 6 confirms that a very diverse microbial population exists in all groundwater zones tested, including dominant strains of *Proteobacteria*, *Bacteroidetes* and *Actinobacteria*. Though the survey does not identify specific microorganisms that can be directly linked to RDX degradation in any of the aquifers, it reveals the presence of *Rhodococcus* and *Pseudomonas* in the perched-intermediate zone associated with the highest RDX concentrations. This suggests that these species may have been enriched by the contamination. The microbial diversity survey results are consistent with monitoring-well observations that indicate the shallow alluvial aquifers are likely to support intermittent biodegradation activity during transitions from aerobic to anaerobic conditions associated with recurring postfire and snowmelt flooding events. High ratios of MNX (hexahydro-1-nitroso-3,5-dinitro-1,3,5-triazine), DNX (hexahydro-1,3-dinitro-5-nitro-1,3,5-triazine), and TNX (2,4,6-trinitroxylene) to RDX observed in shallow aquifers support the hypothesis of intermittent RDX biodegradation in shallow aquifers. Conversely, the deeper perched-intermediate and regional aquifers represent stable oxic environments, so RDX biodegradation is unlikely even though a diverse population of microbes is present. We conclude that the detection of RDX degradation products MNX, DNX, and TNX in the deeper aquifers is due to the transport of these compounds from shallower groundwater zones and not to in situ biodegradation.

2.7 Attachment 7: RDX Degradation in Sediments Treated Both Chemically and with Biostimulant Amendments

Exploratory experiments designed to assess the rate of degradation of RDX contamination in sediments treated by chemical and biostimulant amendments under simulated TA-16 site-specific conditions offer qualitative insights on the feasibility of subsurface remediation. Treatment of sediments using chemical additives that produce either reducing, oxidizing, or alkaline conditions resulted in effective degradation of RDX with degradation rates varying from 0.02 to 0.54 h^{-1}. Sediments treated by sodium dithionate to induce strong reducing conditions had the fastest RDX degradation rates, and the alkaline treatment had the slowest degradation rate. In column testing, sodium dithionate was the only treatment that effectively removed RDX from solution. However, the alkaline treatment might also be very effective if sufficient residence time is allowed and should be investigated further. Biostimulation tests using both molasses and safflower oil in sediments from the Puye Formation revealed that both biostimulants could be effective at creating conditions favorable for RDX degradation in column flow tests because of the establishment of strictly anaerobic conditions. However, biostimulation requires a more rigorous control to limit and manage biofouling.

2.8 Attachment 8: Hydrogeology and Model Calibration for Contaminant Fate and Transport at Technical Area 16

The observations from laboratory and field tests described in the previous amendments are important to the design of RDX field contaminant mitigation protocols. Should corrective actions be required, the efficiency of any treatment options is dependent on local hydrologic and geochemical heterogeneity and the homogeneity of amendment distribution in the subsurface. Ongoing field tests and hydrologic modeling help better understand the complex geochemical and hydrogeologic mechanisms that operate in the subsurface at TA-16.

A 3-D flow and transport model of the VZ and upper SZs in the vicinity of the Cañon de Valle area is being developed as a platform for the integration of site information and models developed over the past several years. The model allows quantitative predictions of the fate and transport of RDX at TA-16. It honors the key hydrologic, geochemical, and transport data collected at the site and is used to predict transport rates, concentrations, and the long-term mass flux of RDX to the regional aquifer beneath the contaminated source. Ultimately, this model is critical to a system model that simulates the behavior of future RDX migration in the regional aquifer and is the basis for uncertainty quantification of key model parameters. For example, (1) RDX concentrations at hypothetical compliance locations downstream of TA-16, (2) HE concentration attenuation rates as a result of dispersion, and (3) the dissipation of finite VZ contaminant sources can all be derived from these models.

Attachment 8 also presents (1) a new computationally efficient, analytical three dimensional VZ/SZ “pipe-and-disk” model, used to assess multiple contaminant transport scenarios from surface sources to deeper aquifers; and (2) results from a blind source separation machine-learning data analysis that identifies and explores mixing scenarios for various groundwater source types using saturated zone chemistries. From this work, the chemistry, flow pathways, and evolution of RDX subsurface contaminant sources in the regional aquifer can be evaluated and potentially used to refine remediation corrective actions.

2.9 Attachment 9: 2017 Status Report: Tracer Tests at Consolidated Unit 16-021(c)-99, Technical Area 16

This report provides information on tracer monitoring in perched-intermediate and regional groundwaters in the vicinity of TA-16 at Los Alamos National Laboratory. Results from a series of large scale, multiyear tracer tests are presented based on (1) a previous 2017 status report that describes the deployment details and monitoring results through September 2016 (LANL 2017, 602161) and (2) new monitoring results through December 2017. The primary objective of the TA-16 tracer study is to test the connectivity between various parts of the TA-16 hydrological system and how it might affect HE transport. The study also supports potential evaluation activities related to remedial alternatives for HE-contaminated groundwater. Implementation of the tracer study is based on a work plan approved by NMED (LANL 2015, 600535).

Large-scale tracer deployments in wells R-25b, CdV-9-1(i) (i.e., with screen 1, piezometer 1, and piezometer 2), and CdV-16-1(i) were initiated in November 2015. Tracers were monitored in these wells on a quarterly basis through December 2017 and in perched-intermediate wells CdV-16-2(i)r, CdV-16-4ip, and R-47i and regional aquifer wells R-18, R-25, R-47, R-48, R-58, and R-63. This report also includes results from pump tests and some high water-level events during which higher frequency sampling was used.

Overall, the large tracer tests from all three deployment wells show clear dilution effects. In addition, differences in tracer concentrations between wells suggest that (1) the groundwater flow velocity in well R-25b, with the highest concentrations, is very low and (2) the flow velocity in well CdV-9-1(i) is higher than the velocity in well CdV-16-1(i).

Pump tests in CdV-9-1(i) and CdV-16-1(i) affected the tracer concentrations in the vicinity of these wells, removing some of the mass from the groundwater. Mass removal is minor in CdV-9-1(i) and restricted to bromide and the tracers introduced into the piezometers. Conversely, mass removal of the original tracer mass during the aquifer test in well CdV-16-1(i) is substantially higher (i.e., 29%). More importantly, tracers from both CdV-9-1(i) piezometers have been detected in screen 1, proving the existence of vertical flow path connections.

Since the last status report (LANL 2017, 602161), substantial pulses of both the piezometer tracers in CdV-9-1(i) were observed in screen 1 during the spring of 2017. By August 2017, the pulses had dissipated for both tracers. These pulses appear to be related to substantial increases in water levels observed in CdV-9-1(i) during this period. As noted in in the last status report (LANL 2017,602161), it is unclear whether these detections represent naturally occurring flow conditions or if they are the result of short-circuiting along the well bore or in the adjacent damaged zone (from drilling). Despite ambiguity about the nature of the vertical flow path connections at CdV-9-1(i), the spring 2017 pulses demonstrate the importance of seasonally transient recharge conditions at TA-16. This is also consistent with isotopic and aqueous geochemistry data presented in the updated HGCM, which suggest that MFR from the canyon bottom occurs in part via subvertical fracture pathways (see section 2.3 above). The CdV-9-1(i) screen 1 and CdV-16-1(i) tracers have moved beyond the vicinity of the deployment screens, which indicates that although no credible observations have been made to date, cross-well detections may occur in the future. Continued long-term tracer breakthrough monitoring is recommended to realize the full benefits of the TA-16 tracer study. Specifically the groundwater monitoring activities at TA-16 are needed to elucidate the connection between contaminant pathways and seasonally variable MFR.

3.0 CONCLUSIONS

The RDX technical reports and modeling activities conducted over the last several years and summarized in this compendium will feed into the deep groundwater IR which is currently proposed for submittal to NMED in March 2019 (the 2016 Compliance Order on Consent, or, the Consent Order). Together, the reports presented in this document help reduce uncertainty in key components of the site conceptual model, including the following:

- The estimated RDX mass remaining in the subsurface below and in the vicinity of the 260 Outfall and downgradient of the outfall in Cañon de Valle (Attachment 1).
- The refined site geologic model (Attachment 2) with additional data on geologic features that influence groundwater pathways and flow directions. New data on the location and distribution of fractures, depositional structures, stratigraphic contacts, and bedding orientations have been collected and used to update stratigraphic contacts and geologic cross-sections. The updated contacts have been incorporated in a 3-D variably saturated flow and transport model.

- The updated HGCM (Attachment 3) that includes results from new studies presented in the attachments from this report. Findings include estimates for (1) the percentage of MBR in perched-intermediate and the upper part of the regional aquifer and (2) the dilution effects from MBR that influence all contaminant concentrations in perched-intermediate and regional groundwaters and mitigate RDX concentrations via dilution. The effects of HE perched-intermediate groundwater contamination by episodic local flooding events in the Cañon de Valle are also discussed.
- Laboratory batch and column studies that provide retardation factors and equilibrium partitioning coefficients (Kd) for RDX in the subsurface environment at TA-16 (Attachment 4). These studies confirm that the underlying lithologies have little to no capacity to delay RDX under the aerobic conditions typical of the subsurface environment.
- The presence and diversity of biosomes in groundwater samples from the TA-16 perched-intermediate zone suggest that under strict anaerobic conditions, RDX can be degraded (Attachment 5). Given these findings, in situ bioremediation of RDX in groundwater may be a potentially feasible alternative, should corrective action be required.
- Microbial surveys of perched-intermediate and regional groundwater at TA-16 that document diverse microbial populations in all wells tested (Attachment 6). High ratios of MNX/RDX, DNX/RDX, and TNX/RDX observed in shallow groundwater further support the hypothesis that intermittent RDX biodegradation occurs in shallow groundwater. Conversely, the deeper perched-intermediate and regional aquifers are stable oxic environments where RDX biodegradation is unlikely, even though a diverse population of microbes is present. In terms of pathways, the detection of RDX degradation products MNX, DNX, and TNX in the deeper aquifers may be because of the transport of these compounds from shallow groundwater rather than from in situ biodegradation in deep groundwater.
- Laboratory batch and column studies that demonstrate that RDX can be chemically degraded by sodium dithionite or alkaline hydrolysis (Attachment 7). Unlike biostimulation, chemical amendments can potentially reduce in situ RDX concentrations in groundwater without frequent amendments to sustain RDX degradation.

The data collected from these studies, including the updated geologic surfaces and structures, the relative quantification of MBR, MFR and local recharge sources, and the geochemical retardation factors and equilibrium partitioning coefficients for RDX, were used to build a calibrated 3-D VZ/SZ model that accurately reproduces observed site data (contaminant concentrations, hydraulic heads), and incorporates the geometries of perched zones within the VZ at TA-16. Although preliminary, the model captures the significant heterogeneity of the TA-16 site, along with the transient initial conditions and boundary conditions that simulate the hydrologic environment in deep perched groundwaters (Attachment 8). This calibrated model may be used to assess the potential impacts of the RDX inventory on the regional aquifer and simulate potential corrective action scenarios.

These compendium studies complement the recently completed or ongoing characterization activities being conducted in support of the RDX remediation campaign (Attachment 9), most of which have been summarized in deliverables to NMED. These include the cross-borehole aquifer testing conducted in 2016 (LANL 2017, 602288), the initial tracer deployment and quarterly tracer breakthrough sampling (LANL 2017, 602161), the deep groundwater investigation activities to assess the nature and extent of contamination in the regional aquifer, including the installation of regional monitoring well R-68 (LANL 2017, 602539), and the planned installation of R-69 (LANL 2017, 602646). All of these activities address uncertainties in the HGCM at TA-16, and the original NMED request to conduct additional characterization to evaluate the feasibility of potential corrective actions in a deep groundwater CME and to assess the nature and extent of contamination in perched-intermediate groundwater and in the regional aquifer (NMED 2008, 101311).

Data from these studies will feed into the deep groundwater IR, proposed for submittal to NMED in March 2019. The IR will summarize the updated hydrogeologic conceptual model, and will address the remaining data gaps identified by the NMED in the NOD related to the deep groundwater CME (NMED 2008, 101311). The IR will also address the more recently identified data gaps identified in the GIWP (LANL 2016, 601779) and the "Summary Report for R-68 and Drilling Work Plan for R-69, Revision 1" (LANL 2017, 602646).

The IR will include a groundwater risk assessment to help define the path forward for the RDX remediation campaign. Should the risk assessment results indicate that corrective actions may be necessary to mitigate the potential impacts of RDX to the regional aquifer, the data from these compendium studies and the groundwater flow and transport models developed could be used for identifying and assessing potential corrective actions to mitigate RDX in the subsurface environment.

4.0 REFERENCES AND MAP DATA SOURCES

4.1 References

The following reference list includes documents cited in this report. Parenthetical information following each reference provides the author(s), publication date, and ERID or ESHID. This information is also included in text citations. ERIDs were assigned by the Associate Directorate for Environmental Management's (ADEM's) Records Processing Facility (IDs through 599999), and ESHIDs are assigned by the Environment, Safety, and Health Directorate (IDs 600000 and above). IDs are used to locate documents in the Laboratory's Electronic Document Management System and in the Master Reference Set. The NMED Hazardous Waste Bureau and ADEM maintain copies of the Master Reference Set. The set ensures that the NMED has the references to review documents. The set is updated when new references are cited in documents.

Gard, M.O., and B.D. Newman, November 2005. "The High Explosives Source Term at TA-16," Los Alamos National Laboratory document LA-UR-05-9433, Los Alamos, New Mexico. (Gard and Newman 2005, 093651)

LANL (Los Alamos National Laboratory), November 2003. "Corrective Measures Study Report for Solid Waste Management Unit 16-021(c)-99," Los Alamos National Laboratory document LA-UR-03-7627, Los Alamos, New Mexico. (LANL 2003, 085531)

LANL (Los Alamos National Laboratory), August 2007. "Corrective Measures Evaluation Report, Intermediate and Regional Groundwater, Consolidated Unit 16-021(c)-99," Los Alamos National Laboratory document LA-UR-07-5426, Los Alamos, New Mexico. (LANL 2007, 098734)

LANL (Los Alamos National Laboratory), June 2008. "Supplemental Investigation Work Plan for Intermediate and Regional Groundwater at Consolidated Unit 16-021(c)-99," Los Alamos National Laboratory document LA-UR-08-3991, Los Alamos, New Mexico. (LANL 2008, 103165)

LANL (Los Alamos National Laboratory), March 2010. "Summary Report for the Corrective Measures Implementation at Consolidated Unit 16-021(c)-99," Los Alamos National Laboratory document LA-UR-10-0947, Los Alamos, New Mexico. (LANL 2010, 108868)

LANL (Los Alamos National Laboratory), January 2012. "Work Plan for a Tracer Test at Consolidated Unit 16-021(c)-99, Technical Area 16," Los Alamos National Laboratory document LA-UR-12-0440, Los Alamos, New Mexico. (LANL 2012, 210352)

LANL (Los Alamos National Laboratory), March 2012. “Technical Area 16 Well Network Evaluation and Recommendations,” Los Alamos National Laboratory document LA-UR-12-1082, Los Alamos, New Mexico. (LANL 2012, 213573)

LANL (Los Alamos National Laboratory), July 2014. “Geophysical Investigation of Cañon de Valle,” Los Alamos National Laboratory document LA-UR-14-25096, Los Alamos, New Mexico. (LANL 2014, 259157)

LANL (Los Alamos National Laboratory), July 2015. “Work Plan for a Tracer Test at Consolidated Unit 16-021(c)-99, Technical Area 16, Revision 1,” Los Alamos National Laboratory document LA-UR-15-24089, Los Alamos, New Mexico. (LANL 2015, 600535)

LANL (Los Alamos National Laboratory), August 2015. “Work Plan for Intermediate Groundwater System Characterization at Consolidated Unit 16-021(c)-99,” Los Alamos National Laboratory document LA-UR-15-24545, Los Alamos, New Mexico. (LANL 2015, 600686)

LANL (Los Alamos National Laboratory), September 2016. “Groundwater Investigation Work Plan for Consolidated Unit 16-021(c)-99, Including Drilling Work Plans for Wells R-68 and R-69,” Los Alamos National Laboratory document LA-UR-16-26493, Los Alamos, New Mexico. (LANL 2016, 601779)

LANL (Los Alamos National Laboratory), February 2017. “Status Report for the Tracer Tests at Consolidated Unit 16-021(c)-99, Technical Area 16,” Los Alamos National Laboratory document LA-UR-17-20782, Los Alamos, New Mexico. (LANL 2017, 602161)

LANL (Los Alamos National Laboratory), April 2017. “Summary Report for Intermediate Groundwater System Characterization Activities at Consolidated Unit 16-02l(c)-99,” Los Alamos National Laboratory document LA-UR-17-22550, Los Alamos, New Mexico. (LANL 2017, 602288)

LANL (Los Alamos National Laboratory), July 27, 2017. “Completion Report for Regional Aquifer Well R-68,” Los Alamos National Laboratory document LA-UR-17-26063, Los Alamos, New Mexico. (LANL 2017, 602539)

LANL (Los Alamos National Laboratory), September 2017. “Summary Report for R-68 and Drilling Work Plan for R-69, Revision 1,” Los Alamos National Laboratory document LA-UR-17-28551, Los Alamos, New Mexico. (LANL 2017, 602646)

NMED (New Mexico Environment Department), April 22, 2008. “Notice of Disapproval Corrective Measures Evaluation Report, Intermediate and Regional Groundwater Consolidated Unit 16-021(c)-99,” New Mexico Environment Department letter to D. Gregory (DOE-LASO) and D. McInroy (LANL) from J.P. Bearzi (NMED-HWB), Santa Fe, New Mexico. (NMED 2008, 101311)

NMED (New Mexico Environment Department), February 7, 2012. “Approval with Modification, Work Plan for a Tracer Test at Consolidated Unit 16-021(c)-99, Technical Area 16,” New Mexico Environment Department letter to G.J. Rael (DOE-LASO) and M.J. Graham (LANL) from J.E. Kieling (NMED-HWB), Santa Fe, New Mexico. (NMED 2012, 210098)

NMED (New Mexico Environment Department), June 20, 2012. “Approval with Modifications, Technical Area 16 Well Network Evaluation and Recommendations,” New Mexico Environment Department letter to P. Maggiore (DOE-LASO) and M.J. Graham (LANL) from J.E. Kieling (NMED-HWB), Santa Fe, New Mexico. (NMED 2012, 520747)

4.2 Map Data Sources

Hillshade; Los Alamos National Laboratory, ER-ES, As published; \\slip\gis\Data\HYP\LiDAR\2014\Bare_Earth\BareEarth_DEM_Mosaic.gdb; 2014.

Structures; Los Alamos National Laboratory, KSL Site Support Services, Planning, Locating and Mapping Section; 06 January 2004; as published 29 November 2010.

Unpaved road;; Los Alamos National Laboratory, ER-ES, As published, GIS projects folder; \\slip\gis\GIS\Projects\14-Projects\14-0062\project_data.gdb; digitized_site_features; digitized_road; 2017.

Paved Road Arcs; Los Alamos National Laboratory, FWO Site Support Services, Planning, Locating and Mapping Section; 06 January 2004; as published 29 November 2010.

Drainage channel; Los Alamos National Laboratory, ER-ES, As published, GIS projects folder; \\slip\gis\GIS\Projects\11-Projects\11-0108\gdb\gdb_11-0108_generic.mdb; drainage; 2017.

Approximate extent of RDX contamination in deep perched groundwater, based on current knowledge; Los Alamos National Laboratory, ER-ES, As published, GIS projects folder; \\slip\gis\GIS\Projects\15-Projects\15-0041\shp\perched_aquifer.shp; 2016.

Approximate extent of deep perched groundwater, based on current knowledgePerched intermediate groundwater elevation contour, 100-ft interval.

Primary Electric Grid; Los Alamos National Laboratory, KSL Site Support Services, Planning, Locating and Mapping Section; 06 January 2004; as published 29 November 2010.

Perched intermediate groundwater elevation contour, 100-ft interval; Los Alamos National Laboratory, ER-ES, As published, GIS projects folder; \\slip\gis\GIS\Projects\15-Projects\15-0041\shp\sketch_contour.shp; 2016.

May 2017 groundwater elevation, 50-ft contours; Los Alamos National Laboratory, ER-ES, As published, GIS projects folder; \\slip\gis\GIS\Projects\16-Projects\16-0027\project_data.gdb\contour_wl2017may_2ft; 2017.

wqh_npdes_outfalls_pnt; WQH NPDES Outfalls; Los Alamos National Laboratory, ENV Water Quality and Hydrology Group; Edition 2002.01; 01 September 2003.

5.0 LIST OF CONTRIBUTORS

Main Text:

Gilles Bussod (EES-14), Tim Goering (ADEM), Danny Katzman (ADEM)

Maps and GIS Support:

Dave Frank (ADEM)

Attachment 1: 2017 Update of the RDX Inventory Report

Brendan Brady (ADEM), Brent Newman (EES-14), Tim Goering (ADEM), Daniel Strobridge (Weston Solutions Inc.)

Attachment 2: Geology of Technical Area 16 and Vicinity, Los Alamos National Laboratory

Dave Broxton (EES-14), Elaine Jacobs (EES-14), Giday WoldeGabriel (EES-14),
Daniel Strobridge (Weston Solutions Inc.)

Attachment 3: A Refined Hydrogeochemical Conceptual Model for the RDX Project

Brent Newman (EES-14), Jace Koger (EES-14), Brendan Brady (ADEM), Allison Chan (ADEM),
Emily Schulze (ADEM), Heather Throckmorton (EES-14), Tim Goering (ADEM), Dave Frank (ADEM)

Attachment 4: Fate and Transport of Hexahydro-1,3,5-trinitro-1,3,5-triazine (RDX) and its Degradation Products in Sedimentary and Volcanic Rocks, Los Alamos New Mexico

Brent Heerspink (EES-14), Sachin Pandey (EES-14), Hakim Boukhalfa (EES-14), Doug Ware (EES-14),
Oana Marina (EES-14), George Perkins (EES-14), Velimir Vesselinov (EES-16),
Giday WoldeGabriel (EES-14)

Attachment 5: Biostimulation and Microbial Community Profiling Reveal Insights on RDX Transformation in Groundwater

Dongping Wang (EES-14), Hakim Boukhalfa (EES-14), Oana Marina (EES-14), Doug Ware (EES-14),
Tim Goering (ADEM), Fengjie Sun (School of Science and Technology, Georgia Gwinnett College),
Hajnalka Daligault (B-11), Chien-Chi Lo (B-11), Momchilo Vuyisich (B-11), Shawn Starkenburg (B-11)

Attachment 6: Characterization of the Microbial Population and RDX Degradation in Groundwater at Technical Area 16

Hakim Boukhalfa (EES-14), Dongping Wang (EES-14), Oana Marina (EES-14), Bennie Martinez (EES-14),
Tim Goering (ADEM), Zhenghua Li (EES-14), Doug Ware (EES-14), Chien-Chi Lo (B-11)

Attachment 7: RDX Degradation in Sediments Treated Both Chemically and with Biostimulant Amendments

Hakim Boukhalfa (EES-14), Brent Porter Heerspink, Dongping Wang (EES-14), Doug Ware (EES-14),
Oana Marina (EES-14), George Perkins (EES-14), Kai Williams (EES-14), David Chu (EES-14)
Giday WoldeGabriel (EES-14), Tim Goering (ADEM)

Attachment 8: Hydrogeology and Model Calibration for Contaminant Fate and Transport at Technical Area 16

Velimir Vesselinov (EES-16), Zhiming Lu (EES-16), Sachin Pandey (EES-16), Daniel O'Malley (EES-16),
Terry Miller (EES-16), Boian Alexandrov (T-1), Bruce Robinson (ADEM), Gilles Bussod (EES-14)

Attachment 9: 2017 Status Report: Tracer Tests at Consolidated Unit 16-021(c)-99, Technical Area 16

Brent Newman (EES-14), Jace Koger (EES-14), Oana Marina (EES-14), and George Perkins (EES-14)

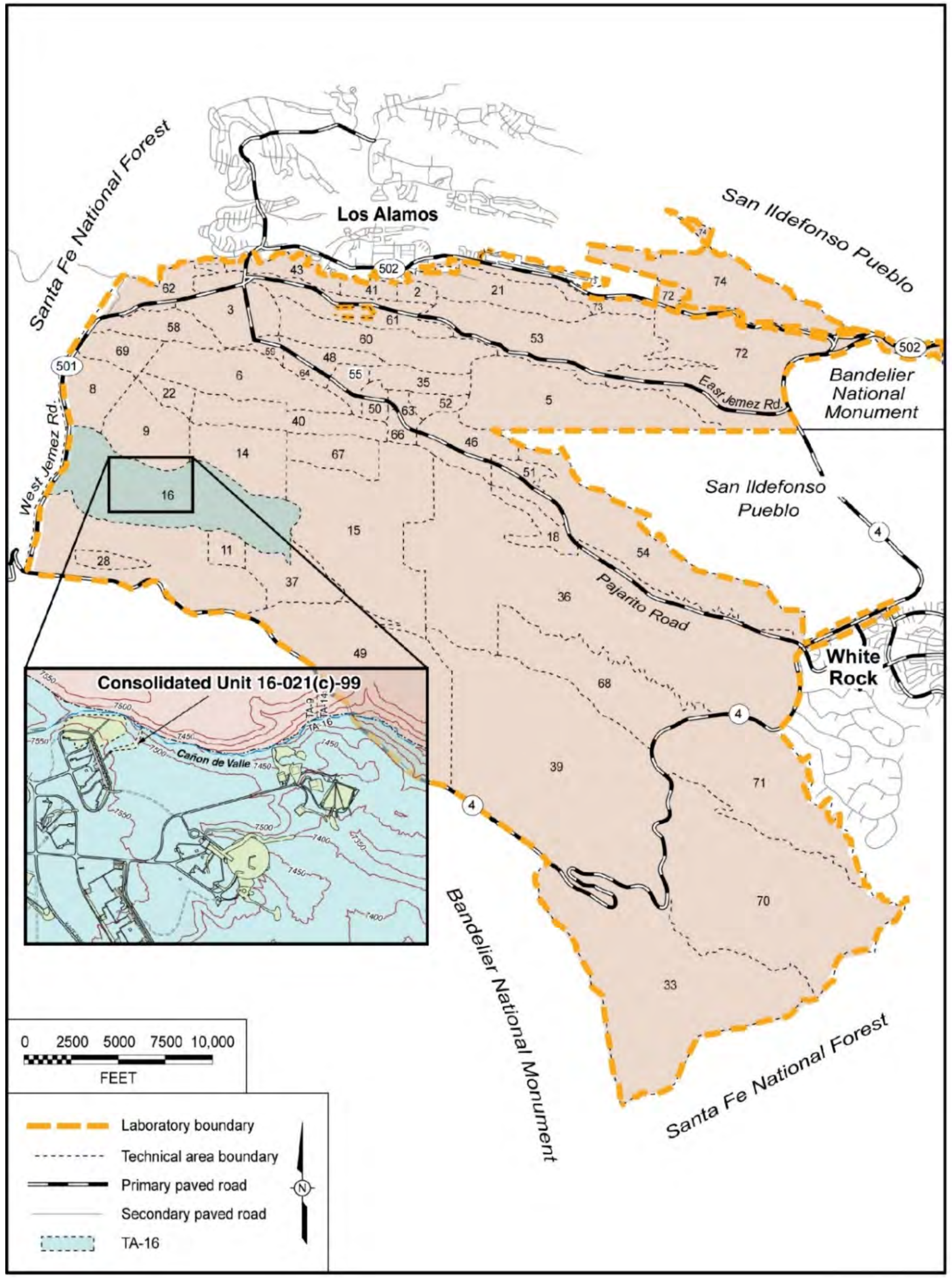

Figure 1.0-1 Location of TA-16 with respect to Laboratory TAs and surrounding landholdings

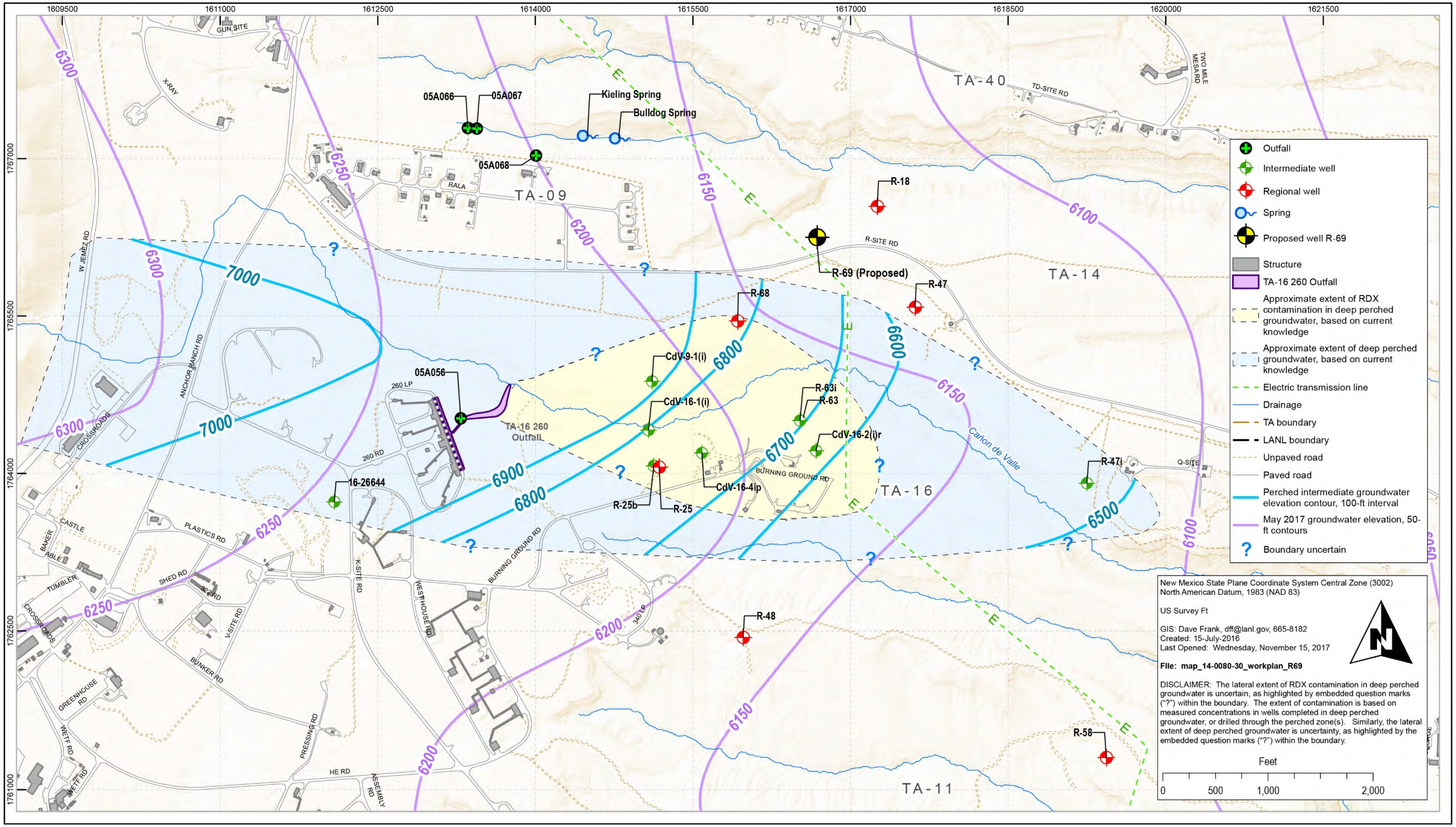

New Mexico State Plane Coordinate System Central Zone (3002)
North American Datum, 1983 (NAD 83)

US Survey Ft

GIS: Dave Frank, dff@lanl.gov, 665-8182
Created: 15-July-2016
Last Opened: Wednesday, November 15, 2017

File: map_14-0080-30_workplan_R69

DISCLAIMER: The lateral extent of RDX contamination in deep perched groundwater is uncertain, as highlighted by embedded question marks ("?") within the boundary. The extent of contamination is based on measured concentrations in wells completed in deep perched groundwater, or drilled through the perched zone(s). Similarly, the lateral extent of deep perched groundwater is uncertainty, as highlighted by the embedded question marks ("?") within the boundary.

Figure 1.0-2 Location Map of the 260 Outfall and the TA-16 study area. Deep perched-intermediate and regional monitoring well network in the vicinity of Consolidated Unit 16-021(c)-99 and water table contours for the intermediate zone and regional aquifer

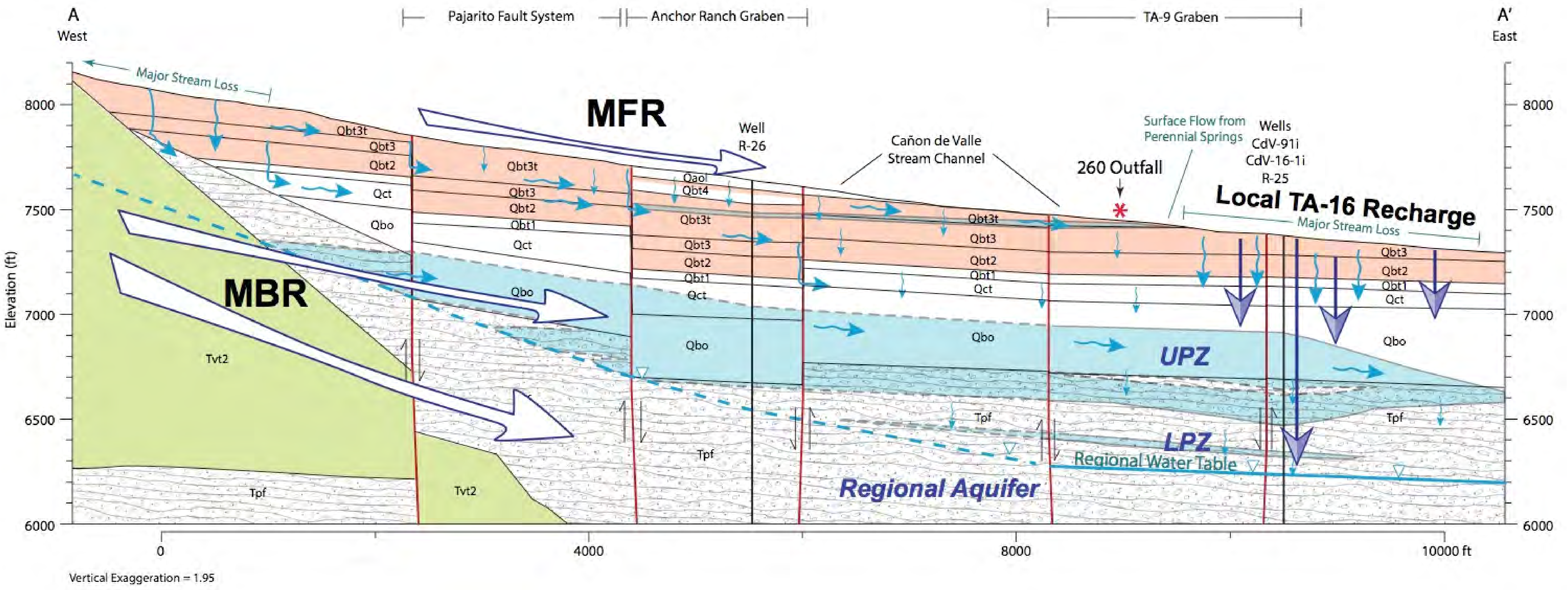

Figure 2.3-1 Conceptual hydrogeologic east-west cross-section for the Cañon de Valle in the vicinity of the 260 Outfall at TA-16. Represented are the three principal recharge sources, which include mountain block recharge (MBR), mountain front recharge (MFR), and local TA-16 recharge. The latter is an HE-contaminant source for the alluvial aquifer, the upper perched zone (UPZ), the lower perched zone (LPZ) and the regional aquifer. Note that local recharge to deeper aquifers at TA-16 occurs downstream of the 260 Outfall, via matrix and fracture flow (fast pathway), as indicated by vertical blue arrows.

LA-UR-18-21326
March 2018
EP2018-0018

2017 Update of the RDX Inventory Report

Attachment 1

Los Alamos
NATIONAL LABORATORY
EST. 1943

Prepared by the Associate Directorate for Environmental Management

CONTENTS

Figures

Tables

1.0 INTRODUCTION

Wastewater from the machining of high explosive (HE) charges was produced at Technical Area 16 (TA-16) at Los Alamos National Laboratory (LANL or the Laboratory) over several decades, much of which was discharged at the surface through Consolidated Unit 16-021(c)-99, the 260 Outfall. Although other types of HE wastewater, including HMX (octahydro-1,3,5,7-tetranitro-1,3,5,7-tetrazocine); TNT (2,4,6-trinitrotoluene); and TATB (triaminotrinitrobenzene), were released at the outfall, the principal waste component was RDX (hexahydro-1,3,5-trinitro-1,3,5-triazine). RDX is characterized as toxic, potentially carcinogenic, and environmentally stable in the absence of light. It has high solubility and a low octanol-water partition coefficient (Log K_{ow} = 0.87) (EPA 2014), indicating a tendency to remain in solution in organic carbon-poor environments (Reid et al. 2005, p.745). RDX is therefore highly mobile in the subsurface. With a retardation factor calculated as 1.13, it moves at nearly the same rate as groundwater (Broxton et al. 2002, p. H-1). A 2005 inventory study estimated the quantity and distribution of RDX in soil, vadose zone, and aquifer at TA-16 based upon limited data available (LANL 2006). This report is intended to update those estimates with more extensive and recent data.

TA-16 is located near the western edge of the Pajarito Plateau, on a mesa where shallow soils overlie a thick unsaturated zone of Bandelier Tuff (Figure 1.0-1). To the west are the Pajarito fault and the Jemez Mountains. Below the HE outfall, a settling pond area leads to a steep lower channel that drains into the adjacent Cañon de Valle. Transient saturation in and beneath these source areas, especially during the period of outfall operation, allows percolation and downward transport of RDX from the surface to groundwater, as detailed in various site conceptual models (LANL 2003; Birdsell et. al. 2005; Newman et al. 2007). From the outfall pond, subsurface flow pathways are believed to include fractures in the welded Bandelier Tuff as well as surge beds within the tuff that can promote lateral transport. Because the outfall pond drains into a perennial reach of Cañon de Valle, the canyon also acts as an area for enhanced downward transport of HE (LANL 2003). A conceptual model of groundwater in the vicinity of TA-16 is shown in Figure 1.0-1.

The 2005 inventory study estimated RDX contamination in seven discrete components of the TA-16 hydrologic system (LANL 2006) (Table1.0-1). For comparison, the same components are evaluated here. Although that study was based on a limited body of data from a smaller network of monitoring wells than are installed currently, it concluded that significant RDX masses may persist in intermediate and regional groundwater: up to 8109 kg and 6053 kg, respectively. These would be the most contaminated of the seven hydrologic components evaluated. However, both the concentrations of RDX and contaminated aquifer volumes were largely unknown. Only 12 samples, collected from 2 wells, informed the intermediate estimate. With respect to regional groundwater in particular, the report stated that even the minimum values could be overestimated because only one well sampled RDX, with variable results, in the regional aquifer. Otherwise, potentially large amounts of RDX were identified in unsaturated zones of tuff beneath the pond area and the alluvial aquifer in Cañon de Valle. Although new or more varied core samples from the vadose zone are not available, data collected from six new alluvial wells improve the estimates in Cañon de Valle. This update to the 2005 report first describes a "simple geometry" approach for estimating the seven TA-16 hydrological components. An alternative "geostatistical" approach was also used to estimate inventories for the alluvial, perched-intermediate, and regional zones, and this approach and the results are discussed herein.

2.0 METHODS

Estimates of RDX in the TA-16 hydrologic system are useful for constraining the scope and evaluating the results of any proposed corrective measures. The inventory presented here couples available data, provided by groundwater sampling and analysis, with hydrogeological observations used to constrain the volumetric extent of RDX contamination. Together, they result in a projection of overall mass of RDX in the vicinity of TA-16, including Cañon de Valle. The concentrations in each part of the system are compiled and partitioned, in most cases, using a quartile approach. The first quartile is taken to represent the lower bound of concentration for a given unit, while the third quartile represents the upper bound for that unit. This is considered the best way to account for the skewed distributions of concentrations, as seen in histogram plots. In other parts of the system, where data points are more scarce, or close to detection limits, maximum or average concentrations are chosen as more useful for making conservative estimates. Aquifer volumes are estimated with simple geometry; for intermediate groundwater, well-drilling reports provide both an approximate areal extent and thickness of the water-bearing unit. The area multiplied by an assumed “average” thickness provides a bulk volume for the unit, which is then reduced by considering the porosity of the formation. For regional groundwater, a similar calculation is made, although the volume constraint is the demonstrated extent of contamination rather than the size of the aquifer itself.

This inventory study employs more recent data from a wider network; however, a high degree of uncertainty is still associated with all estimates. The main sources of uncertainty are the areal extent and volume of contaminated zones and aquifer porosity and variability. Error may also be associated with the heterogeneity of groundwater characteristics and fracture flow-type preferential pathways and RDX degradation over time.

Though the primary focus of this study is groundwater contamination, surface “source area” RDX is addressed first, with calculations based on an estimate from the interim measures report (LANL 2002). Discharges from the 260 Outfall were greatest in the 1950s; they then fell significantly, although were sustained at low levels for more than 30 yr afterward (Gard and Newman 2005, p. 19). The 260 Outfall was deactivated in 1996 as remediation programs commenced. Near the surface, efforts have been made to restrict downward migration of RDX; including source removals in 2000 and 2001 (LANL 2002, p. 31) and 2009 (LANL 2010, p. 8) from the pond area, placement of crushed tuff and bentonite layers in excavated areas, and grouting of a highly porous surge bed zone beneath the settling pond (LANL 2010, pp. 11–12).

3.0 HYDROLOGIC COMPONENT INVENTORIES, INCLUDING BASIS AND ASSUMPTIONS

This section describes the data and assumptions that were used to estimate inventories for each of the seven TA-16 components. It also discusses how and why inventories were revised from the 2005 inventory estimates. A comparison of the 2005 and the current inventories for each of the components is provided in Table 3.0-1.

3.1 260 Outfall Former Settling Pond Area

During 2000–2001 interim measure activities, soil exceeding 100 mg RDX/kg soil was targeted for removal from the settling pond area. At that time, more than 990 m^3 of contaminated soil was removed (LANL 2003), some of the material with high explosives (HE) concentrations of 2 wt% (20,000 ppm) or more. In a study summarized in the 2002 interim measure report (LANL 2002, p. 72), the HE compounds removed were estimated at 8500 kg, or 90% of the total. The remaining part was estimated at 650 kg, based on post-removal analytical data, high-performance liquid chromatography screening data, and estimates of volume and bulk density in each of three zones below the outfall. The zones, as identified in the 2002 interim measure report (p. 49), are described as follows:

Zone A – Surface material from the excavated drainage channel between the outfall and the edge of the cliff. Includes upper drainage and settling pond.

Zone B – Surface material from the drainage channel between the base of the cliff and the drainage channel's confluence with Cañon de Valle (includes lower drainage).

Zone C – Subsurface material from the center of the drainage channel between the outfall and the cliff.

Additionally, the 650 kg estimate includes HE present in a surge bed located below the settling pond area (LANL 2002, p. 72). Surge beds are highly discontinuous, non-welded structures in tuff, resulting from the viscous flow of hot ash. Within them, porosity and surface area are greatly increased, apparently along with the capacity to retain HE compounds. In boreholes below the settling pond area, RDX is concentrated up to 4500 mg/kg (4500 ppm) in a surge bed at about 5 m below the ground surface (LANL 1998, pp. 2–66).

Since 1996, precipitation may have caused the dissolution of some RDX associated with surface deposits. However, since the outfall area is no longer receiving discharge from the 260 Outfall, percolation rates are likely to be low, and it is reasonable to assume that the same 650 kg would be preserved, either in the soil or the unsaturated zone directly beneath it. It is assumed that storm water retention controls would also reduce the downward movement of dissolved and particulate RDX. Although the 2005 inventory places the entire 650 kg in the pond area, according to the interim measure report (LANL 2002), this value represents the entire Consolidated Unit 16-021(c)-99, which includes the upper and lower sections of the drainage channel as well as the surge bed.

In 2009, cleanup activities associated with the corrective measures implementation (CMI) plan followed the site-specific screening action level of 36.9 mg/kg for RDX (LANL 2010, p.8). A field analysis method was used to guide soil removal, and subsequent laboratory analysis was used to validate results. Three locations within the settling pond area were excavated, yielding approximately 30 m^3 of soil (LANL 2010, p. 7).

During the previous interim measure activities, soil with concentrations exceeding 100 mg/kg had been targeted for removal; therefore, the calculation here assumes that the 30 m^3 of soil removed had an average RDX concentration of 100 mg/kg. Assuming a conservative density value of 1900 kg/m^3, the corrective measures implementation (CMI) would have removed less than 6 kg of RDX from the 260 Outfall settling pond area. Subtracted from the 650-kg value given in the interim measure report, 644 kg of RDX would remain in the pond area. This would be distributed in a large amount of soil at concentrations below 36.9 mg/kg; at this concentration, 644 kg of RDX would occupy about 9200 m^3 of soil in and around the drainage channel (Table 3.0-1). However, a large part of this inventory apparently resides in the surge bed, which was grouted in an effort to immobilize RDX associated with unsaturated tuff (LANL 2010, p. 12). Although there is no way to know how completely the surge bed was filled with grout and no way to monitor RDX within that zone afterward, a dry condition in the settling pond area would suggest a substantial amount of surge bed–associated HE is probably immobilized. It should be noted that because the effect of grouting cannot be well quantified, the amount of immobilized HE is not included in the inventory estimate.

3.2 Vadose Zone Directly under 260 Outfall Area

The interim measure report presents core data from borehole 16-6370, drilled to a depth of 25 m below the settling pond area (LANL 2002, p. 35). In samples collected at 1.5-m intervals, the highest RDX concentration is 1.48 mg/kg. It is worth noting that far greater concentrations occur sporadically in localized near-surface zones (e.g., see section 1.0). Their distribution, consistent with the site conceptual model (Figure 1.0-1), is understood to be along preferential fracture-flow pathways and in surge beds where lateral transport of shallow groundwater occurs (LANL 2002, p. 13). Of 46 samples collected from Bandelier Tuff in this area, 3 are above 1000 mg/kg, with the highest, 4500 mg/kg, in a surge bed beneath the pond area (LANL 1998, pp. 2–66). All but 12 of the samples are below 15 mg/kg, and the median is 1.74 mg/kg. This value is used to calculate the minimum RDX mass in the 260 Outfall vadose zone. Although it underrepresents some locally contaminated areas in the upper section of the tuff, the RDX profile of borehole 16-6370 supports the assumption that nearly 200 m of underlying tuff have contamination levels well below the median. Below 20 m, RDX drops to below 0.1 mg/kg (LANL 2002, p. 40). Surge bed–associated RDX is accounted for in the 260 Outfall component (in 2006, 650 kg of RDX); as in the 2005 inventory, some double counting is possible between these components. However, a few high concentrations do not result in elevated median concentrations.

Somewhat larger and more variable RDX concentrations are detected in samples collected along the length of the upper and lower drainage channel, as presented in Table 2.2-1 of the "Phase III RFI Report for Solid Waste Management Unit 16-021(c)-99" (LANL 2003). The highest of these numbers is in surface samples collected from the center of the drainage channel and is considered potentially representative of concentrations in underlying tuff. The median concentration among them, 3 mg/kg, is used to constrain the higher end of RDX mass in the 260 Outfall vadose zone.

Figure 3.2-1 shows the distribution of solid-phase RDX results from various sources (LANL 2003; LANL 1998; LANL 2002).

To give an estimate of the solid phase RDX present in the vadose zone, concentrations are multiplied by the estimated mass of the overburden (see Figure 1.0-1 for a conceptual view of the extent of overburden). The area is considered as the size of the former settling pond (approximately 15 m × 6 m), together with the drainage channel (approximately 192 m × 5 m). The depth to the first screen in a saturated zone [CdV-16-4(i)p] is 250 m; this is used to complete the vadose zone volume. A bulk density of 1.19 g/cm^3, or 1190 kg/m^3, representative of the Otowi Member of the Bandelier Tuff (Rogers and Gallaher 1995), is used to conservatively estimate the contaminated mass at 3.13×10^8 kg.

Using this approach, a range of RDX mass was estimated to be between 545 kg and 940 kg (Table 3.0-1). The vadose zone is understood to be highly heterogeneous and dominated by fracture flow, and thus the uncertainty of the estimate is great.

3.3 Mesa Vadose Zone Encountered by Saturated Zones Feeding Sanitary Wastewater Systems Consolidation and Burning Ground Springs

In the 2005 inventory, maximum and minimum RDX concentrations in springs sample water were multiplied by maximum and minimum flow rates, yielding figures for maximum and minimum yearly releases. A 100-yr release period was assumed. In the 2005 study, the calculated minimum mass of RDX (3 kg) would be discharged in 100 (minimum) yr, while in 100 maximum-flow yr a total of 482 kg would be discharged from the springs. For this current report, the aim has been to balance such extremes of flow with more typical conditions. In Figure 3.3-1 histograms show RDX concentrations in samples collected from springs at TA-16.

For the current report, volume is taken as an average and applied to a range of RDX concentration data from spring samples. Flow data from Sanitary Wastewater Systems Consolidation (SWSC) and Burning Ground Springs were gathered for Water Years (WYs) 1997 through 2010 (WYs begin on October 1 and end on September 30). The median value for each was used to project a volume of discharge over a span of 100 yr; as in the 2005 study, it was assumed that RDX would be depleted from the springs in that time. No relationship between springs flow rates and concentrations is easily discernable. Spring discharge flows have not been sufficient for measurement since 2010 (although spring monitoring has been reestablished at Burning Ground and Martin Springs).

The ranges of mass discharge are estimated by multiplying the 100-yr average discharge volumes by upper and lower concentrations, selected as the first and third quartiles in each set of samples. The minimum mass discharge is defined by the value of the first quartile, and the maximum is defined by the value of the third quartile. The 33 to 56 kg range given in Table 3.0-1 are sums for the two springs and represent a minor fraction of the total RDX inventory at TA-16. The lower end of this range is similar to the mass calculated from average annual Burning Ground and SWSC spring flow and concentration data for the last 11 yr (reported in LANL 2016**,** which discusses future CMI activities at the TA-16 springs).

3.4 Alluvial Sediments in the Bottom of Cañon de Valle

The 2005 inventory cites the value of 5 kg RDX in alluvial sediments of Cañon de Valle from Reid et al. (2005, p. 753). This estimate is based on a geomorphic assessment of canyon bottom sediments. The 2011 Water Canyon/Cañon de Valle investigation report (LANL 2011, p. 45) approximates the mass of RDX in alluvium as 11 kg, 66% (7.3 kg) of which is located in Cañon de Valle, and 24% (2.6 kg) of which is located in Water Canyon below the confluence with Cañon de Valle. Together, the RDX present in these two reaches are taken as the maximum value (10 kg), while the 5-kg value provided in Reid et al. (2005, 093660) is considered the minimum value (Table 3.0-1).

3.5 Vadose Zone beneath Cañon de Valle and above the Intermediate Groundwater Zone

Because of the combination of perennial and frequent ephemeral surface flow in this part of Cañon de Valle, this compartment meets the criteria of a saturated pathway from the surface to the intermediate zone. However, few data on the vadose zone RDX concentrations in the unsaturated zone beneath Cañon de Valle are available. Calculation of the RDX mass transfer can be made using values assumed for mass flux and area, where the area is described by a line equal in width to the flowing stream. Appendix N of the Phase III RFI gives the length of the Cañon de Valle aquifer as 7750 ft (LANL 2003), and in the water balance study for the report, infiltration to the underlying tuff is estimated at 2.6 gal./ft*d (LANL 2003, p. 5–11). It is assumed that RDX concentrations in the tuff vadose zone do not exceed RDX concentrations in shallow wells in the overlying alluvial sediment. The third quartile concentration value from alluvial wells, 23.1 µg/L, is used as a maximum, and the first quartile value, 2.7 µg/L, is used as a minimum. Together, these figures allow for the estimation of mass flux per day of RDX, downward and out of the alluvium. As with the Burning Ground and SWSC Springs calculations, it is assumed that the supply of RDX in alluvial material will be exhausted in 100 yr. By this estimate, a maximum of 64 kg, or a minimum of 8 kg, would move from the alluvial aquifer of Cañon de Valle into the unsaturated zone above perched groundwater. Because of the lack of actual concentration data in the vadose zone below Cañon de Valle, estimates of inventory are highly uncertain for this component.

3.6 Intermediate Groundwater

A “concentration × volume mass estimate” approach is used to estimate RDX residing in groundwater zones.

3.6.1 Intermediate Zone RDX Concentrations

Since 2005, RDX has been detected in three new wells in the intermediate zone [CdV-16-4(i)p, R-25b, and CdV-9-1(i)]. The data provided by these wells, as well as continued sampling data from intermediate wells CdV-16-1(i) and CdV-16-2(i)r, informs the current inventory study. Figures 3.6-1, 3.6-2, and 3.6-3 are cross-sections of the perched-intermediate zone showing well screens. Table 3.6-1 is a summary of samples from intermediate well screens where RDX occurs, and Figure 3.6-4 represents these samples in a histogram.

A quartile method was used to constrain a likely range of concentrations. High and low concentrations for the upper intermediate zone were determined by the third and first quartile values, respectively, from a set of 41 groundwater samples. For the upper intermediate zone, RDX concentrations from the LANL Interim Facility-Wide Groundwater Monitoring Plan (IFGMP) samples were used to calculate these values. By constraining the sampling dates to 2015–2017, roughly equal weighting was given to the five well screen locations.

A thin, deeper perched zone is apparent between 1000 ft and 1200 ft below the surface. Most of the samples from this zone (23 of 26) are from screen 4 of well R-25; the other 3 are from CdV-16-4ip screen 2, from a depth of 1110–1141.1 ft. One of the 3 samples (the first sample) collected has a concentration of 167 µg/L. As with the early data from R-25, this value is considered unreliable; it was most likely introduced to this depth from above, during drilling and well development. Less than two months later, the same screen produced a sample containing 22.2 µg/L RDX. The screen was abandoned in April 2011; the last sample collected indicated an RDX detection of 19.9 µg/L. For the purpose of the inventory, 20 µg/L is assumed as a reasonable concentration for the entire lens of deep perched groundwater. Although the samples from R-25 screen 4 are not used here for calculation, they are useful in assessing the validity of this assumption: the highest value among them is 26.7 µg/L, and the mean value is 12.4 µg/L.

3.6.2 Intermediate Zone Volume

The volume of groundwater present in the intermediate zone is approximated from maps and cross-sections related to this study, created with information gained during well drilling and development. These calculations are naturally subject to a high degree of uncertainty. In Figure 3.6-5, the area of RDX contamination in the upper perched zone is bounded in green; this area is computed as 435,433 m^2 using GIS tools (ArcGIS 10.3.1). Figure 3.6-6 approximates the areal extent of deep and shallow perched water zones, with building 16-260 and the 260 Outfall at the western edge of the lower zone. As the entire deep (lower) zone lies downgradient of building 260, and the contamination within it is not well constrained by available data, it is considered as a whole. The area of the deep zone is computed to be 513,940 m^2 using geographic information system (GIS) tools (ArcGIS 10.3.1).

Though the saturated intermediate zones are lens-shaped, their volumes are estimated by considering their thicknesses to be uniform. At its thickest, the upper zone lies within about 134 vertical m, perhaps divided into two bodies. For the calculation a 76.2-m thickness is used. In cross-section, the contact between the Otowi Member and the Puye Formation occurs approximately halfway through the saturated upper zone; this places 38.1 m in each formation. The bulk volumes are therefore equal, although the volumes of groundwater differ according to porosity. A key sensitivity is the volume of RDX contamination. The inventory will scale with volume, thus errors in the volume will affect the mass estimate. The volume assumed is considered at this time to be a conservative best estimate. If additional wells are drilled, the volumes and inventories can be recalculated if it appears that the new data might substantially impact the current estimate.

Statistical analyses of porosity for each formation are taken from a spreadsheet based on Schlumberger, Inc., geophysical logs. The data were derived from well R-26, where a mud-drilled borehole provided nearly ideal logging conditions, and includes combined magnetic resonance, density porosity, thermal and epithermal neutron logs (Kleinfelder 2005). The spreadsheet, entitled "Summary of Borehole Porosity Measurements by Geologic Unit for Well R-26," is attached as Appendix A.

The porosity values within 1 standard deviation of the median are multiplied by the bulk volumes to calculate a range of volumes of pore water. The Otowi Member of the Bandelier Tuff is significantly more porous, at between 40% and 46%, while the Puye Formation has porosity of between 18% and 33%. The pore water estimated in the Otowi Member is between 5.4 and 6.1 billion L; in the Puye Formation, it is between 2.5 and 4.4 billion L. The total of the two lower volume estimates is 7.9 billion L and the total of the two upper volume estimates is 10.5 billion L.

For the lower intermediate zone, a thickness of 7.6 m was assumed. Though it is perhaps 18 m thick in some places, it also would taper to thin edges. The 7.6-m thickness, multiplied by the area shown in Figure 3.6-6 and upper and lower Puye porosities, gives a range of pore water volumes from 0.72 to 1.28 billion L for the lower intermediate zone.

3.6.3 Intermediate Groundwater Results

To estimate minimum RDX mass in the upper zone, the smaller volume, 7.9 billion L, is multiplied by the first quartile intermediate RDX concentration, 25.4 µg/L. The larger volume, 10.5 billion L, is multiplied by the third quartile concentration, 111 µg/L, to give the maximum mass in the upper zone. The range in the upper perched zone is between 205 and 862 kg. For the lower perched zone, the assumed concentration of 20 µg/L is multiplied by the high- and low-volume estimates to yield another range of RDX mass: 14 to 26 kg. The high-mass estimate is added to the high for the upper perched zone, and the low-mass estimate is added to the low value for the upper zone, to obtain a range of RDX mass for the entire perched system: between 263 and 1478 kg (Table 3.0-1). The minimum is based on 40% porosity in the Otowi Member and 18% porosity in the Puye Formation, with an RDX concentration of 25.4 µg/L in the upper zone and 20 µg/L in the lower zone. The maximum is based on respective porosities of 46% and 33%, and RDX concentrations of 111 µg/L in the upper zone and 20 µg/L in the lower zone. Although the distribution of HE is not thought to be uniform within perched groundwater zones, the assumption of uniformity is used to constrain the mass to upper and lower limits.

3.7 Regional Groundwater

Data gathered since the 2005 study allows for a markedly different interpretation, both of the overall mass as well as the distribution of RDX that could be expected in the regional aquifer below the 260 Outfall. The following contrasts in data availability between the study presented here and the 2005 study are worth noting.

The 2005 inventory relied on early data from R-25, which then was the only well showing RDX in regional groundwater. However, those data are now considered unreliable (LANL 2011). Although various observations from that borehole contribute to understanding of the geology and regional groundwater, all sampling data from R-25 have been excluded in the calculation of the concentrations applied to regional and intermediate groundwater compartments for the revised inventory. R-25 data have an impact both in the concentrations of RDX thought to be present in the aquifer as well as the volume expected to be contaminated. The 2005 study, guided by early data from the deep screens of R-25, considered that RDX could be present as far as 400 m below the regional water table surface. However, these data are now thought to result from downward leakage during drilling and are not representative of actual conditions in the regional aquifer. In recent years, RDX has been detected in screen 6 of R-25 (top of screen is 27.7 m below the water table) but is not apparent in screen 7 (top of screen is 91.8 m below the water table).

Since 2005, RDX has been detected in three new wells developed in the regional zone: R-18, R-63, and R-68. Other new wells in the regional aquifer that have not detected RDX are useful for constraining the areal extent of contamination. The 2005 study speculated, for lack of regional well data, a contaminated area equal in size to the upper perched-intermediate zone. Here, a far smaller footprint of contamination is indicated by the regional groundwater gradient and absence of RDX in samples from wells R-47, R-47i, and R-48.

3.7.1 Regional Zone Volume

For the 2005 inventory, a large, somewhat arbitrary contaminated volume was assumed below the regional water table. The principal reason for this was the data from R-25 showing RDX in groundwater at the deeper screens. The idea then was to assume a depth within the aquifer at which no RDX could reasonably be present and then calculate the largest possible volume of potential contamination. The inventory presented a maximum of 6053 kg RDX, and a minimum of 135 kg, while acknowledging that the real mass of RDX in the regional zone may in fact be less than 135 kg. For the 2017 inventory update, the matter of contaminated volume is addressed differently, and lower inventories are in fact the case.

Here, a far shallower depth of the regional aquifer is considered to be contaminated, based on the more recent sampling data from R-25. Small concentrations of RDX, just above the detection limits, persist in screen 6. This is at a depth of 27.7 m below the water table (LANL 2012) (http://www.intellusnm.com). Because screens 7 and 8 show no detectible RDX since 2007, the depth of contamination in the aquifer is assumed to be 46 m (below R-25 screen 6 and above screen 7). Given the anisotropic character of Puye Formation sediments, flow velocities along bedding planes (laterally) are thought to far exceed velocities across bedding planes (vertically). Observations from deep wells developed for the Chromium Groundwater Project at the Laboratory support this assumption, where a high degree of anisotropy is observed in the Puye Formation.

The area of contamination is also defined differently because of new wells and includes the wells where RDX is present and is constrained by those where it is not detected. Well R-18, to the northeast of the 260 Outfall, shows increasing concentrations of RDX, although R-47, south and slightly east of R-18, shows none. The plume is conceptualized as a triangle spreading out to the east of building 260. One vertex is located to the north of R-18, with another to the south of Fish Ladder Canyon in the direction of new well R-58. Because RDX has not been detected at well R-48, it constrains the contaminated area on the southwest. The other two wells where RDX has been detected, R-63 and R-68, are within the triangle, on opposite sides of Cañon de Valle. The area, bounded by an orange polygon in Figure 3.6-6, is 1.214×10^6 m^2. The bulk volume is calculated as 37 million m^3. As with the intermediate-perched zone, the porosity of the Puye Formation is within the range of 18% to 33% (Kleinfelder 2005). The pore volume of this zone as defined above is estimated to range between 10.3 and 18.3 billion L.

3.7.2 Regional Zone RDX Concentration

In the 2005 inventory, regional groundwater was estimated using RDX concentrations from screens 5 and 8 of well R-25, zones that are now thought to have been contaminated by intermediate groundwater during time that the borehole was left undeveloped (LANL 2011). Well R-25 data are not used for RDX mass calculation here, although it is worth noting the decline in RDX concentration over the past several years at each of the lower (regional) screens of that well. These data are represented in Figure 3.7-1; the most recent samples in R-25 had concentrations below 1 µg/L. Also, RDX has not been detected in screens 7 and 8 of R-25 since 2007. This information is presented to validate the omission of R-25 data from this inventory and to suggest those data skewed the results of the 2005 inventory. Similarly, two samples from well R-63 with RDX concentrations of 15 µg/L and 15.9 µg/L are omitted because they appear to contain water from well development (Figure 3.7-2). Two days after the 15.9 µg/L sample was collected, the concentration had dropped to below 1 µg/L and has remained below 2 µg/L since that time.

For the current inventory study, maximum and minimum concentrations were multiplied by an estimated volume to capture a range of values for RDX mass. Regional aquifer mass estimates are sensitive to the assumed volume (just like the intermediate zone estimates) and if future data suggest that the contaminated volume is substantially different than assumed here, mass will need to be recalculated. The concentrations used were from the regional aquifer wells with RDX detections, R-18, R-63, and R-68, minus the two data points discussed above (Table 3.7-1). Table 3.7-1 is a summary of samples from regional well screens where RDX occurs, and Figure 3.7-3 represents these samples in a histogram.

For the maximum, the highest measured concentration among them, 17.1 µg/L, is used. The increasing RDX trend in R-18 (Figure 3.7-4) suggests the highest value recorded, rather than the third quartile value, should be used to calculate a conservative estimate. The minimum concentration is estimated conservatively as the median of all detected samples, calculated as 1.21 µg/L. This is a somewhat arbitrary number derived from a set of data that excludes all “nondetect” samples. With the analytical method usually applied for RDX, accuracy is lost below 0.33 µg/L, although the detection limit is 0.13 µg/L. Samples below 0.13 µg/L are reported at the higher value of 0.325 µg/L, although they are omitted from this study as nondetections. Note that because R-18 is screened several meters below the top of the regional aquifer, that this adds uncertainty to the mass estimate because concentrations in R-18 could be higher in the shallower part of the aquifer. Like the volume sensitivity mentioned above, revised mass estimates may be needed if new well data suggest higher concentrations are more representative.

3.7.3 Regional Groundwater Results

The minimum mass is calculated with the minimum pore water volume, 10.3 billion L, and the median concentration of all regional samples detecting RDX, 2.58 µg/L. The pore water volume maximum, 18.3 billion L, is multiplied by the maximum RDX concentration from regional groundwater sampling, 17.1 µg/L. The regional zone is estimated by this method to contain between 35 kg and 415 kg RDX.

4.0 SUMMARY OF RESULTS

The most significant differences between this study and the 2005 estimate are in the areas of regional and intermediate groundwater, respectively (Table 3.0-1). In 2017, the regional groundwater zone was estimated to contain between 35 and 415 kg, compared with between 135 and 6053 kg in 2005, representing a decrease in the estimate of between 74% and 93%. The intermediate groundwater zone was estimated to contain between 263 and 1478 kg, compared with 476 and 8109 kg in 2005, representing a 45% to 82% decrease in the estimate. The saturated zones feeding SWSC and Burning Ground Springs are estimated to contain between 33 and 56 kg, compared with between 3 and 482 kg in 2005; this represents either a 1000% increase (from 3 kg to 33 kg), or a decrease of 88% on the maximum end.

During the CMI in 2009, it was estimated that only 5 kg of RDX was removed by excavation, leaving 644 kg in soils within the Consolidated Unit 16-021(c)-99 area that includes the former pond, outfall area, drainage channel, and surge bed below the pond. Compared with 650 kg estimated in 2005, this represents a decrease of 0.9%. Grouting has likely immobilized a substantial fraction of this inventory, but it was not accounted for in these estimates because of uncertainties related to where the grout actually traveled in the subsurface. A more recent geomorphology study of alluvial sediments estimated slightly more RDX in Cañon de Valle sediments (LANL 2011), also suggesting it has migrated into Water Canyon as a result of post-fire runoff. The range is between 5 and 10 kg compared with 5 kg in 2005. A different approach to assessment of vadose zone RDX contamination resulted in a smaller maximum value and a larger minimum compared with the 2005 inventory. The range is between 545 kg and 940 kg compared with 234 kg and 4311 kg (2005); this represents either a 133% increase or a 78% decrease from 2005. In the vadose zone beneath the Cañon de Valle alluvial aquifer, values between 8 and 64 kg are possible, compared with 17 kg and 3724 kg in 2006; this represents a 53% to 98% decrease from 2005.

Overall, the values range between 1533 and 3608 kg of RDX estimated to be in all components of the hydrologic system at TA-16. In 2005, the numbers were 1520 kg and 23,334 kg, respectively. On the low end, the decrease from 2005 figures is 2.4%, and on the high end the decrease is 85.8%.

Considering the work that has been done to restrict downward movement of RDX associated with the surface, some of the compartments discussed here have contamination that has been stabilized or that has limited mobility in the environment. The areas of concern remain the intermediate and regional groundwater zones, along with the zone beneath Cañon de Valle alluvium. Recent data from monitoring wells has improved the understanding of RDX concentrations in perched-intermediate and regional zones, although uncertainty associated with estimating volumes of contaminated groundwater is still significant. Information from future samples and new wells will help to evaluate the current inventory estimates, and revision of the calculations may need to be done if future results indicate substantially different conditions.

5.0 ALTERNATIVE INVENTORY APPROACH

Results comparable to those described above were produced using a geostatistical approach (Table 5.0-1), as detailed in the report “TA-16 Groundwater RDX Evaluation,” prepared by Weston, Inc., and included in the “Geology Report for Technical Area 16 and Vicinity” (Weston 2016). An existing geologic framework model was used with EarthVision software (Dynamic Graphics 2015) to model volumes of the contaminated saturated zones, and to spatially interpolate subsurface distribution of RDX in three dimensions. Mass estimates for RDX were produced by the integration of three-dimensional (3-D) models. The geostatistical method focuses on aqueous phase RDX distribution within regional, intermediate, and alluvial aquifers; it corresponds to three of the seven hydrologic compartments considered in the simple geometry method, excluding those related to HE contaminants in currently dry or transiently saturated environments.

With the geostatistical approach, the centroid of the plume is placed at the location of the highest sample concentration, and decreasing concentrations of RDX are interpolated outwardly across the other sample locations. Though the resulting volume of perched intermediate water considered is nearly 47 billion L, which far exceeds the 8 to 10 billion L calculated for the simple geometry approach, much of it has very low concentrations of RDX. In Figure 5.0-1, volumes represented in blue-green to blue have concentrations below 26 µg/L, which was the quartile value used to estimate the minimum RDX in the simple geometry study.

The mass of RDX estimated for intermediate zones (UPZ + LPZ) is between 650 and 1581 kg, which corresponds to simple geometry minimum and maximum values of 263 kg and 1478 kg.

Similarly, the volume of regional aquifer material is greater than the volume considered in the simple geometry approach. While the Weston study integrates RDX concentrations across approximately 85 billion L, the simple geometry study uses a range of regional aquifer water volumes between 10.3 and 18.3 billion L. However, the concentrations are interpolated outward to 0.04 µg/L, resulting in smaller mass of RDX (1.8 to 8.5 kg) than calculated by the simple geometry approach (10 to 42 kg).

In the simple geometry study, 5 to 10 kg RDX was estimated in the alluvium in Cañon de Valle, based on a geomorphic assessment of surface sediments (Reid et al. 2005; LANL 2011). By contrast, the geostatistical approach employs shallow well samples interpolated across the extent of alluvial saturation, where concentrations range from 2.5 to 17.6 µg/L. If this method is used, only 0.16 kg of RDX is estimated, although RDX associated with the dry solid-phase sediment materials in Cañon de Valle is not accounted for.

By the geostatistical approach a range of between 651 and 1589 kg RDX was estimated, while using simple geometry a range between 1533 and 3608 kg RDX was estimated. In the simple geometry study, aquifers account for approximately 298 to 1893 kg; this range encompasses the geostatistical range of 651 to 1589 kg. Overall, the two new studies, as a result of more extensive data, yield narrower ranges that contrast markedly with the 2005 estimates, where the corresponding aquifer compartments were thought to contain between 616 and 14,167 kg. This difference, as well as the agreement of new mass estimates, suggests both new estimates are more reasonable than the 2005 estimates.

6.0 IMPLICATIONS OF THE INVENTORY RESULTS

The revised estimates presented here indicate there may be substantially lower total inventory of RDX in the environment than the previous 2005 estimate which was based on limited data, particularly for the deep-perched and regional groundwater. The current minimum total RDX estimates are only slightly lower than the 2005 estimates, but the current estimate of the maximum total RDX is over 85% lower than in 2005. For the intermediate and regional aquifers, the current estimates are between 45% and 93% lower.

The inventory evaluation provides valuable information regarding the distribution of RDX in the subsurface environment at TA-16. For the groundwater systems, the perched intermediate zone has significantly more mass of RDX than the alluvial or regional aquifers. This information will be useful during development of the upcoming TA-16 investigation report (IR), and evaluation of potential future corrective actions, if necessary.

The only other components with fairly significant known inventories of RDX are the former 260 Outfall settling pond area and the vadose zone beneath the settling pond area. Given the fact that the outfall is no longer operational, and given that much of the RDX in the underlying surge bed was immobilized through in situ grouting during the corrective measures implementation at Consolidated Unit 16-021(c)-99 in 2009–2010 (LANL 2010), it is believed that the transport of RDX from these contaminated areas has been significantly reduced. RDX concentrations in downgradient alluvial monitoring wells in Canon de Valle show long-term declines to levels near the New Mexico tap water screening level of 7.02 ug/L. This may reflect the reduction in available RDX inventory as a result of the interim measures conducted in 2000–2001 (LANL 2002), and the CMI conducted in 2009–2010.

7.0 REFERENCES AND MAP DATA SOURCES

7.1 References

The following reference list includes documents cited in this report.

Birdsell, K.H., B.D. Newman, D.E. Broxton, and B.A. Robinson. "Conceptual Models of Vadose Zone Flow and Transport beneath the Pajarito Plateau, Los Alamos, New Mexico," *Vadose Zone Journal*, Vol. 4, pp. 620–636 (2005).

Broxton, D., R. Warren, P. Longmire, R. Gilkeson, S. Johnson, D. Rogers, W. Stone, B. Newman, M. Everett, D. Vaniman, S. McLin, J. Skalski, and D. Larssen. "Characterization Well R-25 Completion Report," Los Alamos National Laboratory report LA-13909-MS, Los Alamos, New Mexico (2002).

EPA (U.S. Environmental Protection Agency). "Technical Fact Sheet - Hexahydro-1,3,5- trinitro-1,3,5-triazine (RDX)," U.S. Environmental Protection Agency Region 6, Dallas, Texas (2014).

Gard, M.O., and B.D. Newman. "The High Explosives Source Term at TA-16," Los Alamos National Laboratory document LA-UR-05-9433, Los Alamos, New Mexico (2005).

Kleinfelder, January 25, 2005. "Final Well R-26 Completion Report, Revision No. 1," report prepared for Los Alamos National Laboratory, Project No. 37151, Albuquerque, New Mexico.

LANL (Los Alamos National Laboratory). "RFI Report for Potential Release Site 16-021(c)," Los Alamos National Laboratory document LA-UR-98-4101, Los Alamos, New Mexico (1998).

LANL (Los Alamos National Laboratory). "Interim Measure Report for Potential Release Site 16-021(c)-99," Los Alamos National Laboratory document LA-UR-02-4229, Los Alamos, New Mexico (2002).

LANL (Los Alamos National Laboratory). "Phase III RFI Report for Solid Waste Management Unit 16-021(c)-99," Los Alamos National Laboratory document LA-UR-03-5248, Los Alamos, New Mexico (2003).

LANL (Los Alamos National Laboratory). "Investigation Report for Intermediate and Regional Groundwater, Consolidated Unit 16-021(c)-99," Los Alamos National Laboratory document LA-UR-06-5510, Los Alamos, New Mexico (2006).

LANL (Los Alamos National Laboratory). "Summary Report for the Corrective Measures Implementation at Consolidated Unit 16-021(c)-99," Los Alamos National Laboratory document LA-UR-10-0947, Los Alamos, New Mexico (2010).

LANL (Los Alamos National Laboratory). "Investigation Report for Water Canyon/ Cañon de Valle," Los Alamos National Laboratory document LA-UR-11-5478, Los Alamos, New Mexico (2011).

LANL (Los Alamos National Laboratory). "Technical Area 16 Well Network Evaluation and Recommendations," Los Alamos National Laboratory document LA-UR-12-1082, Los Alamos, New Mexico (2012).

LANL (Los Alamos National Laboratory). "Work Plan for a Tracer Test at Consolidated Unit 16-021(c)-99, Technical Area 16, Revision 1," Los Alamos National Laboratory document LA-UR-15-24089, Los Alamos, New Mexico (2015).

LANL (Los Alamos National Laboratory). “Evaluation Report for Surface Corrective Measures Implementation Closure, Consolidated Unit 16-02l(c)-99,” Los Alamos National Laboratory document LA-UR-16-27153, Los Alamos, New Mexico (2016).

Newman, B.D., D.D. Hickmott, and P. Gram. “Flow and High Explosives Transport in a Semiarid Mesa in New Mexico, USA,” unpublished manuscript (2007).

Reid, K.D., S.L. Reneau, B.D. Newman, and D.D. Hickmott. “Barium and High Explosives in a Semiarid Alluvial System, Cañon de Valle, New Mexico,” *Vadose Zone Journal*, Vol. 4, pp. 744–759 (2005).

Rogers, D.B., and B.M. Gallaher. “The Unsaturated Hydraulic Characteristics of the Bandelier Tuff,” Los Alamos National Laboratory report LA-12968-MS, Los Alamos, New Mexico (1995).

Weston (Roy F. Weston, Inc.). “TA-16 Groundwater RDX Evaluation, Los Alamos National Laboratory, Los Alamos, New Mexico,” Los Alamos, New Mexico (2016).

7.2 Map Data Sources

Hillshade; Los Alamos National Laboratory, ER-ES, As published; \\slip\gis\Data\HYP\LiDAR\2014\Bare_Earth\BareEarth_DEM_Mosaic.gdb; 2014

Structures; Los Alamos National Laboratory, KSL Site Support Services, Planning, Locating and Mapping Section; 06 January 2004; as published 29 November 2010.

Unpaved road;; Los Alamos National Laboratory, ER-ES, As published, GIS projects folder; \\slip\gis\GIS\Projects\14-Projects\14-0062\project_data.gdb; digitized_site_features; digitized_road; 2017

Paved Road Arcs; Los Alamos National Laboratory, FWO Site Support Services, Planning, Locating and Mapping Section; 06 January 2004; as published 29 November 2010.

Drainage channel; Los Alamos National Laboratory, ER-ES, As published, GIS projects folder; \\slip\gis\GIS\Projects\11-Projects\11-0108\gdb\gdb_11-0108_generic.mdb; drainage; 2017

Approximate extent of RDX contamination in deep perched groundwater, based on current knowledge; Los Alamos National Laboratory, ER-ES, As published, GIS projects folder; \\slip\gis\GIS\Projects\15-Projects\15-0041\shp\perched_aquifer.shp; 2016

Point features; As published; EIM data pull; 2017.

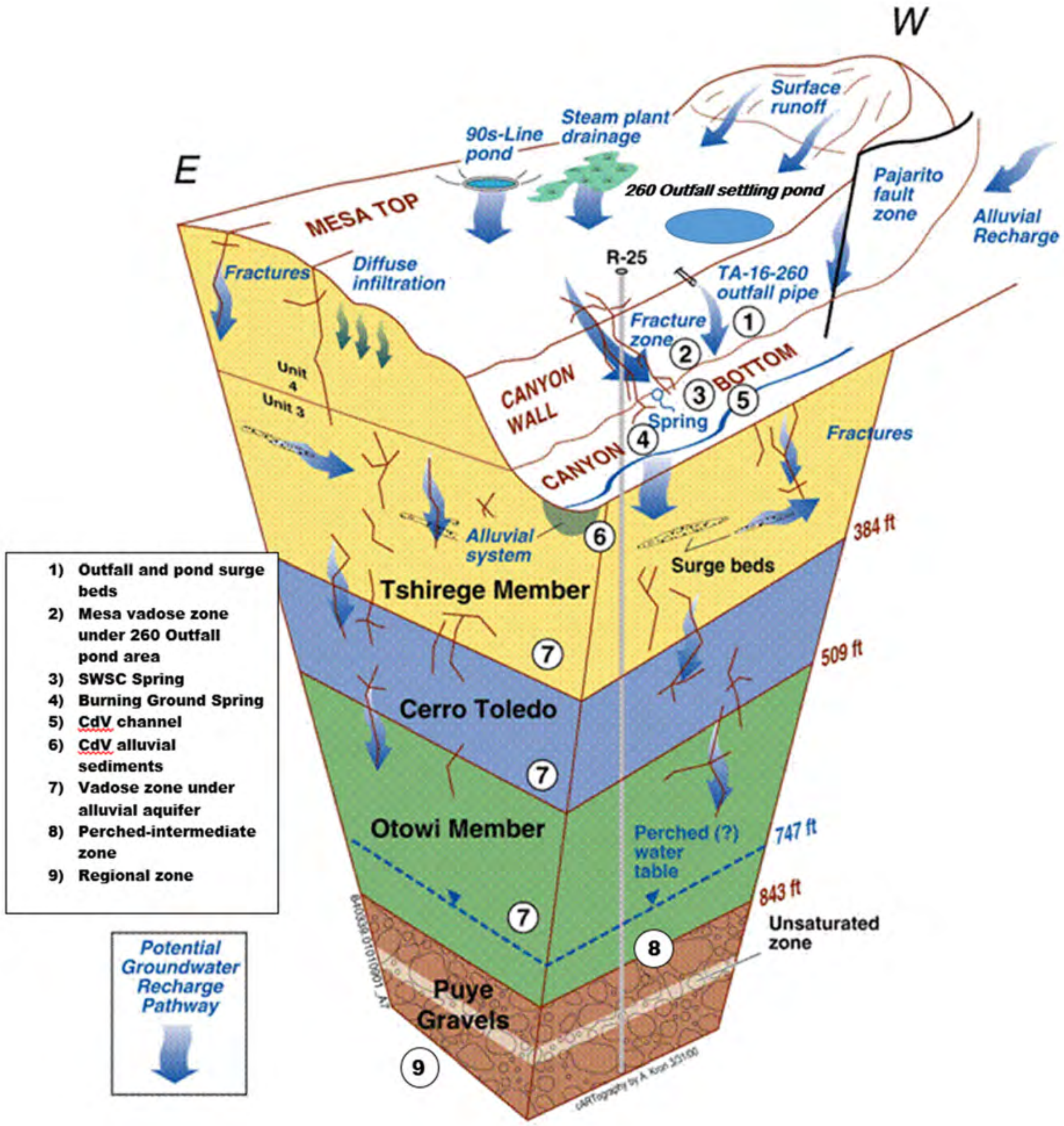

Figure 1.0-1 **Conceptual model of groundwater in the vicinity of TA-16**

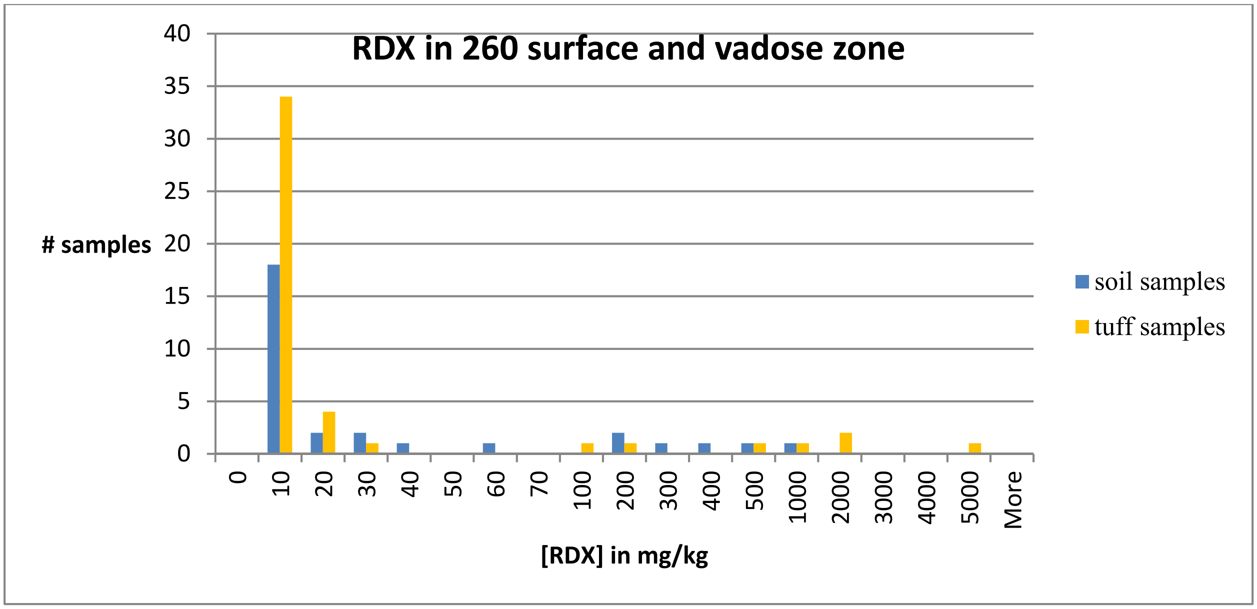

Figure 3.2-1 RDX concentrations in solid-phase samples

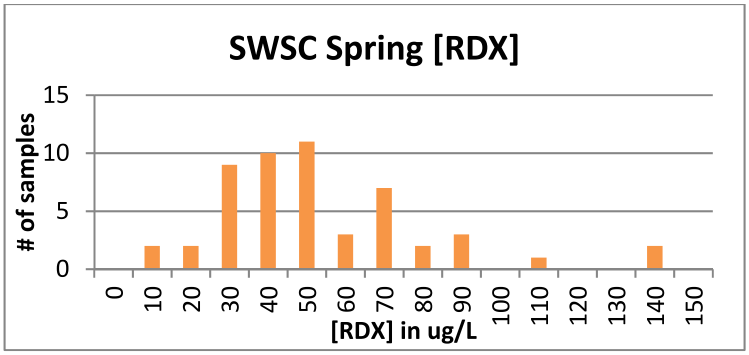

Note: Median concentration for SWSC Spring is 44 µg/L. Minimum is 31 µg/L. Maximum is 61 µg/L.

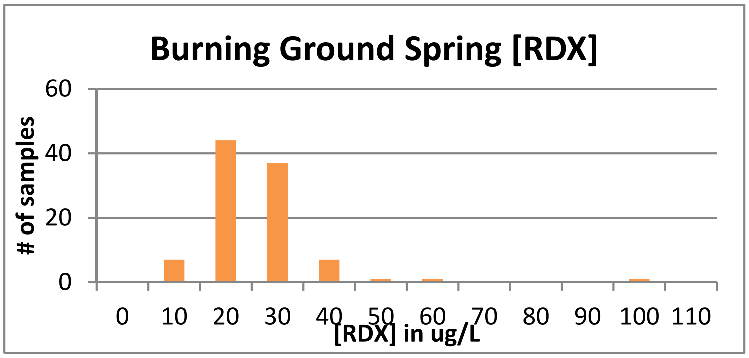

Note: Median concentration for Burning Ground Spring is 20 µg/L. Minimum is 16 µg/L. Maximum is 24 µg/L.

Figure 3.3-1 Histograms showing RDX concentrations in spring discharges

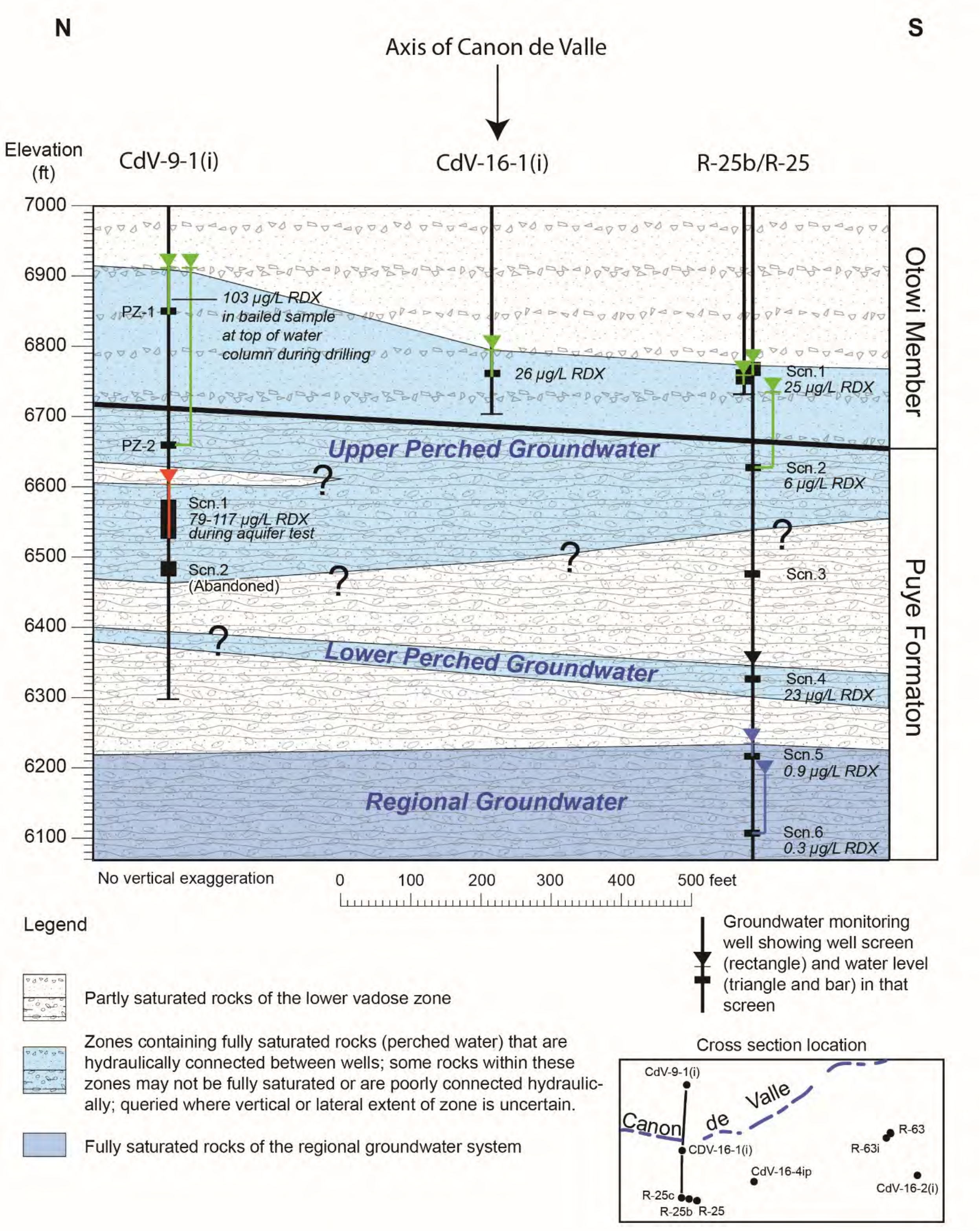

Figure 3.6-1 North-south geologic cross-section for the lower part of the vadose zone showing geologic contacts and groundwater occurrences in wells CdV-9-1(i), CdV-16-1(i), R-25b, and R-25

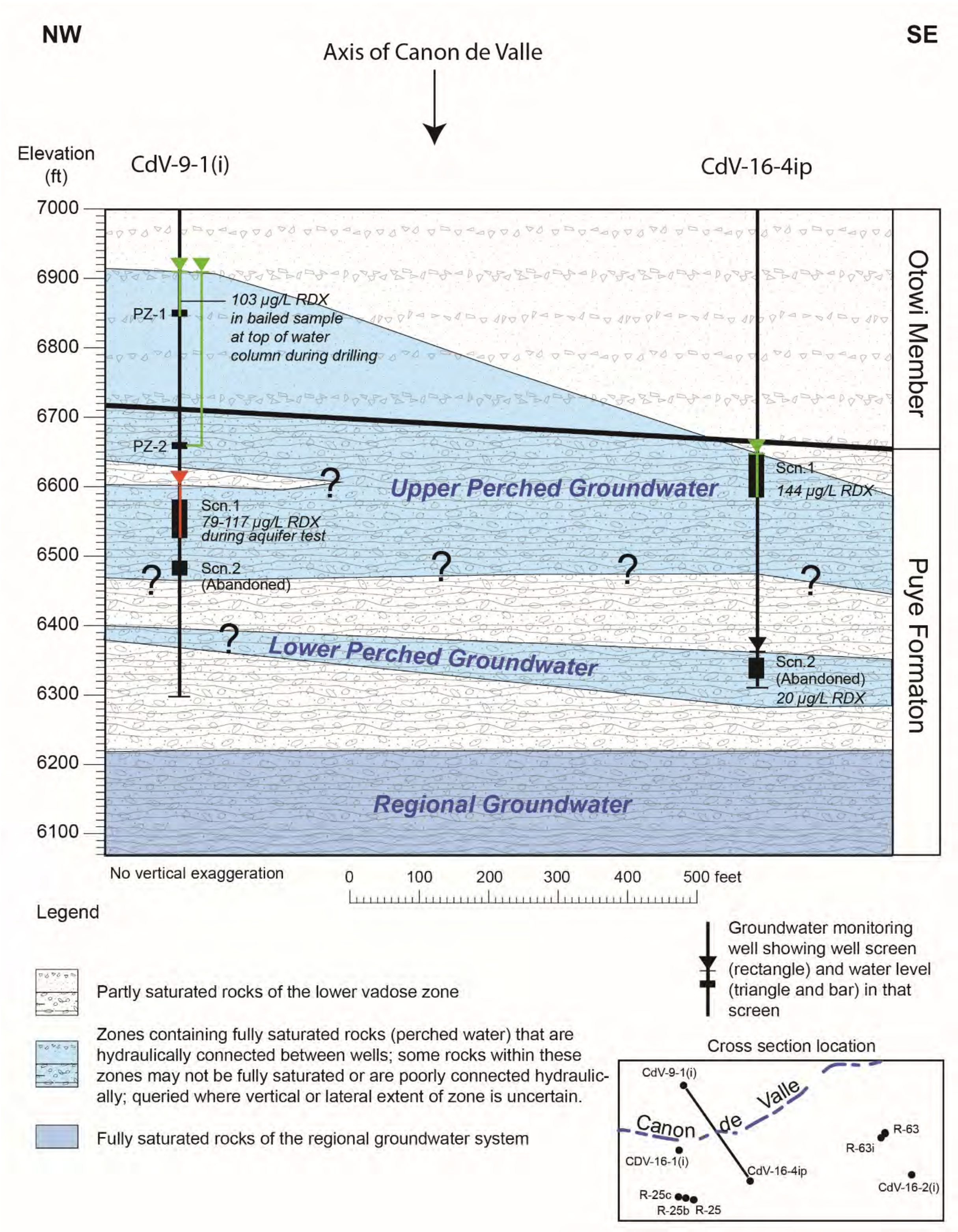

Figure 3.6-2 Northwest-southeast geologic cross-section for the lower part of the vadose zone showing geologic contacts and groundwater occurrences in wells CdV-9-1(i) and CdV-16-4ip

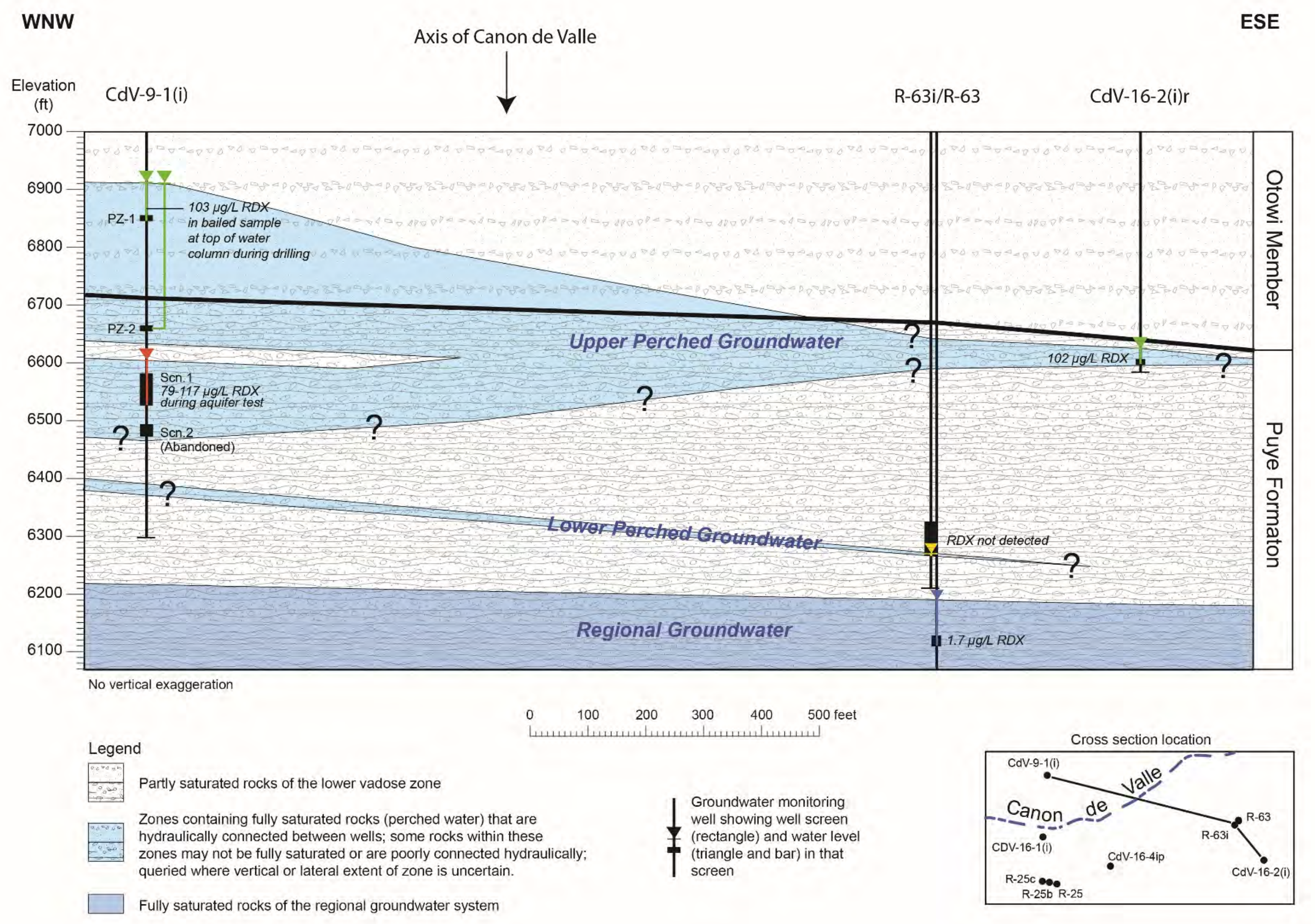

Figure 3.6-3 West-northwest to east-southeast geologic cross-section for the lower part of the vadose zone showing contacts and groundwater occurrences in wells CdV-9-1(i), R-63i, R-63, and CdV-16-2(i)r

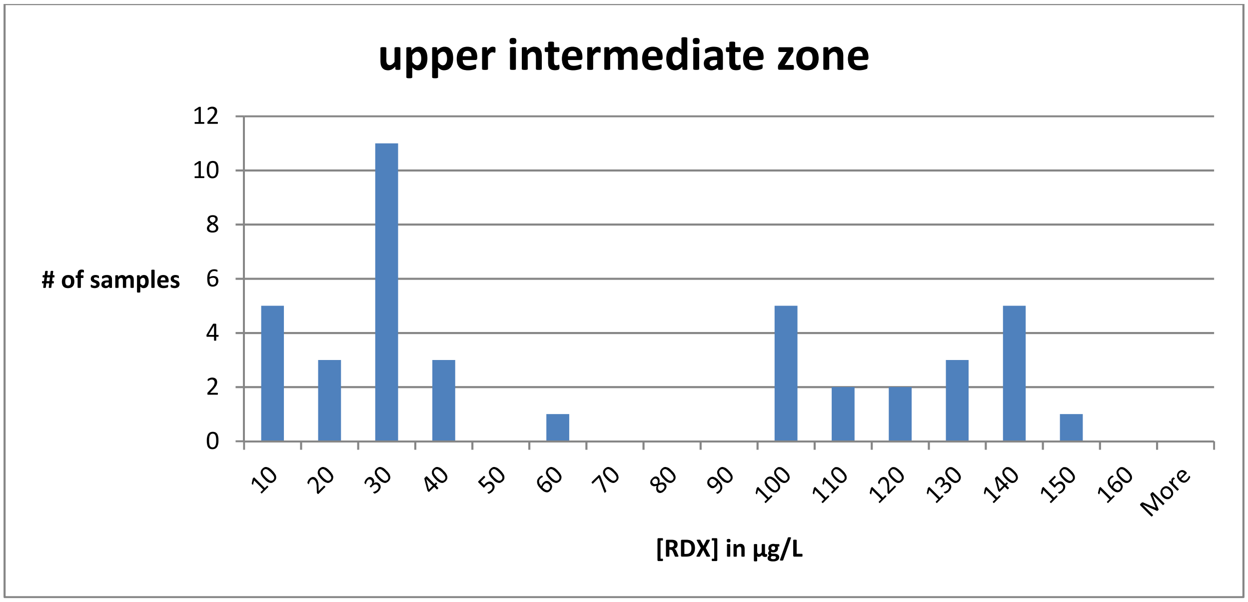

Figure 3.6-4 **Histogram showing RDX concentrations in intermediate groundwater**

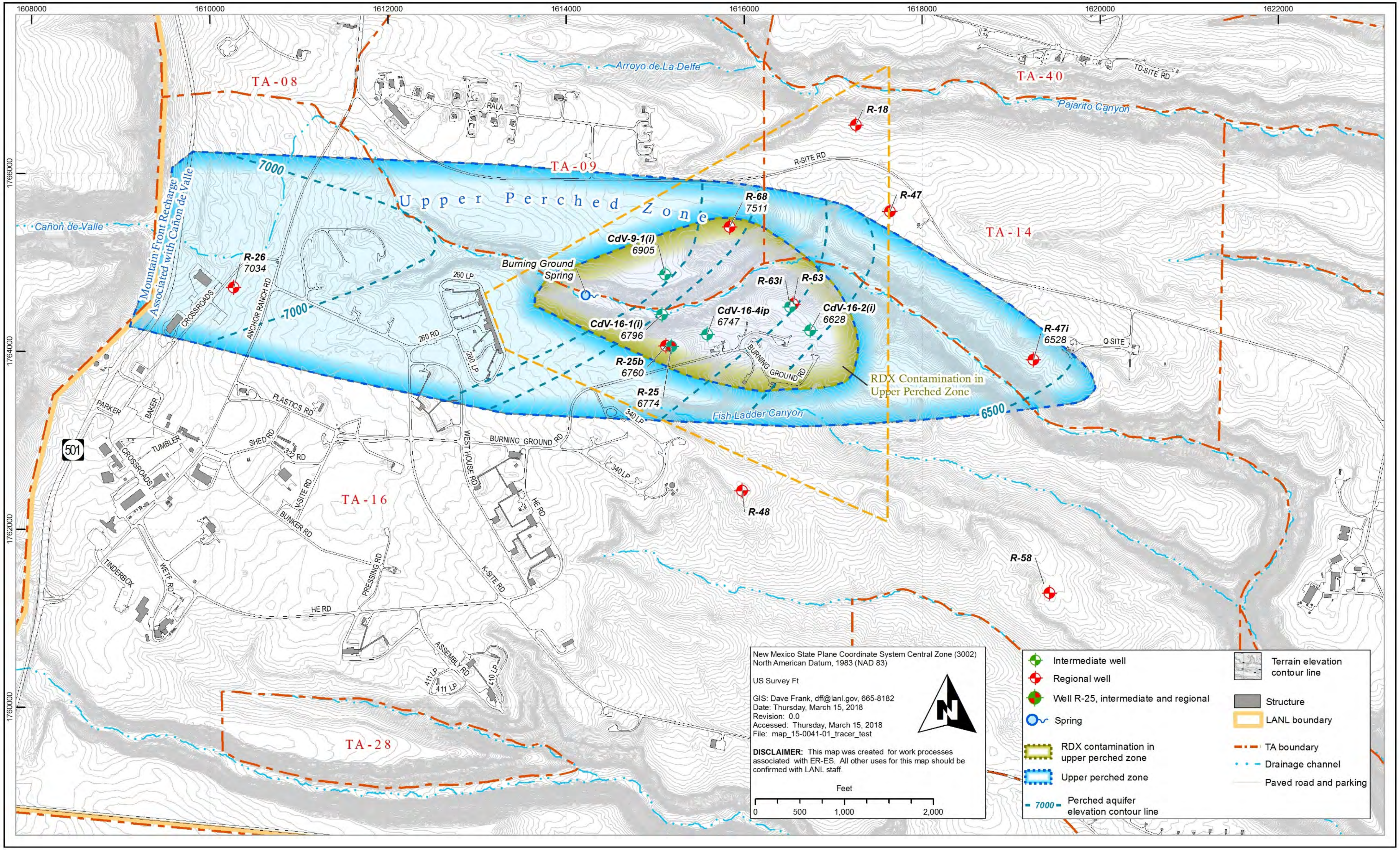

New Mexico State Plane Coordinate System Central Zone (3002)
North American Datum, 1983 (NAD 83)

US Survey Ft

GIS: Dave Frank, dff@lanl.gov, 665-8182
Date: Thursday, March 15, 2018
Revision: 0.0
Accessed: Thursday, March 15, 2018
File: map_15-0041-01_tracer_test

DISCLAIMER: This map was created for work processes associated with ER-ES. All other uses for this map should be confirmed with LANL staff.

Figure 3.6-5 Contaminated groundwater zones within TA-16. Orange dashed line represents assumed regional contaminated zone. Green inner zone is extent of RDX contamination in perched zone (LANL 2015).

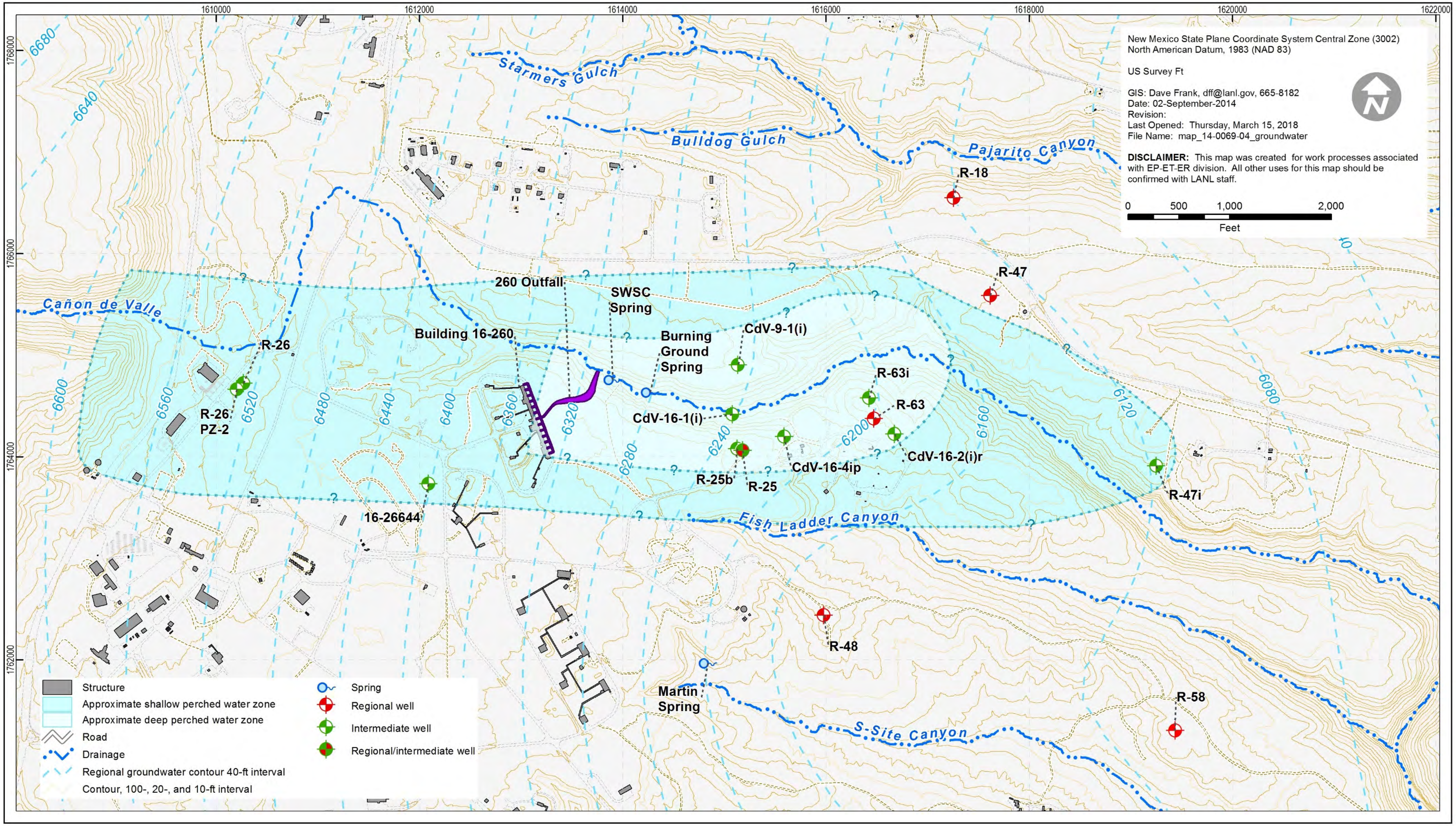

Figure 3.6-6 Map showing approximate extent of perched-intermediate zones at TA-16

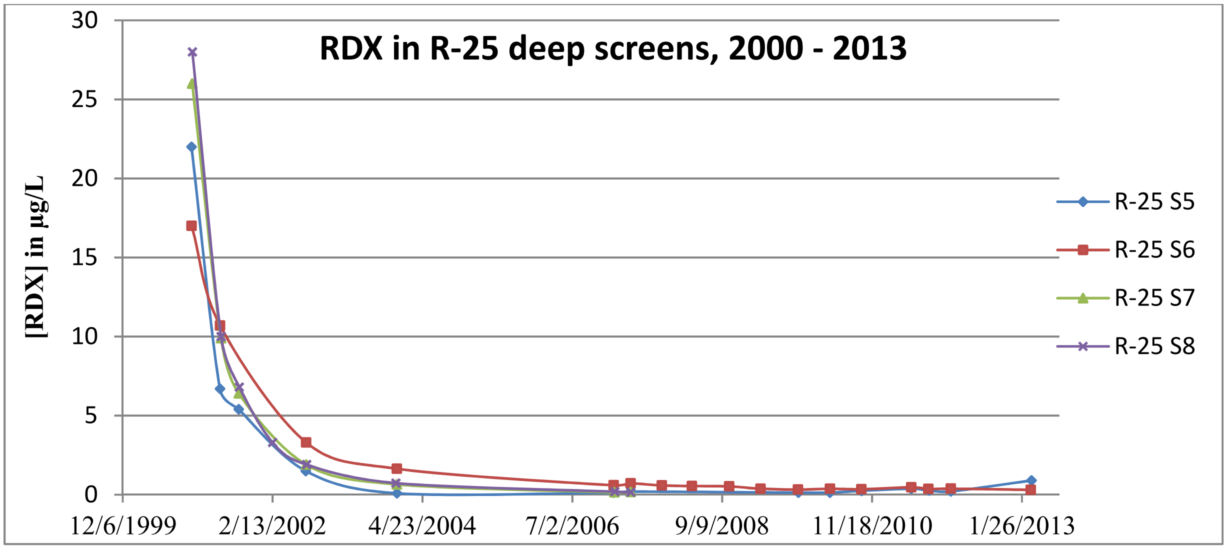

Figure 3.7-1 RDX concentrations in well R-25 screens in regional groundwater

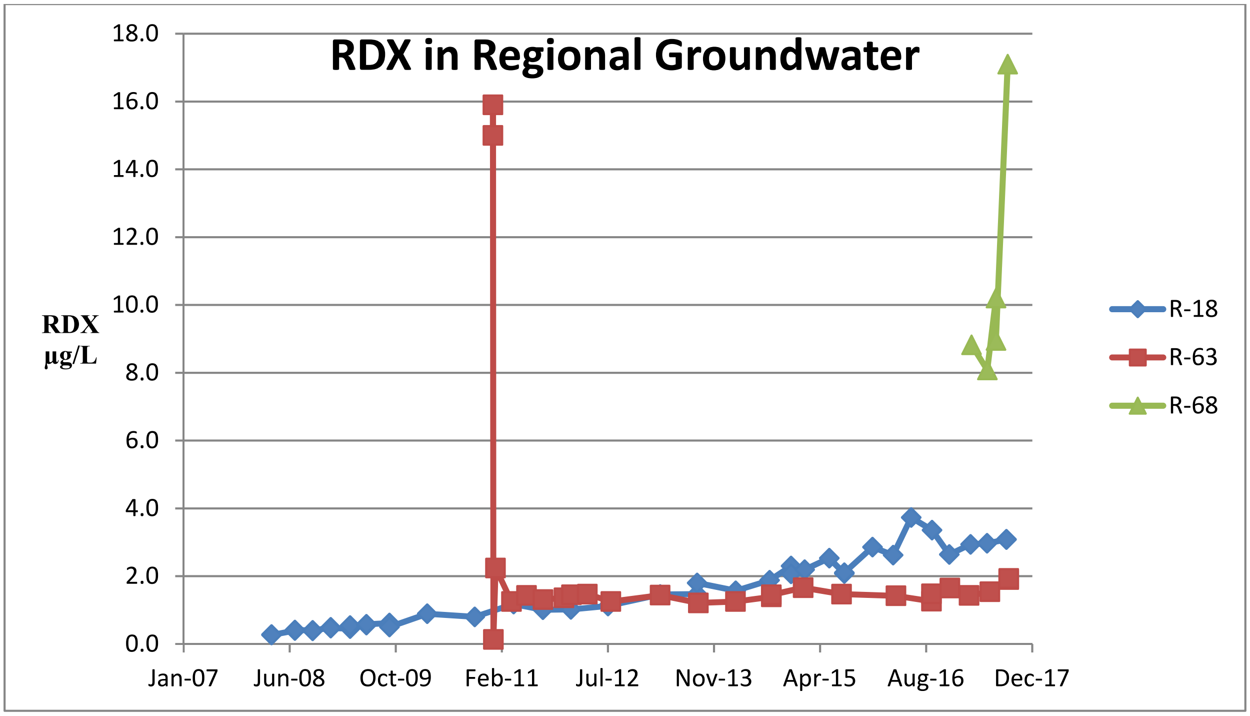

Figure 3.7-2 Regional well RDX concentrations over time

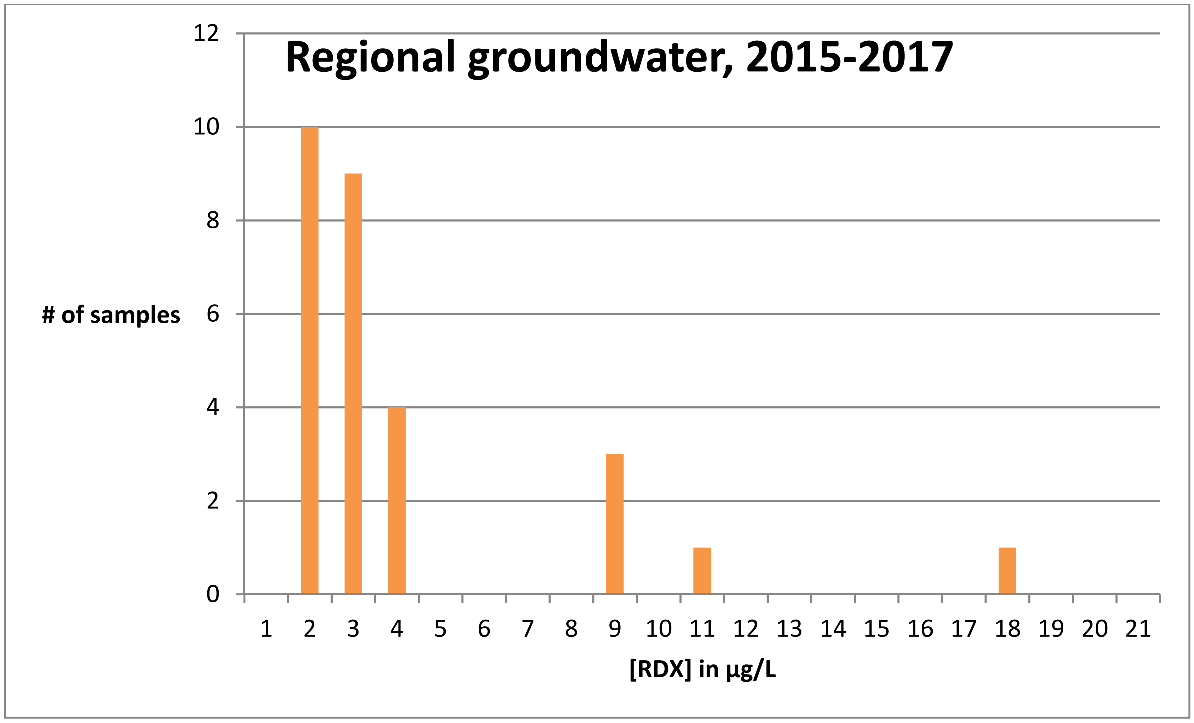

Figure 3.7-3 Histogram showing RDX in three regional wells over time

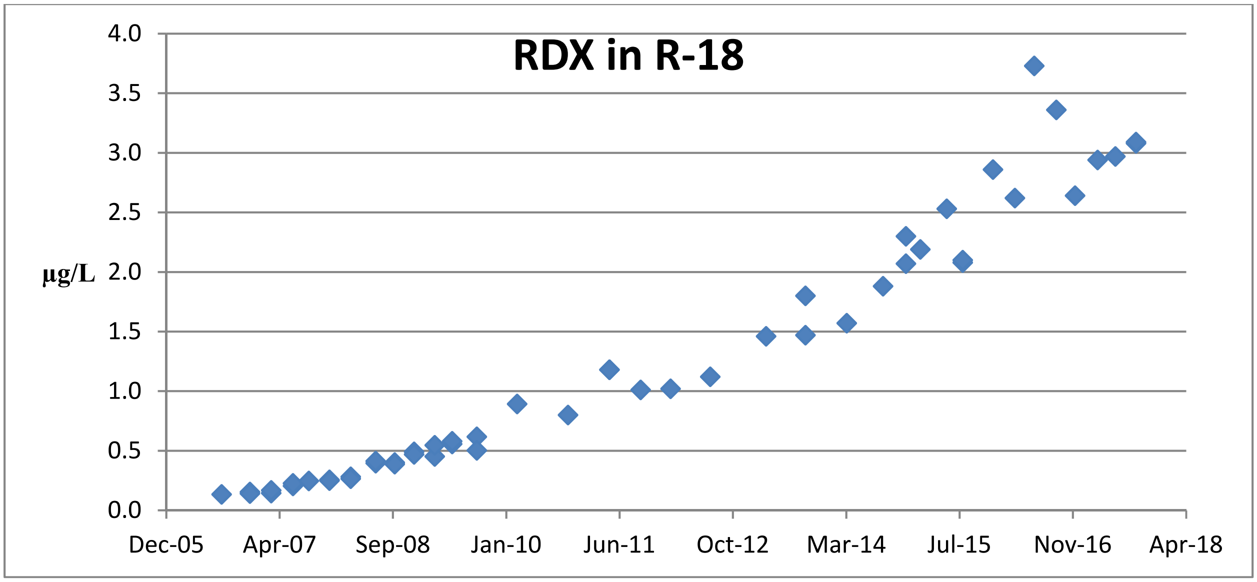

Figure 3.7-4 RDX concentrations in R-18

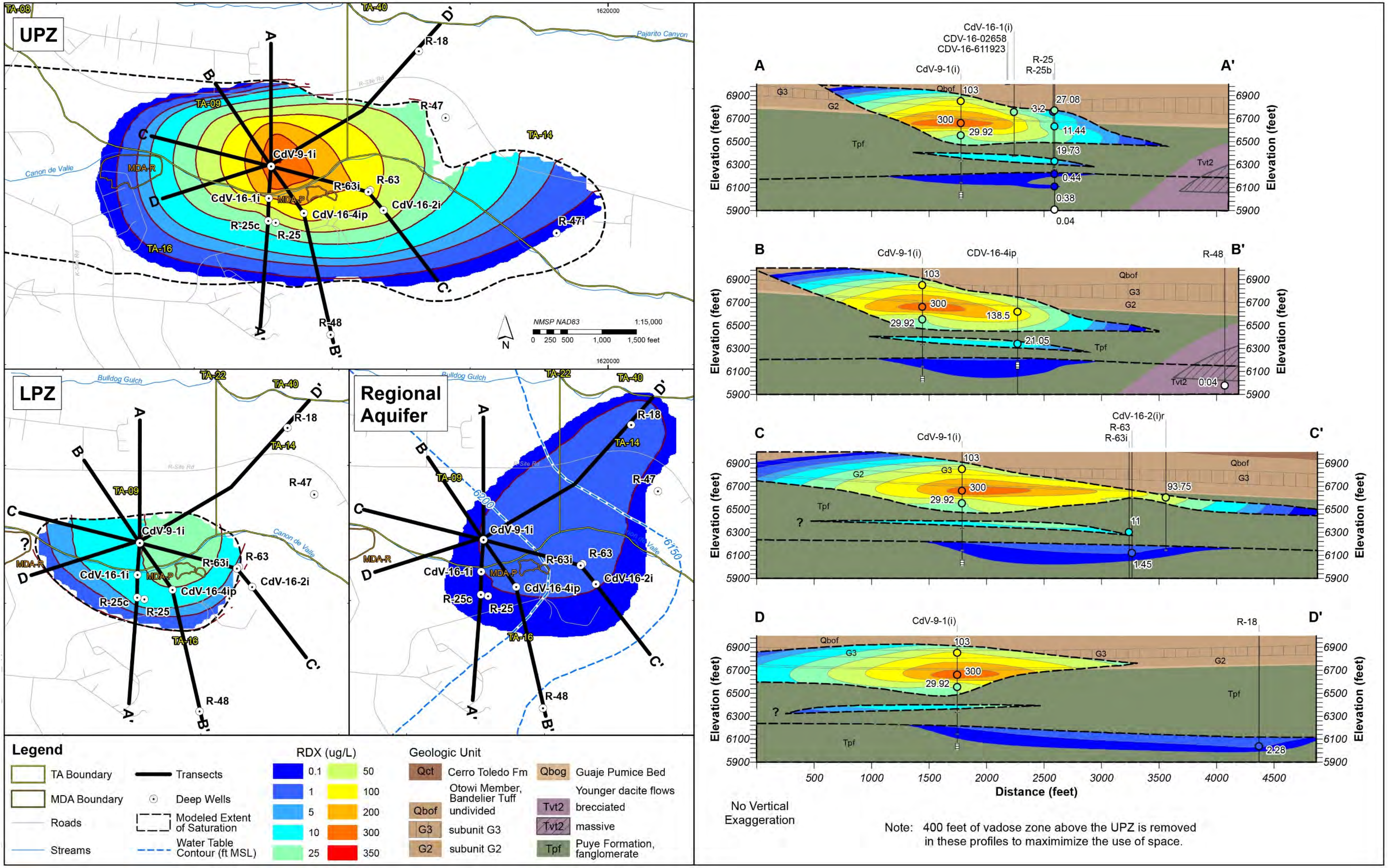

Figure 5.0-1 Example of 3-D RDX interpolation (from Weston 2016)

Table 1.0-1
Estimated Ranges of Total RDX Inventories in Hydrologic Components, 2005

Location	Maximum Mass of RDX (kg)	Minimum Mass of RDX (kg)
260 Outfall former settling pond area, after interim measure	650	650
Vadose zone directly under 260 Outfall former settling pond area	4311	234
SWSC and Burning Ground Springs	482	3
Cañon de Valle alluvial sediments	5	5
Vadose zone under Cañon de Valle alluvial aquifer	3724	17
Intermediate to regional groundwater (747–1132 ft)	8109	476
Regional groundwater (1286–1942 ft)	6053	135
Total	**23,334**	**1520**

Source: LANL 2006, 093798.

Table 3.0-1
RDX Inventory Summary for 2005 and 2017

Location	Maximum (2005) kg	Minimum (2005) kg	Maximum (2017) kg	Minimum (2017) kg	Maximum % Change	Minimum % Change
260 Outfall former settling pond area, after interim measure	650	650	644	644	-0.9%	-0.9%
Vadose zone directly under 260 Outfall former settling pond area	4311	234	940	545	-78.2%	132.9%
SWSC and Burning Ground Springs	482	3	56	33	88.4%	1000.0%
Cañon de Valle alluvial sediments	5	5	10	5	100.0%	0.0%
Vadose zone under Cañon de Valle alluvial aquifer	3724	17	64	8	-98.3%	-52.9%
Intermediate to regional groundwater (228–345 m)	8109	476	1478	263	-81.8%	-44.7.0%
Regional groundwater (392–438 m)	6053	135	415	35	-93.1%	-74.1%
Total	**23,334**	**1520**	**3608**	**1533**	**-84.5%**	**0.9%**

Table 3.6-1
Summary of Intermediate Groundwater Well Samples

Well Screen	# of Samples	Time span of Sampling	Screen depth (ft)	Most Recent (RDX)
CdV-16-4ip S1	10	1/2015–8/2017	815.6-879.2	134 µg/L
CdV-16-2(i)r	9	1/2015–8/2017	850-859.7	99.1 µg/L
CdV-16-1(i)	9	5/2015–9/2017	624-634	27.5 µg/L
R-25b	5	1/2015–3/2017	750-770.8	0.324 µg/L
CdV-9-1(i)	8	5/2015–8/2017	937.4- 992.4	20 µg/L

Notes: The median from this data set is 37.3 µg/L. The first quartile value is 25.4 µg/L, and the third quartile value is 111 µg/L. To calculate the maximum and minimum masses of RDX in the intermediate zone, the third quartile and first quartile concentrations, respectively, were multiplied by the estimated maximum and minimum volumes for pore water in the zone.

Table 3.7-1
Summary of Regional Groundwater Well Samples

Well screen	# of samples	Time span of Sampling	Screen depth (ft)	Most recent [RDX]
R-18	13	1/2015-8/2017	1358–1381	3.09 µg/L
R-63	10	1/2015-9/2017	1325–1345.3	1.93 µg/L
R-68	5	3/2017-9/2017	1340–1360.4	17.1 µg/L

Notes: The maximum concentration seen in R-68, 17.1 µg/L, was used to estimate maximum RDX mass in the regional zone. The median of all 28 samples, 2.58 µg/L, was used to estimate the minimum RDX mass in the regional zone.

Table 5.0-1
Comparison of 2017 Simple Geometry and Geostatistically Based Inventories

Location	Simple Geometry Minimum (kg)	Simple Geometry Maximum (kg)	Geostatistical Minimum (kg)	Geostatistical Maximum (kg)
260 Outfall former settling pond area, after interim measure	644	644	na*	na
Vadose zone under 260 Outfall former settling pond area	545	940	na	na
SWSC and Burning Ground Springs	33	56	na	na
Cañon de Valle alluvial sediments	5	10	0.16	0.16
Vadose zone under Cañon de Valle alluvial aquifer	8	64	NA	NA
Intermediate groundwater (228–345 m)	263	1478	650	1581
Regional groundwater (392–438 m)	35	415	1.8	8.5
Total	**1533**	**3608**	**na**	**na**

* na = Not available.

LA-UR-18-21326
March 2018
EP2018-0019

Geology of Technical Area 16 and Vicinity, Los Alamos National Laboratory

Attachment 2

Prepared by the Associate Directorate for Environmental Management

CONTENTS

Figures

Appendixes

1.0 INTRODUCTION

This report describes geologic investigations in Technical Area 16 (TA-16) and vicinity in the southwest corner of Los Alamos National Laboratory (LANL or the Laboratory) between the Pajarito fault zone and the confluence of Cañon de Valle and Water Canyon. These studies were undertaken to support the RDX (hexahydro-1,3,5-trinitro-1,3,5-triazine) investigation to evaluate corrective actions and remedial alternatives for contaminated groundwater associated with high explosives (HE) releases from Consolidated Unit 16-021(c)-99 (also known as the 260 Outfall). Figure 1.0-1 shows the location of TA-16 with respect to other Laboratory TAs, the location of the 260 Outfall, and the locations of wells discussed in this report.

The 260 Outfall is the primary source of HE contamination that impacted groundwater at TA-16 (LANL 2011c). The 260 Outfall released large quantities of contaminants, particularly RDX, at high concentrations and large volumes of water that provided a significant hydrologic driving force for infiltration of contaminants (LANL 2011c; LANL 2012). Based on the extent of perennial surface water and alluvial groundwater, the main infiltration pathway for contaminated water in Cañon de Valle is located downcanyon of the 260 Outfall and extends east to the vicinity of Material Disposal Area (MDA) P (LANL 2011c). Infiltration of surface water and alluvial groundwater into bedrock units results in the vertical and lateral transport of contaminants through bedrock units of the vadose zone. Contaminated recharge has reached two deep perched groundwater zones downgradient of the 260 Outfall; these two perched zones are important contaminant pathways and are possible sources of recharge to the regional aquifer.

Major uncertainties in the site conceptual model for TA-16 include recharge pathways for HE-contaminated groundwater through the vadose zone and the areal extent of deep perched groundwater near Cañon de Valle (LANL 2011c; LANL 2012). This work addresses uncertainties in the current site geologic model about the distribution, thickness, and properties of key geologic units that make up the vadose zone and upper regional aquifer. During unsaturated conditions, water percolating through the vadose zone is likely to be diverted laterally at capillary barriers associated with bedding contacts. Similarly, perching horizons for perched groundwater systems are generally thought to be stratigraphically controlled. If correct, the direction of groundwater flow is controlled by the dip of bedding planes at the contacts and within the major stratigraphic units. The focus of this work is to improve the site geologic model and to provide a summary of site geologic conditions at TA-16 with an emphasis on geologic features such as fractures and bedding orientations that influence groundwater pathways and flow directions.

This work supports the optimal placement of monitoring wells and provides information to help constrain the nature and extent of HE-contaminated deep perched groundwater. Assessment of potential remedial alternatives requires the integration of geology, structure, hydrology, and geochemistry to understand aquifer conditions, hydraulic properties, groundwater flow, and contaminant properties. Geological and structural data are critical components of the site conceptual model and provide an overall framework for planning groundwater remediation strategies.

1.1 Report Organization

This report is divided into three major sections that describe the scope of work, the methods used to address and resolve the issues, and a geological synthesis that describes and integrates the stratigraphic units within the context of the tectonic/structural and volcanic settings at TA-16. Section 1 presents a brief narrative about the scope of work and identifies the geologic tasks undertaken to refine the conceptual model that is required to understand groundwater pathways. Section 2 details issues related to determining the correct stratigraphic contacts of the major lithologic units, describes field and laboratory methods used, and provides a detailed description of the internal bedding features of the Otowi Member of the Bandelier Tuff, described herein for the first time. Section 3 summarizes the regional geologic setting, provides descriptions of the stratigraphic units, and describes important structural features that may influence recharge and groundwater movement within the RDX investigation area.

The appendixes of this report provide supporting information and are intended to serve as a reference for future studies in this area. Appendix A provides lithologic descriptions of SHB-3 core, photographs of fault gouges from different depth levels of SHB-3, whole-rock geochemical data from x-ray fluorescence (XRF), electron microprobe analysis of selected pumices from the volcanic units intersected in SHB-3, and variation diagram plots of major and trace elements versus depth for SHB-3 samples. Appendix B provides laser ablation inductively coupled plasma mass spectrometry (LA-ICP-MS) results of pumice samples analyzed from nine wells and the SHB-3 core hole. Appendix C contains structure contour maps for the major stratigraphic units at TA-16. Appendix D discusses the Anchor Ranch graben, a subsidiary structure of the Pajarito fault system crossed by Cañon de Valle. Appendix E provides a table that summarizes borehole porosity measurements determined by geophysical logs for each geologic unit in well R-26. Appendix F contains a report by Weston, Inc., that summarizes updates to the WC15c three-dimensional (3-D) geologic framework model that was developed in 2016. Appendix G contains a table of geologic contacts for wells at TA-16 and vicinity.

1.2 Scope of Work

Several tasks were identified to help refine the TA-16 conceptual model for RDX and other subsurface contamination, inform placement of future regional groundwater monitoring wells, and guide assessment of remedial alternatives. These tasks focused on compilation and review of geological, structural, and geophysical logging data from new and existing boreholes. Specific tasks are described below.

- Stratigraphic contacts of some rock units intersected in wells at TA-16 and the surrounding area are not firmly established. Drill cuttings and cores of key stratigraphic units from selected wells were reexamined, and contacts of geologic units were confirmed using geochemical and geophysical data.
- Once contacts were reliably established, they were used to generate structure contour maps of major stratigraphic units and internal bedding surfaces. Bedding orientations of the various rock units influence infiltration pathways through the vadose zone and flow directions in perched groundwater.
- The revised information on stratigraphic contacts and internal bedding orientation was used to update structural features (e.g., faults, grabens, fractures, etc.) and dips along and beneath Cañon de Valle. Finally, east-west and north-south geologic cross-sections were generated from the geologic framework model to show the distribution and orientation of the units in the Cañon de Valle area.

Field and laboratory methods were used to resolve the issues related to stratigraphic contacts, internal bedding orientations, and structural features in the surface and subsurface environments in the vicinity of TA-16. For example, a field survey of the north and south walls of Cañon de Valle between wells CdV-9-1(i) and R-63 was conducted and positively confirmed the published lithologic types, stratigraphic contacts, and structural features. To resolve issues encountered in the placement of stratigraphic contacts, several pumice samples from drill cuttings and core were selected from nine wells and one core hole for major and trace element analyses using LA-ICP-MS. This method generates semiquantitative values of major and trace elements from individual pumice clasts for use in chemical fingerprinting and cross-well correlations using elemental ratios. The SHB-3 core hole, drilled for paleoseismic hazard investigations and located about 1.3 mi to the west of Cañon de Valle, serves as an important reference section for the subsurface geological and structural studies of TA-16 and vicinity. Cores from the SHB-3 were carefully reexamined to ascertain the type of rocks, contacts, and associated structural features for comparison with drill-hole cuttings from other wells in the vicinity of Cañon de Valle (Appendix A). The refined stratigraphic contact information was then used to update the 3-D geological framework model of the TA-16 site.

2.0 SUMMARY OF GEOLOGIC TASKS AT TA-16

The geological tasks highlighted above were investigated in detail to establish reliable surface and subsurface lithologic contacts for identifying internal bedding surfaces and orientations and to determine structural dips of the bedding planes at TA-16. Each of these criteria is discussed in the following sections.

2.1 Qct-Qbof Lithologic Contact Criteria

Despite differences in lithologic types, the stratigraphic contact between the Cerro Toledo Formation (Qct) and the Otowi Member ash-flow tuff (Qbof) has not been easy to delineate in most TA-16 wells because of the poor quality of the drill cuttings resulting from the loss of textural information as well as the winnowing of fines, grinding of cuttings, and mixing of the Qbof and Qct units along the contact. Unit Qct is mostly composed of alluvial sediments, whereas Qbof represents a primary ash-flow tuff deposit. However, both units contain variable amounts and clast sizes of pumices in a glassy matrix. The Qct pumices are generally reworked, subrounded to rounded, and lightly coated with tuffaceous sediments that make up the matrix. Quartz and feldspars are the dominant minerals and are generally fine-grained and sparse compared with the abundant and coarse primary minerals present within the underlying Qbof. The Qbof ash-flow tuff is a nonwelded and fairly consolidated primary deposit with inflated light gray pumice clasts in a glassy matrix. The tuff contains abundant coarse quartz and feldspar grains and minor dacite lava clasts. The top of the Qbof is generally partially weathered and forms a reddish-orange layer. In outcrop, the contact is clearly defined by lithologic variations and sedimentological features. For example, at the Camp Hamilton Trail section located north of the Laboratory in Pueblo Canyon on the east side of the Los Alamos Airport, massive Qbof ash-flow tuff underlies bedded, sorted, and clast-supported pumice fallout assigned to Qct. In the SHB-3 core hole, about 1.3 mi west of Cañon de Valle, the Qct-Qbof contact is at the 408.5-ft depth (Figure 1.0-1, Appendix A). In descending stratigraphic order, the lowermost part of Qct consists of a light gray moderately consolidated tuff, white pumice-rich bed, and a light brownish-gray reworked pumice deposit. In contrast, the underlying Qbof consists of partially weathered ash-flow tuff containing coarse inflated pumice clasts with rusty stain patches in a poorly sorted, glassy matrix that is underlain by devitrified ash-flow tuff. In well R-26, located about 0.72 mi north of SHB-3, the Qct-Qbof contact occurs at the 662-ft depth and is marked by bedded alluvial sands of Qct capping massive ash-flow tuff (Qbof).

Drill cuttings from several wells in the vicinity of Cañon de Valle were reexamined using a binocular microscope to redefine the Qct-Qbof contact. In most cases, the criteria used to define the Qct-Qbof contact varies by location. In general, the following factors, including color variation of pumices and associated matrix, the amount and size of crystals, pumice morphology, abundance and types of lithic fragments, types of matrix and degree of sediment coating on minerals and lithic fragments, presence or absence of perlite and obsidian, and type of lithology, are used to establish the contact. For example, at the R-47 well, the Qct-Qbof contact is at the 445-ft depth, and Qct consists of brown and wood chip–like pumice fragments mixed with abundant lithic clasts. The underlying Qbof is also lithic-rich and contains dacite lava fragments, inflated gray pumice, and no wood chip–like pumice clasts. The Qct-Qbof contact in well R-63, located about 0.3 mi southwest of R-47, is at about the 410-ft depth. Reworked tuff, containing grayish-orange poorly sorted pumice clasts mixed with minor dacite and perlite fragments in a tuffaceous matrix defines the base of Qct. The top of the Qbof is a lithic-rich ash-flow tuff. The abundant dacite and pumice clasts are lightly coated with grayish-orange tuffaceous silt. The contact at the CdV-9-1(i) well closest to the 260 Outfall occurs at the 450-ft depth. The Qct unit (420–450-ft depth) is lithic-rich and contains partially rounded pumice clasts mixed with minor minerals and dacite, devitrified tuff, and scoria fragments. In contrast, the uppermost part of the Qbof (450–598-ft depth) consists of grayish-orange pumice mixed with abundant dacite clasts and minerals.

2.2 Use of Chemical Signatures to Define Lithologic Contacts

The Qct-Qbof contact in select wells in the vicinity of TA-16 was verified using chemical fingerprinting of pumice clasts collected above and below the contact zone. Fifty-six samples of pumice were selected from various stratigraphic levels in nine wells [CdV-9-1(i), CdV-16-3i/R-48, CdV-16-4ip, CdV-R-15-3, R-18, R-26, R-58, R-63, and R-25] and one core hole (SHB-3) for LA-ICP-MS analysis (Appendix B, Table B-1.0). LA-ICP-MS is a new semiquantitative technique that generates major and trace elemental values by performing several laser scans of individual pumice grains. A full description of the technique, along with a list of samples and table of results, is provided in Appendix B. Ratios of LA-ICP-MS major and trace elemental results were plotted against stratigraphic position to verify the proposed lithologic contacts within the selected wells and to identify potential cross-well correlations (Figure 2.2-1). Plots were created using GCD Kit software (available at http://www.gcdkit.org/). Elemental ratios of Fe/Ti, U/Ti, Th/Ti, and Zr/Ti appeared to be the most useful for distinguishing between Qct and Qbof pumices (Figure 2.2-2). The Qct samples generally contain lower elemental ratios than the Qbof samples. There is high confidence in the assignment of samples to the Qct at SHB-3 because the availability of core from SHB-3 allows observation of in situ textural relations between rock components and removes the issues with mixing that occur with cuttings. In addition, the Qct sample set from SHB-3 spans the full interval of the Qct deposits within this core hole. Thus, the SHB-3 samples provide the most robust data for defining the “Cerro Toledo compositional field” shown in Figure 2.2-2. The value of chemical fingerprinting is apparent in Figure 2.2-2 where several pumice samples initially assigned to the Qct during sample selection plot outside the “Cerro Toledo compositional field,” whereas a few samples initially assigned to the Qbof during sample selection plot within the “Cerro Toledo compositional field.” Samples obtained from drill cuttings could plot incorrectly because of (1) erroneous assignment of the Qct-Qbof stratigraphic contact, (2) mixing of samples as a result of drilling processes, or (3) reworking of Qbof into the Qct, resulting in compositional overlap. SHB-3 sample “a” at the 403.5–408.5-ft depth below ground surface (bgs) and sample R-25_498_b at the 498-ft depth bgs are examples of Qbof pumices that have been reworked into Qct deposits. Refinement of geologic contacts based on these plots is in progress.

The LA-ICP-MS data for SHB-3 are augmented by electron microprobe (EMP) and XRF data previously analyzed by the seismic hazards program (Gardner et al. 2001); the data are presented in Appendix A. The EMP major element composition of glass shards from various stratigraphic levels exhibit discrete chemical compositions that allow confident placement of the contact between Qct and Qbof (Figure 2.2-3) and are useful for cross-well correlations. Extraction of additional core should be considered when planning future wells to allow the expansion of this chemical correlation framework for defining the Qct-Qbof contact with greater confidence across the RDX investigation area.

2.3 Internal Bedding in the Otowi Member, Bandelier Tuff

This section describes stratification within the Otowi Member and examines how this stratification may influence groundwater pathways in the subsurface of the TA-16 site. Well R-26 is used as a type section for the Otowi Member to describe lithologies and bedding characteristics that give rise to stratification. The section also posits a new approach to mapping bedding orientations in the tuffs based on the identification and correlation of key marker horizons between wells using geophysical data. Structure contour maps were prepared for key subunits of the Otowi Member most closely associated with deep perched groundwater in the RDX investigation area. In the following discussion, the TA-16 site refers to the area between the Pajarito fault system and confluence of Cañon de Valle and Water Canyon. The RDX investigation area refers to the area where active investigations are underway to characterize HE-contaminated perched groundwater in the vicinity of wells such as R-25, CdV-9-1(i), and CdV-16-4ip.

The Otowi Member of the Bandelier Tuff is a regional tuff sheet made up of multiple rhyolitic flow units with a cumulative thickness up to 430 ft (131 m) thick in the TA-16 site. A flow unit represents deposits laid down by a single pyroclastic flow and can usually be subdivided into layers with differing characteristics that reflects processes operating within the flow (Sparks 1976; Wilson 1986). Outcrops of Otowi Member contain as many as 20 individual flow units 3 to 20 m thick south and southeast of the Valles Caldera (Potter and Oberthal 1987).

Otowi Member tuffs form a significant portion of the vadose zone in the RDX investigation area and include both unsaturated and saturated layers (LANL 2011c). Modeling activities commonly treat these tuffs as a single, homogenous hydrogeologic unit with isotropic properties. This classification works well for many modeling applications because the individual tuff deposits making up the unit are highly porous, nonwelded, vitric tuffs that have similar physical, chemical, and mineralogic properties, especially when compared with subjacent lithologically complex units such as the Tshirege Member and Puye Formation.

However, stacking of individual flow units results in widespread stratification within the Otowi Member, with the potential to affect hydrologic properties such as vertical anisotropy and preferred groundwater pathways. Individual tuff beds are volcaniclastic deposits made up of poorly sorted pumices, crystals (silicate minerals), and lithic fragments supported by a matrix of glassy volcanic ash, except in the case of SHB-3, where a portion of the ash-flow tuff is devitrified (Appendix A, Lithologic Descriptions). Flow dynamics during transport and emplacement of flow units commonly result in grain-size variations within and between tuff beds (Sparks 1976; Fisher and Schmincke 1984; Wilson 1986). Clasts in some individual tuff beds are vertically and laterally graded in size as fine ash, pumices, and lithics become segregated and concentrated within flow units (Sparks 1976, 601887; Wilson 1986, 601888). In some cases, thin co-ignimbrite sandy surge deposits or fine ash falls are deposited below or on top of pyroclastic flows. Grain-size and textural variations between flow units can result in abrupt changes of hydrologic properties at bed contacts.

Capillary barriers may form under unsaturated conditions in layered, porous soils and formations (Miyazaki 1988; Ross 1990). Capillary barriers occur in tuffs at layer contacts where a unit with relatively small pores or fractures overlies a unit with relatively large pores or fractures (Montazer and Wilson 1984). Modeling results for Paintbrush nonwelded tuffs at Yucca Mountain, Nevada, a unit similar to the Otowi Member (Qbof) and Cerro Toledo Formation (Qct), demonstrate that significant lateral flow can develop in the presence of layered rock that exhibits contrasting fracture-matrix hydraulic properties, low percolation flux, and sloping layer interfaces (Wu et al. 2002). Fractures and faults are potential downward pathways for laterally diverted percolation flows.

2.3.1 The Otowi Member in Well R-26

A lithological log for well R-26 was prepared to document bedding features of the Otowi Member (Figure 2.3-1). Well R-26 was selected as a type section for describing the Otowi Member because borehole geophysical logs, collected by Schlumberger, Inc., are unusually complete and include a formation microimager (FMI) log that was especially important for identifying bedding characteristics and rock textures. FMI logs are rarely available for the Otowi Member because such logs require fluid-filled boreholes. The Otowi Member is typically well above fluid levels in boreholes (typically the regional water table) except in rare circumstances where drilling is terminated before perching horizons (e.g., well CdV-16-1i) are penetrated. In the case of well R-26, fluid levels were unusually high during logging because the borehole was drilled by mud-rotary methods. The mud-filled borehole allowed FMI imaging of the basal Tshirege Member and all of the underlying rock units, including the Otowi tuffs.

2.3.1.1 Revision to Unit Contacts

Before bedding characteristics for the Otowi Member (Qbof) are described, information about revisions to unit contacts in well R-26 is presented. The lithologic log in the well completion report for well R-26 placed the upper and lower contacts for the Otowi Member at depths of 865 ft and 955 ft bgs, respectively (Kleinfelder 2004), resulting in a unit thickness of only 90 ft. Upper and lower contacts for the overlying Cerro Toledo Formation (Qct) were placed at depths of 472 ft and 865 ft bgs, respectively (Kleinfelder 2004), resulting in a unit that is unusually thick (393 ft). In the R-26 well completion report, the contact between the Qct and Qbof was placed at the 865-ft depth to assign all stratified deposits, including a thick sequence of dacitic boulders and gravels in the 778.4–826-ft interval in the Qct. Stratified deposits, including dacitic boulders and gravels, are found in Qct deposits at other locations but have not been described for the Qbof. However, based on reexamination of the FMI and other geophysical logs, the contact between the Qct and Qbof can be placed at a depth of 662.4 ft bgs (Figures 2.3-1, 2.3-2, and 2.3-3). This marks the top of a 110-ft-thick stratigraphic sequence identified as nonwelded ash-flow tuffs based on bedding and textural characteristics that are similar to ash flows in subunit Qbt 1g of the Tshirege Member and the base of Qbof at well R-26. Similar bedding and textural characteristics are also found in a partial FMI log for the Qbof at well CdV-16-1i. This thick sequence of nonwelded ash-flow tuffs is assigned to the Qbof because the Qct in this area contains only alluvial deposits and intercalated ash and pumice falls.

Placing the upper Qbof contact at the 662.4-ft depth means that dacitic clastic deposits found in the 778.4–826-ft interval represent a 47.6-ft-thick sedimentary sequence intercalated in the Otowi tuffs. Alluvial deposits have not been described for the Qbof by other researchers. In R-26, the unusual occurrence of these sedimentary units within the Qbof tuffs may be related to the location of the depositional environment near the western margin of the Española basin, adjacent to the steep eastern flank of the Jemez Mountains. Eleven beds of matrix- and clast-supported boulders, cobbles, and pebbles were identified using the FMI logs (Figures 2.3-1 and 2.3-4), suggesting these coarse deposits are the result of alluvial or colluvial processes next to a steep faulted mountain front. Other explanations for these deposits, such as landslides or traction deposits at the base of ash-flow tuffs, are considered unlikely because of their bedded nature. The absence of coarse sedimentary deposits in the Qbof in the RDX investigation area farther to the east indicates this subunit has limited distribution and may be confined to a small area near the Pajarito fault zone.

Coarse-grained dacitic clastic deposits were also found within the lowermost tuffs of the Tshirege Member at well R-26 (Figure 2.3-1). The well completion report for well R-26 placed the top of the Qct at a depth of 473 ft bgs, at the top of a 12-ft-thick sequence of dacitic boulders, cobbles, and pebbles. Based on reexamination of the FMI log, the contact between the Tshirege Member and Qct can be placed at a depth of 505 ft bgs (Figure 2.3-1). This marks the base of an 18-ft-thick nonwelded ash-flow tuff that overlies a 2-ft-thick pumice fall (Tsankawi Pumice Bed). These tuffs underlie the dacitic clastic deposits from 473 to 485 ft bgs. The nonwelded tuff has a unique high natural gamma signature that is characteristic of subunit Qbt 1g throughout the Pajarito Plateau. The dacitic clastic deposits apparently occupy the stratigraphic interval between units Qbt 1v and Qbt 1g of the Tshirege Member.

2.3.1.2 Bedding Characteristics of the Otowi Member

The revised lithological log for the base of the Tshirege Member, Qct, and Qbof in well R-26 was prepared by integrating bedding and textural information from the FMI log with compositional, physical property, and mineralogical information from drill cuttings and the other geophysical logs (Figure 2.3-2). Correlations between the FMI log and other geophysical logs were particularly useful for identifying rock types and stratal boundaries. Drill cuttings also provided useful information about rock types and mineralogy but were affected by mixing of cuttings over a range of depths and sorting of clast sizes when mud was used as the circulation fluid during drilling.

The Qbof at well R-26 is overlain by well-stratified alluvial sands of the Qct (Figure 2.3-3). Spectral gamma and elemental capture survey (ECS) logs indicate the base of the Qct is largely made up of silicic low-gamma sand and is probably rich in quartz (Figure 2.3-2). The base of the Qct is a 1-ft-thick electrically conductive fine-grained deposit that may represent a soil. A sharp contact separates the base of the Qct from massive rhyolitic ash-flow tuffs of the Qbof (Figure 2.3-3).

The Qbof at well R-26 is made up of two tuff sequences separated by coarse sedimentary deposits in the 778.4–826-ft interval (Figure 2.3-1). The upper tuff sequence is 116 ft thick and made up of 12 nonwelded ash flow tuffs 1.1 to 10.6 ft thick. Individual ash-flow deposits are separated by thin sandy layers (possibly surge deposits), ash falls, or horizontal partings that are highlighted by increased electrical conductivity. Contacts between beds are sharp and commonly represent abrupt changes in lithology (e.g., rock texture and pore structure) across stratal boundaries. Figure 2.3-4 is an example of the massive nature of the ash-flow tuffs making up the upper tuff sequence in the Otowi Member.

The lower tuff sequence in the Qbof is 123.7 ft thick and is more heterogeneous than the upper tuff sequence. The lower tuff sequence is capped by two thick (19 ft and 15.1 ft) nonwelded ash-flow tuffs that overlie a 1.8-ft-thick bed, tentatively identified as an ash fall in the 863–864.8-ft depth interval. The ash fall overlies a stack of five nonwelded ash-flow tuffs in the 864.8–930.4-ft depth interval that are 3–21.6 ft thick and separated by very thin sandy layers (possibly surge deposits), ash falls, or horizontal partings. The stacked ash-flow tuffs overlie 10.6 ft of well-stratified deposits in the 930.4–941-ft depth interval (Figure 2.3-5). These stratified deposits include at least nine individual beds that are interpreted as intercalated 0.3–1-ft-thick ash falls and 1–2-ft-thick pumice falls. The base of the lower tuff sequence is made up of two ash-flow tuffs 6.2 ft and 2.8 ft thick that are separated by a horizontal parting (Figure 2.3-6). The two ash-flow tuffs overlie the Guaje Pumice Bed (Qbog).

The Qbog in well R-26 includes thin ash and pumice falls in the 949.7–951.5-ft depth interval and a massive pumice fall deposit in the 951.5–956-ft depth interval (Figure 2.3-6). The Qbog deposits are electrically resistive, suggesting little alteration of the volcanic glass to clay minerals occurs. Unit Qbog overlies the Puye Formation at a depth of 956 ft. The top of the Puye Formation is made up of dacite boulders supported by an electrically conductive silt-rich matrix (Figure 2.3-6). These silt-rich deposits have been observed in other wells in the TA-16 area and may represent a widespread soil horizon (section 3.4-2.4). The silt-rich clastic deposit at the top of the Puye Formation is a potential perching horizon for groundwater in the Qbof and Qbog units.

2.3.1.3 Mapping the Orientation of Bedding in the Otowi Member

R-26 is the only well in the TA-16 area for which complete imaging data of textural and bedding features in the Qbof are available. FMI and downhole video logs provide good quality image data for several wells in the RDX investigation area, but the logs are incomplete because fluid levels were too low for FMI logging of the Qbof and video logs were commonly obscured by drilling-induced coatings that covered borehole walls. Therefore, other geophysical logs (e.g., natural gamma, spectral gamma, and ECS logs) were used to identify bedding features within the Qbof that could be correlated over the RDX investigation area (e.g., Figure 2.3-2).

During the evaluation of the lithological characteristics of rock units in well R-26, spectral gamma logs were used to differentiate between dacitic and rhyolitic rock compositions based on their gross gamma activity and uranium, thorium, and potassium concentrations. Additionally, the spectral gamma logs showed that gamma activity for the rhyolitic tuffs of the Qbof varied as a function of stratigraphic position, becoming more radiogenic towards the bottom of the unit (Figure 2.3-1). The progressive change in gamma activity as a function of stratigraphic position reflects the progressive tapping of a chemically zoned magma chamber during eruption of Qbof tuffs. Chemical zonation is a common characteristic of large-volume silicic tuffs (Lipman et al. 1966; Hildreth 1981) and is well documented for the Bandelier Tuff (Smith and Bailey 1966; Smith 1979; Stix et al. 1988; Stimac et al. 2002; Warren et al. 2007).

The progressive trends towards more radiogenic tuffs with depth in the Qbof include abrupt shifts to higher gamma activity downhole at several depths in TA-16 wells (Figures 2.3-7 and 2.3-8). These abrupt shifts in gamma activity are also found in other wells on the Pajarito Plateau, suggesting these features are widespread and can be used to map correlative subunits within the Qbof. Each gamma shift probably represents a brief hiatus in the Qbof eruption, after which a new batch of magma with a slightly less evolved composition was erupted. Sequences of tuffs bounded by gamma shifts were probably deposited in rapid succession during discrete eruption events. The gamma shifts occur at stratal boundaries and are useful marker horizons for correlating Qbof subunits between wells. Subunits are defined as coerupted tuffs bound by upper and lower marker horizons. Mapping these subunits provides a way to determine bedding orientations in the Qbof deposit.

Subunits in the Qbof are correlated between wells in the TA-16 area using natural gamma, spectral gamma, and ECS logs, where available. The spectral gamma logs collected by Schlumberger, Inc., are particularly useful for correlations because the log responses in American Petroleum Institute (API) units are corrected for borehole conditions and calibrated to industry standards using a calibration pit at the University of Houston. Figure 2.3-7 illustrates how API units were useful in correlating subunits of the Qbof between wells R-26 and R-63. Spectral gamma logs also provide information about uranium, thorium, and potassium concentrations that are useful for identifying chemical variations in rock units. The spectral gamma logs are supplemented by natural gamma logs that record gross radioactive responses of rocks as counts per second. Although not directly comparable to API units, natural gamma logs provide useful information about relative radioactivity and record the same trends as the spectral gamma logs. Correlations of spectral gamma and natural gamma logs between wells are shown as a series of elevation-corrected stratigraphic logs in Figures 2.3-7 and 2.3-8. Correlations of the gamma logs are aided by the relatively dense spacing of wells in the RDX investigation area. Structure contour maps were prepared for the two lowermost marker beds because they host the deep perched groundwater system at TA-16, and their dips may be important indicators of flow direction. Elevations for the two lower marker beds were hand-contoured and the resulting maps digitized by Weston, Inc., for inclusion into the recent update of the 3-D site geologic model (see Appendixes C and F).

For discussion purposes, gamma marker beds are labeled G1 through G7 in Figure 2.3-8. Marker bed G1 is the top of the Qbog, G2 through G4 are marker beds for subunits in the Qbof, G5 is the inferred contact between the Qct and Qbof, G6 is the contact between subunit Qbt 1g of the Tshirege Member and the Cerro Toledo Formation, G7 is the contact between subunits Qbt 1v and Qbt 1g of the Tshirege Member, and G8 is the contact between subunits Qbt 2 and Qbt 1v of the Tshirege Member. The following discussion focuses on correlation of subunits in the Otowi Member. Characteristics of the other stratigraphic units are discussed in section 3.

The sharp increase in gamma activity in the Qbog compared with the underlying Puye Formation reflects higher concentrations of uranium and thorium in the rhyolitic tuffs compared with dacitic fanglomerate. Interestingly, the Qbog has a distinctive low gamma signature relative to overlying Qbof ash-flow tuffs bracketed by the G1 and G2 marker beds (Figures 2.3-7 and 2.3-8). The lower gamma activity in the Qbog relative to overlying tuffs is a characteristic of the TA-16 site; by contrast, in the chromium investigation area near Mortandad Canyon, the Qbog is more radiogenic. More work is needed to understand these relationships, but one possible explanation is that the highly radiogenic ash flows making up the base of the Qbof in the TA-16 site were deposited only in areas proximal to the source caldera and did not reach more distal locations in the central part of the Pajarito Plateau.

The Qbof subunit bracketed by marker beds G1 and G2 represents the most radiogenic tuffs identified in the TA-16 site. These tuffs correlate to a well-stratified sequence of interbedded ash flows, ash falls, and pumice falls at well R-26 that record deposition of small volume units that characterized the initial stages of the Qbof eruption (Figure 2.3-5). The G2 gamma shift at R-26 coincides with a change in eruption style and thick-bedded ash-flow tuffs were deposited above the marker bed. Although borehole image data are not available for wells in the RDX investigation area, the subunit bracketed by G1 and G2 is also likely to be made up of thin tuff beds that are well stratified. The highly stratified nature of this subunit may provide important controls on groundwater flow directions locally. A structure contour map for the G2 gamma marker horizon shows that the top of this subunit dips to the southeast (Figure C-8), similar to the base of the Qbog (Figure C-10) that lies below. Most likely, tuffs bracketed by the G1–G2 marker horizons dip to the southeast as well. Saturation of this subunit is documented by well screens installed at wells CdV-16-1i and R-25 (Figure 2.3-8a). At CdV-9-1(i) piezometers PZ-1 and PZ-2, water levels are higher than this subunit (Figure 2.3-8a); however, it is uncertain whether the lower Qbof is fully saturated at this location.

The Qbof subunit bracketed by marker beds G2 and G3 is characterized by a gamma signature that is similar to that found in the Qbog and Qbt 1g of the Tshirege Member. Comparison between the Qbog and Qbt 1g is useful to constrain the relative strength of the gamma signal when correlating this subunit between boreholes. At well R-26, tuffs in this subunit are dominated by thick-bedded ash-flow tuffs separated by very thin sandy beds, ash beds, and partings. The gamma break at the top of this subunit in R-26 coincides with the base of a 1.8-ft-thick bed tentatively identified as an ash fall. Saturation of this subunit is documented by the piezometer PZ-1 installed at well CdV-9-1(i) (Figure 2.3-8a). Water levels at wells CdV-16-1i and R-25 suggest this subunit is also saturated at those locations (Figure 2.3-8a). The thick bedded subunit suggests fewer stratigraphic factors exist for controlling groundwater pathways compared with the underlying G1–G2 subunit.

The Qbof subunit bracketed by marker beds G3 and G4 is characterized by a gamma signature that is intermediate in strength for the Qbof member. Comparison between higher gamma values of Qbt 1g and lower gamma values of Qbt 1v/Qbt 2 in the Tshirege Member is useful to constrain the relative strength of the gamma signal when correlating this subunit between boreholes. At well R-26, this subunit is characterized by two thick ash-flow tuffs overlain by boulder and cobble deposits, which have their own unique low-gamma signature (Figure 2.3-1). The boulder and cobble deposits are absent in the RDX investigation area, and the gamma shift associated with the G4 marker bed represents a compositional break between overlying and underlying tuffs (Figure 2.3-8). A similar gamma shift is apparent when comparing baseline gamma levels in tuffs separated by the boulder and cobble deposits at well R-26 (Figure 2.3-1). The thickness of the G3–G4 subunit appears to vary from north to south (Figure 2.3-8b). The subunit is absent at well R-18 but then forms a wedge-shaped deposit that thickens towards well R-63. A structure contour map for the G3 marker horizon shows a southeast dipping surface with a southeast-oriented drainage-like feature in the vicinity of wells CdV-16-1i, CdV-16-4ip, and CdV-16-2ir (Figure C-8). The origin of the drainage feature is not fully understood because Qbof tuffs are believed to have been erupted in rapid succession, leaving little time for erosion between eruptive pulses. However, the boulder and cobble deposits intercalated in the Qbof and Tshirege (Qbt) Members at well R-26 suggest these eruptions took place over long enough periods of time (e.g., weeks or months) that alluvial sediments were deposited over partially eroded surfaces between eruptive pulses. Although no well screens are located in this subunit in the RDX investigation area, water levels in CdV-9-1(i) PZ-1 suggest this subunit may be fully saturated at that location (Figure 2.3-8).

The uppermost Qbof subunit is bracketed by marker beds G4 and G5, except at well R-18 where it is bracketed by G3 and G5. This subunit represents the least radiogenic tuffs in the Qbof member and has a gamma signature that is comparable to Qbt 1v/Qbt 2 in the Tshirege Member. Based on image logs from well R-26, this subunit is likely made up of thick-bedded ash-flow tuffs (Figures 2.3-3 and 2.3-4). The upper screen at well R-26 spans the upper part of this subunit, suggesting the upper Otowi tuffs may be saturated at that location (Figure 2.3-1). In the RDX investigation area, water levels in wells and piezometers are lower than this subunit, suggesting it is unsaturated (Figure 2.3-8).

2.3.2 Investigation Summary

The Qbof member is a regional tuff sheet made up of multiple rhyolitic flow units. Stacking of individual flow units results in widespread stratification within the Qbof member. Grain-size and textural variations between flow units may result in abrupt changes of hydrologic properties at bed contacts and affect groundwater pathways. Well R-26 is used as a type section for the Qbof member to describe lithologies and bedding characteristics that give rise to stratification. Well R-26 was selected as a type section because its geophysical logs are unusually complete and include an FMI log for identifying bedding characteristics and rock textures. Based on comparisons with other localities, well R-26 also appears to represent a nearly complete stratigraphic sequence of the Qbof member. Reevaluation of the geophysical logs and other available data resulted in revision of the unit contact between the Qct and Qbof member and provided a detailed lithological log for tuffs making up the Qbof member. The R-26 studies also showed that the gamma log for the Qbof member varied as a function of stratigraphic position, becoming more radiogenic towards the bottom of the unit. The progressive trends towards more radiogenic tuffs with depth include abrupt shifts to higher gamma activity downhole at several depths in all TA-16 wells. These abrupt shifts in gamma activity provide marker horizons that were correlated between wells in the TA-16 area, providing a method for mapping subunits within the Qbof member. Characteristics of the Qbof subunits were inferred from the detailed lithologic information prepared for the R-26 type section. The lowermost tuffs in the Qbof member (G1–G2 subunit) are well stratified compared with overlying tuffs that tend to be dominated by thick-bedded ash-flow deposits. The apparent continuity of these lowermost tuffs and the underlying Qbog and the stratification in the G1–G2 subunit may provide important controls on groundwater flow directions locally, directing flow down dip towards the southeast. Stratification is not as pronounced in the overlying Otowi subunits, but the numerous bedding contacts between the individual flow units may also provide local controls on groundwater pathways.

3.0 GEOLOGY OF TA-16 AND VICINITY

The following discussion describes the site-wide geology for TA-16. Griggs and Hem (1964) and Broxton and Vaniman (2005) provide an overview of the geologic framework of the Pajarito Plateau. The geology of TA-16 is known through detailed mapping of surface geology for seismic hazards investigations (Gardner et al. 2001; Lewis et al. 2002) and borehole logging of environmental monitoring wells and investigation boreholes summarized in the “Investigation Report for Water Canyon/Cañon de Valle” (LANL 2011). Additional information about vadose-zone and regional-aquifer geology was collected during installation of perched-intermediate and regional groundwater monitoring wells CdV-9-1(i) (LANL 2015a); CdV-16-1(i) (Kleinfelder 2005c); CdV-16-2(i)r (Kleinfelder 2005b); CdV-16-4ip (LANL 2011a); CdV-R-15-3 (Kopp et al. 2002); CdV-R-37-2 (Kopp et al. 2003); CdV-37-1i (LANL 2010c); R-18 (Kleinfelder 2005a); R-25 (Broxton et al. 2002); R-25b (LANL 2008b); R-25c (LANL 2008a); R-26 (Kleinfelder 2005c); R-47 (LANL 2014); R-47i (LANL 2010b); R-48 (LANL 2010a); R-58 (LANL 2016); R-63 (LANL 2011b); R-63i (LANL 2015b); and R-68 (LANL 2017). Cores collected at seismic hazard borehole SHB-3 provide additional information about geologic units and structural features in the TA-16 area (Gardner et al. 1993, Appendix A). Locations of intermediate and regional monitoring wells in the vicinity of TA-16 and the locations of geologic cross-sections for the site are shown in Figure 1.0-1. A stratigraphic column showing geologic units at TA-16 is shown in Figure 3.0-1. Figures 3.0-2 and 3.0-3 are east-west and north-south geologic cross-sections for TA-16, based on the geologic framework model (WC15c). The structure contour maps for the major stratigraphic units are presented in Appendix C. Figure D-1 in Appendix D is a geologic map of TA-16 and vicinity.

3.1 Regional Tectonic Setting

TA-16 is located in the western part of the Española basin near the active rift basin margin defined by the Pajarito fault system. The Española basin of the Rio Grande rift is a west-tilted, half graben (Kelley 1978) filled with Miocene and Pliocene sedimentary deposits derived from highlands located to the west, north, and east (Griggs and Hem 1964; Galusha and Blick 1971; Cavazza 1989; Turbeville et al. 1989). These deposits thicken westward across the basin and may be as much as 9000 ft thick near the Pajarito fault system (Kelley 1978). Ferguson et al. (1995) identified a northeast-trending intrabasin graben beneath the western Pajarito Plateau based on gravity data; this structure represents the deepest part of the Española basin. The deepest well in the TA-16 area, well R-25, was drilled to a depth of 1942 ft, but it did not fully penetrate basin-fill sediments of Pliocene age.

During early stages of volcanism in the Jemez Mountains volcanic field, the western structural margin of the Española basin coincided with a broad zone of north-trending faults that traversed the central part of the volcanic field (Gardner and Goff 1984). These early rift-margin faults became inactive about 6 Ma ago, and the active rift margin migrated eastwards to the Pajarito fault system. However, field studies and ^{40}Ar/^{39}Ar data from surface and subsurface lavas along the western part of the Pajarito Plateau indicate the Pajarito fault system has been active since at least the mid-Miocene before initial volcanism to the west of the fault zone (Golombek 1983; WoldeGabriel et al. 2013). The Pajarito fault system is a narrow band of north- and northeast-trending normal faults with displacement dominantly down to the east (Griggs and Hem 1964; Smith et al. 1970; Gardner and Goff 1984). West of NM 501, the fault forms a 400-ft- (120-m-) high escarpment that has the surface expression of a large, north-trending, faulted monocline (Gardner et al. 1999; Gardner et al. 2001). Along strike, the fault varies from a simple normal fault to broad zones of small faults and faulted and unfaulted monoclines. These varied styles of deformation are all expressions of deep-seated normal faulting (Gardner et al. 1999). On the western boundary of TA-16, the fault zone is segmented into two major splays that form stepped, east-facing escarpments. The Anchor Ranch graben, a subsidiary structure located next to the Pajarito fault system, is discussed in Appendix D and shown in Figure D-1. Stratigraphic separation on the Tshirege Member of the Bandelier Tuff (1.22 Ma) ranges between 260 and 400 ft along the fault west of the Laboratory (Gardner et al., 2001). Episodic faulting is indicated by progressively larger offsets in older rock units (Griggs and Hem 1964, 092516), though fault displacement for older rock units is poorly known because thick deposits of Bandelier Tuff cover critical relations. Continuing displacement along this fault system is reflected by Holocene movements and historic seismicity (Gardner and House 1987; Gardner et al. 1990).

The Pajarito fault system exerts a major influence on the thickness and juxtaposition of geologic units at the mountain block/basin interface. It is the principal structural feature in the area and probably plays a significant, but poorly understood, role in the movement of groundwater across the mountain block/basin interface. Because of intense fracturing, the fault zone probably is also an important infiltration zone for mountain front recharge.

3.2 Structural Geology of the 260 Outfall Area

High-precision bedrock mapping of a 2.9 mi^2 area, including most of the RDX study area, found that a broad zone of deformation extends eastwards from the Pajarito fault system to the 260 Outfall area (Gardner et al. 2001; Figure D-1 in Appendix D; Lewis et al. 2002). The mapping conducted by the Laboratory's Seismic Hazards program identified the following structural elements in this zone of deformation: (1) a north-south graben, referred to as the TA-09 graben that lies between building 16-260 and MDA P; (2) north-northwest-striking fractures and rare faults that bound the zone of deformation and may be the surface expression of deeper faulting; (3) northeast trending open or rubble-filled fissures within the Tshirege Member, some of which are very large; and (4) rare small east-west-trending faults (Gardner et al. 2001; Lewis et al. 2002).

The largest structure in the 260 Outfall area is the north-trending TA-09 graben (Figure D-1 and Lewis et al., 2002, 073785). The graben is about 2000 ft wide at its southern end between building TA-16-260 and MDA P, narrowing to about 1000 ft wide at its northern end in Pajarito Canyon west of building TA-22-52. The western bounding fault of the TA-09 graben is a high-angle normal fault with 5 ft of down-to-the-east displacement. The eastern boundary of the graben is defined by three closely spaced high-angle normal faults with a total of 20 ft of down-to-the-west displacement. A shallow north-trending syncline adjacent to the eastern bounding fault accounts for an additional 10 ft of down-to-the-west displacement (Figure D-1). The bounding faults of the TA-09 graben offset old mesa top alluvial fan deposits (age in part 1.13 Ma), indicating some displacements post-date the Tshirege Member (Lewis et al. 2002).

Lewis et al. (2002) conducted a total station survey of open and filled fractures of large aperture (up to 3.3 ft wide) at MDA P. A total of 454 fractures were measured in units Qbt 4, Qbt 3t, and Qbt 3 to determine possible tectonic influences on fracturing. The Qbt 4 fractures are generally steep and have a statistically significant north-northwest-preferred orientation (mean direction of N14W ± 16°). Fractures in the densely welded Qbt 3t are generally subhorizontal and have a statistically significant east-northeast preferred orientation (mean direction of N69E ± 32°). Fractures in densely welded Qbt 3 are subhorizontal to steep and have north-northwest-preferred orientation (mean direction of N25W ± 32°). The overall map pattern of high-angle fractures in all units is polygonal, suggesting most are cooling joints (Lewis et al. 2002). Subhorizontal fractures within densely welded units Qbt 3t and Qbt 3 appear to be associated with compaction foliation and some may be partings between flow units. The presence of tectonic fractures is indicated by fracture densities and apertures that are greater on the western side of MDA P near the eastern border faults of the TA-09 graben. The association of elevated fracture density and fractures of large aperture with the TA-09 graben appears to mark a north-northwest-trending zone of diffuse deformation (Lewis et al. 2002).

Faults and fractures in the area between the 260 Outfall and MDA P, including the TA-09 graben, are likely important vertical pathways for infiltration of HE-contaminated surface water and alluvial groundwater. The floor of Cañon de Valle is underlain by bedrock units Qbt 3t and Qbt 3. These tuffs are densely welded, and their rock matrix is relatively impermeable. Faults and fractures (including cooling joints, tectonic fractures, subhorizontal compaction fractures) provide groundwater pathways through these impermeable tuffs. Similar fractures likely provide similar pathways through the densely welded tuffs of Qbt 2.

3.3 Regional Volcanic Setting

The Jemez volcanic field began to develop ~13 to 10 Ma with the eruption of predominantly basaltic and rhyolitic rocks of the Keres Group (Gardner et al. 1986). From 10 to 7 Ma, 240 mi^3 (1000 km^3) of andesite and subordinate basalt and rhyodacite were erupted as part of the Paliza Canyon Formation (Gardner and Goff 1984; Gardner et al. 1986). High-silica rhyolite plugs, domes, and tuffs of the Bearhead Rhyolite, including thick tuffaceous deposits of the Peralta Canyon Member, were erupted ~6.15 to 7.06 Ma (Smith 2001). The period from 6 to 7 Ma also coincided with a transition to predominantly dacitic volcanism throughout the volcanic field (Gardner et al. 1986, 059104). Pliocene dacite lavas of the Tschicoma Formation were erupted over a wide area, including the large, overlapping Tschicoma volcanic centers that make up the mountain block (Sierra de los Valles) west of TA-16 (Goff et al. 2002; Kempter and Kelley 2002; Broxton et al. 2007). These dacite volcanos shed the thick alluvial fans of the Puye Formation into the actively subsiding Española basin.

Activity in the volcanic field reached a climax with eruption of the Bandelier Tuff (Griggs and Hem 1964; Smith and Bailey 1966; Bailey et al. 1969; Smith et al. 1970). The Bandelier Tuff has two members, each consisting of a basal pumice fall overlain by a petrologically related succession of ash-flow tuffs (Bailey et al. 1969). Eruption of the two members was accompanied in each case by caldera collapse. The Otowi Member (1.61 Ma, Izett and Obradovich 1994, 048817; Spell et al. 1996, 055542) was erupted from the earlier of the two calderas. This early caldera was coincident with, and largely destroyed by, the younger Valles Caldera that formed during the eruption of the Tshirege Member (Izett and Obradovich 1994; Spell et al. 1996). Deposition of widespread ash-flow tuff sheets over the western Española basin formed the Pajarito Plateau, an east-sloping tableland bounded on the west by the eastern Jemez Mountains (Sierra de los Valles) and on the east by the Rio Grande.

An interval of about 390,000 yr separated eruptions of the two Bandelier members. During this time, domes of Cerro Toledo rhyolite and Rabbit Mountain rhyolite were emplaced northeast and southeast of the Toledo caldera (formed during eruption of the Otowi Member [Qbof]). Tephras from these domes were deposited as ash and pumice falls over the eastern mountain block and western Española basin. These tephras were quickly stripped from the mountain block and deposited as alluvial tuffaceous sediments of the Qct (Cerro Toledo Formation) over broad areas of the Pajarito Plateau, including the TA-16 area (Gardner et al. 2010).

Post–Valles Caldera volcanic events were restricted to the floor of the Valles Caldera, but tephras from these eruptions and their reworked equivalents were deposited over the eastern mountain block and large parts of the Pajarito Plateau (Reneau and McDonald 1996). These deposits were largely removed by stream incision across the plateau, but erosional remnants are locally intercalated with young alluvial fans that are preserved atop the Bandelier Tuff in the TA-16 site (Lewis et al. 2002).

3.4 TA-16 Stratigraphy

The character of volcanic and sedimentary rocks at TA-16 reflect their deposition in the western Española basin near the tectonically active Pajarito fault system during periods of active volcanism in the Jemez Mountains volcanic field. Rock units include thick Quaternary ash-flow tuff sheets erupted from calderas located in the central part of the volcanic field and Pliocene alluvial fan deposits shed from the mountain block west of the Pajarito fault system. The stratigraphy in the vicinity of TA-16 includes surficial deposits, ash-flow tuffs of Quaternary Bandelier Tuff (including interbedded sedimentary deposits of the Cerro Toledo Formation), fanglomerate deposits of the Pliocene Puye Formation, and Pliocene dacite lavas of the Tschicoma Formation (Figure 3.0-1).

3.4.1 Surficial Deposits

There is a large variety of surficial deposits at TA-16, including canyon-bottom alluvium and colluvium, mesa-top soils, and older alluvial fans on mesa tops. In Cañon de Valle near the 260 Outfall and MDA P, the thickness of alluvium ranges between 5.0 ft (1.5 m) in well CdV-16-02657 and 9.0 ft (2.7 m) in well CdV-16-1(i) (LANL 1998; Kleinfelder 2004). Alluvium in Cañon de Valle includes crystal-rich medium-to fine-grained sands derived from the Tshirege Member and dacitic cobbles, gravels, and sands derived from the Tschicoma Formation. These deposits host persistent alluvial groundwater in the vicinity of the 260 Outfall and MDA P; the saturated thickness of this alluvial groundwater ranges from 3.3 to 6.6 ft (1 to 2 m) (LANL 2011c).

Mesa tops at TA-16 include widespread remnants of dacite-rich gravels deposited by early Pleistocene streams draining the Sierra de los Valles that pre-dated incision of the canyons (Reneau and McDonald 1996; Reneau et al. 1996). These older fan deposits include early Valles rhyolite pumice falls and reworked tephras. The older fans are locally overlain by late Quaternary fans near the base of the Pajarito fault escarpment (Lewis et al. 2002). These younger fan deposits contain dacite and Bandelier Tuff detritus. The occurrence of pumice from the youngest eruptions of the Valles Caldera (El Cajete pyroclastic beds, East Fork Member of the Valles rhyolite) in some fan deposits indicates they are relatively young (Zimmerer et al. 2016). Because of their thickness and high porosity, mesa top alluvial fans may play a role storing water from storm runoff and snowmelt. This may be particularly important where Cañon de Valle crosses a thick, widespread fan deposit east of the Pajarito fault system. Infiltration of water stored in fan deposits may be a source of recharge to moisture in the vadose zone.

3.4.2 Bandelier Tuff and Cerro Toledo Formation

The following description of Bandelier Tuff uses the term *welding* to distinguish between tuff that is less compacted (or noncompacted) and porous (nonwelded) as opposed to tuff that is more compacted, dense (welded), and less porous. In the field, the degree of welding in tuff is quantified by the degree of flattening of pumice fragments (a higher degree of flattening and elongation equals a higher degree of welding). Petrographically, welded tuff shows adhesion (welding) of pumice and ash, but nonwelded tuff does not. The term *vitric* is applied to tuff whose volcanic glass is largely unaltered and intact. The term *devitrified* is applied to tuff whose volcanic glass has crystallized to a fine-grained mineral assemblage of alkali feldspar and silica polymorphs (quartz, cristobalite, and tridymite). *Devitrification* includes deposition of alkali feldspar and silica polymorphs in open pores by pervasive vapor-phase alteration associated with degassing of the tuffs. Extensive chemical, mineralogic, and petrographic data for the Bandelier Tuff are published in numerous Laboratory reports (Broxton et al. 1995; Reneau and Raymond 1995; Broxton et al. 1996; Warren et al. 1997; Lewis et al. 2002; Stimac et al. 2002).

3.4.2.1 Tshirege Member, Bandelier Tuff (Qbt)

The Tshirege Member of the Bandelier Tuff is a compound cooling unit that resulted from emplacement of successive rhyolite ash-flow tuffs separated by periods of inactivity that allowed for partial cooling before subsequent flows were deposited (Smith and Bailey 1966; Broxton and Reneau 1995). Because of the episodic nature of deposition, physical properties such as density, porosity, degree of welding, fracture density, and mineralogy vary as a function of stratigraphic position. Vertical variations in tuff properties were used to subdivide the Tshirege Member into mappable subunits that reflect localized emplacement temperature, thickness, gas content, and composition of the tuff deposits (Broxton and Reneau 1995; Lewis et al. 2002). The Tshirege Member is 430 ft (131 m) thick in well CdV-9-1(i).

3.4.2.1.1 Tshirege Member Unit 4 (Qbt 4)

Qbt 4 is a lithologically complex unit that forms the caprock of mesas in the TA-16 site. Qbt 4 is 85 ft (26 m) thick at well CdV-9-1(i). A measured section of Qbt 4 on the north wall of Cañon de Valle found, in ascending order (1) poorly indurated, white to light-gray, nonwelded ash-flow tuff; (2) indurated, light tan, nonwelded, cliff-forming ash-flow tuff capped by talus-covered slope; (3) varicolored, nonwelded, cliff-forming ash-flow tuff that includes a devitrified base and vitric upper part; (4) crystal-rich surge bed 0.8 ft (0.25 m) thick, and (5) hard, densely-welded ash-flow tuff that has a vitric base and hematite-stained devitrified upper part (Broxton et al. 1996). Lewis et al. (2009) subdivided Qbt 4 into an upper (Qbt 4u) and a lower unit (Qbt 4l) (Figure D-1), whereas Goff et al. (2014) differentiated the uppermost flow units of Qbt 4 into Qbt 5l and Qbt 5u. The base of Qbt 4 dips east-southeast and includes a trough-shaped structure south of well R-25 (Figure C-1).

Qbt 4 may play an important hydrologic role on mesa tops where local areas of increased infiltration occur, such as beneath ponds (e.g., the 260 Outfall pond) or beneath tributary drainages that flow during snowmelt and storm events or that received historical effluent releases (LANL 2011c). Martin Spring, located in Martin Spring Canyon, discharges at the Qbt 4/Qbt 3t contact, which is characterized by several localized sandy base surge deposits. The trough-shaped structure at the base of the unit may provide local control for groundwater flow in the vicinity of the 260 Outfall pond (Figure C-1).

3.4.2.1.2 Tshirege Member Unit 3t (Qbt 3t)

Qbt 3t is 20 ft thick at well CdV-9-1(i) and is a local bedrock unit that is largely confined to the western part of the Laboratory and the east slopes of the Jemez Mountains. Qbt 3t is a moderately to densely welded, devitrified ash-flow tuff exposed in the walls of Cañon de Valle in the vicinity of MDA P. These cliff-forming tuffs grade up into a broad, gently sloping bench that marks the contact with Qbt 4. The contact with underlying Qbt 3 is marked by a welding break characterized by poorly welded tuffs. Because of strong welding, Qbt 3t's rock matrix generally has low porosity and is characterized by low permeability. Fractures are common in canyon wall exposures. Locally, crystal-rich pyroclastic surges occur within Qbt 3t as well as at the contact with overlying Qbt 4 (Lewis et al. 2002). The base of Qbt 3t dips east-southeast and includes a trough-shaped structure south of well R-25 that is not as pronounced as the trough at the base of unit Qbt 4 (Figure C-2).

At the TA-16 site, unit Qbt 3t is above the floor of Cañon de Valle east of the 260 Outfall and does not play a role in infiltration beneath the canyon bottom. However, Burning Ground and SWSC Springs discharge from unit Qbt 3t and provide a source of persistent surface water in Cañon de Valle that extends between 0.4 mi and 2 mi (0.6 km to 3.2 km) downstream from Burning Ground Spring (LANL 2011c). This unit appears to be an important perching horizon throughout the western part of the Laboratory because springs discharge at similar elevations from these tuffs in upper Pajarito and

Twomile Canyons to the north. A number of mesa-top wells south of Cañon de Valle encountered small zones of perched groundwater in unit Qbt 3t and underlying unit Qbt 3, including well 16-26644 near the 90s Line Pond, well MSC-16-02665 near the headwaters of S-Site Canyon, and R-26 piezometer PZ-2 near the Pajarito fault system (LANL 2011c). Well 16-260E-02712 near the 260 Outfall showed sporadic saturation before it was plugged and abandoned. These groundwater occurrences probably form ribbon-like zones of saturation of limited extent as defined by dry nearby boreholes and wells installed to similar depths (LANL 2011c).

3.4.2.1.3 Tshirege Member Unit 3 (Qbt 3)

Qbt 3 is about 125 ft thick and forms the lower cliffs of Cañon de Valle and underlies canyon-floor alluvium along the main infiltration pathway for contaminated water downcanyon of the 260 Outfall. Qbt 3 is a moderately to densely welded, devitrified ash-flow tuff. Welding decreases down-section in unit Qbt 3, and the base of the unit is poorly welded and highly porous. Locally, crystal-rich pyroclastic surges occur within Qbt 3 as well as at the contact with overlying Qbt 3t (Lewis et al. 2002). Unit Qbt 3 dips eastward beneath the main infiltration zone and southeast farther downcanyon in the vicinity of well R-47i (Figure C-3). The base of Qbt 3 forms a broad east-dipping trough that parallels the axis of Cañon de Valle near wells R-25 and CdV-9-1(i).

As described above, mesa-top wells south of Cañon de Valle encountered small zones of perched groundwater in unit Qbt 3, which is made up of stacked flow units that were emplaced in rapid succession with little time between eruptions. Individual flows are commonly densely welded throughout, including at their upper and lower contacts. Because the tuff is densely welded, the rock matrix generally has low porosity and is characterized by low permeability. Contacts between flows are commonly marked by partings (horizontal fractures) that locally grade laterally into sandy pyroclastic surge deposits. Groundwater accumulation and movement in the tuff are probably controlled by a combination of horizontal fracture flow along partings and porous flow in sandy pyroclastic surge deposits with flow generally towards the east and southeast. Diversion and vertical stair-stepping of perched zones probably occurs along fractures and faults.

3.4.2.1.4 Tshirege Member Unit 2 (Qbt 2)

Unit Qbt 2 is about 100 ft thick and forms a significant part of the upper vadose zone beneath the main infiltration pathway for contaminated water downcanyon of the 260 Outfall. Similar to overlying unit Qbt 3, Qbt 2 is a moderately to densely welded, devitrified ash-flow tuff made up of stacked flow units that were emplaced in rapid succession. The upper part of Qbt 2 is strongly welded, and a sharp break occurs in hydrological properties from porous nonwelded tuffs at the base of Qbt 3 to densely welded tuffs at the top of Qbt 2. Because Qbt 2 is densely welded, the rock matrix generally has low porosity and is characterized by low permeability. Welding decreases down-section in the lower part of unit Qbt 2, and the contact with the underlying unit Qbt 1v is gradational. The contact between Qbt 2 and Qbt 1v is somewhat arbitrarily placed at the top of nonwelded porous tuffs (Broxton and Reneau 1995). Qbt 2 dips eastward beneath the main infiltration zone and southeast farther downcanyon in the vicinity of well R-47i (Figure C-4). Where exposed, Qbt 2 is characterized by numerous well-developed vertical fractures, although some horizontal and low-angle fractures are also present (Broxton and Reneau 1995). Most fractures are cooling joints formed by contraction of the tuff during cooling; other fractures are tectonic in origin. Typically, Qbt 2 cooling joints die out down-section in the poorly consolidated rocks of Qbt 1v. Tectonic fractures are more likely to form continuous structures across unit contacts. There are no reported occurrences of perched groundwater in unit Qbt 2 for wells installed in the TA-16 area. As with the welded tuffs in Qbt 3, groundwater accumulation and movement in the tuff are probably controlled by a combination of horizontal fracture flow along partings and porous flow in sandy pyroclastic surge deposits with flow generally towards the east and southeast. Diversion and vertical stair-stepping of perched zones probably occur along fractures and faults.

3.4.2.1.5 Tshirege Member Unit 1v (Qbt 1v)

Qbt 1v is about 45 ft thick and is made up of nonwelded devitrified ash-flow tuffs. The tuffs are poorly sorted and include abundant pumice relicts supported by a porous ashy matrix with abundant crystals and sparse lithics. Where exposed in outcrop, the lower part of Qbt 1v is well consolidated and displays a distinctive columnar fracture pattern (Qbt 1vc of Broxton and Reneau 1995). Near-vertical fractures of the colonnade tuff typically die out at the boundary with underlying Qbt 1g; however, a few fractures persist across contact. Unit Qbt 1v dips eastward beneath the main infiltration zone and southeast farther downcanyon in the vicinity of well R-47i (Figure C-5). There are no reported occurrences of perched groundwater in Qbt 1v, but a prominent moisture spike occurs at the contact between Qbt 1v and underlying Qbt 1g in wells 49-700-1 (Stimac et al. 2002, 073391) and LADP-4 (Broxton et al. 1995), suggesting the contact may be an important capillary barrier. The Qbt 1v/Qbt 1g contact marks the abrupt transition between tuffs containing abundant volcanic glass in Qbt 1g and glass-free (devitrified) tuffs in Qbt 1v. Clastic deposits occupy the stratigraphic interval between units Qbt 1v and Qbt 1g of the Tshirege Member in several of the TA-16 wells including at R-26, R-47i, R-63, and R-68. These clastic deposits, which range in thickness from 12 to 16 ft, contain beds of matrix- and clast-supported angular to subangular boulders, cobbles, gravels, and sands made up of dark intermediate-composition lavas. These clastic deposits are characterized by low gamma activity compared to the rhyolitic tuffs of Qbt 1v and Qbt 1g. The bedded nature of the clastic deposits suggests they represent fluvial sediments rather than traction deposits at the base of Qbt 1v ash-flow tuffs. The presence of these deposits between units Qbt 1v and Qbt 1g suggests the Tshirege eruption was episodic and that a hiatus in the eruption was long enough to allow deposition of fluvial sediments. These clastic deposits are not associated with the perched groundwater at TA-16, but their stratification may divert percolating moisture along bedding contacts under unsaturated conditions.

3.4.2.1.6 Tshirege Member Unit 1g (Qbt 1g)

Qbt 1g is about 55 ft thick and is made up of nonwelded vitric ash-flow tuffs and a 2-ft-thick basal pumice fall (Tsankawi Pumice Bed). The ash-flow tuffs are poorly sorted and contain abundant glassy pumice supported by a highly porous matrix of ash, glass shards, broken pumice fragments, phenocrysts (primarily sanidine and quartz), and volcanic lithics. The Tsankawi Pumice Bed is a stratified, fines-depleted deposit of gravel-sized vitric pumice and quartz and sanidine crystals. The base of Qbt 1g forms a well-defined east-draining trough beneath the main contaminant infiltration zone and that turns towards the southeast in the vicinity of well R-47i (Figure C-6). This trough is probably a paleodrainage developed on top of the underlying Cerro Toledo Formation before the eruption of Qbt 1g tuffs. There are no reported occurrences of perched groundwater in Qbt 1g, but a prominent moisture spike occurs at the contact between the ash-flow tuffs and the basal pumice fall in wells 49-700-1 (Stimac et al. 2002) and LADP-4 (Broxton et al. 1995b). Capillary barriers may occur at layer contacts where a unit with relatively small pores overlies a unit with relatively large pores (Montazer and Wilson 1984). Conditions for a capillary barrier may occur at the base of Qbt 1g where ash-flow tuffs characterized by a fine-grained matrix overlie the ash-poor clast-supported Tsankawi Pumice.

3.4.2.2 Cerro Toledo Formation (Qct)

Sedimentary deposits of the Cerro Toledo Formation are commonly referred to as the Cerro Toledo interval in other Laboratory reports (e.g., Broxton and Reneau 1995). However, these deposits were recently incorporated into the newly revised Cerro Toledo Formation consisting of extrusive volcanic domes, lava flows, tephras, and sedimentary rocks that record landscape evolution in the time interval between the Tshirege and Otowi Members of the Bandelier Tuff (Gardner et al. 2010). The newly defined Pueblo Canyon Member of the Cerro Toledo Formation is stratigraphically equivalent to the deposits identified as the Cerro Toledo interval in previous reports. The Cerro Toledo Formation is a well-stratified alluvial sequence deposited on partly eroded Otowi Member ash-flow tuffs on the west alluvial slope and marginal grabens of the Española basin. The Pueblo Canyon member of the Cerro Toledo Formation is made up of beds of tuffaceous sandstone, siltstone, and ash and pumice falls (e.g., Figure 3.0-1) derived from erosion of Cerro Toledo tephras and Otowi Member tuffs from the east slopes of the Jemez Mountains and western Pajarito Plateau. The Cerro Toledo Formation also includes localized dacitic gravel- and cobble-rich alluvial deposits eroded from the Tschicoma Formation exposed in the eastern Jemez Mountains. Based on the structure contour map (Figure C-7), the base of the Cerro Toledo Formation was deposited on a well-defined east-southeast draining trough that is interpreted as a paleodrainage incised into partly eroded Otowi ash-flow tuffs. The axis of this trough lies beneath Cañon de Valle near well R-25 but diverges to the south in the vicinity of well R-63. The stratified nature of the deposit may play a role diverting percolating moisture to the east and southeast along bedding contacts. Identification of the Cerro Toledo Formation/Otowi Formation contact has proven to be a difficult challenge in the TA-16 site (section 2.1), and the structure contour map for this surface has significant uncertainties, as described in section 2.3. For example, new LA-ICP-MS data indicate the base of the Cerro Toledo Formation is bracketed between depths 425 ft and 550 ft in well R-63 (Table B-2.0), or somewhat deeper than shown on Figure C-7. Despite the uncertainties, it is clear the Cerro Toledo Formation was deposited over a surface with a regional dip to the east and southeast. There are no reported occurrences of perched groundwater in Cerro Toledo deposits in the vicinity of the 260 Outfall, but perched groundwater at least 50 ft thick occurs in the lower part of the Cerro Toledo Formation at well R-26. This perched groundwater is tritium dead and does not respond to infiltration events (e.g., snowmelt and storm runoff), suggesting it is recharged by the regional groundwater through connections to the mountain block to the west. Perched groundwater at well R-26 may be connected laterally with deep perched water in the lower Otowi Member in the vicinity of the 260 Outfall. Appendix D describes how rocks at well R-26 may be down-faulted relative to rocks in the 260 Outfall area.

3.4.2.3 Otowi Member, Bandelier Tuff (Qbof)

The Otowi Member is about 360 ft thick and is made up of stacked flows of porous nonwelded vitric ash-flow tuffs and thin beds of intercalated ash and pumice falls. The unit is characterized by fully inflated vitric pumices whose supporting tubular structures have not collapsed as a result of welding. The pumices are supported by a matrix of poorly sorted ash, glass shards, broken pumice fragments, phenocrysts (primarily sanidine and quartz), and volcanic lithics. The sequential deposition of flow and fall deposits resulted in stratification of the unit on a regional scale. At well R-26, the Otowi Member is made up of two tuff sequences separated by coarse sedimentary deposits that are 47.6 ft thick. The sedimentary deposits intercalated within the Otowi tuffs at R-26 appear to be a local feature and are not present in other wells at TA-16. The lithologic characteristics and stratification of the Otowi Member are discussed in more detail in section 2.3 of this report. Deep-perched groundwater zone beneath Cañon de Valle occurs within the lower part of the Otowi Member at wells CdV-16-1(i), R-25, and CdV-9-1(i). In an effort to determine how bedding might affect groundwater flow direction, an investigation was undertaken to characterize the nature of bedding in the Otowi Member (section 2.3.1.2). Bedding orientations internal to the Otowi Member were defined by mapping distinctive gamma shifts in borehole spectral gamma and natural gamma logs (section 2.3.1.3). The gamma shifts occur at stratal boundaries and are useful marker horizons for correlating Otowi subunits between wells.

Structure contour maps were prepared for marker horizons G3 and G2 in the lower part of the Otowi Member (Figure C-8) because they are associated with deep perched groundwater in the vicinity of the 260 Outfall. The structure contour map for the base of the Otowi Member ash-flow tuffs (equivalent to marker horizon G1 in Figures 2.3-7 and 2.3-8) was generated from the recent Weston WC15c sitewide geologic model (Figure C-9). The structure contour map for marker bed G3 (Figure C-8) forms an east-southeast-draining trough that lies beneath Cañon de Valle near the 260 Outfall but diverges to the southeast in the vicinity of well R-47i. Structure contour maps for subunits G2 and G1 (Figures C-8 and C-9) show similar orientations, dipping uniformly to the southeast in the vicinity of the 260 Outfall.

Stratified fine-grained deposits such as ash falls are especially prominent in the Otowi tuffs between marker beds G1–G2 (e.g., Figure 2.3-5) and may act as confining or semi-confining beds for groundwater flow in the uppermost part of the upper perched groundwater zone. Fractures may also act as groundwater pathways in the Otowi Member. High-angle open fractures were intersected in the perched groundwater zone at well R-25 and observed in borehole videos. Multiple fault gouges were also noted within the Otowi Member in the SHB-3 core hole (Appendix A, Photographs of SHB-3 Core Hole Fault Gouges). The photos show the fractures to be sharp well-defined breaks, suggesting the Otowi tuffs were well consolidated despite being nonwelded. Two high-angle fractures were also intersected in the perched groundwater zone at well CdV-16-1(i) and observed in an FMI log. Fractures were intersected at depths of 597 ft and 619 ft and had orientations of N34E, 84˚NE and N53W, 85˚NW, respectively. The 619-ft-deep fracture (Figure 3.4-1) is within the well screen at CdV-16-1(i).

3.4.2.4 Guaje Pumice Bed (Qbog)

The Guaje Pumice Bed is the basal fall deposit of the Otowi Member. It was deposited atop the Puye Formation on the west alluvial slope of the Española basin. The Guaje Pumice Bed is a stratified, fines-depleted deposit of gravel-sized vitric pumice, quartz and sanidine phenocrysts, and subordinate volcanic lithics. At well R-26, the Guaje Pumice Bed is made up of thin ash and pumice falls that overlie a thick basal pumice fall (Figure 2.3-6). Borehole data indicate the thickness of this unit at TA-16 ranges between 5 ft (1.5 m) and 15 ft (4.6 m). The Guaje Pumice Bed dips to the southeast in the vicinity of the 260 Outfall (Figure C-10). The Guaje Pumice Bed is potentially an important groundwater pathway because higher moisture content and zones of saturation occur within this unit at other areas of the Laboratory beneath wet canyons (e.g., Los Alamos Canyon). At TA-16, deep perched groundwater occurs in the Guaje Pumice Bed at wells R-25 and CdV-9-1(i). Potential clay-silt soil horizons have been identified at the top of the underlying Puye Formation in wells CdV-16-4ip, SHB-3, R-25, and R-26 and may act as confining beds for perched groundwater (Figures 2.3-6 and 3.4-2).

3.4.3 Puye Formation

The Pliocene Puye Formation was deposited as broad, coalescing alluvial fans shed eastward from the Jemez Mountains volcanic field into the western Española basin (Griggs and Hem 1964; Bailey at el. 1969). The sources for these alluvial-fan deposits were overlapping dacite to low-silica rhyolite dome complexes of the Tschicoma Formation that were active in the eastern Jemez Mountains between about 3 and 5 Ma (Broxton et al. 2007). The Puye Formation is more than 1092 ft thick in well R-25, but the base of the unit was not penetrated by wells in the TA-16 area.

Rocks of the Puye Formation are commonly referred to as fanglomerates, a type of conglomerate consisting of heterogeneous volcanic rock fragments of all sizes deposited in an alluvial fan. At TA-16, Puye fanglomerates are a heterogeneous assemblage of clast- to matrix-supported conglomerates, with associated gravels and lithic sandstones. Boulders up to 2 ft (0.6 m) or larger are common and tend to be subangular to subrounded, based on borehole video and FMI logs. The deposits lack cementation and clay minerals are sparse to absent. They are commonly poorly sorted and poorly to moderately consolidated. Debris flow deposits are common throughout the unit. Boulder and cobble deposits tend to be thickly bedded up to 5.0 ft (1.5 m) and are commonly separated by thin beds of sandy gravels and silty sands (Figure 3.4-2).

The Puye Formation is an important component of the two deep perched groundwater zones beneath Cañon de Valle in the vicinity of the 260 Outfall. The lateral extents of the two perched zones suggest that bedding and lithologic variations in the Puye Formation play an important role in confining perched water and in controlling the direction of groundwater flow. Though relatively uncommon in the stratigraphic sequence, silt beds 1 ft to 3 ft (0.3 m to 0.9 m) thick may be important perching horizons for the two deep perched zones based on water-level data collected during drilling of wells in the area. The depositional environment for the silt beds is uncertain, but they may form aquicludes over relatively large areas. Attempts to map silt beds between wells were unsuccessful because the extreme heterogeneity of the Puye Formation, and the quality of the drill cuttings makes it difficult to recover fine sediments and to correlate individual beds.

Confining conditions may also develop above matrix-supported conglomerate beds. Dacite boulders, cobbles, and pebbles have low permeability; thus, moisture flow in these deposits is controlled by the grain size and sorting of the rock matrix. Permeability in a poorly sorted matrix containing abundant silt and fine sand will be significantly less than a matrix of well sorted medium- to coarse-grain sand. At well R-47i, perched water appears to be confined above a bed of cobbles and boulders supported by a matrix containing abundant silt and fine sand.

The top of the Puye Formation (equivalent to the base of the Guaje Pumice Bed in Figure C-10) dips southeast in the vicinity of Cañon de Valle. However, dips of individual beds within the unit may vary because of the complex depositional patterns associated with aggrading alluvial fans. The locations and orientations of streams on the fan change over time as channels aggrade and migrate laterally. This study attempted to identify unique marker beds within the Puye Formation to better understand bedding orientations internal to the unit. Geophysical data and drill cuttings were examined to determine if unique lithologies or marker beds such as tephra deposits could be correlated among the wells of the area. Attempts to identify unique marker beds in the upper Puye Formation have been unsuccessful thus far because no unique correlative lithologies were recognized in the cuttings and the geophysical logs. Interpretation of the geophysical logs is further complicated by the need to apply corrections for borehole conditions, such as number and depth of drill casings and air versus water in the boreholes. The geophysical data hold promise for identifying mappable marker beds, but more work is needed to process the data to make the borehole logs comparable.

3.4.4 Tschicoma Formation, Dacite of Cerro Grande (Tvt2)

In the southern part of the TA-16 area, a thick lobe of Tschicoma dacite lava originating in the mountain block to the west flowed eastward into the western part of the Española basin; this lava was subsequently down-faulted and buried by younger Puye fan deposits. This dacite lava correlates to the dacite of Cerro Grande exposed in the mountain block to the west based on similarities in rock chemistry and petrography (Samuels et al. 2007). Dacite lava is not present in areas of perched groundwater beneath Cañon de Valle, but it is a major component of the regional aquifer over a broad area in the southern part of TA-16, TA-11, and probably most, if not all, of TA-37 and TA-28. The dacite of Cerro Grande was partially penetrated in wells CdV-R-37-2, R-48, and R-58. Well R-48 drilled through 750 ft of dacite lava but did not penetrate the base of the unit. A structure contour map for the top of the dacites, collectively called Tvt2 in the WC15c model, is shown in Figure C-11. The dacite of Cerro Grande is differentiated from other dacites identified by Samuels et al. (2007) in the area shown in Figure C-11.

The Cerro Grande dacite has two main facies: (1) monolithologic flow breccia and (2) massive, dense, flow-banded lava. The flow breccia consists of large, clast-supported angular blocks of dacite with no apparent bedding or structure. The breccia both overlies and underlies the interior zone of the massive flow-banded lava and appears to be a thick carapace of chilled dacite lava that was disrupted as the molten interior zone continued to flow. At well R-58, the cuttings of the flow breccia are pervasively hydrothermally altered to a brick-red color. Figure 3.4-3 shows FMI images of the dacite breccia and massive lavas. Parts of the massive interior of the dacite lava are characterized by a well-developed and pervasive flow foliation. At well R-48, azimuths of flow foliation determined from FMI logs show that the north margin of the dacite lava was moving towards the northeast during emplacement (Figure 3.4-4). The flow breccia portion of the dacite lava is a porous medium, and groundwater flow will be dominantly breccia-controlled. The massive interiors of the dacite lavas are highly fractured, with fractures having little or no preferred orientation. Groundwater flow in the massive lavas is probably fracture-dominated and heterogeneous, and permeability is likely to be greater in the zones of high fracturing. The WC15c geologic model for Tvt2 was updated as part of this investigation to account for the different hydrologic properties in flow breccia versus massive lava. Tvt2 was subdivided into Tvt2 flow breccia and Tvt2 massive lava by assigning the upper 200 ft and lower 250 ft of the unit to flow breccia, based on logs from wells R-48, CdV-R-37-2, and R-58. The model update now includes a massive core of Tvt2 surrounded by a carapace of brecciated lava 200–250 ft thick.

4.0 SUMMARY AND CONCLUSIONS

New data and interpretations presented in this report augment the sitewide geologic model that is currently used to assess hydrogeologic site conditions. The new data provide information about geologic contacts and internal bedding features for rocks that make up the vadose zone. These bedding features have the potential to influence groundwater pathways and flow directions. These data are relevant for assessing groundwater remediation strategies by providing information about groundwater pathways in the site conceptual model and by helping to constrain numerical models that examine contaminant transport through the vadose zone.

The geological investigations at TA-16 focused on three tasks to improve the geologic model that underpins the site conceptual model for contaminant transport. The three tasks consisted of (1) updating the stratigraphic contacts within the Bandelier Tuff and the Cerro Toledo Formation, (2) using the contacts to define internal bedding surfaces and orientations within the major units, and (3) updating the geological and structural features at TA-16 and adjacent areas using results obtained from the tasks 1 and 2 above.

Stratigraphic contacts were examined and updated using multiple lines of evidence, including binocular microscope examination of borehole cuttings, lithologic examinations of cores, chemical fingerprinting of pumices, and analysis of geophysical logs. Updated contacts were used to make cross-well correlations, to generate structure contour maps showing the bedding orientations and dips of units, and to locate and measure displacements of faults. Internal bedding and orientation features observed within the Otowi Member were correlated between wells in the TA-16 site.

Percolation of surface water beneath Cañon de Valle has penetrated thick deposits of tuff and alluvial fan sediment to contaminate deep perched groundwater in the lower Otowi Member and Puye Formation. At unsaturated conditions, moisture movement through the vadose zone is likely dominated by vertical, gravity-driven flow through porous rocks. Moisture is probably diverted laterally at capillarity barriers associated with bedding contacts. Similarly, perching horizons for perched groundwater systems are thought to be stratigraphically controlled. Direction of groundwater flow is controlled by the dip of bedding within the major stratigraphic units. Based on this investigation, moisture flux through the vadose zone will have a tendency to be diverted towards the east and southeast.

Infiltration pathways in the upper vadose zone are dominated by strongly welded ash-flow tuffs of Tshirege units Qbt 3 and Qbt 2. Because these tuffs are characterized by low porosity and low permeability, groundwater accumulation and movement are probably controlled by a combination of horizontal fracture flow along partings and porous flow in sandy pyroclastic surge deposits. Bedding orientations suggest groundwater flow may be diverted towards the east and southeast. Vertical pathways through the tuffs probably occur where horizontal flows intersect abundant fractures and faults.

Tshirege units Qbt 1v and Qbt 1g, Cerro Toledo Formation, Otowi Member, and Guaje Pumice Bed are highly porous and variably stratified deposits. Vertical, gravity-driven moisture flow through these rocks is likely to be diverted laterally at bedding contacts, particularly in the Cerro Toledo Formation, lower part of the Otowi Member, and Guaje Pumice Bed. Bedding orientations favor diversion of moisture flow towards the east and southeast in these units. Although fractures are less common than in the overlying welded tuffs, they may provide vertical pathways through saturated portions of the lower Otowi Member.

This report also highlights the role of faults and fractures as potential moisture pathways in the upper vadose zone. The TA-09 graben and its associated structures crosses Cañon de Valle downstream of the 260 Outfall where quantities of HE at high concentrations were released in large volumes of water that provided a significant hydrologic driving force for infiltration of contaminants. The faults and fractures may be important infiltration pathways through the strongly welded tuffs that underlie the canyon floor.

Groundwater flow directions are poorly known for deep perched groundwater at TA-16, presenting challenges for evaluation and design of remedial alternatives for the corrective measures evaluation. New data from this investigation suggest HE-contaminated moisture flow through the vadose zone will tend to stair-step towards the east and southeast before entering the upper deep perched groundwater zone. Flow directions for perched groundwater in the lower Otowi Member are likely to be towards the southeast based on the orientation of potential perching horizons. These gradients support the interpretations for flow directions inferred from the water table map for the upper deep perched zone. These data contribute to the site conceptual model about contaminant recharge pathways and will help constrain the placement and locations of future wells targeting deep perched groundwater in the area.

5.0 REFERENCES AND MAP DATA SOURCES

5.1 References

The following reference list includes documents cited in this report.

Bailey, R.A., R.L. Smith, and C.S. Ross. "Stratigraphic Nomenclature of Volcanic Rocks in the Jemez Mountains, New Mexico," in *Contributions to Stratigraphy*, U.S. Geological Survey Bulletin 1274-P, Washington, D.C. (1969).

Broxton, D., R. Warren, P. Longmire, R. Gilkeson, S. Johnson, D. Rogers, W. Stone, B. Newman, M. Everett, D. Vaniman, S. McLin, J. Skalski, and D. Larssen. "Characterization Well R-25 Completion Report," Los Alamos National Laboratory report LA-13909-MS, Los Alamos, New Mexico (2002).

Broxton, D., G. WoldeGabriel, L. Peters, J. Budahn, and G. Luedemann. "Pliocene Volcanic Rocks of the Tschicoma Formation, East-Central Jemez Volcanic Field: Chemistry, Petrography, and Age Constraints," New Mexico Geological Society Guidebook: 58th Field Conference, Geology of the Jemez Mountains Region II, pp. 284–295 (2007).

Broxton, D.E., G.H. Heiken, S.J. Chipera, and F.M. Byers, Jr.. "Stratigraphy, Petrography, and Mineralogy of Bandelier Tuff and Cerro Toledo Deposits," in *Earth Science Investigation for Environmental Restoration—Los Alamos National Laboratory, Technical Area 21*, Los Alamos National Laboratory report LA-12934-MS, Los Alamos, New Mexico, pp. 33-63 (1995a).

Broxton, D.E., P.A. Longmire, P.G. Eller, and D. Flores. "Preliminary Drilling Results for Boreholes LADP-3 and LADP-4," in *Earth Science Investigation for Environmental Restoration—Los Alamos National Laboratory, Technical Area 21*, Los Alamos National Laboratory report A-12934-MS, Los Alamos, New Mexico, pp. 93-109 (1995b).

Broxton, D.E., and S.L. Reneau. "Stratigraphic Nomenclature of the Bandelier Tuff for the Environmental Restoration Project at Los Alamos National Laboratory," Los Alamos National Laboratory report LA-13010-MS, Los Alamos, New Mexico (1995c).

Broxton, D.E., R.T. Ryti, D. Carlson, R.G. Warren, E.C. Kluk, and S.J. Chipera. "Natural Background Geochemistry of the Bandelier Tuff at MDA P, Los Alamos National Laboratory," Los Alamos National Laboratory document LA-UR-96-1151, Los Alamos, New Mexico (1996).

Broxton, D.E., and D.T. Vaniman. "Geologic Framework of a Groundwater System on the Margin of a Rift Basin, Pajarito Plateau, North-Central New Mexico," *Vadose Zone Journal,* Vol. 4, No. 3, pp. 522–550 (2005).

Cavazza, W.. "Sedimentation Pattern of a Rift-Filling Unit, Tesuque Formation (Miocene), Española Basin, Rio Grande Rift, New Mexico," *Journal of Sedimentary Petrology,* Vol. 59, No. 2, pp. 287–296 (1989).

Ferguson, J.F., W.S. Baldridge, L.W. Braile, S. Biehler, B. Gilpin, and G.R. Jiracek. "Structure of the Española Basin, Rio Grande Rift, New Mexico, from Stage Seismic and Gravity Data," New Mexico Geological Society Guidebook: 46th Field Conference, Geology of the Santa Fe Region, pp. 105-110 (1995).

Fisher, R.V., and H.-U. Schmincke. *Pyroclastic Rocks*, Springer-Verlag, Berlin, Germany (1984).

Galusha, T., and J.C. Blick. “Stratigraphy of the Santa Fe Group, New Mexico,” *Bulletin of the American Museum of Natural History,* Vol. 144, No. 1, pp. 1–128 (1971).

Gardner, J.L., S.L. Reneau, C.J. Lewis, A. Lavine, D.J. Krier, G. WoldeGabriel, and G.D. Guthrie. “Geology of the Pajarito Fault Zone in the Vicinity of S-Site (TA-16), Los Alamos National Laboratory, Rio Grande Rift, New Mexico,” Los Alamos National Laboratory report LA-13831-MS, Los Alamos, New Mexico (2001).

Gardner, J.N., W.S. Baldridge, R. Gribble, K. Manley, K. Tanaka, J.W. Geissman, M. Gonzales, and G. Baron. “Results from Seismic Hazards Trench #1 (SHT-1) Los Alamos Seismic Hazards Investigations,” Los Alamos National Laboratory document EES1-SH90-19, Los Alamos, New Mexico (1990).

Gardner, J.N., F. Goff, S. Kelley, and E. Jacobs. “Rhyolites and Associated Deposits of the Valles-Toledo Caldera Complex,” *New Mexico Geology,* Vol. 32, No. 1, pp. 3–18 (2010).

Gardner, J.N., and F.E. Goff. “Potassium-Argon Dates from the Jemez Volcanic Field: Implications for Tectonic Activity in the North-Central Rio Grande Rift,” New Mexico Geological Society Guidebook: 35th Field Conference, Rio Grande Rift, Northern New Mexico, University of New Mexico, Albuquerque, New Mexico (1984).

Gardner, J.N., F.E. Goff, S.R. Garcia, and R.C. Hagan. “Stratigraphic Relations and Lithologic Variations in the Jemez Volcanic Field, New Mexico,” *Journal of Geophysical Research,* Vol. 91, No. B2, pp. 1763–1778 (1986).

Gardner, J.N., and L.S. House. “Seismic Hazards Investigations at Los Alamos National Laboratory, 1984 to 1985,” Los Alamos National Laboratory report LA-11072-MS, Los Alamos, New Mexico (1987).

Gardner, J.N., T. Kolbe, and S. Chang. “Geology, Drilling, and Some Hydrologic Aspects of Seismic Hazards Program Core Holes, Los Alamos National Laboratory, New Mexico,” Los Alamos National Laboratory report LA-12460-MS, Los Alamos, New Mexico (1993).

Gardner, J.N., A. Lavine, G. WoldeGabriel, D. Krier, J., D.T. Vaniman, F.A. Caporuscio, C.J. Lewis, M.R. Reneau, E.C. Kluk, and M.J. Snow. “Structural Geology of the Northwestern Portion of Los Alamos National Laboratory, Rio Grande Rift, New Mexico: Implications for Seismic Surface Rupture Potential from TA-3 to TA-55,” Los Alamos National Laboratory report LA-13589-MS, Los Alamos, New Mexico (1999).

Goff, F., J.N. Gardner, and S.L. Reneau. “Geology of the Frijoles 7.5-minute Quadrangle, Los Alamos and Sandoval Counties, New Mexico,” New Mexico Bureau of Geology and Mineral Resources Open-File Digital Geologic Map OF-GM 42, Socorro, New Mexico (2002).

Goff, F., R.G. Warren, C.J. Goff, and N. Dunbar. “Eruption of Reverse-Zoned Upper Tshirege Member, Bandelier Tuff from Centralized Vents within Valles Caldera, New Mexico,” *Journal of Volcanology and Geothermal Research,* Vol. 276, pp. 82–104 (2014).

Golombek, M.P. “Geology, Structure, and Tectonics of the Pajarito Fault Zone in the Española Basin of the Rio Grande Rift, New Mexico,” *Geological Society of America Bulletin,* Vol. 94, pp. 192–205 (1983).

Griggs, R.L., and J.D. Hem. “Geology and Ground-Water Resources of the Los Alamos Area, New Mexico,” U.S. Geological Survey Water Supply Paper 1753, Washington, D.C. (1964).

Hildreth, W.. “Gradients in Silicic Magma Chambers: Implications for Lithospheric Magmatism,” *Journal of Geophysical Research,* Vol. 86, No. B11, pp. 10153–10192 (1981).

Izett, G.A., and J.D. Obradovich. “^{40}Ar/^{39}Ar Age Constraints for the Jaramillo Normal Subchron and the Matuyama-Brunhes Geomagnetic Boundary,” *Journal of Geophysical Research,* Vol. 99, No. B2, pp. 2925–2934 (1994).

Kelley, V.C.. “Geology of Española Basin, New Mexico,” Map 48, ISSN: 0545-2899, New Mexico Bureau of Mines and Mineral Resources, Socorro, New Mexico (1978).

Kempter, K.A., and S. Kelley. “Preliminary Geologic Map of Guaje Mountain 7.5 Minute Quadrangle, Los Alamos and Sandoval Counties, New Mexico,” scale 1:24000, Map 55, New Mexico Bureau of Mines & Mineral Resources, New Mexico Institute of Mining and Technology, Socorro, New Mexico (2002).

Kleinfelder. “Final Well CdV-16-1(i) Completion Report,” report prepared for Los Alamos National Laboratory, Project No. 37151/9.12, Albuquerque, New Mexico (2004).

Kleinfelder. “Final Completion Report, Characterization Well R-18,” report prepared for Los Alamos National Laboratory, Project No. 37151, Albuquerque, New Mexico (2005a).

Kleinfelder. “Final Completion Report, Characterization Well CdV-16-2(i)r,” report prepared for Los Alamos National Laboratory, Project No. 49436, Albuquerque, New Mexico (2005b).

Kleinfelder. “Final Well R-26 Completion Report, Revision No. 1,” report prepared for Los Alamos National Laboratory, Project No. 37151, Albuquerque, New Mexico (2005c).

Kopp, B., A. Crowder, M. Everett, D. Vaniman, D. Hickmott, W. Stone, N. Clayton, S. Pearson, and D. Larssen. “Well CdV-R-15-3 Completion Report,” Los Alamos National Laboratory report LA-13906-MS, Los Alamos, New Mexico (2002).

Kopp, B., M. Everett, J.R. Lawrence, G. WoldeGabriel, D. Vaniman, J. Heikoop, W. Stone, S. McLin, N. Clayton, and D. Larssen. “Well CdV-R-37-2 Completion Report,” Los Alamos National Laboratory report LA-14023-MS, Los Alamos, New Mexico (2003).

LANL (Los Alamos National Laboratory). “RFI Report for Potential Release Site 16-021(c),” Los Alamos National Laboratory document LA-UR-98-4101, Los Alamos, New Mexico (1998).

LANL (Los Alamos National Laboratory). “Completion Report for Well R-25c,” Los Alamos National Laboratory document LA-UR-08-5878, Los Alamos, New Mexico (2008a).

LANL (Los Alamos National Laboratory). “Completion Report for Well R-25b, Revision 1,” Los Alamos National Laboratory document LA-UR-08-7831, Los Alamos, New Mexico (2008b).

LANL (Los Alamos National Laboratory). “Completion Report for Regional AquiferWell R-48,” Los Alamos National Laboratory document LA-UR-10-0864, Los Alamos, New Mexico (2010a).

LANL (Los Alamos National Laboratory). “Completion Report for Intermediate Aquifer Well R-47i,” Los Alamos National Laboratory document LA-UR-10-2207, Los Alamos, New Mexico (2010b).

LANL (Los Alamos National Laboratory). “Completion Report for Intermediate Aquifer Well CdV-37-1i,” Los Alamos National Laboratory document LA-UR-10-1771, Los Alamos, New Mexico (2010c).

LANL (Los Alamos National Laboratory). “Completion Report for Intermediate Well CdV-16-4ip,” Los Alamos National Laboratory document LA-UR-11-0187, Los Alamos, New Mexico (2011a).

LANL (Los Alamos National Laboratory). “Completion Report for Regional Well R-63,” Los Alamos National Laboratory document LA-UR-11-3673, Los Alamos, New Mexico (2011b).

LANL (Los Alamos National Laboratory). “Investigation Report for Water Canyon/Cañon de Valle,” Los Alamos National Laboratory document LA-UR-11-5478, Los Alamos, New Mexico (2011c).

LANL (Los Alamos National Laboratory). “Technical Area 16 Well Network Evaluation and Recommendations,” Los Alamos National Laboratory document LA-UR-12-1082, Los Alamos, New Mexico (2012).

LANL (Los Alamos National Laboratory). “Completion Report for Regional Aquifer Well R-47,” Los Alamos National Laboratory document LA-UR-14-28638, Los Alamos, New Mexico (2014).

LANL (Los Alamos National Laboratory). “Completion Report for Intermediate Aquifer Well CdV-9-1(i),” Los Alamos National Laboratory document LA-UR-15-23954, Los Alamos, New Mexico (2015a).

LANL (Los Alamos National Laboratory). “Completion Report for Intermediate Aquifer Well R-63i,” Los Alamos National Laboratory document LA-UR-15-26729, Los Alamos, New Mexico (2015b).

LANL (Los Alamos National Laboratory) “Completion Report for Regional Aquifer Well R-58,” Los Alamos National Laboratory document LA-UR-16-21912, Los Alamos, New Mexico (2016).

LANL (Los Alamos National Laboratory). “Completion Report for Regional Aquifer Well R-68,” Los Alamos National Laboratory document LA-UR-17-26063, Los Alamos, New Mexico (2017).

Lewis, C.J., A. Lavine, S.L. Reneau, J.N. Gardner, R. Channell, and C.W. Criswell. “Geology of the Western Part of Los Alamos National Laboratory (TA-3 to TA-16), Rio Grande Rift, New Mexico,” Los Alamos National Laboratory report LA-13960-MS, Los Alamos, New Mexico (2002).

Lewis, C.L., J.N. Gardner, E.S. Schultz-Fellenz, A. Lavine, and S.L. Reneau. “Fault Interaction and Along-Strike Variation in Throw in the Pajarito Fault System, Rio Grande Rift, New Mexico,” *Geosphere,* Vol. 5, No. 3, pp. 252–269 (2009).

Lipman, P.W., R.L. Christensen, and J.T. O'Connor. “A Compositionally Zoned Ash-Flow Sheet in Southern Nevada,” *U.S. Geological Survey Professional Paper,* Vol. Paper 524-F, pp. 1–54 (1966).

Miyazaki, T.. “Water Flow in Unsaturated Soil in Layered Slopes,” *Journal of Hydrology,* Vol. 102, pp. 201–214 (1988).

Montazer, P., and W.E. Wilson. “Conceptual Hydrologic Model of Flow in the Unsaturated Zone, Yucca Mountain, Nevada,” *U.S. Geological Survey Water-Resources Investigation Report,* Vol. 84-4345, pp. 1–59 (1984).

Potter, D.B., and C.M. Oberthal. “Vent Sites and Flow Directions of the Otowi Ash Flows (Lower Bandelier Tuff), New Mexico,” *Geological Society of America Bulletin,* Vol. 98, pp. 66-76 (1987).

Reneau, S.L., and E.V. McDonald, September 12–15. “Landscape History and Processes on the Pajarito Plateau, Northern New Mexico,” in *Rocky Mountain Cell, Friends of the Pleistocene Field Trip Guidebook*, Los Alamos National Laboratory document LA-UR-96-3035, Los Alamos, New Mexico (1996a).

Reneau, S.L., E.V. McDonald, J.N. Gardner, T.R. Kolbe, J.S. Carney, P.M. Watt, and P.A. Longmire. “Erosion and Deposition on the Pajarito Plateau, New Mexico, and Implications for Geomorphic Responses to Late Quaternary Climatic Changes,” New Mexico Geological Society Guidebook: 47th Field Conference, Jemez Mountains Region, New Mexico, pp. 391-398 (1996b).

Reneau, S.L., and R. Raymond, Jr. (Eds.). “Geological Site Characterization for the Proposed Mixed Waste Disposal Facility, Los Alamos National Laboratory,” Los Alamos National Laboratory report LA-13089-MS, Los Alamos, New Mexico (1995).

Ross, B.. “The Diversion Capacity of Capillary Barriers,” *Water Resources Research,* Vol. 26, No. 5, pp. 2625-2629 (1990).

Samuels, K.E., D.E. Broxton, D.T. Vaniman, G. WoldeGabriel, J.A. Wolff, D.D. Hickmott, E.C. Kluk, and M.M. Fittipaldo. “Distribution of Dacite Lavas beneath the Pajarito Plateau, Jemez Mountains, New Mexico,” New Mexico Geological Society Guidebook: 58th Field Conference, Geology of the Jemez Mountains Region II, pp. 296–308 (2007).

Smith, G.A.. “Development of a Pyroclastic Apron Adjacent to Rhyolite Domes in a Subsiding Basin: Upper Miocene Peralta Tuff, Jemez Mountains, New Mexico,” *Volcanology in New Mexico, New Mexico Natural History and Science Bulletin,* Vol. 18, pp. 85-96 (2001).

Smith, R.L.. “Ash-Flow Magmatism,” *U.S. Geological Survey,* Vol. 951, No. Special Paper 180, pp. 5-27 (1979).

Smith, R.L., and R.A. Bailey. “The Bandelier Tuff: A Study of Ash-Flow Eruption Cycles from Zoned Magma Chambers,” *Bulletin Volcanologique,* Vol. 29, pp. 83-103 (1966).

Smith, R.L., R.A. Bailey, and C.S. Ross. “Geologic Map of the Jemez Mountains, New Mexico,” U.S. Geological Survey Miscellaneous Investigations Series, Map I-571, Washington, D.C. (1970).

Sparks, R.S.J.. “Grain Size Variations in Ignimbrites and Implications for the Transport of Pyroclastic Flows,” *Sedimentology,* Vol. 23, pp. 147-188 (1976).

Spell, T.L., I. McDougall, and A.P. Doulgeris. “Cerro Toledo Rhyolite, Jemez Volcanic Field, New Mexico: ^{40}Ar/^{39}Ar Geochronology of Eruptions between Two Caldera-Forming Events,” *Geological Society of America Bulletin,* Vol. 108, No. 12, pp. 1549-1566 (1996).

Stimac, J.A., D.E. Broxton, E.C. Kluk, S.J. Chipera, and J.R. Budahn. “Stratigraphy of the Tuffs from Borehole 49-2-700-1 at Technical Area 49, Los Alamos National Laboratory, New Mexico,” Los Alamos National Laboratory report LA-13969, Los Alamos, New Mexico (2002).

Stix, J., F.E. Goff, M.P. Gorton, G. Heiken, and S.R. Garcia. “Restoration of Compositional Zonation in the Bandelier Silicic Magma Chamber Between Two Caldera-Forming Eruptions: Geochemistry and Origin of the Cerro Toledo Rhyolite, Jemez Mountains, New Mexico,” *Journal of Geophysical Research,* Vol. 93, No. B6, pp. 6129-6147 (1988).

Turbeville, B.N., D.B. Waresback, and S. Self. “Lava-Dome Growth and Explosive Volcanism in the Jemez Mountains, New Mexico: Evidence from the Pilo-Pliestocene Puye Alluvial Fan,” *Journal of Volcanology and Geothermal Research,* Vol. 36, pp. 267–291 (1989).

Warren, R.G., F. Goff, E.C. Kluk, and J.R. Budahn. “Petrography, Chemistry, and Mineral Compositions for Subunits of the Tshirege Member, Bandelier Tuff within the Valles Caldera and Pajarito Plateau,” Geology of the Jemez Region II. New Mexico Geological Society, 58th Annual Field Conference, Socorro, New Mexico, pp. 316-332 (2007).

Warren, R.G., E.V. McDonald, and R.T. Ryti. “Baseline Geochemistry of Soil and Bedrock, Tshirege Member of the Bandelier Tuff at MDA P,” Los Alamos National Laboratory report LA-13330-MS, Los Alamos, New Mexico (1997).

Wilson, C.J.N., 1986. “Pyroclastic Flows and Ignimbrites,” *Science Progress Oxford,* Vol. 70, pp. 171-207.

WoldeGabriel, G., D.J. Koning, D. Broxton, and R.G. Warren. “Chronology of Volcanism, Tectonics, and Sedimentation Near the Western Boundary Fault of the Española Basin, Rio Grande Rif, New Mexico,” *Geological Society of America Special Papers,* Vol. 494, pp. 221-238 (2013).

Wu, Y.-S., W. Zhang, L. Pan, J. Hinds, and G.S. Bodvarsson. “Modeling Capillary Barriers in Unsaturated Fractured Rock,” *Water Resources Reseach,* Vol. 38, No. 11, pp. 1255-1259 (2002).

Zimmerer, M.J., J. Lefferty, and M.A. Coble. “The Eruptive and Magmatic History of the Youngest Pulse of Volcanism at the Valles Caldera: Implications for Successfully Dating Late Quaternary Eruptions,” *Journal of Volcanology and Geothermal Research,* Vol. 310, pp. 50–57 (2016).

5.2 Map Data Sources

Hillshade; Los Alamos National Laboratory, ER-ES, As published; \\slip\gis\Data\HYP\LiDAR\2014\Bare_Earth\BareEarth_DEM_Mosaic.gdb; 2014

Structures; Los Alamos National Laboratory, KSL Site Support Services, Planning, Locating and Mapping Section; 06 January 2004; as published 29 November 2010.

Paved Road Arcs; Los Alamos National Laboratory, FWO Site Support Services, Planning, Locating and Mapping Section; 06 January 2004; as published 29 November 2010.

Drainage channel; Los Alamos National Laboratory, ER-ES, As published, GIS projects folder; \\slip\gis\GIS\Projects\11-Projects\11-0108\gdb\gdb_11-0108_generic.mdb; drainage; 2017

Contour, 100-, 20-, and 10-ft interval; Hypsography; Los Alamos National Laboratory, ENV Environmental Remediation and Surveillance Programt; 1991.

Regional groundwater contour 40-ft interval; Los Alamos National Laboratory, ER-ES, As published, GIS projects folder; \\slip\gis\GIS\Projects\12-Projects\12-0020\shp\contour_10_ft_interval.shp; 2012

Approximate extent of RDX contamination in deep perched groundwater, based on current knowledge; Los Alamos National Laboratory, ER-ES, As published, GIS projects folder; \\slip\gis\GIS\Projects\12-Projects\12-0020\shp\perched_water_zones.shp; 2014

Approximate extent of RDX contamination in deep perched groundwater, based on current knowledge; Los Alamos National Laboratory, ER-ES, As published, GIS projects folder; \\slip\gis\GIS\Projects\15-Projects\15-0041\shp\perched_aquifer.shp; 2016.

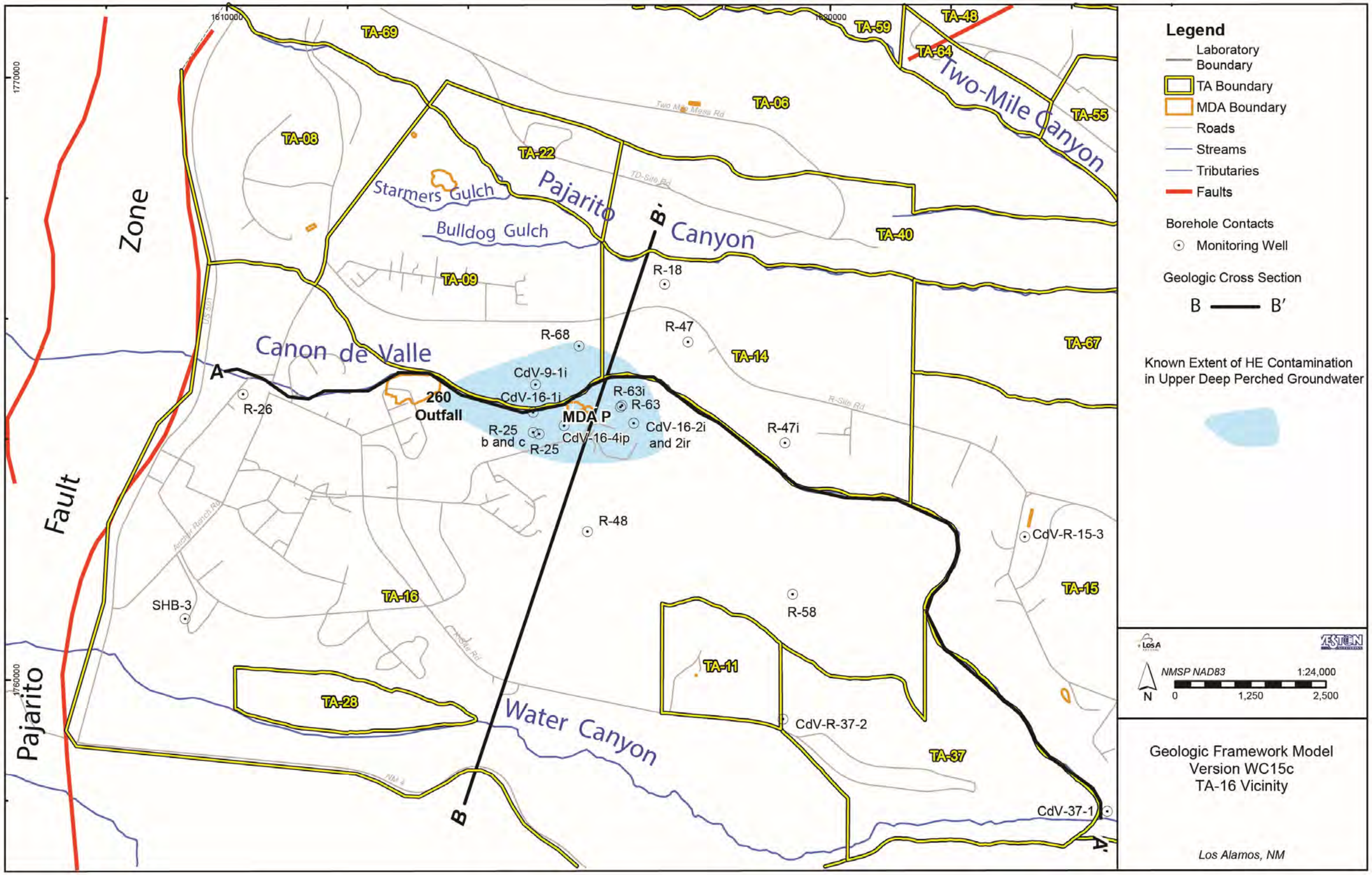

Figure 1.0-1 Location of the 260 Outfall, regional and intermediate wells in the vicinity of TA-16, and the lines of section for geologic cross-sections shown in Figures 3.0-2 and 3.0-3

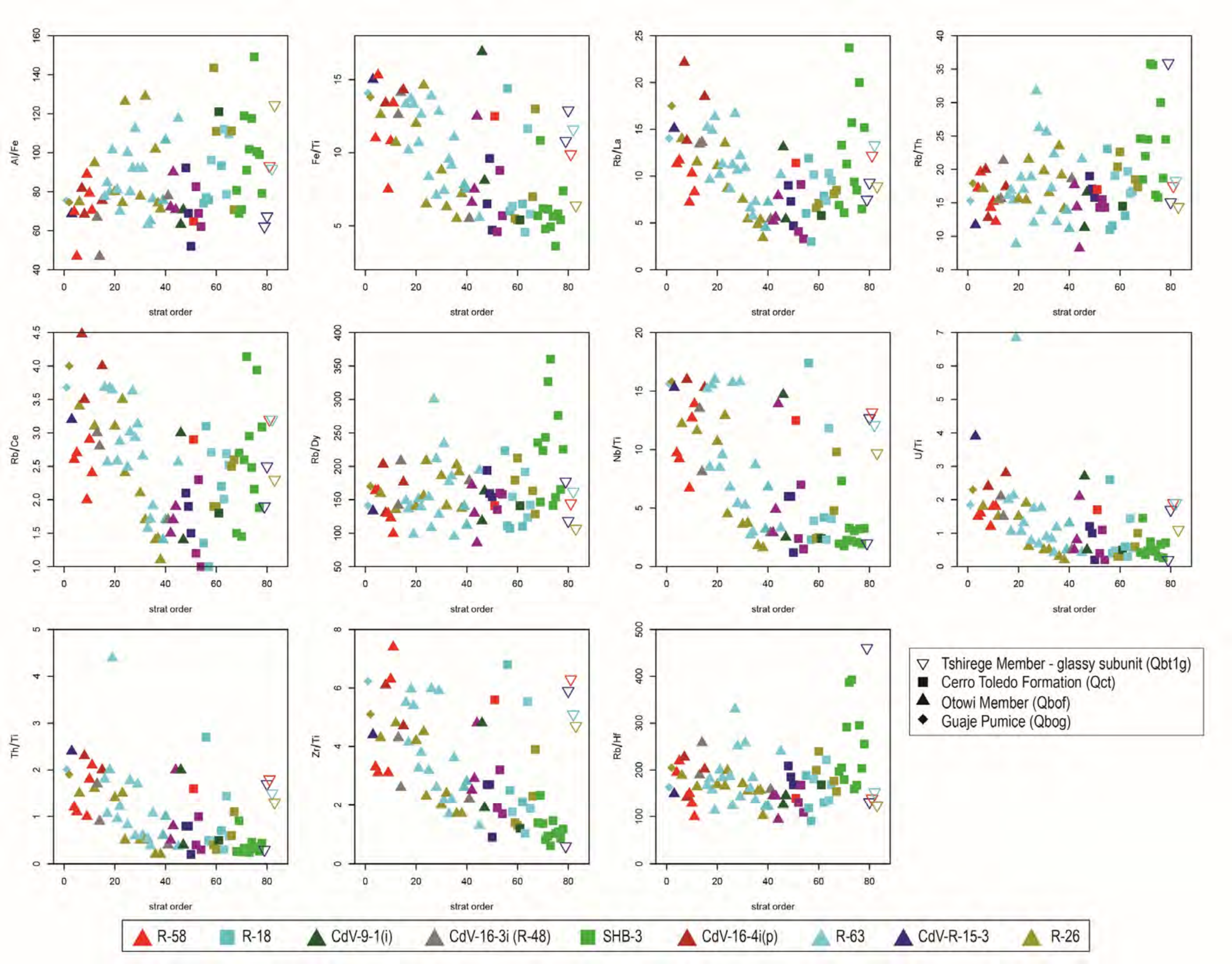

Figure 2.2-1 Plots of elemental ratios versus stratigraphic order for samples analyzed by LA-ICP-MS of pumice grains. Lowest stratigraphic units are assigned the lowest values, highest stratigraphic units are assigned the highest values of stratigraphic order.

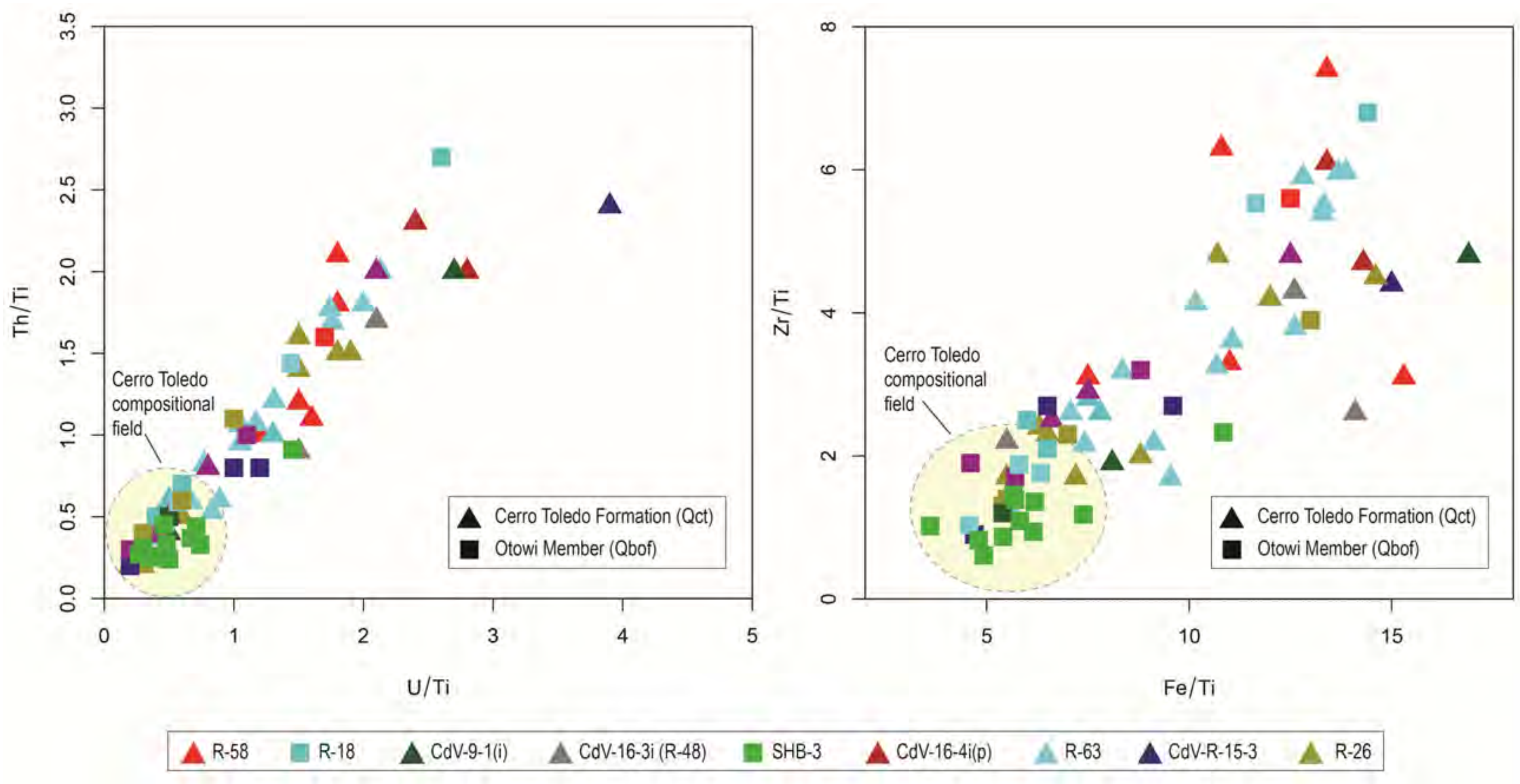

Figure 2.2-2 Plots of trace element ratios determined by LA-ICP-MS of pumice grains from eight wells and one core hole (SHB-3) within the RDX investigation area. The Cerro Toledo Formation samples generally show lower ratios than the Otowi Member samples. However, some samples identified as Otowi Member plot within the Cerro Toledo compositional field and some samples identified as the Cerro Toledo Formation plot outside the Cerro Toledo compositional field.

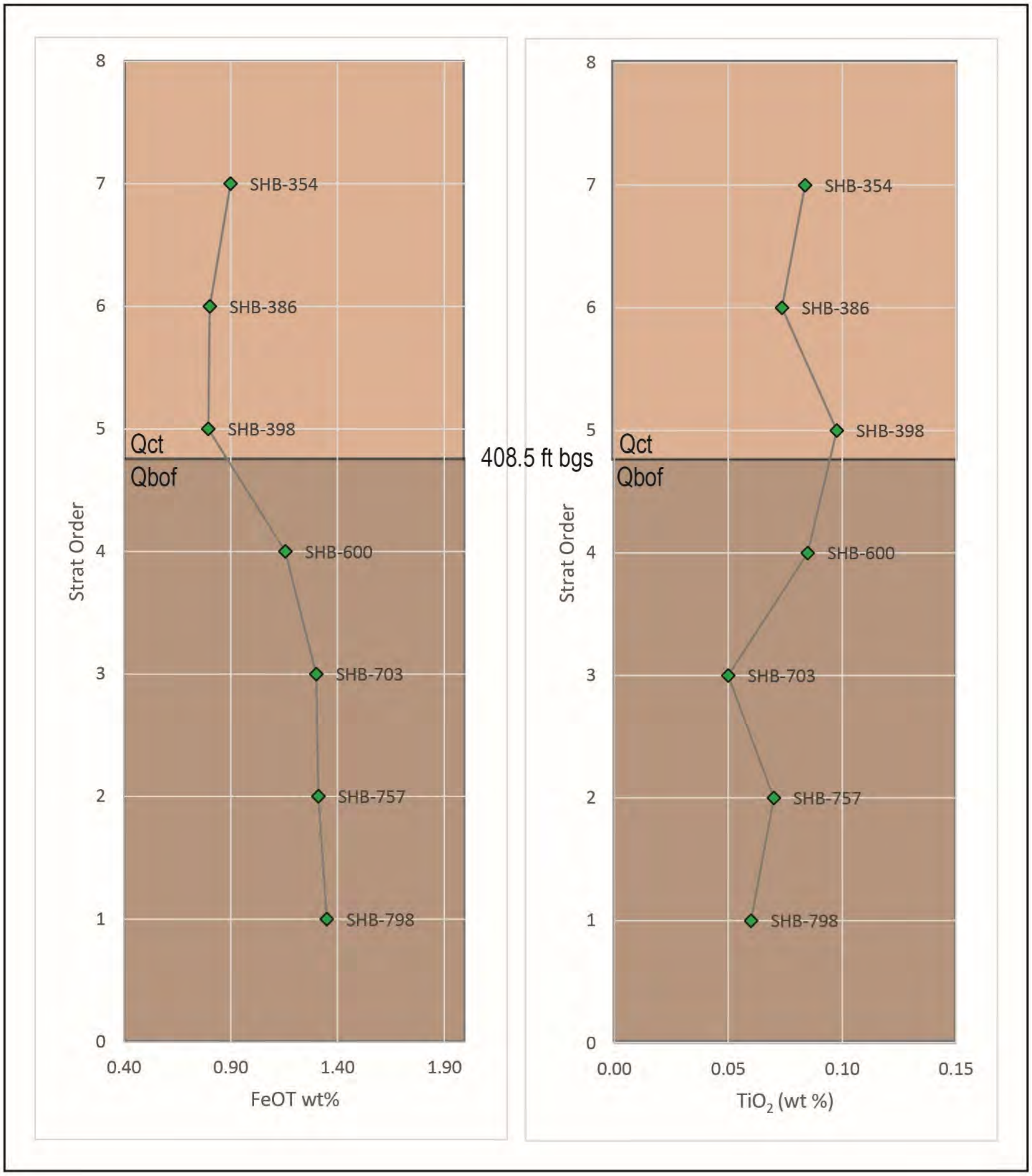

Figure 2.2-3 **Electron microprobe iron oxide (total) and titanium oxide data for SHB-3 glass showing the chemical transition up-section from the Otowi Member to the Cerro Toledo Formation. The weight percent of iron is higher, and the weight percent of titanium is lower in the Otowi Member compared with the Cerro Toledo Formation in this borehole.**

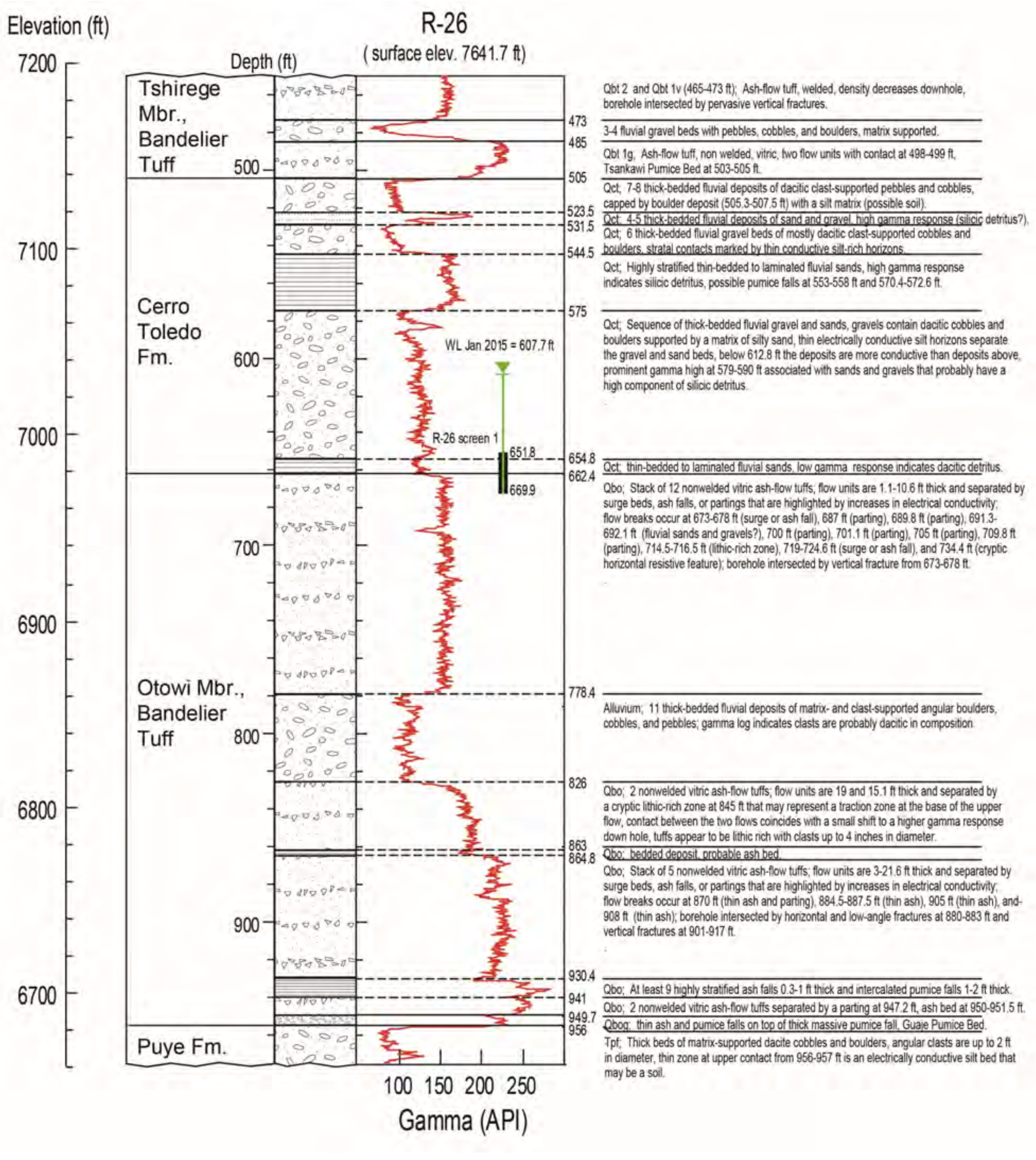

Qbt 2 and Qbt 1v (465-473 ft); Ash-flow tuff, welded, density decreases downhole, borehole intersected by pervasive vertical fractures.

3-4 fluvial gravel beds with pebbles, cobbles, and boulders, matrix supported.

Qbt 1g; Ash-flow tuff, non welded, vitric, two flow units with contact at 498-499 ft, Tsankawi Pumice Bed at 503-505 ft.

Qct; 7-8 thick-bedded fluvial deposits of dacitic clast-supported pebbles and cobbles, capped by boulder deposit (505.3-507.5 ft) with a silt matrix (possible soil).

Qct; 4-5 thick-bedded fluvial deposits of sand and gravel, high gamma response (silicic detritus?).

Qct; 6 thick-bedded fluvial gravel beds of mostly dacitic clast-supported cobbles and boulders, stratal contacts marked by thin conductive silt-rich horizons.

Qct; Highly stratified thin-bedded to laminated fluvial sands, high gamma response indicates silicic detritus, possible pumice falls at 553-558 ft and 570.4-572.6 ft.

Qct; Sequence of thick-bedded fluvial gravel and sands, gravels contain dacitic cobbles and boulders supported by a matrix of silty sand, thin electrically conductive silt horizons separate the gravel and sand beds, below 612.8 ft the deposits are more conductive than deposits above, prominent gamma high at 579-590 ft associated with sands and gravels that probably have a high component of silicic detritus.

Qct; thin-bedded to laminated fluvial sands, low gamma response indicates dacitic detritus.

Qbo; Stack of 12 nonwelded vitric ash-flow tuffs; flow units are 1.1-10.6 ft thick and separated by surge beds, ash falls, or partings that are highlighted by increases in electrical conductivity; flow breaks occur at 673-678 ft (surge or ash fall), 687 ft (parting), 689.8 ft (parting), 691.3-692.1 ft (fluvial sands and gravels?), 700 ft (parting), 701.1 ft (parting), 705 ft (parting), 709.8 ft (parting), 714.5-716.5 ft (lithic-rich zone), 719-724.6 ft (surge or ash fall), and 734.4 ft (cryptic horizontal resistive feature); borehole intersected by vertical fracture from 673-678 ft.

Alluvium; 11 thick-bedded fluvial deposits of matrix- and clast-supported angular boulders, cobbles, and pebbles; gamma log indicates clasts are probably dacitic in composition.

Qbo; 2 nonwelded vitric ash-flow tuffs; flow units are 19 and 15.1 ft thick and separated by a cryptic lithic-rich zone at 845 ft that may represent a traction zone at the base of the upper flow; contact between the two flows coincides with a small shift to a higher gamma response down hole, tuffs appear to be lithic rich with clasts up to 4 inches in diameter.

Qbo; bedded deposit, probable ash bed.

Qbo; Stack of 5 nonwelded vitric ash-flow tuffs; flow units are 3-21.6 ft thick and separated by surge beds, ash falls, or partings that are highlighted by increases in electrical conductivity; flow breaks occur at 870 ft (thin ash and parting), 884.5-887.5 ft (thin ash), 905 ft (thin ash), and 908 ft (thin ash); borehole intersected by horizontal and low-angle fractures at 880-883 ft and vertical fractures at 901-917 ft.

Qbo; At least 9 highly stratified ash falls 0.3-1 ft thick and intercalated pumice falls 1-2 ft thick.

Qbo; 2 nonwelded vitric ash-flow tuffs separated by a parting at 947.2 ft, ash bed at 950-951.5 ft.

Qbog; thin ash and pumice falls on top of thick massive pumice fall, Guaje Pumice Bed.

Tpf; Thick beds of matrix-supported dacite cobbles and boulders, angular clasts are up to 2 ft in diameter, thin zone at upper contact from 956-957 ft is an electrically conductive silt bed that may be a soil.

Figure 2.3-1 Lithologic log and spectral gamma log for the base of the Tshirege Member, Cerro Toledo Formation, and Otowi Member (depth interval 450 ft to 980 ft) in well R-26. Geologic contacts and lithologic log were revised based on reexamination and reinterpretation of borehole geophysical logs and cuttings. Well screen interval (black rectangle) and water level (inverted green triangle) are shown for the upper well screen.

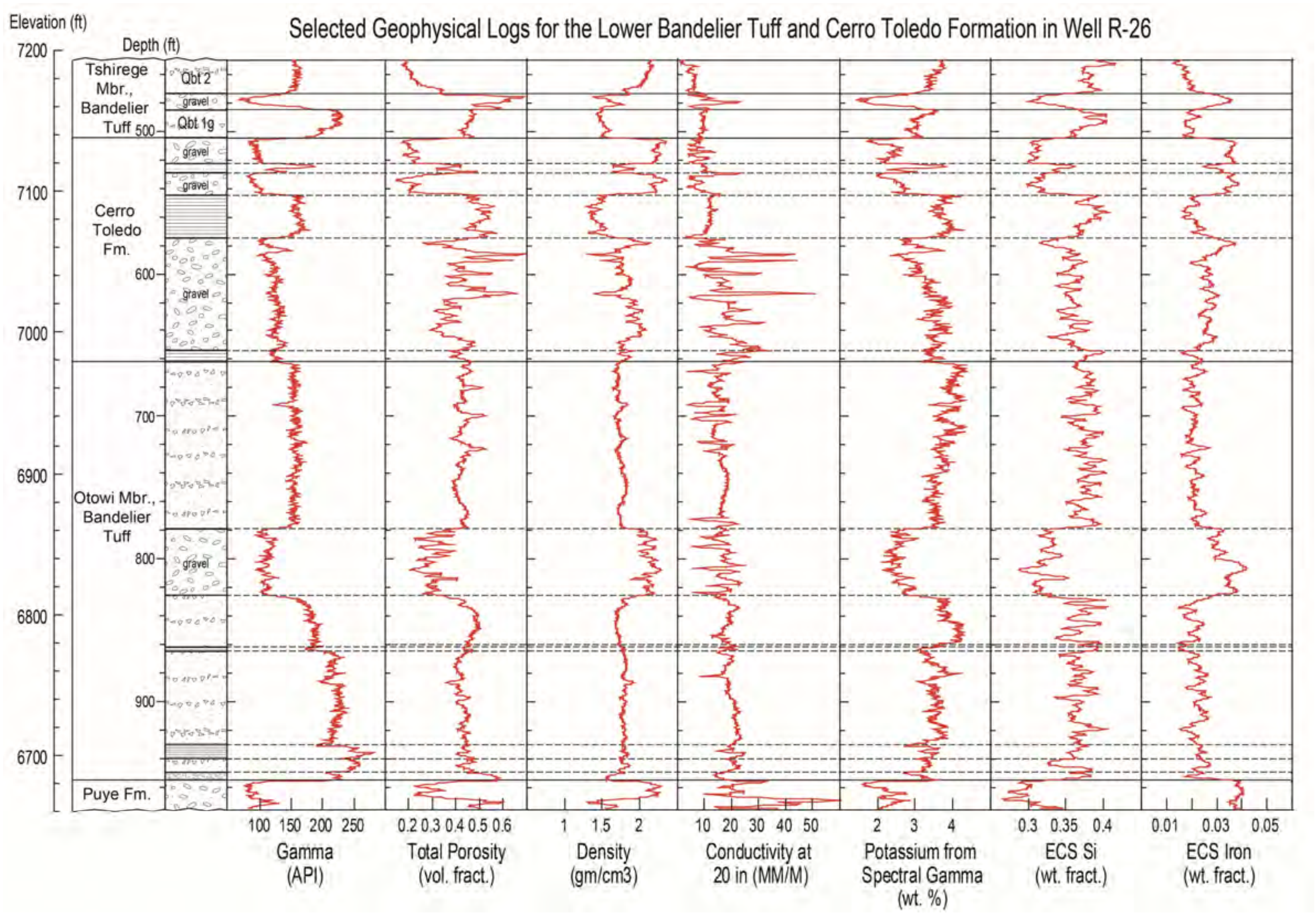

Figure 2.3-2 **Selected geophysical logs of the base of the Tshirege Member, Cerro Toledo Formation, and Otowi Member in well R-26. The logs were collected in a mud-filled open borehole by Schlumberger, Inc. See Figure 2.3-1 for details about lithologies in this depth interval. Log responses reflect variations in rock compositions, physical properties, and electrical properties.**

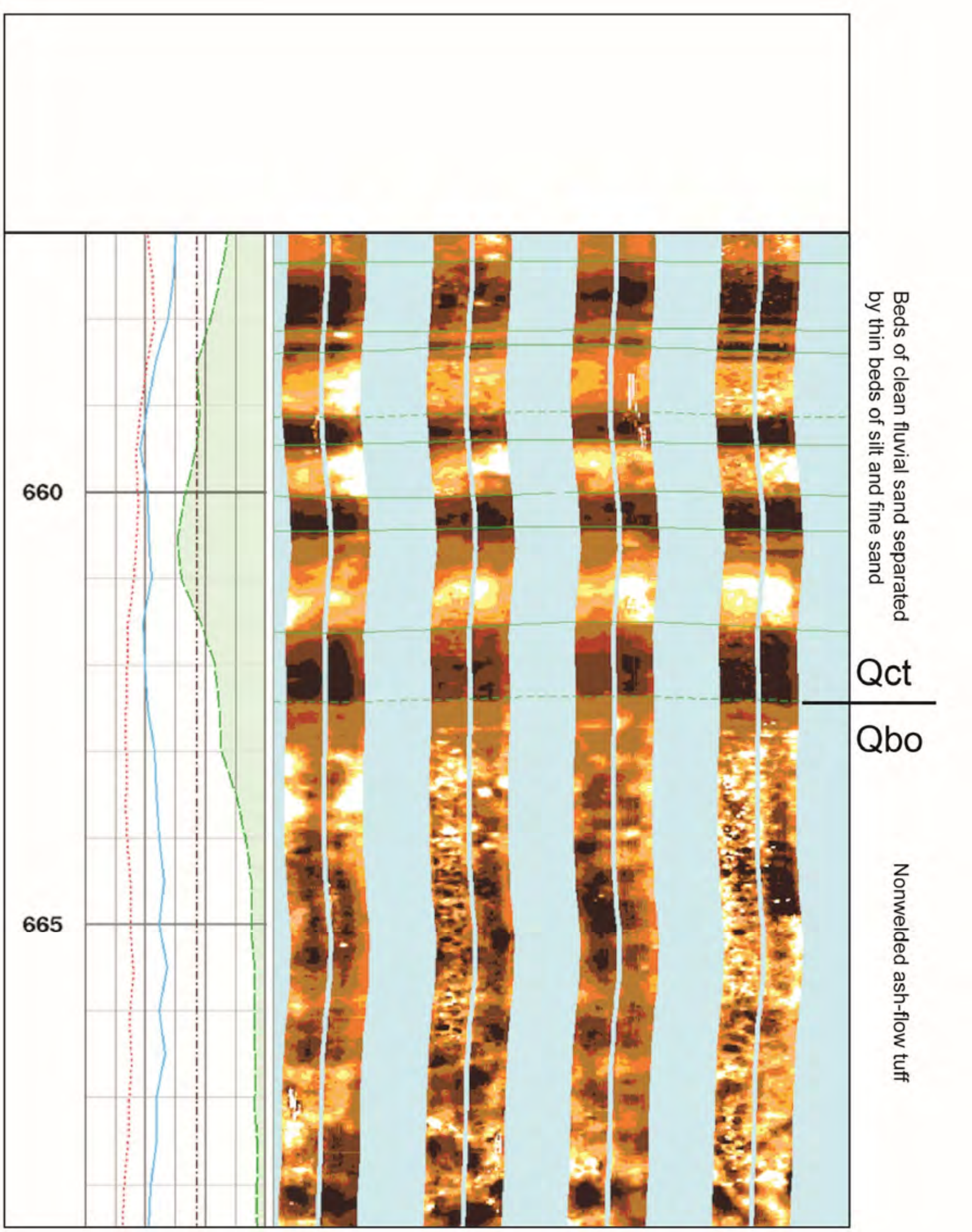

Figure 2.3-3 **FMI log showing the contact between stratified dacitic sands of the Cerro Toledo Formation (Qct) and nonwelded ash-flow tuffs in the upper part (G4–G5 subunit) of the Otowi Member (Qbo) in well R-26. The depth interval for the image is 657 ft to 668.5 ft.**

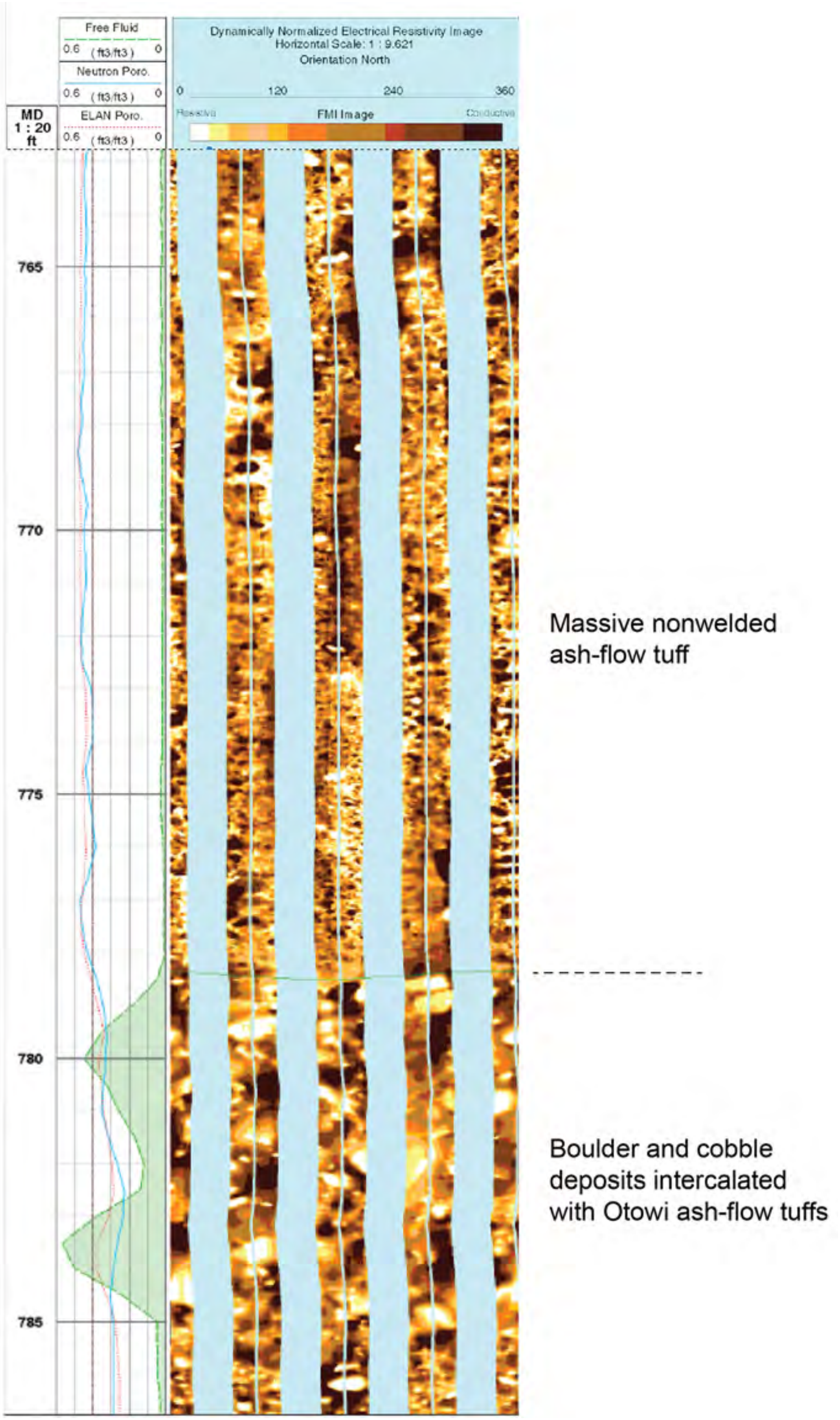

Massive nonwelded ash-flow tuff

Boulder and cobble deposits intercalated with Otowi ash-flow tuffs

Figure 2.3-4 FMI log showing the massive nature of thick nonwelded ash-flow tuffs in the upper part of the Otowi Member (G4–G5 subunit) in well R-26. The tuffs overlie boulder and cobble that separate the upper and lower tuff sequences in the Otowi Member at this location. The depth interval for the image is 762.8 ft to 786.7 ft.

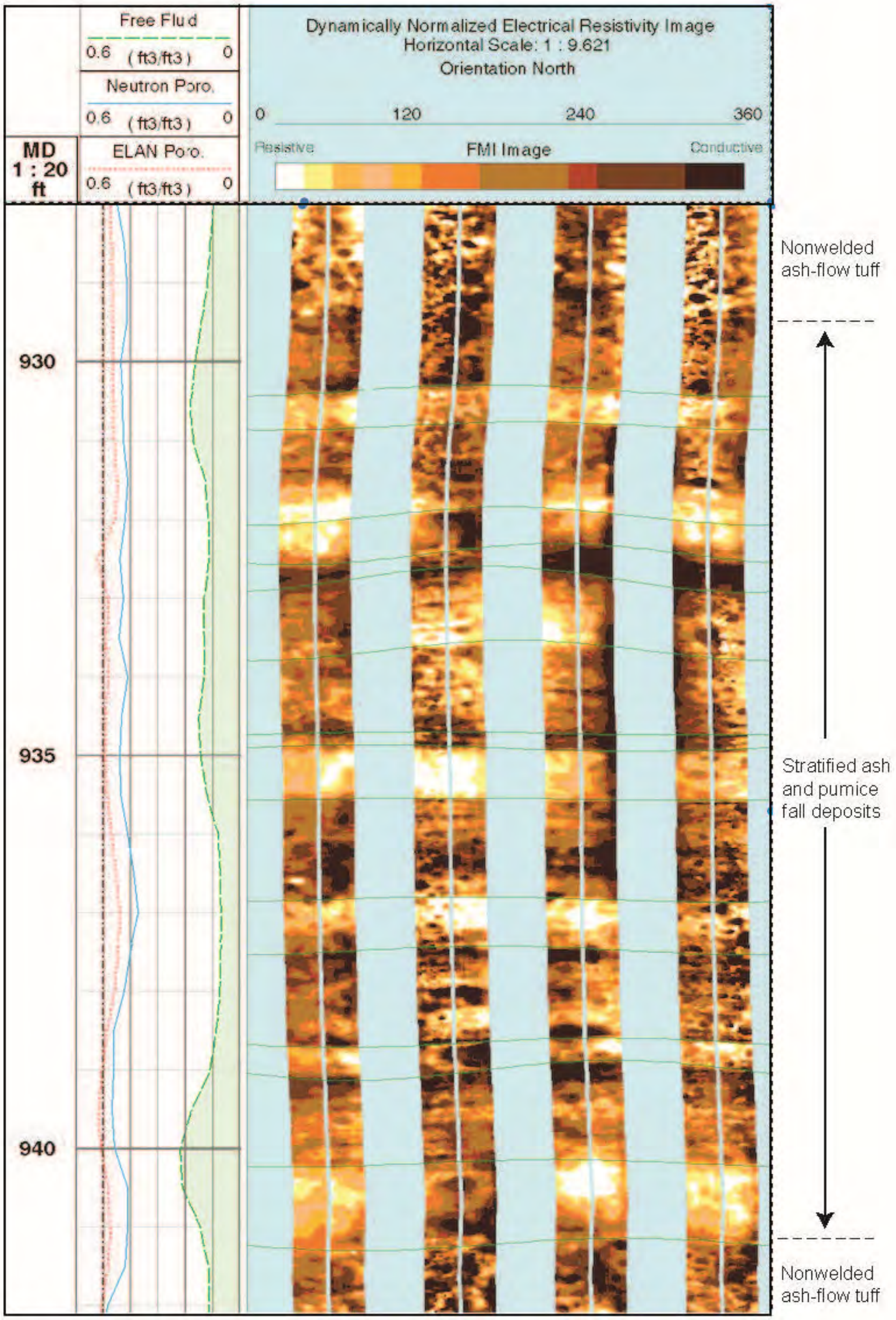

Figure 2.3-5 **FMI log showing well-stratified ash and pumice fall deposits in the lower part of the Otowi Member (G1–G2 subunit) in well R-26. The depth interval for the image is 928 ft to 942 ft. The G2 gamma marker horizon occurs at the 930.4-ft depth.**

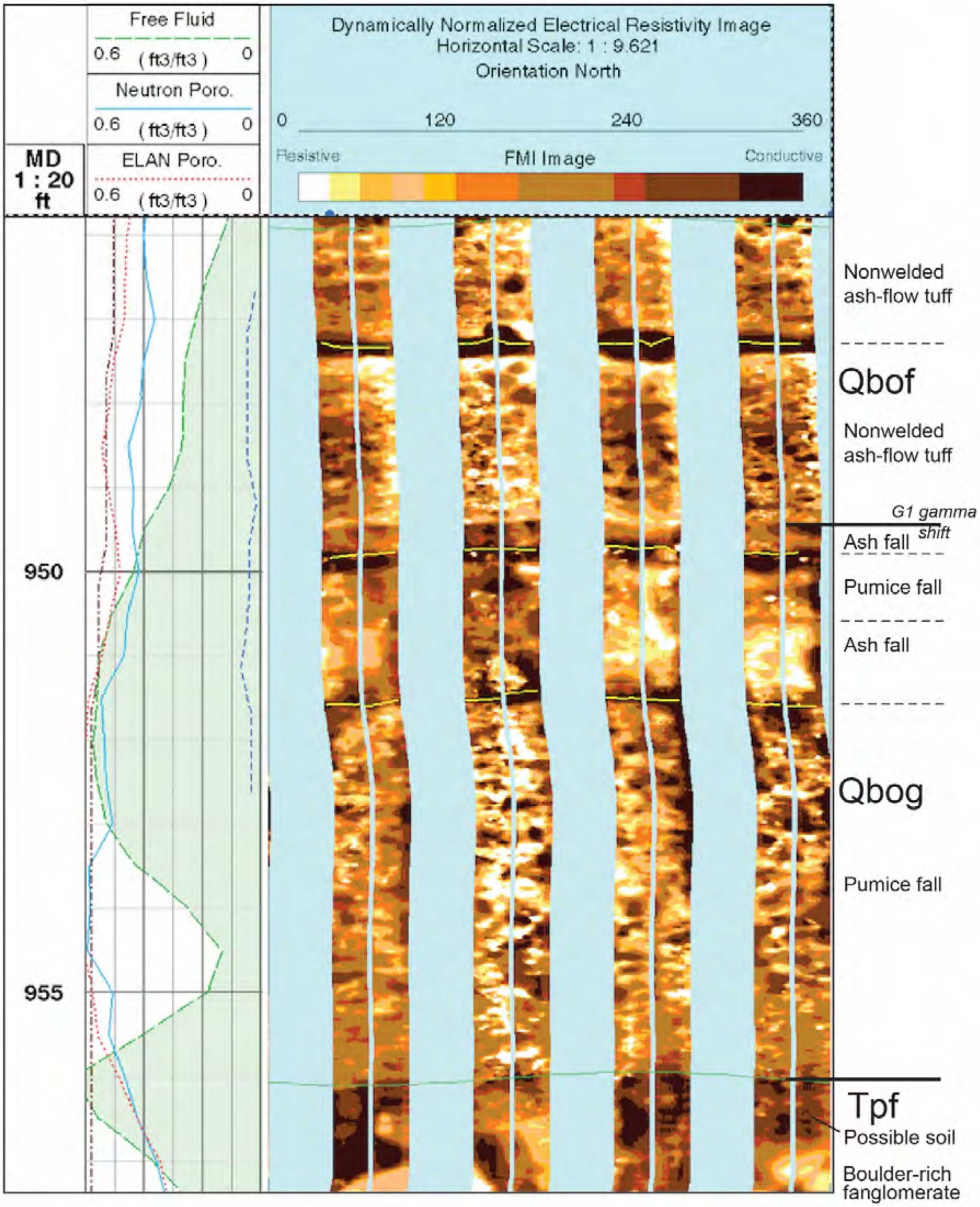

Figure 2.3-6 **FMI log showing thick-bedded ash-flow tuffs in the lower part of the Otowi Member (G1–G2 subunit) overlying ash and pumice fall deposits of the Guaje Pumice Bed in well R-26. The contact between the Otowi ash-flow tuffs and the Guaje Pumice Bed (G1 gamma marker horizon) occurs at the 949.8-ft depth. The depth interval for the image is 945.8 ft to 957.4 ft.**

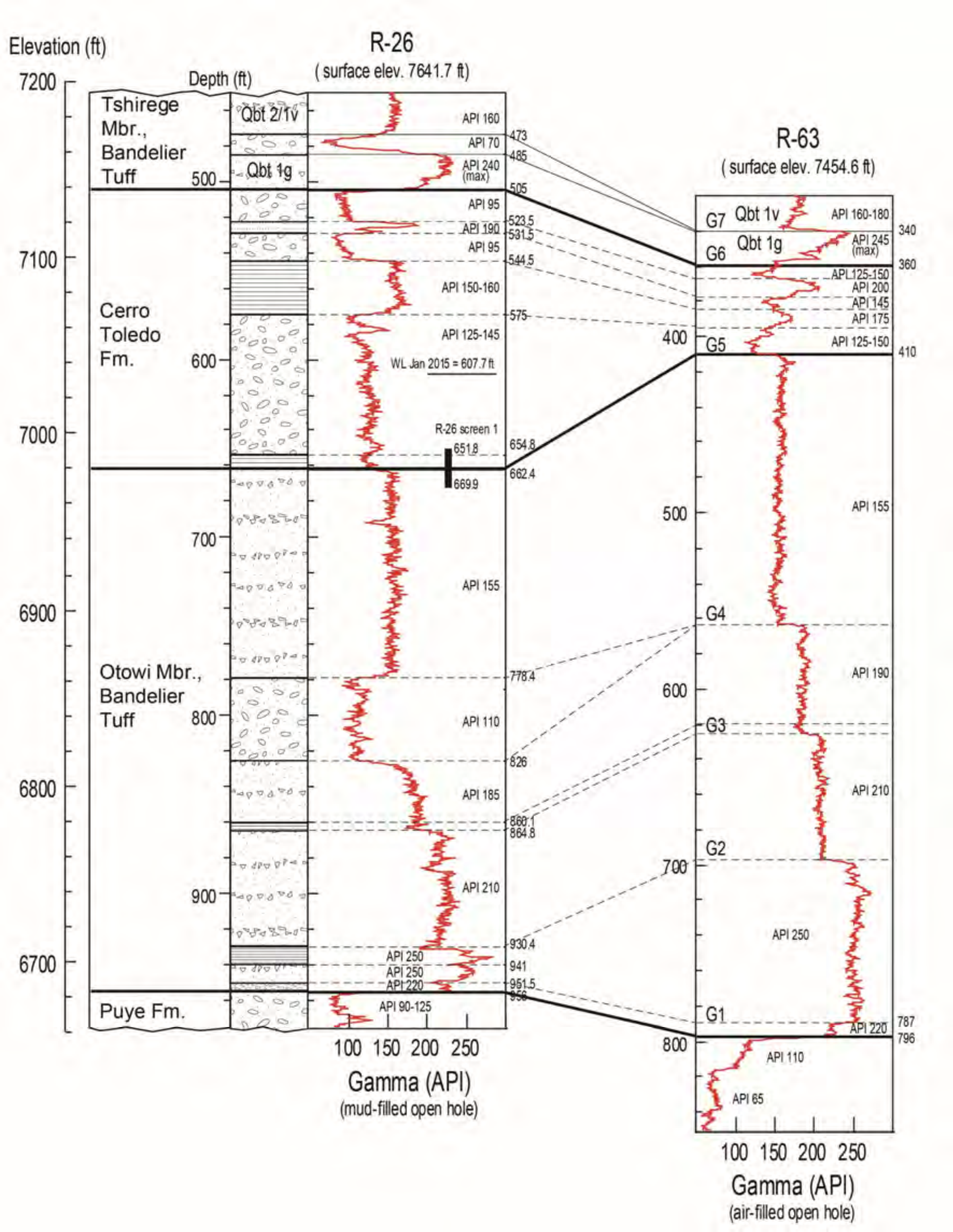

Figure 2.3-7 West-to-east cross-section showing spectral gamma logs for the base of the Tshirege Member, Cerro Toledo Formation, and Otowi Member in wells R-26 and R-63. Subunits for the major rock units are identified by abrupt shifts in gamma activity downhole. Proposed correlations of subunits between wells R-26 and R-63 are shown as dashed lines. Gamma activity levels (in API units) are shown for comparison in the correlated subunits. See Figure 2.3-1 for explanation of lithologies shown for well R-26.

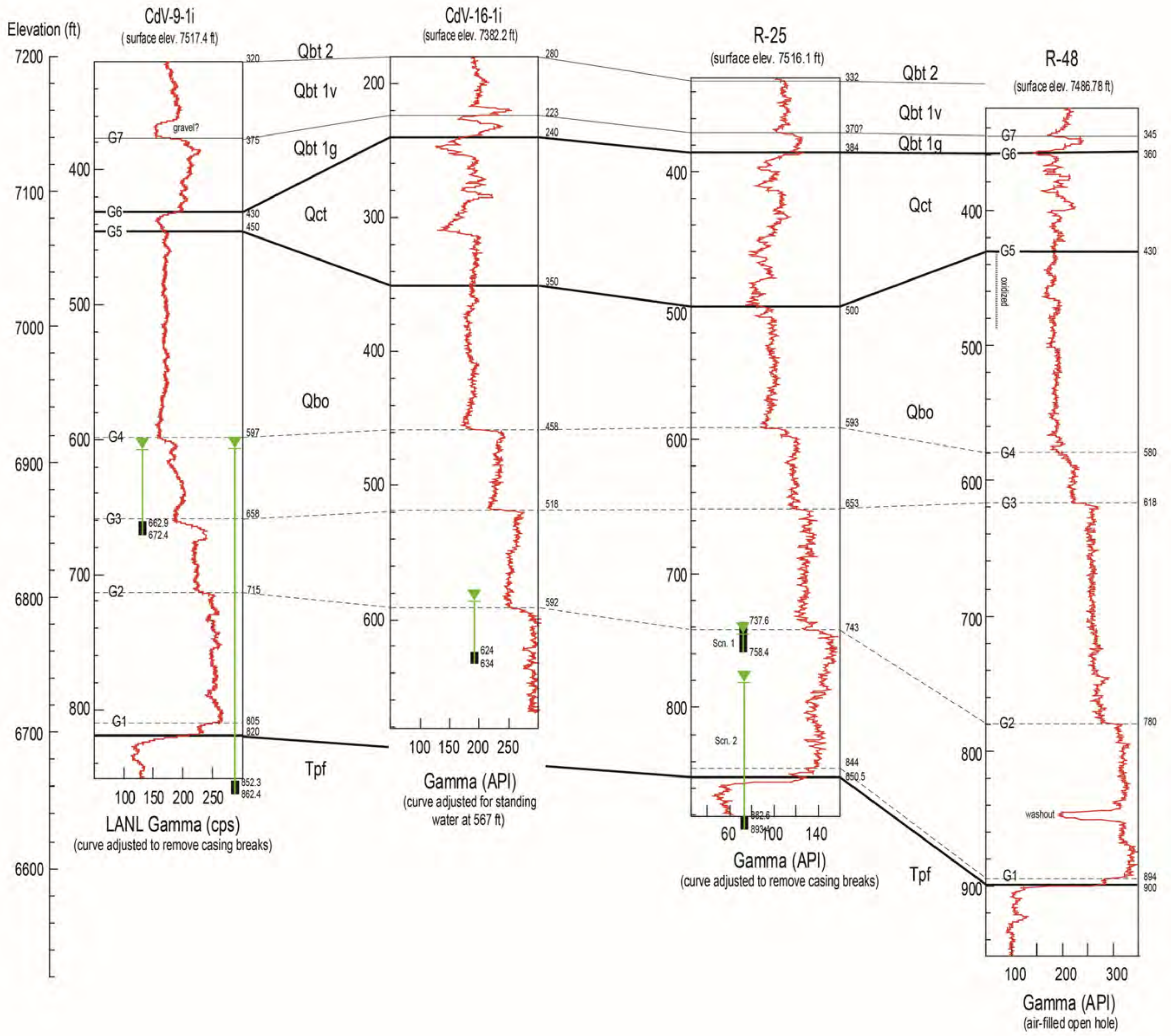

a.

Figure 2.3-8 Cross-sections showing correlation of gamma logs for the base of the Tshirege Member, Cerro Toledo Formation, and Otowi Member in wells of the RDX investigation area. The gamma logs include spectral gamma logs collected by Schlumberger, Inc. (API units) and natural gamma logs collected by the Laboratory (counts per second [cps] units). Proposed correlations of gamma marker horizons are shown as dashed lines. Cross-sections are arranged north to south (Figures 2.3-8a and 2.3-8b) and east to west (Figure 2.3-8c). Locations of wells are shown in Figure 1.0-1.

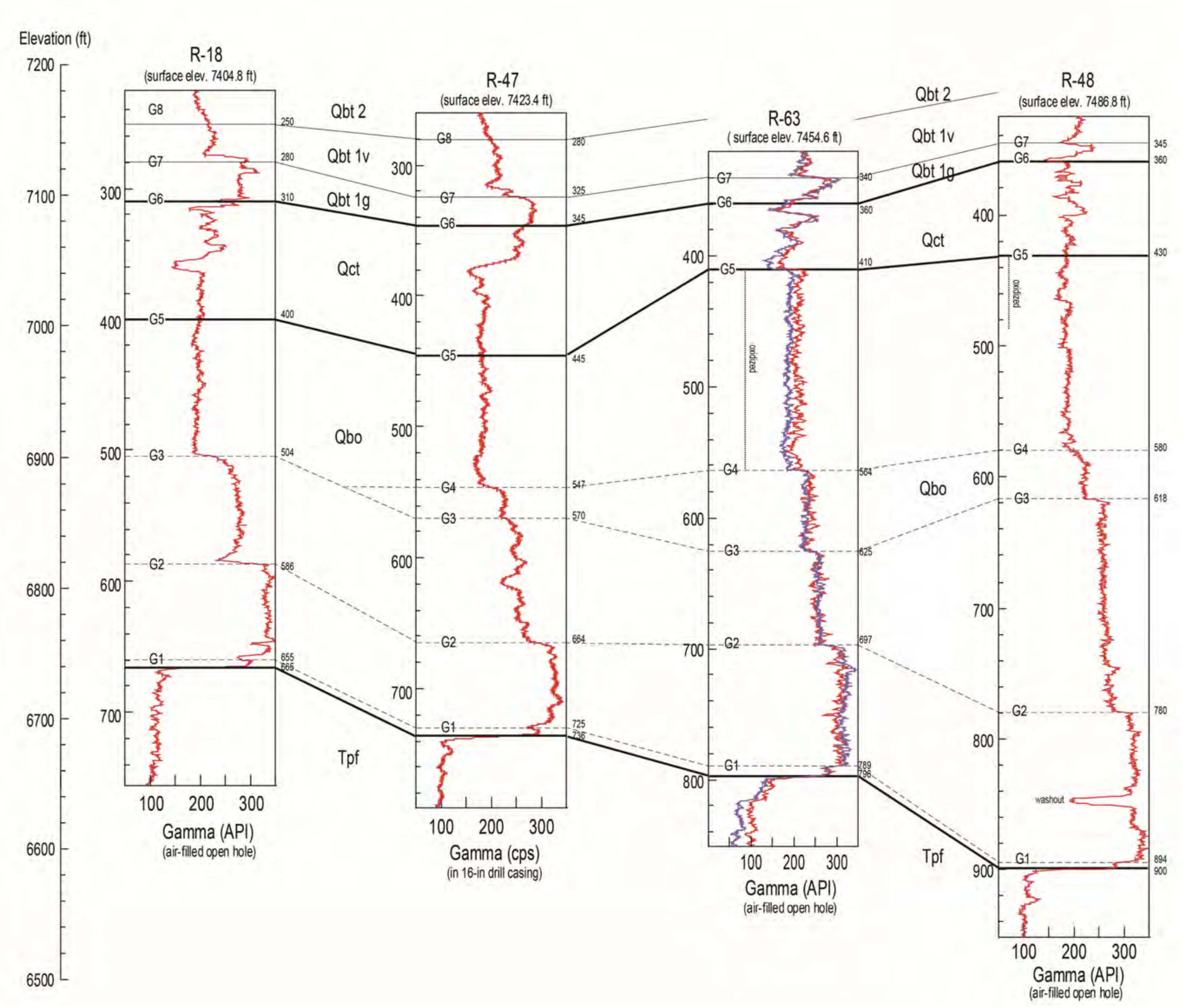

b.

Figure 2.3-8 (continued) **Cross-sections showing correlation of gamma logs for the base of the Tshirege Member, Cerro Toledo Formation, and Otowi Member in wells of the RDX investigation area. The gamma logs include spectral gamma logs collected by Schlumberger, Inc. (API units) and natural gamma logs collected by the Laboratory (cps units). Proposed correlations of gamma marker horizons are shown as dashed lines. Cross-sections are arranged north to south (Figures 2.3-8a and 2.3-8b) and east to west (Figure 2.3-8c). Locations of wells are shown in Figure 1.0-1.**

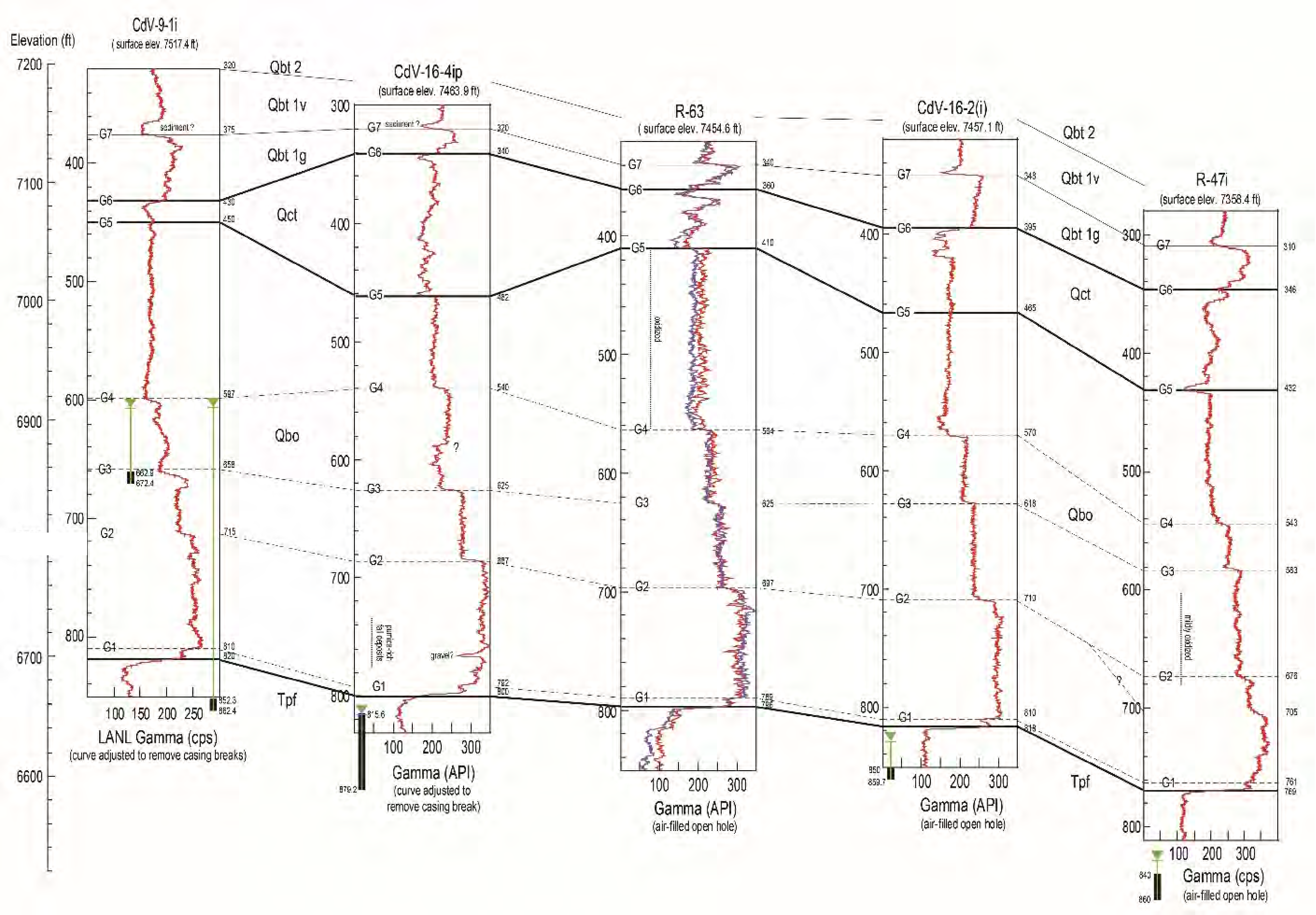

c.

Figure 2.3-8 (continued) **Cross-sections showing correlation of gamma logs for the base of the Tshirege Member, Cerro Toledo Formation, and Otowi Member in wells of the RDX investigation area. The gamma logs include spectral gamma logs collected by Schlumberger, Inc. (API units) and natural gamma logs collected by the Laboratory (cps units). Proposed correlations of gamma marker horizons are shown as dashed lines. Cross-sections are arranged north to south (Figures 2.3-8a and 2.3-8b) and east to west (Figure 2.3-8c). Locations of wells are shown in Figure 1.0-1.**

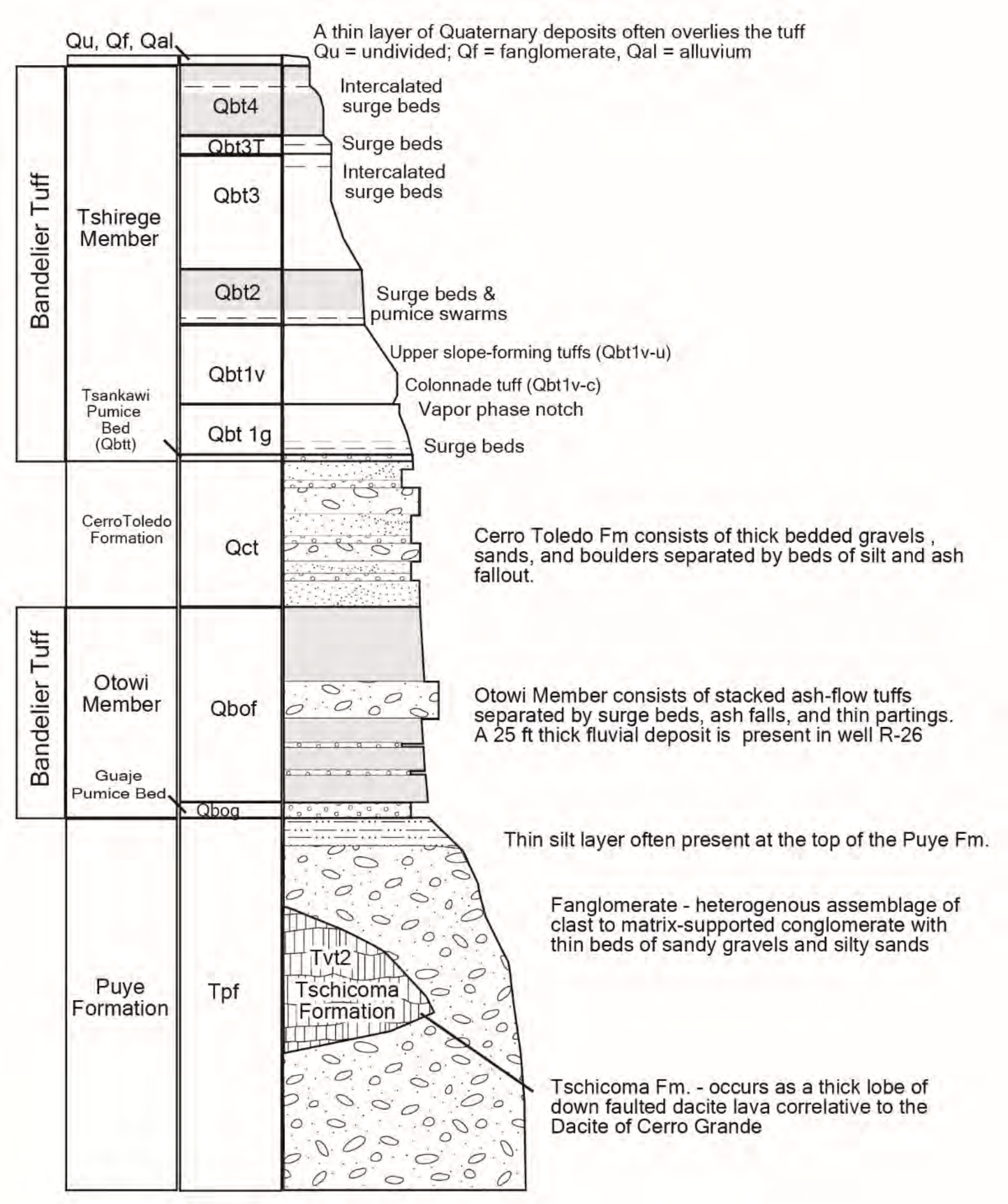

Figure 3.0-1 Stratigraphy of the geologic units at TA-16. Section is schematic; thickness of units taken from well CdV-9-1(i) with descriptions of units compiled from lithologic descriptions of wells and outcrops. Only Qbt 4 is treated as a single unit based on the geologic mapping performed by the Seismic Hazards mapping; however, other workers have created a new unit Qbt 5 out of the upper part of Qbt4 based on petrochemical differences (Goff et al. 2014).

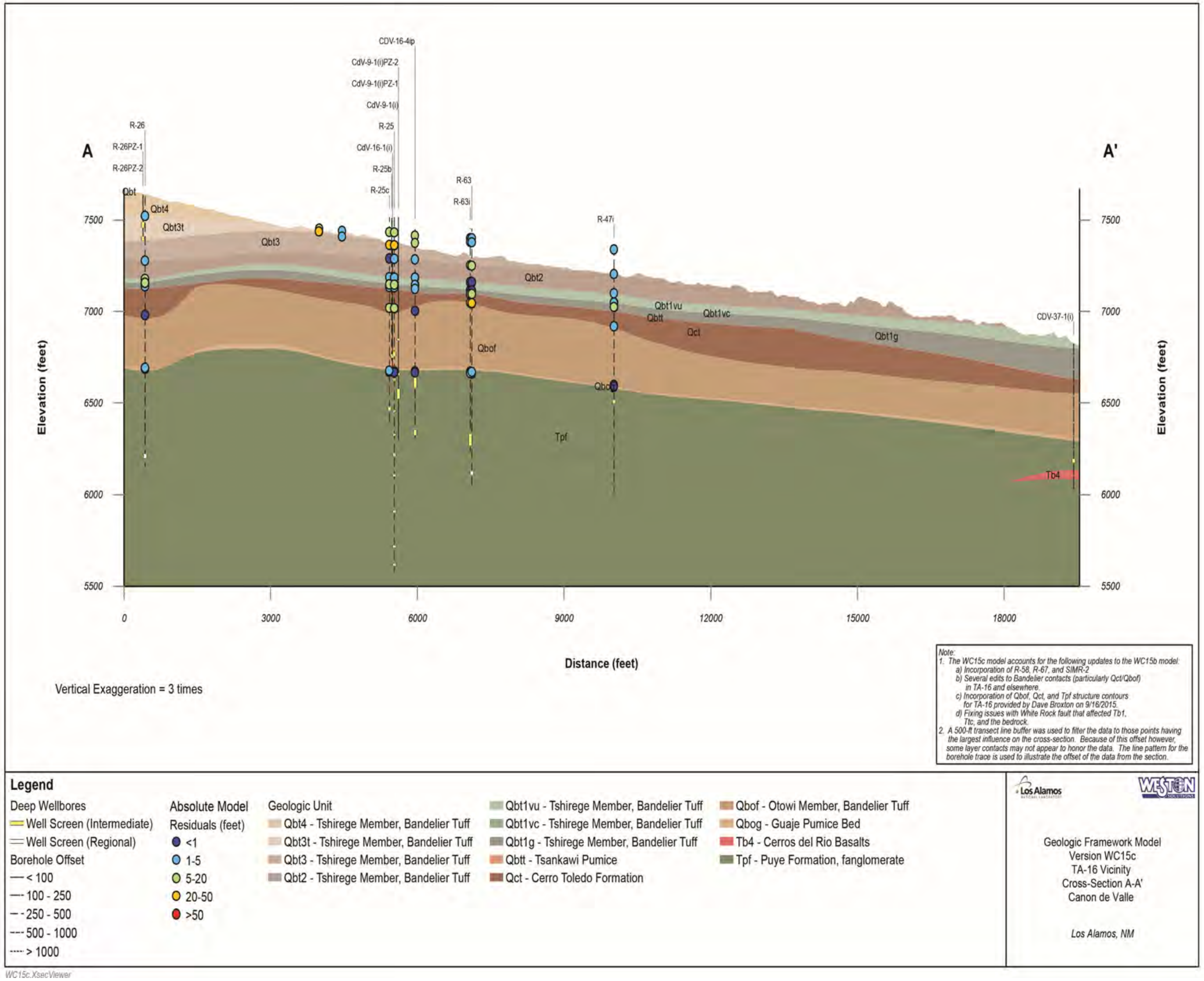

Note:
1. *The WC15c model accounts for the following updates to the WC15b model:*
   - *a) Incorporation of R-58, R-67, and SIMR-2*
   - *b) Several edits to Bandelier contacts (particularly Qct/Qbof) in TA-16 and elsewhere.*
   - *c) Incorporation of Qbof, Qct, and Tpf structure contours for TA-16 provided by Dave Broxton on 9/16/2015.*
   - *d) Fixing issues with White Rock fault that affected Tb1, Ttc, and the bedrock.*
2. *A 500-ft transect line buffer was used to filter the data to those points having the largest influence on the cross-section. Because of this offset however, some layer contacts may not appear to honor the data. The line pattern for the borehole trace is used to illustrate the offset of the data from the section.*

Figure 3.0-2 West-to-east geologic cross-section A-A' along the axis of Cañon de Valle. See Figure 1.0-1 for location of cross-section.

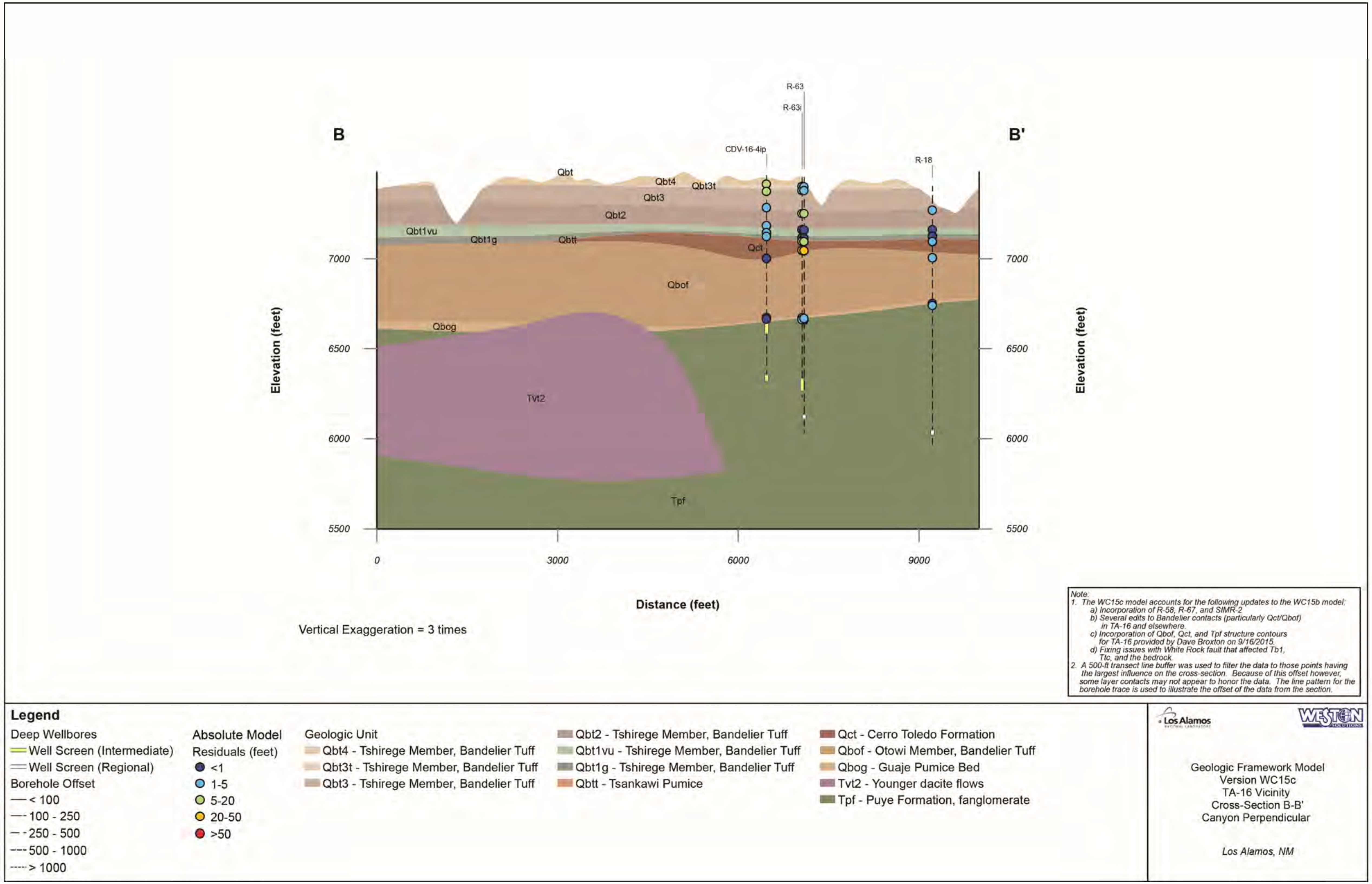

Note:

1. *The WC15c model accounts for the following updates to the WC15b model:*
    - *a) Incorporation of R-58, R-67, and SIMR-2*
    - *b) Several edits to Bandelier contacts (particularly Qct/Qbof) in TA-16 and elsewhere.*
    - *c) Incorporation of Qbof, Qct, and Tpf structure contours for TA-16 provided by Dave Broxton on 9/16/2015.*
    - *d) Fixing issues with White Rock fault that affected Tb1, Ttc, and the bedrock.*
2. *A 500-ft transect line buffer was used to filter the data to those points having the largest influence on the cross-section. Because of this offset however, some layer contacts may not appear to honor the data. The line pattern for the borehole trace is used to illustrate the offset of the data from the section.*

Figure 3.0-3 North-to-south geologic cross-section B-B' perpendicular to Cañon de Valle. See Figure 1.0-1 for location of cross-section.

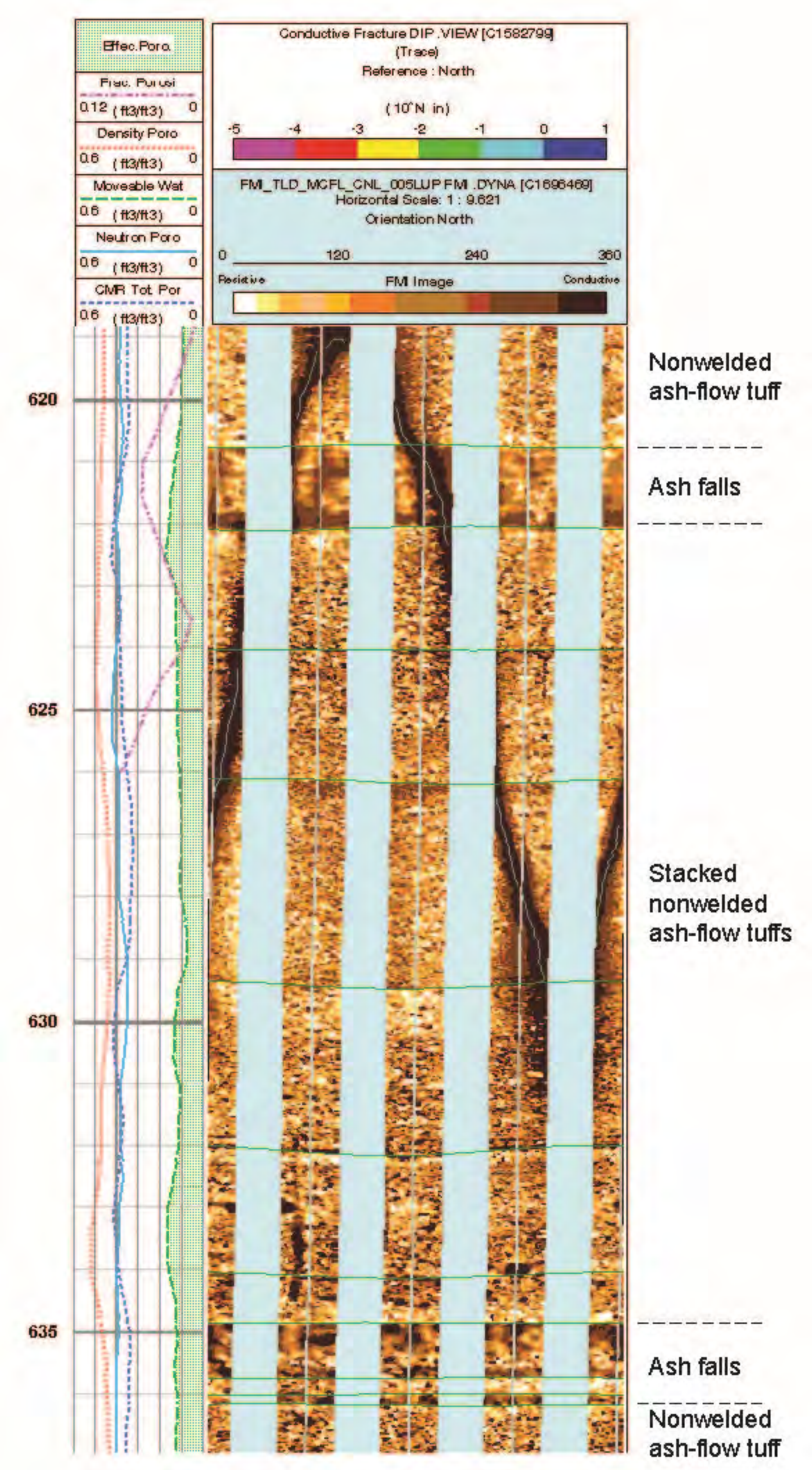

Figure 3.4-1 **FMI log showing high-angle fracture cutting nonwelded ash-flow tuffs in well CdV-16-1(i)**

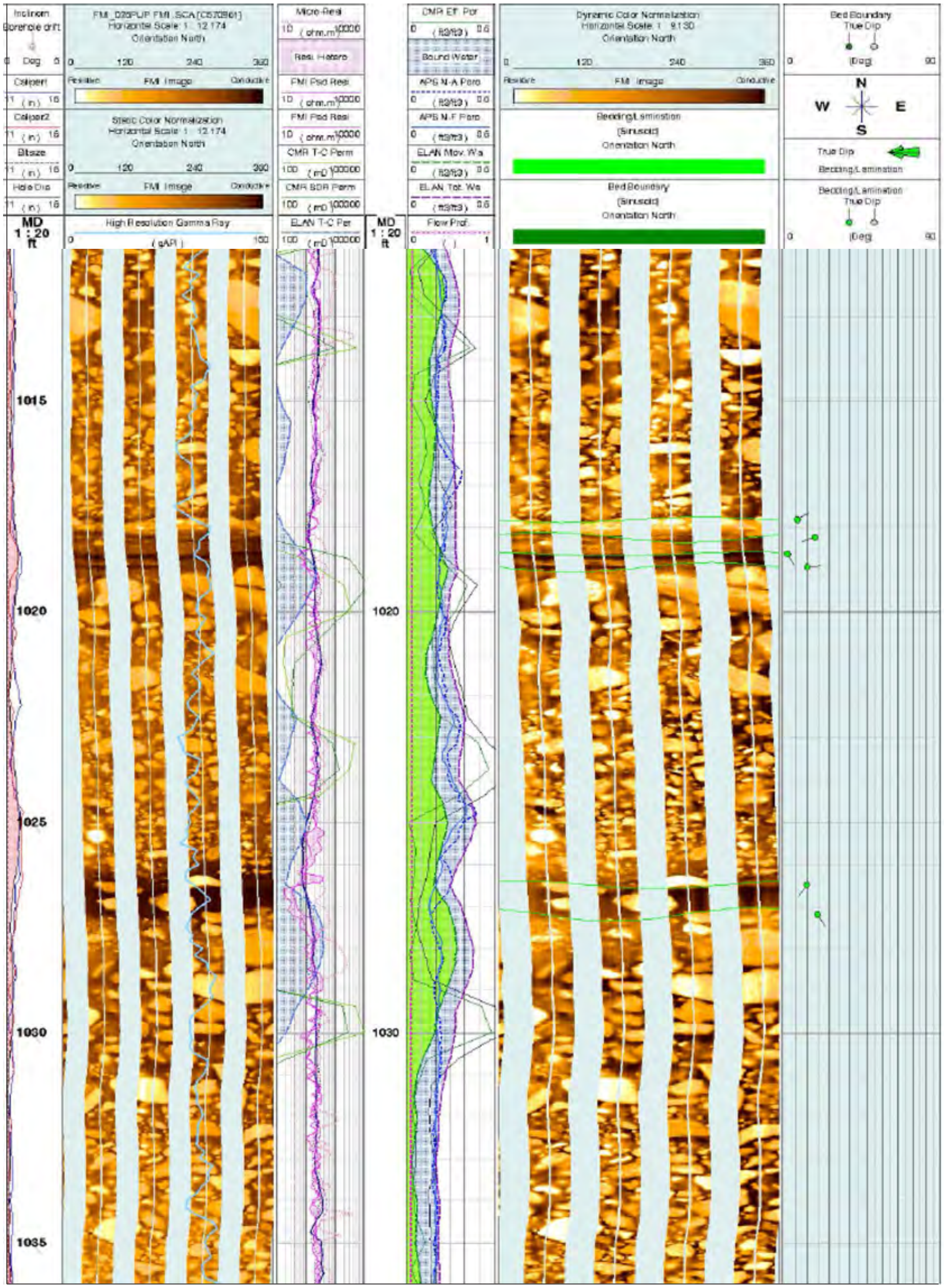

Figure 3.4-2 FMI log showing thick-bedded, poorly sorted, coarse-grain deposits of the Puye Formation in well CdV-16-4ip

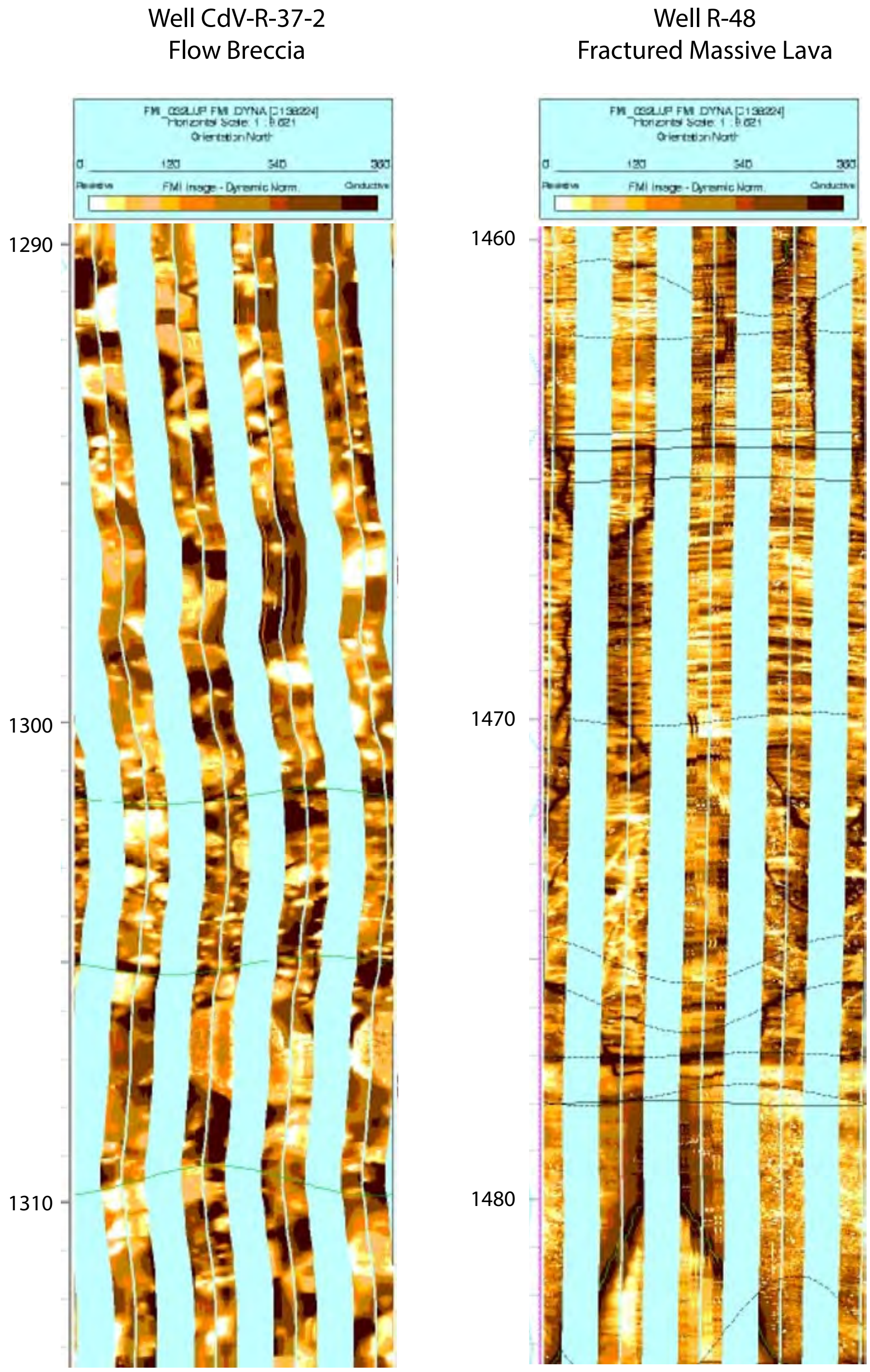
Well CdV-R-37-2
Flow Breccia

Well R-48
Fractured Massive Lava

Figure 3.4-3 **FMI log showing flow breccia and massive lava facies of the Cerro Grande dacite in wells R-48 and CdV-R-37-2. The massive lava exhibits strong flow foliation in this image.**

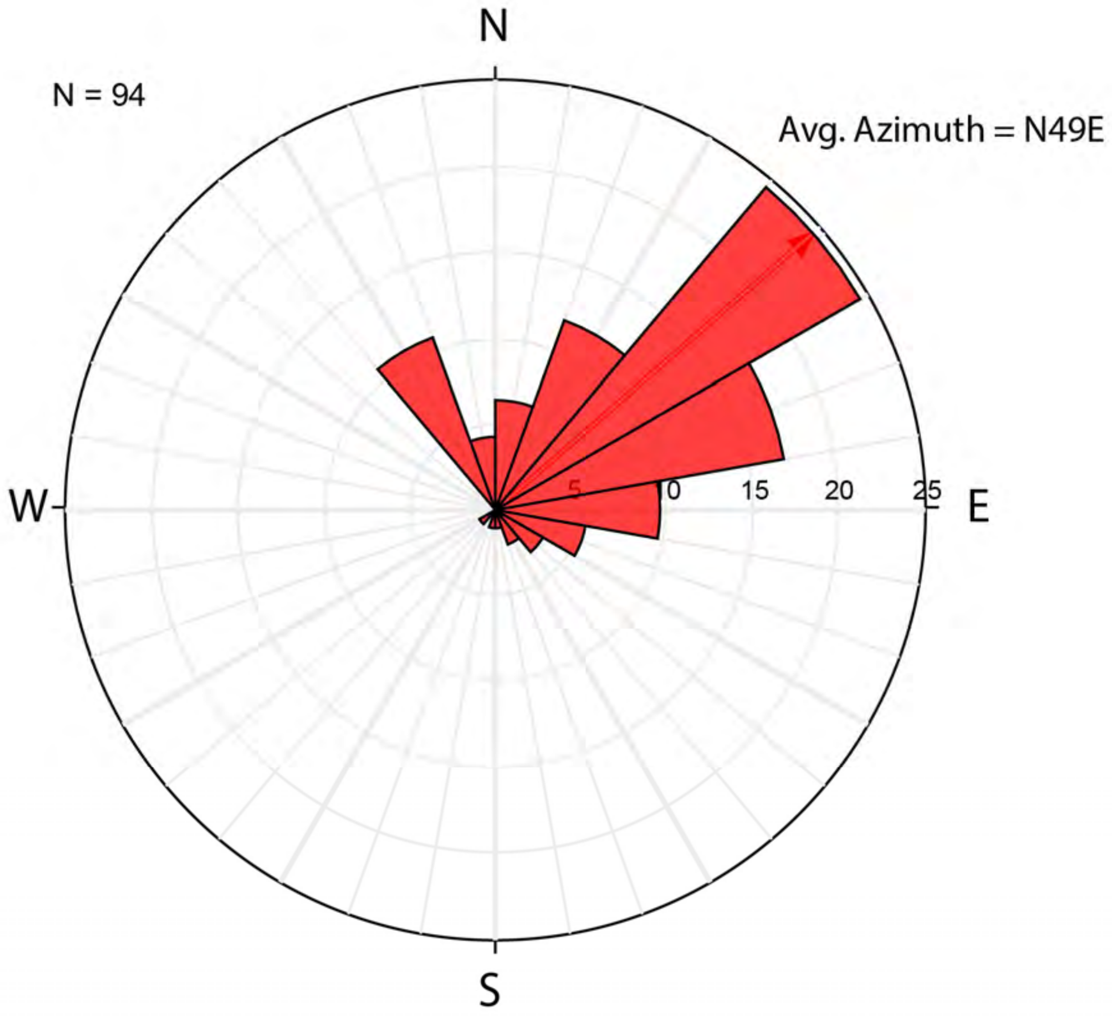

Figure 3.4-4 **Rose diagram showing the orientation of flow foliation in massive lava at well R-48**

Appendix A

SHB-3 Core Hole Lithologic Descriptions

A-1.0 INTRODUCTION

The SHB-3 core hole was drilled to a depth of 860 ft west of the Tritium Facility at Technical Area 16 (TA-16), also known as S-Site, as part of Los Alamos National Laboratory's Seismic Hazards Investigations Program (Gardner et al. 1993). The SHB-3 core hole was continuously cored with conventional wire line diamond coring techniques. Nearly 70% core recovery was achieved using light muds. Recently, the SHB-3 cores were reexamined to analyze the lithologic units, the stratigraphic contacts, and sedimentological and structural features relevant to the conceptual model refinement of the RDX Investigation Project. Brief descriptions of the various lithologic units and photographs of fracture zones are presented in Figures A-1.0-1a to A-1.0-1e.

Electron microprobe (EMP) major element chemistry of discrete glassy pumices and x-ray fluorescence (XRF) major and trace element compositions of whole rock samples from SHB-3 are provided in Tables A-1.0-1 and A-1.0-2, respectively. EMP iron oxide (total) and titanium oxide for SHB-3 glass are plotted in Figure 2.2-3 of the report. Variation diagram plots of major and trace elements versus depth in whole rock samples are shown in Figure A-1.0-2. The plots show chemical variations of the samples with depth that are consistent with the stratigraphic contacts. The distinct chemical compositions from the EMP and XRF analyses are used for cross-well correlations and to identify contacts between units.

A-2.0 LITHOLOGIC DESCRIPTIONS

Alluvium (0–5 ft below ground surface [bgs])

Grayish-brown silty clay mixed with minor rock fragments.

Tshirege Member, Qbt 5 (5–10 ft bgs)

Weathered tuff, partially welded, crystal-rich, and medium gray. The fault gouge consists of reddish-brown clay and altered tuff partially coated with patches of white carbonate crust. Few devitrified and weathered pumice clasts also noted. Tuff and devitrified pumice fragments are coated with fault gouge matrix.

Tshirege Member, Qbt 5 (10–25 ft bgs)

The middle part is medium gray, partially welded, and fractured. Pumice clasts are devitrified and partially welded. Fine-grained vapor-phase mineral aggregates are present in devitrified pumice cavities. Core contains reddish-brown fault gouge. It coats the fractured and slightly weathered tuff.

Tshirege Member, Qbt 5 (25–53 ft bgs)

The lowermost part is welded, grayish-pink, and crystal-rich. Quartz and feldspars are abundant. Mafic minerals are mostly weathered. The basal part of the unit is nonwelded.

Tshirege Member, Qbt 3t (53–85 ft bgs)

Tuff is medium gray, crystal-rich, and strongly welded with large collapsed and devitrified pumices. It breaks to platy fragments throughout the section. Abundant quartz and feldspars along with partially altered minor mafic minerals are commonly noted. Weathered and clay-filled fractured zones are commonly noted in the upper part of the unit (e.g., 76 ft, 83.25 ft, 108.75–109 ft, and 112–113 ft).

Tshirege Member, Qbt 3t (85–114 ft bgs)

The lithology and welding features are similar to the overlying core. It is welded, crystal-rich, light to medium gray, and devitrified. Isolated dark spots are probably altered mafic minerals. Brown weathered patches are also noted. Fractures filled with brown clay and clay-coated tuff fragments occur at a couple of intervals (e.g., 108.75–109 ft and 112 ft–113 ft bgs).

Tshirege Member, Qbt 3t (114–157.5 ft bgs)

The tuff is welded, crystal-rich, light to medium gray much like the overlying cores. The core appears darker gray with depth. More fractures and fracture walls partially coated with clay are present at 116 ft. The lowermost part of the unit appears more welded and fractured. A fault gouge consisting of brown clay and weathered and pulverized tuff occur at multiple intervals (e.g., 133–135 ft bgs and 143–144.5 ft bgs) (Figure A-1.0-1a). The basal tuff is broken into less welded light gray and crystal-rich platy discs within the interval.

Tshirege Member, Qbt 3 (157.5–185 ft bgs)

The tuff is light to medium gray, nonwelded, crystal-rich, and fractured into plates of thin discs. Welding appears to randomly increase with depth. In most cases, the more welded cores are less fractured. Figure A-1.0-1b shows more fractured discs and a fault gouge filled with clay-cemented tuff fragments occur in the interval (183–183.5 ft bgs).

Tshirege Member, Qbt 3 (185–233 ft bgs)

The tuff is moderately welded, light pinkish-gray, crystal-rich, and strongly fractured, resulting in thin platy discs. The section transitions to moderately welded, nonwelded, and friable core with depth. In the lowermost part of the interval (218.5–233 ft bgs), the tuff is light pinkish-gray, crystal-rich, nonwelded, and friable.

Tshirege Member, Qbt 2 (233–242.5ft bgs)

The pale red nonwelded tuff is weathered and transitions to moderately welded tuff that is strongly fractured. The matrix is light pinkish-gray. The crystal-rich tuff contains abundant quartz and feldspars. Lithic fragments are generally sparse. A fault gouge of crushed tuff and brown clay occurs at the base of the interval (242.5 ft bgs).

Tshirege Member, Qbt 2 (242.5–326.5 ft bgs)

Densely welded tuff, crystal-rich, and pinkish-gray matrix. The upper part of the core is fractured and welding appears to increase with depth. Multiple fracture zones coated and partially filled with brown clay randomly occur throughout the interval. Other fracture zones are marked by thinly sliced discs of welded tuff that show no alteration or fault gouge. These features might be related to drilling. A few nonwelded tuff fragments with alteration rims occur within the matrix. Some fractures are coated with manganese and clay (e.g., 265–267 ft bgs). A fault gouge was noted in the lower part of the interval (298.5–299.5 ft bgs).

Tshirege Member Qbt 1v/1g (326.5–334 ft bgs)

No recovery but the high gamma reading suggests a glassy interval that is consistent with the Tsankawi Pumice Bed.

Cerro Toledo Formation, Qct (334–368.5 ft bgs)

Fine-grained sediment with minor reworked pumice and felsic lava fragments underlie the upper Bandelier Tuff. A few large (5 in.), medium gray dacite cobbles occur within the upper part of the unit. More reworked, poorly sorted pumice occurs within fairly consolidated brownish-gray silty clay matrix.

Cerro Toledo Formation, Qct (368.5–398.5 ft bgs)

The tuffaceous sediments transition to abundant white to gray, unconsolidated, pumice bed in a glassy matrix. Pumice fragments are angular to subangular and are mixed with minor dark gray dacite fragments. The unit appears to be a fallout deposit.

Cerro Toledo Formation, Qct (398.5–408.5 ft bgs)

The tuffaceous deposit is light gray, crystal-rich, and moderately consolidated. It transitions to light orange unconsolidated tuff that contains porphyritic pumice clasts.

Otowi Member (408.5–413.5 ft bgs)

The uppermost unit is light brownish-gray tuff. It contains large rusty and glassy pumice fragments in a silty glassy matrix. It is crystal-rich and poorly consolidated.

Otowi Member (413.5– 445 ft bgs)

The nonwelded brownish-gray tuff overlies devitrified ash-flow tuff. It is medium to purplish gray, crystal-rich, and fairly consolidated. It becomes moderately welded with depth.

Otowi Member (445–454.5 ft bgs)

The ash-flow tuff is fractured and weathered. The devitrified tuff fragments are coated with brown clay, and fractures are partially filled with similar material. The core becomes densely welded and transitions to nonwelded, fairly consolidated tuff.

Otowi Member (454.5–463.5 ft bgs)

No recovery from this interval.

Otowi Member (463.5–499.5 ft bgs)

The core is light pinkish-gray, densely welded, and devitrified. It is crystal-rich. The intact core transitions to fractured platy discs and becomes nonwelded and friable with depth. The lowermost part of the core within the interval is light pinkish-gray, welded, and devitrified tuff.

Otowi Member (499.5–558.5 ft bgs)

Lithic-rich tuff contains large devitrified pumice and dacite fragments in a light pinkish-gray matrix. Pumices are more abundant and coarser than dacite fragments. The tuff is moderately welded. A fractured zone with fault gouge occurs within the lower part (549 ft) of the interval. Fractures are filled and coated with clay (Figure A-12).

Otowi Member (558.5–613 ft bgs)

The tuff is nonwelded, gray, crystal-rich, and glassy. The pumice and dacite fragments are less abundant and smaller in size. A fault gouge marked by fractured tuff and dark brown clay occurs within the interval. The tuff becomes less consolidated and friable with depth. Most pumice clasts are gray with rust-like patches. A fault gouge occurs at the base of the interval. The zone contains silty clay mixed with crushed tuff and appears sandy (Figures A-1.0-1c and A-1.0-1d).

Otowi Member (613–626 ft bgs)

No recovery from this interval.

Otowi Member (626–674.5 ft bgs)

Light to medium gray tuff is matrix-supported, poorly consolidated, friable, and sorted. Pumice and dacite clasts are sparse. Pumice clasts with rust-like patches are partially collapsed and variable in size. The pumice contents generally increase with depth.

Otowi Member (674.5–703 ft bgs)

The light pinkish-gray tuff is nonwelded but consolidated, poorly sorted and matrix-supported. Although pumice and dacite clast are generally sparse, the few dacite fragments are up to 2 in. in size. The light gray pumices, which are embedded within light pinkish-gray glassy matrix, have rust-like patches.

Otowi Member (703–767 ft bgs)

The fairly lithic-rich ash-flow tuff is unconsolidated and friable. It is light gray, sorted, and contains more pumice and dacite clasts than overlying cores. The pumices are larger in size. The tuff becomes light pinkish-gray with depth within the interval.

Otowi Member (767–772 ft bgs)

The pumice fallout deposit is white, unconsolidated, clast-supported, and poorly sorted. Pumice clasts are angular to subangular. Dacite fragments and minerals are sparse.

Otowi Member (772–773 ft bgs)

Fault gouge consists of light brown silty clay and fractured tuff with minor lava fragments and minerals (Figure A-1.0-1e).

Otowi Member (773–838 ft bgs)

The upper part of the core interval contains light brownish silty clay, fractured and partially altered tuff, minerals, and rock fragments (772–773 ft bgs). The ash flow tuff is nonwelded and friable and contains white pumice clasts, and a few reworked pumice that are coated light brown. Dacite fragments are present but sparse. The white pumice clasts are poorly sorted and increase with depth.

Otowi Member (838–839 ft bgs)

The fallout pumice core is white, consolidated, clast-supported, and poorly sorted. The pumice clasts are angular to subangular.

Puye Formation (839–848 ft bgs)

Gravely sandstone, containing large medium gray dacite cobbles (>5 in. long) in a medium brown silty sand. The core is massive and poorly sorted and strongly consolidated.

A-3.0 PHOTOGRAPHS OF SHB-3 CORE HOLE FAULT GOUGES

The representative images of fault gouges in SHB-3 cores show crushed tuffs mixed with silty clays taken using a binocular microscope. Several fault gouges of variable sizes were encountered throughout the SHB-3 core hole. Gouge forms along zones of faulting and are mostly pulverized and altered compared with adjacent host rocks. In most cases, the finer matrix is foliated and/or laminated, whereas the coarser fraction is massive and unconsolidated (Figures A-1.0-1a to 1.0-1e). The fault gouges in SHB-3 core hole probably represent multiple fault episodes related to the nearby Pajarito fault system.

4.0 REFERENCES

The following reference list includes documents cited in this report.

Gardner, J.L., S.L. Reneau, C.J. Lewis, A. Lavine, D.J. Krier, G. WoldeGabriel, and G.D. Guthrie. “Geology of the Pajarito Fault Zone in the Vicinity of S-Site (TA-16), Los Alamos National Laboratory, Rio Grande Rift, New Mexico,” Los Alamos National Laboratory report LA-13831-MS, Los Alamos, New Mexico (2001).

Gardner, J.N., T. Kolbe, and S. Chang. “Geology, Drilling, and Some Hydrologic Aspects of Seismic Hazards Program Core Holes, Los Alamos National Laboratory, New Mexico,” Los Alamos National Laboratory report LA-12460-MS, Los Alamos, New Mexico (1993).

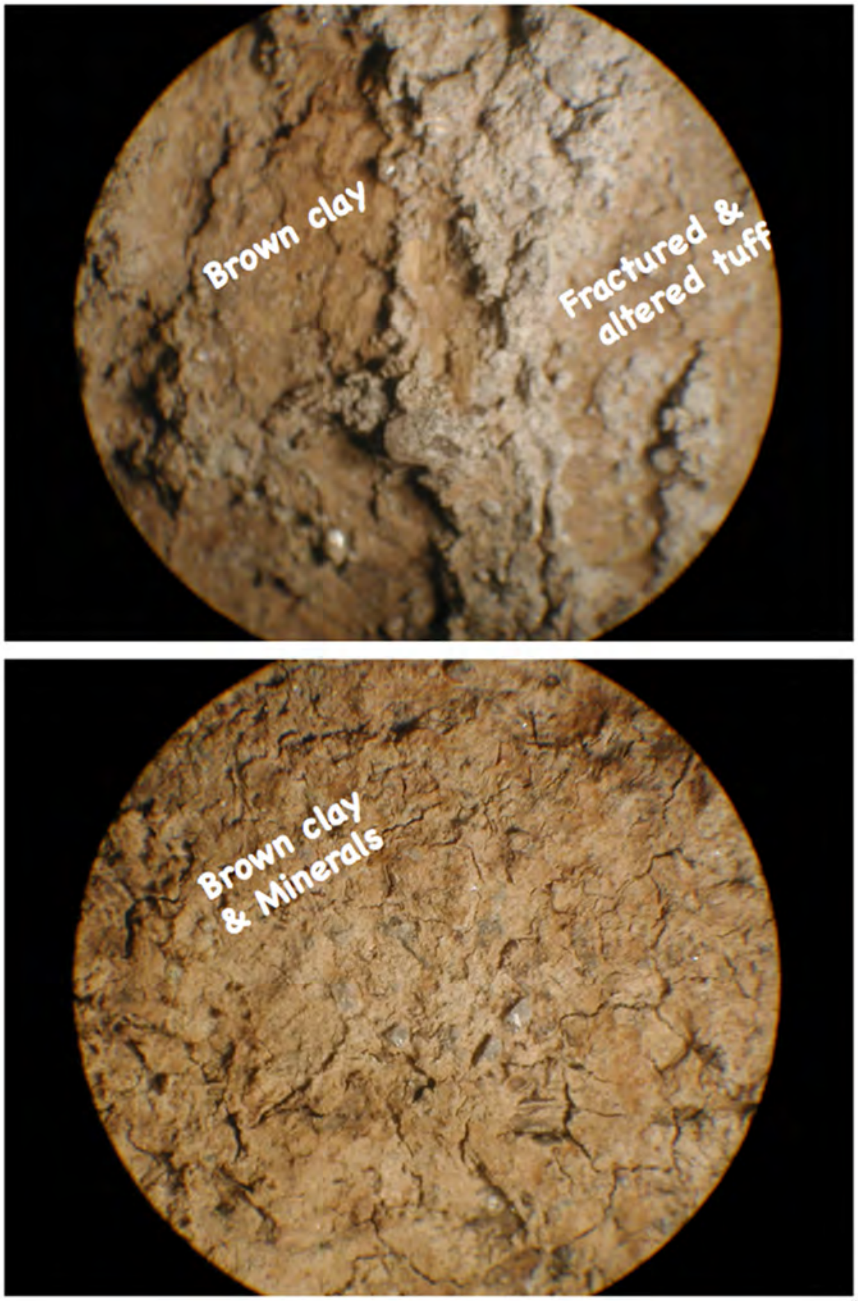

Figure A-1.0-1a **Brown silty clay mixed with fractured and altered Qbt 3t tuff at the 133-ft depth in the SHB-3 core hole**

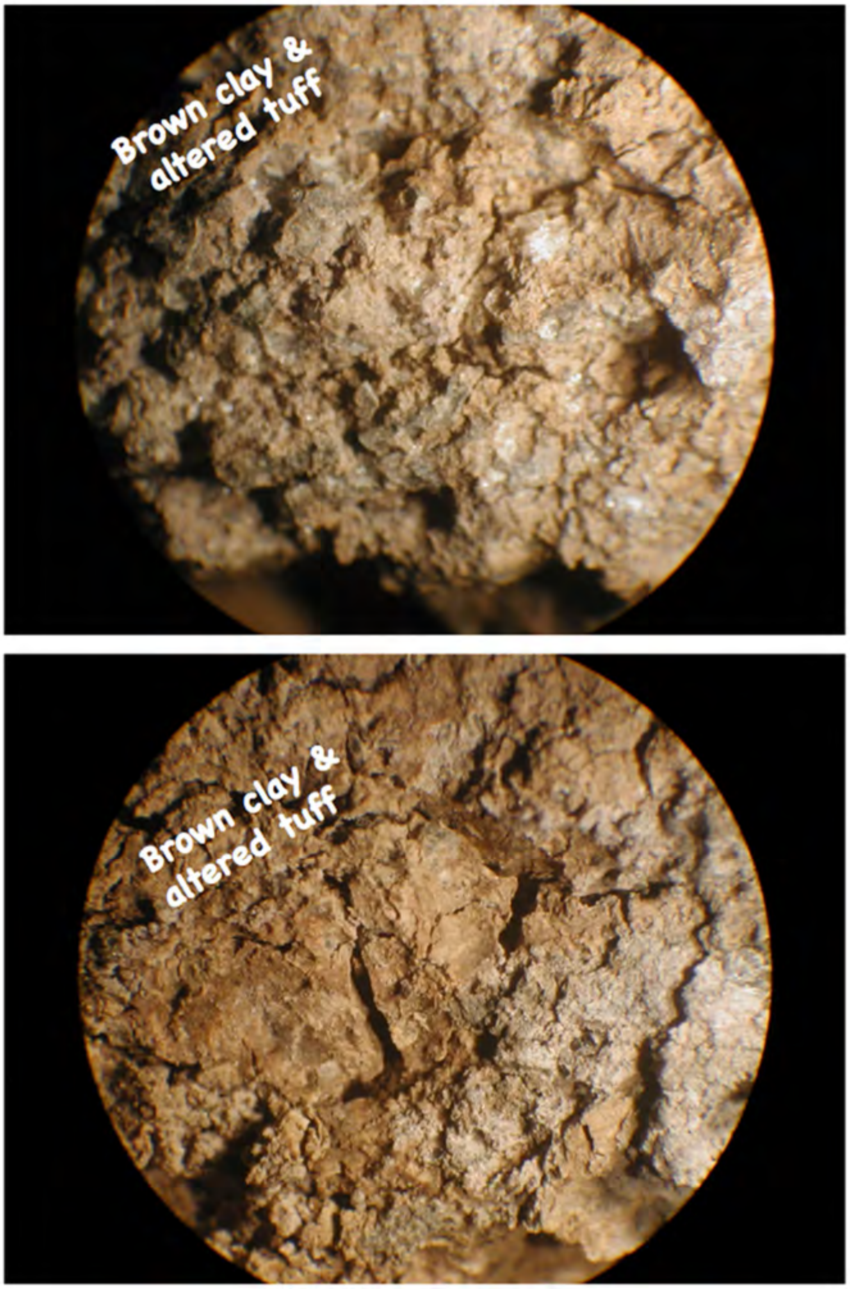

Figure A-1.0-1b Brown silty clay mixed with fractured and altered Qbt 3 tuff (upper) and the Otowi Member ash-flow tuff (lower) at the 183-ft and 549-ft depths, respectively, in the SHB-3 core hole

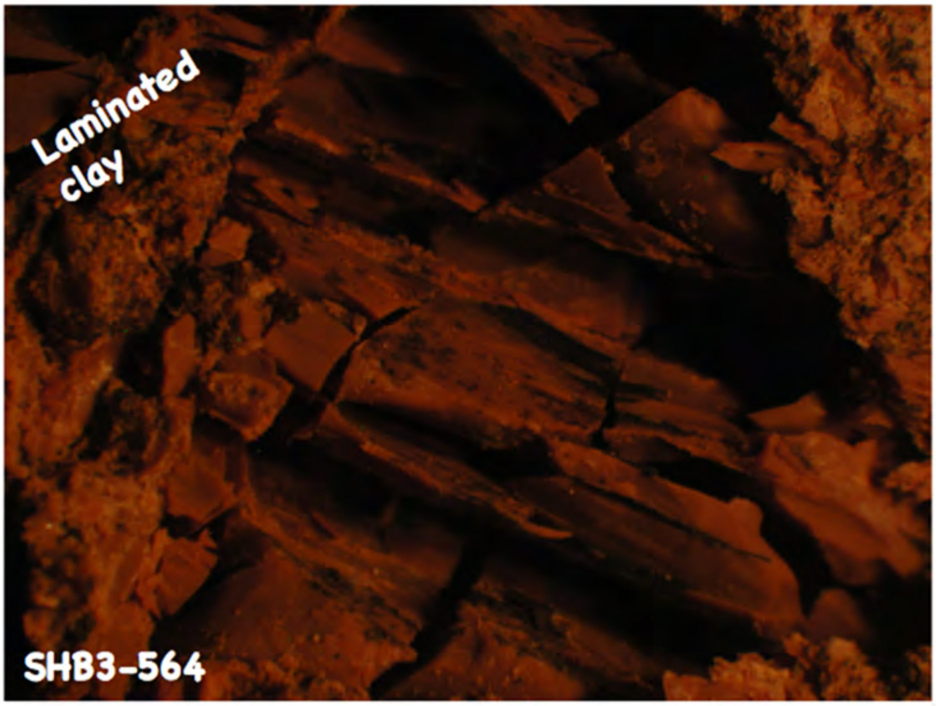

Figure A-1.0-1c Laminated brown clay within a fractured and altered Otowi Member ash-flow tuff at the 564-ft depth in the SHB-3 core hole

Figure A-1.0-1d **Light brown silty clay mixed with fractured and altered Otowi Member ash-flow tuff at the 608–613-ft depth interval in the SHB-3 core hole**

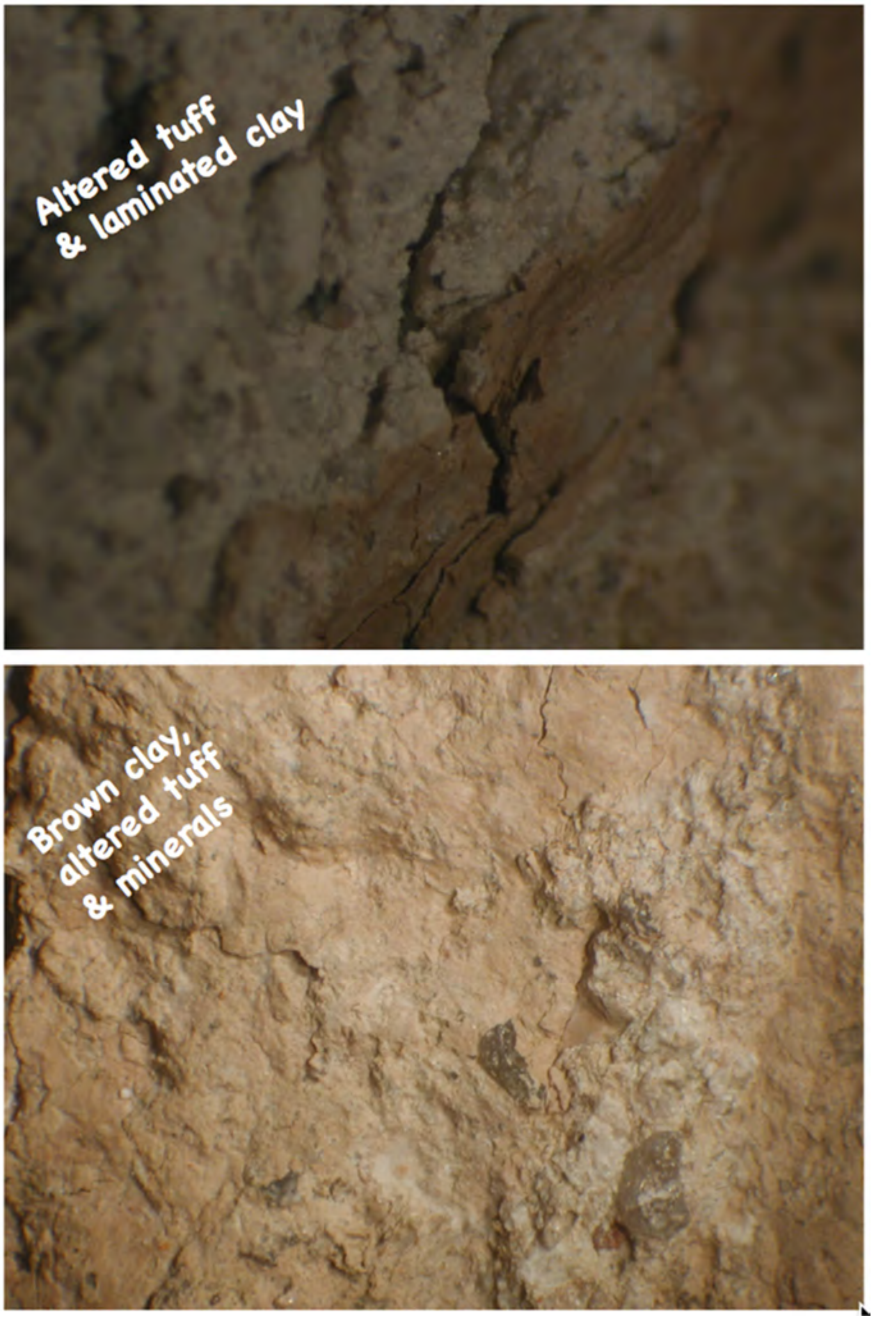

Figure A-1.0-1e **Light brown laminated (upper) and silty clay (lower) within a fractured and altered Otowi Member ash-flow tuff at the 772–773-ft depth interval in the SHB-3 core hole**

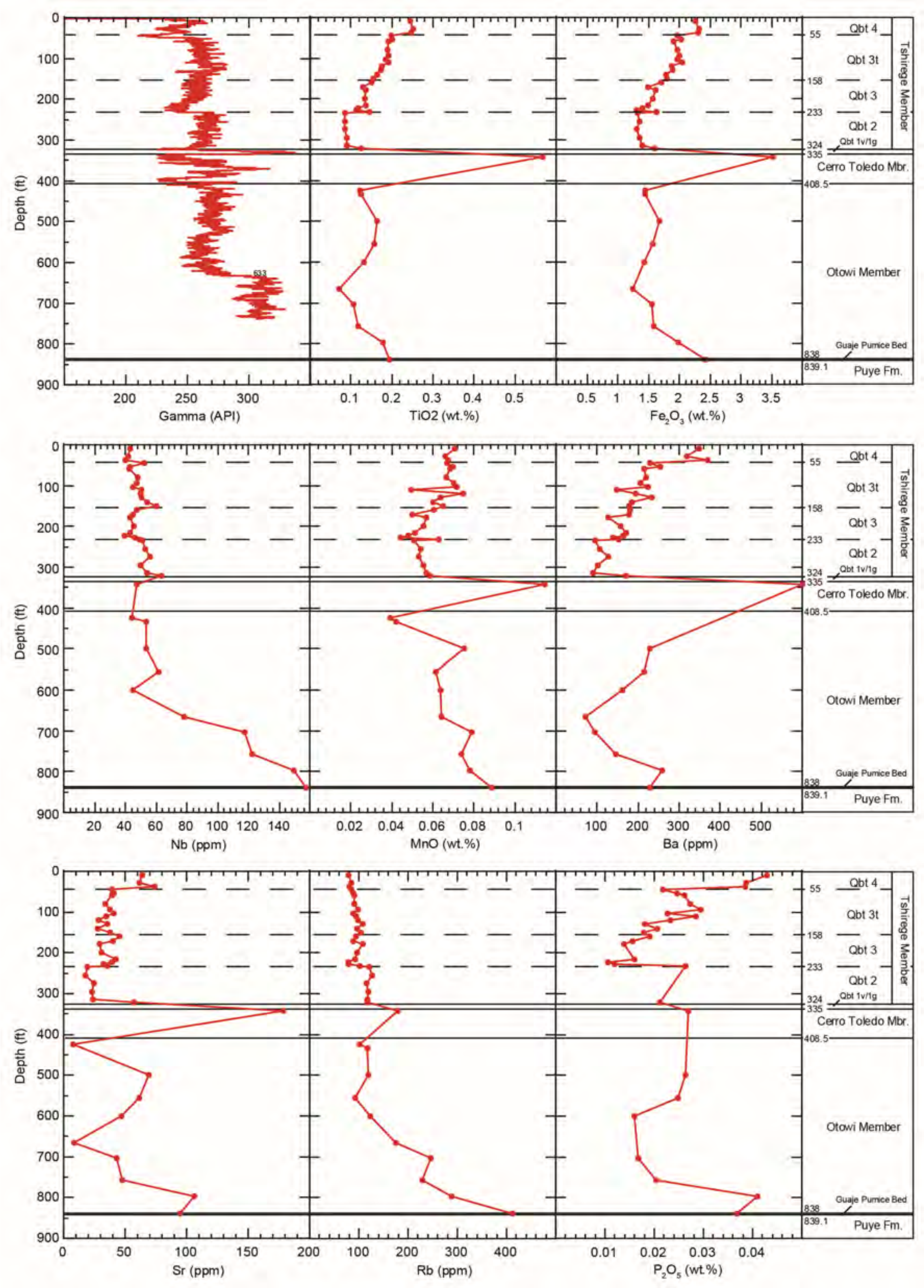

Figure A-1.0-2 **Variation diagrams for major and trace elements for whole rock samples from the SHB-3 core hole**

Table A-1.0-1
Electron Microprobe Analyses of Volcanic Glasses from Core Hole SHB-3

Sample	SiO_2	TiO_2	Al_2O_3	FeO (Total)	MnO	MgO	CaO	Na_2O	K_2O	P_2O_5	SrO	BaO	Total
Pueblo Canyon Member, Cerro Toledo Formation													
SHB3_353.5	75.26	0.10	11.98	0.93	0.09	0.02	0.29	2.90	5.05	0.00	0.00	0.00	96.62
SHB3_353.5	74.23	0.01	11.94	1.26	0.06	0.00	0.14	3.49	4.96	0.00	0.00	0.00	96.08
SHB3_353.5	75.52	0.11	12.04	0.94	0.04	0.02	0.35	2.87	4.54	0.03	0.00	0.01	96.46
SHB3_353.5	75.67	0.14	12.14	0.77	0.04	0.03	0.38	3.09	4.86	0.00	0.00	0.00	97.12
SHB3_353.5	74.82	0.09	11.89	0.82	0.06	0.01	0.31	2.93	4.96	0.00	0.01	0.05	95.95
SHB3_353.5	75.04	0.08	12.05	0.95	0.03	0.02	0.31	3.03	4.82	0.03	0.00	0.00	96.34
SHB3_353.5	75.12	0.11	12.03	0.78	0.03	0.00	0.33	3.18	4.80	0.03	0.00	0.00	96.41
SHB3_353.5	74.29	0.08	11.94	0.94	0.06	0.01	0.28	3.05	4.80	0.01	0.00	0.00	95.45
SHB3_353.5	76.33	0.10	11.98	0.86	0.09	0.01	0.28	3.03	4.85	0.00	0.01	0.02	97.55
SHB3_353.5	75.68	0.11	12.01	0.83	0.07	0.02	0.33	2.85	4.73	0.01	0.00	0.03	96.67
SHB3_353.5	76.14	0.07	11.99	0.89	0.11	0.01	0.28	3.07	4.91	0.02	0.00	0.00	97.49
SHB3_353.5	74.57	0.07	11.96	0.84	0.08	0.01	0.29	3.06	4.78	0.00	0.00	0.00	95.65
SHB3_353.5	75.66	0.11	11.98	0.89	0.07	0.02	0.28	3.17	4.80	0.00	0.00	0.01	96.98
SHB3_353.5	75.91	0.09	12.05	0.89	0.08	0.00	0.33	3.06	4.83	0.05	0.00	0.00	97.28
SHB3_353.5	74.57	0.09	12.01	0.93	0.06	0.00	0.34	3.10	4.99	0.01	0.00	0.05	96.14
SHB3_353.5	75.50	0.08	12.09	0.78	0.06	0.02	0.37	2.78	4.48	0.00	0.00	0.05	96.20
SHB3_353.5	76.65	0.11	12.02	0.91	0.06	0.01	0.38	2.87	5.03	0.00	0.00	0.03	98.07
SHB3_353.5	76.57	0.03	12.09	0.83	0.07	0.01	0.30	3.29	4.85	0.00	0.02	0.01	98.08
SHB3_353.5	76.04	0.07	11.94	0.80	0.04	0.01	0.28	3.03	4.57	0.00	0.04	0.00	96.84
SHB3_353.5	75.71	0.04	12.03	0.84	0.07	0.01	0.32	3.15	4.82	0.04	0.00	0.00	97.02
SHB3_353.5	75.97	0.13	11.97	0.84	0.10	0.02	0.33	2.97	4.69	0.00	0.00	0.00	97.01
SHB3_353.5	75.59	0.15	12.01	0.87	0.08	0.01	0.29	3.23	4.80	0.00	0.00	0.01	97.04
SHB3_353.5	76.82	0.08	12.01	0.77	0.09	0.02	0.37	2.95	4.74	0.00	0.00	0.00	97.85
SHB3_353.5	76.29	0.11	11.98	0.83	0.07	0.01	0.29	2.97	4.87	0.00	0.00	0.00	97.40

Table A-1.0-1 (continued)

Sample	SiO_2	TiO_2	Al_2O_3	FeO (Total)	MnO	MgO	CaO	Na_2O	K_2O	P_2O_5	SrO	BaO	Total
Pueblo Canyon Member, Cerro Toledo Formation													
SHB3_353.5	75.49	0.05	11.97	0.93	0.07	0.00	0.30	2.86	4.66	0.00	0.00	0.02	96.36
SHB3_353.5	75.16	0.08	11.95	0.78	0.11	0.01	0.31	2.99	4.84	0.04	0.00	0.00	96.27
SHB3_353.5	75.28	0.09	11.90	0.90	0.06	0.00	0.30	2.92	4.85	0.04	0.00	0.07	96.40
SHB3_353.5	75.38	0.07	11.91	0.77	0.07	0.00	0.30	3.02	4.93	0.02	0.00	0.00	96.48
SHB3_353.5	75.80	0.00	11.95	0.93	0.09	0.02	0.32	3.28	4.82	0.00	0.00	0.02	97.23
SHB3_353.5	76.22	0.01	12.18	1.03	0.07	0.02	0.34	2.99	4.75	0.00	0.00	0.00	97.62
SHB3_353.5	75.59	0.12	11.84	0.85	0.12	0.02	0.29	2.80	4.93	0.02	0.00	0.00	96.57
SHB3_353.5	75.47	0.06	11.99	0.75	0.07	0.01	0.33	3.06	4.75	0.00	0.00	0.01	96.50
SHB3_353.5	75.74	0.04	11.99	0.79	0.06	0.02	0.37	2.95	4.69	0.00	0.00	0.00	96.64
Mean	**75.58**	**0.08**	**11.99**	**0.87**	**0.07**	**0.01**	**0.31**	**3.03**	**4.81**	**0.01**	**0.00**	**0.01**	**96.78**
Stdev	**0.64**	**0.04**	**0.07**	**0.10**	**0.02**	**0.01**	**0.04**	**0.15**	**0.13**	**0.01**	**0.01**	**0.02**	**0.66**

Table A-1.0-1 (continued)

Sample	SiO_2	TiO_2	Al_2O_3	FeO (Total)	MnO	MgO	CaO	Na_2O	K_2O	P_2O_5	SrO	BaO	Total
Pueblo Canyon Member, Cerro Toledo Formation													
SHB3_385.9	74.91	0.05	12.01	0.82	0.04	0.02	0.32	3.06	4.53	0.00	0.02	0.00	95.79
SHB3_385.9	74.84	0.04	12.02	0.79	0.09	0.03	0.35	3.07	4.78	0.00	0.00	0.00	96.01
SHB3_385.9	74.22	0.09	11.92	0.82	0.04	0.01	0.35	3.11	4.67	0.00	0.00	0.00	95.23
SHB3_385.9	73.15	0.11	11.77	0.73	0.05	0.02	0.33	2.42	5.35	0.00	0.00	0.00	93.92
SHB3_385.9	73.53	0.05	11.81	0.73	0.04	0.03	0.32	2.64	5.05	0.02	0.01	0.02	94.25
SHB3_385.9	74.89	0.12	11.93	0.79	0.03	0.02	0.33	2.86	4.88	0.00	0.02	0.00	95.86
SHB3_385.9	74.70	0.08	11.92	0.73	0.02	0.02	0.35	2.94	4.63	0.00	0.00	0.00	95.39
SHB3_385.9	73.83	0.09	11.95	0.78	0.06	0.03	0.36	3.12	4.47	0.06	0.01	0.00	94.76
SHB3_385.9	75.56	0.13	12.03	0.77	0.03	0.03	0.37	2.88	4.57	0.04	0.00	0.07	96.48
SHB3_385.9	74.28	0.08	12.01	0.78	0.04	0.01	0.36	3.05	4.62	0.00	0.00	0.03	95.26
SHB3_385.9	75.57	0.07	12.02	0.75	0.02	0.02	0.33	3.23	4.55	0.03	0.00	0.00	96.59
SHB3_385.9	74.87	0.11	12.00	0.71	0.06	0.03	0.39	2.89	4.76	0.00	0.00	0.00	95.82
SHB3_385.9	76.08	0.04	11.99	0.78	0.04	0.02	0.36	3.02	4.51	0.00	0.00	0.00	96.83
SHB3_385.9	74.68	0.11	12.08	0.78	0.07	0.02	0.37	3.23	4.62	0.00	0.00	0.06	96.00
SHB3_385.9	74.31	0.00	11.86	0.74	0.08	0.01	0.34	2.88	4.75	0.01	0.00	0.00	94.98
SHB3_385.9	75.09	0.09	12.06	0.74	0.05	0.02	0.36	3.05	4.52	0.00	0.00	0.00	95.98
SHB3_385.9	74.08	0.03	11.99	0.81	0.09	0.02	0.33	3.02	4.64	0.01	0.00	0.10	95.12
SHB3_385.9	75.06	0.05	11.94	0.83	0.05	0.02	0.34	3.03	4.84	0.04	0.00	0.03	96.24
SHB3_385.9	73.96	0.04	11.95	0.78	0.05	0.03	0.35	3.13	4.51	0.00	0.00	0.00	94.80
SHB3_385.9	74.25	0.04	11.90	0.72	0.00	0.02	0.39	3.27	4.53	0.01	0.01	0.01	95.14
SHB3_385.9	74.96	0.03	11.87	0.74	0.06	0.01	0.32	2.85	4.79	0.00	0.01	0.00	95.64
SHB3_385.9	74.06	0.04	12.00	0.81	0.06	0.02	0.35	3.02	4.54	0.03	0.00	0.04	94.96
SHB3_385.9	73.48	0.16	11.93	0.74	0.03	0.02	0.35	2.96	4.73	0.00	0.00	0.01	94.40
SHB3_385.9	75.67	0.09	12.02	0.75	0.05	0.04	0.36	3.07	4.68	0.02	0.00	0.02	96.77

Table A-1.0-1 (continued)

Sample	SiO_2	TiO_2	Al_2O_3	FeO (Total)	MnO	MgO	CaO	Na_2O	K_2O	P_2O_5	SrO	BaO	Total
Pueblo Canyon Member, Cerro Toledo Formation													
SHB3_385.9	73.74	0.10	11.83	0.77	0.05	0.02	0.36	3.10	4.57	0.00	0.00	0.01	94.54
SHB3_385.9	74.25	0.08	11.79	0.73	0.09	0.02	0.34	3.10	4.58	0.00	0.00	0.00	94.99
SHB3_385.9	73.52	0.01	11.93	0.76	0.08	0.02	0.35	3.15	4.61	0.00	0.00	0.00	94.42
SHB3_385.9	74.62	0.08	11.95	0.72	0.06	0.01	0.30	2.99	4.71	0.02	0.00	0.00	95.46
SHB3_385.9	74.45	0.06	11.96	0.77	0.06	0.03	0.34	2.98	4.82	0.00	0.00	0.00	95.46
SHB3_385.9	74.26	0.08	11.93	0.78	0.02	0.01	0.37	2.86	4.70	0.01	0.00	0.00	95.03
SHB3_385.9	75.41	0.01	12.04	0.76	0.02	0.04	0.36	3.08	4.73	0.03	0.00	0.04	96.51
SHB3_385.9	74.63	0.08	12.05	0.73	0.09	0.02	0.35	3.08	4.62	0.01	0.00	0.00	95.65
SHB3_385.9	74.65	0.08	11.96	0.80	0.03	0.03	0.36	3.17	4.43	0.03	0.00	0.04	95.58
Mean	**74.53**	**0.07**	**11.95**	**0.77**	**0.05**	**0.02**	**0.35**	**3.01**	**4.67**	**0.01**	**0.00**	**0.01**	**95.45**
Stdev	**0.69**	**0.04**	**0.08**	**0.03**	**0.02**	**0.01**	**0.02**	**0.17**	**0.18**	**0.02**	**0.01**	**0.02**	**0.75**

Table A-1.0-1 (continued)

Sample	SiO_2	TiO_2	Al_2O_3	FeO (Total)	MnO	MgO	CaO	Na_2O	K_2O	P_2O_5	SrO	BaO	Total
Pueblo Canyon Member, Cerro Toledo Formation													
SHB3_398	73.88	0.11	11.55	0.81	0.08	0.03	0.34	3.17	4.89	0.03	0.03	0.01	94.93
SHB3_398	75.14	0.11	11.66	0.73	0.08	0.03	0.33	3.37	4.92	0.04	0.02	0.03	96.45
SHB3_398	73.91	0.10	11.51	0.73	0.05	0.03	0.38	2.93	5.16	0.00	0.03	0.09	94.90
SHB3_398	74.51	0.07	11.64	0.77	0.04	0.03	0.34	3.14	5.06	0.02	0.05	0.00	95.66
SHB3_398	75.49	0.11	11.63	0.77	0.06	0.03	0.37	3.34	4.85	0.03	0.06	0.00	96.71
SHB3_398	75.19	0.11	11.56	0.73	0.03	0.01	0.35	2.74	5.38	0.00	0.00	0.05	96.16
SHB3_398	74.00	0.11	11.62	0.75	0.01	0.02	0.30	3.02	5.23	0.01	0.05	0.04	95.15
SHB3_398	75.04	0.07	11.53	0.79	0.08	0.02	0.34	2.69	5.60	0.00	0.05	0.02	96.22
SHB3_398	74.37	0.11	11.48	0.81	0.03	0.04	0.35	2.95	5.09	0.00	0.07	0.00	95.29
SHB3_398	74.90	0.08	11.69	0.74	0.07	0.02	0.35	2.81	5.41	0.00	0.00	0.00	96.06
SHB3_398	74.57	0.10	11.55	0.73	0.04	0.04	0.35	2.89	5.24	0.00	0.00	0.02	95.53
SHB3_398	74.28	0.10	11.60	0.79	0.02	0.01	0.36	2.82	5.07	0.02	0.05	0.00	95.12
SHB3_398	74.00	0.10	11.54	0.70	0.05	0.04	0.36	2.57	5.59	0.00	0.04	0.00	95.00
SHB3_398	74.29	0.07	11.61	0.79	0.03	0.03	0.35	3.05	5.08	0.06	0.03	0.06	95.46
SHB3_398	74.67	0.11	11.60	0.73	0.07	0.02	0.35	3.07	5.04	0.00	0.04	0.00	95.70
SHB3_398	75.73	0.12	11.65	0.76	0.05	0.03	0.35	3.15	4.92	0.05	0.00	0.03	96.83
SHB3_398	74.55	0.08	11.67	0.70	0.06	0.02	0.33	2.98	5.22	0.00	0.05	0.00	95.65
SHB3_398	74.37	0.09	11.49	0.69	0.06	0.02	0.34	3.03	5.15	0.01	0.03	0.00	95.27
SHB3_398	74.15	0.07	11.49	0.72	0.06	0.02	0.33	2.96	4.98	0.00	0.02	0.03	94.82
SHB3_398	73.61	0.12	11.73	0.77	0.06	0.04	0.31	3.27	4.79	0.00	0.02	0.06	94.78
SHB3_398	75.22	0.09	11.63	0.79	0.03	0.03	0.34	2.92	5.08	0.00	0.04	0.04	96.21
SHB3_398	75.12	0.09	11.56	0.79	0.04	0.01	0.35	2.13	5.14	0.02	0.03	0.00	95.28
SHB3_398	74.18	0.09	11.65	0.71	0.06	0.02	0.34	2.97	4.98	0.00	0.06	0.00	95.04
SHB3_398	74.31	0.07	11.54	0.78	0.03	0.01	0.36	2.88	5.36	0.00	0.01	0.00	95.35

Table A-1.0-1 (continued)

Sample	SiO_2	TiO_2	Al_2O_3	FeO (Total)	MnO	MgO	CaO	Na_2O	K_2O	P_2O_5	SrO	BaO	Total
Pueblo Canyon Member, Cerro Toledo Formation													
SHB3_398	74.41	0.09	11.49	0.77	0.11	0.03	0.36	2.59	5.66	0.00	0.01	0.01	95.51
SHB3_398	74.51	0.08	11.51	0.76	0.04	0.02	0.33	2.80	5.35	0.00	0.08	0.06	95.54
SHB3_398	74.49	0.05	11.56	0.79	0.06	0.02	0.33	2.76	5.45	0.02	0.03	0.00	95.57
SHB3_398	74.57	0.14	11.53	0.86	0.07	0.03	0.33	2.91	5.50	0.00	0.09	0.00	96.01
SHB3_398	74.95	0.10	11.72	0.82	0.06	0.01	0.38	3.11	4.95	0.00	0.02	0.09	96.21
SHB3_398	74.21	0.08	11.61	0.65	0.06	0.03	0.34	3.25	4.98	0.00	0.04	0.00	95.24
SHB3_398	74.42	0.08	11.61	0.83	0.08	0.03	0.32	3.24	4.87	0.03	0.03	0.00	95.53
SHB3_398	74.83	0.10	11.57	0.75	0.07	0.03	0.33	3.13	5.01	0.00	0.02	0.00	95.82
SHB3_398	75.30	0.10	11.56	0.81	0.06	0.03	0.36	3.26	4.81	0.02	0.01	0.00	96.31
Mean	**74.58**	**0.09**	**11.58**	**0.76**	**0.05**	**0.02**	**0.34**	**2.97**	**5.14**	**0.01**	**0.03**	**0.02**	**95.62**
Stdev	**0.50**	**0.02**	**0.07**	**0.04**	**0.02**	**0.01**	**0.02**	**0.25**	**0.24**	**0.02**	**0.02**	**0.03**	**0.55**

Table A-1.0-1 (continued)

Sample	SiO_2	TiO_2	Al_2O_3	FeO (Total)	MnO	MgO	CaO	Na_2O	K_2O	P_2O_5	SrO	BaO	Total
Otowi Member, Bandelier Tuff													
SHB3_600	75.49	0.00	11.98	1.19	0.05	0.00	0.21	3.50	4.99	0.00	0.01	0.01	97.43
SHB3_600	75.60	0.13	12.04	1.30	0.02	0.01	0.24	3.59	4.98	0.00	0.03	0.01	97.93
SHB3_600	76.21	0.12	11.97	1.17	0.04	0.01	0.23	3.44	5.08	0.02	0.00	0.00	98.29
SHB3_600	75.54	0.00	11.98	1.25	0.00	0.00	0.22	3.55	5.04	0.00	0.01	0.00	97.59
SHB3_600	75.92	0.14	11.94	1.04	0.06	0.00	0.21	3.42	5.10	0.01	0.00	0.00	97.84
SHB3_600	75.41	0.13	11.94	1.22	0.04	0.01	0.24	3.42	5.07	0.00	0.03	0.00	97.51
SHB3_600	75.36	0.06	11.92	1.26	0.02	0.00	0.23	3.35	5.05	0.03	0.00	0.00	97.27
SHB3_600	75.21	0.11	11.93	1.27	0.03	0.01	0.20	3.50	5.03	0.01	0.00	0.00	97.31
SHB3_600	75.55	0.06	11.84	1.30	0.00	0.01	0.24	3.45	5.00	0.03	0.04	0.00	97.53
SHB3_600	75.72	0.13	11.98	0.75	0.05	0.00	0.20	3.32	5.32	0.00	0.03	0.04	97.55
SHB3_600	75.72	0.07	11.96	1.01	0.06	0.00	0.21	3.41	5.06	0.02	0.00	0.02	97.55
SHB3_600	75.87	0.12	11.93	0.21	0.02	0.00	0.19	2.61	6.02	0.00	0.02	0.02	97.00
SHB3_600	76.04	0.05	11.99	0.83	0.06	0.00	0.27	3.49	4.94	0.02	0.02	0.01	97.74
SHB3_600	75.07	0.08	11.83	1.23	0.06	0.00	0.18	3.56	5.03	0.00	0.01	0.00	97.06
SHB3_600	75.16	0.08	12.00	1.25	0.09	0.01	0.20	3.62	5.06	0.03	0.05	0.00	97.53
SHB3_600	75.51	0.04	11.95	1.06	0.08	0.01	0.21	3.46	5.03	0.00	0.02	0.02	97.38
SHB3_600	75.91	0.00	11.89	1.12	0.01	0.00	0.22	3.44	5.13	0.00	0.00	0.00	97.73
SHB3_600	76.79	0.13	12.09	0.45	0.03	0.00	0.17	3.41	5.38	0.00	0.00	0.09	98.54
SHB3_600	76.19	0.21	11.98	1.20	0.03	0.01	0.23	3.42	4.98	0.00	0.01	0.00	98.26
SHB3_600	75.73	0.05	12.02	1.01	0.06	0.00	0.21	3.52	5.08	0.02	0.02	0.00	97.74
SHB3_600	75.15	0.13	11.97	1.29	0.07	0.00	0.20	3.46	4.98	0.00	0.03	0.00	97.28
SHB3_600	75.15	0.06	11.98	1.20	0.04	0.01	0.17	3.50	5.20	0.00	0.02	0.04	97.35
SHB3_600	76.11	0.14	11.97	1.24	0.04	0.02	0.20	3.61	4.96	0.00	0.00	0.00	98.28
SHB3_600	76.50	0.07	12.02	1.12	0.02	0.01	0.24	3.48	4.93	0.02	0.00	0.06	98.47
SHB3_600	75.50	0.01	11.90	1.22	0.06	0.00	0.20	3.30	5.02	0.00	0.04	0.00	97.23

Table A-1.0-1 (continued)

Sample	SiO_2	TiO_2	Al_2O_3	FeO (Total)	MnO	MgO	CaO	Na_2O	K_2O	P_2O_5	SrO	BaO	Total
Otowi Member, Bandelier Tuff													
SHB3_600	74.46	0.06	11.85	1.22	0.01	0.01	0.19	3.55	5.05	0.00	0.05	0.00	96.43
SHB3_600	75.72	0.02	11.97	1.19	0.08	0.01	0.23	3.38	5.05	0.00	0.05	0.00	97.69
SHB3_600	75.24	0.10	12.01	1.09	0.04	0.01	0.21	3.40	5.08	0.02	0.02	0.02	97.21
SHB3_600	75.46	0.14	11.89	1.16	0.06	0.01	0.20	3.46	5.07	0.01	0.01	0.02	97.51
SHB3_600	75.46	0.02	11.88	1.25	0.08	0.02	0.20	3.29	5.06	0.00	0.03	0.00	97.29
SHB3_600	75.72	0.08	11.96	1.28	0.02	0.00	0.19	3.59	4.92	0.00	0.07	0.02	97.86
SHB3_600	75.29	0.05	11.88	1.21	0.06	0.01	0.21	3.47	5.00	0.00	0.04	0.01	97.24
SHB3_600	75.22	0.08	11.81	1.22	0.01	0.00	0.21	3.52	5.06	0.00	0.00	0.09	97.23
SHB3_600	75.46	0.16	12.04	1.13	0.05	0.02	0.22	3.64	4.94	0.00	0.00	0.03	97.70
SHB3_600	75.18	0.08	12.02	1.03	0.08	0.00	0.21	3.61	5.01	0.01	0.00	0.07	97.31
SHB3_600	74.78	0.13	11.92	1.27	0.02	0.01	0.21	3.34	5.06	0.00	0.00	0.00	96.73
SHB3_600	75.26	0.05	11.87	1.24	0.04	0.01	0.20	3.38	4.97	0.01	0.00	0.03	97.06
SHB3_600	75.46	0.06	11.85	1.22	0.04	0.00	0.21	3.40	5.02	0.00	0.02	0.01	97.28
SHB3_600	74.96	0.11	11.84	1.26	0.03	0.01	0.22	3.44	4.94	0.00	0.00	0.00	96.83
Mean	**75.54**	**0.08**	**11.94**	**1.13**	**0.04**	**0.01**	**0.21**	**3.44**	**5.07**	**0.01**	**0.02**	**0.02**	**97.51**
Stdev	**0.46**	**0.05**	**0.07**	**0.22**	**0.02**	**0.01**	**0.02**	**0.16**	**0.18**	**0.01**	**0.02**	**0.02**	**0.46**

Table A-1.0-1 (continued)

Sample	SiO_2	TiO_2	Al_2O_3	FeO (Total)	MnO	MgO	CaO	Na_2O	K_2O	P_2O_5	SrO	BaO	Total
Otowi Member, Bandelier Tuff													
SHB3_703	74.07	0.00	11.85	1.26	0.02	0.00	0.25	3.96	4.49	0.00	0.02	0.12	96.04
SHB3_703	73.01	0.10	11.81	1.23	0.06	0.00	0.26	4.22	4.45	0.00	0.00	0.00	95.14
SHB3_703	74.50	0.01	11.85	1.37	0.08	0.00	0.28	4.13	4.51	0.01	0.00	0.00	96.72
SHB3_703	73.78	0.10	11.72	1.23	0.10	0.01	0.25	4.05	4.52	0.05	0.00	0.00	95.81
SHB3_703	73.84	0.01	11.81	1.26	0.16	0.00	0.25	4.07	4.51	0.00	0.00	0.00	95.91
SHB3_703	73.57	0.01	11.70	1.23	0.08	0.00	0.23	4.03	4.48	0.01	0.01	0.08	95.43
SHB3_703	73.99	0.08	11.81	1.16	0.04	0.00	0.28	3.96	4.54	0.04	0.00	0.00	95.90
SHB3_703	73.23	0.05	11.66	1.39	0.11	0.00	0.26	4.03	4.50	0.00	0.04	0.00	95.26
SHB3_703	74.24	0.03	11.86	1.22	0.04	0.01	0.26	4.02	4.56	0.01	0.02	0.02	96.31
SHB3_703	73.64	0.07	11.83	1.28	0.07	0.00	0.28	4.16	4.47	0.02	0.03	0.00	95.85
SHB3_703	73.52	0.08	11.83	1.27	0.05	0.00	0.23	4.03	4.45	0.02	0.03	0.02	95.52
SHB3_703	73.50	0.00	11.71	1.33	0.08	0.00	0.25	4.18	4.41	0.00	0.03	0.02	95.52
SHB3_703	74.74	0.13	11.98	1.18	0.14	0.00	0.29	4.06	4.51	0.00	0.01	0.00	97.03
SHB3_703	73.43	0.00	11.76	1.18	0.08	0.00	0.28	3.93	4.53	0.00	0.00	0.00	95.19
SHB3_703	74.75	0.07	11.94	1.23	0.09	0.01	0.26	4.07	4.51	0.01	0.02	0.00	96.95
SHB3_703	73.64	0.04	11.75	1.24	0.05	0.00	0.24	3.99	4.46	0.06	0.03	0.00	95.51
SHB3_703	73.71	0.01	11.77	1.22	0.07	0.00	0.29	4.08	4.49	0.00	0.00	0.08	95.72
SHB3_703	73.55	0.07	11.80	1.19	0.07	0.00	0.22	3.89	4.71	0.01	0.02	0.00	95.53
SHB3_703	73.89	0.00	11.76	1.26	0.10	0.00	0.24	3.98	4.56	0.05	0.00	0.00	95.86
SHB3_703	74.22	0.09	11.81	1.24	0.10	0.00	0.26	4.01	4.36	0.04	0.04	0.04	96.20
SHB3_703	74.06	0.00	11.87	1.37	0.11	0.01	0.24	4.12	4.45	0.01	0.02	0.03	96.31
SHB3_703	74.12	0.06	11.85	1.43	0.09	0.00	0.27	4.12	4.40	0.02	0.00	0.07	96.43
SHB3_703	73.56	0.11	11.86	1.21	0.06	0.01	0.28	3.86	4.45	0.02	0.00	0.00	95.41
SHB3_703	73.89	0.00	11.76	1.20	0.08	0.00	0.25	3.97	4.41	0.00	0.03	0.00	95.59
SHB3_703	72.59	0.04	11.58	1.12	0.08	0.00	0.24	4.03	4.59	0.02	0.00	0.00	94.28

Table A-1.0-1 (continued)

Sample	SiO_2	TiO_2	Al_2O_3	FeO (Total)	MnO	MgO	CaO	Na_2O	K_2O	P_2O_5	SrO	BaO	Total
Otowi Member, Bandelier Tuff													
SHB3_703	73.85	0.10	11.73	1.22	0.06	0.00	0.28	4.08	4.54	0.01	0.04	0.04	95.95
SHB3_703	73.74	0.12	11.55	1.23	0.08	0.00	0.25	4.09	4.49	0.00	0.00	0.00	95.54
SHB3_703	73.13	0.01	11.80	1.26	0.07	0.00	0.25	4.21	4.44	0.00	0.03	0.00	95.21
SHB3_703	73.19	0.14	11.91	1.19	0.06	0.00	0.22	3.99	4.54	0.01	0.01	0.05	95.31
SHB3_703	73.88	0.00	11.74	1.21	0.12	0.00	0.27	4.12	4.41	0.00	0.00	0.00	95.75
SHB3_703	73.51	0.04	11.96	1.22	0.03	0.00	0.26	4.00	4.57	0.00	0.01	0.02	95.61
SHB3_703	73.40	0.00	11.76	1.27	0.03	0.00	0.26	4.01	4.44	0.00	0.05	0.00	95.22
SHB3_703	73.61	0.11	11.80	1.22	0.10	0.01	0.24	4.07	4.46	0.02	0.04	0.00	95.68
SHB3_703	74.79	0.10	11.93	1.21	0.08	0.00	0.27	3.98	4.49	0.00	0.01	0.09	96.96
SHB3_703	73.98	0.00	11.83	1.26	0.01	0.01	0.23	4.15	4.38	0.01	0.05	0.00	95.90
Mean	**73.77**	**0.05**	**11.80**	**1.25**	**0.08**	**0.00**	**0.26**	**4.05**	**4.49**	**0.01**	**0.02**	**0.02**	**95.79**
Stdev	**0.49**	**0.05**	**0.10**	**0.07**	**0.03**	**0.00**	**0.02**	**0.08**	**0.07**	**0.02**	**0.02**	**0.03**	**0.58**

Table A-1.0-1 (continued)

Sample	SiO_2	TiO_2	Al_2O_3	FeO (Total)	MnO	MgO	CaO	Na_2O	K_2O	P_2O_5	SrO	BaO	Total
Otowi Member, Bandelier Tuff													
SHB3-757	75.28	0.12	11.93	1.12	0.08	0.00	0.26	4.13	4.35	0.00	0.00	0.01	97.28
SHB3-757	73.46	0.07	11.77	1.21	0.03	0.01	0.27	4.12	4.39	0.03	0.01	0.01	95.37
SHB3-757	73.78	0.04	11.73	1.28	0.11	0.00	0.27	4.13	4.42	0.00	0.02	0.03	95.81
SHB3-757	75.22	0.06	11.86	1.42	0.09	0.01	0.27	4.15	4.40	0.02	0.00	0.00	97.49
SHB3-757	74.50	0.00	11.81	1.25	0.04	0.00	0.28	4.10	4.40	0.00	0.02	0.00	96.39
SHB3-757	74.12	0.09	11.78	1.35	0.08	0.00	0.23	4.18	4.42	0.00	0.03	0.01	96.28
SHB3-757	74.31	0.09	11.88	1.20	0.00	0.00	0.27	3.95	4.41	0.00	0.00	0.00	96.11
SHB3-757	74.11	0.07	11.77	1.26	0.11	0.00	0.27	4.00	4.48	0.00	0.03	0.00	96.10
SHB3-757	73.49	0.05	11.81	1.24	0.08	0.00	0.29	4.00	4.43	0.00	0.02	0.00	95.40
SHB3-757	74.09	0.13	11.92	1.25	0.10	0.00	0.28	4.12	4.37	0.02	0.02	0.00	96.30
SHB3-757	74.10	0.03	11.89	1.26	0.11	0.00	0.27	4.22	4.48	0.00	0.02	0.01	96.39
SHB3-757	74.80	0.12	11.94	1.29	0.09	0.00	0.27	4.13	4.38	0.00	0.00	0.00	97.02
SHB3-757	75.87	0.08	11.94	1.29	0.05	0.00	0.27	3.88	4.49	0.00	0.01	0.03	97.90
SHB3-757	75.02	0.05	11.90	1.32	0.03	0.00	0.29	4.02	4.44	0.00	0.00	0.00	97.06
SHB3-757	74.05	0.05	11.89	1.27	0.07	0.00	0.26	4.22	4.46	0.02	0.02	0.03	96.31
SHB3-757	74.92	0.10	12.06	1.26	0.08	0.01	0.28	4.16	4.38	0.03	0.02	0.03	97.32
SHB3-757	74.40	0.12	11.89	1.32	0.07	0.00	0.27	4.17	4.33	0.02	0.00	0.02	96.61
SHB3-757	73.93	0.09	11.96	1.17	0.12	0.00	0.26	4.03	4.43	0.02	0.02	0.00	96.04
SHB3-757	74.30	0.05	11.89	1.31	0.06	0.01	0.30	3.96	4.34	0.00	0.01	0.00	96.22
SHB3-757	74.71	0.08	12.03	1.28	0.08	0.00	0.27	3.99	4.44	0.00	0.00	0.01	96.90
SHB3-757	75.05	0.10	11.96	1.22	0.09	0.00	0.29	4.02	4.51	0.00	0.00	0.05	97.30
SHB3-757	74.21	0.08	11.92	1.27	0.12	0.01	0.26	3.91	4.53	0.00	0.00	0.00	96.32
SHB3-757	73.48	0.03	11.84	1.29	0.09	0.00	0.29	3.91	4.44	0.00	0.00	0.00	95.36
SHB3-757	74.45	0.10	11.97	1.27	0.06	0.00	0.27	4.06	4.34	0.00	0.00	0.00	96.50
SHB3-757	74.74	0.00	12.03	1.27	0.11	0.00	0.26	4.20	4.50	0.00	0.01	0.00	97.11

Table A-1.0-1 (continued)

Sample	SiO_2	TiO_2	Al_2O_3	FeO (Total)	MnO	MgO	CaO	Na_2O	K_2O	P_2O_5	SrO	BaO	Total
Otowi Member, Bandelier Tuff													
SHB3-757	74.42	0.07	11.87	1.27	0.09	0.01	0.27	4.07	4.40	0.00	0.01	0.00	96.49
SHB3-757	74.28	0.05	11.93	1.28	0.12	0.00	0.29	4.11	4.42	0.00	0.01	0.01	96.50
SHB3-757	74.10	0.05	11.91	1.22	0.06	0.00	0.27	4.16	4.44	0.00	0.04	0.03	96.28
SHB3-757	73.64	0.00	11.86	1.23	0.08	0.00	0.25	4.17	4.35	0.00	0.01	0.03	95.61
SHB3-757	73.63	0.04	11.96	1.18	0.10	0.01	0.27	4.03	4.42	0.00	0.03	0.02	95.69
SHB3-757	74.11	0.12	11.88	1.23	0.09	0.00	0.28	4.12	4.39	0.02	0.03	0.04	96.31
SHB3-757	55.43	0.06	27.21	0.52	0.03	0.02	9.87	5.57	0.38	0.08	0.20	0.09	99.47
Mean	**73.75**	**0.07**	**12.37**	**1.24**	**0.08**	**0.00**	**0.57**	**4.12**	**4.29**	**0.01**	**0.02**	**0.01**	**96.54**
Stdev	**3.39**	**0.04**	**2.71**	**0.14**	**0.03**	**0.01**	**1.70**	**0.28**	**0.72**	**0.02**	**0.03**	**0.02**	**0.83**

Table A-1.0-1 (continued)

Sample	SiO_2	TiO_2	Al_2O_3	FeO (Total)	MnO	MgO	CaO	Na_2O	K_2O	P_2O_5	SrO	BaO	Total
Otowi Member, Bandelier Tuff													
SHB3_798	73.29	0.10	11.73	0.24	0.07	0.00	1.20	3.94	4.48	0.04	0.01	0.00	95.11
SHB3_798	72.28	0.03	11.66	0.26	0.09	0.00	1.29	4.37	4.19	0.01	0.03	0.00	94.20
SHB3_798	72.45	0.03	12.23	0.23	0.06	0.00	1.17	4.49	4.39	0.00	0.01	0.00	95.07
SHB3_798	72.56	0.04	11.87	0.23	0.09	0.00	1.34	4.18	4.15	0.05	0.02	0.00	94.53
SHB3_798	73.64	0.03	11.95	0.24	0.12	0.00	1.28	4.24	4.18	0.00	0.00	0.00	95.67
SHB3_798	72.76	0.08	11.89	0.23	0.12	0.00	1.19	4.28	4.17	0.00	0.03	0.04	94.79
SHB3_798	73.09	0.10	11.72	0.24	0.10	0.00	1.28	4.12	4.25	0.00	0.00	0.06	94.94
SHB3_798	72.73	0.06	11.85	0.25	0.06	0.00	1.19	4.17	4.28	0.02	0.01	0.08	94.69
SHB3_798	73.72	0.04	11.80	0.23	0.09	0.00	1.28	4.19	4.22	0.04	0.00	0.00	95.60
SHB3_798	75.17	0.07	11.85	0.23	0.03	0.00	1.28	4.31	4.27	0.00	0.01	0.00	97.20
SHB3_798	73.85	0.09	11.84	0.26	0.08	0.00	1.25	4.02	4.24	0.03	0.02	0.00	95.66
SHB3_798	73.42	0.04	11.65	0.25	0.08	0.00	1.26	4.15	4.27	0.06	0.00	0.00	95.17
SHB3_798	72.97	0.09	11.91	0.26	0.07	0.00	1.34	4.09	4.25	0.02	0.00	0.07	95.08
SHB3_798	73.44	0.01	11.89	0.26	0.04	0.00	1.35	4.07	4.44	0.00	0.02	0.02	95.53
SHB3_798	73.42	0.09	11.71	0.24	0.08	0.00	1.26	4.10	4.25	0.00	0.03	0.02	95.20
SHB3_798	72.80	0.08	11.80	0.27	0.08	0.00	1.31	4.09	4.28	0.00	0.03	0.04	94.78
SHB3_798	72.67	0.06	11.56	0.24	0.10	0.00	1.24	3.88	4.41	0.01	0.01	0.02	94.19
SHB3_798	72.80	0.05	11.74	0.27	0.11	0.00	1.36	4.02	4.30	0.01	0.04	0.00	94.70
SHB3_798	73.20	0.07	11.86	0.23	0.13	0.00	1.30	4.22	4.28	0.00	0.05	0.00	95.34
SHB3_798	73.11	0.03	11.77	0.25	0.09	0.00	1.28	4.05	4.48	0.02	0.00	0.03	95.10
SHB3_798	73.43	0.08	11.75	0.25	0.06	0.00	1.32	3.92	4.29	0.00	0.01	0.01	95.12
SHB3_798	71.39	0.04	11.47	0.38	0.12	0.00	1.20	3.45	5.00	0.00	0.02	0.00	93.07
SHB3_798	73.28	0.03	11.96	0.25	0.08	0.00	1.30	3.97	4.46	0.01	0.02	0.00	95.36
SHB3_798	72.91	0.07	11.87	0.23	0.10	0.00	1.33	4.29	4.10	0.00	0.00	0.04	94.95
SHB3_798	73.05	0.09	11.83	0.24	0.09	0.00	1.29	4.16	4.43	0.03	0.00	0.01	95.22

Table A-1.0-1 (continued)

Sample	SiO_2	TiO_2	Al_2O_3	FeO (Total)	MnO	MgO	CaO	Na_2O	K_2O	P_2O_5	SrO	BaO	Total
Otowi Member, Bandelier Tuff													
SHB3_798	72.75	0.04	11.74	0.26	0.10	0.00	1.30	4.18	4.27	0.00	0.00	0.06	94.71
SHB3_798	72.39	0.01	11.70	0.26	0.06	0.00	1.27	4.15	4.22	0.00	0.02	0.00	94.09
SHB3_798	72.44	0.05	11.87	0.24	0.10	0.00	1.27	4.14	4.26	0.01	0.04	0.00	94.39
SHB3_798	71.12	0.00	11.70	0.25	0.10	0.00	1.32	4.07	4.20	0.03	0.03	0.00	92.81
SHB3_798	73.74	0.12	11.88	0.26	0.09	0.00	1.32	4.14	4.27	0.04	0.00	0.03	95.89
Mean	**72.99**	**0.06**	**11.80**	**0.25**	**0.09**	**0.00**	**1.28**	**4.11**	**4.31**	**0.01**	**0.02**	**0.02**	**94.94**
Stdev	**0.74**	**0.03**	**0.14**	**0.03**	**0.02**	**0.00**	**0.05**	**0.18**	**0.16**	**0.02**	**0.01**	**0.02**	**0.81**

Note: These data were originally reported in Gardner et al (2001).

Table A-1.0-2
Major and Trace Element Whole Rock Geochemistry of Samples from Core Hole SHB-3

Sample Number	SHB3-8.5	SHB3-28	SHB3-38	SHB3-45	SHB3-53	SHB3-58	SHB3-79	SHB3-93	SHB3-102.75	SHB3-109	SHB3-119	SHB3-130	SHB3-140	SHB3-151	SHB3-158.5	SHB3-170	SHB3-178.5	SHB3-199	SHB3-215	SHB3-223
Elevation (ft)	**7599.2**	**7579.7**	**7569.7**	**7562.7**	**7554.7**	**7549.7**	**7528.7**	**7514.7**	**7504.9**	**7498.7**	**7488.7**	**7477.7**	**7467.7**	**7456.7**	**7449.2**	**7437.7**	**7429.2**	**7408.7**	**7392.7**	**7384.7**
Depth (ft)	**8.5**	**28**	**38**	**45**	**53**	**58**	**79**	**93**	**102.75**	**109**	**119**	**130**	**140**	**151**	**158.5**	**170**	**178.5**	**199**	**215**	**223**
Major Elements (wt%)																				
SiO_2	72.97	72.94	72.17	75.35	74.93	74.22	74.60	74.27	75.81	75.39	74.56	76.18	74.49	76.31	75.30	77.99	75.62	76.32	75.98	78.26
TiO_2	0.24	0.25	0.25	0.20	0.20	0.19	0.19	0.19	0.18	0.19	0.17	0.17	0.16	0.16	0.15	0.13	0.14	0.13	0.14	0.12
Al_2O_3	13.42	13.65	13.73	12.89	13.05	12.99	12.70	12.82	12.78	12.72	12.63	12.83	12.51	12.93	12.34	12.05	12.26	12.10	11.89	11.79
$Fe_2O_{3\,T}$	2.26	2.32	2.31	1.98	2.03	1.91	1.97	2.00	1.96	2.04	1.88	1.89	1.79	1.80	1.71	1.50	1.62	1.56	1.50	1.39
MnO	0.07	0.07	0.07	0.07	0.07	0.07	0.07	0.07	0.07	0.05	0.07	0.06	0.06	0.07	0.06	0.05	0.06	0.06	0.05	0.05
MgO	0.09	0.10	0.12	—*	0.11	0.09	0.10	0.10	—	—	0.08	—	—	—	0.10	—	—	—	—	—
CaO	0.46	0.44	0.48	0.45	0.47	0.45	0.39	0.38	0.36	0.26	0.33	0.33	0.29	0.35	0.42	0.35	0.27	0.31	0.33	0.33
Na_2O	4.60	4.63	4.80	4.45	4.52	4.55	4.45	4.49	4.46	4.42	4.42	4.42	4.39	4.40	4.20	4.17	4.24	4.22	4.09	4.10
K_2O	4.76	4.72	4.65	4.74	4.77	4.78	4.75	4.81	4.76	4.80	4.73	4.78	4.67	4.77	4.49	4.41	4.63	4.48	4.38	4.30
P_2O_5	0.04	0.04	0.04	0.02	0.02	0.03	0.03	0.03	0.02	0.03	0.02	0.02	0.02	0.02	0.02	0.02	0.01	—	0.02	0.01
LOI %	0.32	0.52	0.36	0.15	0.13	0.20	0.22	0.23	0.16	0.26	0.28	0.18	0.25	0.20	0.29	0.12	0.21	0.21	0.15	0.14
Total	**99.35**	**99.80**	**99.09**	**100.40**	**100.41**	**99.59**	**99.58**	**99.49**	**100.68**	**100.25**	**99.27**	**100.96**	**98.72**	**101.10**	**99.18**	**100.87**	**99.14**	**99.55**	**98.60**	**100.56**
Trace Elements (ppm)																				
Ba	349.26	318.27	370.36	228.87	252.95	215.60	220.03	206.16	224.19	146.78	193.73	233.89	183.51	176.55	179.24	177.03	126.83	157.84	170.37	162.96
Nb	42.80	41.95	40.20	52.44	43.16	42.36	48.15	47.16	44.90	50.50	49.86	50.26	53.92	60.30	47.48	44.98	43.13	45.36	42.87	39.66
Rb	78.66	84.69	80.36	84.00	88.95	90.35	90.60	97.53	89.02	94.95	98.85	107.35	97.05	104.31	94.28	88.86	107.58	97.00	91.76	78.07
Sr	63.89	61.32	73.64	39.60	40.87	39.33	33.83	37.71	40.95	34.67	28.67	35.71	27.75	37.39	45.70	40.37	29.37	30.88	42.13	39.01
Y	46.00	35.02	35.70	32.71	28.00	39.14	35.75	36.22	32.71	39.35	38.79	32.78	38.18	46.68	38.47	35.00	39.53	37.64	27.91	27.29
Zn	42.92	49.55	57.16	47.73	52.07	36.32	58.68	56.27	68.98	64.03	57.60	68.41	44.40	67.19	56.96	58.25	59.57	45.22	43.24	42.60
Zr	376.20	373.23	376.78	377.00	368.99	324.49	336.32	337.10	341.48	332.65	319.14	325.75	300.47	289.92	248.02	246.44	254.42	239.13	218.06	200.63

Table A-1.0-2 (continued)

Sample Number	**SHB3-228.5**	**SHB3-233**	**SHB3-235**	**SHB3-255**	**SHB3-275**	**SHB3-295**	**SHB3-314**	**SHB3-321.5**	**SHB3-342.4**	**SHB3-423.5**	**SHB3-433.5**	**SHB3-499**	**SHB3-555.2**	**SHB3-600**	**SHB3-665**	**SHB3-703**	**SHB3-757**	**SHB3-798**	**SHB3-838.1**
Elevation (ft)	**7379.2**	**7374.7**	**7372.7**	**7352.7**	**7332.7**	**7312.7**	**7293.7**	**7286.2**	**7265.3**	**7184.2**	**7174.2**	**7108.7**	**7052.5**	**7007.7**	**6942.7**	**6904.7**	**6850.7**	**6809.7**	**6769.6**
Depth (ft)	**228.5**	**233**	**235**	**255**	**275**	**295**	**314**	**321.5**	**342.4**	**423.5**	**433.5**	**499**	**555.2**	**600**	**665**	**703**	**757**	**798**	**838.1**
Major Elements (wt%)																			
SiO_2	78.71	77.53	77.30	77.32	77.21	77.68	77.63	78.28	70.69	77.25	77.05	76.31	76.44	76.04	76.46	75.45	75.47	73.25	72.41
TiO_2	0.11	0.15	0.08	0.08	0.09	0.09	0.09	0.13	0.57	0.12	0.12	0.16	0.16	0.13	0.07	0.11	0.12	0.18	0.19
Al_2O_3	11.56	11.71	11.43	11.38	11.34	11.35	11.50	11.57	14.08	12.17	12.13	12.49	12.20	11.93	11.81	12.15	12.30	12.76	12.17
$Fe_2O_{3\,T}$	1.30	1.63	1.33	1.35	1.31	1.36	1.40	1.60	3.53	1.44	1.44	1.67	1.58	1.44	1.24	1.55	1.59	1.98	2.43
MnO	0.04	0.06	0.05	0.05	0.05	0.06	0.06	0.06	0.11	0.04	0.04	0.08	0.06	0.06	0.06	0.08	0.07	0.08	0.09
MgO	—	0.15	—	—	—	—	—	0.11	0.98	—	—	0.13	0.15	0.12	—	—	0.11	0.23	0.56
CaO	0.29	0.31	0.20	0.19	0.22	0.22	0.22	0.42	0.90	0.20	0.18	0.51	0.52	0.48	0.19	0.41	0.47	0.76	0.68
Na_2O	3.98	3.97	3.94	3.97	3.93	4.02	3.99	3.88	1.63	4.03	4.27	4.25	3.94	3.30	3.41	3.69	3.72	3.69	2.87
K_2O	4.26	4.31	4.31	4.31	4.26	4.24	4.23	4.05	2.92	4.67	4.72	4.33	4.36	4.78	5.25	4.79	4.78	4.58	5.16
P_2O_5	0.01	0.03	—	—	—	—	—	0.02	0.03	—	—	0.03	0.02	0.02	—	0.02	0.02	0.04	0.04
LOI %	0.18	0.25	0.23	0.15	0.20	0.22	0.23	0.32	4.35	0.42	0.20	0.37	0.62	1.71	1.79	2.12	2.17	2.70	3.54
Total	**100.52**	**100.18**	**98.94**	**98.89**	**98.68**	**99.35**	**99.42**	**100.52**	**99.98**	**100.39**	**100.22**	**100.44**	**100.15**	**100.09**	**100.35**	**100.47**	**100.91**	**100.39**	**100.31**
Trace Elements (ppm)																			
Ba	138.94	152.33	95.44	106.87	127.47	100.81	90.61	171.68	599.78	—	—	228.80	214.86	162.16	71.61	93.80	146.51	259.44	229.11
Nb	45.93	49.11	51.35	53.14	55.83	49.82	54.42	63.15	47.22	44.57	53.32	53.44	61.43	44.95	78.09	117.52	122.74	149.83	157.70
Rb	79.51	101.16	121.06	126.27	115.81	119.98	118.05	117.03	179.74	102.62	117.55	118.98	92.42	123.58	174.59	245.86	228.39	288.36	412.43
Sr	32.33	35.26	19.07	17.48	24.56	22.70	23.79	56.98	178.10	7.92	—	68.91	61.18	47.21	8.72	42.96	47.65	106.47	94.61
Y	30.50	38.88	44.23	38.29	47.00	40.31	46.67	38.62	52.88	30.27	26.09	37.89	32.40	34.37	45.71	78.62	70.49	82.21	96.84
Zn	43.95	73.97	58.59	51.26	49.71	51.79	73.90	62.46	84.53	50.16	51.48	88.61	47.26	62.38	77.09	88.86	84.34	107.17	128.79
Zr	205.37	213.93	190.26	189.23	188.47	190.65	187.60	195.54	324.95	249.91	251.13	212.71	212.68	171.79	162.36	192.52	191.86	245.48	246.07

Notes: V, Cr, Ni concentrations are below detection limits and therefore not reported. Data originally published in Gardner et al. (2001).

*— = Not detected.

Appendix B

Laser Ablation Inductively Coupled Plasma Mass Spectrometry Methods and Results

Fifty-six samples of pumice fragments were selected from several stratigraphic levels within the upper and lower Bandelier Tuffs and the Cerro Toledo Formation in nine wells and one core hole located in the vicinity of Technical Area 16 (TA-16) (Table B-1). The pumices were all glassy and varied in clast sizes. Each pumice fragment was polished to create a smooth surface to be scanned using the laser ablation inductively coupled plasma mass spectrometry (LA-ICP-MS) beam. Pumices from the same stratigraphic level in each well were mounted on a glass slide for analysis. Table B-2 presents information on the analysis of glassy pumices by LA-ICP-MS.

The LA-ICP-MS analyses were carried out on pumice samples using an Electro Scientific Industries New Wave Research NWR 213 laser ablation system equipped with a Nd:YAG deep ultraviolet (213 nm) laser coupled to a Thermo Scientific iCAP Q ICP-MS. Before the samples were analyzed, the ICP-MS parameters were optimized using National Institute of Standards and Testing 612 glass sample. The LA-ICP-MS parameters included a plasma power of 1550W, an argon nebulizer gas flow of 0.5707 Lmin^{-1}, and dwell times of 10 milliseconds per isotope except for ^{57}Fe and ^{47}Ti, which had dwell times of 50 milliseconds.

Two to three line scans per pumice piece (3–6 pieces per sample) for each well depth were collected. Line scans were approximately 0.5-mm apart on each piece of pumice. Line scans were carried out under the following conditions: 30 s in duration at a scan speed of 8 μm/s, with a laser spot size of 30 μm, operating at 10 Hz, and with a laser power of 4 J/cm^2. Helium carrier gas was used to deliver the ablated material to the ICP-MS at a flow rate of 1 L/min. The samples were probed for ^{27}Al, ^{44}Ca, ^{47}Ti, ^{48}Ti, ^{57}Fe, ^{85}Rb, ^{90}Zr, ^{93}Nb, ^{133}Cs,^{139}La, ^{140}Ce, ^{146}Nd, ^{147}Sm, ^{153}Eu, ^{163}Dy, ^{172}Yb, ^{175}Lu, ^{178}Hf, ^{232}Th, and ^{238}U. The integration time for each analysis was 15 s.

Table B-1
List of Samples Selected for LA-ICP-MS Analysis

Priority	Well Name	Depth (ft bgs)	Initial Unit Assignment and Description	Unit Assignment after Review of Chemical Fingerprinting Results
1	R-26	500	Qbt 1g	Unchanged
2	R-26	510	Qct	Likely Qbt1g from mixing during drilling; Qbt 1g/Qct contact is at 505 ft
3	R-26	545	Qct	Unchanged
4	R-26	575	Qct	Unchanged
5	R-26	580	Qct	Unchanged
6	R-26	665	Qbof above gravels	Sample plots within but at the edge of Qct compositional boundary
7	R-26	700	Qbof above gravels	Sample plots within Qct compositional field; Qct/Qbof contact at 662.4 ft—review contact
8	R-26	755	Qbof above gravels	Unchanged
9	R-26	785	Qbof in gravels	Unchanged
10	R-26	835	Qbof below gravels	Unchanged
11	R-26	870	Qbof below gravels	Unchanged
12	R-26	900	Qbof below gravels	Unchanged
13	R-26	930	Qbof below gravels	Unchanged
14	R-26	945	Qbof below gravels	Unchanged
15	R-26	955	Qbog	Unchanged
16	R-63	365	Qct	Sample R-63-365a_d could be Qbt 1g from mixing during drilling or reworked Qbof based on chemistry
17	R-63	380	Qct	Unchanged
18	R-63	405	Qct	Unchanged
19	R-63	425	Qbof	Chemistry overlaps Qbof and Qct, contact unchanged
20	R-63	550	Qbof	Unchanged
21	R-63	560	Qbof	Unchanged
22	R-63	585	Qbof	Unchanged
23	R-63	610	Qbof	Unchanged
24	R-63	625	Qbof	Unchanged
25	R-63	690	Qbof	Unchanged
26	R-63	705	Qbof	Unchanged
27	R-63	715	Qbof	Unchanged
28	R-63	725	Qbof	Unchanged
29	R-63	790	Qbog	Unchanged
30	CdV-9-1(i)	450	Qct	Unchanged
31	CdV-9-1(i)	465	Qbof	Unchanged
32	R-18	295	Qbt 1g	Unchanged

Table B-1 (continued)

Priority	Well Name	Depth (ft bgs*)	Initial Unit Assignment and Description	Unit Assignment after Review of Chemical Fingerprinting Results
33	R-18	335	Top of Qct, obsidian grain present	Qct, based on chemistry
34	R-18	380	Base of Qct	Qbof, based on chemistry
36	R-18	415	Top of Qbof	Qbof
37	CdV-16-4ip	740	Qbof	Unchanged
38	CdV-16-4ip	760	Qbof	Unchanged
39	R-25	498	Qct	Sample R-25_498_b near Qct/Qbof compositional boundary; contact at 500 ft
40	R-25	514	Qbof	Unchanged
41	CdV-16-3(i)	490	Qbof	Plots within but at edge of Qct compositional boundary; contact at 430 ft bgs
42	CdV-16-3(i)	770	Qbof	Unchanged
43	CdV-R-15-3	357	Base of Qbt 1g	Qbt1g
44	CdV-R-15-3	402	Top of Qct- 2 types of pumice	Unchanged
45	CdV-R-15-3	577	Base of Qct	Near Qct/Qbof compositional boundary; contact at 582 ft bgs
46	CdV-R-15-3	602	Top of Qbof	Unchanged
47	R-58	460	Qbt 1g or Qct (?)	Unchanged
48	R-58	495	Qct	Qbt1g?, reexamine cuttings to determine if contact should be moved
49	R-58	660	Qct or Qbof (?); white pumices	Qbof, based on chemistry
50	R-58	690	Qct or Qbof (?)	Qbof, based on chemistry
51	SHB-3	338.5-.339.5	Qct	Unchanged
52	SHB-3	353.5-358.5	Qct	Unchanged
53	SHB-3	373.5-378.5	Qct	Unchanged
54	SHB-3	386-387.5	Qct	Unchanged
55	SHB-3	403.5-408.5	Qct	Sample 403.5 a appears to be reworked Qbof
56	SHB-3	408.5-413.5	Qbof	Sample 408.5_a_f plots in Qct compositional boundary; review contact

*bgs = Below ground surface.

Table B-2
LA-ICP-MS Analysis for Glassy Pumices from Wells at TA-16 and Vicinity

Well Depth (ft)	Samples	Al/Fe	Fe/Ti	Rb/La	Rb/Th	Rb/Ce	Rb/Dy	Nb/Ti	U/Ti	Th/Ti	Zr/Ti	Rb/Hf	N*
450	CdV-9-1(i)_450	121	5.4	5.8	14.5	1.8	141	2.4	0.5	0.5	1.2	168.4	5
465	CdV-9-1(i)_465_ab	63.2	16.9	13.1	11.3	3	118.3	14.7	2.7	2	4.8	125.5	3
465	CdV-9-1(i)_465_cd	70.7	8.1	5.4	16.6	1.4	162.9	2.5	0.5	0.4	1.9	144.7	4
295	R-18-295	91.8	11.6	13.3	18.3	3.2	162.1	12.1	1.9	1.5	5.1	152.4	5
335	R-18-335	93.3	6.5	7.9	13.1	2.2	110.2	4.2	0.6	0.7	2.1	129.9	10
380	R-18-380_a	77	14.4	11.9	11	3.1	111.1	17.4	2.6	2.7	6.8	117.8	3
380	R-18-380_b	75.8	6	3	11.6	1	107.3	2.3	0.4	0.5	2.5	90.5	3
415	R-18-415_ab	75.5	7.8	4.5	13.9	1.4	140	3.2	0.5	0.6	2.6	120.9	6
415	R-18-415_c	106.4	7.5	7.2	11.1	1.7	111.7	6.8	1.3	1	2.8	121.8	2
740	CdV-16-4i(p)-740	75.5	14.3	18.5	17.4	4	176.2	15.3	2.8	2	4.7	201.4	6
760	CdV-16-4i(p)-760	68.4	13.4	13.8	12.8	3.5	130.5	16	2.4	2.3	6.1	141.4	5
498	R-25_498_a	82.6	4.6	4.1	14.3	1.2	135.3	2.4	0.4	0.4	1.9	129.9	2
498	R-25_498_b	68.9	8.8	9.1	15.5	2.3	159.8	7	1.1	1	3.2	167.6	2
498	R-25_498_cd	62.1	5.7	3.3	14.3	1	158.1	1.5	0.2	0.3	1.7	108.8	4
514	R-25-514_a	72.2	6.6	5.2	17.7	1.5	171.9	2.9	0.5	0.5	2.5	144.9	2
514	R-25-514_b	90.1	7.5	5.6	14.4	1.7	129.9	4.9	0.8	0.8	2.9	144.2	2
514	R-25-514_c	70.8	12.5	7.9	8.2	1.9	85.5	13.9	2.1	2	4.8	93.8	2
490	CdV-16-3(i)-490	77.8	5.5	5.4	18.6	1.7	178.2	2.9	0.5	0.4	2.2	158.3	6
770	CdV-16-3(i)-770_b,d	66.9	12.6	13.4	15.6	3	141.3	13.5	2.1	1.7	4.3	188.8	4
770	CdV-16-3(i)-770_c	46.8	14.1	13.6	21.3	2.8	208.2	8.1	1.5	0.9	2.6	258	2
357	CdV-R-15-3-357-a	62.2	10.8	7.5	35.9	1.9	177.3	2	0.2	0.3	0.6	460.5	2
357	CdV-R-15-3-357-b,c	67.4	12.9	9.3	15.1	2.5	118.3	12.7	1.7	1.7	5.9	131.1	4
402	CdV-R-15-3-402-a,c	68.9	9.6	7.3	17.1	1.9	159.3	6	1	0.8	2.7	184.7	4

Table B-2 (continued)

Well Depth (ft)	Samples	Al/Fe	Fe/Ti	Rb/La	Rb/Th	Rb/Ce	Rb/Dy	Nb/Ti	U/Ti	Th/Ti	Zr/Ti	Rb/Hf	N
402	CdV-R-15-3-402-b	52	4.7	4.7	15.8	1.5	154.1	1.2	0.2	0.2	0.9	168.3	2
577	CdV-R-15-3-577	92.2	6.5	9	19	2.1	193.8	6	1.2	0.8	2.7	208.5	4
602	CdV-R-15-3-602	68.7	15	15.1	11.7	3.2	133.2	15.3	3.9	2.4	4.4	148.8	4
460	R-58-460	93.2	9.9	12.2	17.5	3.2	144.5	13.2	1.9	1.8	6.3	138.9	6
495	R-58-495	64.8	12.5	11.4	17	2.9	141.1	12.5	1.7	1.6	5.6	139.1	6
660	R-58_660_a	89	7.5	7.2	14.3	2	129.5	6.7	1.2	1	3.1	149.2	2
660	R-58_660_b,c	79.2	10.8	10.3	15.2	2.9	122.6	12.7	1.8	1.8	6.3	128.3	4
660	R-58_660_d	70.5	13.4	8.3	12.2	2.4	99.4	13.9	1.8	2.1	7.4	99.5	2
690	R-58-690-a,c	69.7	11	11.3	17.2	2.6	163.5	9.7	1.5	1.2	3.3	194.4	4
690	R-58-690-b	46.9	15.3	11.7	19.6	2.7	164	9.2	1.6	1.1	3.1	218.9	2
R-26 Well depth (ft)													
500	500	124.4	6.4	8.9	14.4	2.3	106.7	9.7	1.1	1.3	4.7	123.9	5
510	510	70.8	13	8.5	17.4	2.6	128.5	9.8	1	1.1	3.9	153.9	5
545	545	111.3	7	8.1	18.5	2.5	163.4	4.8	0.6	0.6	2.3	176.4	12
575	575	111	5.4	7.1	22.6	1.9	212.2	2.5	0.3	0.3	1.3	239.6	15
580	580	143.5	5.5	6.6	20.4	1.9	179.2	2.4	0.3	0.4	1.4	199.4	10
665	665	71	7.2	3.4	14.1	1.1	136.9	1.6	0.2	0.2	1.7	101.7	10
700	700	101.8	5.5	4.8	23.5	1.4	201.9	1.8	0.3	0.2	1.7	154.3	8
755	755	128.9	6.3	5.4	16.5	1.7	140.9	3.7	0.5	0.5	2.4	154.4	8
785	785	77.6	8.8	7.5	19.8	2.1	185.8	3.6	0.5	0.5	2	170.4	8
835	835	126.2	6.5	8.7	21.5	2.4	208.4	4.5	0.6	0.5	2.3	198.7	8
870	870	74.3	14.6	13.5	15.4	3.5	155.8	12.9	1.9	1.5	4.5	165.4	6
900	900	80	12	11.1	15.6	3.1	140.3	10.7	1.5	1.4	4.2	168	6
930	930	94.7	10.7	11.5	15.4	3.1	135.3	11.6	1.5	1.6	4.8	163.6	10

Table B-2 (continued)

Well Depth (ft)	Samples	Al/Fe	Fe/Ti	Rb/La	Rb/Th	Rb/Ce	Rb/Dy	Nb/Ti	U/Ti	Th/Ti	Zr/Ti	Rb/Hf	N
945	945	74.7	12.6	14	17.1	3.4	159.3	12.2	1.8	1.5	4.3	187.8	9
955	955	74.6	13.8	17.5	17.9	4	170.3	15.8	2.3	1.9	5.1	204.6	10
R-63 Well depth (ft)													
365	365a-d	78.71	11.64	10.3	16.43	2.69	123.51	11.83	1.44	1.44	5.53	134.63	8
365	365e	109.53	5.8	9.51	16.72	2.52	142.17	4.1	0.57	0.59	1.88	168.42	2
380	380	111.98	4.57	7.37	19.7	2.01	191.56	2.32	0.3	0.3	1.03	221.37	8
405	405	96.24	6.34	10.15	19.04	2.71	154.45	3.92	0.47	0.47	1.76	180.5	8
425	425	117.53	5.56	10.14	21.52	2.56	194.29	3.29	0.42	0.37	1.29	239.32	8
550	550a-d	65.09	9.13	5.73	22.28	1.71	185.04	2.95	0.41	0.38	2.18	183.11	8
550	550e	76.23	11.06	7.25	12.14	1.91	95.42	8.69	1.17	1.07	3.61	134.63	2
560	560	63.11	9.54	6.57	17.22	1.57	176.81	2.68	0.83	0.53	1.69	160.05	8
585	585	91.91	7.42	10.9	25.63	2.65	233.83	5.22	0.89	0.6	2.16	257.56	8
610	610a	112.39	7.08	10.6	26.19	2.93	211.07	5.39	0.67	0.59	2.6	250.48	3
610	610bc	91.72	12.81	12.16	13.8	3.13	128.14	15.78	1.76	1.69	5.9	142.04	6
625	625ad	100.06	8.35	8.6	18.84	2.49	154.04	6.78	0.77	0.82	3.18	185.64	4
625	625 bc	79.81	13.87	11.19	12.03	3.01	108	15.74	1.74	1.77	5.97	123.65	4
690	690	69.93	12.61	11.26	16.95	2.87	139.19	9.55	1.31	1.21	3.79	182.76	8
705	705	80.88	10.68	10.19	18.78	2.58	151.31	8.47	1.05	0.95	3.25	199.64	8
715	715b-e	79.75	13.68	14.86	15.39	3.67	139.93	15.52	2.13	2	5.96	156.99	8
715	715a	101.32	13.29	16.34	8.85	3.64	97.93	16	6.84	4.39	5.39	112.98	2
725	725a-d	77.45	13.32	15.19	16.07	3.68	148.36	15.19	2	1.8	5.5	166.23	8
725	725e	84.54	10.16	9.62	16.88	2.56	136.19	8.5	1.05	1.06	4.14	180.7	2
790	790	75.49	14.07	14.04	15.3	3.68	141.26	15.63	1.85	2.01	6.23	162.77	10

Table B-2 (continued)

Well Depth (ft)	Samples	Al/Fe	Fe/Ti	Rb/La	Rb/Th	Rb/Ce	Rb/Dy	Nb/Ti	U/Ti	Th/Ti	Zr/Ti	Rb/Hf	N
SHB-3 Well depth (ft)													
338.5-339.5	a-f	79.2	7.39	15.2	24.5	3.09	225.4	3.28	0.71	0.44	1.18	255.2	11
353.5-358.5	a,d	117.6	5.66	9.4	16.2	2.48	141.5	3.07	0.46	0.45	1.46	159.6	6
353.5-358.5	b	149.1	3.61	8.5	15.8	2.16	153.8	2.07	0.3	0.31	1.02	167.4	2
353.5-358.5	c,f	100.6	5.82	20	30	3.94	275.9	3.22	0.67	0.37	1.09	295.4	4
353.5-358.5	e	99	5.41	6.5	18.7	1.88	165.6	1.93	0.27	0.27	0.87	203.2	2
373.5-378.5	a-e	91.1	6.15	23.7	35.8	4.14	326.9	3.3	0.74	0.33	0.94	386.9	10
373.5-378.5	f	101.8	4.93	15.7	35.6	2.95	360.2	2.2	0.5	0.24	0.61	392.7	2
386-387.5	a-f	118.9	4.8	11.3	24.5	2.6	243.3	2.27	0.48	0.33	0.82	291.6	12
403.5-408.5	a	68.9	10.84	13.3	18.5	2.7	146.7	7.31	1.45	0.91	2.33	204.6	2
403.5-408.5	b-f	70.9	6.19	6.1	22	1.45	223.5	1.76	0.36	0.25	1.36	179.3	12
408.5-413.5	a-f	80.7	5.7	6.9	24.6	1.5	235.4	1.96	0.42	0.26	1.39	196.4	11

*N= Number of line scans per pumice sample.

Appendix C

Dip of Stratigraphic Units Based on Structure Contour Maps and Possible Influence of Bedding on Preferred Groundwater Pathways

Structure contour maps are presented for the major stratigraphic units at Technical Area 16 (TA-16) (Figures C-1 through C-11). The structure contour maps were generated from the WC15c version of the Los Alamos National Laboratory (LANL or the Laboratory) site geologic model. Structure contour maps for gamma marker horizons G2 and G3 in the lower Otowi Member (Figure C-8) are based on information from the investigations in this report. The maps, presented from youngest to oldest, are discussed as part of the geologic site description presented in section 3.0 of the report.

The western part of the structure contour maps includes the Anchor Ranch graben next to the Pajarito fault escarpment. The structure contour maps depict the Anchor Ranch graben as a north-dipping basin with a steep west-dipping eastern margin and progressively greater displacement of older units. The eastern margin of the basin is faulted, and future updates to the WC15c geologic framework model will replace the steep west-dipping eastern basin margin with a down-to-the-west high-angle normal fault.

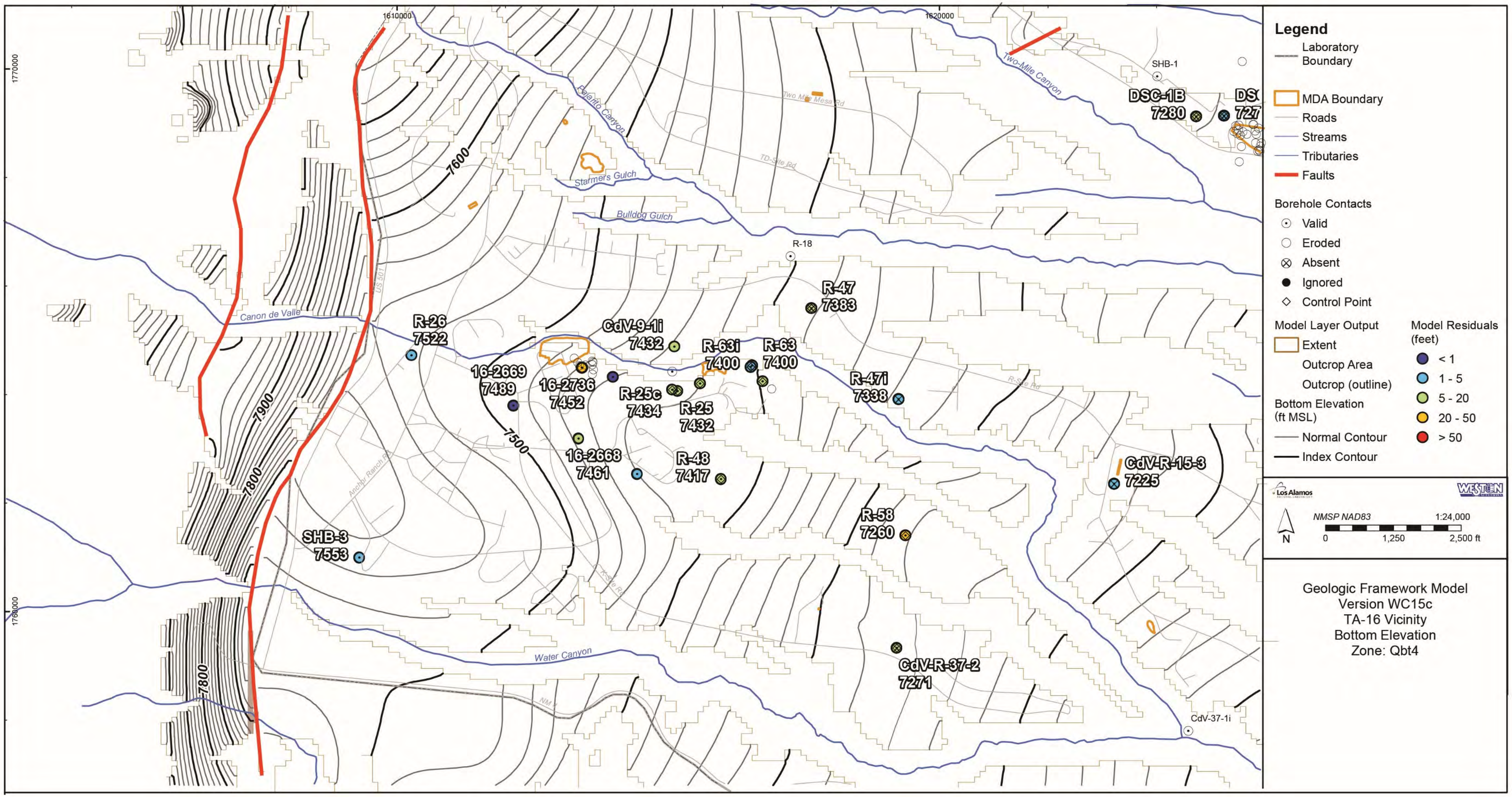

Figure C-1 **Structure contour map for the base of Tshirege Member unit Qbt 4 based on the WC15c version of the Laboratory's site geologic model**

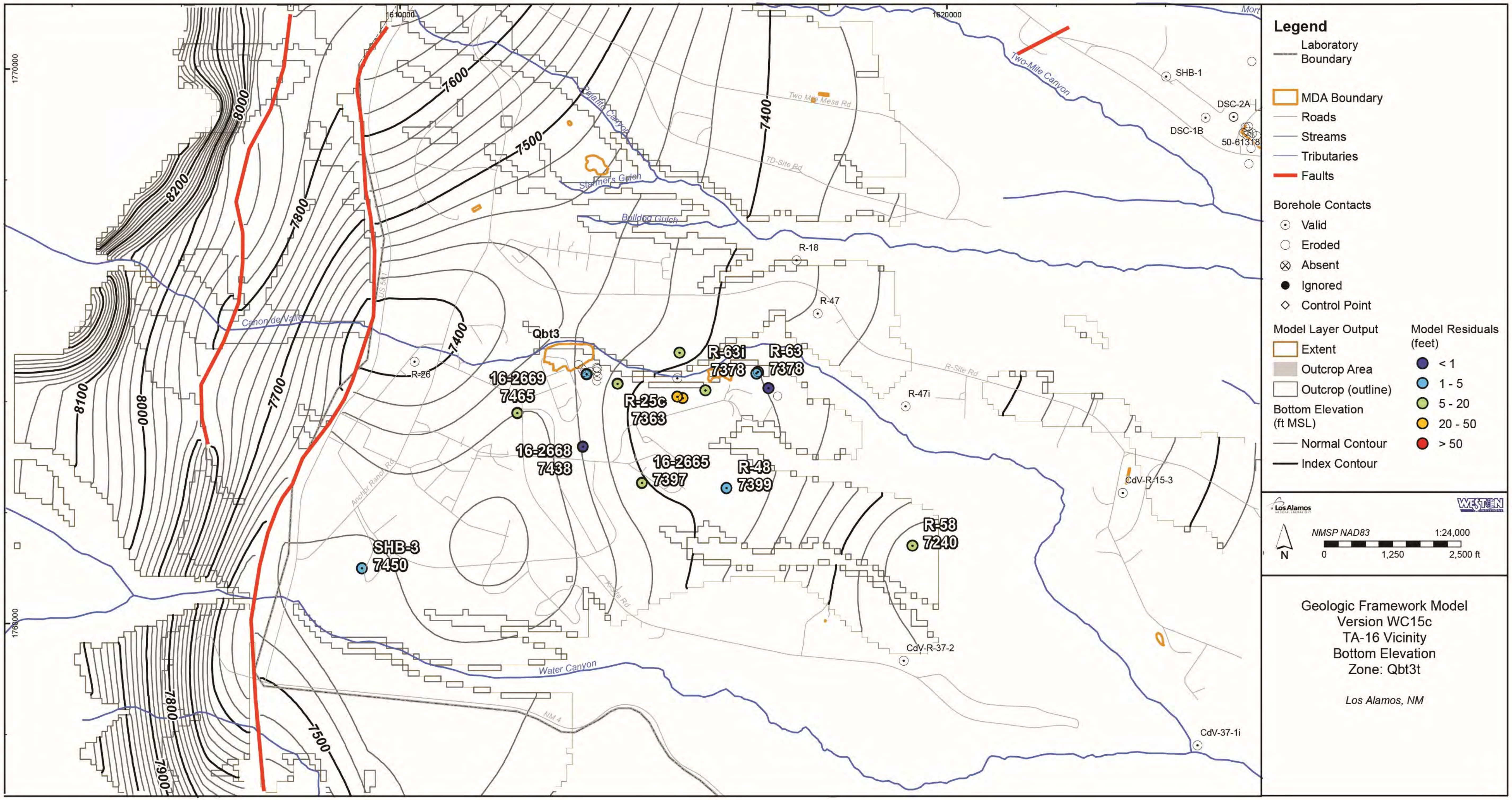

Figure C-2 Structure contour map for the base of Tshirege Member unit Qbt 3t based on the WC15c version of the Laboratory's site geologic model

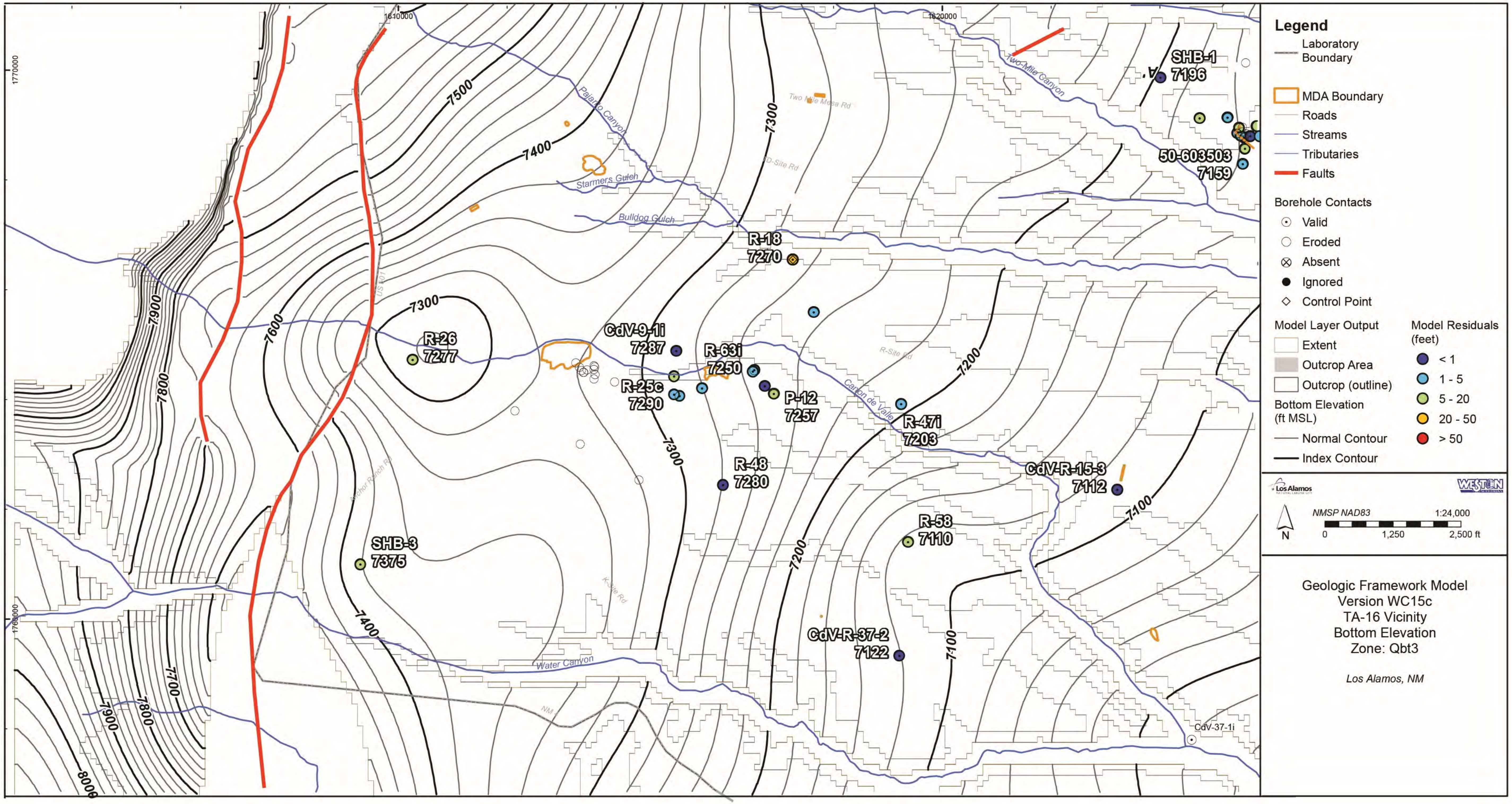

Figure C-3 Structure contour map for the base of Tshirege Member unit Qbt 3 based on the WC15c version of the Laboratory's site geologic model

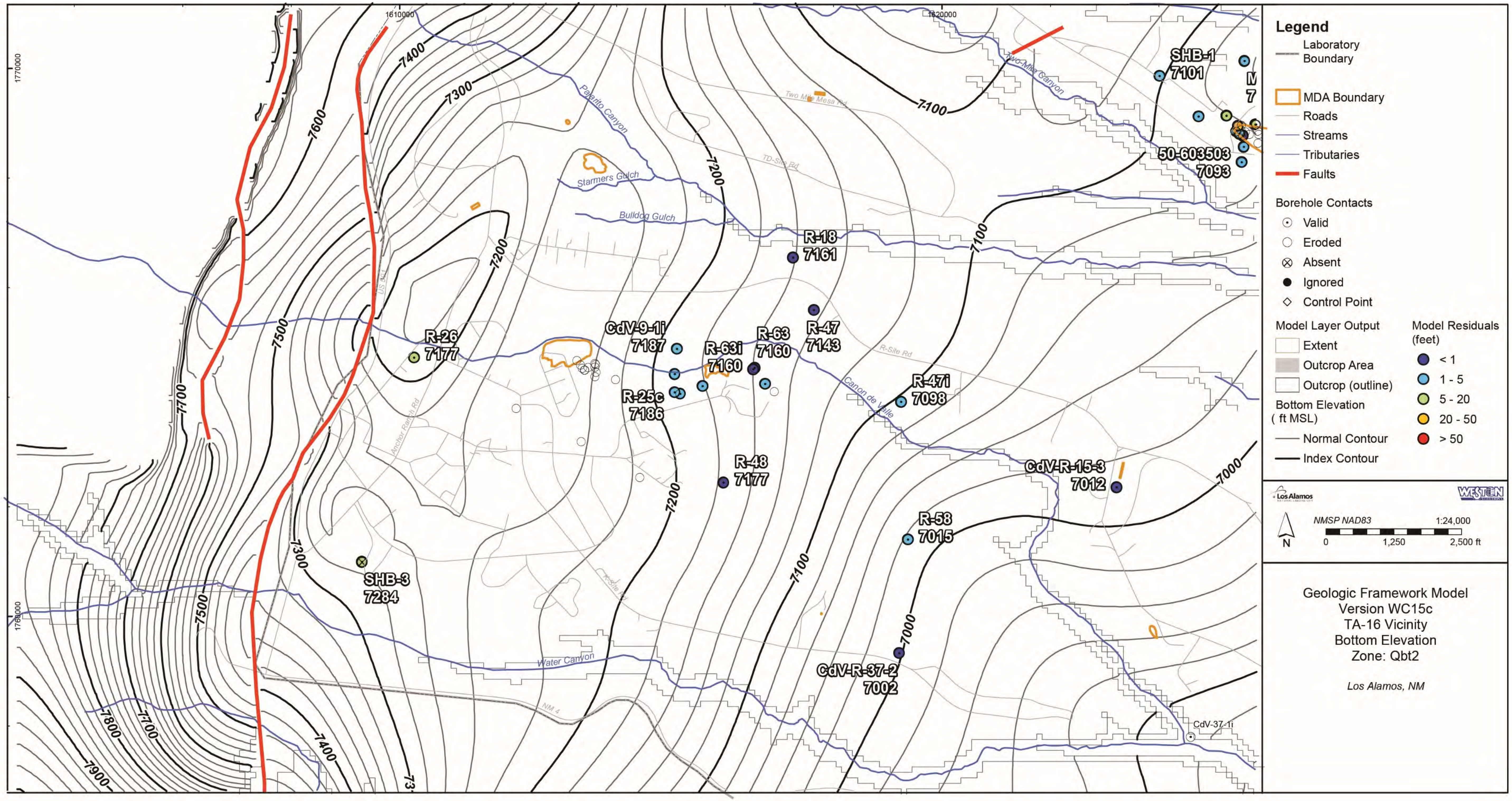

Figure C-4 Structure contour map for the base of Tshirege Member unit Qbt 2 based on the WC15c version of the Laboratory's site geologic model

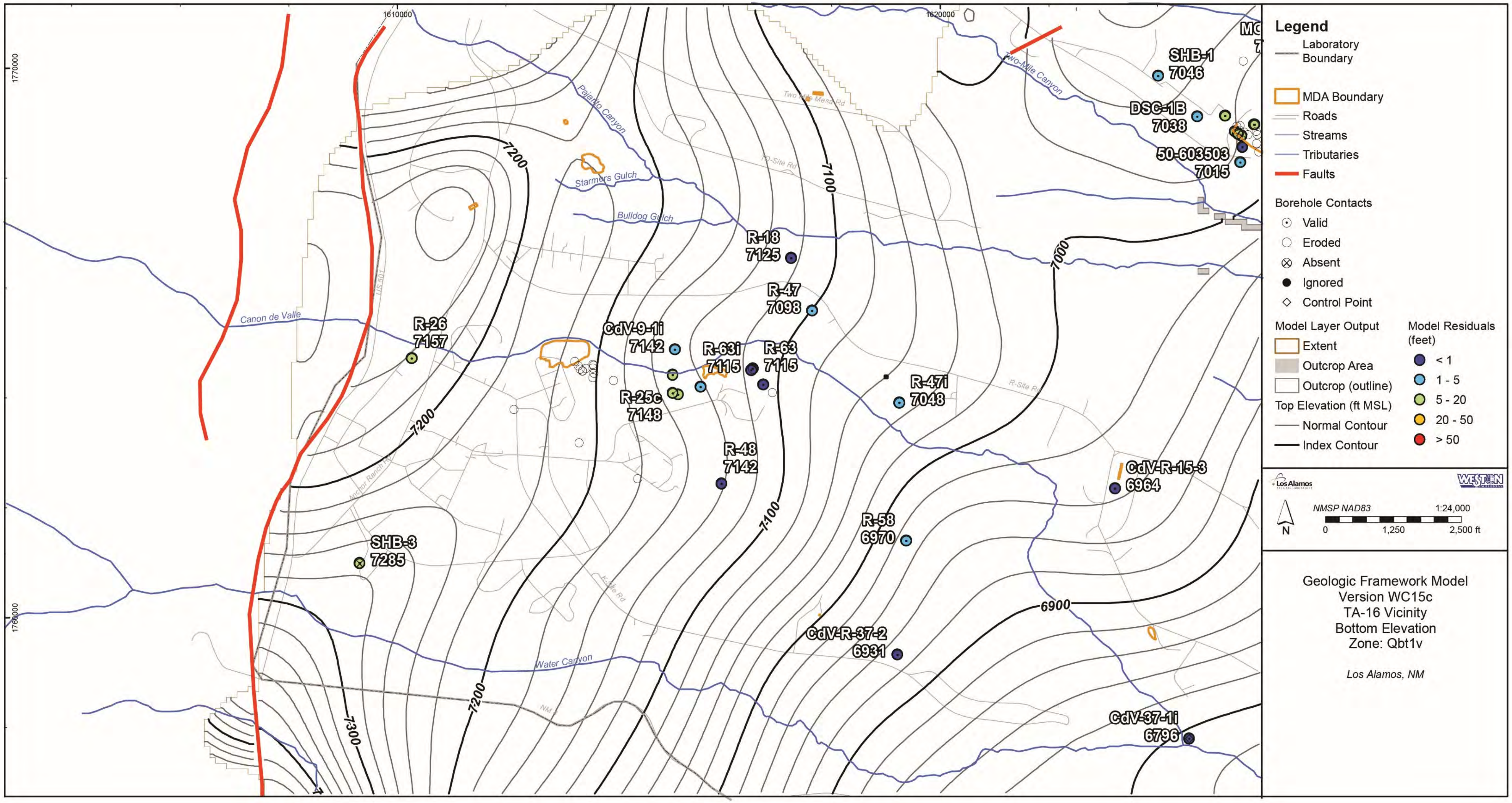

Figure C-5 Structure contour map for the base of Tshirege Member unit Qbt 1v based on the WC15c version of the Laboratory's site geologic model

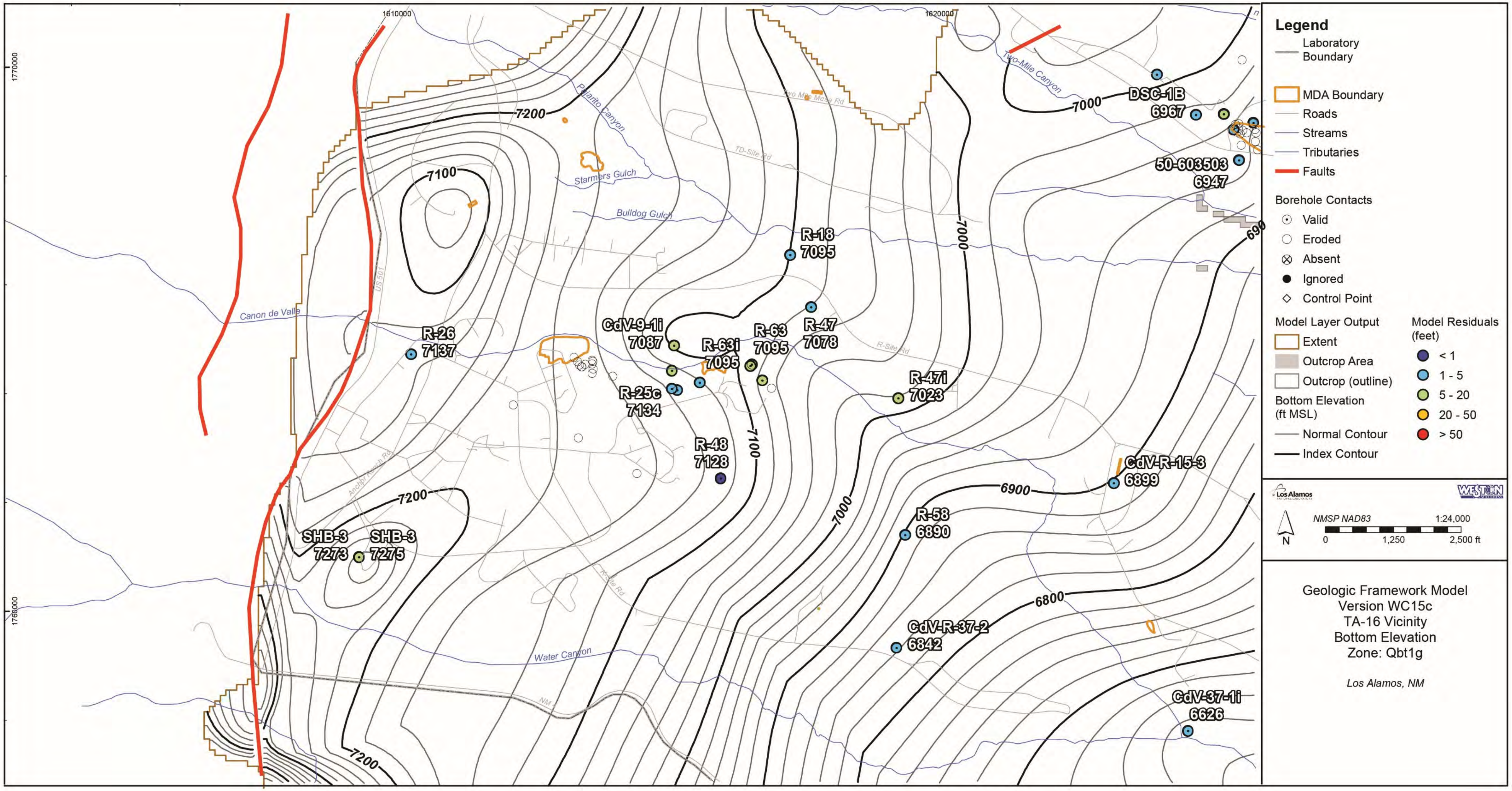

Figure C-6 Structure contour map for the base of Tshirege Member unit Qbt 1g based on the WC15c version of the Laboratory's site geologic model

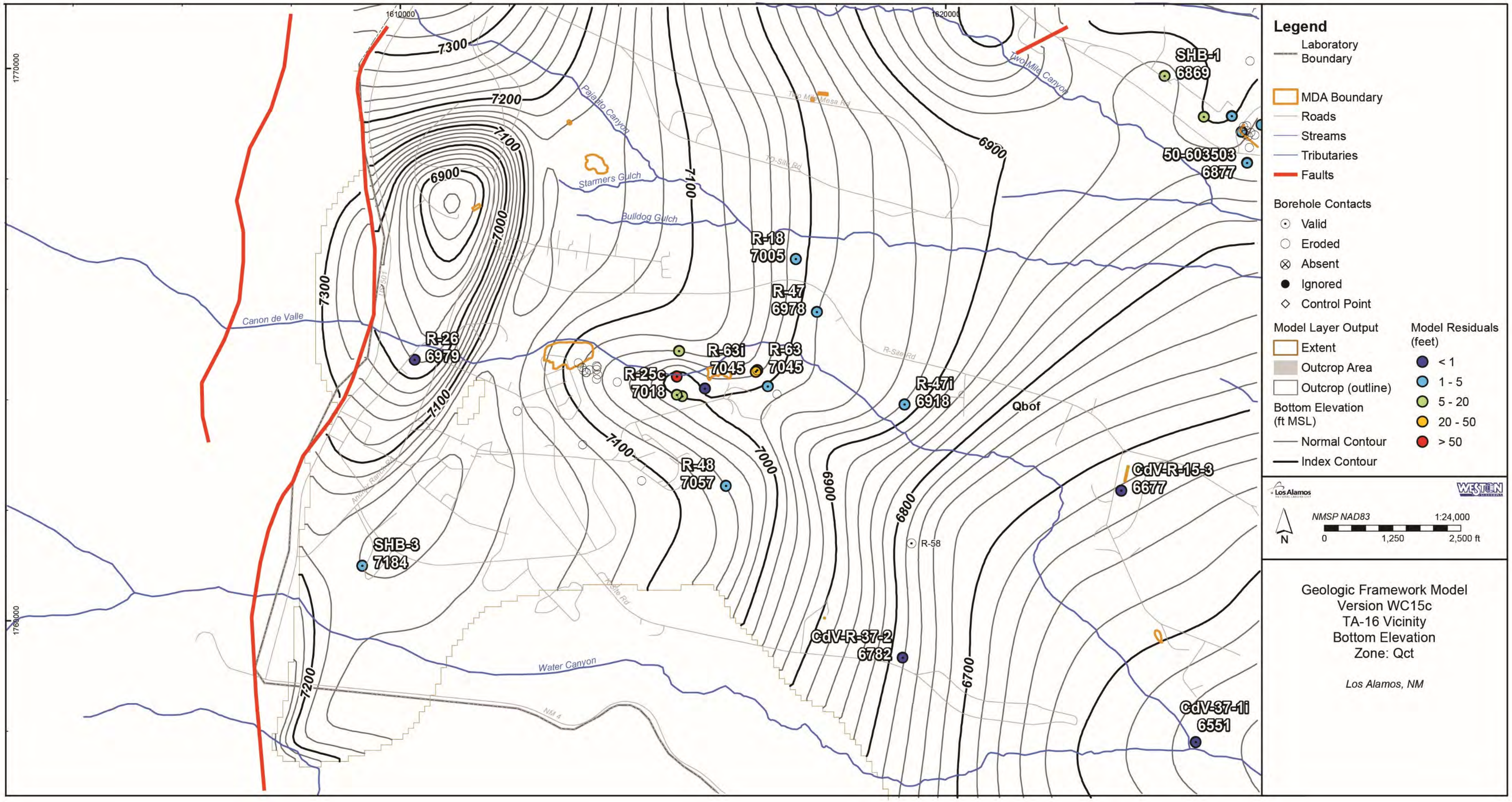

Figure C-7 Structure contour map for the base of the Cerro Toledo Formation (Qct) based on the WC15c version of the Laboratory's site geologic model

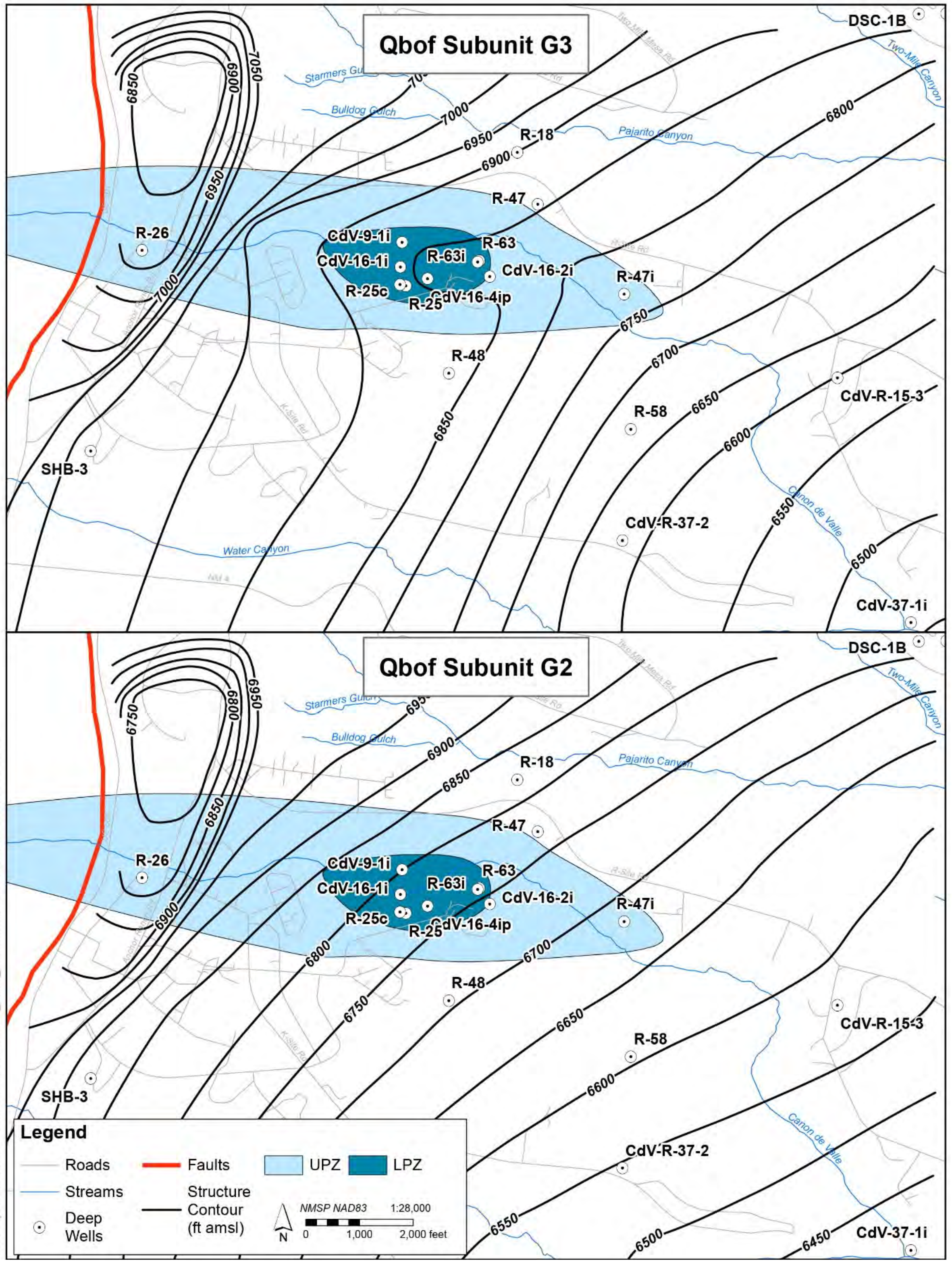

Figure C-8 Structure contour map for the marker horizons G2 and G3 in the Otowi Member–based correlation of gamma logs between wells

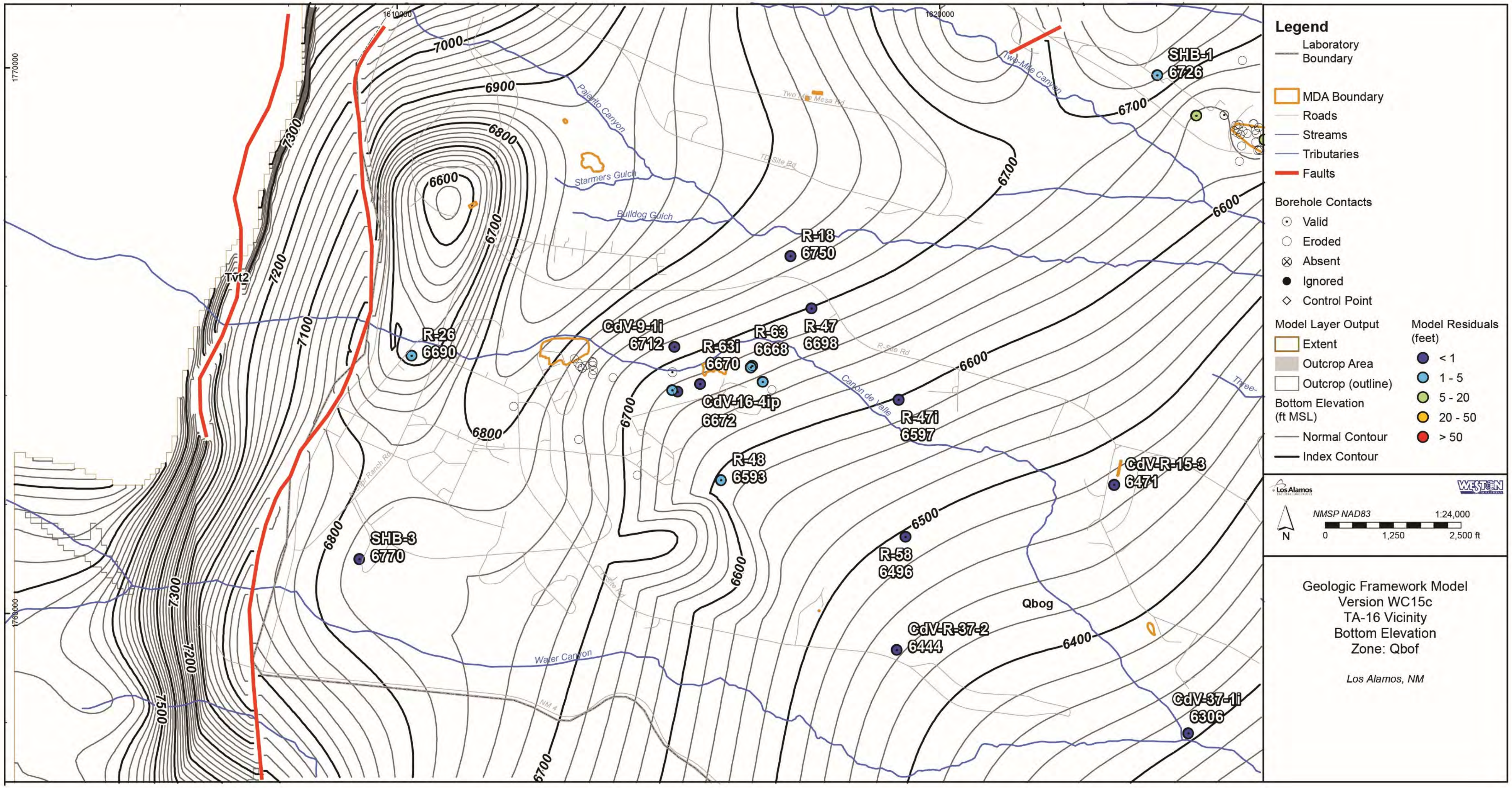

Figure C-9 Structure contour map for the base of Otowi Member ash-flow tuffs (Qbof) based on the WC15c version of the Laboratory's site geologic model. Equivalent to gamma marker horizon G1 in Figures 2.3-7 and 2.3-8 of the report.

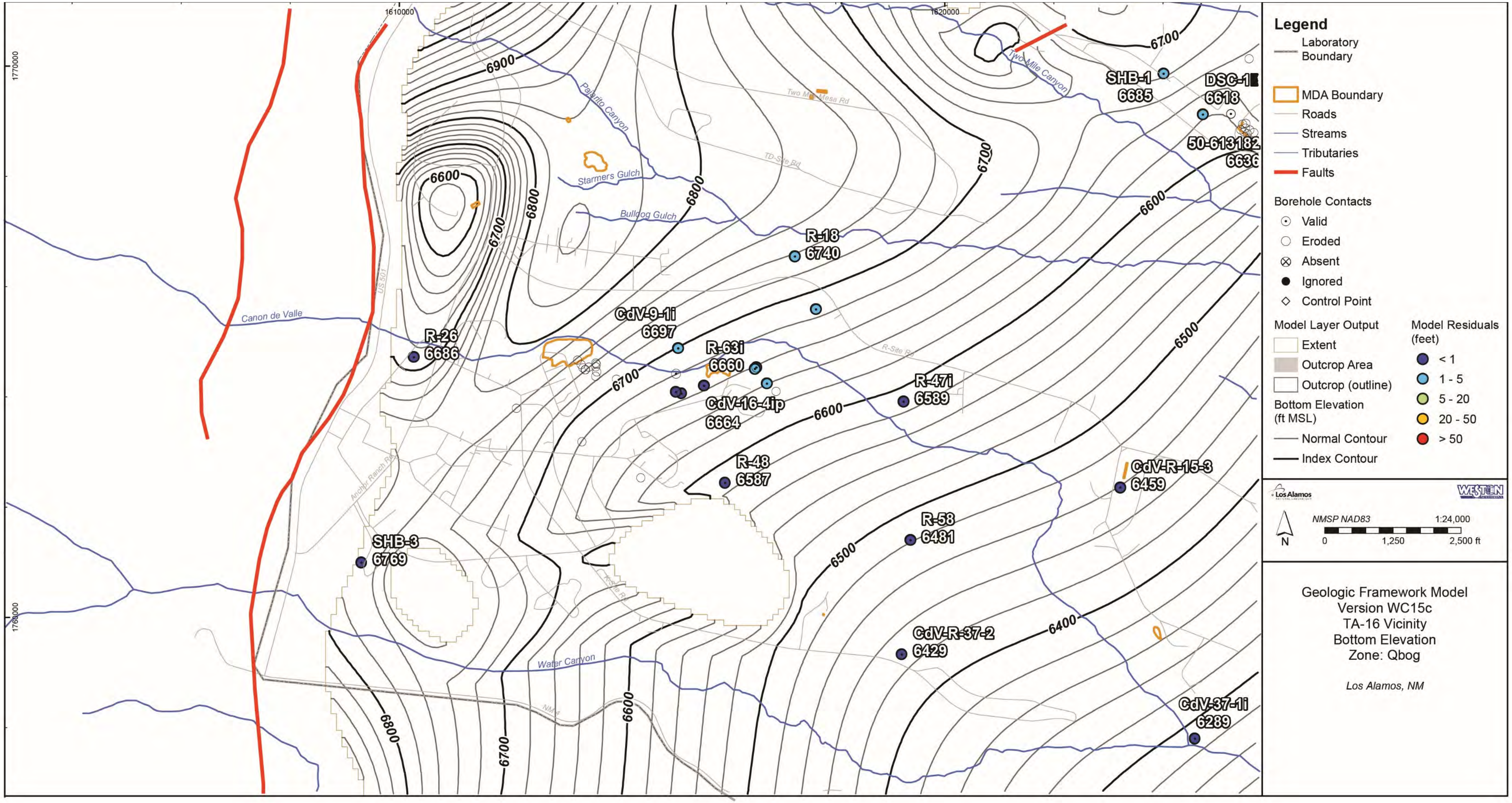

Figure C-10 Structure contour map for the base of Guaje Pumice Bed (Qbog) based on the WC15c version of the Laboratory's site geologic model

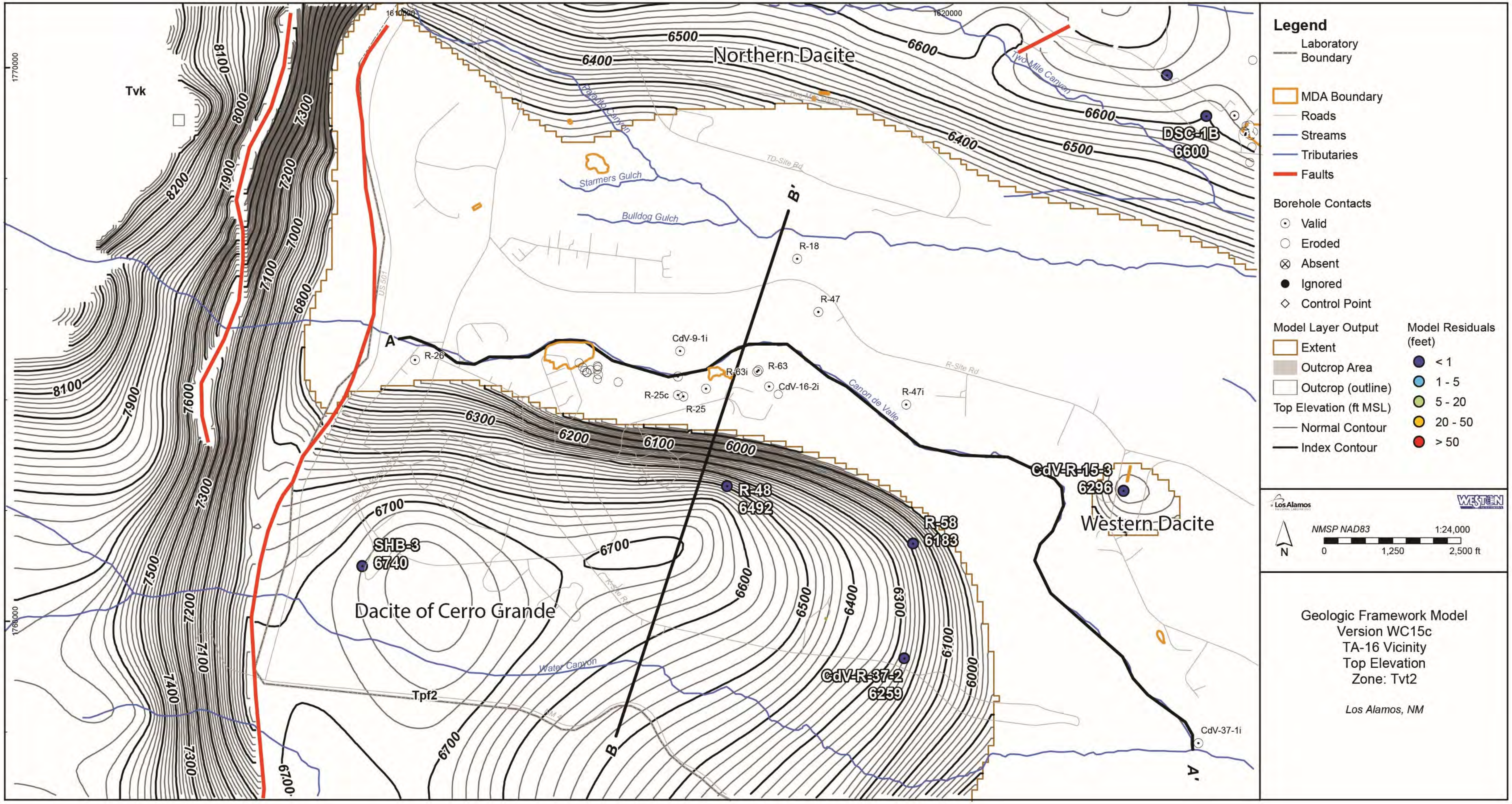

Figure C-11 Structure contour map for the top of the dacite of Cerro Grande (Tvt2) based on the WC15c version of the Laboratory's site geologic model

Appendix D

Anchor Ranch Graben: a Marginal Subbasin Adjacent to the Pajarito Fault Zone in Upper Cañon de Valle

The Anchor Ranch graben is a subsidiary structure of the Pajarito fault system that crosses Cañon de Valle just east of the mountain block escarpment (Figure D-1). Comparisons of elevations of stratigraphic units in well R-26 and core hole SHB-3 at Technical Area 16 (TA-16) at Los Alamos National Laboratory (LANL or the Laboratory) suggest a progressively greater displacement of older rock units occurs across the graben's eastern fault. The two wells also show dramatic facies changes in lithologies and unit thicknesses over a relatively short distance.

Progressive displacement of older units and facies changes suggest the Anchor Ranch graben was active throughout the Quaternary and the graben is a north-plunging basin. Lewis et al. (2009) describe a 500-m-wide graben located next to the Pajarito fault system extending from Water Canyon to Los Alamos Canyon. The graben is bound by the down-to-east east splay of the Pajarito fault system (Anchor Ranch fault) and a down-to-west fault with 30 m of displacement on the Qbt 3/Qbt 2 contact. In this investigation, the graben is referred to as the Anchor Ranch graben and is compared with rock units in well R-26, located in the graben, and core hole SHB-3, located on the eastern shoulder of the graben (Figure D-1).

Wells R-26 and SHB-3 are located 1.06 mi apart, and both wells are about 820 ft m from the eastern strand of the Pajarito fault system. Well R-26 was drilled by mud-rotary methods and was characterized by drill cuttings and an extensive suite of borehole geophysics that included combinable magnetic resonance, array induction, triple detector litho-density, natural gamma ray spectroscopy, elemental capture spectroscopy, epithermal compensated neutron, and full-bore formation microimager (FMI). Core hole SHB-3 was continuously cored (about 70% core recovery) and gamma and neutron logs were collected. Figure D-2 compares elevations of geologic contacts for the lower Tshirege Member, Cerro Toledo Formation, Otowi Member, and the top of the Puye Formation. Elevations of contacts at SHB-3 are higher than those at R-26, consistent with down-to-the-west displacement on the graben's eastern fault boundary. Throw across the eastern margin is related to a growth fault, with older units showing more displacement than younger ones. For example, 98 ft of displacement occurs on the Qbt 3/Qbt 2 contact, 138 ft on the Tshirege Member/Cerro Toledo Formation contact and 220 ft on the Cerro Toledo Formation/Otowi Member contact. Progressive displacement of Bandelier Tuff and Cerro Toledo contacts with depth suggests subsidence within the Anchor Ranch graben occurred throughout the Quaternary and that tectonism overlapped volcanic activity associated with the eruption of the Bandelier Tuff. The graben may also predate the Otowi eruption, but deep well data are insufficient to examine this possibility.

Large facies changes occur within alluvial fan deposits of the Cerro Toledo Formation between well R-26 and core hole SHB-3. The Cerro Toledo Formation is 157 ft thick at well R-26 and 90 ft thick in well SHB-3. In well R-26, Cerro Toledo beds are dominated by three thick subunits of dacitic cobbles and boulders that make up 71% of the deposit. The gamma log for well R-26 shows that high-gamma rhyolitic volcaniclastic rocks (fluvial sands and gravels and fall deposits) are subordinate to the low-gamma sediments derived from dacitic source rocks of the Tschicoma Formation (Figure D-2). At well SHB-3, core recovery was poor through the Cerro Toledo Formation, but the deposits appear to be made up primarily of sands and sandy pumice-bearing gravels containing thin interbedded air-fall tephras. Unlike at well R-26, thick beds of dacitic cobbles and boulders are absent at core hole SHB-3. The gamma log for SHB-3 shows that rhyolitic volcaniclastic rocks make up a significant portion of the Cerro Toledo Formation (Figure D-2). The thick, coarse nature of the Cerro Toledo Formation in well R-26 and its lower elevation compared with SHB-3 is consistent with accumulation of alluvial fan deposits in the actively subsiding Anchor Ranch graben.

Bedding attitudes for the Otowi Member and Cerro Toledo Formation in well R-26 suggest the Anchor Ranch graben is a trap-door structure with the basin deepening northward. Bedding orientations were obtained from the FMI log and binned into Otowi tuffs and the Cerro Toledo Formation (Figure D-3). Bedding in the Otowi Member includes contacts between ash-flow units, ash- and pumice-fall deposits, and the thick, coarse-grain sedimentary sequence in the middle of the unit (see discussion in section 2.3 of the report). The mean dip azimuth for Otowi tuffs is 352.5° and the mean dip 8.3°. The Cerro Toledo Formation has a mean dip azimuth of 8.8° and mean dip of 7°. Bedding orientations for both units indicate the basin floor has been tilted northward.

The Anchor Ranch graben is a major structure on the pathway for movement of groundwater from the mountain block to the perched groundwater bodies in the vicinity of the 260 Outfall. In well R-26, the perched zone at the base of the Cerro Toledo Formation may be recharged in part by underflow from the mountain block. Also, the graben is probably an area of focused recharge for surface water exiting the mountain block via Cañon de Valle. Cañon de Valle forms a deeply incised drainage up- and downcanyon of the Anchor Ranch graben. However, within the graben, Cañon de Valle is poorly defined as it crosses thick alluvial fans atop the Bandelier Tuff. Surface water rarely flows across the alluvial fans except during strong runoff events. The alluvial fans may provide storage for water infiltrating the underlying Bandelier Tuffs. Fractures probably play a major role in infiltration pathways because of the brittle, densely welded nature of upper Bandelier Tuffs and the wide zone of deformation associated with the Pajarito fault system that include the Anchor Ranch graben. Several fracture zones were mapped within the Tshirege and Otowi Members of the Bandelier Tuff in SHB-3 that probably acted as major fluid pathways (Appendix A).

A connection between the perched zone at well R-26 and perched groundwater in the 260 Outfall area has not been established. However, the base of the Cerro Toledo Formation is juxtaposed against middle Otowi tuffs across the east margin of the Anchor Ranch graben. The eastern fault and its associated fractures may act as vertical pathways that provide recharge to perched groundwater in the lower Otowi Member and Puye Formation on the footwall of the fault.

REFERENCES

The following reference list includes documents cited in this report.

Lewis, C.L., J.N. Gardner, E.S. Schultz-Fellenz, A. Lavine, and S.L. Reneau. "Fault Interaction and Along-Strike Variation in Throw in the Pajarito Fault System, Rio Grande Rift, New Mexico," *Geosphere,* Vol. 5, No. 3, pp. 252–269 (2009).

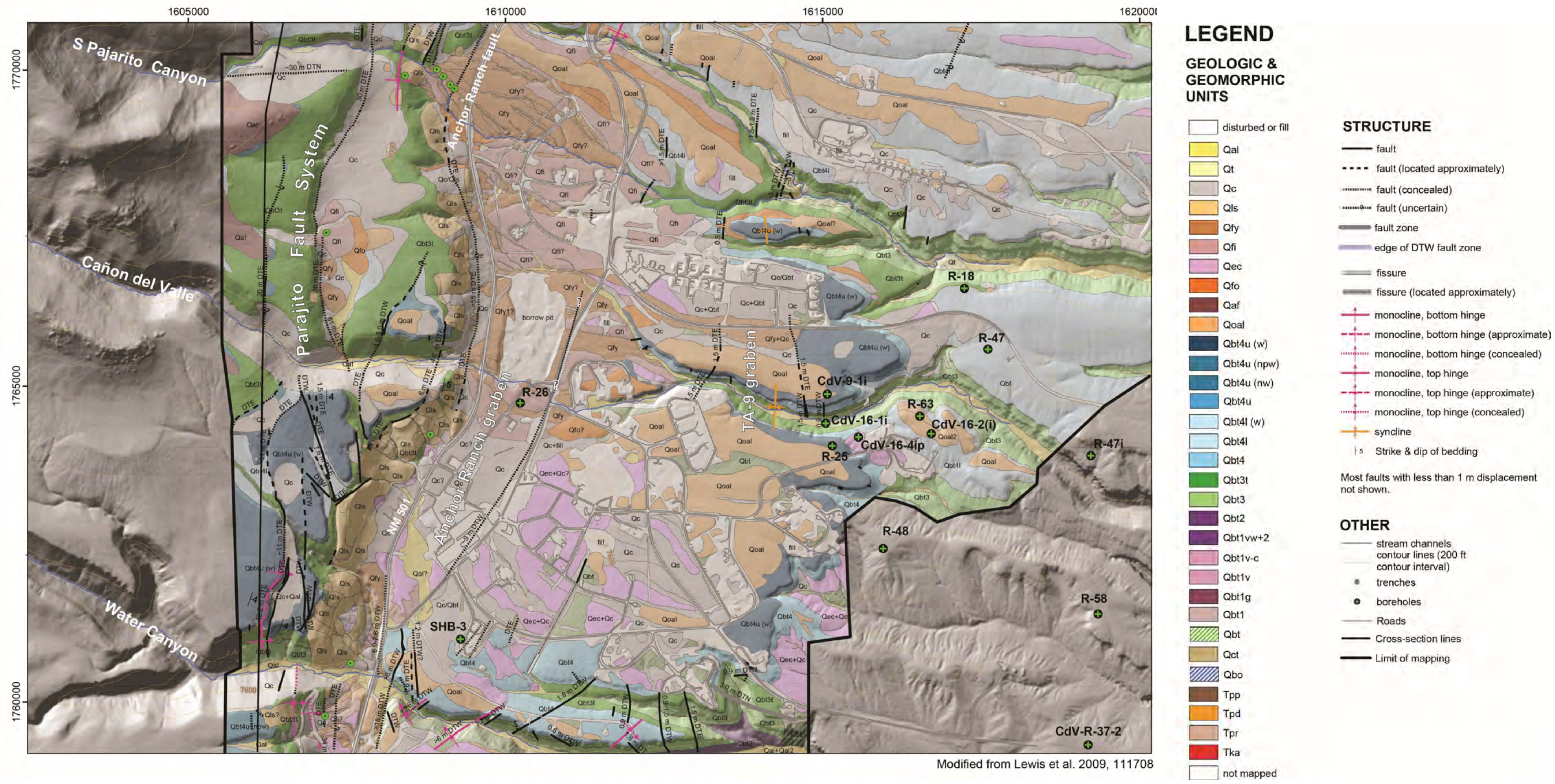

Modified from Lewis et al. 2009, 111708

Figure D-1 Geologic map of TA-16 and vicinity showing surficial and bedrock geology and the tectonic structures

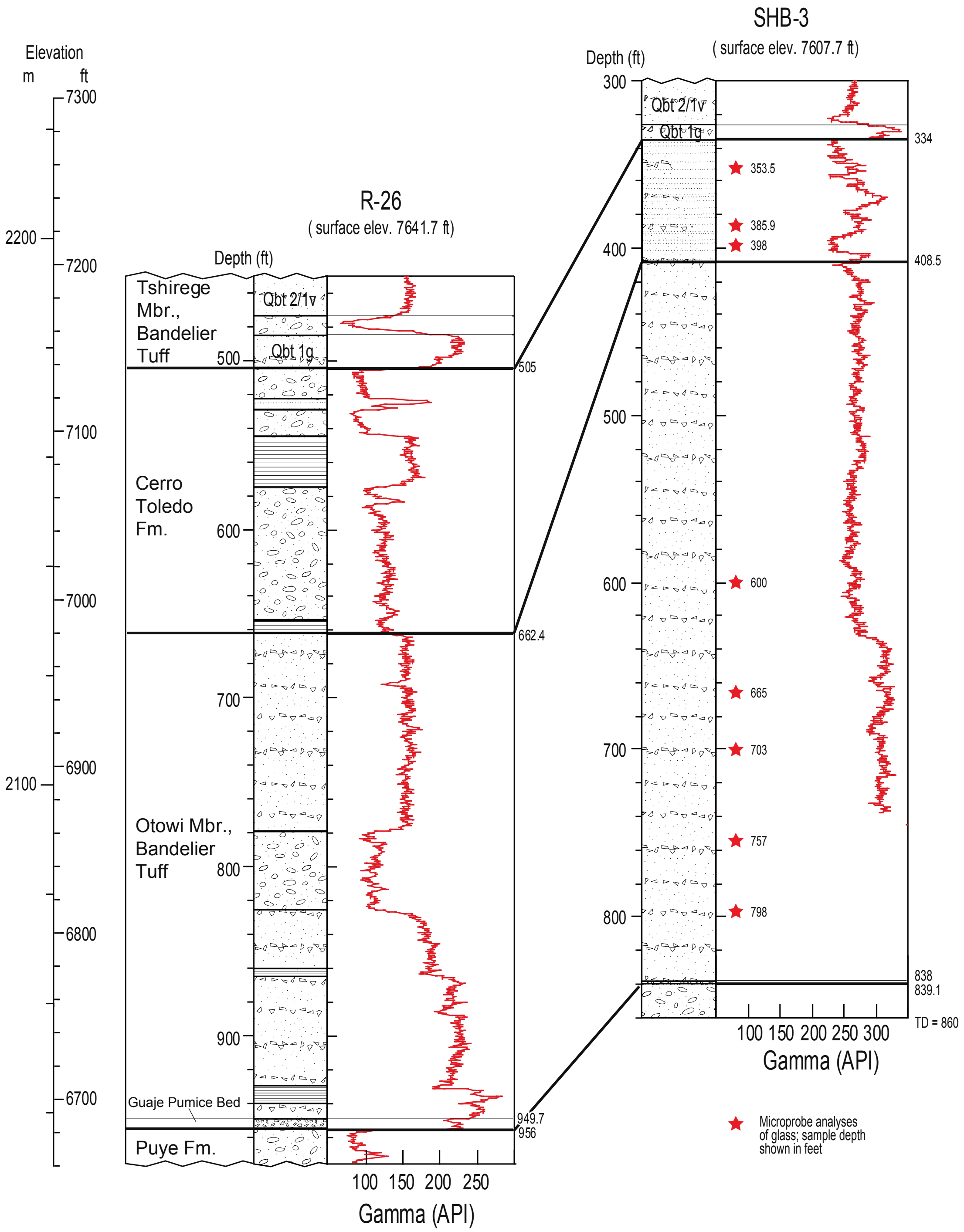

Figure D-2 **Correlation of Cerro Toledo Formation and Otowi Member of the Bandelier Tuff in core hole SHB-3 and well R-26. Correlations are based on lithologic description of drill core (SHB-3, Appendix A) and cuttings (R-26) and borehole natural gamma logs. Samples collected for microprobe analysis of glass pumices in SHB-3 are show**

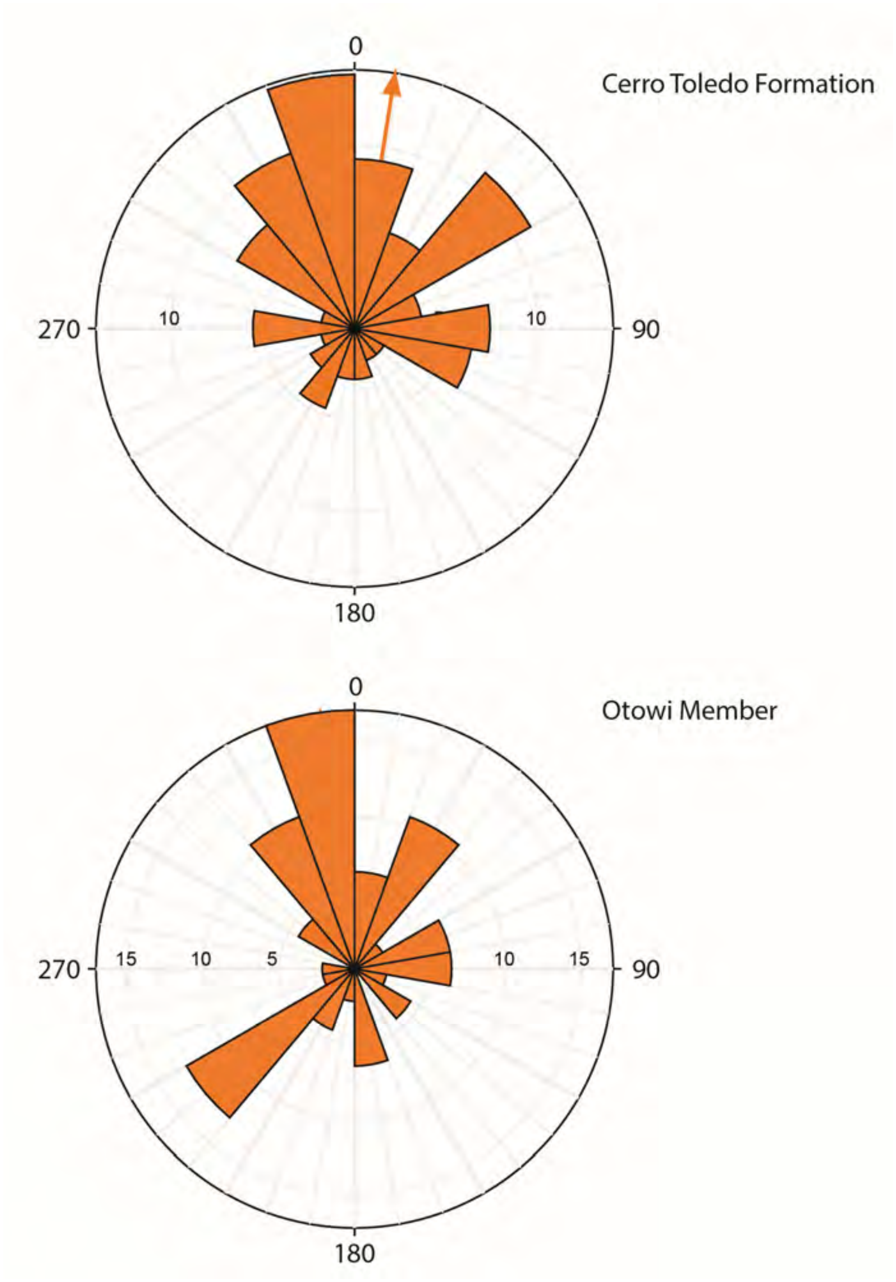

Figure D-3 **Rose diagrams showing bedding orientations for the Cerro Toledo Formation and Otowi Member of the Bandelier Tuff in well R-26. Beds in both units dip predominantly northward.**

Appendix E

Summary of Borehole Porosity Measurements by Geologic Unit for Well R-26

This appendix summarizes porosity data for Technical Area 16 (TA-16) geologic units based on Schlumberger, Inc., borehole geophysical logs for well R-26. Porosity measurements were compiled to support hydrologic modeling for the RDX (hexahydro-1,3,5-trinitro-1,3,5-triazine) investigation. The porosity data were also provided to Weston, Inc., which used the data in conjunction with the geologic model and RDX concentrations in groundwater to calculate RDX mass.

The data are derived from well R-26 where a mud-drilled borehole provided nearly ideal geophysical logging conditions. Porosity measurements were made by combinable magnetic resonance (CMR), density porosity, thermal and epithermal neutron logs. Schlumberger, Inc., processed the data to remove borehole effects and integrated the results to produce a best estimate of porosity. In addition to total porosity, Schlumberger's ELAN analysis also produced estimates of effective porosity based on an analysis of pore-size distribution from the CMR log.

A statistical summary of porosity data for TA-16 geologic units is provided in Figures E-1 through E-13. Effective porosity data are also presented for the Otowi Member and Puye Formation because these units host deep perched groundwater in the TA-16 area.

Tshirege Member Qbt 4 Total Porosity

Minimum	0.33547
Maximum	0.538
Sum	49.22143
Points	119
Mean	0.413625
Median	0.41588
RMS	0.415636
Std Deviation	0.041007
Variance	0.001682
Std Error	0.003759
Skewness	0.558616
Kurtosis	0.443601

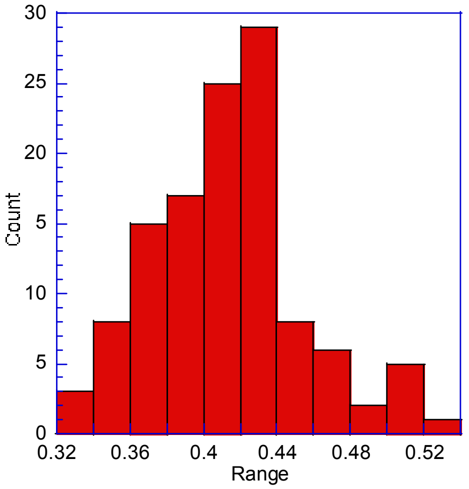

Figure E-1 **Total porosity in Tshirege Member, Qbt 4**

Tshirege Member Qbt 3t Total Porosity

Minimum	0.06822
Maximum	0.63475
Sum	49.13797
Points	359
Mean	0.136875
Median	0.11231
RMS	0.156736
Std Deviation	0.07647
Variance	0.005848
Std Error	0.004036
Skewness	3.390317
Kurtosis	13.42312

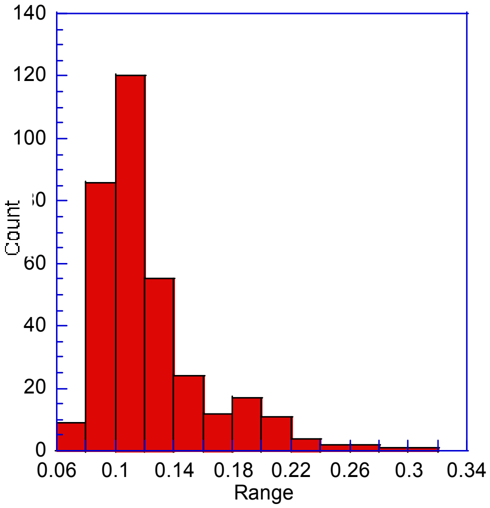

Figure E-2 **Total porosity in Tshirge Member, Qbt 3t**

Tshirege Member Qbt 3 Total Porosity

Minimum	0.04425
Maximum	0.22504
Sum	17.03491
Points	129
Mean	0.132054
Median	0.13312
RMS	0.139841
Std Deviation	0.046193
Variance	0.002134
Std Error	0.004067
Skewness	-0.16015
Kurtosis	-1.0724

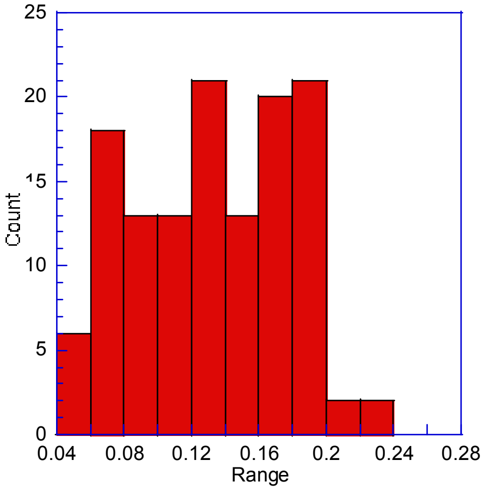

Note: Broad porosity range reflects a poorly welded base and strongly welded upper part in Qbt-3.

Figure E-3 Total porosity in Tshirge Member, Qbt 3

Tshirege Member Qbt 2 Total Porosity

Minimum	0.06989
Maximum	0.34467
Sum	25.79422
Points	201
Mean	0.128329
Median	0.10414
RMS	0.141872
Std Deviation	0.060642
Variance	0.003677
Std Error	0.004277
Skewness	1.685495
Kurtosis	2.254609

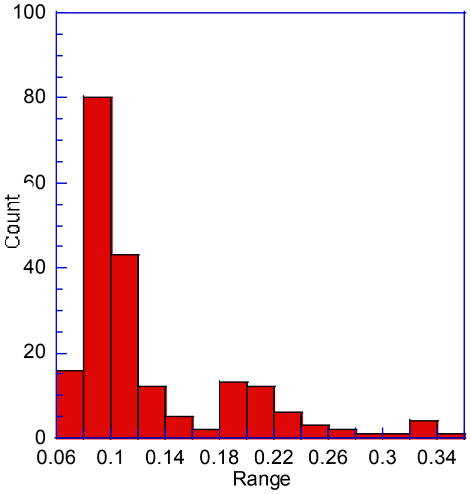

Figure E-4 Total porosity in Tshirge Member, Qbt 2

Tshirege Member Qbt 1v/1g
Undivided Total Porosity

Minimum	0.3908
Maximum	0.48153
Sum	18.59606
Points	41
Mean	0.453562
Median	0.45909
RMS	0.454008
Std Deviation	0.020352
Variance	0.000414
Std Error	0.003178
Skewness	-0.92607
Kurtosis	0.530987

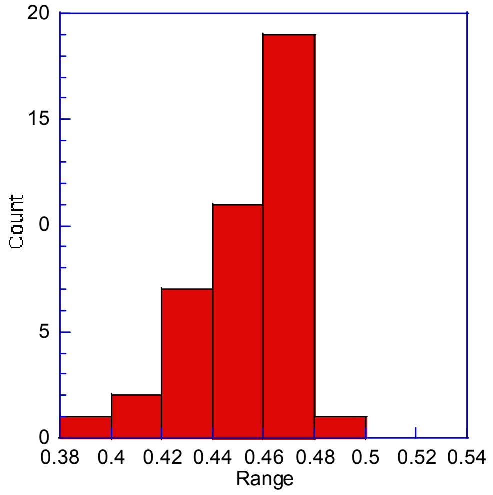

Figure E-5 Total porosity (undivided) in Tshirege Member, Qbt 1v/1g

Cerro Toledo Formation Sandy
Deposits Total Porosity

Minimum	0.23736
Maximum	0.56888
Sum	44.34326
Points	95
Mean	0.466771
Median	0.47735
RMS	0.47174
Std Deviation	0.068647
Variance	0.004712
Std Error	0.007043
Skewness	-1.13059
Kurtosis	1.416683

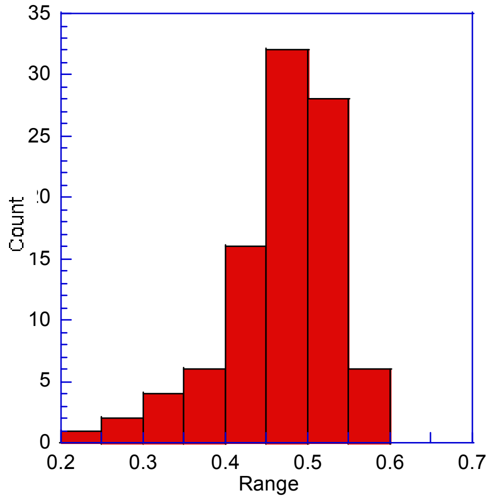

Figure E-6 Total porosity of sandy deposits, Cerro Toledo Formation

Cerro Toledo Formation Cobble and Boulder Deposits Total Porosity	
Minimum	0.15152
Maximum	0.70955
Sum	80.12668
Points	220
Mean	0.364212
Median	0.37552
RMS	0.382983
Std Deviation	0.118698
Variance	0.014089
Std Error	0.008003
Skewness	0.276136
Kurtosis	-0.22372

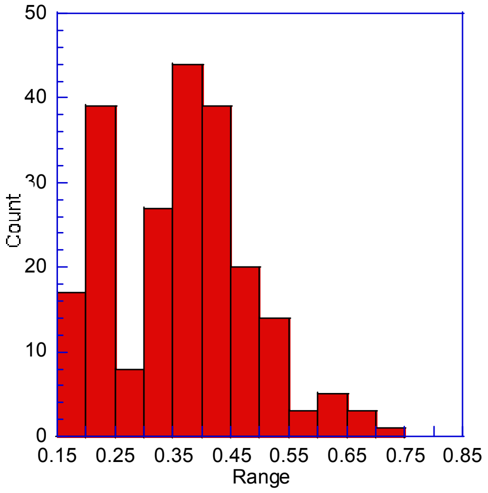

Figure E-7 **Total porosity of cobble and boulder deposits, Cerro Toledo Formation**

Otowi Member Ash-flow Tuffs Total Porosity	
Minimum	0.34721
Maximum	0.52585
Sum	210.0457
Points	482
Mean	0.435779
Median	0.43295
RMS	0.436676
Std Deviation	0.028001
Variance	0.000784
Std Error	0.001275
Skewness	0.410463
Kurtosis	0.515808

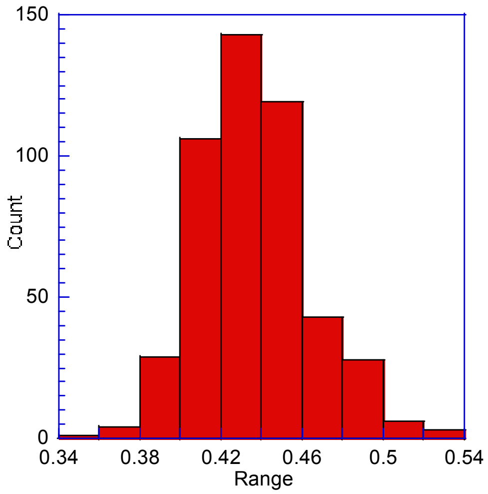

Figure E-8 **Total porosity of ash-flow tuffs, Otowi Member**

Cobble and Boulder Deposits in the Otowi Member Total Porosity

Minimum	0.21134
Maximum	0.41065
Sum	29.15538
Points	95
Mean	0.306899
Median	0.30491
RMS	0.310548
Std Deviation	0.047718
Variance	0.002277
Std Error	0.004896
Skewness	0.284767
Kurtosis	-0.58229

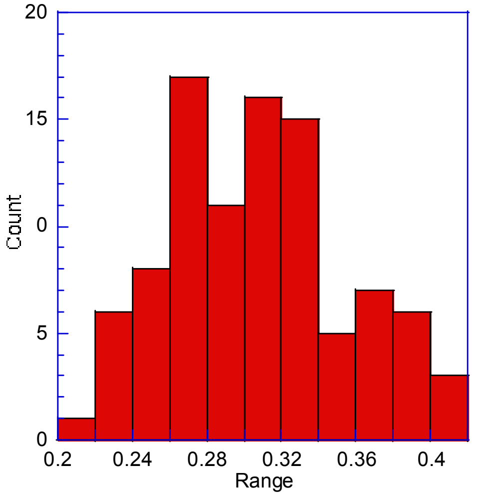

Figure E-9 **Total porosity of cobble and boulder deposits, Otowi Member**

Otowi Member Ash-flow Tuffs Effective Porosity

Minimum	0.09535
Maximum	0.40109
Sum	91.24986
Points	480
Mean	0.190104
Median	0.18431
RMS	0.196361
Std Deviation	0.049225
Variance	0.002423
Std Error	0.002247
Skewness	0.530159
Kurtosis	0.123287

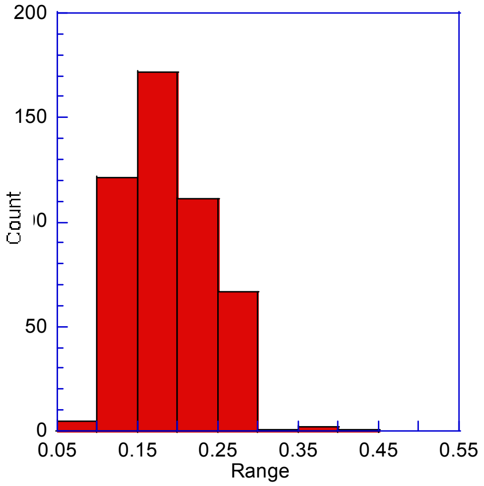

Figure E-10 **Effective porosity of ash-flow tuffs, Otowi Member**

Guaje Pumice Bed Total Porosity

Minimum	0.53472
Maximum	0.58535
Sum	5.09329
Points	9
Mean	0.565921
Median	0.56902
RMS	0.566095
Std Deviation	0.01487
Variance	0.000221
Std Error	0.004957
Skewness	-0.95886
Kurtosis	0.284801

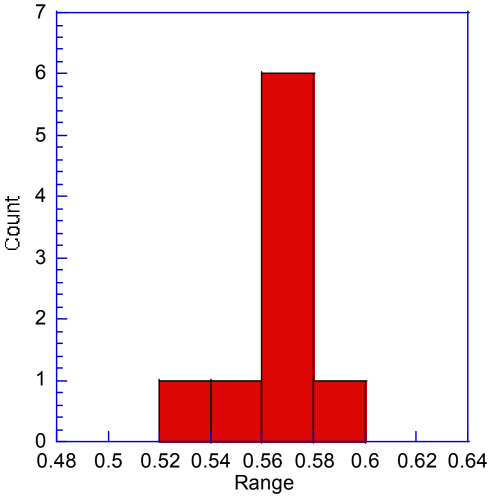

Figure E-11 Total porosity, Guaje Pumice Bed

Puye Formation Total Porosity

Minimum	0.17596
Maximum	0.59777
Sum	297.7946
Points	1057
Mean	0.281736
Median	0.256
RMS	0.290703
Std Deviation	0.071682
Variance	0.005138
Std Error	0.002205
Skewness	1.710916
Kurtosis	3.291937

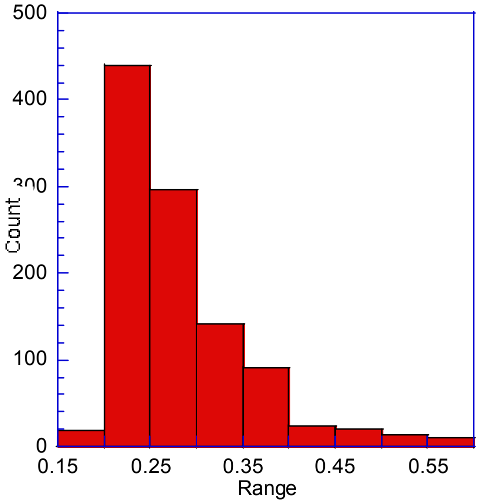

Note: Very low porosities probably represent dacite boulders. Porosities >0.35 generally contain abundant matrix silt, either as thin silt beds or as coarse deposits with a silt-rich matrix.

Figure E-12 Total porosity, Puye Formation

Puye Formation Effective Porosity

Minimum	1.00E-04
Maximum	0.59777
Sum	173.658
Points	1059
Mean	0.163983
Median	0.14665
RMS	0.180069
Std Deviation	0.074429
Variance	0.00554
Std Error	0.002287
Skewness	2.489067
Kurtosis	8.890872

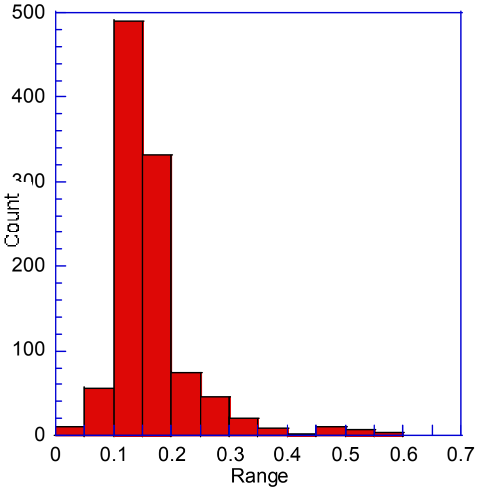

Figure E-13 **Effective porosity, Puye Formation**

Appendix F

Technical Area 16 Groundwater RDX Evaluation

Draft Final

TA-16 GROUNDWATER RDX EVALUATION

Contract No.: 286642

Prepared for

LOS ALAMOS NATIONAL LABORATORY
Los Alamos, New Mexico

February 2016

Prepared by

WESTON SOLUTIONS, INC.
1400 Weston Way
West Chester, Pennsylvania 19380-1499

Table of Contents

Section **Page**

List of Appendices

List of Figures

Title

List of Tables

Title

List of Acronyms

2D	two dimensional
3D	three dimensional
amsl	above mean sea level
CSM	Conceptual Site Model
ft	feet
ft^3	cubic foot
GFM	Geologic Framework Model
kg/ft^3	kilograms per cubic foot
LANL	Los Alamos National Laboratory
LPZ	Lower perched saturation zone
RDX	Research Department Explosive
TA-16	Technical Area 16
ug/L	micrograms per liter
UPZ	Upper perched saturation zone

1 INTRODUCTION

This memo presents estimates of the distribution and mass of Research Department Explosive (RDX) in the saturated media beneath Technical Area 16 (TA-16) at Los Alamos National Laboratory (LANL) in Los Alamos, New Mexico. These estimates were developed for comparison with inventory and disposal records to determine whether the majority of RDX mass released from the Site 260 outfall is accounted for by the conceptual site model (CSM) of subsurface RDX distribution.

2 METHODOLOGY

The distribution of RDX beneath TA-16 was modeled in three dimensions (3D) and makes use of an existing geologic framework model (GFM) developed with EarthVision (Dynamic Graphics, 2015). The existing geologic framework model was supplemented by addition of two new geologic surfaces to better define tuff subunits that host perched groundwater in the Otowi Member of the Bandelier Tuff. RDX groundwater samples from several water bearing zones were interpolated in 3D and then integrated to produce the mass estimates. Input data consisted of interpreted saturated interval extents, porosity values for each geologic unit in the GFM, recent average RDX groundwater concentrations in the Canon de Valle vicinity, and 2D inferences about maximum RDX contamination extents along select profiles as well as at the regional water table.

2.1 Input Data

Two perched groundwater zones are important in terms of contaminant pathways and possible sources of contaminated recharge to the regional aquifer at TA-16. These are referred to as the upper and lower deep perched zones (UPZ and LPZ, respectively) in this report. 3D volumes of the perched zones were created using structure contour maps defining tops and bottoms of these perched zones. These surfaces were used to define the boundaries and volumes of perched water zones.. The available well data allow for a range of interpretations regarding the geometry of the tops and bottoms of perched zones; two of the interpretations were selected for this study and are henceforth referred to as Scenario 1 and Scenario 2. Figure 2-1 depicts the data for both scenarios. Both interpretations taper westward to the Pajarito fault zone but maps are cropped to the region where the most significant differences lie for improved legibility. A full view of each scenario will be provided in Section 3.1. Figure 2-2 provides the data and interpreted contours for the LPZ and the regional water table. The February 2015 regional water table interpretation was used as the top of the regional aquifer.

Processed borehole geophysical data were used as the source of porosity estimates and summary statistics are provided in Table 2-1. Median values for the applicable geologic units were deemed most appropriate for mass estimation based on the skewed distributions for several units. New subunit boundaries G2 and G3 were identified in the Otowi Member based on abrupt shifts in gamma activity observed in borehole geophysical logs. These gamma shifts were mapped in wells throughout the study area and structure contour maps were prepared for these subunit boundaries (Figure 2-3). The G2 and G3 surfaces were used to define a new subunit in the Otowi Member in the model.

Input RDX concentrations, provided in Table 2-2, represent averages from the four most recent quarters of data for most wells. Only two sample events were available for wells CDV-16-4ip S2 and CDV-9-1(i) S1. Screening samples were used for wells CDV-9-1(i) PZ1, PZ2, and R-63i. Well CDV-9-1(i) PZ1 is a bailed sample that may be biased low and the latter two represent an average of two separate intervals. A value of half the detection limit (0.08 ug/L) was used to represent non-detect data during interpolation.

Inferred RDX contours were used in addition to sampling data from wells to inform the shape and extent of the 3D plume. In the UPZ, three sets of extrapolated RDX concentration contours were prepared along cross sections intersecting CdV-9-1i; these extrapolated contours were usedto supplement the well data in modeling RDX distributions in the UPZ.. Well CdV-9-1i is important because it yielded several well-development samples containing the highest concentration of RDX (300-ug/L) beneath TA-16. For mass estimates, RDX distribution was treated as a single contaminant plume that extended from the upper perched zone to the regional aquifer. Vertical RDX concentration gradients were extrapolated between the UPZ and regional aquifer, but RDX mass was calculated only for those rock volumes that were identified are fully saturated. The base of the RDX plume was constrained by sub-horizontal contours at the water table inferred from well data in the regional aquifer. Figure 2-4 provides a visualization of the 3D distribution of RDX data and the interpreted contours. The conceptual model of RDX transport through the system is advection primarily to the east-southeast in the UPZ with symmetric transverse dispersion in the horizontal plane and downward migration through the LPZ and into the regional aquifer, where the plume migrates to the northeast due to mounding at the water table induced by the perched zones above.

2.2 Perched Saturation and Geologic Zone Modeling

Structural contours representing the bounding surfaces for each model zone were interpolated using EarthVision’s 2D minimum tension algorithm. All interpolations were performed using a 50-ft rectangular grid resolution. Each surface was slightly smoothed and damped to yield results that closely honored the contours but without the sharp changes in slope that can occur when contours are used as input. The intersections of the top and bottom surfaces of each perched zone were then used to develop 3D volumes in the model. The addition of G2 and G3 surfaces to the geologic framework model (GFM) partitions the Otowi Member into lower, middle, and upper subunits that are labeled G2, G3, and undivided Otowi in ascending stratigraphic order, for this report. Lastly, perched saturation volumes were intersected with the revised GFM stratigraphy for selection of porosity values to use in mass integration.

2.3 RDX Plume Interpolation

The collection of monitoring well data and associated interpretive contours were interpolated using EarthVision’s 3D minimum tension algorithm. The model domain accounts for all data, regardless of geologic unit or saturation interval, in a single gridding pass so the resulting plume does not exhibit discontinuities at stratigraphic contacts. Although the saturated intervals are interpreted as isolated from one another, it was assumed that there is a correlation in the RDX distribution among them based on the premise that they share the same source. Independent treatment of each saturation zone would have been difficult with the limited number of wells completed in each saturation zone.

The minimum tension algorithm uses a feedback mechanism to minimize sharp changes in concentration gradient wherever possible. However, results in areas of sparse data are sensitive to each of the following parameters: grid resolution, vertical anisotropy, transformation of data prior to interpolation, and boundary conditions imposed at the model edges. A sensitivity analysis consisting of 48 iterations was consequently performed to provide a range of plume distributions for use in mass estimation. These iterations represent all possible combinations from among three selected grid resolutions, four vertical anisotropy factors, and four values used as the exponent in a power function transformation of the data prior to interpolation. The model boundaries, which were selected based on inferred saturation or contaminant extents, were treated as non-detect values and were not varied.

2.4 RDX Mass Estimation

RDX mass estimates were determined for each saturated interval through integration of the interpolated plume. This was accomplished by multiplying the plume by a categorical grid containing the median porosity by geologic layer and the conversion from units of ug/L to kg/ft^3 (2.832E-8). The applicable grid cells for each saturated interval were then isolated in the resulting grid, summed, and multiplied by the dimensions of a grid cell (50 x 50 x 2.5 feet) to yield RDX mass in kilograms. The contributions by each of the strata within each of the saturated intervals were also determined using the same procedure.

The saturated alluvial zone was not incorporated into the plume interpolations and was instead treated as a five-foot thick prism along the segment of Canon de Valle between Peter Spring and ALLV Seep 100E. This segment was divided into an 1850-ft long upstream reach assumed to have a 65-ft width and 1350-ft downstream reach assumed to have a 30-ft width. RDX mass within this zone was determined as the product of the prism dimensions, an assumed porosity of 0.4, and the maximum (17.6-ug/L) from among the four alluvial well average RDX concentrations.

3 RESULTS

3.1 Perched Saturation Zones

Models of saturated intervals are required for isolating cells in the interpolated 3D RDX plume for integration. Figure 3-1 depicts the modeled perched saturation zones using UPZ Scenario 1. Figure 3-2 provides the same views for UPZ Scenario 2. The primary difference between the two UPZ scenarios is how the margins of the zone taper in the absence of well data for dictating this shape. Despite the differences in the isopach maps for the two interpretations, estimates of total UPZ volume for both scenarios were within 1% of a value of 100,000 acre-ft. The volume of water contained in the UPZ, accounting for the variable porosity of the strata it intersects, is approximately 38,000 acre-feet according to each scenario. The lateral extent and thickness of the LPZ is much smaller than that of the UPZ and yielded a total volume of approximately 3,000 acre-feet and a water volume of 766 acre-feet (approximately 3% and 2% of corresponding UPZ volumes, respectively). The regional aquifer was modeled as the volume occupying the interval between the regional water table and a base elevation of 5600-ft above mean sea level (amsl). The volume of water contained within an ~150-ft thick rectangle closely bounding the extents of the UPZ is approximately 69,000 acre-ft (1.8 times that of the UPZ).

3.2 RDX Distribution

Figure 3-3 provides both plan and profile views of the interpolated RDX contaminant distribution within each saturated interval. This figure uses Scenario 1 for the UPZ and Figure 3-4 uses Scenario 2 for comparison. The three plan views in both figures depict maximum RDX concentrations within the applicable saturated interval. Transects A, B, and C on the maps were used to generate the profiles and are extended versions of those used to develop interpreted RDX contours from the data. Transect D was added to depict a profile along the centerline of the dilute plume impacting the regional aquifer.

The RDX plume in the UPZ is centered on the 300-ug/L value at well CdV-9-1i PZ2, which is located at the top of the Puye Formation (Tpf). Due to the influence of the inferred RDX contours used to impose the conceptual model of transport within the UPZ, the plume has the shape of an ellipsoid elongated to the east. The plume in UPZ is nearly symmetric about the major axis to account for dispersion that is observed in the data south of well CdV-9-1i and presumed to be mirrored to the north, where there are currently no data. Well R-47i is the only non-detect sample within the UPZ for constraining the eastern edge of the RDX plume. Non-detect model boundaries were used to constrain the plume in other directions in the absence of data. The western boundary was placed immediately upgradient of the Site 260 outfall, which is the suspected source of contamination. The southern and eastern boundaries were placed just beyond the UPZ extents and the northern boundary was placed approximately 1400-ft north of R-18 to allow some extrapolation beyond this location as indicated by the inferred RDX contours in the regional aquifer. RDX contours were not inferred between well CdV-9-1i and the Site 260 outfall due to a lack of knowledge of where the centroid of the plume truly resides and the uncertainty associated with whether the RDX concentration in the bailed sample at well CdV-9-1(i) PZ1 represents a maximum value in the upper part of the UPZ . Uncertainty about the center of mass as well as the shape of the plume margins in the UPZ was the primary reason for performing the sensitivity analysis.

The magnitude and extent of the RDX plume in the LPZ and regional aquifer are more limited than that of the UPZ. The plume honors the contours inferred for the regional aquifer. The maximum thickness of the plume in the regional aquifer is 180-ft based on the 0.1-ug/L contour but only 80-ft based on the 1-ug/L contour. The average interpolated concentration in the LPZ is approximately 20-ug/L and the plume contours within this zone reflect the concentration gradient between the UPZ and the regional aquifer suggested by the LPZ data.

3.3 RDX Mass

RDX mass was estimated for each applicable combination of saturation zone and stratigraphic unit. The integration procedure described in Section 2.4 was performed for each of the 48 sensitivity runs and Figure 3-5 illustrates that the mass estimates for every zone are normally distributed. Based on this normality, the interpolated plume mean was used in Figures 3-3 and 3-4 to illustrate the central tendency of this batch of realizations designed to account for at least a few sources of uncertainty. Basic statistics calculated from the collection of sensitivity runs are presented in Table 3-1.

The total UPZ RDX mass for the interpolated plume mean was 1,084-kg for Scenario 1 and 987-kg for Scenario 2. The median values are very similar to the means based on the normally distributed values. Estimates for the two scenarios are within 10% of each other and both indicate that the UPZ constitutes just over 98% of the total RDX mass (1,000 to 1,100-kg) in groundwater. The LPZ represents 1.3% of the total RDX mass followed by the regional aquifer and saturated alluvium at 0.4% and 0.02%, respectively. The minimum and maximum estimates for both scenarios are approximately 40% different from the mean and are similar to bounds representing a 95% confidence (two standard deviations away from the mean) for this set of sensitivity runs.

Due to their thickness relative to the other units, the Puye (Tpf) and the Otowi (Qbof) contain the majority of RDX mass. The Puye contains all of the LPZ and regional aquifer mass and approximately 50% of the UPZ mass. The Otowi contains approximately 40% of the UPZ mass and over half of that is in the G2 subunit due to its closer proximity to the center of mass for the current model.

4 CONCLUSIONS

The distribution of RDX in the saturated media beneath TA-16 was modeled in 3D using EarthVision to provide estimates of mass for comparison with values derived through other methods. The advantages of this approach are: a) the holistic treatment of data from different saturation zones and stratigraphic units during interpolation, and b) the ability to use an existing GFM for dissection of the result to account for variable properties of the strata after interpolation. These mass estimates were heavily influenced by professional judgement in the form of hydraulic and RDX contours inferred from the data to compensate for the fact that the interpolation algorithms themselves do not account for the flow regime. Two interpretations for the UPZ shape and a sensitivity analysis of interpolation parameters were used to address some of the sources uncertainty in the mass estimate. The central tendencies of estimates for the two UPZ scenarios were similar. This was because the primary differences in these scenarios occurred near the margins of the zone, which are relatively thin and contain relatively dilute plumes. However, the endpoints of the sensitivity runs suggested that the actual RDX mass could be as much as 40% different from the mean. Although the sensitivity runs allowed for different amounts of extrapolation

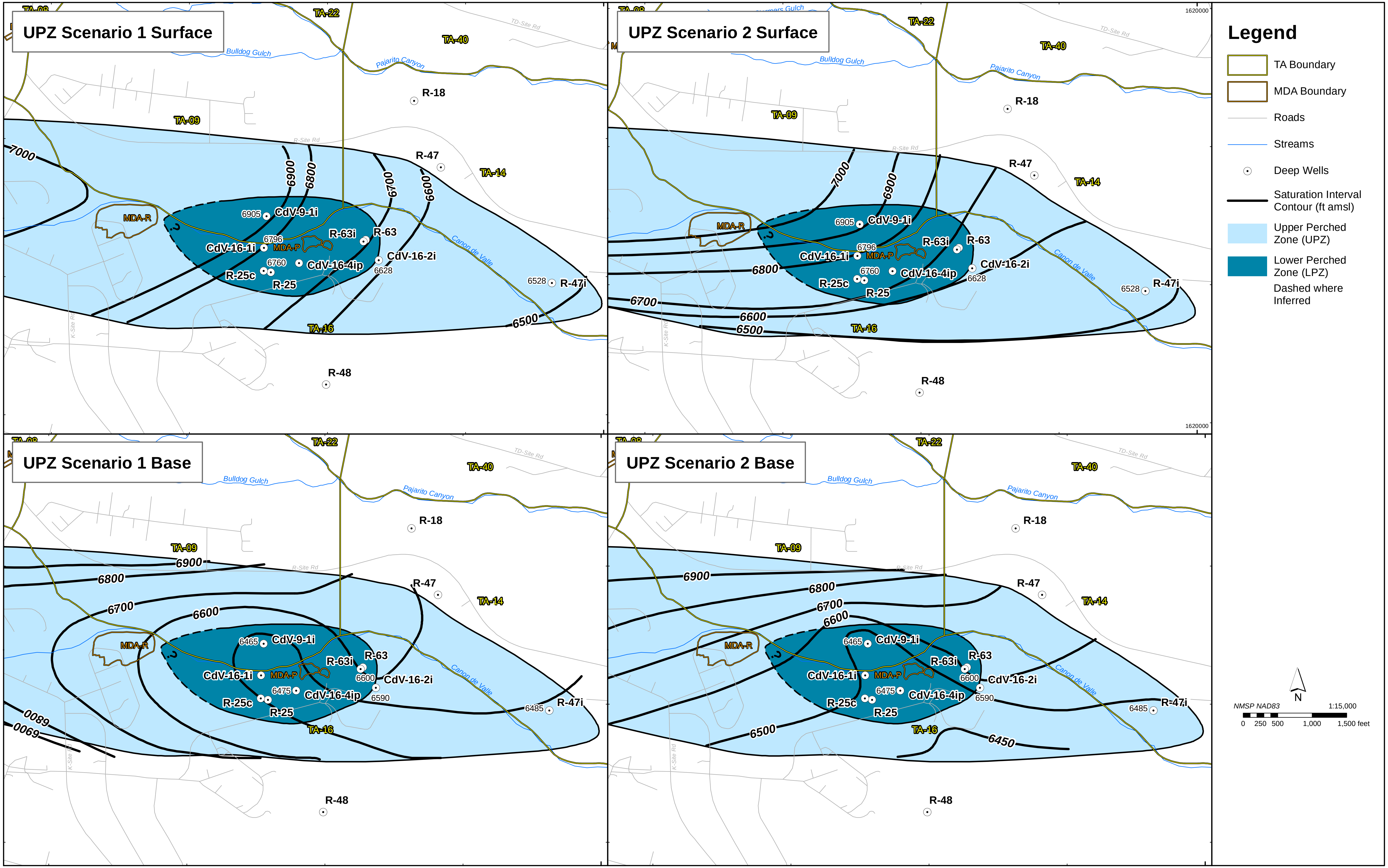

C:\Projects\LANL2014\TA-16\GIS\mxd\TA16_WBZ_Contours_Upper.mxd STROBRID 2/17/2016 10:07

Figure 2-1 TA-16 Upper Perched Saturation Zone Data

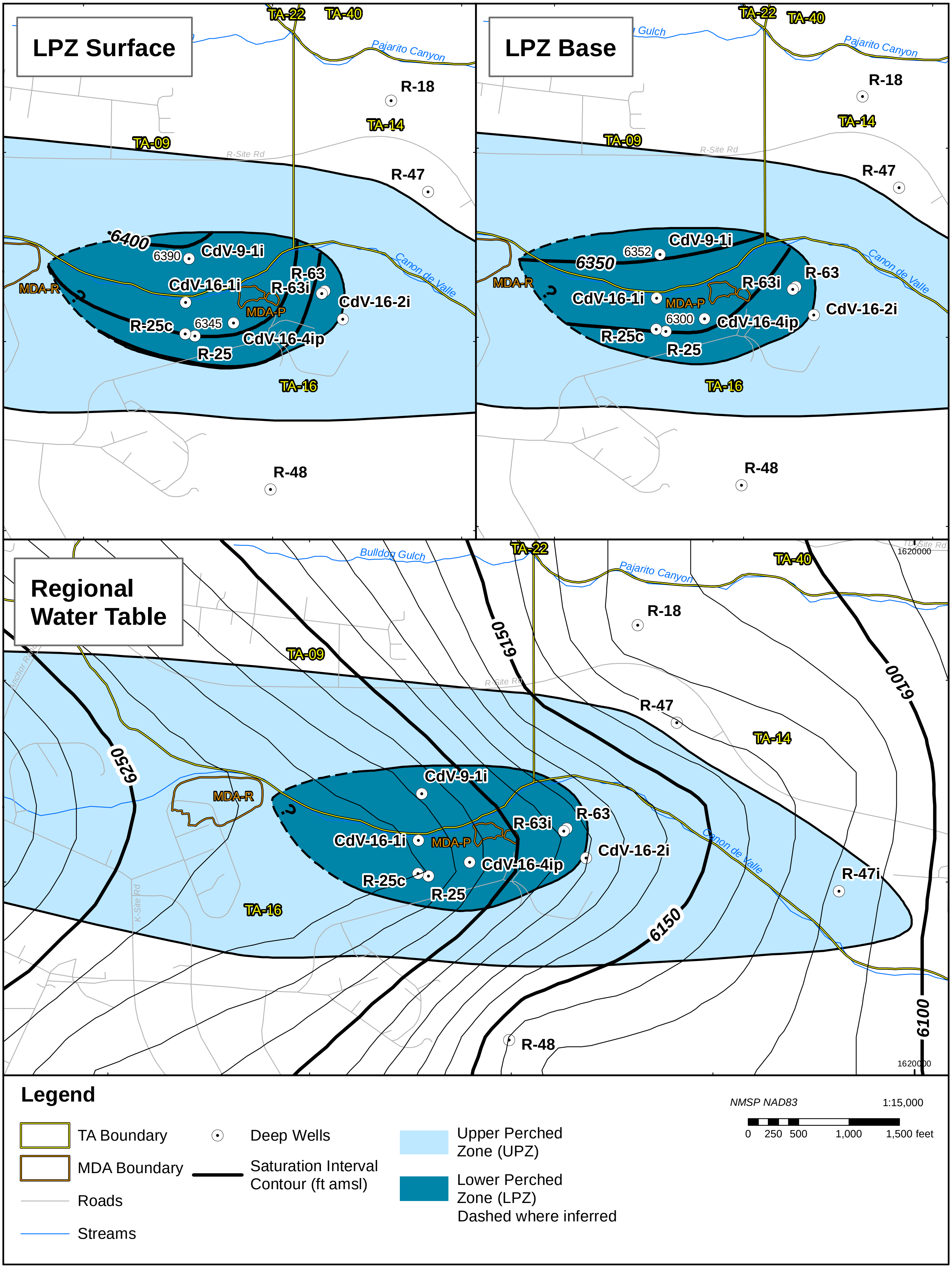

C:\Projects\LANL2014\TA-16\GIS\mxd\TA16_WBZ_Contours_LowerReg.mxd STROBRID 2/17/2016 10:07

Figure 2-2 TA-16 Lower Perched Saturation and Regional Aquifer Data

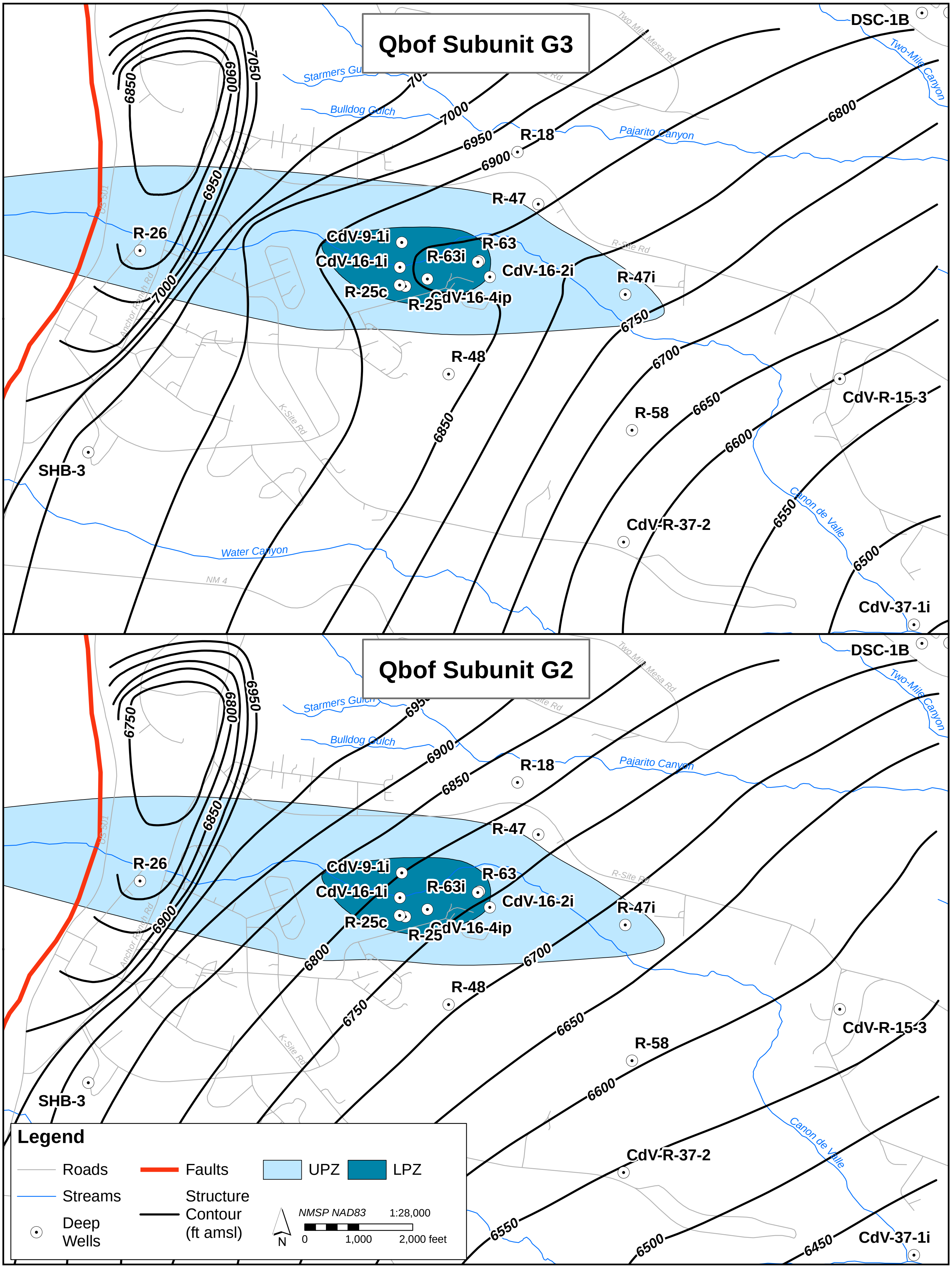

Figure 2-3 Structure Contours for Subunits G2 and G3 of the Otowi Member, Bandelier Tuff

C:\Projects\LANL2014\TA-16\GIS\mxd\TA16_Qbof_Subunits.mxd STROBRID 2/17/2016 13:46

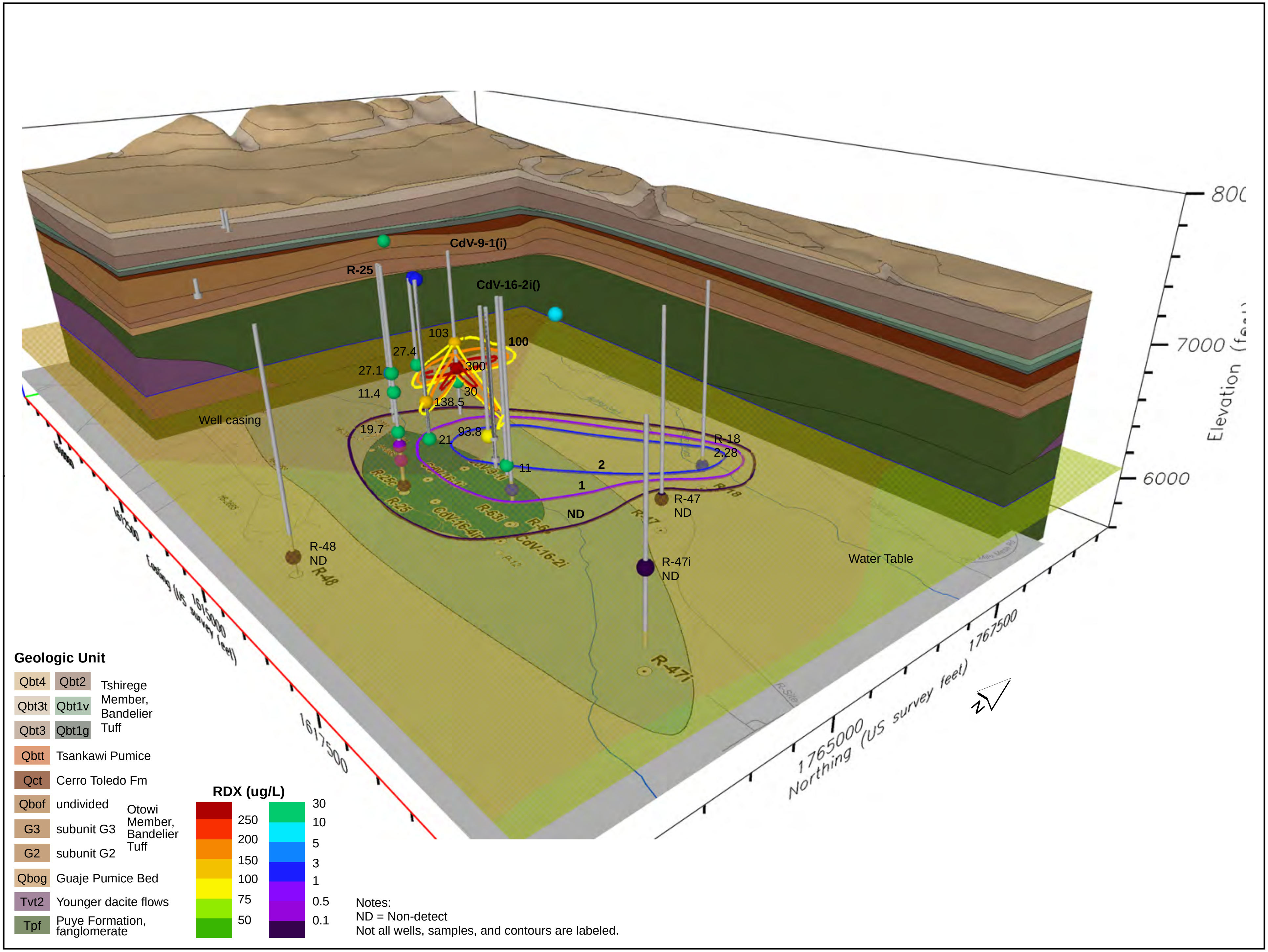

C:\Projects\LANL2014\TA-16\GIS\mxd\TA16_RDX_contours_3D.mxd STROBRID 2/17/2016 11:25

Figure 2-4 TA-16 RDX Groundwater Data and Inferred Plume Contours

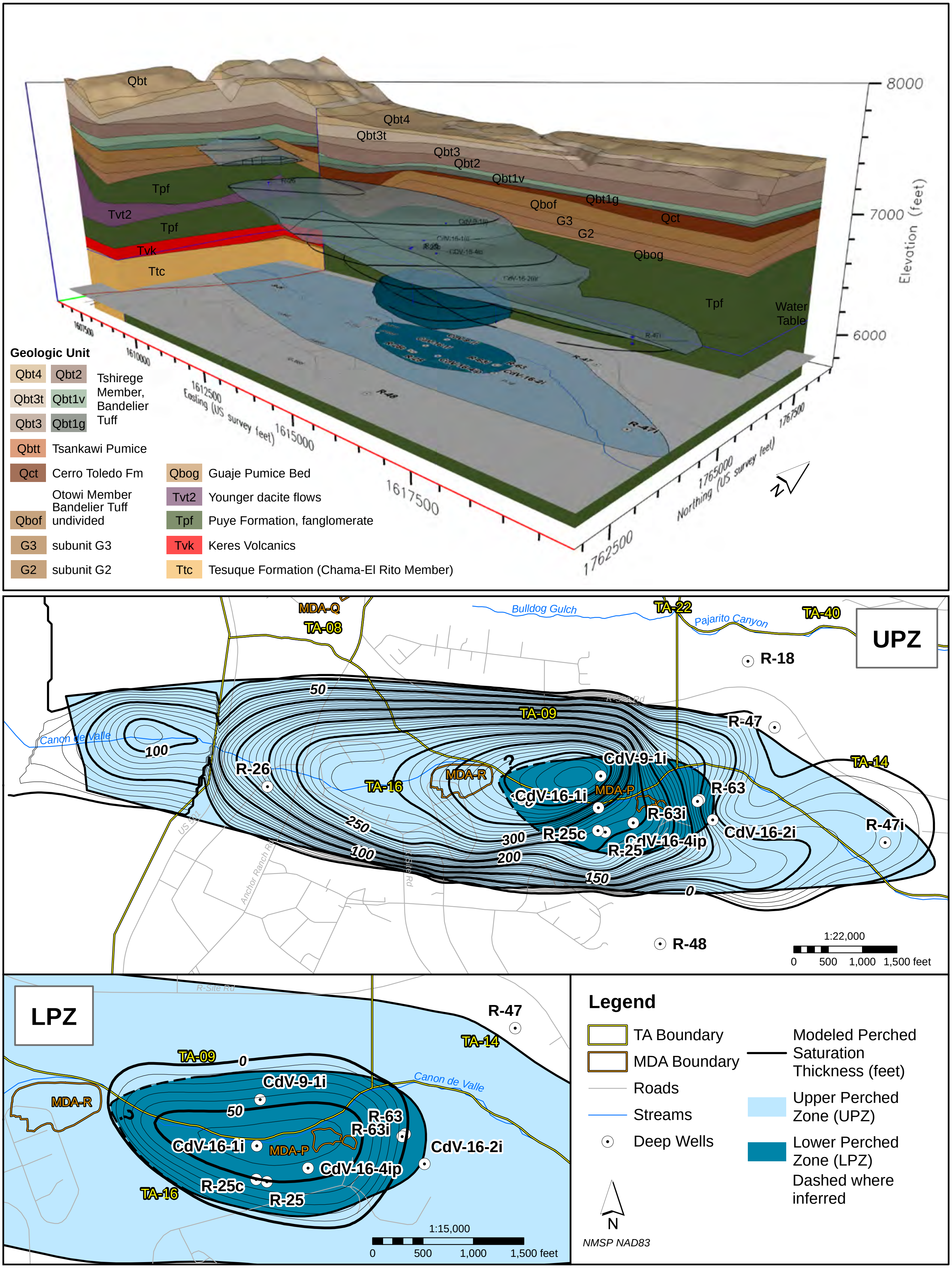

C:\Projects\LANL2014\TA-16\GIS\mxd\TA16_WBZ_3D_Upper2.mxd STROBRID 2/17/2016 10:39

Figure 3-1 Modeled TA-16 Perched Saturation Zones (UPZ Scenario 1)

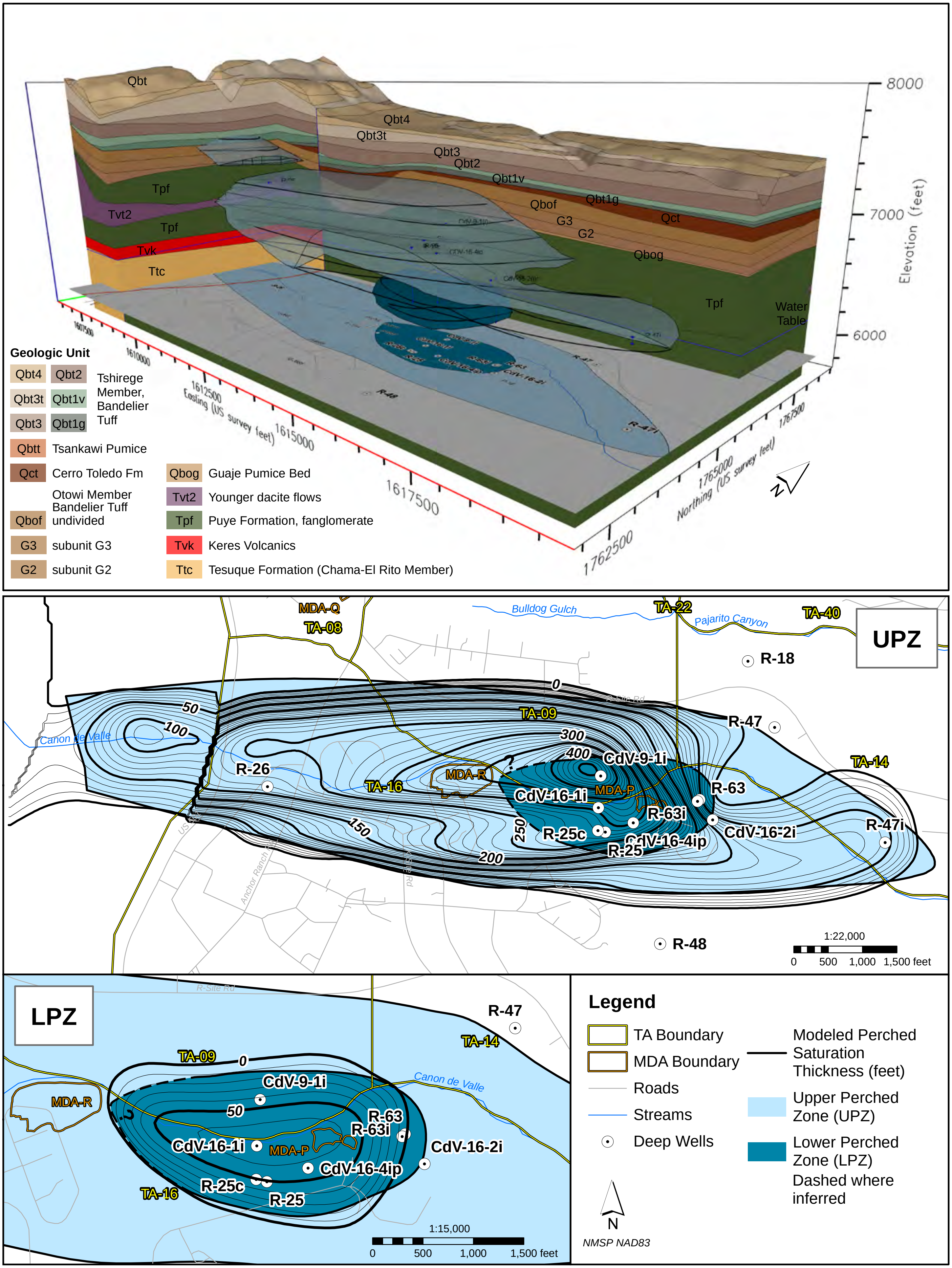

C:\Projects\LANL2014\TA-16\GIS\mxd\TA16_WBZ_3D_Upper4.mxd STROBRID 2/17/2016 10:40

Figure 3-2 Modeled TA-16 Perched Saturation Zones (UPZ Scenario 2)

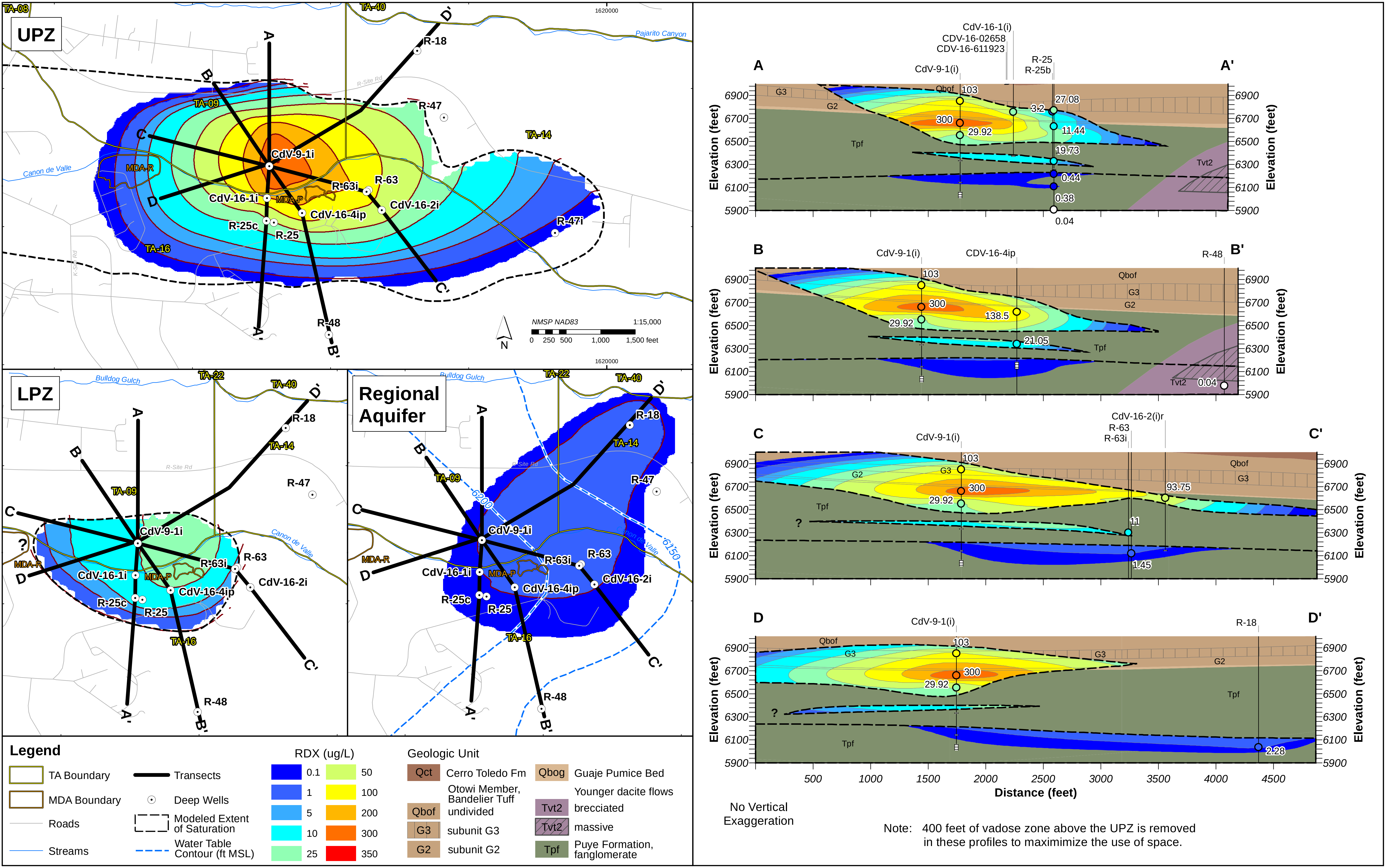

C:\Projects\LANL2014\TA-16\GIS\mxd\TA16_Combo_Upper2.mxd STROBRID 2/17/2016 11:19

Figure 3-3 Modeled TA-16 Lower Vadose and Regional Aquifer RDX Groundwater Distribution (UPZ Scenario 1)

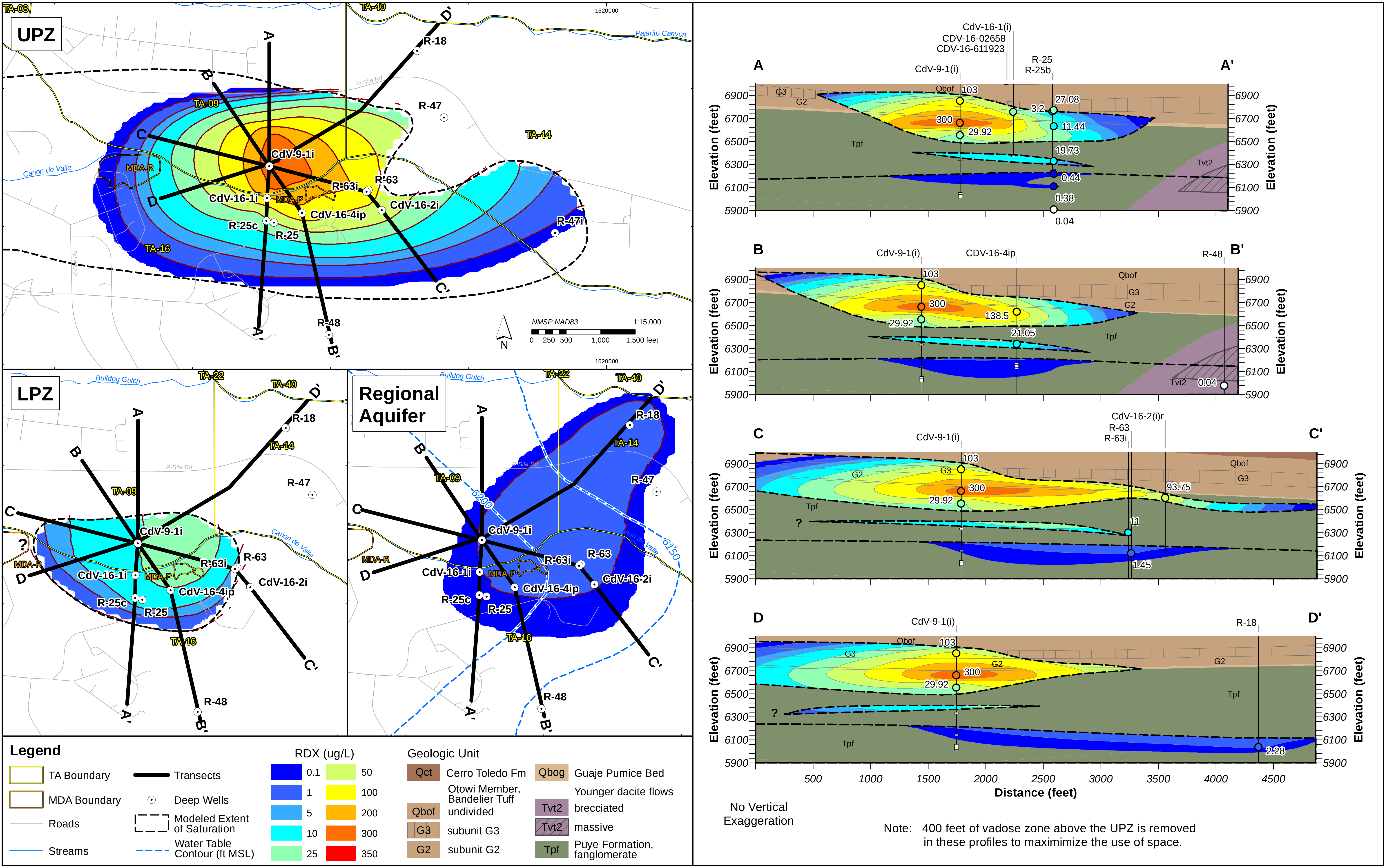

C:\Projects\LANL 2014\TA-16\GIS\mxd\TA16_Combo_Upper4.mxd STROBRID 2/17/2016 11:18

Figure 3-4 Modeled TA-16 Lower Vadose and Regional Aquifer RDX Groundwater Distribution (UPZ Scenario 2)

Figure 3−5
Density Distributions for Sensitivity Analysis of TA−16 RDX Mass Estimates

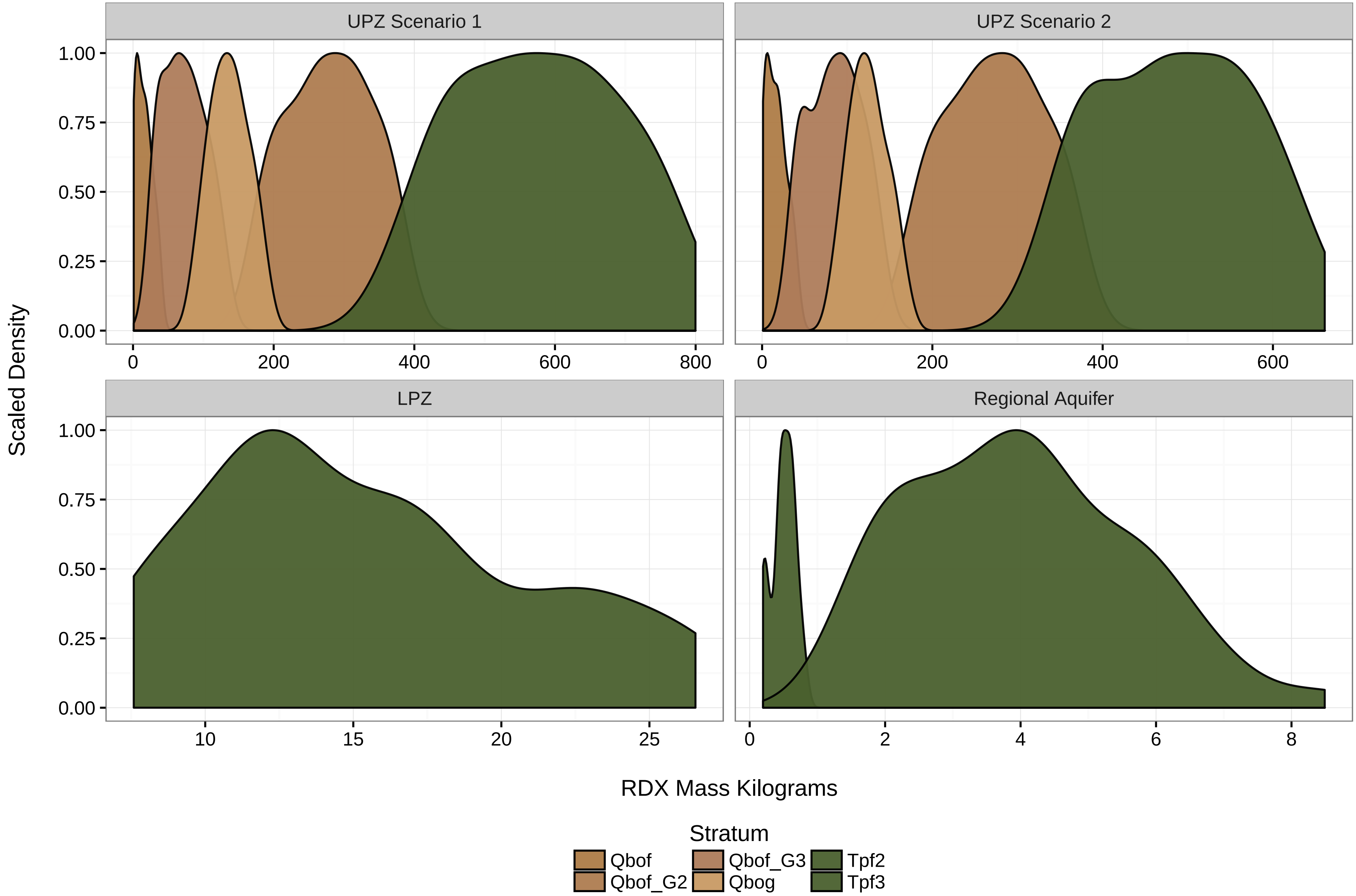

Table 2-1
TA-16 ELAN Porosity Statistics

Zone	Type	Points	Min	Max	Mean	Median	StDev	Var	Skewness	Kurtosis	StdError	RMS	Sum
Qbt4	Total	119	0.335	0.538	0.414	0.416	0.041	0.002	0.559	0.444	0.004	0.416	49.221
Qbt3t	Total	359	0.068	0.635	0.137	0.112	0.076	0.006	3.390	13.423	0.004	0.157	49.138
Qbt3	Total	129	0.044	0.225	0.132	0.133	0.046	0.002	-0.160	-1.072	0.004	0.140	17.035
Qbt2	Total	201	0.070	0.345	0.128	0.104	0.061	0.004	1.685	2.255	0.004	0.142	25.794
Qbt1v	Total	41	0.391	0.482	0.454	0.459	0.020	0.0004	-0.926	0.531	0.003	0.454	18.596
Qbt1g	Total	41	0.391	0.482	0.454	0.459	0.020	0.0004	-0.926	0.531	0.003	0.454	18.596
Qct	Total	95	0.237	0.569	0.467	0.477	0.069	0.005	-1.131	1.417	0.007	0.472	44.343
Qct (Cobbles)	Total	220	0.152	0.710	0.364	0.376	0.119	0.014	0.276	-0.224	0.008	0.383	80.127
Qbof	Effective	480	0.095	0.401	0.190	0.184	0.049	0.002	0.530	0.123	0.002	0.196	91.250
Qbof	Total	482	0.347	0.526	0.436	0.433	0.028	0.001	0.410	0.516	0.001	0.437	210.046
Qbof (Cobbles)	Total	95	0.211	0.411	0.307	0.305	0.048	0.002	0.285	-0.582	0.005	0.311	29.155
Qbof_G3	Total	482	0.347	0.526	0.436	0.433	0.028	0.001	0.410	0.516	0.001	0.437	210.046
Qbof_G2	Total	482	0.347	0.526	0.436	0.433	0.028	0.001	0.410	0.516	0.001	0.437	210.046
Qbog	Total	9	0.535	0.585	0.566	0.569	0.015	0.0002	-0.959	0.285	0.005	0.566	5.093
Tpf	Effective	1059	0.0001	0.598	0.164	0.147	0.074	0.006	2.489	8.891	0.002	0.180	173.658
Tpf	Total	1057	0.176	0.598	0.282	0.256	0.072	0.005	1.711	3.292	0.002	0.291	297.795

Appendix G

Geologic Contacts for Wells Included in the RDX Investigation at Technical Area 16 and Vicinity

G-1.0 INTRODUCTION

This appendix contains the elevations and depths below ground surface (bgs) for contacts of geologic units encountered within wells CdV-16-1i, CdV-16-2i, CdV-16-4ip, CdV-37-1i, CdV-9-1i, CdV-R-15-3, CdV-R-37-2, R-18, R-25, R-25b, R-26, R-47i, R-47, R-48, R-58, R-63i, R-63, R-68 and one core hole, SHB-3, located at Technical Area 16 and nearby (Table G-1.0-1). These contacts are excerpted from file WC15c.xlsx provided by Weston, Inc., and were used to prepare the most recent update to the WC15c three-dimensional (3-D) geologic framework model (Appendix F). In Table G-1.0-1, geologic contacts that were updated in the WC15c 3-D geologic framework model or based on reexamination and reinterpretation of cuttings, borehole geophysics, and borehole video logs that differ from those in the well completion reports are flagged. Contacts for core hole SHB-3 are new and were not included in the WC15c 3-D geologic framework model file. Geologic units include, from oldest to youngest: Puye Formation (Tpf); Tschicoma Formation (Tvt2, 3–3.5 Ma); Guaje Pumice Bed (Qbog); Otowi Member, Bandelier Tuff (Qbof); Cerro Toledo Formation (Qct); Tsankawi Pumice Bed (Qctt); Tshirege Member, Bandelier Tuff (Qbt); and Quaternary Alluvium (Qal).

G-2.0 REFERENCES

The following reference list includes documents cited in this report.

Broxton, D., R. Warren, P. Longmire, R. Gilkeson, S. Johnson, D. Rogers, W. Stone, B. Newman, M. Everett, D. Vaniman, S. McLin, J. Skalski, and D. Larssen. "Characterization Well R-25 Completion Report," Los Alamos National Laboratory report LA-13909-MS, Los Alamos, New Mexico (2002).

Gardner, J.N., T. Kolbe, and S. Chang. "Geology, Drilling, and Some Hydrologic Aspects of Seismic Hazards Program Core Holes, Los Alamos National Laboratory, New Mexico," Los Alamos National Laboratory report LA-12460-MS, Los Alamos, New Mexico (1993).

Kleinfelder. "Final Well CdV-16-1(i) Completion Report," report prepared for Los Alamos National Laboratory, Project No. 37151/9.12, Albuquerque, New Mexico (2004a).

Kleinfelder. "Final Well CdV-16-2(i) Completion Report," report prepared for Los Alamos National Laboratory, Project No. 37151/10.12, Albuquerque, New Mexico (2004b).

Kleinfelder. "Final Completion Report, Characterization Well R-18," report prepared for Los Alamos National Laboratory, Project No. 37151, Albuquerque, New Mexico (2005a).

Kleinfelder, January 25, 2005b. "Final Well R-26 Completion Report, Revision No. 1," report prepared for Los Alamos National Laboratory, Project No. 37151, Albuquerque, New Mexico.

Kopp, B., A. Crowder, M. Everett, D. Vaniman, D. Hickmott, W. Stone, N. Clayton, S. Pearson, and D. Larssen. "Well CdV-R-15-3 Completion Report," Los Alamos National Laboratory report LA-13906-MS, Los Alamos, New Mexico (2002).

Kopp, B., M. Everett, J.R. Lawrence, G. WoldeGabriel, D. Vaniman, J. Heikoop, W. Stone, S. McLin, N. Clayton, and D. Larssen. "Well CdV-R-37-2 Completion Report," Los Alamos National Laboratory report LA-14023-MS, Los Alamos, New Mexico (2003).

LANL (Los Alamos National Laboratory). “Completion Report for Well R-25c,” Los Alamos National Laboratory document LA-UR-08-5878, Los Alamos, New Mexico (2008).

LANL (Los Alamos National Laboratory). “Completion Report for Regional Aquifer Well R-48,” Los Alamos National Laboratory document LA-UR-10-0864, Los Alamos, New Mexico (2010a).

LANL (Los Alamos National Laboratory), April 2010b. “Completion Report for Intermediate Aquifer Well R-47i,” Los Alamos National Laboratory document LA-UR-10-2207, Los Alamos, New Mexico (2010b).

LANL (Los Alamos National Laboratory). “Completion Report for Intermediate Aquifer Well CdV-37-1i,” Los Alamos National Laboratory document LA-UR-10-1771, Los Alamos, New Mexico (2010c).

LANL (Los Alamos National Laboratory). “Completion Report for Intermediate Well CdV-16-4ip,” Los Alamos National Laboratory document LA-UR-11-0187, Los Alamos, New Mexico (2011a).

LANL (Los Alamos National Laboratory). “Completion Report for Regional Well R-63,” Los Alamos National Laboratory document LA-UR-11-3673, Los Alamos, New Mexico (2011b).

LANL (Los Alamos National Laboratory). “Completion Report for Regional Aquifer Well R-47,” Los Alamos National Laboratory document LA-UR-14-28638, Los Alamos, New Mexico (2014).

LANL (Los Alamos National Laboratory). “Completion Report for Intermediate Aquifer Well CdV-9-1(i),” Los Alamos National Laboratory document LA-UR-15-23954, Los Alamos, New Mexico (2015a).

LANL (Los Alamos National Laboratory). “Completion Report for Intermediate Aquifer Well R-63i,” Los Alamos National Laboratory document LA-UR-15-26729, Los Alamos, New Mexico (2015b).

LANL (Los Alamos National Laboratory). “Completion Report for Regional Aquifer Well R-58,” Los Alamos National Laboratory document LA-UR-16-21912, Los Alamos, New Mexico (2016).

LANL (Los Alamos National Laboratory). “Completion Report for Regional Aquifer Well R-68,” Los Alamos National Laboratory document LA-UR-17-26063, Los Alamos, New Mexico (2017).

Table G-1.0-1
Geologic Contacts for Wells within the RDX Investigation Area Based on the Weston WC15c Geologic Framework Model

Location	Easting (ft)	Northing (ft)	Surface elev. (ft)	Contact Elevation (ft)	Contact Depth (ft bgs)	Upper Contact	Lower Contact	Data Reference	Date Modified
CdV-16-1i	1615078.20	1764415.20	7382.2	7382.2	0	Qal	Qal	Kleinfelder 2004a	7/1/2011
CdV-16-1i	1615078.20	1764415.20	7382.2	7373.2	9	Qal	Qbt3	Kleinfelder 2004a	7/1/2011
CdV-16-1i	1615078.20	1764415.20	7382.2	7297.2	85	Qbt3	Qbt2	Kleinfelder 2004a	—[a]
CdV-16-1i	1615078.20	1764415.20	7382.2	7187.2	195	Qbt2	Qbt1vu	Kleinfelder 2004a	—
CdV-16-1i	1615078.20	1764415.20	7382.2	7187.1	195.1	Qbt1vu	Qbt1vu	Kleinfelder 2004a	—
CdV-16-1i	1615078.20	1764415.20	7382.2	7159.3	222.9	Qbt1vc	Qbt1vc	Kleinfelder 2004a	—
CdV-16-1i	1615078.20	1764415.20	7382.2	7159.2	223	Qbt1vc	Qbt1g	Kleinfelder 2004a	—
CdV-16-1i	1615078.20	1764415.20	7382.2	7142.2	240	Qbt1g	Qct	Kleinfelder 2004a	—
CdV-16-1i	1615078.20	1764415.20	7382.2	7032.2	350	Qct	Qbof	This report[b]	—
CdV-16-1i	1615078.20	1764415.20	7382.2	6699.2	683	Qbof	Qbof	Kleinfelder 2004a	—
CdV-16-2i	1616741.20	1764237.20	7457.1	7457.1	0	Qbt4	Qbt4	Kleinfelder 2004b	—
CdV-16-2i	1616741.20	1764237.20	7457.1	7398.1	59	Qbt4	Qbt3t	This report	—
CdV-16-2i	1616741.20	1764237.20	7457.1	7380.1	77	Qbt3t	Qbt3	Kleinfelder 2004b	—
CdV-16-2i	1616741.20	1764237.20	7457.1	7252.1	205	Qbt3	Qbt2	This report	—
CdV-16-2i	1616741.20	1764237.20	7457.1	7152.1	305	Qbt2	Qbt1vu	Kleinfelder 2004b	—
CdV-16-2i	1616741.20	1764237.20	7457.1	7152	305.1	Qbt1vu	Qbt1vu	Kleinfelder 2004b	—
CdV-16-2i	1616741.20	1764237.20	7457.1	7109.2	347.9	Qbt1vc	Qbt1vc	Kleinfelder 2004b	—
CdV-16-2i	1616741.20	1764237.20	7457.1	7109.1	348	Qbt1vc	Qbt1g	Kleinfelder 2004b	—
CdV-16-2i	1616741.20	1764237.20	7457.1	7062.1	395	Qbt1g	Qct	Kleinfelder 2004b	—
CdV-16-2i	1616741.20	1764237.20	7457.1	6992.1	465	Qct	Qbof	—	5/1/2011
CdV-16-2i	1616741.20	1764237.20	7457.1	6655.1	802	Qbof	Qbog	Kleinfelder 2004b	—
CdV-16-2i	1616741.20	1764237.20	7457.1	6639.1	818	Qbog	Tpf	Kleinfelder 2004b	—
CdV-16-2i	1616741.20	1764237.20	7457.1	6394.1	1063	Tpf	Tpf	Kleinfelder 2004b	—
CdV-16-4ip	1615587.10	1764195.70	7463.9	7463.9	0	Qbt4	Qbt4	LANL 2011a	—
CdV-16-4ip	1615587.10	1764195.70	7463.9	7413.9	50	Qbt4	Qbt3t	LANL 2011a	7/7/2011

Table G-1.0-1 (continued)

Location	Easting (ft)	Northing (ft)	Surface Elevation (ft)	Contact Elevation (ft)	Contact Depth (ft bgs)	Upper Contact	Lower Contact	Data Reference	Date Modified
CdV-16-4ip	1615587.10	1764195.70	7463.9	7373.9	90	Qbt3t	Qbt3	LANL 2011a	7/7/2011
CdV-16-4ip	1615587.10	1764195.70	7463.9	7283.9	180	Qbt3	Qbt2	LANL 2011a	—
CdV-16-4ip	1615587.10	1764195.70	7463.9	7183.9	280	Qbt2	Qbt1v	This report	—
CdV-16-4ip	1615587.10	1764195.70	7463.9	7143.9	320	Qbt1v	Qbt1g	This report	—
CdV-16-4ip	1615587.10	1764195.70	7463.9	7123.9	340	Qbt1g	Qct	LANL 2011a	—
CdV-16-4ip	1615587.10	1764195.70	7463.9	7001.9	462	Qct	Qbof	This report	—
CdV-16-4ip	1615587.10	1764195.70	7463.9	6671.9	792	Qbof	Qbog	LANL 2011a	—
CdV-16-4ip	1615587.10	1764195.70	7463.9	6663.9	800	Qbog	Tpf	LANL 2011a	—
CdV-16-4ip	1615587.10	1764195.70	7463.9	6310.2	1153.7	Tpf	Tpf	LANL 2011a	—
CdV-37-1i	1624592.30	1757798.60	6826.5	6826.5	0	Qal	Qal	LANL 2010c	—
CdV-37-1i	1624592.30	1757798.60	6826.5	6786.5	40	Qal	Qbt1g	LANL 2010c	—
CdV-37-1i	1624592.30	1757798.60	6826.5	6626.5	200	Qbt1g	Qct	LANL 2010c	—
CdV-37-1i	1624592.30	1757798.60	6826.5	6551.5	275	Qct	Qbof	LANL 2010c	—
CdV-37-1i	1624592.30	1757798.60	6826.5	6306.5	520	Qbof	Qbog	LANL 2010c	—
CdV-37-1i	1624592.30	1757798.60	6826.5	6289.5	537	Qbog	Tpf	LANL 2010c	—
CdV-37-1i	1624592.30	1757798.60	6826.5	6137.5	689	Tpf	Tb4	LANL 2010c	—
CdV-37-1i	1624592.30	1757798.60	6826.5	6086.5	740	Tb4	Tpf	LANL 2010c	—
CdV-37-1i	1624592.30	1757798.60	6826.5	6023.5	803	Tpf	Tpf	LANL 2010c	—
CdV-9-1i	1615198.00	1764997.00	7517.44	7517.44	0	Qu	Qu	LANL 2015a	—
CdV-9-1i	1615198.00	1764997.00	7517.44	7507.44	10	Qu[c]	Qbt4	LANL 2015a	—
CdV-9-1i	1615198.00	1764997.00	7517.44	7432.44	85	Qbt4	Qbt3t	LANL 2015a	—
CdV-9-1i	1615198.00	1764997.00	7517.44	7412.44	105	Qbt3t	Qbt3	LANL 2015a	—
CdV-9-1i	1615198.00	1764997.00	7517.44	7287.44	230	Qbt3	Qbt2	LANL 2015a	—
CdV-9-1i	1615198.00	1764997.00	7517.44	7227.44	330	Qbt2	Qbt1v	This report	—
CdV-9-1i	1615198.00	1764997.00	7517.44	7142.44	375	Qbt1v	Qbt1g	LANL 2015a	—

Table G-1.0-1 (continued)

Location	Easting (ft)	Northing (ft)	Surface Elevation (ft)	Contact Elevation (ft)	Contact Depth (ft bgs)	Upper Contact	Lower Contact	Data Reference	Date Modified
CdV-9-1i	1615198.00	1764997.00	7517.44	7087.44	430	Qbt1g	Qct	LANL 2015, 600503	—
CdV-9-1i	1615198.00	1764997.00	7517.44	7067.44	450	Qct	Qbof	This report	—
CdV-9-1i	1615198.00	1764997.00	7517.44	6712.44	805	Qbof	Qbog	LANL 2015a	—
CdV-9-1i	1615198.00	1764997.00	7517.44	6697.44	820	Qbog	Tpf	LANL 2015a	—
CdV-9-1i	1615198.00	1764997.00	7517.44	6297.44	1220	Tpf	Tpf	LANL 2015a	—
CdV-R-15-3	1623221.00	1762349.20	7258.9	7258.9	0	Qu	Qu	Kopp et al. 2002	—
CdV-R-15-3	1623221.00	1762349.20	7258.9	7253.9	5	Qu	Qbt4	Kopp et al. 2002	—
CdV-R-15-3	1623221.00	1762349.20	7258.9	7224.9	34	Qbt4	Qbt3	Kopp et al. 2002	—
CdV-R-15-3	1623221.00	1762349.20	7258.9	7117.9	141	Qbt3	Qbt2	This report	—
CdV-R-15-3	1623221.00	1762349.20	7258.9	7022.8	236.1	Qbt1vu	Qbt1vu	Kopp et al. 2002	—
CdV-R-15-3	1623221.00	1762349.20	7258.9	7011.9	247	Qbt2	Qbt1vu	Kopp et al. 2002	—
CdV-R-15-3	1623221.00	1762349.20	7258.9	6969	289.9	Qbt1vc	Qbt1vc	Kopp et al. 2002	—
CdV-R-15-3	1623221.00	1762349.20	7258.9	6963.9	295	Qbt1vc	Qbt1g	This report	—
CdV-R-15-3	1623221.00	1762349.20	7258.9	6908.9	360	Qbt1g	Qbtt	This report	—
CdV-R-15-3	1623221.00	1762349.20	7258.9	6896.9	362	Qbtt	Qct	Kopp et al. 2002	—
CdV-R-15-3	1623221.00	1762349.20	7258.9	6676.9	582	Qct	Qbof	Kopp et al. 2002	—
CdV-R-15-3	1623221.00	1762349.20	7258.9	6508.9	788	Qbof	Qbog	This report	—
CdV-R-15-3	1623221.00	1762349.20	7258.9	6458.9	800	Qbog	Tpf	Kopp et al. 2002	—
CdV-R-15-3	1623221.00	1762349.20	7258.9	6295.9	963	Tpf	Tvt2	—	07/06/2011
CdV-R-15-3	1623221.00	1762349.20	7258.9	6246.9	1012	Tvt2	Tpf	—	07/06/2011
CdV-R-15-3	1623221.00	1762349.20	7258.9	5536.9	1722	Tpf	Tpf	Kopp et al. 2002	—
CdV-R-37-2	1619219.00	1759327.30	7330.6	7330.6	0	Qbt4	Qbt4	Kopp et al. 2003	—
CdV-R-37-2	1619219.00	1759327.30	7330.6	7270.6	60	Qbt4	Qbt3	This report	—
CdV-R-37-2	1619219.00	1759327.30	7330.6	7121.6	209	Qbt3	Qbt2	Kopp et al. 2003	—
CdV-R-37-2	1619219.00	1759327.30	7330.6	7001.6	329	Qbt2	Qbt1v	Kopp et al. 2003	6/5/2011
CdV-R-37-2	1619219.00	1759327.30	7330.6	6906.6	424	Qbt1v	Qbt1g	Kopp et al. 2003	6/5/2011

Table G-1.0-1 (continued)

Location	Easting (ft)	Northing (ft)	Surface Elevation (ft)	Contact Elevation (ft)	Contact Depth (ft bgs)	Upper Contact	Lower Contact	Data Reference	Date Modified
CdV-R-37-2	1619219.00	1759327.30	7330.6	6841.6	489	Qbt1g	Qct	Kopp et al. 2003	—
CdV-R-37-2	1619219.00	1759327.30	7330.6	6781.6	549	Qct	Qbof	Kopp et al. 2003	—
CdV-R-37-2	1619219.00	1759327.30	7330.6	6443.6	887	Qbof	Qbog	Kopp et al. 2003	—
CdV-R-37-2	1619219.00	1759327.30	7330.6	6428.6	902	Qbog	Tpf	Kopp et al. 2003	—
CdV-R-37-2	1619219.00	1759327.30	7330.6	6258.6	1072	Tpf	Tvt2	Kopp et al. 2003	—
CdV-R-37-2	1619219.00	1759327.30	7330.6	5666.6	1664	Tvt2	Tvt2	Kopp et al. 2003	—
R-18	1617254.40	1766545.50	7404.8	7404.8	0	Qbt3		Kleinfelder 2005a	—
R-18	1617254.40	1766545.50	7404.8	7269.8	135	Qbt3	Qbt2	Kleinfelder 2005a	—
R-18	1617254.40	1766545.50	7404.8	7160.8	244	Qbt2	Qbt1vu	Kleinfelder 2005a	—
R-18	1617254.40	1766545.50	7404.8	7160.7	244.1	Qbt1vu	Qbt1vu	Kleinfelder 2005a	—
R-18	1617254.40	1766545.50	7404.8	7126.9	277.9	Qbt1vc	Qbt1vc	Kleinfelder 2005a	—
R-18	1617254.40	1766545.50	7404.8	7124.8	280	Qbt1vc	Qbt1g	This report	—
R-18	1617254.40	1766545.50	7404.8	7094.8	310	Qbt1g	Qct	This report	—
R-18	1617254.40	1766545.50	7404.8	7042.8	362	Qct	Qbof	This report	—
R-18	1617254.40	1766545.50	7404.8	6749.8	655	Qbof	Qbog	Kleinfelder 2005a	—
R-18	1617254.40	1766545.50	7404.8	6739.8	665	Qbog	Tpf	Kleinfelder 2005a	—
R-18	1617254.40	1766545.50	7404.8	5974.8	1430	Tpf	Tpf	Kleinfelder 2005a	—
R-25	1615178.40	1764060.50	7516.1	7516.1	0	Qbt4	Qbt4	Broxton et al. 2002	—
R-25	1615178.40	1764060.50	7516.1	7432.1	84	Qbt4	Qbt3t	Broxton et al. 2002	—
R-25	1615178.40	1764060.50	7516.1	7361.1	155	Qbt3t	Qbt3	This report	—
R-25	1615178.40	1764060.50	7516.1	7287.1	229	Qbt3	Qbt2	Broxton et al. 2002	—
R-25	1615178.40	1764060.50	7516.1	7184.1	332	Qbt2	Qbt1vu	Broxton et al. 2002	—
R-25	1615178.40	1764060.50	7516.1	7184.1	332.1	Qbt1vu	Qbt1vu	Broxton et al. 2002	—
R-25	1615178.40	1764060.50	7516.1	7184.1	369.1	Qbt1vc	Qbt1vc	This report	—
R-25	1615178.40	1764060.50	7516.1	7146.1	370	Qbt1v	Qbt1g	This report	—
R-25	1615178.40	1764060.50	7516.1	7134.3	381.8	Qbt1g	Qbtt	Broxton et al. 2002	—

Table G-1.0-1 (continued)

Location	Easting (ft)	Northing (ft)	Surface Elevation (ft)	Contact Elevation (ft)	Contact Depth (ft bgs)	Upper Contact	Lower Contact	Data Reference	Date Modified
R-25	1615178.40	1764060.50	7516.1	7132.1	384	Qbtt	Qct	Broxton et al. 2002	—
R-25	1615178.40	1764060.50	7516.1	7016.1	500	Qct	Qbof	This report	—
R-25	1615178.40	1764060.50	7516.1	6672.3	843.8	Qbof	Qbog	Broxton et al. 2002	—
R-25	1615178.40	1764060.50	7516.1	6665.6	850.5	Qbog	Tpf	Broxton et al. 2002	—
R-25	1615178.40	1764060.50	7516.1	5574.1	1942	Tpf	Tpf	Broxton et al. 2002	—
R-25c	1615158.00	1764060.00	7516	7516	0	Qbt4	Qbt4	LANL 2008	—
R-25c	1615158.00	1764060.00	7516	7432	84	Qbt4	Qbt3t	LANL 2008	—
R-25c	1615158.00	1764060.00	7516	7361	155	Qbt3t	Qbt3	This report	—
R-25c	1615158.00	1764060.00	7516	7288	228	Qbt3	Qbt2	LANL 2008	—
R-25c	1615158.00	1764060.00	7516	7184	332	Qbt2	Qbt1vu	LANL 2008	—
R-25c	1615158.00	1764060.00	7516	7146	370	Qbt1vu	Qbt1g	This report	—
R-25c	1615158.00	1764060.00	7516	7132	384	Qbt1g	Qct	LANL 2008	—
R-25c	1615158.00	1764060.00	7516	7016	500	Qct	Qbof	This report	—
R-25c	1615158.00	1764060.00	7516	6673	843	Qbof	Qbog	LANL 2008	—
R-25c	1615158.00	1764060.00	7516	6666	850	Qbog	Tpf	LANL 2008	—
R-25c	1615158.00	1764060.00	7516	6376	1140	Tpf	Tpf	LANL 2008	—
R-26	1610267.30	1764721.10	7641.7	7641.7	0	Qu	Qu	This report	—
R-26	1610267.30	1764721.10	7641.7	7581.7	60	Qu	Qbt4	Kleinfelder 2005b	—
R-26	1610267.30	1764721.10	7641.7	7521.7	120	Qbt4	Qbt3t	Kleinfelder 2005b	—
R-26	1610267.30	1764721.10	7641.7	7341.7	300	Qbt3t	Qbt3	Kleinfelder 2005b	—
R-26	1610267.30	1764721.10	7641.7	7276.7	365	Qbt3	Qbt2	Kleinfelder 2005b	—
R-26	1610267.30	1764721.10	7641.7	7176.7	465	Qbt2	Qbt1vu	Kleinfelder 2005b	—
R-26	1610267.30	1764721.10	7641.7	7156.7	485	Qbt1vu	Qbt1g	This report	—
R-26	1610267.30	1764721.10	7641.7	7136.7	505	Qbt1g	Qct	This report	—
R-26	1610267.30	1764721.10	7641.7	6979.3	662.4	Qct	Qbof	This report	—
R-26	1610267.30	1764721.10	7641.7	6690.2	951.5	Qbof	Qbog	This report	—

Table G-1.0-1 (continued)

Location	Easting (ft)	Northing (ft)	Surface Elevation (ft)	Contact Elevation (ft)	Contact Depth (ft bgs)	Upper Contact	Lower Contact	Data Reference	Date Modified
R-26	1610267.30	1764721.10	7641.7	6686.7	956	Qbog	Tpf	This report	—
R-26	1610267.30	1764721.10	7641.7	6151.2	1490.5	Tpf	Tpf	Kleinfelder 2005b	—
R-47	1617641.36	1765581.72	7423.37	7423.37	0	Qbt4	Qbt4	LANL 2014	—
R-47	1617641.36	1765581.72	7423.37	7383.37	40	Qbt4	Qbt3	LANL 2014	—
R-47	1617641.36	1765581.72	7423.37	7254.37	169	Qbt3	Qbt2	This report	—
R-47	1617641.36	1765581.72	7423.37	7143.37	280	Qbt2	Qbt1v	LANL 2014	—
R-47	1617641.36	1765581.72	7423.37	7098.37	325	Qbt1v	Qbt1g	LANL 2014	—
R-47	1617641.36	1765581.72	7423.37	7078.37	345	Qbt1g	Qct	This report	—
R-47	1617641.36	1765581.72	7423.37	6978.37	445	Qct	Qbof	This report	—
R-47	1617641.36	1765581.72	7423.37	6698.37	725	Qbof	Qbog	LANL 2014	—
R-47	1617641.36	1765581.72	7423.37	6687.37	736	Qbog	Tpf	LANL 2014	—
R-47	1617641.36	1765581.72	7423.37	6026.37	1397	Tpf	Tpf	LANL 2014	—
R-47i	1619250.00	1763907.90	7358.4	7358.4	0	Qu	Qu	LANL 2010b	—
R-47i	1619250.00	1763907.90	7358.4	7353.4	5	Qu	Qbt4	LANL 2010b	—
R-47i	1619250.00	1763907.90	7358.4	7338.4	20	Qbt4	Qbt3	LANL 2010b	—
R-47i	1619250.00	1763907.90	7358.4	7203.4	155	Qbt3	Qbt2	LANL 2010b	—
R-47i	1619250.00	1763907.90	7358.4	7098.4	260	Qbt2	Qbt1v	LANL 2010b	—
R-47i	1619250.00	1763907.90	7358.4	7048.4	310	Qbt1v	Qbt1g	This report	—
R-47i	1619250.00	1763907.90	7358.4	7012.4	346	Qbt1g	Qct	This report	—
R-47i	1619250.00	1763907.90	7358.4	6926.4	432	Qct	Qbof	This report	—
R-47i	1619250.00	1763907.90	7358.4	6597.4	761	Qbof	Qbog	LANL 2010b	—
R-47i	1619250.00	1763907.90	7358.4	6589.4	769	Qbog	Tpf	LANL 2010b	—
R-47i	1619250.00	1763907.90	7358.4	6007.9	1350.5	Tpf	Tpf	LANL 2010b	—
R-48	1615977.30	1762436.20	7486.8	7486.8	0	Qbt4	Qbt4	LANL 2010	—
R-48	1615977.30	1762436.20	7486.8	7416.8	70	Qbt4	Qbt3t	LANL 2010	—
R-48	1615977.30	1762436.20	7486.8	7398.8	88	Qbt3t	Qbt3	LANL 2010	—

Table G-1.0-1 (continued)

Location	Easting (ft)	Northing (ft)	Surface Elevation (ft)	Contact Elevation (ft)	Contact Depth (ft bgs)	Upper Contact	Lower Contact	Data Reference	Date Modified
R-48	1615977.30	1762436.20	7486.8	7279.8	207	Qbt3	Qbt2	LANL 2010	—
R-48	1615977.30	1762436.20	7486.8	7176.8	310	Qbt2	Qbt1v	LANL 2010	—
R-48	1615977.30	1762436.20	7486.8	7141.8	345	Qbt1v	Qbt1g	LANL 2010	—
R-48	1615977.30	1762436.20	7486.8	7127.8	359	Qbt1g	Qct	LANL 2010	—
R-48	1615977.30	1762436.20	7486.8	7056.8	430	Qct	Qbof	This report	—
R-48	1615977.30	1762436.20	7486.8	6592.8	894	Qbof	Qbog	LANL 2010	—
R-48	1615977.30	1762436.20	7486.8	6586.8	900	Qbog	Tpf	LANL 2010	—
R-48	1615977.30	1762436.20	7486.8	6491.8	995	Tpf	Tvt2	LANL 2010	—
R-48	1615977.30	1762436.20	7486.8	5781.8	1705	Tvt2	Tvt2	LANL 2010	—
R-58	1619374.00	1761398.00	7370	7370	0	Qbt4	Qbt4	LANL 2016	—
R-58	1619374.00	1761398.00	7370	7260	110	Qbt4	Qbt3t	LANL 2016	—
R-58	1619374.00	1761398.00	7370	7240	130	Qbt3t	Qbt3	LANL 2016	—
R-58	1619374.00	1761398.00	7370	7110	260	Qbt3	Qbt2	LANL 2016	—
R-58	1619374.00	1761398.00	7370	7015	355	Qbt2	Qbt1v	LANL 2016	—
R-58	1619374.00	1761398.00	7370	6970	400	Qbt1v	Qbt1g	LANL 2016	—
R-58	1619374.00	1761398.00	7370	6890	480	Qbt1g	Qct	LANL 2016	—
R-58	1619374.00	1761398.00	7370	6755	615	Qct	Qbof	LANL 2016	—
R-58	1619374.00	1761398.00	7370	6496	874	Qbof	Qbog	LANL 2016	—
R-58	1619374.00	1761398.00	7370	6481	889	Qbog	Tpf	LANL 2016	—
R-58	1619374.00	1761398.00	7370	6183	1187	Tpf	Tvt2	LANL 2016	—
R-58	1619374.00	1761398.00	7370	5992	1378	Tpf	Tpf	LANL 2016	—
R-58	1619374.00	1761398.00	7370	5992	1378	Tvt2	Tvt2	LANL 2016	—
R-63	1616550.70	1764532.50	7454.6	7454.6	0	Qbt4	Qbt4	LANL 2011b	—
R-63	1616550.70	1764532.50	7454.6	7399.6	55	Qbt4	Qbt3t	LANL 2011b	—
R-63	1616550.70	1764532.50	7454.6	7377.6	77	Qbt3t	Qbt3	LANL 2011b	—
R-63	1616550.70	1764532.50	7454.6	7249.6	205	Qbt3	Qbt2	LANL 2011b	—

Table G-1.0-1 (continued)

Location	Easting (ft)	Northing (ft)	Surface Elevation (ft)	Contact Elevation (ft)	Contact Depth (ft bgs)	Upper Contact	Lower Contact	Data Reference	Date Modified
R-63	1616550.70	1764532.50	7454.6	7159.6	295	Qbt2	Qbt1v	This report	—
R-63	1616550.70	1764532.50	7454.6	7114.6	340	Qbt1v	Qbt1g	LANL 2011b	—
R-63	1616550.70	1764532.50	7454.6	7094.6	360	Qbt1g	Qct	This report	—
R-63	1616550.70	1764532.50	7454.6	7044.6	410	Qct	Qbof	This report	—
R-63	1616550.70	1764532.50	7454.6	6667.6	787	Qbof	Qbog	LANL 2011b	—
R-63	1616550.70	1764532.50	7454.6	6658.6	796	Qbog	Tpf	LANL 2011b	—
R-63	1616550.70	1764532.50	7454.6	6030.8	1423.8	Tpf	Tpf	LANL 2011b	—
R-63i	1616520.27	1764507.14	7455.4	7455.4	0	Qbt4	Qbt4	LANL 2011b	—
R-63i	1616520.27	1764507.14	7455.4	7400.4	55	Qbt4	Qbt3t	LANL 2011b	—
R-63i	1616520.27	1764507.14	7455.4	7378.4	77	Qbt3t	Qbt3	LANL 2011b	—
R-63i	1616520.27	1764507.14	7455.4	7250.4	205	Qbt3	Qbt2	LANL 2011b	—
R-63i	1616520.27	1764507.14	7455.4	7160.4	295	Qbt2	Qbt1v	This report	—
R-63i	1616520.27	1764507.14	7455.4	7115.4	340	Qbt1v	Qbt1g	LANL 2015b	—
R-63i	1616520.27	1764507.14	7455.4	7095.4	360	Qbt1g	Qct	This report	—
R-63i	1616520.27	1764507.14	7455.4	7045.4	410	Qct	Qbof	This report	—
R-63i	1616520.27	1764507.14	7455.4	6670.4	785	Qbof	Qbog	LANL 2015b	—
R-63i	1616520.27	1764507.14	7455.4	6660.4	795	Qbog	Tpf	LANL 2015b	—
R-63i	1616520.27	1764507.14	7455.4	6230.4	1225	Tpf	Tpf	LANL 2015b	—
R-68	1615835.26	1765398.48	7511.31	7511.31	0	Qbt4	Qbt4	LANL 2017	—
R-68	1615835.26	1765398.48	7511.31	7409.31	102	Qbt4	Qbt3t	LANL 2017	—
R-68	1615835.26	1765398.48	7511.31	7376.31	135	Qbt3t	Qbt3	LANL 2017	—
R-68	1615835.26	1765398.48	7511.31	7276.31	235	Qbt3	Qbt2	LANL 2017	—
R-68	1615835.26	1765398.48	7511.31	7176.31	335	Qbt2	Qbt1v	LANL 2017	—
R-68	1615835.26	1765398.48	7511.31	7141.31	370	Qbt1v	Cobble bed	LANL 2017	—

Table G-1.0-1 (continued)

Location	Easting (ft)	Northing (ft)	Surface Elevation (ft)	Contact Elevation (ft)	Contact Depth (ft bgs)	Upper Contact	Lower Contact	Data Reference	Date Modified
R-68	1615835.26	1765398.48	7511.31	7125.31	386	Cobble bed	Qbt1g	LANL 2017	—
R-68	1615835.26	1765398.48	7511.31	7052.31	459	Qbt1g	Qct	LANL 2017	—
R-68	1615835.26	1765398.48	7511.31	7046.31	465	Qct	Qbof	LANL 2017	—
R-68	1615835.26	1765398.48	7511.31	6721.31	790	Qbof	Qbog	LANL 2017	—
R-68	1615835.26	1765398.48	7511.31	6701.31	810	Qbog	Tpf	LANL 2017	—
R-68	1615835.26	1765398.48	7511.31	6088.51	1422.8	Tpf	Tpf	LANL 2017	—
SHB-3	1609310.00	1760990.00	7607.7	7607.7	0	Qal	Qal	This report	—
SHB-3	1609310.00	1760990.00	7607.7	7602.7	5	Qal	Qbt5	This report	—
SHB-3	1609310.00	1760990.00	7607.7	7554.7	53	Qbt4	Qbt3t	This report	—
SHB-3	1609310.00	1760990.00	7607.7	7450.2	157.5	Qbt3t	Qbt3	This report	—
SHB-3	1609310.00	1760990.00	7607.7	7374.7	233	Qbt3	Qbt2	This report	—
SHB-3	1609310.00	1760990.00	7607.7	7281.2	326.5	Qbt2	Qbt1v/1g	This report	—
SHB-3	1609310.00	1760990.00	7607.7	7273.7	334	Qbt1g	Qct	This report	—
SHB-3	1609310.00	1760990.00	7607.7	7199.2	408.5	Qct	Qbof	This report	—
SHB-3	1609310.00	1760990.00	7607.7	6769.7	838	Qbof	Qbog	Gardner et al. 1993	—
SHB-3	1609310.00	1760990.00	7607.7	6768.6	839.1	Qbog	Tpf	Gardner et al. 1993	—
SHB-3	1609310.00	1760990.00	7607.7	6747.7	860	Tpf	Tpf	Gardner et al. 1993	—

Qal = Quaternary Alluvium, Qbt = Tshirege Member, Bandelier Tuff; Qbtt = Tsankawi Pumice Bed; Qct = Cerro Toledo Formation; Qbof = Otowi Member, Bandelier Tuff: Qbog = Guaje Pumice Bed; Tvt2 = Tschicoma Formation (3–3.5 Ma); Tpf = Puye Formation.in Table G-1.

[a] This report = Updates to geologic contacts based on reexamination of cuttings by Los Alamos National Laboratory geologists as part of this investigation.

[b] – = Not available.

[C] Qu = Quaternary, undifferentiated.

LA-UR-18-21326
March 2018
EP2018-0020

A Refined Hydrogeochemical Conceptual Model for the RDX Project

Attachment 3

Los Alamos
NATIONAL LABORATORY
EST. 1943

Prepared by the Associate Directorate for Environmental Management

EXECUTIVE SUMMARY

Recent studies of hydrogeochemical and isotopic data from Technical Area 16 (TA-16) and the surrounding area provide valuable insights on the hydrologic system as it pertains to controls on high explosives (HE) transport and extent, as well as how the overall system functions. This report focuses on the main saturated zones at TA-16, including the regional aquifer, perched-intermediate groundwater zones, springs, alluvial groundwater zone, and Cañon de Valle stream flow. Overall, these new results support the previously developed TA-16 site conceptual model, which suggests that the model is robust and representative. However, these results extend the conceptual model in important ways and address some previously identified key gaps in the model.

One data gap for TA-16 is that there has not been a comprehensive evaluation using all of the TA-16 geochemistry samples. So while it is clear there are distinct groundwater zones spatially, it was not clear how similar or different the zones are geochemically, except on a somewhat ad hoc basis. The broad statistical approach helps clarify water sources and flow paths as well as highlight important geochemical differences between zones. Factor analysis was performed to understand the “global” TA-16 geochemistry dataset collected over the last several years and identify possible relations among analytes. Using the factor analysis results, specific analytes were used to test for statistically significant differences between zones. Results show that the groundwater zones that have been spatially recognized as part of the TA-16 conceptual model for many years are also geochemically distinct. These zones include the regional aquifer, upper and lower perched-intermediate zones, springs, and alluvial zone. Thus, these groundwater zone geochemistries are all reflective of different flow paths through different lithologic units. Lithium and chloride were found to be very good indicators of long, deep flow paths where highly statistically significant differences were found between the regional and perched-intermediate zones and the shallower zones.

Concentration-discharge data collected over a 10-year period show relatively constant RDX (hexahydro-1,3,5-trinitro-1,3,5-triazine) and barium concentrations (along with other major ions) on a log basis over a range of discharges for Burning Ground Spring, Sanitary Wastewater Systems Consolidation Spring, and Cañon de Valle surface water. This behavior is known as chemostatic and has important implications for TA-16. First, it suggests there are soluble sources of RDX and barium at TA-16 that behave like natural mineral weathering products. Second, it implies that even though there have been source removals and grouting in and around the 260 Outfall area, there will still be an extended residence time for RDX in the shallower zones at TA-16, and for barium in the alluvial sediments.

The impact of local TA-16 recharge from the reach of Cañon de Valle below the 260 Outfall on perched-intermediate groundwater, and particularly the regional aquifer, is of primary concern because of HE transport. Analyses of stable isotopes, groundwater ages, and RDX data reveal that perched-intermediate groundwater and the top ~100 feet of the regional aquifer in close proximity to the perennial reach of Cañon de Valle below the 260 Outfall are the most impacted compared to areas further away on the TA-16 mesa. Maps of the isotope and RDX data have some variability, but show generally consistent hotspots associated with Cañon de Valle below the 260 Outfall. A limited number of perched-intermediate zone wells in this area show rapid (6 to 12 month) chemical responses to natural tracers of post-fire floods, indicating the presence of preferential flow connections to the perched-intermediate zone.

The relative proportions of local recharge from lower Cañon de Valle, which is the main vector for deep contaminant transport, vs uncontaminated mountain block/mountain front recharge from the Jemez Mountains and upper Cañon de Valle to perched-intermediate groundwater and the regional aquifer is another important aspect. A water balance of streamflow lost in upper Cañon de Valle vs that returned in lower Cañon de Valle at TA-16 suggests significant quantities of mountain block recharge (MBR) to the perched-intermediate zone and the regional aquifer above the Pajarito fault zone. Results show that the majority of this recharge to deep groundwater occurs during snowmelt. To examine the importance of MBR further, and better understand differences in contributions to the perched-intermediate zone and regional aquifer, two separate mixing model approaches were used. Despite using different methods, both models show that MBR dominates within the regional aquifer, having greater than 90% mountain block contributions and perched-intermediate groundwater having greater than 40% contributions. The large quantities of MBR should strongly moderate HE concentrations over time, especially in the regional aquifer. Thus, in addition to the quantities of HE released at TA-16 and the multi-decadal release period, the percentage of MBR is probably one of the most critical factors controlling RDX concentrations and transport over the long term.

CONTENTS

Figures

Tables

Appendix

Appendix A Supplementary Chemical and Stable Isotope Data

1.0 HYDROLOGICAL ZONE STATISTICAL CHEMICAL CHARACTERIZATION AND DIFFERENCES

1.1 Introduction

Seven main hydrological zones have been identified in the Technical Area 16 (TA-16) area, and these form the basis of the site conceptual model (LANL 2003a; LANL 2011). They include (1) the TA-16 vadose zone, (2) the three “perennial” springs, (3) stream water, (4) alluvial groundwater, (5) upper perched-intermediate groundwater, (6) lower perched-intermediate groundwater, and (7) the regional aquifer. This evaluation examines the five “saturated” parts of the system (i.e., everything but the vadose zone and stream water) from a geochemical perspective because there is more uncertainty about their origins than surface or vadose zone waters. Water samples from the vadose zone are sparse and stream water was deemed irrelevant to the key objective of understanding how different ground water zones are from each other. It is clear that the five saturated zones are distinct from a spatial perspective, but there has not been a broad-based statistical examination about how different these zones are from a geochemical point of view. There has been extensive evaluation of concentrations of important contaminants such as RDX (hexahydro-1,3,5-trinitro-1,3,5-triazine) in these zones (LANL 2003a; LANL, 2003b; LANL 2011), but not the broader suite of anions and cations. The TA-16 system is complex, and a broad statistical analysis has the potential to help clarify issues about hydrological connectivity, as well as provide understanding of how different hydrological flow paths might be influencing the zone chemistries. It may also be possible to discern certain geochemical fingerprints that have important implications for how the TA-16 hydrogeochemical system behaves. Insights into any of these aspects are valuable for understanding the potential for breakdown of high explosives (HE) and other controls on contaminant concentrations and transport.

The statistical approach used here is similar to those sometimes used to define hydrochemical facies in groundwater basins (Back 1966; Newman et al. 2016). According to Back (1966), hydrochemical facies “… denote the diagnostic chemical aspect of groundwater solutions occurring in hydrologic systems. Hydrochemical facies reflect the response of chemical processes operating within the lithologic framework and also the pattern of flow of the water.” Although the five TA-16 groundwater zones would not typically be considered as individual hydrochemical facies, the approaches used to define hydrochemical facies are certainly relevant to understanding the TA-16 zones.

One challenge to the TA-16 system is that there is an overwhelming amount of water chemistry data available. However, by using statistical methods, it is possible to identify and distill important observations and relations, and the large data set becomes an advantage.

1.2 Methods

Data used for this analysis were retrieved from the Los Alamos National Laboratory (LANL or the Laboratory) Environmental Information Management System (EIM) on April 9, 2015. Any samples analyzed from the five zones at TA-16 were used, and results for anions, major cations, RDX, and HMX (octahydro-1,3,5,7-tetranitro-1,3,5,7-tetrazocine) were used. Data for other organics were not used because of the high frequency of non-detections. This data set initially started with 130,783 chemical measurements, with each analyte separately listed for every measurement. In this format, different analytes that were measured on the same sample (i.e., from the same well collected on the same day) were reported as completely separate data points. In order to run multivariate analyses, data were restructured, rotated, and reduced based on individual sample water chemistries as identified by (1) well or spring location, and (2) date of sampling. These manipulations were necessary to identify full chemical suites within samples and to compare chemistry across samples. As is typical in statistical analyses, any non-detections were replaced with a value of ½ the detection limit for the particular analyte. The resulting dataset contained 1,410 samples with 31 analytes that could be analyzed by zone.

Data analysis methods consisted of first producing fingerprint diagrams (Mazor 2003; Shoeller 1959) to represent the geochemistry of the different zones. Fingerprint diagrams were generated based on the TA-16 chemical analyses by converting concentration data from mg/L to meq/L, and plotting cations on the left and anions on the right on a semi-logarithmic diagram. Straight lines are used to connect the concentration points forming cation and anion traces that represent a particular water sample. Distinctly different patterns based on concentration differences or relative relationships between ions from different water samples suggest waters have different origins or flow paths. A complete discussion on construction and interpretation of fingerprint diagrams can be found in Mazor (2003). Fingerprint diagrams are different, in that waters from different parts of the groundwater system will have different patterns in their cation and/or anion traces.

Factor analysis is a multivariate technique that has been used to help define hydrochemical facies and understand geochemical relationships (see Newman et al. 2016 and references therein). Factor analysis has similarities to principal components analysis, but in principal components, individual components are calculated as linear combinations of the original variables, whereas in factor analysis the original variables are defined as linear combinations of the factors. Factor analysis is focused on explaining relationships between the variables, whereas in principal components the goal is to explain as much of the total variance in the variables as possible. For this analysis, R-mode factor analysis was used with the varimax rotation approach (see Newman et al. 2016 and references within for additional discussion about factor analysis). Prior to conducting factor analysis, concentration data were log-transformed because water chemistry data are typically not normally distributed. In addition, standard z-scores (Equation 1) were calculated using the transformed data to reduce the influence of one analyte having much higher concentrations than another (which would unduly bias multivariate statistics toward the higher concentration analytes.

$$z_i = \frac{C_i - \mu}{\sigma}$$ **Equation 1**

After the factor analysis was completed, pairwise comparison tests were made to test for statistically significant differences between zones. Because of the non-normal data and unbalanced comparisons (i.e., one zone may have many more sample analyses than another) a standard T-test was not applied. Instead, a permutation approach was used to assess differences (see Newman et al. [2015] for details).

1.3 Results and Discussion

A fingerprint plot of the average major ion concentrations for each zone is shown in Figure 1.3-1. The plot shows broadly similar chemistries across the zones. Calcium and sodium are the dominant cations in the plot and bicarbonate is the dominant anion. Fingerprint plots are also useful for showing changes in ion ratios, and although there are some minor variations, ratios also tend to be similar across zones. The general similarity of the zone chemistries is not surprising given that the Bandelier Tuff, Cerro Toledo, and Puye Formations are all related to Jemez Mountains volcanic activity.

The overall similarity shown in the fingerprint plot does not preclude differences in chemistry between the zones for individual ions, and there are suggestions of this in the fingerprint plot (Figure 1.3-1). For example, calcium in the lower perched zone is elevated relative to sodium, which contrasts with the other zones, and sulfate has a wide range in concentrations across the zones. In order to evaluate differences and geochemical relations more fully, the factor analysis results are discussed next, followed by the comparison tests results.

Results for the factor analysis are shown in Table 1.3-1. The first four factors are shown along with the factor weightings for each analyte. These four factors account for 57% of the total variance. Higher order factors (5 and higher) represent smaller and smaller variance contributions on an individual basis and are thus not presented. Factor 1 is somewhat surprising because of the types of analytes that have high factor weightings. For example, lead, nickel, and lithium are minor analytes, yet have the highest loadings in the number one factor. These results suggest that some of these minor analytes may have some power in helping us understand differences between the zones, and should not be ignored even though their concentrations are typically low compared to the major ions. The importance of these high-weighted but minor analytes is discussed later in the comparison test results. Factor 2 has high weightings for calcium, hardness, total dissolved solids (TDS), chloride, magnesium, and alkalinity. Except for chloride, this factor appears to represent the affinity of calcium and magnesium and their contributions to hardness. Chloride, calcium, and magnesium are major contributors to TDS. Factor 3 has extremely high weightings for potassium and nitrate. Although they are both nutrients, it is unclear what this factor represents since potassium concentrations have a strong mineral weathering control and nitrate is biologically controlled (natural production and possibly through HE degradation). Nevertheless, their high weightings suggest they may be of interest in terms of differences in zone chemistries. Finally, Factor 4 is dominated by the two HE species RDX and HMX. It also has high weightings for iron and aluminum. The connection between these four analytes will be discussed below in the pairwise comparison section.

For the statistical comparisons, pairwise results for all of the analytes for each zone are presented in Table 1.3-2. Pairs deemed to be significantly to highly significantly different are denoted by * to *** respectively in Table 1.3-2. For this discussion, particular attention is given to analytes whose importance was suggested by virtue of having high factor loadings in one of the first four factors. Results for the selected analytes are shown in box and whisker plots which help show similarities and differences between zones graphically.

For Factor 1, lead and nickel show significant differences between the upper perched and regional zones as well as between the springs and alluvium (Table 1.3-2). Strontium shows significant differences for almost all combinations of pairs and is one of the most sensitive analytes in terms of differences in zonal chemistries (Table 1.3-2). Lithium is one of the most interesting of this group, having highly significant differences between the shallower zones and the deeper zones, the regional and the upper perched, and the regional and the upper/lower perched zones. The box and whisker plot for lithium clearly shows the differences between the shallower and deeper zones, and even between the perched-intermediate and regional zones (Figure 1.3-2). Blake et al. (1995) suggest that lithium is unlikely to have been strongly affected by Laboratory releases and so is one of the better indicators of natural processes. In their Pajarito Plateau–wide study, lithium concentrations were positively correlated with temperature, and they noted that lithium increased in deeper, warmer, older waters. Thus, lithium appears to be a good indicator of deep hydrological flow paths. The box and whisker plots in Figure 1.3-2 suggest there are varying contributions of deep vs shallow flow paths even at the TA-16 scale, and it is likely that these differences are at least partially controlled by increasing amounts of mountain block recharge (MBR) (longer/deeper flow paths) in the lower zones. The differences between the perched-intermediate zone and the regional suggest that the relative proportion of MBR is likely lower in the perched-intermediate. Mixing of different water sources is explored later in section 6.0.

The high loadings for calcium, hardness, and magnesium (Table 1.3-1) are consistent with a mineral weathering control for Factor 2. Geochemical modeling using PHREEQC suggests that calcium in feldspars is one of the main weathering contributions at TA-16 (Brady 2017). Calcium and magnesium concentrations tend to be elevated in the lower perched-intermediate zone, which generates significant differences with the adjacent zones, including the upper perched. The high loading for chloride is inconsistent with the calcium and magnesium, but it is consistent with the relatively high loading for TDS. Chloride is similar to strontium in that it shows significant (and often highly significant) differences for many combinations of zones, including the regional vs the upper and lower perched zones (Table 1.3-2a). It also clearly highlights differences in shallow vs deeper zones (Figure 1.3-3, Table 1.3-2b,). Like lithium, chloride appears to be a good indicator of deeper MBR sources. However, as the box and whisker plots in Figures 1.3-2 and 1.3-3 show, chloride appears to be inversely correlated to lithium. In other words, the shallower systems have high chloride relative to the deeper zones. Chloride is useful, because in non-marine geological systems there are typically little to no contributions (or sinks) of chloride from mineral weathering. Given that the TA-16 geology is silicate-dominated, the main source of chloride is atmospheric, and the main mode of concentrating chloride is evapotranspiration. The higher chloride in the shallower zones is probably from waters that have had near-surface flow paths subject to evapotranspiration, while much of the recharge to the deeper zones came from water that rapidly percolated below the depth where evapotranspiration occurs. Thus, the chloride results also indicate that the deeper zones likely have a substantial contribution from deep mountain block flow paths while the shallower zones have a substantial contribution from flow paths within the root zone.

As discussed earlier, Factor 3 has very high loadings for potassium and nitrate (Table 1.3-1). Like strontium and chloride, potassium is another sensitive indicator of differences showing highly significant differences between all combinations of zones (Table 1.3-2) despite overlaps in ranges shown in the box and whisker plot (Figure 1.3-4). Potassium concentrations tend to be highest in the shallower zones, but are distinctive in all zones (dissimilar 2^{nd}+3^{rd} quartiles and 1.5x interquartile distance; Figure 1.3-4) suggesting variations in potassium-bearing minerals across the TA-16 stratigraphy are large enough to drive differences in groundwater concentrations across relatively small depth scales. At TA-16, nitrate has both natural and Laboratory release–related sources. Highly significant differences were found between all combinations of zones except alluvial vs regional, and upper vs lower perched-intermediate zones (Table 1.3-2). The higher levels of nitrate in the springs is notable (Figure 1.3-5), and may be related to the proximity of Sanitary Wastewater Systems Consolidation (SWSC) and Burning Ground Springs to the 260 Outfall.

The high loadings for RDX, HMX, iron, and aluminum in Factor 4 (Table 1.3-1) were initially puzzling because there is no obvious weathering (iron and aluminum) or Laboratory release–based connection (RDX and HMX). However, the box and whisker plots for iron, aluminum, and HMX especially (Figures 1.3-6 to 1.3-8), show higher median and interquartile distances in the springs and alluvial zones, and have similar box and whisker patterns across the zones. RDX shows the same elevated values for the springs (Figure 1.3-9), although the upper and lower perched zone medians are also elevated compared to the pattern for iron, aluminum, and HMX. The similar patterns in concentration distributions across the zones for these analytes appear to be the reason they have high weightings in the same factor. RDX has highly significant differences between all combinations of zones except the upper vs lower perched-intermediate zones (Table 1.3-2). These differences are probably related to a combination of factors, including different flow paths to the various zones and the variable release history of RDX from the 260 Outfall. HMX had substantial numbers samples with below detection values, so some of the comparisons between zones could not be made. However, it does show significant differences between the springs and alluvial zones, and these shallow zones and the regional zone. Despite its high factor loading, iron did not have any significant differences between zones except for the alluvium and the regional. Significant differences were found for aluminum between the springs and upper perched-intermediate zone, alluvium and the upper perched-intermediate zone, springs and the regional, and alluvium and the regional.

Even though they are not highly weighted analytes in the factor analysis, it is worth examining results for boron and barium because of their known historical Laboratory releases at TA-16 (Figures 1.3-10 and 1.3-11). Boron is clearly elevated in the springs (Figure 1.3-10) and significant differences were found for all comparisons with the springs zone (Table 1.3-2). High boron in Martin Spring is well-documented (LANL 2003a) and is what drives these significant differences. Boron in the deepest zones is more likely controlled by water-rock interactions. Releases of barium as a component of Baratol at TA-16 has also been documented (LANL 2003a; Reid et al. 2005). The box and whisker plot (Figure 1.3-11) clearly shows that most of the barium resides within the alluvial zone. All comparisons with alluvial zone barium are highly significantly different (Table 1.3-2). Reid et al. (2005) showed that much of the barium is tied up within the alluvial sediments as witherite or barite. Given that much of the barium in the alluvial zone is in the solid phase, the residence time of barium in this zone will likely be quite long.

1.4 Conclusions

This broad statistical analysis of the geochemistry of the groundwater zones at TA-16 indicates that not only are these zones hydrologically distinct, but that they each have distinct geochemical signatures. For example, one particular area of interest was whether there were any differences between the upper and lower perched-intermediate zones. Some differences were noted above, but looking broadly across all analytes, there were eleven that showed significantly different to highly significantly different results. Boron, barium, calcium, fluorine, potassium, magnesium, sodium, silicon, strontium, sulfate, and TDS were all significantly different, suggesting that these zones are geochemically distinct. Some of these differences appear to be related to a greater influence of the Bandelier Tuff on the upper zone. Potassium feldspar is more prevalent in the rhyolites of the Bandelier Tuff and may explain the generally higher potassium concentrations in the upper perched-intermediate zone. In contrast, the dacitic provenance of the Puye would be consistent with the higher calcium, magnesium, and strontium observed for the lower perched-intermediate zone.

There are also other zones where it is interesting to review comparisons. It seems plausible that the springs and the upper perched-intermediate zones could have a limited flow connection within the mesa via saturated ribbons in the vadose zone that feed the springs (LANL 2011). The site conceptual model (see section 7.0) also suggests there is an important connection from Cañon de Valle to the upper perched-intermediate zone. However, in both cases, 27 of 31 analytes have significant to highly significant differences with the upper perched-intermediate zone (note that they are not the same 27 for the two comparisons). These large differences in geochemistry suggest there must be a substantial change resulting from water rock interaction along any potential flow paths down to the upper perched zone, and/or there must be a substantially large amount of water with a different chemistry that is contributing to the upper perched-intermediate zone that is not from the local TA-16 area. This additional source is explored further in later sections of this report. Finally, there are also distinct differences between the perched-intermediate zones and the regional zone. Thirteen of the 31 analytes are significantly different between the lower perched-intermediate zone and the regional zone, and 19 of 31 are significantly different between the upper perched-intermediate zone and the regional. Among these differences chloride and lithium are particularly noteworthy, and are discussed in more detail in later sections.

2.0 CONCENTRATION-DISCHARGE RELATIONSHIPS

2.1 Introduction

The relationship between concentrations of dissolved species and discharge provides valuable information about the nature of water-rock interaction along hydrological flow paths. Log-log plots of concentration vs discharge are used to assess whether a solute in a hydrologic system behaves chemostatically (concentration varies little relative to discharge) or if its concentration responds to varying discharge in a systematic way. It is often difficult to discern patterns from regular concentration-discharge plots. However, Godsey et al. (2009) showed that plots of log concentration vs log discharge can be highly informative. Zero or slightly negative log concentration-log discharge slopes indicate chemostatic behavior of a system, in other words one that is not supply- or weathering-rate limited (Godsey et al. 2009). Chemostatic behavior is a type of power law behavior ($C = aQ^b$, Godsey et al., 2009) and is closely tied to the average subsurface residence time of water in a catchment, which must be approximately equal to or greater than the time required for groundwater to approach equilibrium with weathering minerals (Maher 2011). This power law behavior is expressed by Equation 2, where *C* is concentration of the analyte, *a* is a constant, *Q* is discharge, and *b* is the log-log slope.

$$C = aQ^b \qquad \textbf{Equation 2}$$

Pre-event water must be a significant component of streamflow during storm events for chemostatic behavior to prevail (Clow & Mast 2010). With the exception of redox (reduction-oxidation) or biogeochemically sensitive species, chemostatic behavior is the rule rather than the exception for most natural stream systems (Godsey et al. 2009). However, substantial dilution behavior is observed in some watersheds (e.g., Shanley et al. 2011). Major weathering ions (e.g., calcium, sodium, magnesium, and silicon) tend to behave chemostatically, whereas biogeochemically active ions (e.g., iron and nitrate) can increase, decrease, or remain constant with increased discharge, depending upon redox conditions and other factors affecting rates of biological processing (Walling & Webb 1986; Godsey et al. 2009; Duncan et al., 2017).

The focus of this study is the mesa/canyon hydrologic system at TA-16. The local springs and surface water provide an ideal opportunity to investigate concentration-discharge relationships in three spring systems and in a perennially-flowing reach of a stream channel that is ephemeral for most of its length. Near-surface water systems of TA-16 have been under intensive investigation and monitoring since the mid-1990s because of HE contamination, generating a large water quality data set. The climate is semiarid and the study area is located on the Pajarito Plateau just downslope from a major mountain block fault along the Jemez Mountains.

Despite the extensive investigation of surface water concentration-discharge relations, few spring systems have been studied in depth for chemostatic behavior. In the state of Florida, large-volume springs with an almost constant discharge and temperature have been characterized as chemostatic (Odum 1957; Nifong et al. 2010). To our knowledge, less geologically buffered springs with variable flow characteristics have not been investigated for chemostatic behavior.

The springs and perennial stream of TA-16 at the Laboratory also present a unique opportunity to study the concentration-discharge relations of contaminants. The concentration-discharge behavior of contaminants is important because it can act as a major control of how quickly contaminants are removed from a hydrological system and can impact selection of remediation measures. RDX and barium related to the HE Baratol (TNT [trinitrotoluene(2,4,6-)] and barium nitrate) are contaminants at this site (LANL 2011). High explosives of concern have been made and processed in the TA-16 area since the early 1940s. The largest releases of HE wastewater, mainly through milling operations, to the mesa and canyons of TA-16 occurred from the early 1950s to the mid-1990s from a processing facility called building 260. Most of the HE inventory was released from building 260’s associated outfall on the mesa adjacent to Cañon de Valle (Figure 2.1-1). Some of the wastewater infiltrated the mesa and some flowed directly into a perennial reach of Cañon de Valle (Figure 2.1-1).

RDX is the primary HE exceeding standards or screening levels in surface water and groundwater at TA-16. Other HE released include HMX; TNT; and TATB (triaminotrinitrobenzene) (LANL 2011). RDX solubility in water at 25°C is 59.7 mg/L (US EPA 2014). HMX behaves much like RDX, but is an order of magnitude less soluble in water than RDX (with a solubility limit of ~5 mg/L), so it is typically present at concentrations lower than RDX. TNT sorbs more strongly to clays and other environmental materials than does RDX. It also biodegrades and breaks down via chemical processes in the environment more rapidly than RDX. TATB is extremely insoluble.

Stream and spring water in the TA-16 area can exceed the New Mexico tap water screening level of 7.02 µg/L RDX (NMED 2014). Dissolved concentrations of RDX have been measured at mg/L levels in spring discharge and surface water in canyons adjacent to the TA-16 mesa (LANL 2011). Barium was released as a component of the explosive baritol, and has also been evaluated as a contaminant in Cañon de Valle (Reid et al. 2005).

2.2 Methods

Chemical concentration and discharge data have been collected quarterly for TA-16 springs and stream water from 1995 to 2017, except for some gaps with no sampling and periods with more frequent sampling. Stream discharges were measured at each sampling location using a portable V-notch weir. A permanent gaging station was also used to measure flow in Cañon de Valle from 2005 to 2017. Spring discharges were measured using permanent V-notch weirs with ultrasonic probes (measurement locations are the same as spring locations shown in Figure 2.1-1).

Concentration and discharge data for this study were obtained from the Intellus New Mexico public database (http://intellusnm.com/). Samples were collected and analyzed at multiple laboratories using standard U.S. Environmental Protection Agency (EPA) procedures. Anions were analyzed using ion chromatography. Cations were analyzed using inductively coupled plasma- (ICP-) atomic emission spectroscopy (AES), ICP-optical emission spectroscopy (OES), or ICP-mass spectrometer (MS). Analytical errors for anion analyses are typically better than or equal to ±5%, and cation errors are better than or equal to ±10%. RDX was analyzed using high-performance liquid chromatography (HPLC).

2.3 Results

Concentration-discharge relationships for three perennial springs (Burning Ground and SWSC Springs in Cañon de Valle, and Martin Spring in Martin Canyon) and stream water samples from the perennially flowing reach of Cañon de Valle are presented in Figures 2.3-1 to 2.3-3. Data are presented in log-log space, with an equal number of log cycles on each axis. Four basic categories are devised for classification of the dominant form of the concentration-discharge relationship; chemostatic (slope of 0 or small negative slope); dilution (slope of −1 or large negative slope); mixed chemostatic and dilution (most data plot within the envelope between chemostatic and a −1 dilution slope); and unsystematic (data plot well outside the “mixed” envelope) (Table 2.3-1). Each analyte for the three springs and Cañon de Valle streamflow is assigned to one of these categories based on a visual approximation of data fit to a log-log slope of 0 (chemostatic) or −1 (dilution). To facilitate comparisons of variability between analytes with concentrations that differ by orders of magnitude, coefficient of variation (CV) (CV = SD/mean) were also calculated for each analyte in each hydrologic system as a means of normalizing the data (Table 2.3-2).

The majority of concentration-discharge relationships show chemostatic behavior, particularly the major cations silicon, calcium, and sodium as well as the anions chloride and sulfate (Table 2.3-1, Figure 2.3-1). Concentration-discharge pairs that have mixed chemostatic and dilution trends have generally high coefficients of variation. These data sets include many analytes from Martin Spring (barium and nitrate, with CV 0.53 and 0.51, respectively), nitrate in most data sets (CV 0.36–0.51), silicon dioxide in Burning Ground (CV 0.24), and iron in surface water (CV 1.35) (Table 2.3-2). Surface water consistently shows the greatest variability for each analyte (excluding chloride) (Table 2.3-2).

Redox and biogeochemically sensitive analytes show more variability than major cations and anions (Table 2.3-2). Iron is the only analyte that is consistently unsystematic and shows high CVs from 1.29–1.35 (Table 2.3-2, Figure 2.3-2). Nitrate exhibits both chemostatic and dilution behaviors (Table 2.3-1, Figure 2.3-2). Sulfate is redox sensitive but has low variability compared with iron and nitrate and tends to follow a chemostatic trend (Tables 2.3-1 and 2.3-2).

Despite the generally high variability, Martin Spring shows predominantly chemostatic behavior, with minor dilution behavior. We observed good evidence for dilution at discharges between 0.0001 and 0.0004 m^3/s (Table 2.3-1, Figures 2.3-1B and 2.3-3B). Measurements of calcium and sodium closely track each other over the same time/discharge interval, implying dilution (Miller and Drever 1977).

RDX concentrations in the springs are most variable (CV 0.54–1.16) compared with other analytes besides iron but have an overall log-log slope close to 0 for the evaluated water systems (Table 2.3-2, Figure 2.3-3). Stream water RDX concentrations in Cañon de Valle plot in a wide spread between the regression and dilution lines, indicating a mixture of both chemostatic and dilution behaviors. RDX in Martin Spring is unsystematic. Barium concentrations are generally chemostatic, with some variability (CV 0.25 – 0.73) (Figure 2.3-3, Tables 2.3-1 and 2.3-2).

2.4 Discussion

At TA-16, we observe chemostatic behavior in Burning Ground and SWSC Springs and Cañon de Valle surface water for all examined analytes except iron and nitrate. Few dissolved analytes are in perfect chemostasis, instead displaying variability and occasional outliers in log-log plots. Analytes sensitive to redox and biogeochemical processes display the most variability or stronger dilution behavior, as do many of the analytes in Martin Spring (Tables 2.3-1 and 2.3-2, Figure 2.3-2). The redox ladder describes how stable ions are with increasingly reducing conditions (nitrate>iron>sulfate) (Borch et al. 2010). The TA-16 results are revealing in the context of the redox ladder. Nitrate displays both chemostatic and dilution behavior (Figure 2.3-2). This duality may be from transient reducing conditions (stable nitrate during oxic conditions and unstable nitrate under more reducing conditions) or from biological influences.

Nitrate contents in the soil are dependent on biologic productivity, with positive slope concentration-discharge relationships in watersheds with relatively high levels of biologic productivity (Walling and Webb 1986). Semiarid climates such as this one are typically nitrogen limited (e.g., Valett et al. 1997). Given the semiarid climate of Los Alamos, NM, and proximity to the mountain front, biologic productivity is lower than catchments with thick organic soil horizons. Biologic productivity in TA-16 hydrologic catchments is likely often insufficient to compensate for higher flows that could result in dilution. Nitrate has also been observed to behave chemostatically on an event scale but shows dilution behavior over longer time scales (Duncan et al., 2017). This behavior occurs because of different concentration-discharge patterns for different events and supports the idea that nitrate can show both dilution and chemostatic concentration-discharge behaviors. Iron displays unsystematic, discharge-independent changes in concentration that indicate transient reducing conditions. Studies of the Rio Calaveras alluvial aquifer, an analog for Cañon de Valle, also located in the Jemez Mountains of northern New Mexico, show that reducing conditions prevail during times of little recharge (e.g., winter) and oxidizing conditions occur during times of high recharge (e.g., spring) (Groffman & Crossey 1999; Newman et al. 2006). Similar conditions likely prevail at TA-16. In contrast to nitrate, sulfate is chemostatic with relatively low variability, showing that reducing conditions typically are not sufficient to reach sulfate reduction.

Martin Spring has been noted to have a unique flow and chemistry, distinct from the two Cañon de Valle springs, even though it discharges on the opposite side of the same mesa (LANL 2003a). However, Martin Spring issues from stratigraphically higher rocks than the two Cañon de Valle springs and the two spring systems are probably not hydrologically connected. It has a variable and generally lower discharge than the other two springs and has ceased to flow during drought years in the recent past (LANL 2011). Calcium and sodium closely track each other on a slope close to −1 between discharges of 0.0001 and 0.0004 m^3/s (during the same period), suggesting dilution behavior (Figure 2.3-1). However, the dominant behavior is chemostatic. RDX follows the same dilution pattern in that discharge range (Figure 2.3-3). This behavior suggests transient, moderately high flow conditions cause dilution in Martin Spring. The stable isotopes $\delta^{18}O$ and $\delta^{2}H$ can be used as tracers to determine the proportion of event (precipitation) vs pre-event (groundwater) water in streams and springs during and following precipitation events. Earlier studies on Martin Spring used this approach to calculate percent of event-water during different precipitation events, finding that flow ranged from 0% to 85% event-water (LANL 2003a). The large range in percent event-water between different precipitation events may account for the different behaviors seen in Martin Spring because of the importance of sufficient residence time to facilitate chemostatic behavior (Maher 2011).

Springs can have longer average hydrological residence times than streams. Logically, longer spring residence times should translate to stronger chemostatic behavior than streams. Martin Spring runs contrary to this assumption. Martin Spring's relatively small catchment size and its hydrologic system's near-surface nature could lower the mean residence time of discharge, making it more chemically sensitive to recent rainfall and snowmelt. The range in behaviors at Martin Spring and the contrast between it and Burning Ground and SWSC Springs highlight the need for further study of the chemical behavior in springs.

RDX concentration-discharge relationships give us insight into what controls RDX fluxes in springs and surface water (Figure 2.3-3). The graphs showing concentration discharge for RDX show general chemostatic behavior, indicating it behaves like a weathering product. This observation is key, demonstrating that chemostatic behavior can extend to anthropogenic contaminants in addition to natural weathering products. RDX's behavior implies a reservoir of solid particulate matter in the mesa that responds to increased flow with increased RDX flux. Weight percent RDX has been measured in soils removed from the vicinity of the outfall retention pond, and particulate phase RDX was produced by milling operations (Gard & Newman 2006). It is also possible chemostatic behavior results from the storage of dissolved RDX in relatively immobile (low permeability, small pore spaces, and/or unsaturated) parts of the extensive vadose zone at TA-16. As these immobile regions saturate, they could mix with mobile fractions of groundwater. These results suggest net RDX flux is not currently supply-limited. Contaminated soil removals from the outfall area were conducted in 2000 and 2001 (LANL 2003b). However, Burning Ground and SWSC Spring RDX concentrations have not declined significantly (Reid et al. 2005; LANL 2017), further supporting the importance of solubility control of RDX coupled with a long enough hydrological residence time to produce chemostatic behavior (Maher et al. 2011).

RDX concentration-discharge data are more variable than most other analytes, despite overall chemostatic behavior (CV 0.54–1.16). RDX is not broadly distributed in the vadose zone, unlike other analytes examined. Given the semiarid conditions, different flow paths are likely utilized during different storm events depending on the antecedent moisture conditions. Preferential flow paths in the vadose zone beneath TA-16 mesas support "ribbons" of saturated flow in a heterogeneous and transient distribution (LANL 2011). These may be responsible for variable RDX concentrations in springs discharge. RDX is also a redox-sensitive species and is prone to photodegradation (EPA 2014), which may account for the high variability observed in Cañon de Valle. A final factor likely influencing variability in discharge concentrations is that RDX releases at TA-16 varied considerably over multiple decades.

Although Martin Spring shows some dilution behavior and RDX concentrations in discharge have gradually decreased over time, Martin Spring Canyon contains only <0.5% of the total estimated RDX inventory (LANL 2011; LANL 2017). The variability in the distribution of concentration-discharge data at Martin Spring may be from heterogeneity in the distribution of RDX source areas and its variable release history. Martin Spring is not impacted by building 260, and other HE-processing areas were located closer to Martin Spring (LANL 2011). As noted earlier, there is a wide range of event-water percentages in Martin Spring based on stable isotopes. This result is also consistent with mixed concentration-discharge behaviors in Martin Spring.

Barium also behaves chemostatically because its primary occurrence in Cañon de Valle is in the minerals barite and witherite (Reid et al. 2005). The chemostatic behavior of barium also supports the interpretation that average residence times of spring and surface waters of the TA-16 area are sufficiently long to equilibrate with barium-bearing minerals.

2.5 Conclusions

The TA-16 area at the Laboratory provides a unique opportunity to study the concentration discharge behavior of both natural weathering products and anthropogenic contaminants in springs and stream water. Most cations and anions in the springs and stream behave chemostatically. The exceptions are iron and nitrate, which are affected by redox and biogeochemical conditions to varying degrees. Martin Spring is also an exception that shows mixed chemostatic/dilution and unsystematic behaviors. The range in behaviors of the springs from chemostatic to unsystematic highlights the natural chemical variability of springs and the need for further study. RDX behavior is dominantly chemostatic (excluding Martin Spring), similar to a natural weathering product and indicates export is discharge-controlled and not supply-controlled. This behavior will extend the residence time for RDX, resulting in a longer time period required to flush RDX from the system. The chemostatic behavior of RDX and barium demonstrated here suggests this approach may be beneficial in other contamination studies, and such results can be incorporated into models of long-term contaminant fluxes and transport.

3.0 CAÑON DE VALLE WATER BALANCE

3.1 Introduction

In many semiarid settings, basins are recharged primarily by melt from snowpack at higher elevations (e.g., Rango 2006). Mountain front recharge (MFR), along with direct transfer of mountain block groundwater to basins, is thought to greatly exceed local recharge within basins (Wilson and Guan 2004). Understanding MFR recharge contributions via the mountain block to perched intermediate and regional groundwater at TA-16 is very important to understand hydrologic functioning of the Cañon de Valle watershed and can have a major control on HE concentrations in the deeper groundwater zones. This section examines the importance of MFR within the Cañon de Valle drainage, based on surface water flow data from the upper and lower sections of the canyon. These include measurement locations above the Pajarito fault zone (along the mountain front), at springs that discharge into the lower canyon at TA-16, and at a channel flow gauge downstream of the springs, also at TA-16.

Snowmelt can recharge groundwater in the mountain block and this can be facilitated by faults and fractures that intersect drainage channels along the mountain front. In Upper Cañon de Valle, termination points of some observed peak snowmelt runoff events occur close to mapped faults. Upper canyon snowmelt flows exceed lower canyon flows, suggesting that the Pajarito fault zone acts as an important conduit from the surface to intermediate and/or regional groundwater, and this study focused on quantifying these mountain front contributions.

3.2 Methods

Cañon de Valle discharge upstream of the fault zone was measured by portable flume gauging under different conditions between March 2016 and May 2017. Historical measurements were also used to provide additional reference points for upper canyon springs and channel discharge (described later). V-notch weir-based discharge measurements at Burning Ground and SWSC Springs were also utilized. These springs feed most of the channel flow in lower Cañon de Valle and are supplied by a shallow saturated zone perched above welded tuff unit Qbt3. It was assumed that these springs represent potential return flow from the mountain front, thus the difference between upper canyon discharge and the total springflow represents recharge to the deeper groundwater zones. This approach represents a maximum bound on MFR estimates because the two springs may not completely account for all of the return flow in lower Cañon de Valle. Small seeps could also be related to return flow, although their volumetric contribution would be substantially smaller than the springs. To determine minimum bounds the difference between upper canyon discharge and flow at gauging station E256 in lower Cañon de Valle was used. E256 discharges are usually larger than the sum of the two springs which lowers the estimates for MFR. However, it should be noted that the E256 based estimates are likely unrealistically low because the E256 measurements include both return flow and any local flow contributions at TA-16. It is difficult to separate the return flow and local contributions, but this approach still provides a useful bounding calculation.

As a first step, estimates of the percentage of return flow in lower Cañon de Valle were made on a monthly basis according to Equation 3:

$$([\text{Total Lower Canyon Spring Flow}])/([\text{Upper Canyon Flow}]) \times 100 = \text{Return Flow \%} \qquad \textbf{Equation 3}$$

where Return Flow is the percentage of upper canyon flow that reappears in the lower canyon. It is worth noting that this quantity also represents <u>potential</u> recharge to the alluvial system in lower Cañon de Valle because all of this flow is typically lost not far downcanyon from the E256 station. The maximum monthly MFR percentage was determined by difference using the Return Flow estimate from Equation 3, where:

$$100\% - \text{Return Flow \%} = \text{MFR \%} \qquad \textbf{Equation 4}$$

Minimum estimates were also determined using Equations 3 and 4, except that E256 discharge is used instead of the Total Lower Canyon Spring Flow.

3.3 Results and Discussion

In the upper canyon above the Pajarito fault zone, discharge data demonstrate distinct gaining and losing reaches (Figure 3.3-1). Springs emerging from Tschicoma Formation bedrock supply the bulk of base flow, which is lost to the subsurface in various places, dependent on season and flow volume. The overall impact is that all upper Cañon de Valle flow is lost at or above the Pajarito fault zone. Flow across the fault, which was occasionally seen in older data from the E253 stream gauge at the base of the fault zone, no longer occurs. This shift occurred as a result of scouring and heavy silting of the stream channel during flood events that followed the Cerro Grande fire. The fault appears to accept virtually all upper canyon surface water, and losses along the fault zone were certainly substantial before the fire.

Flow in the upper canyon is highly variable. Flow measurements provided by historical sources Stearns (1948) and Griggs (1964) suggest that base flow at UCdV-1, the site of an old weir structure, is normally in the range of 7 to 10 gallons per minute (gpm). In 2016 and 2017, base flows have been in the range of 6 to 26 gpm, or 0.01 to 0.06 cubic feet per second (cfs), at the same location. These flow measurements have been taken during relatively dry periods in winter and summer, respectively.

In the relatively dry conditions of late July and mid-December, low amounts of discharge are observed terminating at points less than 30 ft apart, between the UCdV-1 weir location and the confluence with Spring 5.0. This type of stream loss suggests that focused recharge occurs along vertical bedrock fractures expressed at the surface. In contrast, during snowmelt, the stream at UCdV-1 was gauged at 202 gpm on 5/3/16, and flow extended nearly 5000 ft further down the canyon. Even higher snowmelt discharge was observed on 3/30/17, when flow extended to about 6300 ft below the dry season terminus point. These locations, and their proximity to mapped faults, are shown in Figure 3.3-1 (see lower pink colored area). Although variable, springtime flow rates are probably an order of magnitude larger than base flow during the rest of the year. Runoff events related to summer monsoons were not captured by the recent gauging, because of their intermittent occurrence. There is also a lack of monsoon-related data in the historical sources. Monsoon events are expected to follow similar recharge pathways as snowmelt, but may have different recharge rates and volumes because of differences in the durations and sizes of elevated flows.

For the upper canyon, key observations are that snowmelt flows dominate the discharge record, yet snowmelt flows do not typically cross the main front block fault scarps. Lower discharge flows during the rest of the year are lost to the subsurface further west of the faults, in what is assumed to be a zone of deformation underlying alluvium.

Springs discharge into lower Cañon de Valle comes mainly from Burning Ground Spring; SWSC Spring is a secondary and, at least in recent years, intermittent source. Observations at Peter Seep and geophysical transects (LANL 2005) suggest there are also other minor subsurface sources of water to the canyon bottom sediments. The seasonality observed in the upper canyon is also present in the lower canyon, although in a much lower amplitude form. (Figure 3.3-1). Comparison of average monthly total spring flows (Burning Ground + SWSC) with average E256 gauge flows downstream of the flows indicate that, for much of the year, water from these two springs supplies a substantial fraction of the channel flow (Figure 3.3-1). Most of the difference between the total lower canyon spring flow and the E256 gauge is probably attributable to local TA-16 overland flow or interflow contributions to the lower canyon, although there may be some small seepage-related upper canyon contributions. Peak flows in the upper canyon and the lower canyon (at E256) are both in April, while the peak flow in the springs is in June. The lag in peak flow in the springs is consistent with subsurface flow contributions from the mountain block. The timing of peak flow at E256 is best explained by direct snowmelt runoff at TA-16 to the lower canyon because, as noted above, upper canyon snowmelt flows do not cross the Pajarito fault zone.

Results from the water balance calculations described in section 3.1 are shown in Table 3.3-1. As noted earlier, maximum estimates of MFR were made by assuming that total lower canyon spring flow represents all of the return flow from above the fault zone. Minimum estimates were made assuming the typically higher E256 averages represent return flow instead of the springs. Local TA-16 flow sources add uncertainty to the minimum calculations and sometimes resulted in non-physical estimates when using the E256 data. In these instances the monthly minimum values were left blank in Table 3.3-1.

During the fall (September to November), MFR is about 50% although flows are low (Figure 3.3-2 and Table 3.3-1). In the winter (December and January), maximum estimates suggest much lower percentages of MFR. This seems reasonable since most precipitation at that time is stored as snow and upper canyon discharges are low. However, by February the maximum MFR percentage rises as upper canyon discharge increases (likely through early snowmelt). When full snowmelt is in effect during the March–May period upwards of 85% of upper canyon snowmelt runoff appears to recharge deep groundwater zones as MFR. Given that the largest upper canyon discharges occur at this time, the snowmelt period is clearly the most important period for MFR from a volumetric perspective. The June and July period is interesting because the maximum and minimum return flow and MFR percentages invert (i.e., minimums and maximums flip, Table 3.3-1). During these months, spring discharges exceed E256 flows which cause the inversions (Figure 3.3-2 and Table 3.3-1). As noted earlier, spring flow peaks late, and the flow data suggests that springs lag upper canyon and E256 peak flows by about 60 days. The difference between the springs and E256 discharges also leads to the question of what happens to the extra June/July springs discharge along the way to E256? It could be partly related to increased canyon bottom recharge of alluvial groundwater between the springs and E256, but because this period is when evapotranspiration is at its annual maximum. Thus, it is likely that evapotranspiration is a major loss factor.

3.4 Conclusions

Based on the upper and lower canyon discharge measurements, some amount of MFR occurs throughout the year. However, there is strong seasonality where MFR is quite low during the winter but increases dramatically during the snowmelt period. During snowmelt, the percentage of upper canyon water lost to recharge and the amount of upper canyon discharge are both at their maximums (Figure 3.3-2 and Table 3.3-1). Thus, MFR from snowmelt appears to be a very large source of recharge to intermediate and regional groundwater beneath the TA-16 area. Transient increases in spring and early summer water levels observed in 2017 in some TA-16 area perched intermediate wells (data in preparation) are consistent with the importance of snowmelt-driven MFR. MFR in Cañon de Valle appears to be a hydrological process of major importance in terms of understanding the overall watershed flow system, but also has major implications with regard to HE in intermediate and regional groundwater (which is explored in more detail in later sections of this report).

4.0 ISOTOPE HYDROLOGY

4.1 Introduction

The extent of HE contamination from the 260 Outfall at TA-16 has been well-studied (Figure 4.1-1; LANL 2003a; LANL 2003b). This section focuses on new insights on the origin and nature of different water bodies in TA-16 from water stable isotope ($\delta^{18}O$ & $\delta^{2}H$), carbon-14, tritium, temperature, RDX, lithium, and chloride analyses. These are important factors to understand because they have substantial impacts on contaminant distributions and transport at TA-16. TA-16 water bodies are split into six main zones; surface water, springs, alluvial groundwater, upper perched-intermediate groundwater, lower perched-intermediate groundwater, and regional aquifer, consistent with the conceptual model in the “Investigation Report for Water Canyon,” 2011 (Figure 4.1-2). The objective of this study is to compile the existing isotope data from various sources and analyze it in a comprehensive TA-16 context. Note that this section also includes some geochemical and other, non-isotopic data (e.g., groundwater temperatures) when they help to place the isotope data in better context for understanding the TA-16 hydrological system.

4.2 Methods

Surface water, springs, and alluvial groundwater sample locations, and perched-intermediate (or intermediate) and regional aquifer well locations used for this study are shown in Figures 4.2-1 and 4.2-2. Data used for analyses were collected periodically since 1998. The majority of data were obtained from the Intellus New Mexico public database (http://intellusnm.com/). Carbon-14 data were obtained from Michael Dale (NMED personal communication). Stable isotope values for precipitation are from S-Site and TA-49 data in Adams et al. (1995). Stable isotope values of surface and groundwater were analyzed using an isotope ratio mass spectrometer (IR-MS), with errors typically less than ±0.2 ‰ ($\delta^{18}O$) and ±0.4 ‰ ($\delta^{2}H$). Statistical analyses were conducted using a Kruskal-Wallis One Way Analysis of Variance on Ranks, followed by Dunn’s Method pairwise comparison between hydrologic zones. Statistical analyses were performed using the SigmaPlot software package. Additional field collection and analytical information can be found in Longmire et al., 2007.

4.3 Results

Water temperatures, stable isotope ratios of oxygen and hydrogen, activities of tritium and carbon-14, and concentrations of lithium and chloride (see section 1.0) are presented for the hydrologic systems of the Cañon de Valle watershed. These systems are separated into near-surface waters (stream water, alluvial groundwater, springs) and deep waters (upper vadose zone, perched-intermediate zone, and regional aquifer). For this study surface water is restricted to water from canyon drainage channels. Much of Cañon de Valle and adjacent canyons contain perennial and ephemeral stream reaches. The alluvial groundwater zone is composed of any groundwater directly connected to stream water in the canyons, typically <2 m thick and 1–3 m wide. Springs discharge within the canyons but above the canyon bottoms. The subsurface area below the mesas, but at greater elevation than the canyons comprises the upper vadose zone, which contains saturated ribbons of groundwater (Figure 4.1-2). Perched-intermediate groundwater is separated into upper and lower perched zones. The upper perched zone occurs in the Otowi Member of the Bandelier Tuff and the Puye Formation, and the lower perched zone occurs only in the Puye Formation. The regional aquifer occurs in the Puye Formation as well.

4.3.1 General Stable Isotope Observations and Statistics

There are some overarching isotopic differences between the hydrologic systems (Figures 4.3-1 to 4.3-3). Surface water, springs, and alluvial groundwater all show a larger variability of $\delta^{2}H$ and $\delta^{18}O$ than intermediate and regional aquifer samples, with the largest standard deviation (SD) in alluvial groundwater samples (Figures 4.3-3 and 4.3-4, Table 4.3-1). In contrast, perched-intermediate zone and regional aquifer samples have low SDs (~0.3 ‰ $\delta^{18}O$ and ~2 ‰ $\delta^{2}H$) only slightly greater than analytical error (typically 0.1 ‰ $\delta^{18}O$ and 1 ‰ $\delta^{2}H$). All group averages plot close to the local meteoric water line (LMWL), suggesting minimal loss through evaporation (Figure 4.3-3). The $\delta^{18}O$ and $\delta^{2}H$ isotope ratio averages by group, from highest to lowest, are as follows; alluvial groundwater, springs, regional aquifer, perched-intermediate groundwater, and surface water. The largest gap between any two averages is between springs and the regional aquifer.

Surface water samples are significantly lighter and show less variance than the other near-surface hydrologic zones (Figures 4.3-1 and 4.3-3). Intuitively, this does not make sense because the other near-surface hydrologic zones are fed by surface water. Surface water samples were preferentially collected during the second quarter, because of the ephemeral nature of many of the surface water sample locations (Figure 4.3-5). Thus, the dataset is not fully representative of the isotopic characteristics of surface water because of seasonal sample bias. The average isotopic value calculated for surface water may be close to the volumetrically weighted average because of the relative importance of springtime snowmelt, but analysis requires a more complete discharge and stable isotope dataset.

The perched-intermediate zone and regional aquifer share many isotopic similarities, although they are on the margin of statistical difference (Table 4.3-2). The upper and lower perched-intermediate zones are grouped together, as there were not enough samples for statistical tests when separated. Upper vadose zone samples are omitted from analysis, because there are not enough samples for statistical tests and they are not directly connected to the deeper perched groundwater zones.

Statistically significant differences were found between all but three system pairs (Table 4.3-2). There are no significant differences between the alluvial and springs zones, surface water and perched-intermediate zones, and the regional vs the perched-intermediate zone. However, the regional and perched-intermediate zones have relatively low P-values ($\delta^{18}O$ P-value = 0.113, $\delta^{2}H$ P-value = 0.127), so it is likely that a statistical difference may occur if more analyses were available.

4.3.2 Surface Water, Alluvial Groundwater, and Springs

4.3.2.1 Stable Isotopes of Surface and Near-Surface Waters

As noted in the previous section, there are unique isotopic characteristics in the near-surface zones. Alluvial groundwater and springs samples have similar stable isotope ratios, while surface water samples are closer to perched-intermediate and regional aquifer signatures (Figure 4.3-3). Alluvial and spring water samples are responsible for the most extreme outlier values (Figure 4.3-6). Surface water isotopes cluster towards the low end of the isotopic range for near-surface waters (Figures 4.3-7 and 4.3-8). Some samples, predominantly from Martin Spring Canyon, lie to the right of the LMWL showing possible evidence for minor evaporative enrichment (Figure 4.3-8).

Alluvial and spring water values have similar isotope ratio distributions (Figures 4.3-9 to 4.3-12). Alluvial groundwater samples extend over a larger range, with higher $\delta^{18}O$ and $\delta^{2}H$ values than spring water. Martin Spring Canyon alluvial groundwater and Martin Spring samples comprise the most extreme values (Figures 4.3-9 and 4.3-11). This indicates that alluvial groundwater is closely connected to the springs that feed them. Alluvial groundwater isotopic composition is a function of the proportion of recharge from spring water vs surface water and spring water is typically a substantial if not major component of surface water, (see section 3.0).

4.3.2.2 Tritium and RDX of Surface and Near-Surface Waters

Cañon de Valle near-surface waters show highly time variable tritium and RDX concentrations (Figures 4.3-13 to 4.3-18). Because of this temporal variability, time-averaged values for a given location are used for analysis. Average tritium activity ranges from 6.9 to 74.4 tritium units (TUs) for surface water samples, 11.7 to 57.2 TU for alluvial groundwater samples, and 3.1 to 40.8 TU for spring water samples (Table A-1.0, in Appendix A of this document). Average RDX concentrations range from 0.2 to 105.8 µg/L for surface water samples, 0.2 to 62.2 µg/L for alluvial groundwater samples, and 0.2 to 109.0 µg/L for spring water samples (Table A-1.0). Tritium and RDX concentrations are similar for all near-surface systems by canyon, and differ between different canyons (Table A-2.0, in Appendix A of this document). Tritium and RDX concentrations show a loose correlation; the three canyon systems with the highest activity of tritium (Cañon de Valle, Martin Spring Canyon, and Fish Ladder Canyon) are also the only three to have average RDX concentrations >1 µg/L (Figure 4.3-19).

4.3.3 Perched-Intermediate Groundwater Zone and Regional Aquifer

4.3.3.1 Stable Isotopes of the Perched-Intermediate Groundwater Zone and Regional Aquifer

Both intermediate and regional aquifer wells show loose clustering by well and well screen (Figures 4.3-20 and 4.3-21). CdV-37-1(i) and PCI-2 have heavier isotope values than most of the other regional aquifer wells. R-17 tends to consistently have heavier values as well. No other trends are apparent for regional or perched-intermediate groundwater well stable isotope data without looking at other thermochemical data.

4.3.3.2 Tritium and Carbon-14, Temperature, RDX, Lithium, and Chloride of the Perched-Intermediate Zone

Isotope based ages and chemical information shed light on the nature of the perched-intermediate groundwater zone and regional aquifer. There are many trends that only become apparent when stable isotopes, tritium, carbon-14, temperature, lithium, and chloride are examined together. This section discusses the relationships, highlighting the meaningful comparisons.

Intermediate groundwater well stable isotope ratios do not show any dependence on tritium concentrations, carbon-14 age, temperature, lithium concentrations, or chloride concentrations. Most of the perched-intermediate zone wells show average tritium concentrations >0.8 TU, indicating a component of modern (younger than 1950) recharge (Table 4.3-3) (Clark and Fritz 1997). Perched-intermediate zone wells have good coverage for tritium, but only four well screens have carbon-14 data; CDV-37-1(i), PCI-2, R-26 S1, and R-47i (Table 4.3-3). Unadjusted ages for these wells range from 336–2075 years. Temperature is consistent at ~10.5°C in all perched-intermediate zone wells, except those that are close to tritium-dead and have elevated temperatures (Figure 4.3-22).

RDX concentrations vary with time for most perched-intermediate zone well screens, so a time-averaged value is used for analysis (Figure 4.3-23). CdV-16-2ir shows a gradual increase in RDX concentration (Figure 4.3-24). A notable observation is that detectable RDX concentrations are found only in wells that also have tritium concentrations >0.8 TU (Figure 4.3-25). There is no correlation between RDX concentrations and chloride, lithium, δ^2H, or δ^{18}O. Tritium concentrations show a negative correlation with lithium and a positive correlation with chloride (Figures 4.3-26 and 4.3-27), suggesting that these ions are indicators of mountain front/deep flow paths as suggested in section 1.0.

Regional aquifer wells show many interesting relationships between δ^2H and δ^{18}O and other chemical parameters. Stable isotope ratios show a positive correlation with average unadjusted carbon-14 age (Figures 4.3-28 and 4.3-29). R-17 and R-27 are outliers, and they are the two wells farthest from the mountain front considered in this study (Figure 4.2-2), and may have a different hydrologic relationship to mountain front and local recharge.

Geothermal gradients can be derived from regional aquifer well data. Temperature data show a correlation with both screen elevation and unadjusted carbon-14 age. Fitting a global linear regression to temperature as a function of screen elevation results in a fairly low r^2 (0.42), but the data appear to fit two different geothermal gradients (Figure 4.3-30). After splitting the data into steep and flatter geothermal gradients, much stronger linear correlations appear (r^2 values of 0.93 and 0.87 for a steeper and shallower geothermal gradient, respectively [Figure 4.3-30]). The steep geothermal gradient (wells CdV-R-15-3, R-18, R-25, and R-27) is 40.7°C/km and the flatter gradient (wells CdV-R-37-2, R-17, and R-48) is 17.4°C/km. The two groups of wells appear to be influenced by differing amounts of local recharge, which is discussed below.

All of the data show a linear correlation between unadjusted carbon-14 age and temperature (Figure 4.3-31). The trend shows higher temperature with older ages. Temperature and carbon-14 age data are summarized for each well in Table 4.3-4.

Well screens with average screen depth in the top ~100 ft below the water table show the greatest variability in average unadjusted carbon-14 age, from ~500 to 3250 ybp (Figure 4.3-32). Average unadjusted carbon-14 age sharply increases with depth of screen below the water table at ~10–12 yrs/ft in the top 100 ft for wells which show a significant (>250 yrs) change with depth (Figure 4.3-32). One regional aquifer well, CdV-R-37-2 does not show an increase in carbon-14 age with depth, and has the oldest carbon-14 age for a well screen in the top 100 ft of the regional aquifer (Figure 4.3-32).

In contrast to the perched-intermediate zone wells, regional aquifer well screens contain predominantly submodern (TU < 0.8) waters, making carbon-14 data the most useful for understanding relative ages (Table 4.3-5). Only R-25 contains levels of tritium considered to be younger than submodern and lacks carbon-14 data. The most recent RDX concentration measurement for each well screen is used for analysis. RDX concentration measurements taken in 2015 and 2016 show only four well screens with detectable levels of RDX (Table 4.3-5). These wells are R-18, the shallowest two regional screens of R-25, and R-63. RDX concentrations in R-18 have been increasing since 2006. A common theme between these wells is that they show tritium concentrations >0.8 TU (R-25) or the youngest carbon-14 ages (R-18 and R-63). With a combination of detectable RDX and relatively young radiogenic ages, these four wells contain a component of modern recharge. Similar to the steep carbon-14 age gradient observed in the shallowest 100 ft for regional aquifer wells (Figure 4.3-32), all four well screens with detectable RDX are also within the shallowest 100 ft (Figure 4.3-33). Wells with steep geothermal and age gradients show a spatial correlation with drainages, suggesting a significant local recharge component, as discussed in section 4.4.

Lithium concentrations show an important correlation in regional aquifer wells, a positive correlation with average unadjusted carbon-14 age (Figure 4.3-34). The stable isotope ratios of oxygen and hydrogen follow this trend as well, as they are correlated with carbon-14 age. Chloride concentrations are not as informative in regional aquifer wells as in perched-intermediate zone wells since the range and concentrations are considerably lower (1.4–3.2 mg/L vs 1.2–24.3 mg/L) (Figure 4.3-34).

4.4 Discussion

4.4.1 Surface Water, Alluvial Groundwater, and Springs

4.4.1.1 Stable Isotopes

The isotopic characteristics of the surface water, springs, and the alluvial groundwater have differences, even though these three systems are hydrologically connected. Surface water is more negative than alluvial or spring water, isotopically similar to the perched-intermediate zone and regional aquifer (Figure 4.3-3). The surface water data set is biased towards second quarter samples, possibly skewing the results to reflect springtime snowmelt (Figure 4.3-5). Spring and alluvial groundwater samples are not statistically different (Table 4.3-2). This suggests that alluvial groundwater is primarily recharged by steady flow from the springs, rather than seasonal surface water. Spring and alluvial groundwater samples from Martin Spring Canyon have the largest spread of isotopic values, indicating that they are the most responsive to individual storm events and are relatively poorly homogenized, being dominated by fast subsurface flow paths and possibly evaporation effects (Figures 4.3-9 and 4.3-11).

Recharge elevation can be estimated from the elevation vs average annual precipitation $\delta^{18}O$ curve for the Jemez Mountains region (Table 4.4-1) (Vuataz and Goff 1986). Recharge elevations greater than ~7800 ft, the slope break between the mountain front and the mesa top, can be considered mountain-sourced precipitation. This reveals that perched-intermediate groundwater, and regional aquifer water are dominated by high elevation recharge (see section 3.0), whereas spring and alluvial zone water are recharged by lower elevation precipitation. However, in the case of Burning Ground and SWSC Springs recharge elevations, while lower than the deeper zones, suggest recharge at the elevation of the Pajarito fault zone. Isotope averages of each water system lie near the LMWL (Figure 4.3-3), suggesting no systematic shift in the isotopes that would indicate geothermal alteration or strong evaporation (Figure 4.3-1) (Craig 1963; Panichi and Gonfiantini 1978).

The average isotopic values of each hydrologic zone and the spread in each data set can be used to approximate their precipitation sources and homogeneity. Surface water, springs, and alluvial groundwater stable isotope data sets have the greatest SD, whereas regional and perched-intermediate samples have the smallest SD (Figure 4.3-4). Another useful way to assess the homogeneity of a hydrologic system is to look at the ratio of SDs (σ) between surface or ground water stable isotope data and local precipitation stable isotope data (Equation 5; e.g., $\sigma_{\delta 18O\ \text{surface water}}/\sigma_{\delta 18O\ \text{precipitation}}$) (DeWalle et al. 1997; Tetzlaff et al. 2009).

$$st\ dev\ ratio = \frac{\sigma_{\delta 18O\ \text{hydro zone}}}{\sigma_{\delta 18O\ \text{precipitation}}}$$ **Equation 5**

Stable isotope values of precipitation are taken from Adams et al. (1995). Lower ratios indicate greater homogeneity and mixing of the data set. The ratio of SDs reveals that the isotopic range of precipitation is damped in surface, spring, and alluvial zone waters (SD ratios of 0.22–0.40) (Table 4.4-2). However, for the perched-intermediate zone and regional aquifer waters substantially more dampening has occurred (SD ratio of 0.09). These low values indicate a clear increase in mixing/homogeneity in the deep groundwaters compared to near-surface waters. Sections 3.0 and 5.0 discuss transient recharge to the deeper groundwater zones in more detail.

4.4.1.2 Tritium and RDX

Tritium values vary with time for all near-surface TA-16 hydrologic systems. Average values are dependent on the individual canyon system and proximity to the mountain front (Figure 4.3-19). Sample sites closest to the mountain front generally have the lowest tritium values (Figure 4.4-1), indicating longer flow paths and/or a greater proportion of MBR vs mesa-top recharge. TA-16, Cañon de Valle and Martin Spring Canyon have the highest tritium, receive substantial amounts of modern recharge, and because they are in proximity to TA-16 HE facilities, have the highest RDX concentrations (Figures 4.2-1 and 4.3-19).

4.4.2 Perched-Intermediate Groundwater Zone and Regional Aquifer

Spatial differences of isotopic and chemical composition and their relationships account for the majority of variation in the perched-intermediate zone and regional aquifer (Figures 4.4-1 to 4.4-5).

4.4.2.1 Stable Isotopes

On an individual well/well screen basis, stable isotope measurements in perched-intermediate and regional aquifer wells show tight clustering (Figures 4.3-20 and 4.3-21). However, there are differences between different wells and well screens, indicating some isotopic heterogeneity in the perched-intermediate zone and regional aquifer despite an overall SD slightly above analytical error (Figure 4.3-3). Isotopic homogeneity of groundwater is typically a measure of the overall homogeneity of the system (Gat 1971). Differences in flow paths and recharge sources/locations explain the heterogeneity between different wells and screens within the same hydrologic zone.

4.4.2.2 Tritium, Carbon-14, Temperature, RDX, Lithium, and Chloride

Correlations between stable isotopes, tritium, carbon-14, temperature, RDX, lithium, and chloride data inform ideas about recharge timing and origin for the perched-intermediate zone and regional aquifer. Most perched-intermediate zone wells have average tritium concentrations of >0.8 TU, indicating they have a component of modern (since 1952) recharge (Table 4.3-3). These wells are located either directly beneath or adjacent to canyons (Figures 4.4-1 and 4.4-2). Perched-intermediate zone well screens with >0.8 TU have temperatures around 11°C, closely matching average annual air temperatures between 5600 and 6500 ft in the area (Manning 2009). Temperatures in perched-intermediate zone well screens with <0.8 TU are the only ones that differ from ~11°C, indicating their average residence times are long enough for the water to be heated by the regional geotherm (Figure 4.3-22). RDX is only found in wells that also have tritium concentrations >0.8 TU (Figure 4.3-25). Low lithium and high chloride concentrations are associated with high tritium concentrations, providing additional support for some contribution of post-1950 modern recharge (Figures 4.3-26 and 4.3-27).

Recharge events have been observed in some perched-intermediate zone wells (see section 5.0). A recent example was observed in well CdV-9-1i, with a water level increase greater than 85 ft during spring of 2017 (Figure 4.4-6). The recharge event is most likely driven by pressure from upgradient infiltration of snowmelt. The isotopic similarity of water sampled during the recharge event to other perched-intermediate zone well samples, as well as an increase in temperature during the recharge event supports the concept that it is old, well-mixed water derived from the mountain block to the west rather than direct snowmelt recharge through the canyon in the vicinity of the 260 Outfall (Figures 4.3-20 and 4.4-6).

Regional aquifer well data show some of the same trends as perched-intermediate zone well data, but also show trends between stable isotope ratios and temperature/chemical data. Stable isotope ratios are higher (less negative) for wells with a greater unadjusted carbon-14 age, indicating that the source of older recharge is different and isotopically heavier than younger recharge (Figures 4.3-28 and 4.3-29). Climate change has been proposed as a possible explanation (Yanicak et al. 2014). However, there is not strong evidence for this because there has been little variability in the average annual temperature of the Española Basin over the past ~3,000 years (Manning 2009). There are two separate geothermal gradients, a sharp and a shallow one (Figure 4.3-30). Carbon-14 age and temperature are positively correlated in TA-16 wells and regional aquifer wells in the Española Basin, suggesting that temperature increases with residence time in the saturated zone and that higher temperatures indicate deeper flow paths and longer residence times (Manning 2009). Both temperature and carbon-14 age show sharp depth gradients beneath and adjacent to canyons for regional aquifer wells and the few perched-intermediate zone wells with carbon-14 data (Figures 4.3-30, 4.3-32, and 4.4-3). Altogether, perched-intermediate zone groundwater and the top ~100 ft of the regional aquifer beneath and adjacent to canyons get a younger, isotopically lighter component of recharge (possibly snowmelt related) than beneath mesas. This recharge can be attributed to infiltration from stream flow in the canyons, and mixing with MBR. Manning conducted a noble gas study of regional aquifer wells in the Rio Grande Valley in 2009 showing at least 50% MBR in R-18, coinciding well with R-18's low isotopic signature (Figure 4.3-21) and presence of RDX (Table 4.3-5) indicating a combination of mountain block and modern canyon bottom recharge (Manning 2009). Hydrological mixing is discussed further in section 6.0. The two wells that do not follow these trends (R-17 and R-27) are farthest from the mountain front, and may not share the same hydrologic balance between MBR and canyon bottom recharge (Figure 4.2-2). Noble gas ages of regional aquifer wells on the east side of the Rio Grande Valley show the youngest ages in the top 30 m and nearest to the mountain front (Manning and Caine 2007). RDX concentrations above the detection limit in regional aquifer wells are present in wells with tritium concentrations >0.8 TU or unadjusted carbon-14 ages <1000 years, again showing that a component of modern recharge is linked to RDX contamination (Table 4.3-5). Well R-18 has increasing concentrations of RDX, starting in 2005. Well R-25 has detectable RDX and tritium >0.8 TU, and displays fire-pulse chemical signatures mere months after a regional fire (Table 4.3-5) (see section 5.0). All wells with detectable RDX are beneath or adjacent to canyons (Figures 4.4-2 and 4.4-4). Lithium concentrations show a positive correlation with carbon-14 ages and can be used as a proxy for groundwater age, similar to low chloride as a proxy for greater ages observed for the perched-intermediate zone (Figure 4.3-34). High lithium is an indicator of deeper, longer flow paths whereas high chloride is an indicator of relatively young surface water recharge. Perched-intermediate groundwater samples show higher concentrations of chloride (1.2–24.3 vs 1.4–2.8 mg/L) than regional aquifer samples and lower lithium concentrations (0.2–15.1 vs 14.1–23.5 mg/L).

4.5 Conclusions

The near-surface and deep groundwater hydrology of TA-16 are greatly informed by stable isotope, age, temperature, and chemical data. Stable isotope signatures reveal that alluvial groundwater is primarily recharged by spring water and that perched-intermediate groundwater and the regional aquifer likely share similar recharge sources, being nearly statistically identical with regards to water stable isotopes (Table 4.3-2). Surface, springs, and alluvial zone waters are highly variable compared to perched-intermediate and regional waters, indicating increased mixing and homogenization deeper in the hydrologic system. Younger aged samples, as indicated by tritium activity or carbon-14 age, are correlated with more negative isotopic signatures, RDX contamination, and low lithium concentrations in the perched-intermediate zone and regional aquifer. Groundwater samples with young, contaminated signatures are concentrated in close proximity to the perennial reach of Cañon de Valle and in the top ~100 ft where they occur in the regional aquifer (Figures 4.4-1 to 4.4-5). These observations highlight the impact that the stream flow in Cañon de Valle has on the perched-intermediate zone and regional aquifer, providing recharge via fractured damage zone conduits in the vadose zone. Young, contaminated recharge to the regional aquifer is localized in a “hotspot” around the perennial reach of Cañon de Valle. Evidence for local recharge to the regional aquifer is limited elsewhere in the Pajarito Plateau area.

5.0 FIRE AND SUBSEQUENT FLOOD PULSES

5.1 Introduction

Water chemistry data collected after the Cerro Grande and Las Conchas fires from springs and alluvial, intermediate, and regional groundwater wells was evaluated to determine if fire-induced changes to water chemistry can be used as a natural tracer of flood waters. All water chemistry data is from TA-16 at the Laboratory (Table 5.1-1). Calcium and total alkalinity are the focus of this study because they showed increased concentrations in runoff following the Cerro Grande fire (Bitner et al. 2001).

5.2 Methods

Concentration and water level data for this study were obtained from the Intellus New Mexico public database (http://intellusnm.com/). Samples were collected and analyzed at multiple laboratories using standard EPA procedures. Anions were analyzed using ion chromatography. Cations were analyzed using ICP-AES, ICP-OES, or ICP-MS. Analytical errors for anion analyses are typically better than or equal to ±5%, and cation errors are better than or equal to ±10%. RDX was analyzed using HPLC.

5.3 Results

5.3.1 Cerro Grande Fire

The Cerro Grande fire burned approximately 43,000 acres of the Pajarito Plateau in northern New Mexico in May of 2000. Changes to the landscape following the fire increased runoff and impacted water quality. Runoff events were intensely monitored in the four years following the fire and detailed assessments of effects on surface water quality are available in a report by Gallagher and Koch (2004).

The first precipitation event following the Cerro Grande fire occurred on June 2, 2000. Although not a large event, elevated levels of calcium were seen at SWSC Spring (Figure 5.3-1). It is not until after the first major flood event on June 28 that most responses were observed. During this event, record high flows were observed in Water Canyon, Pajarito Canyon, and Cañon de Valle and several stream gages were destroyed (Gallagher and Koch 2004). Concentrations of calcium at Water Canyon above SR 501, a gage station located to the west of Laboratory property, increased dramatically from background levels to 574 mg/L (Figure 5.3-2); however, this flooding signal was not immediately evident in any of the nearby wells.

Several more substantial precipitation events occurred throughout the summer of 2000, namely between July 16–19, although a few localized events occurred in August as well. In the years following the Cerro Grande fire, there was a major runoff event on July 2, 2001 and floods on July 25, 2002 and May 2005. Unfortunately, most collected groundwater data do not go back far enough to capture this time period. However, despite a limited sample size, responses were observed in R-25 screen 1, R-25 screen 4, and CdV-16-02656 (Figures 5.3-3 and 5.3-4, Table 5.3-1).

R-25 screen 1 showed slightly elevated calcium in May and August 2001 (Figure 5.3-3B). R-25 screen 4 showed a large increase in calcium concentration in December 2000 and August 2005 (Figure 5.3-4). CdV-16-02656, an alluvial well, showed an increase in calcium concentration in late September 2000 (Figure 5.3-4A). Additionally, alkalinity at CdV-16-1i was responsive (Table 5.3-1) to snowmelt water during high snowfall years (Figure 5.3-5).

5.3.2 Las Conchas Fire

In June 2011, a second large wildfire swept through the area. The Las Conchas fire burned a total of 156,000 acres. After the Las Conchas fire, the first flooding event occurred in August 2011. Burning Ground Spring showed an increase in total alkalinity in September 2011 (Figure 5.3-1) and Water Canyon above SR 501 had increased calcium concentrations in October 2011 (Figure 5.3-2).

A second flood occurred in July 2012. There is a slight increase in calcium concentration at CdV-16-02656 in July (Figure 5.3-4A) and a very large increase in calcium concentrations at Water Canyon above SR 501 in August (Figure 5.3-2).

5.4 Discussion

Overall, fire-induced changes to water chemistry are difficult to trace through the groundwater system in Los Alamos. Large spikes in calcium concentration occurred following both fires at Water Canyon above SR 501 (Gage E252), but responses were only observed at a small number of the groundwater wells investigated (Tables 5.1-1 and 5.3-1). Calcium and alkalinity are both considered natural tracers, but groundwater wells show stronger and more reliable flood water-induced signals of calcium. Although alkalinity showed a response in some cases, alkalinity and calcium were never both indicators for the same flood event (Table 5.3-1).

The initial spike in calcium that was observed at Water Canyon above SR 501 on June 28, 2000 could be seen first at CdV-16-02656, an alluvial well, in late September 2000. Calcium concentration was approximately twice as high as baseline level. This signal was next observed at R-25 screen 4 in early December 2000 when calcium concentration was about seven times higher than baseline levels. While this initially appeared to be a fire signal, the data here are complicated by development activities that were occurring at the well during this time. Cement was being used to repair screen 3 (120 ft above screen 4), which was likely affecting water chemistry at screen 4 (Longmire 2004). Screen 4 was isolated from the screens above in October 2000. Although the high calcium concentration described was measured in December 2000, it is still likely to be an artifact of development activities, and therefore, unreliable. R-25 screen 1 showed a weaker and more delayed response in May 2001, with slightly elevated calcium evident (Table 5.3-1). This is an indication that rapid recharge pathways may have a more direct connection to the deeper screens of R-25.

R-25 screen 4 showed the clearest indication of a flood water response in 2005. Following a flood event in May 2005, R-25 screen 4 had very elevated levels of calcium, with concentration being about four times higher than baseline level (Figure 5.3-3). Interestingly, it did not respond to the large floods following the Las Conchas fire. It is by far the deepest of the wells examined with a screen depth between 1184.6 and 1194.6 ft below ground surface (bgs) (Table 5.1-1). Previous pumping tests conducted in the area have shown that R-25 screen 4 has little to no hydrologic connectivity with the other wells in this study. Water levels at R-25 screen 4 roughly track calcium concentration with higher water level corresponding to higher calcium concentration (Figure 5.3-3).

Although CdV-16-1i was not responsive to flooding events after the Cerro Grande or Las Conchas fires, it is worth noting that this well showed a strong snowmelt signal. Alkalinity and water level both increased during the snowmelt period, although this response was only evident during years with relatively high snowfall (Figure 5.3-5). Of the groundwater wells examined, CdV-16-1i was the only one that showed alkalinity as an indicator. Previous studies have shown that alkalinity increases in snowmelt water moving over rock and soil (Clayton 1998). The relatively longer transport time of snowmelt water vs flood water may contribute to the difference in indicators between CdV-16-1i and the other groundwater wells.

Despite being a much larger fire, there was little effect of the Las Conchas fire on groundwater chemistry. The alluvial well, CdV-16-02656, was the only well that showed any response to the floods following the Las Conchas fire, suggesting that the flood water signal did not make it to lower depths. Although groundwater wells showed inconsistent responses following the two fires, this study is useful in demonstrating the potential for water chemistry data to be used to qualitatively trace flood water transport through the groundwater system.

6.0 MIXING MODELS: MOUNTAIN BLOCK VS LOCAL RECHARGE

6.1 Introduction

Using the geochemical and isotopic data from the TA-16 area, the previous sections have shown that mixing between mountain block and local TA-16 recharge is a major aspect of how the TA-16 hydrological system functions. It is also clear that MBR is likely very important in the perched-intermediate zones and the regional aquifer (e.g., section 3.0). However, the previous data do not provide any quantitative estimates about the relative proportions of mountain block and local recharge in these zones (Figure 6.1-1). Therefore, this section discusses two mixing model approaches that provide quantitative recharge proportion estimates for the deep systems. These proportions have major controls on HE concentrations and how they might vary between the perched-intermediate and regional zones, playing a key role in evaluation of any remedial action options. The section consists of a simple zone-based “average” approach using chloride and a more sophisticated flow path approach using the geochemical code PHREEQC. The benefit of this dual approach is that comparison of results will lead to a better understanding about how realistic model estimates might be.

6.2 Hydrologic Zone-Based Averages Mixing Model

6.2.1 Methods

Mixing models assume that potential source waters being mixed are somehow different in their chemistry or isotope content such that they represent distinct “end members.” As discussed in section 1.0, there are significant differences in chemistry between the different TA-16 waters, which make it possible to implement mixing models for the site. If the number of end members is small enough (typically less than three) simple algebraic equations can be used to quantify the fraction of each end member that when mixed will represent the chemistry or isotope content of a particular hydrologic zone or well sample. Thus, these kinds of models are powerful ways of understanding the relative importance of, for example, different recharge sources at a particular location or zone. For this work, a simple binary (two source) mixing model was used in conjunction with the conservative tracer chloride to determine sources of recharge to deep groundwater at TA-16 (Equation 6). Hydrologic systems evaluated include the perched-intermediate zone and regional aquifer, further separated into young (carbon-14 age <1500 ybp or tritium activity ≥0.8 TU) (Figure 6.2-1) vs old and canyon (within ~1/4 mile of a wet canyon) vs mesa categories (Figure 6.2-2).

$$\%_{\mathrm{MBR}}=\left[\frac{[\mathrm{Cl}]_{\text{sample set}}-[\mathrm{Cl}]_{\mathrm{local}}}{[\mathrm{Cl}]_{\mathrm{MBR}}-[\mathrm{Cl}]_{\mathrm{local}}}\right]\times 100 \qquad \textbf{Equation 6}$$

Equation 6 is a binary mixing equation for the percent of MBR (end member 1) vs local recharge (end member 2, e.g. surface water, alluvial water, or springs) in a certain zone or group of wells (e.g., “young” regional aquifer wells). The equation terms include the average concentration of chloride for the zone or group in question ($[Cl]_{sample\ set}$), the average concentration in the local recharge source chosen ($[Cl]_{local}$), and the average concentration in MBR ($[Cl]_{MBR}$). Chloride was chosen as the mixing tracer since it is typically a conservative ion in groundwater, except in aquifers containing evaporite minerals (Manning 2009). Evaporite minerals are not present in the volcanic and volcaniclastic rocks of the Pajarito Plateau and Jemez Mountains. Because chloride is an anion, it does not adsorb to mineral phases, and its high solubility prevents it from precipitating in typical groundwater. $\delta^{18}O$ was also explored as a conservative tracer, but was discarded because end members (e.g., MBR vs local recharge) were not as distinct as for chloride. The lack of good end member separation for $\delta^{18}O$ frequently resulted in non-physical results. End members for the model were based on average chloride concentrations from R-26 screen 1 (representing MBR), average Cañon de Valle surface water values (potential shallow recharge source), average alluvial groundwater values (potential shallow recharge source), and average springs values (potential shallow recharge source). The three shallow endmembers represent the range of possible sources of local TA-16 recharge. R-26 was selected as representing MBR because of its proximity to the mountain front, and apparent lack of any significant local TA-16 recharge component (i.e., it is tritium-dead and has no RDX).

6.2.2 Simple Mixing Model Results

Proportions for the average values of mountain block vs local recharge are shown in Table 6.2-1 along with values based on minimum and maximum end member values to help illustrate the range in potential estimates. Results show that MBR is a major component in both the perched-intermediate zone and regional aquifer regardless of the local recharge endmember used. They also show that the local recharge proportion is substantially higher in the perched-intermediate zone compared to the regional aquifer.

Across all comparisons, the percent of MBR is >86% for all regional aquifer wells, suggesting that very high inputs of MBR is a characteristic of the regional zone regardless of age or location in or near a canyon, or on a mesa (Table 6.2-2). Similar to the data in Table 6.2-1, perched-intermediate zone wells have higher proportions of local recharge than regional aquifer wells and the wells that contain the highest proportions of local recharge are young perched-intermediate zone wells or perched-intermediate zone wells located beneath a canyon. This result is consistent with the isotope and RDX hotspots shown in Figures 4.4-4 and 4.4-5. It is also interesting that the single “old” perched-intermediate zone well has low local recharge proportions approaching those of the regional aquifer.

6.2.3 Discussion

Many studies have used conservative tracer mixing models to estimate recharge rates of aquifers by precipitation from different provenances (Anderholm 1994; Lee and Krothe 2001; Custodio 2010). An analogous study was conducted by Anderholm (1994) assessing the amount of MBR and local recharge to the regional aquifer in the Santa Fe area in the southeastern Española Basin near Los Alamos, NM. Anderholm used chloride as a conservative tracer for determining volumes of recharge from different sources and $\delta^{18}O$ for relative proportions as an independent estimate. Based on chloride concentrations of 40–60 mg/L in surface water in arroyos and typically less than 5 mg/L in groundwater, they concluded that surface water was not a significant component of groundwater recharge. The TA-16 study lacked the necessary information to calculate accurate volumes of recharge, and instead relies on relative proportions. Nevertheless, the dominance of MBR estimated here is consistent with the results of Anderholm (1994). The higher proportion of local recharge in the TA-16 perched-intermediate zone does differ from Anderholm's (1994) overall results, but this may be related to the close proximity of TA-16 to the mountain front, and the basin scale perspective of Anderholm's study.

In terms of the simple mixing model for TA-16, regional aquifer and perched-intermediate zone wells show fundamental differences in proportions of MBR vs local recharge. Regional aquifer wells, regardless of grouping by age or location show >90% average MBR vs local recharge (Table 6.2-2). Perched-intermediate zone wells show 60% to 70% average MBR for "young" or "canyon" wells, and 94% to 100% MBR for "old" or "mesa" wells (Table 6.2-2; Figures 6.2-1 and 6.2-2). The perched-intermediate zone within ¼ mile of a canyon appears to be the most impacted by local recharge. This observation is in agreement with increased tritium activity (≤17 TU) and RDX concentrations (≤152 µg/L) in perched-intermediate zone wells in the vicinity of Cañon de Valle (section 4.0).

Regional aquifer wells, even those that are considered relatively "young" or within ½ mile of a canyon receive greater than 86% MBR. Perched-intermediate zone wells in the same category show averages of 60% to 67% MBR, with some wells falling outside of the bounds of the mixing model (0% MBR) (Table 6.2-2). These ratios indicate that the perched-intermediate zone close to and beneath Cañon de Valle are the most susceptible to RDX contamination and that the regional aquifer is more homogenous and less influenced by local recharge. It is important to point out that these estimates and conclusions are based on a simple "average" mixing model approach, and we examine another approach in the next section as a way of testing these results.

6.3 PHREEQC Mixing Model Approach

As an alternative to the simple mixing model approach above, the geochemical code PHREEQC (Parkhurst and Appelo 2013) was used to examine mountain block vs local TA-16 recharge. The approach used a combination of forward, inverse, and mixing models to constrain groundwater chemistries along assumed specific flow paths (e.g., upper Cañon de Valle springs to individual TA-16 wells, or well to well flow paths). The advantage of this approach is that it begins with developing and identifying models that generate representative TA-16 water-rock interaction behaviors before any application of mixing models. Thus, with this approach, any mixing model will not only be based on the mixing end member tracer, but will be internally consistent with the local geochemical evolution along the selected flow path. This section represents a summary of the modeling process and results. For additional details and all of the modeling results, see Brady (2017).

The PHREEQC analysis is based in background hydrochemistry of TA-16 wells and potential source waters (e.g. MBR), and the potentially relevant water/rock interactions. Mineral dissolution, precipitation, and ion exchange are the chemical processes considered. The modeling combines an inverse mass balance function, which accounts for chemical changes in water along flow pathways, with a mixing function; the purpose of this is to constrain likely ratios of mixing between waters representing MBR flow and local recharge from TA-16.

The models employ aggregated water chemistry data from four individual sources (Table 6.3-1). Spring 5.29, which emanates from dacite bedrock in upper Cañon de Valle and contributes to surface flow above the fault, and R-26 S1, the westernmost perched-intermediate zone well screen, are used to characterize water chemistry from mountain block sources. Local recharge sources are represented by Burning Ground Spring, which discharges from a horizon within welded tuff, and three alluvial wells in the TA-16 reach of Cañon de Valle.

In Phase I of the modeling, solubilities of rock materials present in Bandelier Tuff and Puye Formation fanglomerate are evaluated by forward modeling in PHREEQC. In dilute waters such as these, there is undersaturation with respect to various mafic silicates. Plagioclase feldspar, as a solid solution containing both sodium and calcium, is near equilibrium, though dissolution is indicated by the activity of sodium in groundwaters as they evolve. Metastable glass, present in rapidly quenched tuff and brecciated dacite rocks, is considered important as a contributor of dissolved silica.

Once key reactive phases were identified for the TA-16 area using the forward models, inverse models were determined for Phase II. Inverse mass-balance modeling was used to identify the dominant geochemical reactions (i.e., mass transfers between mineral phases and groundwater) taking place along an assumed groundwater flow pathway between two specific locations (i.e., springs or wells). The general concept is to constrain and quantify the mass transfers likely to occur as water moves from the upgradient location to the downgradient location. Model construction for each pathway is based on the key mineral phases identified in the forward modeling (Phase I). The models include both primary soluble minerals and observed secondary clays, iron oxides and silica solids. Phases within the aquifer that are indicated to potentially dissolve or precipitate are explicitly used as input to PHREEQC running in inverse mode. PHREEQC identifies specific sets of reactions that would mediate mass transfer between the solids present and fluid, satisfying chemical constraints of the water at either end of the flow path. An important aspect is that PHREEQC will identify multiple possible models because there is typically not a unique solution to the problem. In other words, there are different combinations of mass transfers that can represent the changes in chemistry along the flow path. Inverse models appear as groups of mass transfer coefficients and once a set of reasonable inverse models were generated, mixing was evaluated in Phase III.

Mixing between mountain block water and local TA-16 sources was explored with sets of models that combine the inverse mass-balance function with a mixing function. When mixing is used with the inverse models, groups of results expressing the same reactions as Phase II are considered as valid. However, multiple models are again generated and it is difficult to assess which models are the most representative. To address this non-uniqueness issue chloride mass balance was used to identify which of the mixing models were most representative.

In PHREEQC, only elements that participate in dissolution/precipitation reactions are tracked as mass balance constraints. Because chloride is not involved in any of these reactions it makes an ideal tracer to evaluate mixing. In other words, in deep groundwater without any significant chloride-bearing mineral phases, mixing is the only process that would alter chloride concentrations.

The water mixing fractions generated for a given PHREEQC model for the two end members were multiplied by their respective chloride concentrations and then summed to get a model-based estimate of the total amount of chloride. The sum was then subtracted from the actual chloride concentration of the final (downgradient) water, resulting in a chloride mass balance error, in mg/L. Mass balance errors were calculated for each model, and the models with the lowest chloride mass balance errors are considered to be the most representative for that particular flow path. Mixing results for the top three models for each well location (downgradient "final" water chemistry) are shown in Table 6.3-2 along with the associated mass balance errors. Mass balance errors for the top three models are almost all below 2 mg/L and the best models for each flow path have errors that are typically less than 1 mg/L. These low errors strongly support that the estimated mixing proportions are reasonable.

6.4 Summary and Conclusions

There is a great deal of similarity between the PHREEQC-based estimates and the simple estimates in section 6.2, despite the fact that one is an individual flow path approach and the other is based on bulk averages for the perched-intermediate zone and regional aquifer. The PHREEQC results confirm the simple model results that MBR is dominant in both the perched-intermediate and regional zones (>50% MBR for all the top models in both zones). They also confirm the conclusion from the simple models that regional aquifer recharge is nearly all from mountain block sources (>90% MFR) and that the perched-intermediate zone has a much larger component of local TA-16 recharge (typically 10%–40%). A generalization of the mixing model proportions in a TA-16 cross- sectional context is shown in Figure 6.4-1. These results have major implications on long-term HE concentrations. The high proportions of MBR should act to moderate concentrations in both zones and should play a major role in buffering concentrations in the regional aquifer. There are RDX hotspots in the regional aquifer and as discussed in previous sections these seem to be related to localized higher infiltration areas in and around Cañon de Valle. As RDX and other HE species migrate further downgradient, these concentrations should be altered via dispersive and diffusional processes by the large volume of mountain block water.

7.0 RELEVANCE OF FINDINGS FROM SECTIONS 1–6 TO THE TA-16 SITE CONCEPTUAL MODEL

7.1 Previous Conceptual Model Summary

The most recent conceptual hydrologic model of the TA-16 site was discussed in the "2011 Water Canyon Investigation Report" (Figures 7.1-1 to 7.1-3) (LANL 2011). According to the conceptual model, water in the TA-16 area can be split into five different saturated zones; surface water, alluvial groundwater, mesa waters feeding springs, intermediate-perched groundwater, and regional groundwater (Figure 7.1-3). These zones are connected by complex flow paths, dominated by vertical fracture flow (Figures 7.1-1 to 7.1-3).

Contaminant nature and extent, particularly of RDX, is the primary concern from the former HE milling operations at TA-16. The majority of contaminant mass was transported to Cañon de Valle via the building 260 Outfall. The main infiltration pathway for contaminated water in Cañon de Valle is downcanyon of the 260 Outfall and extends east of alluvial well CdV-16-02659 based on perennial surface water and alluvial groundwater reach, as well as widespread presence of RDX and HMX in shallow perched groundwater. Additional details of the 2011 conceptual model can be found in LANL (2011).

The rest of this section discusses how the results of current studies (i.e., sections 1–6) affect the TA-16 site conceptual model. Overall, the findings described in the previous sections support rather than contradict the 2011 conceptual model, and thus provide good evidence that the existing site model is a representative and robust one. However, what is also important about these new results is that they address some major gaps including the relative importance of mountain block vs local recharge, definition of recharge pathways, lack of a TA-16 site-wide synthesis of groundwater ages/isotopes and a comprehensive statistical assessment of the geochemical characteristics of the different hydrological zones.

7.2 Shallow Hydrological Zones

According to the 2011 conceptual model, ribbons of saturation are the main source of water for the perennial springs (Figures 7.1-1 and 7.1-2). Burning Ground and SWSC Springs are hydrologically and geochemically similar, whereas Martin Spring is distinct. Burning Ground Spring and to a lesser extent SWSC Spring are important sources of base flow and alluvial groundwater recharge in lower Cañon de Valle. A stable isotope study of the springs demonstrated that they are fed though long recharge pathways with some contributions from local fast recharge pathways (LANL 2003a). The importance of long flow path contributions to the springs was also supported by a frequency domain analysis of spring discharge time series (Newman et al. 2001). Maximum recharge elevation estimates presented in LANL (2003) using stable isotopes suggested Burning Ground and SWSC Springs recharge elevations are consistent with the elevation of the Pajarito fault zone. A reanalysis presented in Table 4.4-1 using a larger stable isotope data set confirms the findings of LANL (2003) including the fact that Martin Spring appears to be recharged at a lower elevation than the Cañon de Valle springs, although as discussed in LANL (2003) the Martin Spring recharge elevation estimates may be biased low. The association of the springs recharge elevations with the Pajarito fault zone implies that MBR or MFR is an important source of water in at least the Cañon de Valle springs. Both surface water and shallow vadose zone/springs contribute recharge to alluvial groundwater. Alluvial groundwater is not isotopically homogenous and responds rapidly to precipitation and runoff events (Figure 4.3-4), showing the dynamic interplay between recharge by base flow (springs) and precipitation. From a geochemical perspective, the springs, alluvial groundwater, and surface waters are distinct. Statistical comparison tests found significant differences for multiple analytes (including RDX) between each of these zones (Table 4.3-2).

High explosives were also transported into the mesa vadose zone via fractures and surge beds, and these now act as secondary sources for subsurface groundwater contamination. The chemostatic behavior (i.e., low variability of concentrations over the range of discharge values) of RDX in springs (excluding Martin Spring) and surface water (Figures 2.3-1 to 2.3-3) is an important finding and supports the conceptual model in that there is a reservoir of RDX in the vadose zone acting as a long-term source. The source could be solid-phase RDX, dissolved RDX in relatively immobile zones, or both. Residence times of local groundwater recharge are long enough to interact with the sources and produce chemostatic behavior. The chemostatic behavior of SWSC and Burning Ground Springs, compared to the mixed chemostatic and dilution behaviors of Martin Spring, reinforces the hydrologic and geochemical differences of Martin Spring. Chemostatic behavior indicates extended residence times for RDX in the TA-16 area, and is consistent with the lack of decrease in RDX concentrations in SWSC and Burning Ground Springs, despite source removals and grouting in the 260 Outfall pond and drainage. This finding modifies the 2011 conceptual model statement that contaminant concentrations will decrease over time because of cessation of 260 Outfall HE discharges and source removals (Figure 7.1-2). The general statement of “decreases over time” is correct, but chemostatic behavior implies that declines will likely occur over a prolonged time frame.

7.3 Perched-Intermediate Groundwater

The 2011 conceptual model indicates the perched-intermediate zone in the TA-16 area is separated into upper and lower zones (Figure 7.1-2), although other small saturated zones occur at localized features like silt beds. These zones are laterally discontinuous. Statistical analysis of groundwater chemistry in the upper and lower perched zones show that they are geochemically distinct (section 1.0), implying that the flow paths into these zones are different because the waters must be encountering different lithological zones to develop unique chemistries. This also implies that behaviors of HE may also be different in these zones.

In addition to the presence of RDX in some deeper perched-intermediate locations, there is additional evidence for connections between shallow zones and the perched-intermediate, and within the perched-intermediate. Perched-intermediate groundwater responses to seasonal runoff, water level responses in monitoring wells from drilling of new boreholes, and water level responses in monitoring wells during pump tests all indicate connections with shallower zones or connectivity within the perched-intermediate zone (sections 4.0 and 5.0, LANL 2011). Perched-intermediate groundwater level responses occur in wells close to Cañon de Valle and Burning Ground Spring (wells R-25/S-1 & S-2, CdV-16-1(i), and R-25b) and some perched-intermediate zone wells show chemical responses to post-fire flood pulses and snowmelt within 6 to 12 months, showing relatively rapid surface connectivity and transport (section 5.0). It is assumed this recharge occurs via fractured rocks of the Pajarito fault zone and in fractured tuffs underlying Cañon de Valle. In contrast, temperature and isotope data from CdV-9-1(i) suggests that rapid water table responses from snowmelt in shallow perched-intermediate zone wells is not from direct transport, but rather a pressure response to upgradient recharge (section 4.0). See section 7.5 for additional discussion of perched-intermediate recharge sources.

The upper perched zone is highly heterogeneous and both upper and lower perched zones show hydraulic disconnection between most wells during pumping tests. This observation is consistent with the distinct chemistries of these zones, discussed in section 1.0. RDX detections in the top of the regional aquifer suggest some localized downward connections between the perched-intermediate zone and the regional aquifer, although pump tests in perched-intermediate zone wells have not affected regional aquifer wells, which suggests that the perched-intermediate zone and regional aquifer connection may be limited.

7.4 Regional Aquifer

The regional aquifer is primarily contained within the Puye Formation in the TA-16 area (Figure 7.4-1). Figure 7.4-1 is similar to Figure 7.1-1 (2011 conceptual model). However, Figure 7.4-1 is an updated version that more accurately reflects current understanding of the stratigraphy, geologic structures, and hydrology of the TA-16 area. This updated conceptual model figure is based on new wells and reanalysis of older well cores and cuttings. According to the 2011 conceptual model and Figure 7.4-1, the regional aquifer is laterally heterogeneous and vertical hydraulic conductivities are much lower than horizontal, indicating significant stratification. The sharp age gradient with depth in the top ~100 ft of the regional aquifer supports the idea of vertical hydraulic stratification and predominantly lateral flow (Figures 4.3-32 and 7.1-2). Water supply pumping has little impact on the levels or flow directions near the regional water table at TA-16 (LANL 2011). Flow in the aquifer is generally from west to east or southeast. The regional aquifer is mounded beneath the perched-intermediate zone, which occurs beneath the wet reach of Cañon de Valle. This suggests a vertical recharge connection from Cañon de Valle to the perched-intermediate zone, and from the perched-intermediate zone to the regional aquifer. The mounded regional water table beneath Cañon de Valle coincides with a zone of younger ages and RDX contamination in the perched-intermediate zone and the top 100 ft of the regional aquifer, supporting this conclusion (Figures 4.4-1 to 4.4-5 and 7.4-2). It appears that the intermediate perched zones help to buffer recharge and HE transport to the regional aquifer.

7.5 Deep Groundwater – Recharge Sources

The 2011 conceptual model indicates that recharge to the perched-intermediate zone and regional aquifer comes from three proposed sources; MBR and MFR along the Pajarito fault zone, local recharge from canyon bottoms, and local recharge from mesa tops. Water percolation into bedrock is likely greater beneath canyon floors than mesa tops because of surface flow and alluvial groundwater hydrologic drivers for infiltration. Mesas may have local areas of increased infiltration because of ponding, but these are limited (Newman et al. 2007). The spatial extent of RDX contamination and “young” water in the perched-intermediate zone and regional aquifer supports this proposed infiltration pathway (Figures 4.4-1, 4.4-3, and 4.4-4). Fractures in the shallow bedrock tuffs in Cañon de Valle's bottom are likely pathways for contaminant transport to deeper groundwater bodies. Contaminants transported to deeper hydrologic zones are limited to soluble constituents such as RDX.

Groundwater chemistry provides general information about recharge sources. Comparison tests show that the perched-intermediate zone and regional aquifer are geochemically distinct (section 1.0). However, this is likely because of the difference in lithology of flow paths rather than recharge sources. Two of the most useful parameters were found to be lithium and chloride. The high lithium and low chloride in these zones are suggestive of long, deep flow paths consistent with a mountain block source. In addition, the perched-intermediate and regional groundwater stable isotope SDs of values are extremely low, indicating the recharge flow paths to these zones are much longer than for the shallow systems.

According to the conceptual model, groundwater in springs, shallow bedrock mesa saturation, perched-intermediate zone, and the regional aquifer is largely recharged by infiltration in the mountain block including surface water in upper Cañon de Valle. This groundwater follows mountain front and fault zone fractures and is then diverted laterally at different depths along high permeability horizons (e.g. partings and surge beds) (Figure 7.4-1). Water from higher elevations that doesn't discharge at the TA-16 springs percolates deeper to provide recharge to the perched-intermediate zone and regional aquifer (Figure 7.4-1). To test the conceptual model, the proportion of MBR to deep groundwater via upper Cañon de Valle and the Pajarito fault zone was estimated using water balance data (section 3.0). The highest estimated mountain block loss to deeper zones was found to occur during spring (up to 98% of upper Cañon de Valle streamflow), when snowmelt runoff dominates. The lowest values occurred during June through July and December through January (<10%). Based on this analysis, the majority of net recharge to deep groundwater is sourced from above the Pajarito fault zone during the snowmelt period.

The water balance is a crude but convincing assessment of the potential for significant MBR and MFR to the deeper groundwater zones. However, a quantitative assessment of relative proportions of mountain block vs local TA-16 provides information useful to further hydrologic modelling. As discussed in section 6.0, a simple binary mixing model using chloride as a conservative tracer suggests MBR contributes 60% to 90% of the water in the perched-intermediate zone and 94% to 95% for the regional aquifer. The lowest MBR values were for perched-intermediate zone wells near or directly beneath Cañon de Valle. A more sophisticated mixing model approach using water chemistry data, specific flow paths, and geologic constraints using PHREEQC yielded results similar to the simple mixing model (i.e., 49% to 99% MBR) with the lowest proportions also being found at the top of perched-intermediate zone wells close to Cañon de Valle. Findings of high proportions of uncontaminated MBR have favorable implications for the long-term fate of HE contaminants, particularly in the regional aquifer. The high proportions of MBR in the perched-intermediate zone will help buffer concentrations over time and the very high proportions in the regional system will help moderate concentrations both vertically and laterally.

Stable isotopes, tritium, and carbon-14 data also help refine the conceptual model, particularly with regards to perched-intermediate and regional aquifer sources (sections 1.0 and 4.0). There are two main recharge pathways to the perched-intermediate zone and the regional aquifer; mountain block and MFR from the Pajarito fault zone, and local TA-16 recharge from lower Cañon de Valle streamflow. The volumetrically important component is mountain block/front recharge. Although relatively low-volume, contaminated, local TA-16 recharge to the perched-intermediate zone and regional aquifer does occur. Maps of stable isotope, RDX, tritium, and carbon-14 data show a hotspot of isotopically light, contaminated, and relatively young water in the perched-intermediate zone and regional aquifer in an area around the perennial reach of Cañon de Valle (Figures 4.4-1 to 4.4-5).

7.6 Future Work

There are still knowledge gaps in our understanding of the TA-16 area hydrology, despite strengthening of the TA-16 hydrologic model. Filling in spatial data gaps in water stable isotopes, tritium, and carbon-14 in recently drilled wells would serve to flesh out the extent of young, contaminated water recharge from Cañon de Valle to the regional aquifer. Robust high-resolution quarterly monitoring of existing wells and near-surface TA-16 hydrologic systems would help to temporally balance the TA-16 database, which is currently skewed to late 1990s and early 2000s data. Monitoring should also continue for the deep groundwater tracer study which will help improve understanding of connectivity between perched-intermediate zone wells and deeper hydrologic zones. Additional modeling of future RDX concentrations in deep wells, factoring in the proportion of MBR is suggested.

8.0 REFERENCES AND MAP DATA SOURCES

8.1 References

The following reference list includes documents cited in this report.

Adams, A.L., G. Fraser, and D. Counce. "Chemical and Isotopic Variations of Precipitation in the Los Alamos Region, New Mexico," Los Alamos National Laboratory report LA-12895-MS, Los Alamos, New Mexico (1995).

Anderholm, S.K.. "Ground-water recharge near Santa Fe, north-central New Mexico," U.S. Geological Survey Water-Resources Investigations Report 94-4078, Albuquerque, New Mexico (1994).

Back, W.. "Hydrochemical facies and ground-water flow patterns in northern part of Atlantic coastal plain," U.S. Geological Survey Professional Paper 498-A, Washington, D.C. (1966).

Bitner, K., B. Gallaher, and K. Mullen. "Review of Wildfire Effects on Chemical Water Quality," Los Alamos National Laboratory report LA-13826-MS, Los Alamos, New Mexico (2001).

Blake, W.D., F. Goff, A.I. Adams, and D. Counce. "Environmental geochemistry for surface and subsurface waters in the Pajarito Plateau and outlying areas, New Mexico," Los Alamos National Laboratory report LA-12912-MS, Los Alamos, New Mexico (1995).

Borch, T., R. Kretzchmar, A. Kappler, P.V. Cappellen, M. Ginder-Vogel, A. Voegelin, and K. Campbell. "Biogeochemical Redox Processes and their Impact on Contaminant Dynamics," *Environmental Science & Technology*, Vol. 44, No. 1, pp. 15-23 (2010).

Brady, B.W.. "Hydrogeochemical Investigaton of Recharge Pathways to Intermediate and Regional Groundwater in Cañon de Valle and Technical Area 16, Los Alamos National Laboratory," MS Thesis, University of New Mexico (2017).

Clark, I.D., and P. Fritz. *Environmental Isotopes in Hydrogeology*, CRC Press LLC, Boca Raton, Florida (1997).

Clayton, J.L.. "Alkalinity Generation in Snowmelt and Rain Runoff during Short Distance Flow over Rock," Res. Pap. RMRS-RP-12. Ogden, UT: U.S. Department of Agriculture, Rocky Mountain Research Station (1998).

Clow, D. W., and M. Mast. "Mechanisms for chemostatic behavior in catchments: Implications for CO2 consumption by mineral weathering," *Chemical Geology*, Vol. 269, No. 1, pp. 40-51 (2010).

Craig, H.. “The isotopic geochemistry of water and carbon in geothermal areas,” Nuclear Geology on Geothermal Areas, Spoleto Conference Proceedings, 1963, Pisa, Italy, pp. 17-53 (1963).

Custodio, E.. “Estimation of aquifer recharge by means of atmospheric chloride deposition balance in the soil,” *Contributions to Science*, Vol. 6, No. 1, pp. 81-97 (2010).

DeWalle, D.R., P.J. Edwards, B.R. Swistock, R. Aravena, and R.J. Drimmie. “Seasonal isotope hydrology of three Appalachian forest catchments,” *Hydrological Processes*, Vol. 11, pp. 1895-1906 (1997).

Duncan, J.M., L.E. Band, and P.M. Groffman, 2017. “Variable nitrate concentration-discharge relationships in a forested watershed,” *Hydrological Processes*, Vol. 31, No. 9, pp. 1817-1824.

EPA (U.S. Environmental Protection Agency). “Technical Fact Sheet Hexahydro-1,3,5-trinitro- 1,3,5-triazine (RDX)” (2014).

Gallaher, B.M., and R.J. Koch. “Cerro Grande Fire Impacts to Water Quality and Stream Flow near Los Alamos National Laboratory: Results of Four Years of Monitoring,” Los Alamos National Laboratory report LA-14177-MS, Los Alamos, New Mexico (2004).

Gard, M., and B. Newman. “High Explosives Source Term at TA-16”. Los Alamos National Laboratory report LA-UR-05-9433, Los Alamos, New Mexico (2006).

Gat, J.R.. “Comments on the stable isotope method in regional groundwater investigations” *Water Resources Research*, Vol. 7, No. 4, pp. 980-993 (1971).

Godsey, S.E., J.W. Kirchner, and D.W. Clow. “Concentration-discharge relationships reflect chemostatic characteristics of US catchments,” *Hydrological Processes*, Vol. 23, No. 13, pp. 1844-1864 (2009).

Griggs, R.L.. “Geology and ground-water resources of the Los Alamos area, New Mexico,” Geological Survey Water-Supply Paper 1753, U.S. Department of the Interior. United States Government Printing Office, Washington, D.C. (1964).

Groffman, A.R., and L.J. Crossey. “Transient redox regimes in a shallow alluvial aquifer,” *Chemical Geology*, Vol. 161, No. 4, pp. 415-442 (1999).

Lee, E.S., and Krothe, N.C.. “A four-component mixing model for water in a karst terrain in south-central Indiana, USA. Using solute concentration and stable isotopes as tracers,” *Chemical Geology*, Vol. 179, pp. 129-143 (2001).

Longmire, P.. “Characterization Well R-25 Geochemistry Report,” Los Alamos National Laboratory report LA-14198-MS, Los Alamos, New Mexico (2004).

Longmire, P., M. Dale, D. Counce, A. Manning, T. Larson, K. Granzow, R. Gray, and B. Newman. “Radiogenic and Stable Isotope and Hydrogeochemical Investigation of Groundwater, Pajarito Plateau and Surrounding Area, New Mexico,” Los Alamos National Laboratory report LA-14333, Los Alamos, New Mexico (2007).

LANL (Los Alamos National Laboratory). “Phase III RFI Report for Solid Waste Management Unit 16-021(c)-99,” Los Alamos National Laboratory report LA-UR-03-5248, Los Alamos, New Mexico (2003a).

LANL (Los Alamos National Laboratory). “Corrective Measures Study Report for Solid Waste Management Unit 16-021(c)-99,” Los Alamos National Laboratory report LA-UR-03-7627, Los Alamos, New Mexico (2003b).

LANL (Los Alamos National Laboratory). “Hydrogeologic Studies of the Pajarito Plateau: A Synthesis of Hydrogeologic Workplan Activities (1998-2004),” Los Alamos National Laboratory document LA-14263-MS, Los Alamos, New Mexico (2005).

LANL (Los Alamos National Laboratory). “Water Canyon/Cañon de Valle Investigation Report,” Los Alamos National Laboratory report LA-UR-11-5478, Los Alamos, New Mexico (2011).

LANL (Los Alamos National Laboratory). “Remedy Completion Report for Corrective Measures,” Los Alamos National Laboratory report LA-UR-17-27678, Los Alamos, New Mexico (2017).

Maher, K.. “The role of fluid residence time and topographic scales in determining chemical fluxes from landscapes,” *Earth and Planetary Science Letters*, Vol. 312, No. 1, pp. 48-58 (2011).

Manning, A.H.. “Ground-water temperature, noble gas, and carbon isotope data from the Española Basin, New Mexico,” U.S. Geological Survey Scientific Investigations Report No. 2008-5200 (2009).

Manning, A.H., and J.S. Caine. “Groundwater noble gas, age, and temperature signatures in an Alpine watershed: Valuable tools in conceptual model development,” *Water Resources Research*, Vol. 43, No. 4 (2007).

Mazor, E.. *Chemical and isotopic groundwater hydrology*, Vol. 98, Marcel Dekker Inc., New York, New York (2004).

Miller, W.R., and J.I. Drever. “Water chemistry of a stream following a storm, Absaroka Mountains, Wyoming,” *Geological Society of America Bulletin*, Vol. 88, No. 2, pp. 286-290 (1977).

Newman, B.D., C.J. Duffy, and D.D. Hickmott. “Evaluating the hydrogeochemical response of springs using singular spectrum analysis and phase-plane plots,” *New Approaches to Characterizing groundwater flow,* Balkema Publishers, Tokyo, Japan. pp. 763-767 (2001).

Newman, B.D., K.C. Havenor, and P. Longmire. “Identification of hydrochemical facies in the Roswell Artesian Basin, New Mexico (USA), using graphical and statistical methods,” *Hydrogeology Journal*, Vol. 24, No. 4, pp. 819-839 (2016).

Newman, B.D., D.D. Hickmott, and P. Gram. “Flow and high explosives transport in a semiarid mesa in New Mexico, U.S.A.,” Los Alamos National Laboratory report ERID-095632, Los Alamos, New Mexico (2007).

Newman, B.D., H.M. Throckmorton, D.E. Graham, B. Gu, S.S. Hubbard, L. Liang, Y. Wu, J.M. Heikoop, E.M. Herndon, T.J. Phelps, C.J. Wilson, and S.D. Wullschleger. “Microtopographic and Depth Controls on Active Layer Chemistry in Arctic Polygonal Ground,” *Geophysical Research Letters*, Vol. 42, No. 6, pp. 1808-1817 (2015).

Newman, B.D., E.R. Vivoni, and A.R. Groffman. “Surface water-groundwater interactions in semiarid drainages of the American southwest,” *Hydrological Processes*, Vol. 20, No. 15, pp. 3371-3394 (2006).

NMED (New Mexico Environment Department). “Risk Assessment Guidance for Site Investigations and Remediation,” Vol. 1, Santa Fe, New Mexico (2014).

Nifong, R.L., M.J. Cohen, and W.P. Cropper Jr.. “Homeostasis and nutrient limitation of benthic autotrophs in natural chemostats,” *Limnology and Oceanography*, Vol. 59, No. 6, pp. 2101–2111 (2010).

Odum, H.T.. “Trophic structure and productivity of Silver Springs, Florida,” *Ecological monographs*, Vol. 27, No. 1, pp. 55-112 (1957).

Panichi, C., and R. Gonfiantini. “Environmental isotopes in geothermal studies,” *Geothermics*, Vol. 6, pp. 143-161 (1978).

Parkhurst, D.L., and C.A.J. Appelo. “Description of input and examples for PHREEQC version 3--A computer program for speciation, batch- reaction, one-dimensional transport, and inverse geochemical calculations,” U.S. Geological Survey Techniques and Methods, Book 6, Chap. A43 (2013).

Rango, A.. “Snow: the real water supply for the Rio Grande Basin,” *New Mexico Journal of Science*, Vol. 44, pp. 99-118 (2006).

Reid, K.D., S.L. Reneau, B.D. Newman, and D.D. Hickmott. “Barium and high explosives in a semiarid alluvial system, Cañon de Valle, New Mexico,” *Vadose Zone Journal*, Vol. 4, No. 3, pp. 744-759 (2005).

Shanley, J.B., W.H. McDowell, and R.F. Stallard. “Long-term patterns and short-term dynamics of stream solutes and suspended sediment in a rapidly weathering tropical watershed,” *Water Resources Research*, Vol. 47, No. 7 (2011).

Stearns, H.T.. “Ground-water supplies for Los Alamos, New Mexico,” Los Alamos National Lab document ER Record ID# 0011871 (1948).

Tetzlaff, D., J. Seibert, K.J., McGuire, H. Laudon, D.A. Burns, S.M. Dunn, and C. Soulsby. “How does landscape structure influence catchment transit time across different geomorphic provinces?” *Hydrological Processes*, Vol. 23, pp. 945-953 (2009).

Valett, H.M., C.N. Dahm, M.E. Campana, J.A. Morrice, M.A. Baker, and C.S. Fellows. “Hydrologic influences on groundwater-surface water ecotones: heterogeneity in nutrient composition and retention,” *Journal of the North American Benthological Society*, Vol. 16, No. 1, pp. 239–247 (1997).

Vuataz, F.D., and F. Goff. “Isotope Geochemistry of Thermal and Nonthermal Waters in the Valles Caldera, Jemez Mountains, Northern New Mexico,” *Journal of Geophysical Research*, Vol. 91, No. B2, pp. 1835-1853 (1986).

Walling, D.E., and B.W. Webb. “Solutes in River Systems,” *Solute Processes*, pp. 251–327 (1986).

Wilson, J.L., and H. Guan. “Mountain-Block Hydrology and Mountain-Front Recharge,” *Groundwater Recharge in a Desert Environment: The Southwestern United States*, AGU, Washington, D.C., pp. 113-137 (2004).

Yanicak, S.M., M. Dale, K. Granzow, P. Longmire, G. Perkins, and J. Fabryka-Martin. “Use of Groundwater Tracers to Assess Climate Change in North-Central New Mexico during the Holocene Epoch,” poster presented at the American Geophysical Union Fall Meeting, Dec., 2014, San Francisco, California (2014).

8.2 Map Data Sources

Point features; As published; EIM data pull; 2017.

SWMU or AOC boundary: Potential Release Sites; Los Alamos National Laboratory, ESH&Q Waste & Environmental Services Division, Environmental Data and Analysis Group.

Point features; As published; EIM data pull; 2017.

Drainage channel; Los Alamos National Laboratory, ER-ES, As published, GIS projects folder; \\slip\gis\GIS\Projects\15-Projects\15-0080\project_data.gdb\correct_drainage; 2017.

Technical Area Boundaries; Los Alamos National Laboratory, Site Planning & Project Initiation Group, Infrastructure Planning Office; September 2007; as published 13 August 2010.

Paved Road Arcs; Los Alamos National Laboratory, FWO Site Support Services, Planning, Locating and Mapping Section; 06 January 2004; as published 29 November 2010.

Contour, 5-, and 1- m intervals; os Alamos National Laboratory, ER-ES, As published, GIS projects folder; \\slip\gis\GIS\Projects\14-Projects\14-0080\project_data.gdb\jace_contour_meters; 2017.

Terminus location; Los Alamos National Laboratory, ER-ES, As published, GIS projects folder; \\slip\gis\GIS\Projects\14-Projects\14-0080\shp\bendan_CDV.shp; 2017.

er_faults_arc; Fault Traces; Los Alamos National Laboratory, ENV Remediation Services Project, ER2005-0007; 1:24,000 Scale Data; 04 January 2005.

Hillshade; Los Alamos National Laboratory, ER-ES, As published; \\slip\gis\Data\HYP\LiDAR\2014\Bare_Earth\BareEarth_DEM_Mosaic.gdb; 2014.

Structures; Los Alamos National Laboratory, KSL Site Support Services, Planning, Locating and Mapping Section; 06 January 2004; as published 29 November 2010.

wqh_postfire_floodplains_ply; Post Fire Floodplains; Los Alamos National Laboratory; ENV Water Quality & Hydrology Group; First edition, 17 May 2004.

Gain/Loose stream reach; Los Alamos National Laboratory, ER-ES, As published, GIS projects folder; \\slip\gis\GIS\Projects\14-Projects\14-0080\project_data.gdb\gain_loose_buffer; 2017.

SWMU or AOC boundary: Potential Release Sites; Los Alamos National Laboratory, ESH&Q Waste & Environmental Services Division, Environmental Data and Analysis Group.

Drainage channel; Los Alamos National Laboratory, ER-ES, As published, GIS projects folder; \\slip\gis\GIS\Projects\11-Projects\11-0108\gdb\gdb_11-0108_generic.mdb; drainage; 2017.

Approximate extent of RDX contamination in deep perched groundwater, based on current knowledge; Los Alamos National Laboratory, ER-ES, As published, GIS projects folder; \\slip\gis\GIS\Projects\15-Projects\15-0041\shp\perched_aquifer.shp; 2016.

Approximate extent of deep perched groundwater, based on current knowledgePerched intermediate groundwater elevation contour, 100-ft interval.

Perched intermediate groundwater elevation contour, 100-ft interval; Los Alamos National Laboratory, ER-ES, As published, GIS projects folder; \\slip\gis\GIS\Projects\15-Projects\15-0041\shp\sketch_contour.shp; 2016.

May 2017 groundwater elevation, 50-ft contours; Los Alamos National Laboratory, ER-ES, As published, GIS projects folder; \\slip\gis\GIS\Projects\16-Projects\16-0027\project_data.gdb\contour_wl2017may_2ft; 2017.

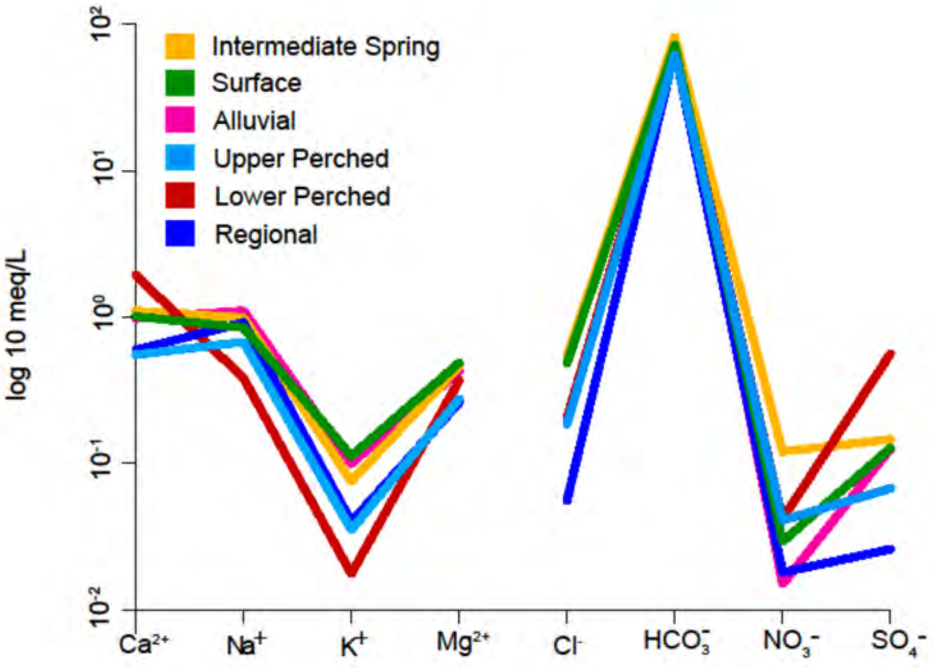

Figure 1.3-1 **Fingerprint diagram of TA-16 waters. Cations are plotted on the left and anions on the right. Concentrations are in meq/L.**

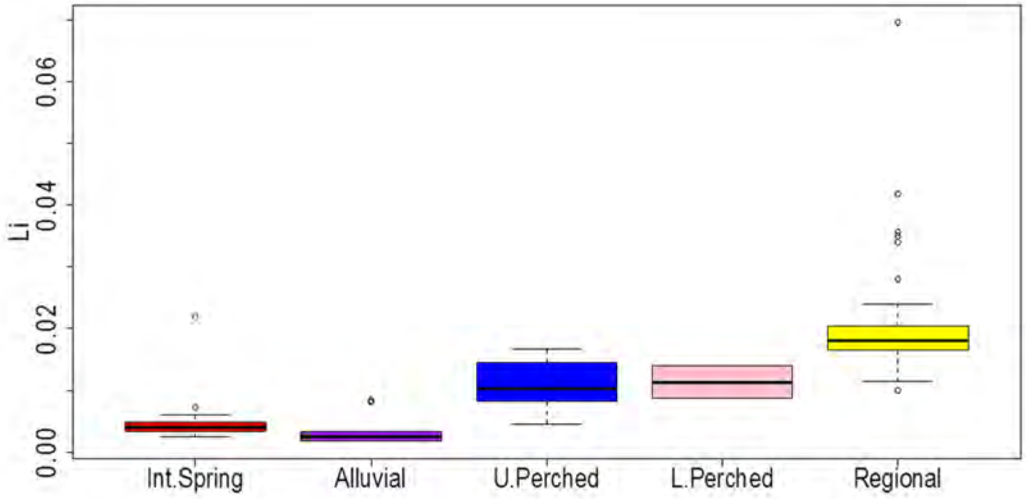

Figure 1.3-2 **Box and whisker plots for lithium (mg/L). For each zone, the bold line indicates the median, and the box indicates the second and third quartiles. Whiskers represent 1.5x the interquartile distance. Circles represent values outside the whisker range.**

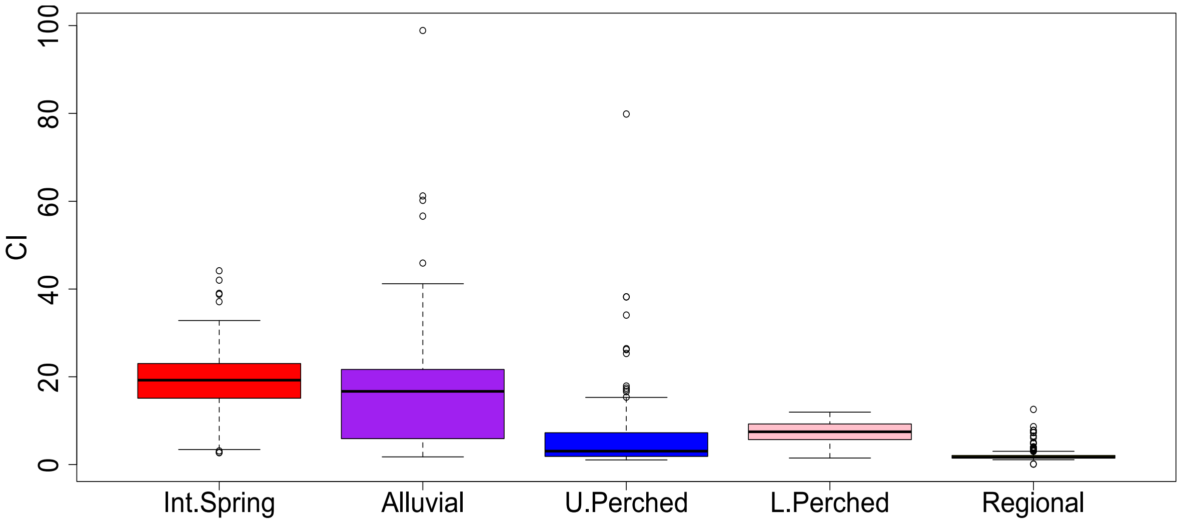

Figure 1.3-3 Box and whisker plots for chloride (mg/L). For each zone, the bold line indicates the median, and the box indicates the second and third quartiles. Whiskers represent 1.5x the interquartile distance. Circles represent values outside the whisker range.

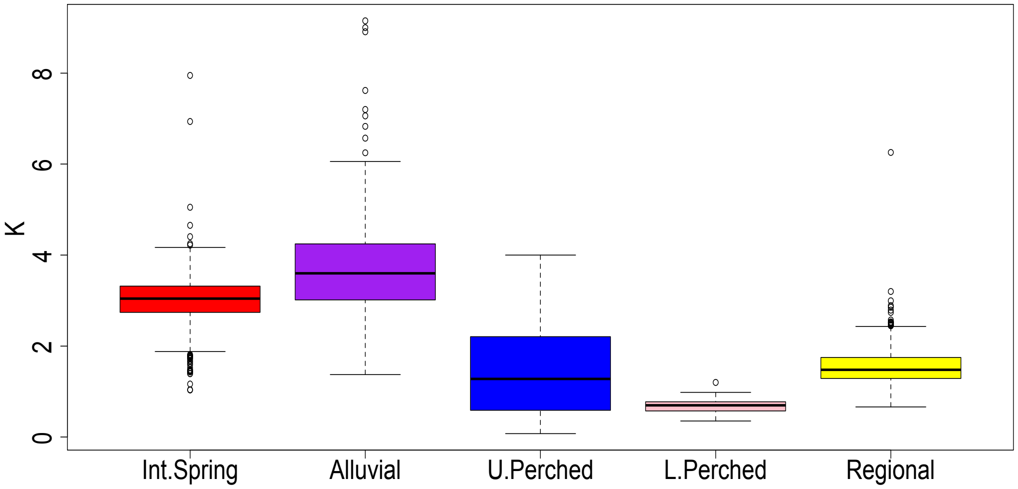

Figure 1.3-4 Box and whisker plots for potassium (mg/L). For each zone, the bold line indicates the median, and the box indicates the second and third quartiles. Whiskers represent 1.5x the interquartile distance. Circles represent values outside the whisker range.

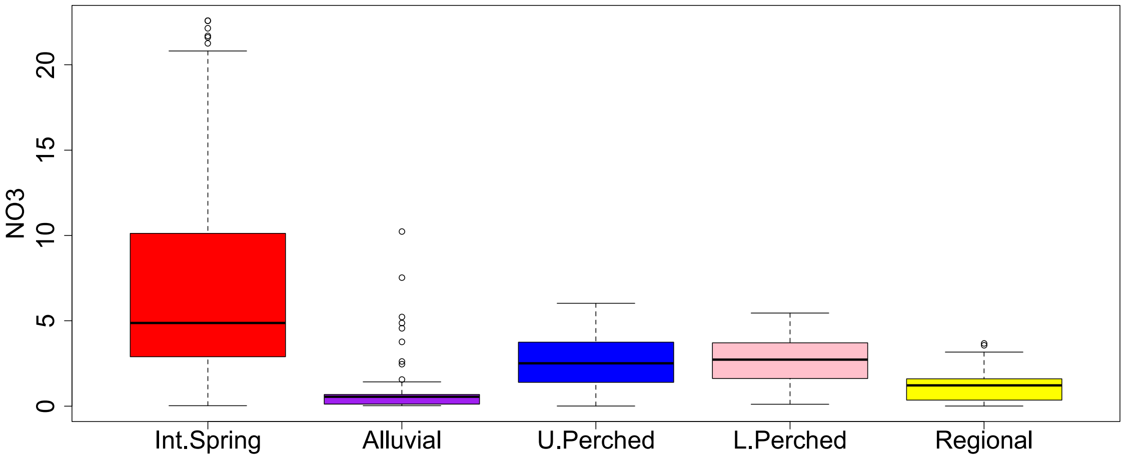

Figure 1.3-5 **Box and whisker plots for nitrate (mg/L). For each zone, the bold line indicates the median, and the box indicates the second and third quartiles. Whiskers represent 1.5x the interquartile distance. Circles represent values outside the whisker range.**

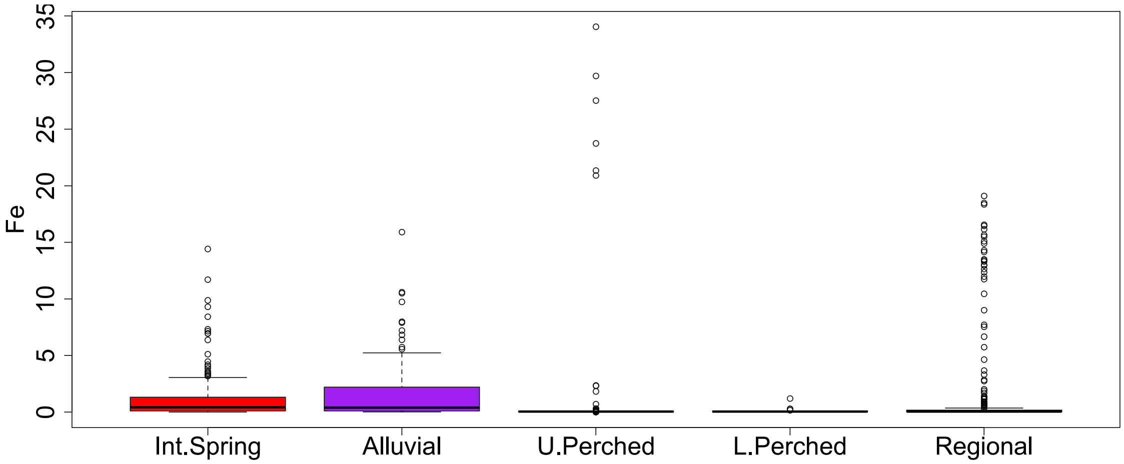

Figure 1.3-6 **Box and whisker plots for iron (mg/L). For each zone, the bold line indicates the median, and the box indicates the second and third quartiles. Whiskers represent 1.5x the interquartile distance. Circles represent values outside the whisker range.**

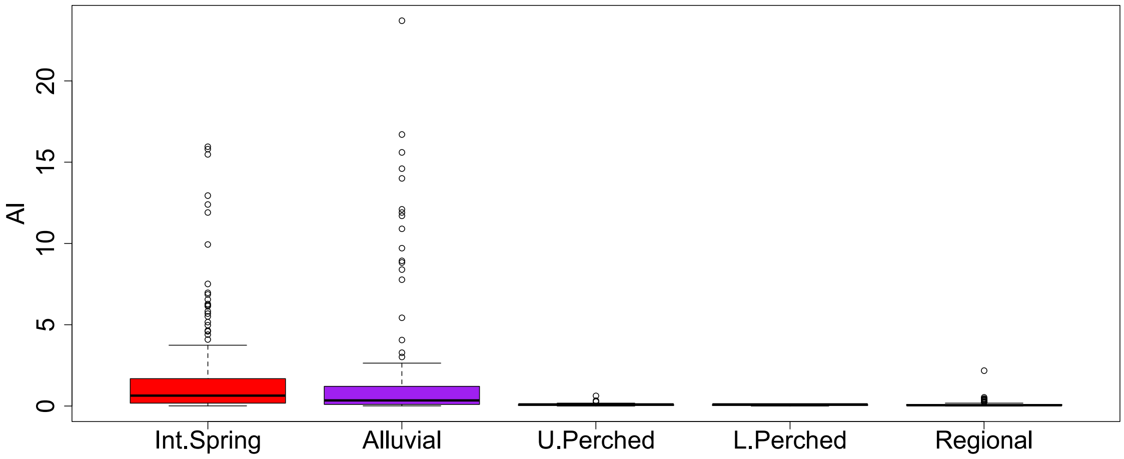

Figure 1.3-7 **Box and whisker plots for aluminum (mg/L). For each zone, the bold line indicates the median, and the box indicates the second and third quartiles. Whiskers represent 1.5x the interquartile distance. Circles represent values outside the whisker range.**

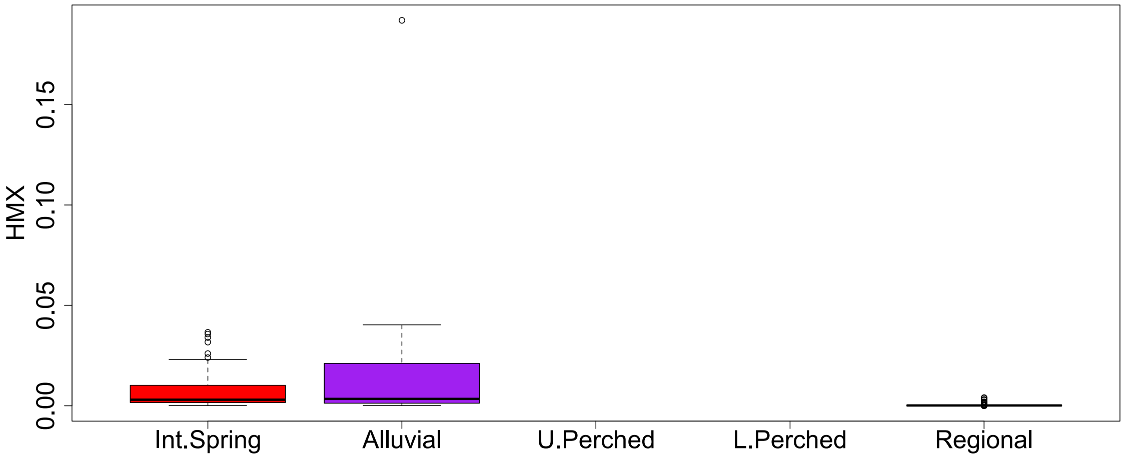

Figure 1.3-8 **Box and whisker plots for HMX (mg/L). For each zone, the bold line indicates the median, and the box indicates the second and third quartiles. Whiskers represent 1.5x the interquartile distance. Circles represent values outside the whisker range.**

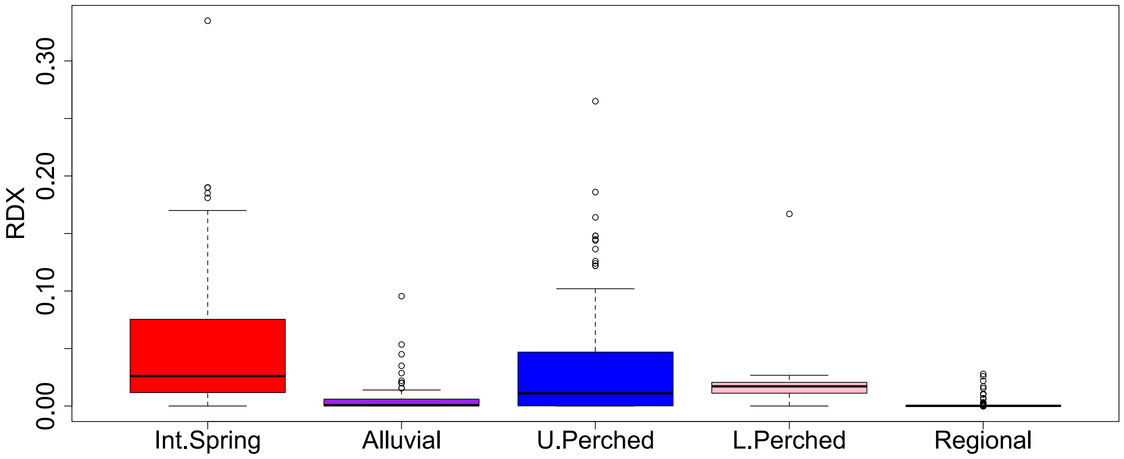

Figure 1.3-9 Box and whisker plots for RDX (mg/L). For each zone, the bold line indicates the median, and the box indicates the second and third quartiles. Whiskers represent 1.5x the interquartile distance. Circles represent values outside the whisker range.

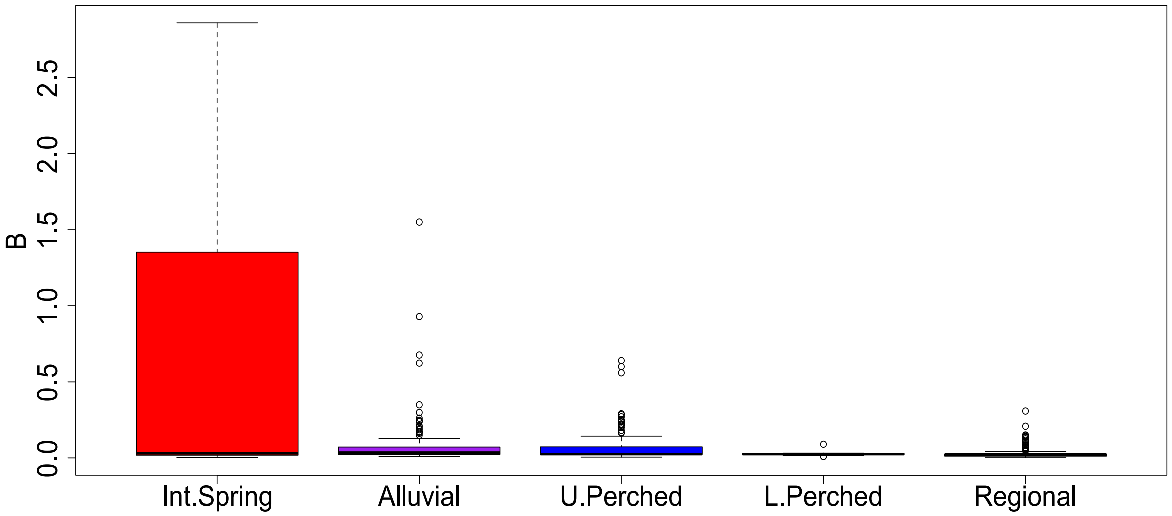

Figure 1.3-10 Box and whisker plots for boron (mg/L). For each zone, the bold line indicates the median, and the box indicates the second and third quartiles. Whiskers represent 1.5x the interquartile distance. Circles represent values outside the whisker range.

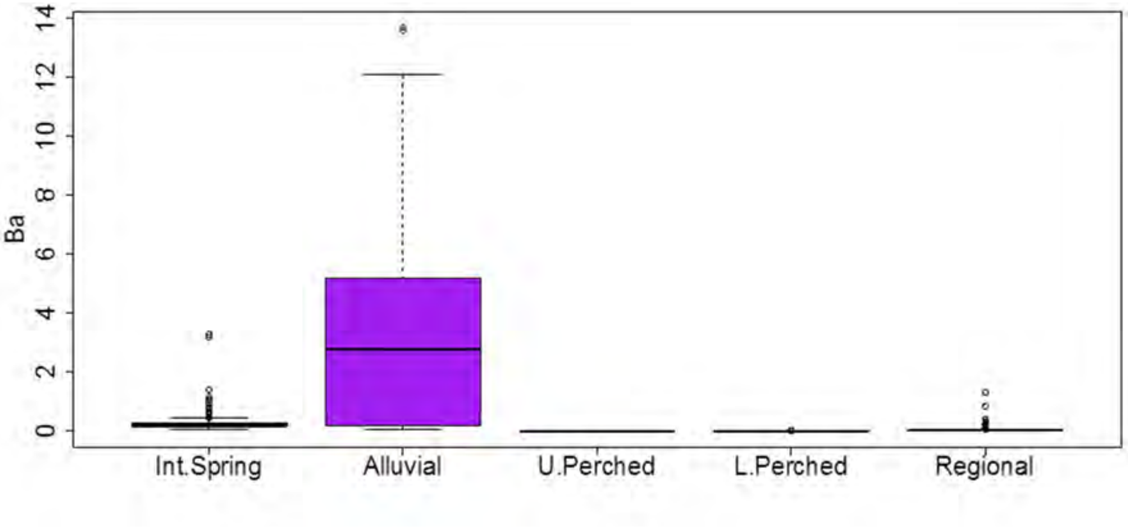

Figure 1.3-11 **Box and whisker plots for barium (mg/L). For each zone, the bold line indicates the median, and the box indicates the second and third quartiles. Whiskers represent 1.5x the interquartile distance. Circles represent values outside the whisker range.**

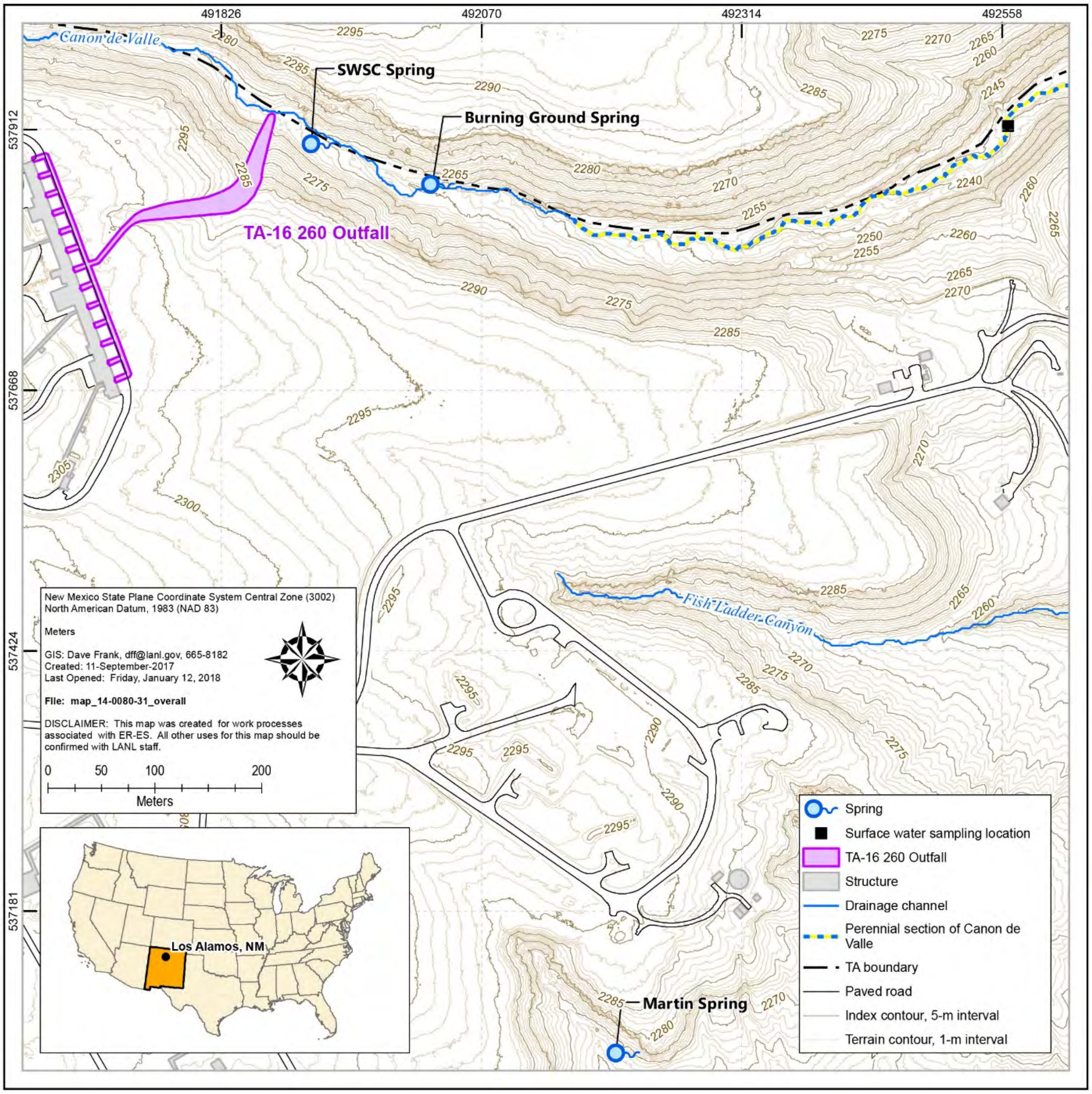

Figure 2.1-1 TA-16 study area, showing locations of springs, surface water samples, and the 260 Outfall with HE contamination. Discharge was measured at the sampling locations.

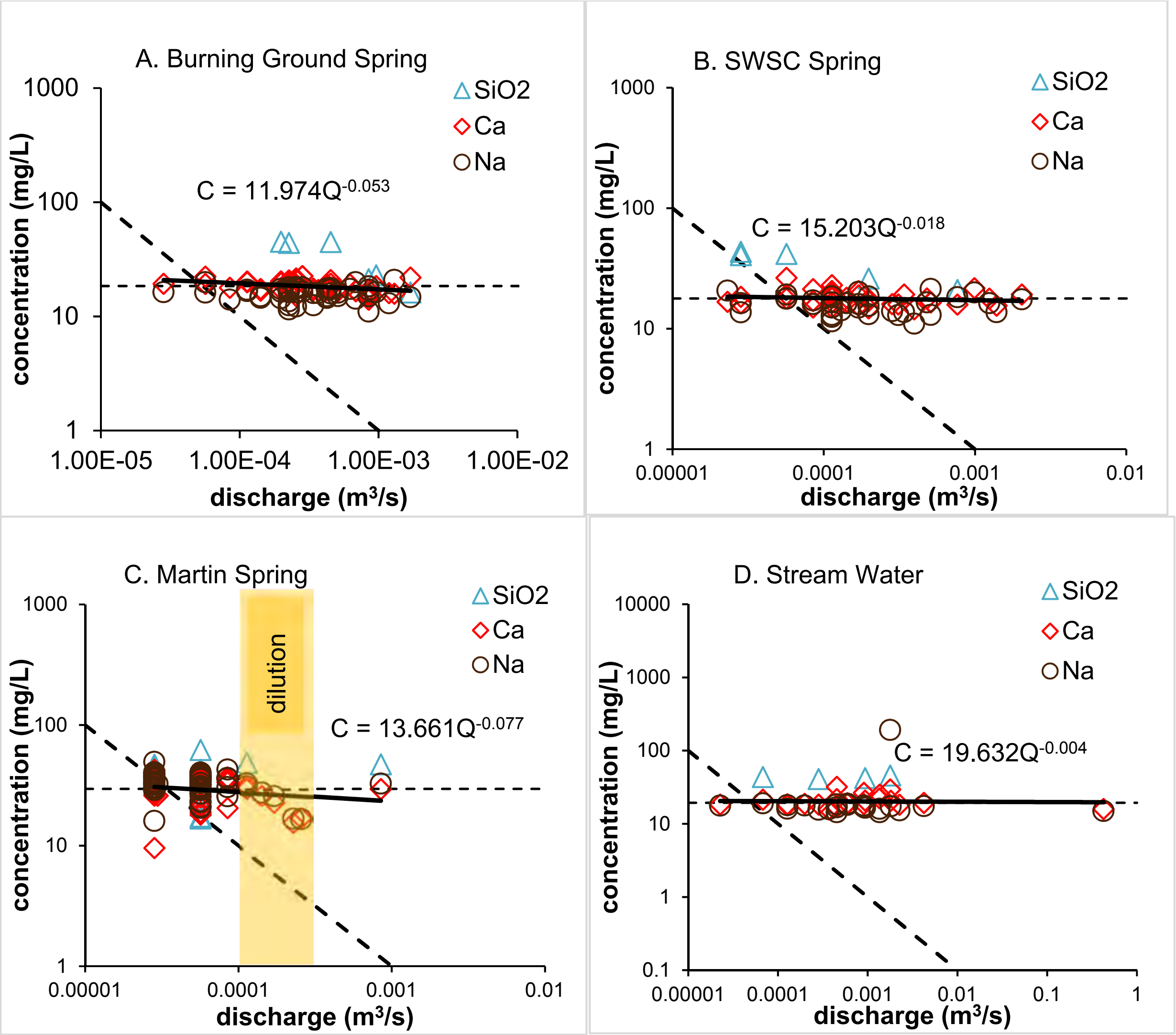

Figure 2.3-1 Log-log concentration-discharge plots of major cations for (A) Burning Ground Spring, (B) SWSC Spring, (C) Martin Spring with the discharge range of possible dilution-dominated behavior highlighted in yellow, and (D) Cañon de Valle stream water (note change in scale). The linear regression line (solid) of calcium concentration for each water system, the average calcium concentration line (dashed), and the arbitrary -1 slope dilution line (bold dashed) are displayed.

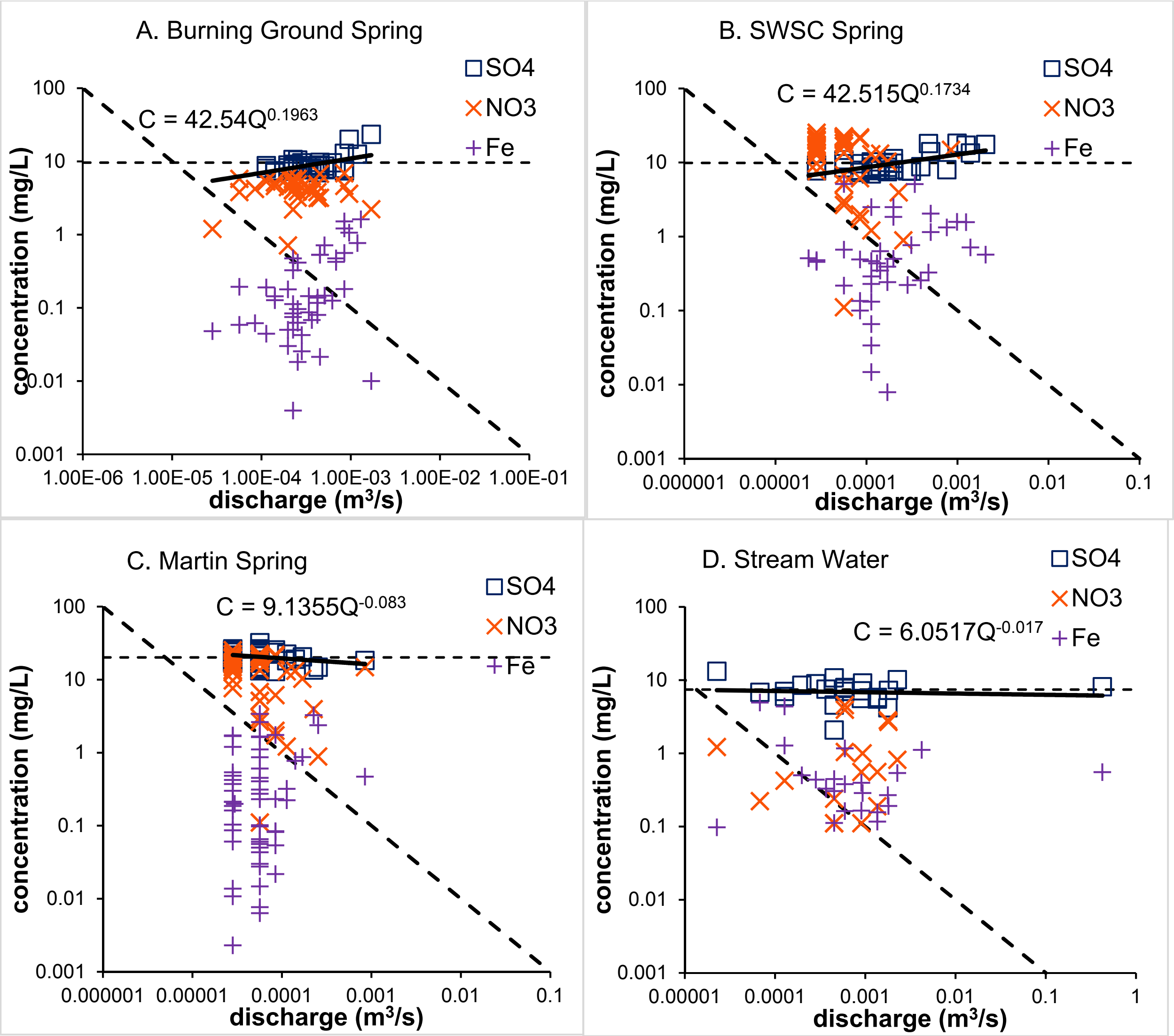

Figure 2.3-2 **Log-log concentration-discharge plots of redox-sensitive analytes for (A) Burning Ground Spring, (B) SWSC Spring, (C) Martin Spring, and (D) Cañon de Valle stream water. The linear regression line (solid) of sulfate concentration for each water system, the average sulfate concentration line (dashed), and the arbitrary -1 slope dilution line (bold dashed) are displayed.**

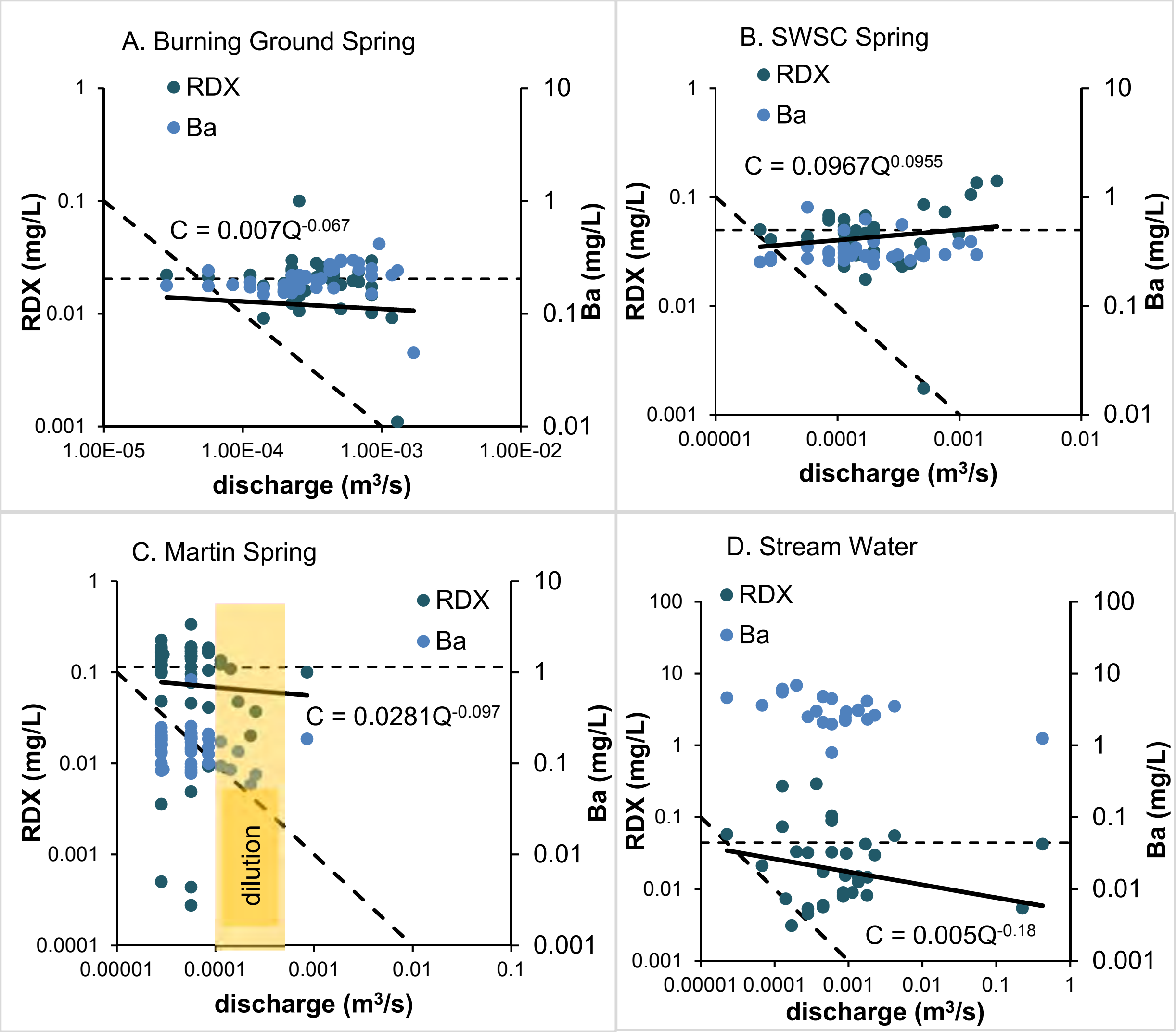

Figure 2.3-3 Log-log concentration-discharge plots of RDX and barium for (A) Burning Ground Spring, (B) SWSC Spring, (C) Martin Spring, and (D) Cañon de Valle stream water. The linear regression line (solid) of RDX concentration for each water system, the average RDX concentration line (dashed), and the arbitrary −1 slope dilution line (bold dashed) are displayed.

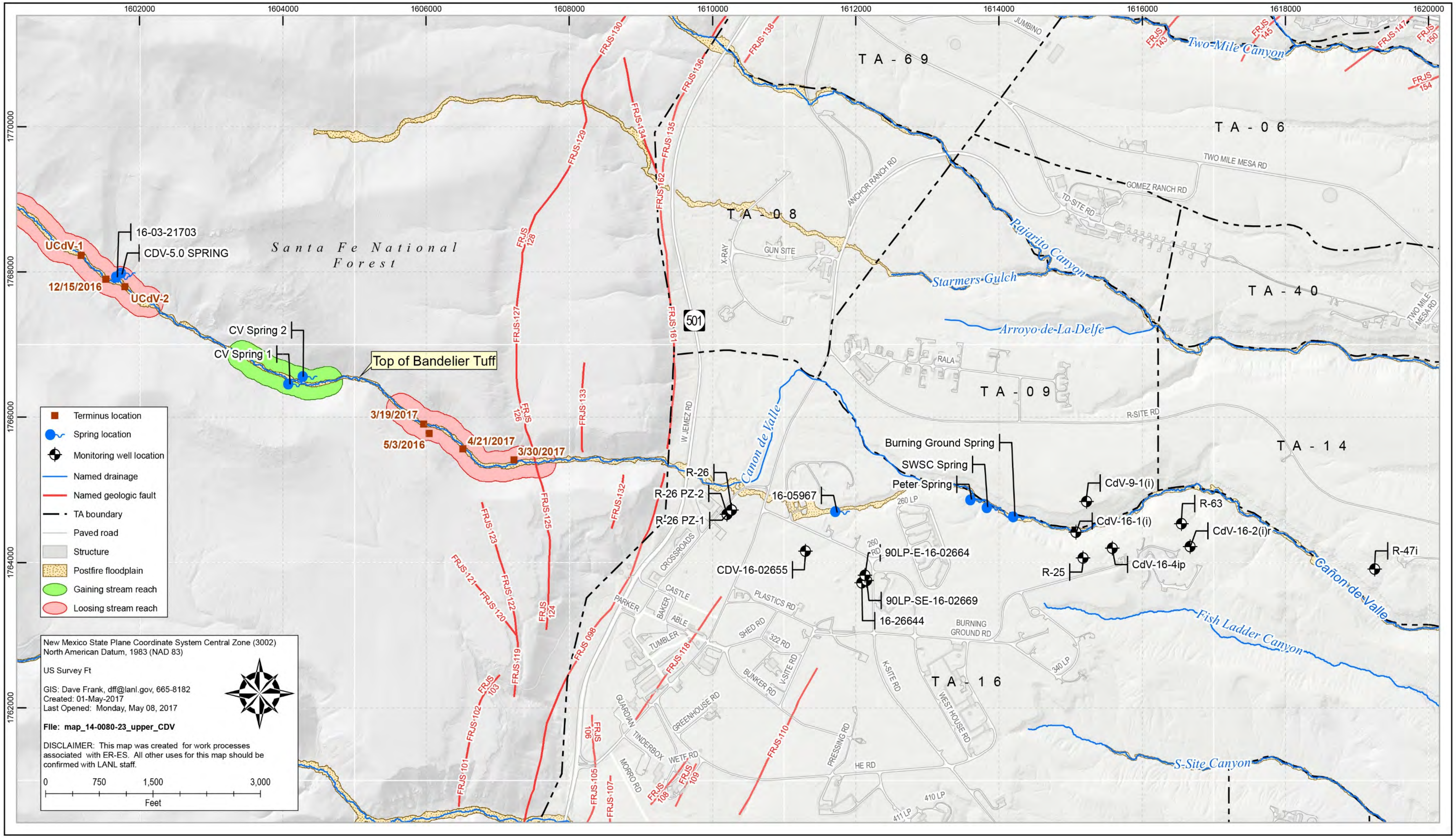

Figure 3.3-1 Stream reaches of upper Cañon de Valle west of the Pajarito fault and lower Cañon de Valle at TA-16, Los Alamos National Laboratory. Gaining reaches are indicated in green and loosing reaches in pink. Flow termination points are denoted by the red squares and the date of observation.

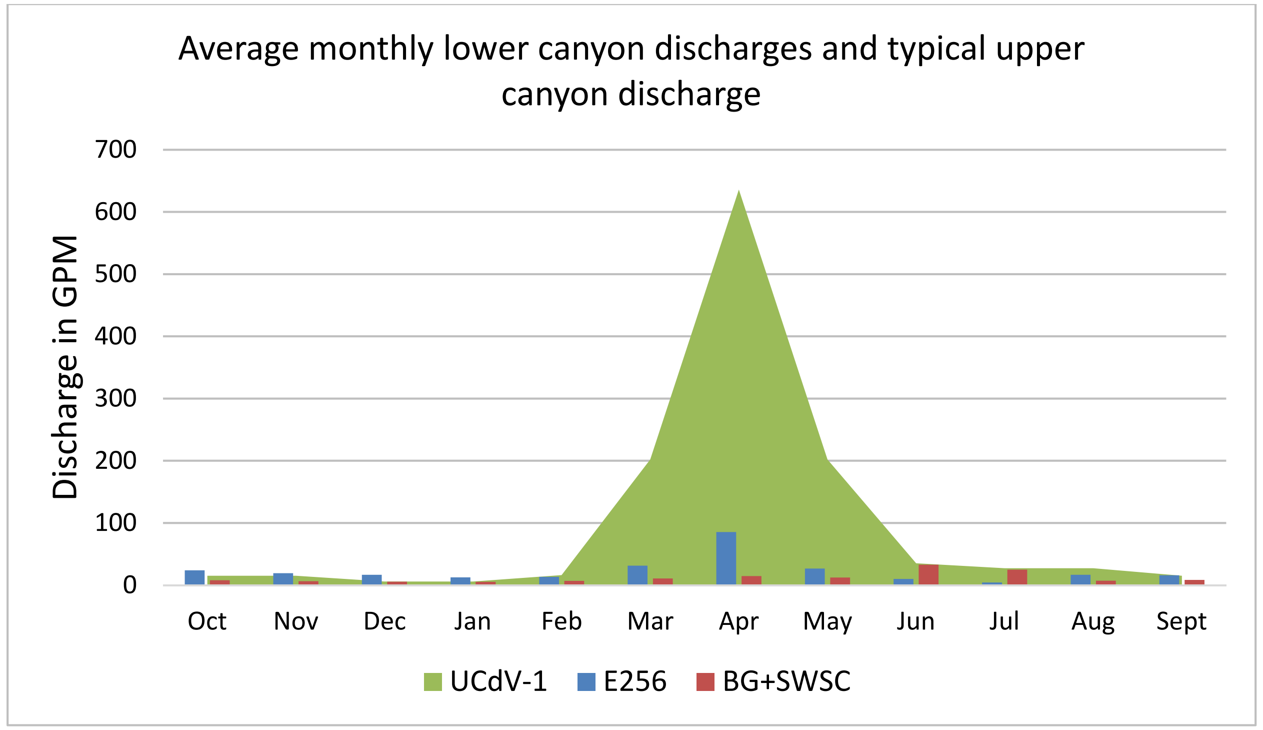

Figure 3.3-2 **Comparison of monthly average upper canyon discharge (UCdV-1 in green) and lower canyon discharges from TA-16 springs (BG+SWSC, in red) and the E256 gauging station (in blue) based on recent and historical upper canyon discharge data.**

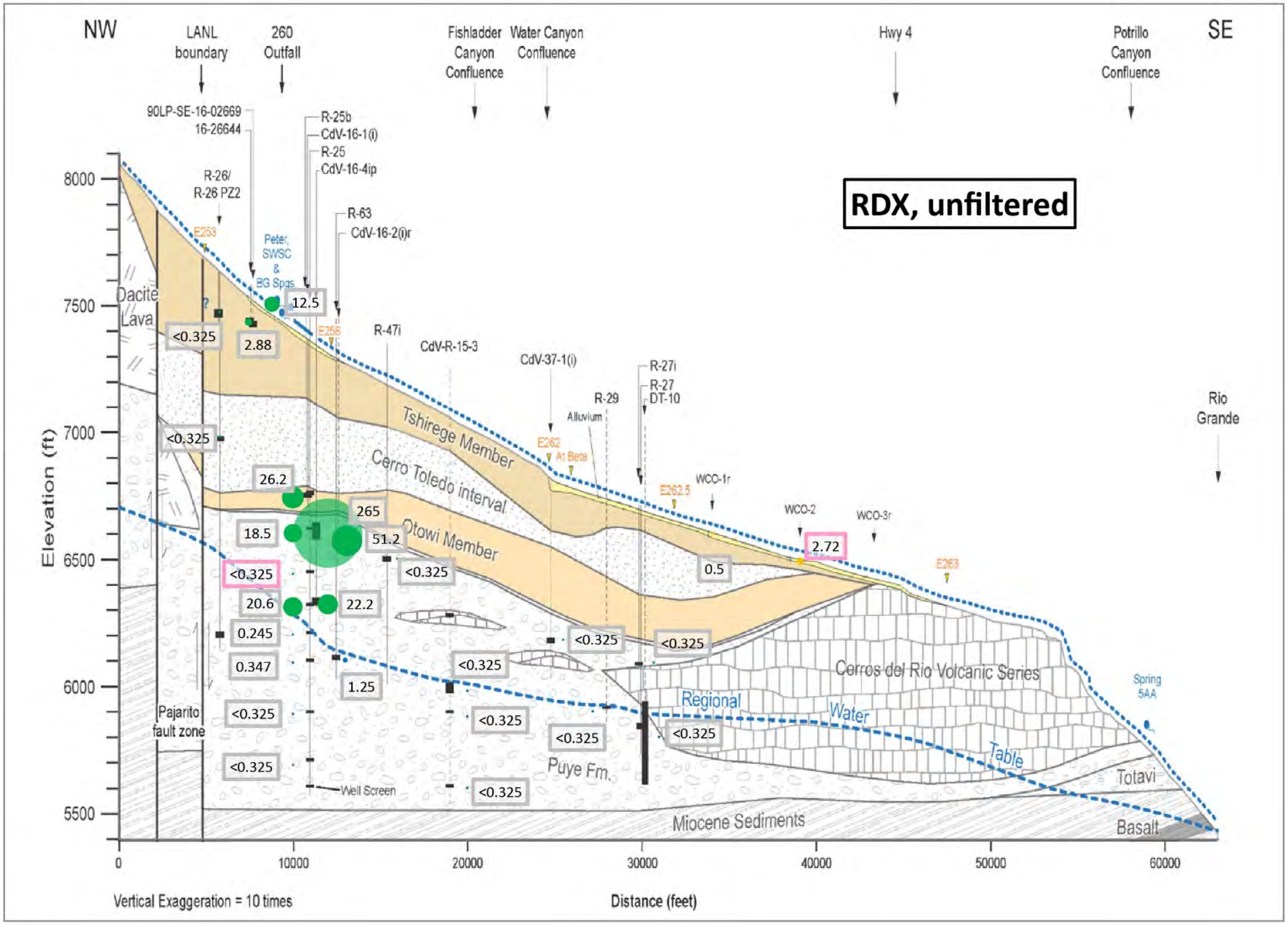

Figure 4.1-1 Cañon de Valle/Water Canyon cross section showing RDX concentrations in µg/L (LANL 2011)

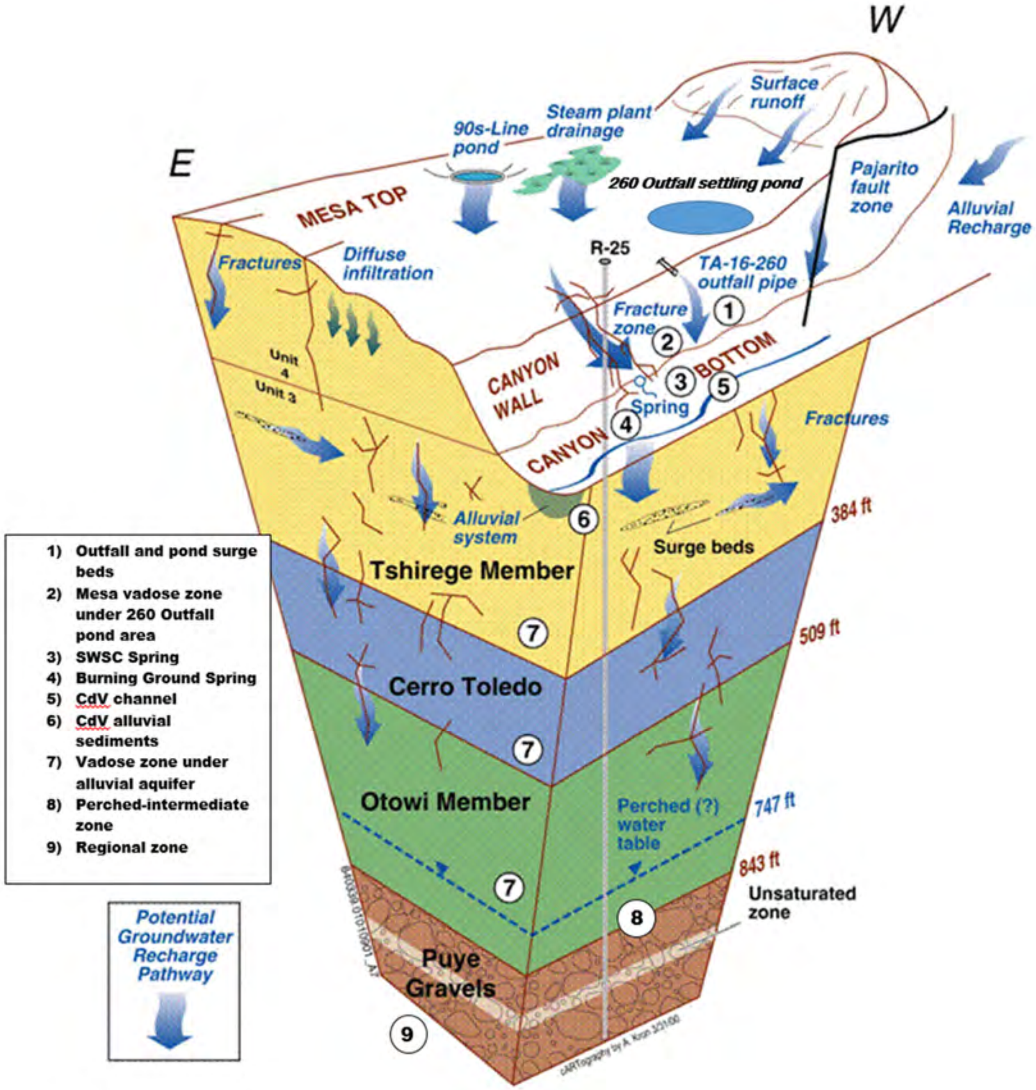

Figure 4.1-2 Conceptual block diagram showing the hydrologic zones in relation to the geologic units beneath TA-16

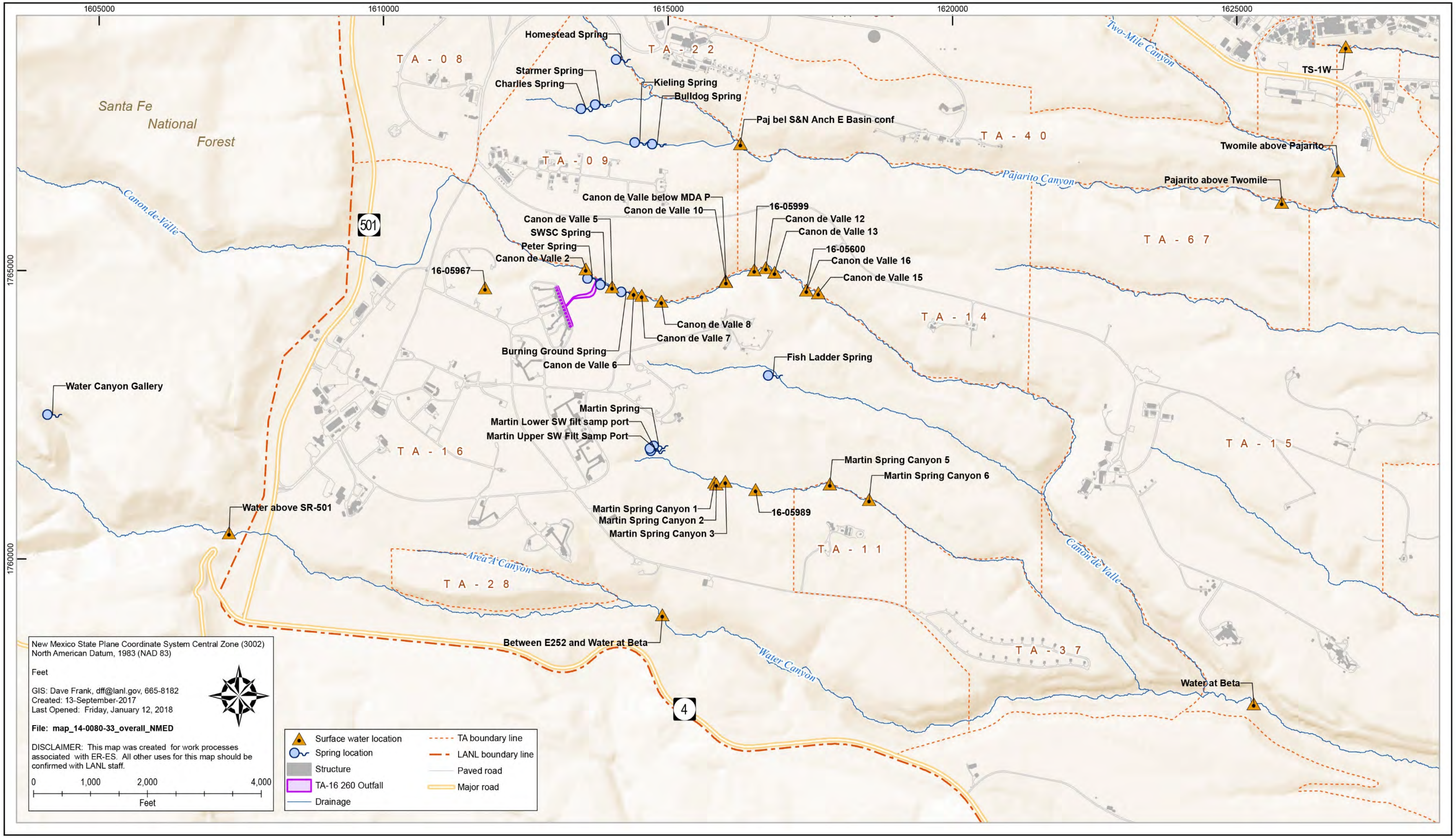

Figure 4.2-1 Surface water samples and springs location map

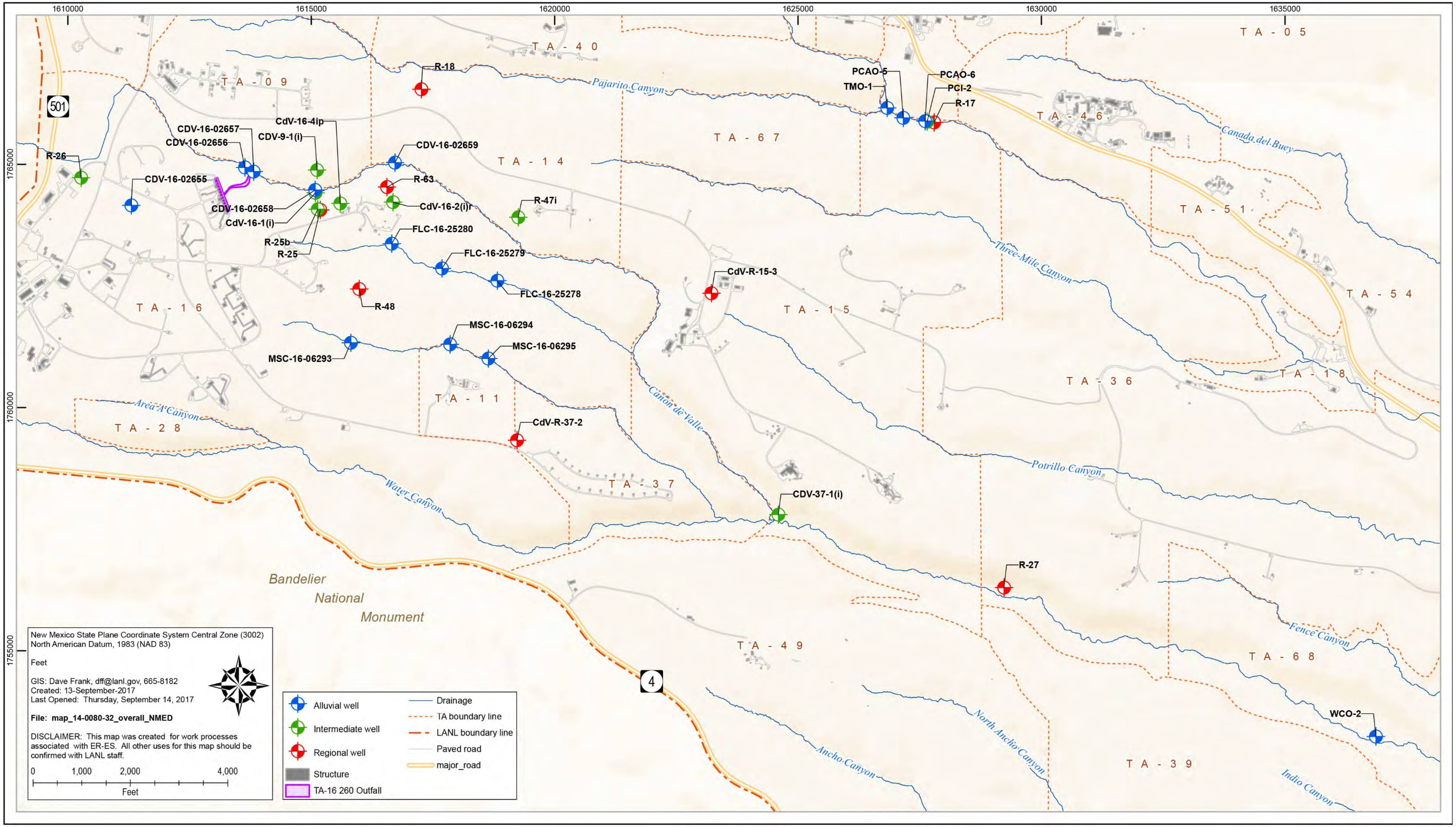

Figure 4.2-2 Alluvial, perched-intermediate, and regional wells location map

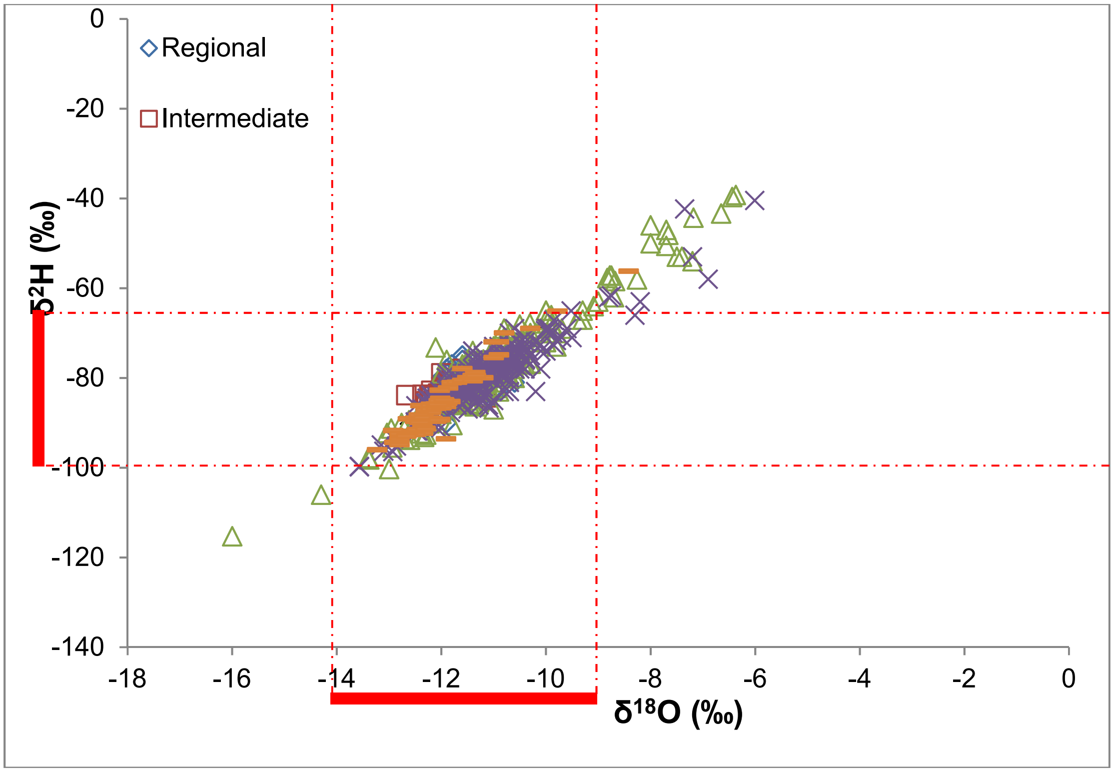

Figure 4.3-1 **Stable isotope ratios, grouped by hydrologic system**

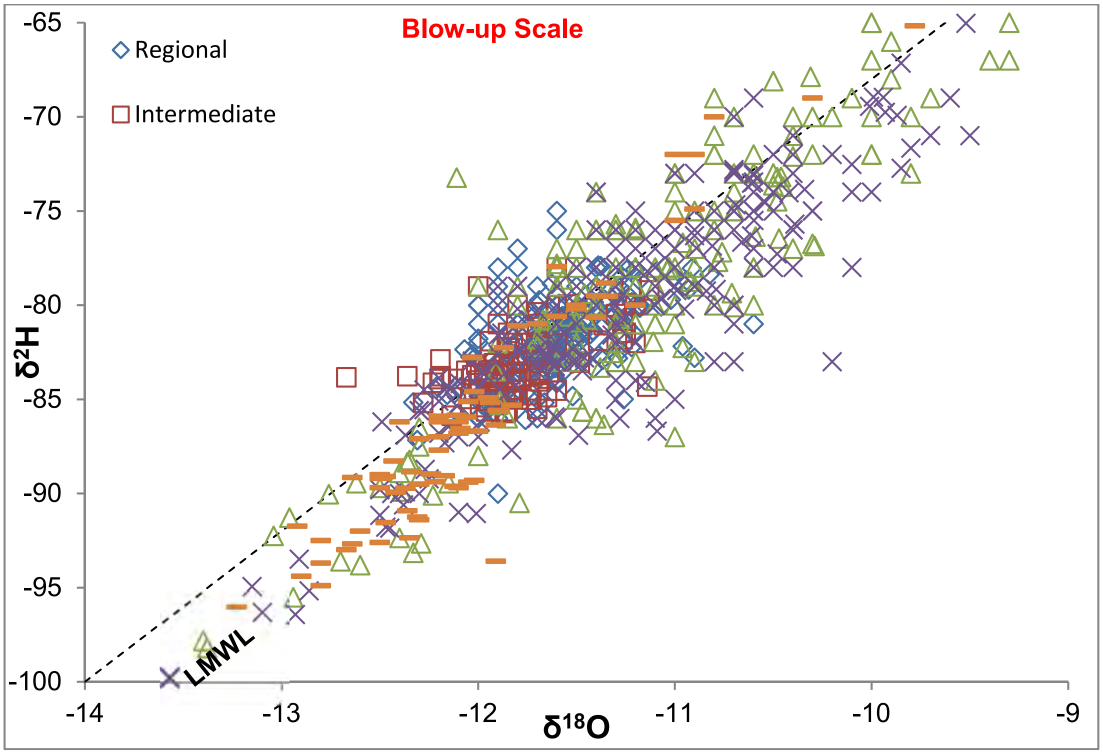

Figure 4.3-2 **Blow-up view of stable isotope ratios, grouped by hydrologic system. The local meteoric water line is from Vuataz & Goff, 1986.**

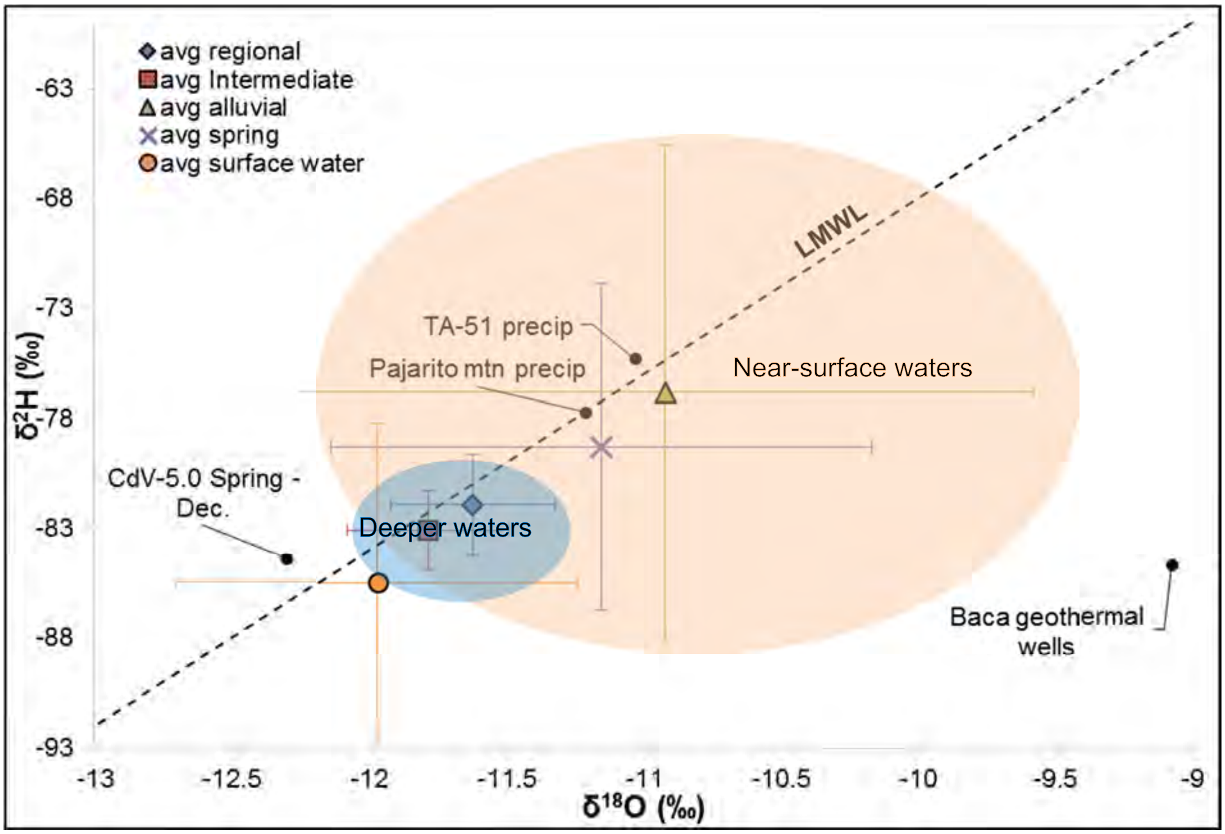

Figure 4.3-3 **Stable isotope averages and SDs, grouped by hydrologic system, vs average isotope ratios of local precipitation and surface water values**

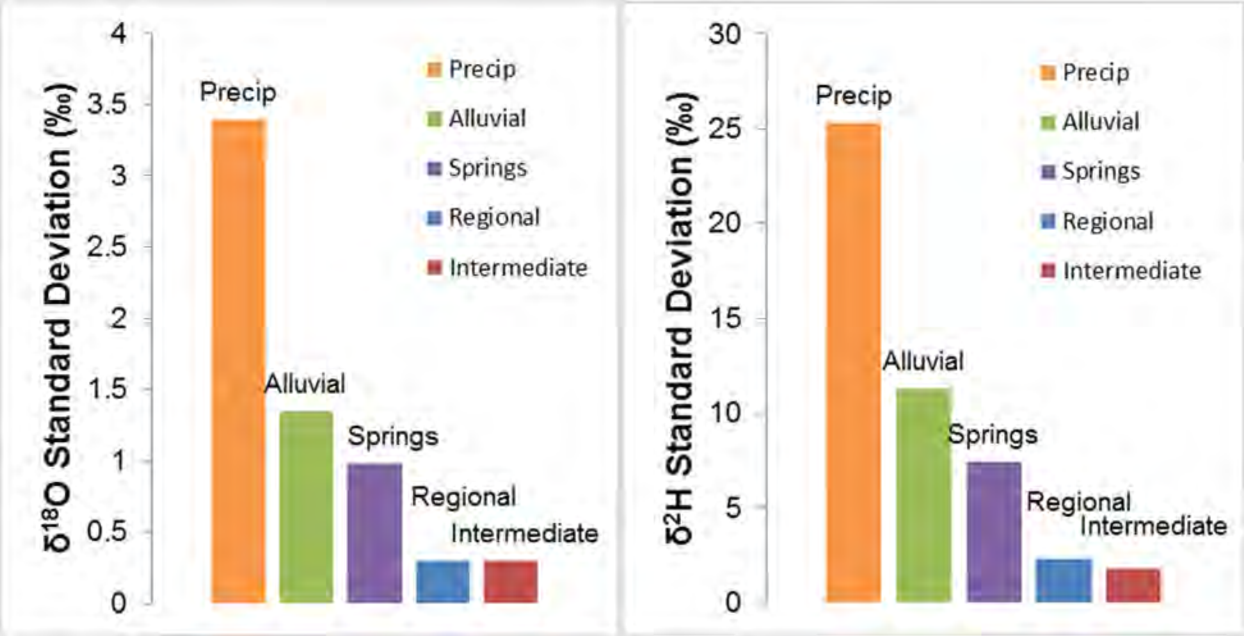

Figure 4.3-4 **Histograms of the SD for δ^{18}O and δ^{2}H separated by each hydrologic system. Because of sampling bias, surface water is not included.**

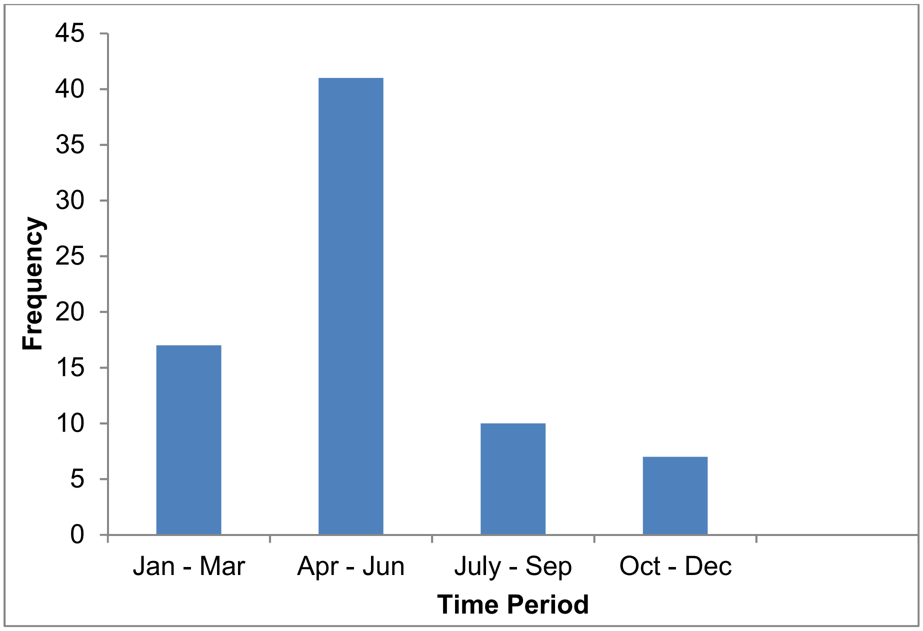

Figure 4.3-5 **Histogram of sample collection dates for surface water samples**

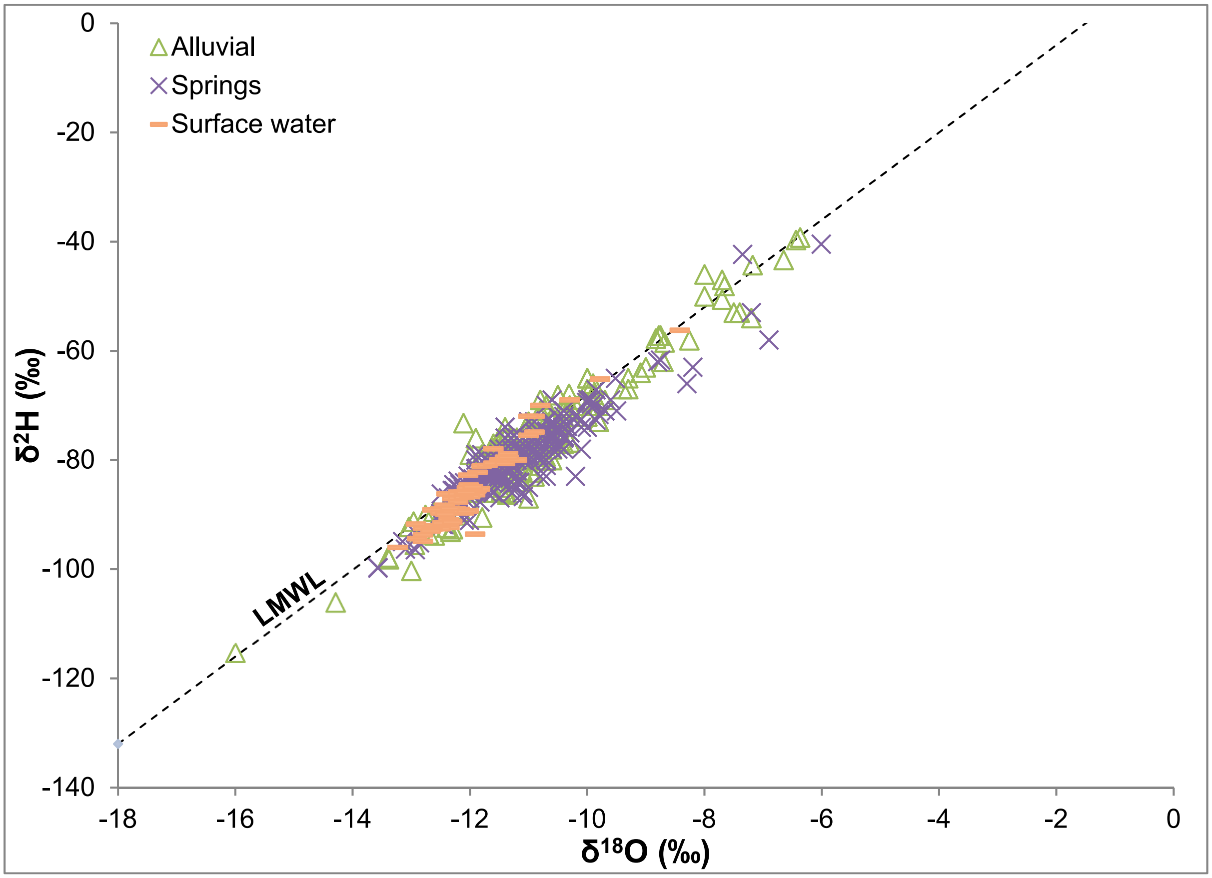

Figure 4.3-6 **Stable isotope ratios of alluvial zone, springs, and surface water samples**

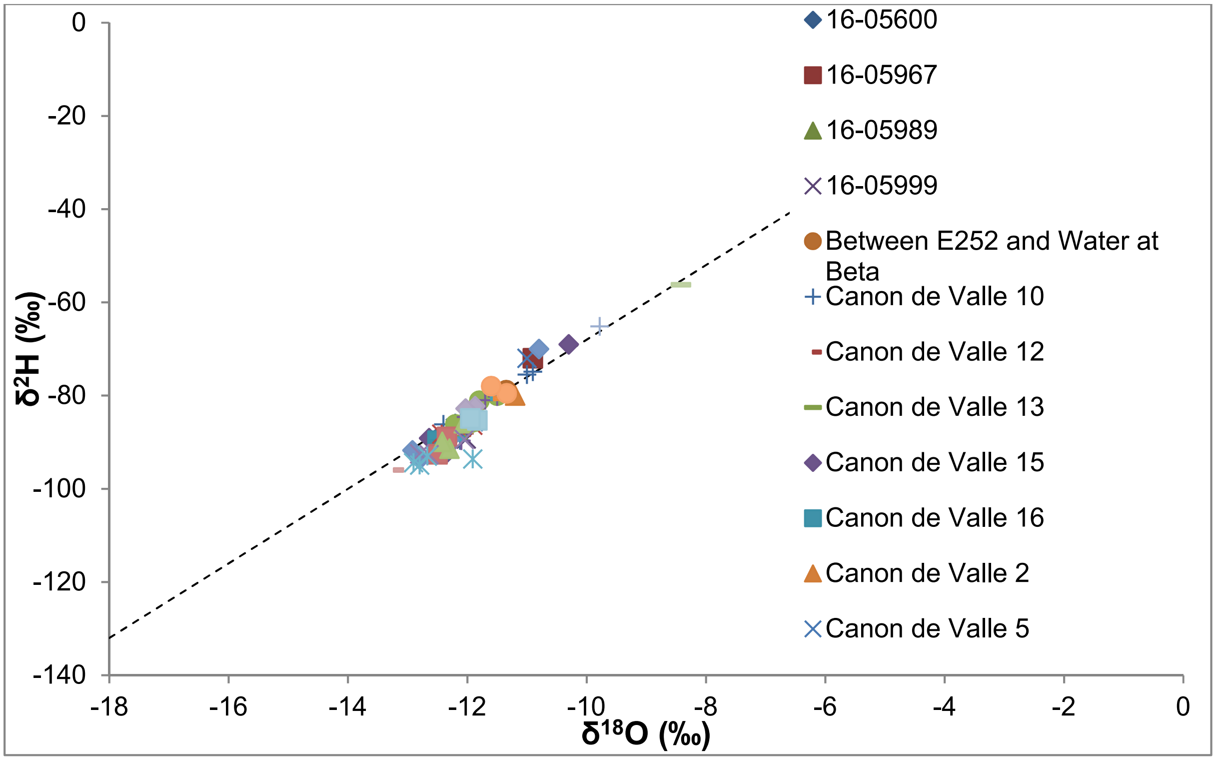

Figure 4.3-7 **Stable isotope ratios for surface water samples**

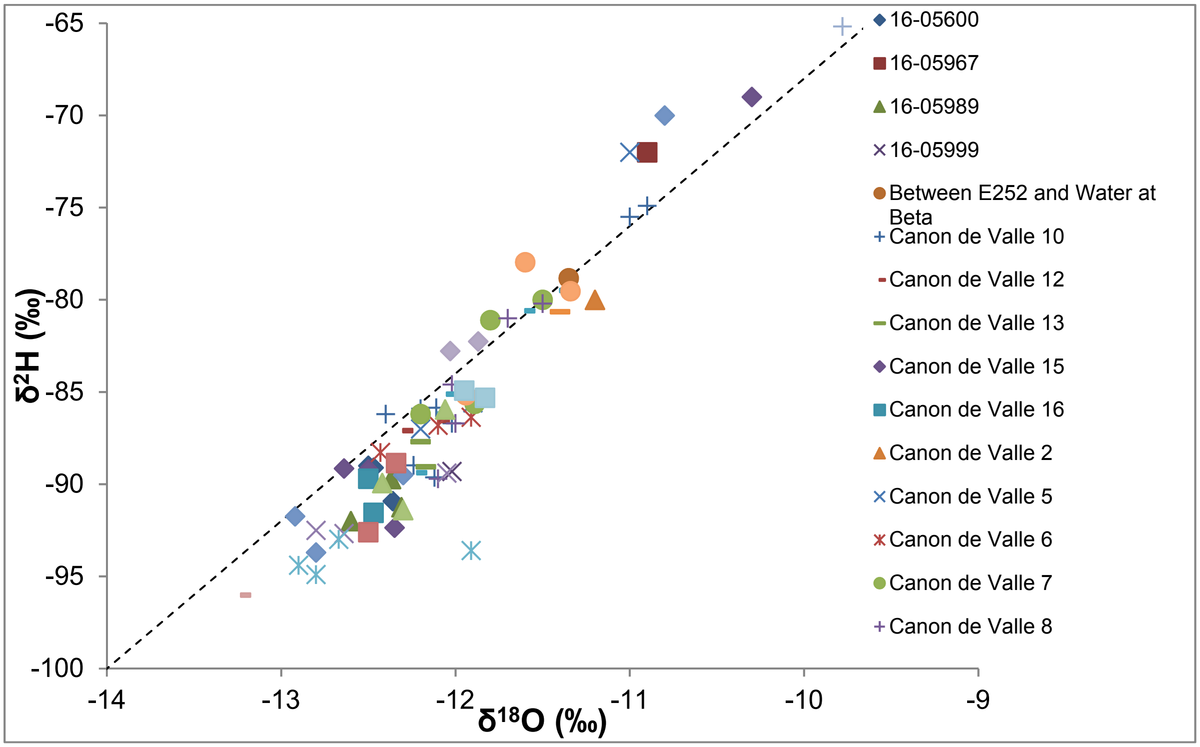

Figure 4.3-8 **Blow-up view of stable isotope ratios for surface water samples**

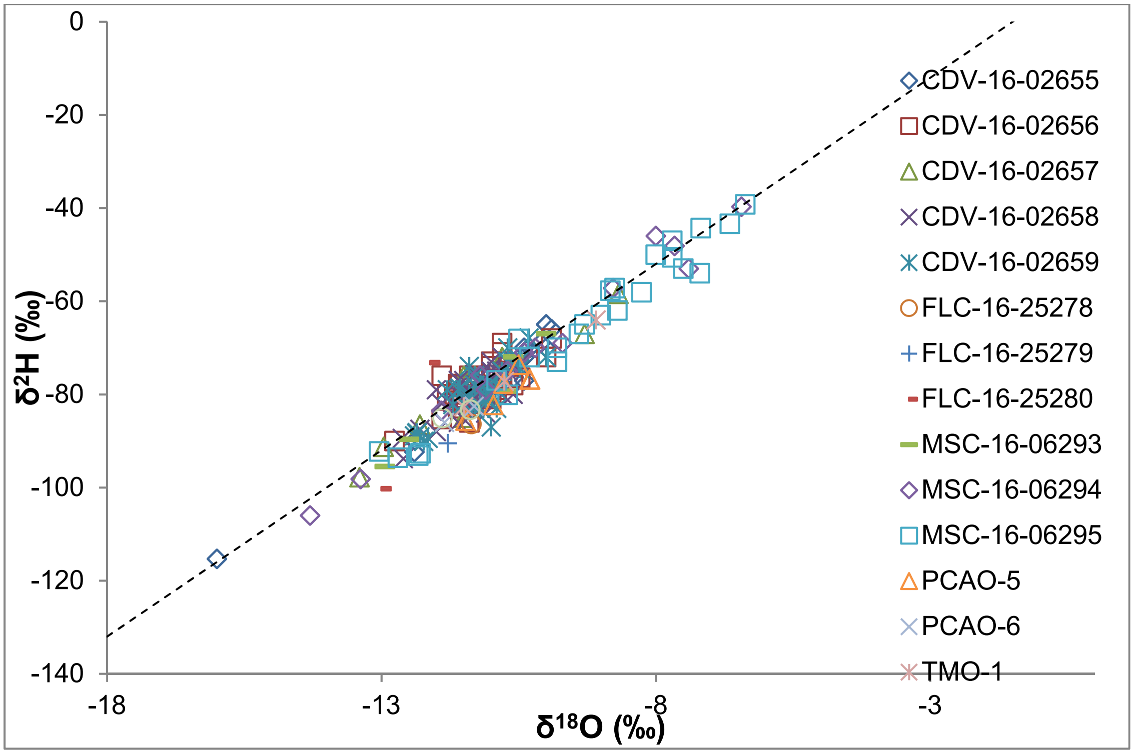

Figure 4.3-9 Stable isotope ratios of alluvial groundwater samples

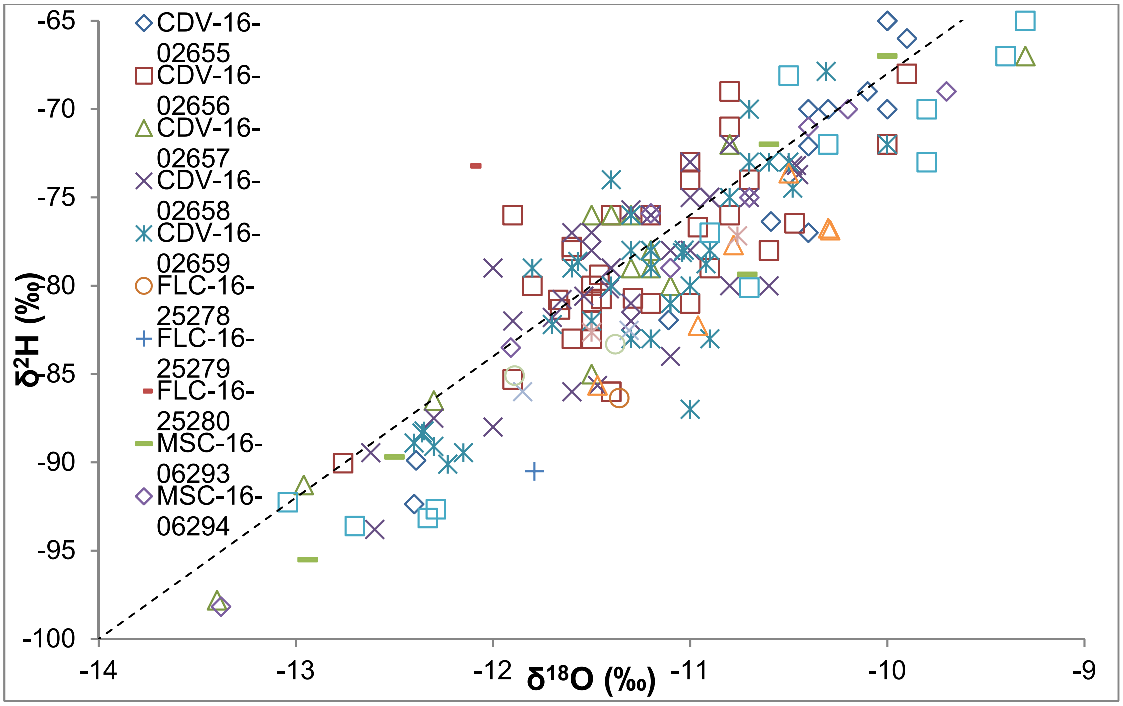

Figure 4.3-10 Stable isotope ratios of alluvial groundwater samples. Blow-up scale.

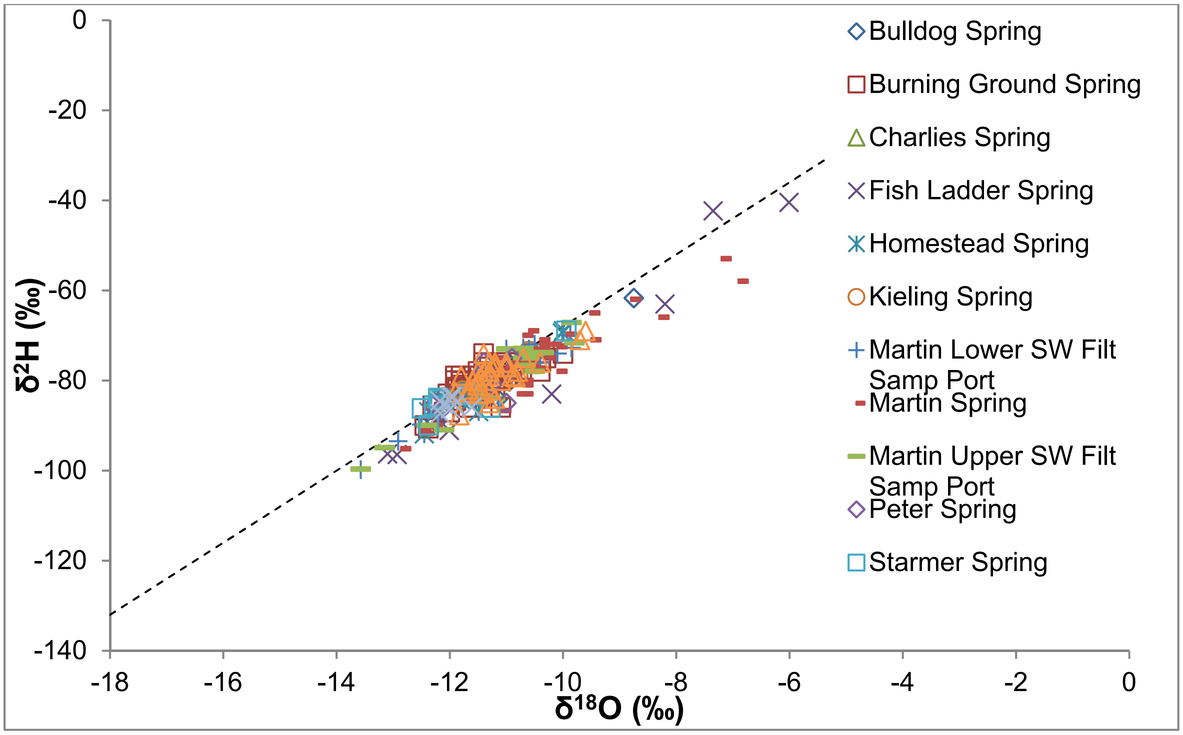

Figure 4.3-11 Stable isotope ratios of springs samples

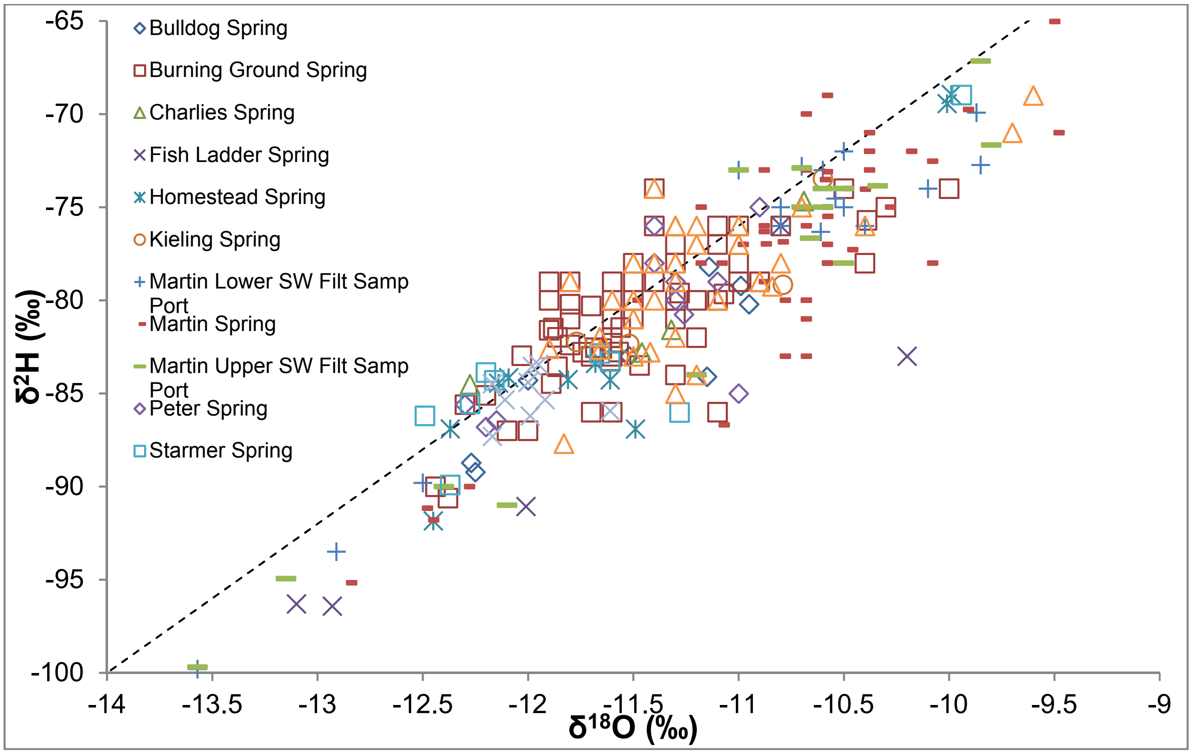

Figure 4.3-12 Stable isotope ratios of springs samples. Blow-up scale.

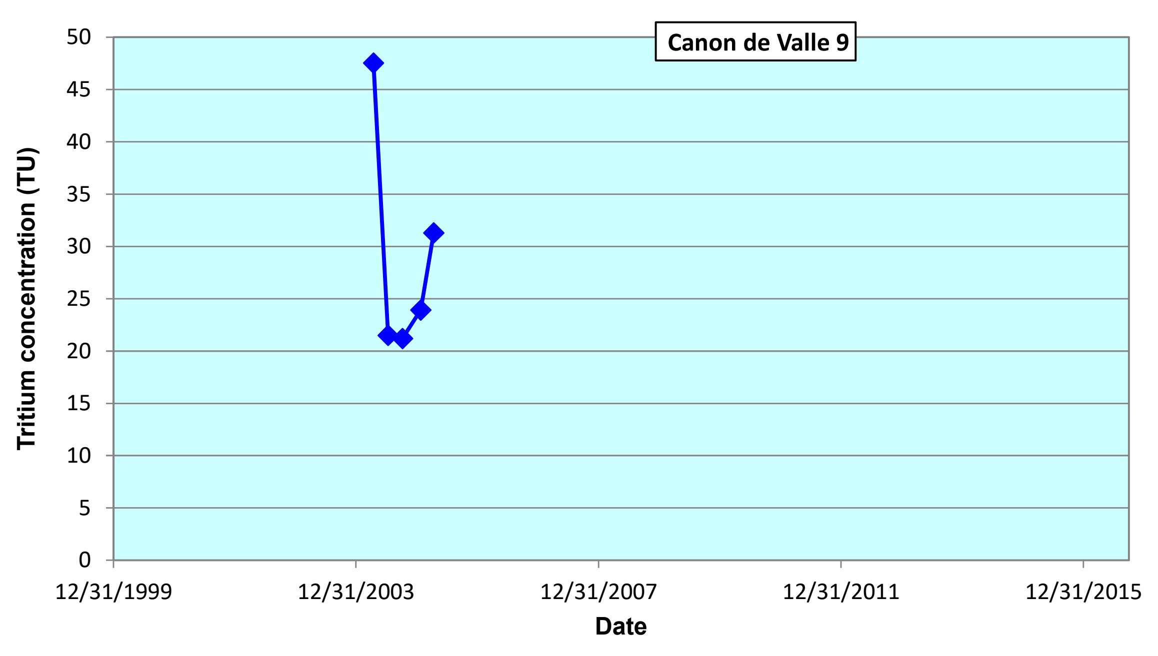

Figure 4.3-13 Tritium concentration with time for surface water samples at Cañon de Valle 9

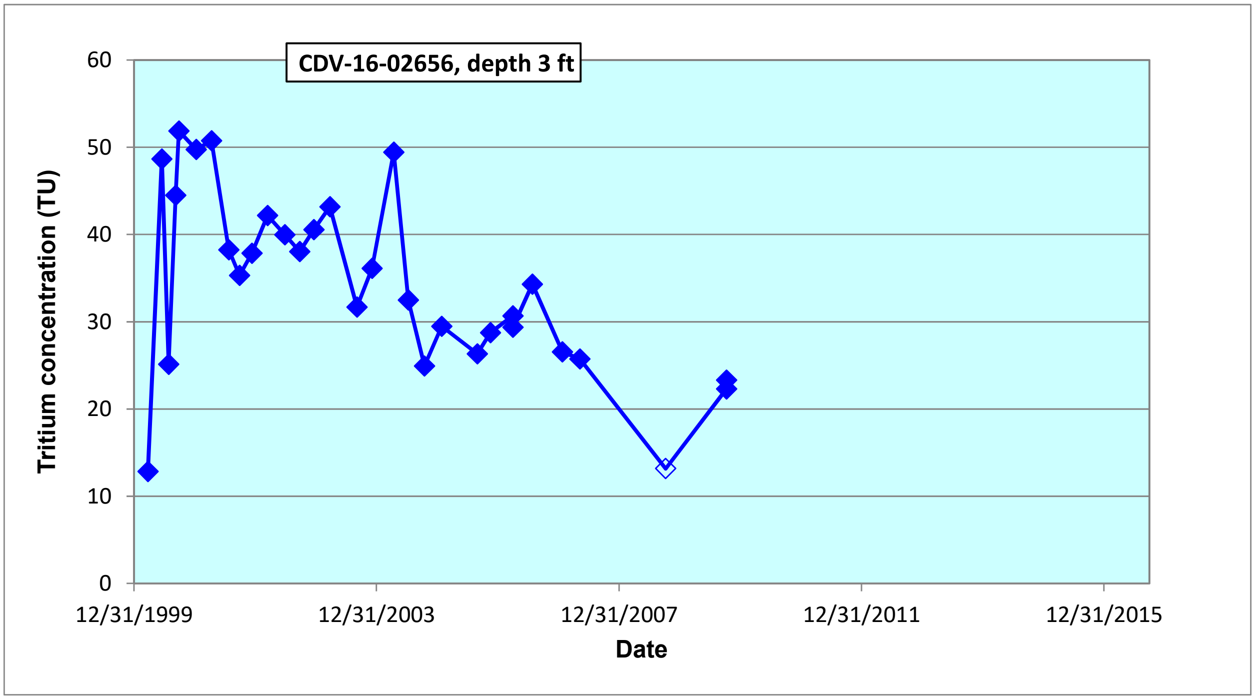

Figure 4.3-14 Tritium concentration with time for alluvial groundwater samples at CDV-16-02656

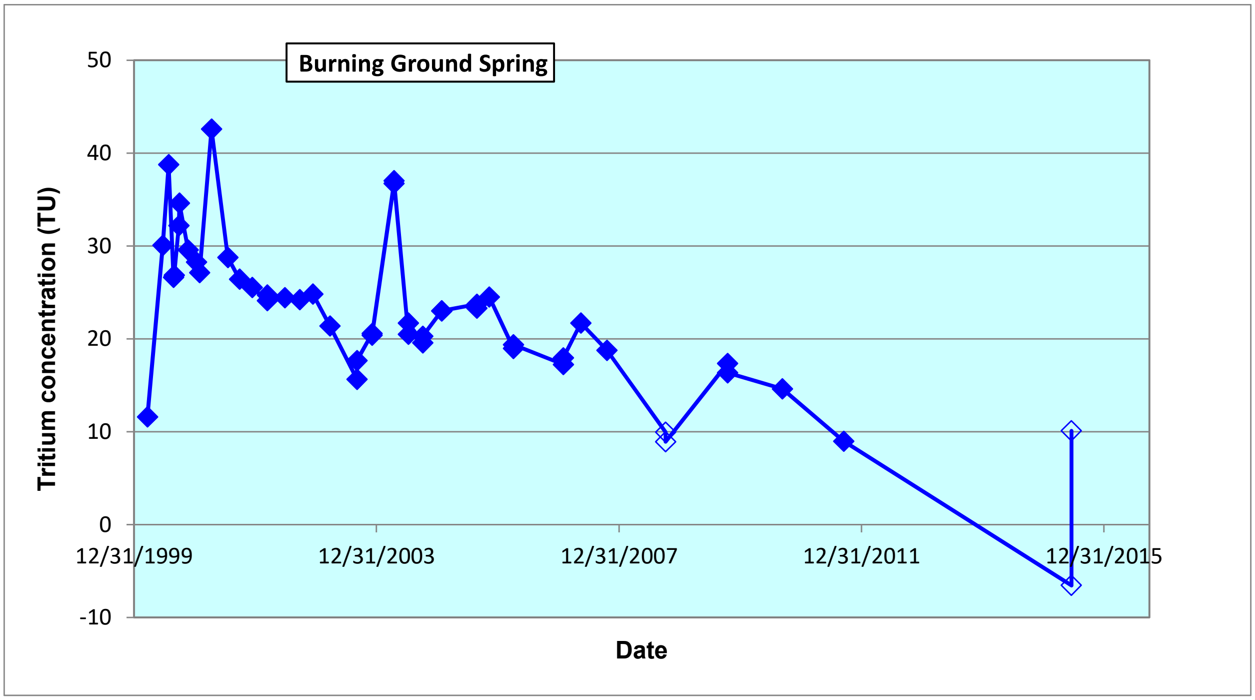

Figure 4.3-15 Tritium concentration over time for Burning Ground Spring in Cañon de Valle

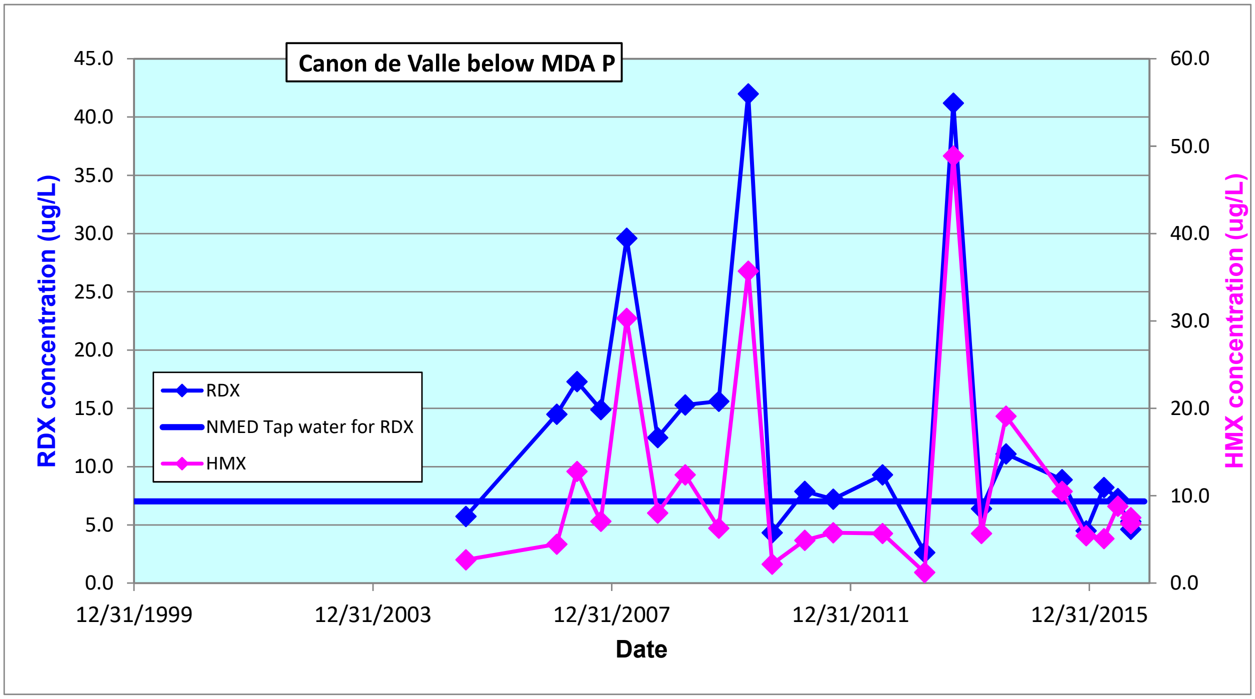

Figure 4.3-16 RDX concentration over time for surface water samples at Cañon de Valle below MDA P

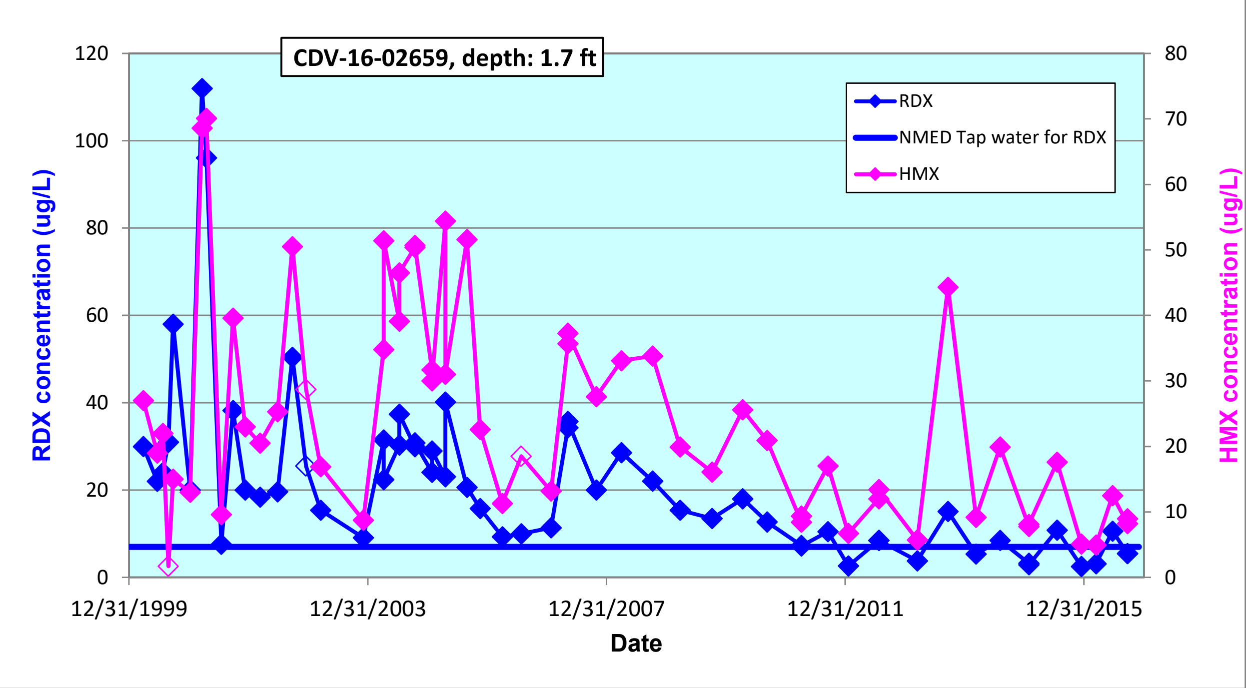

Figure 4.3-17 RDX concentration over time for alluvial groundwater samples at CDV-16-02659

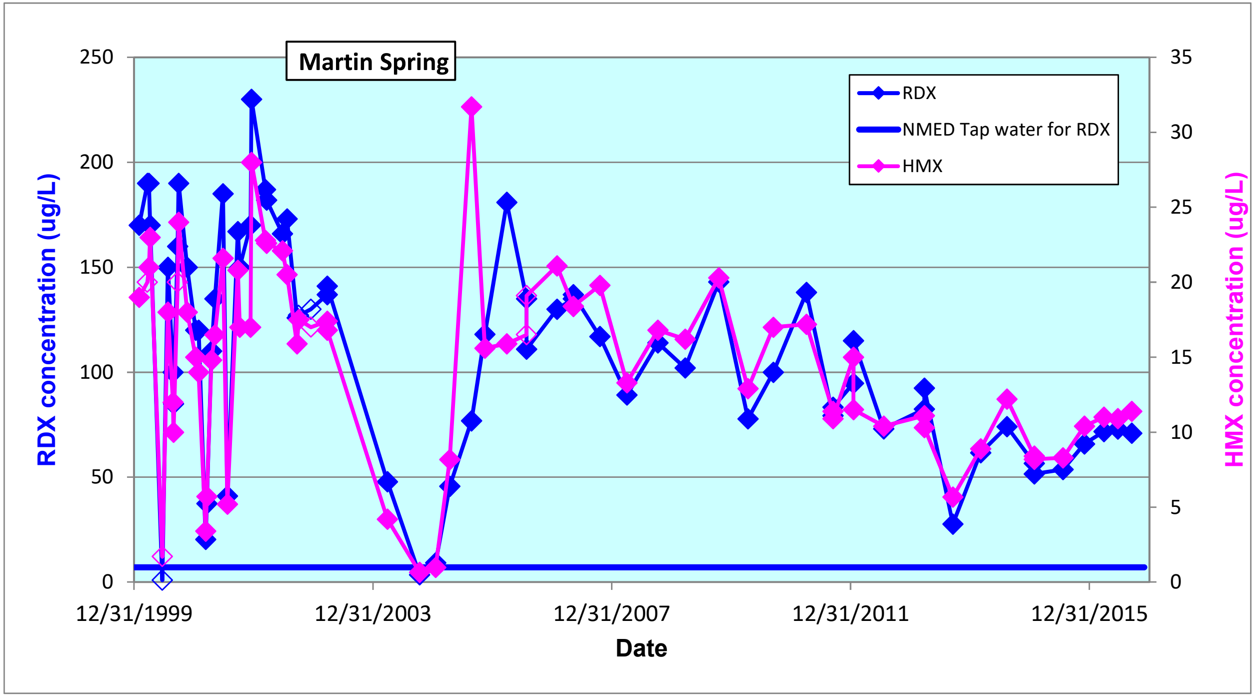

Figure 4.3-18 RDX concentration over time for spring water samples at Martin Spring

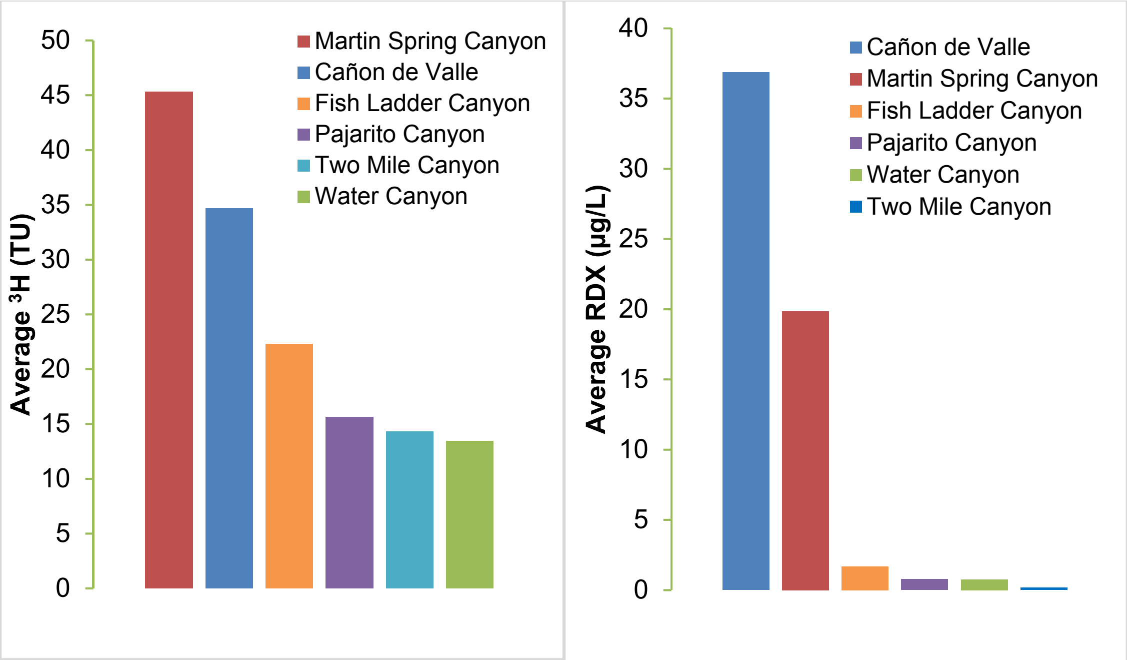

Figure 4.3-19 **Tritium and RDX concentration averages across all surface water, alluvial groundwater, and springs samples, broken out by canyon system**

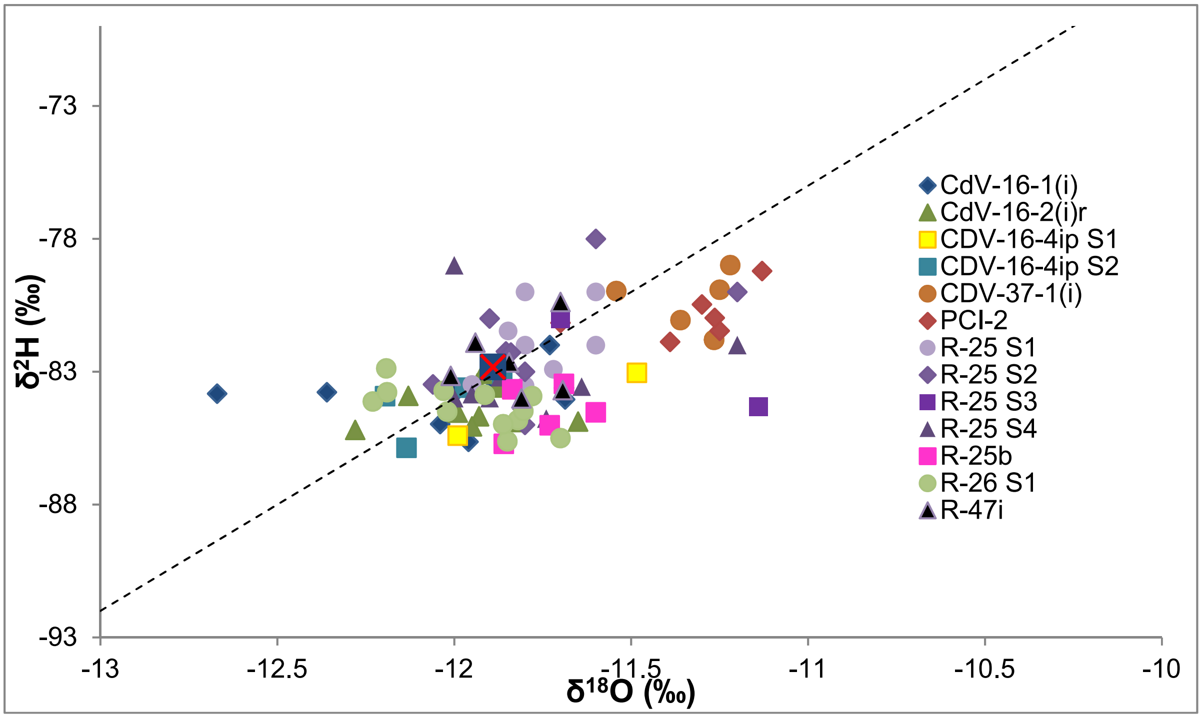

Figure 4.3-20 **Perched-intermediate well stable isotope ratios, grouped by well and screen**

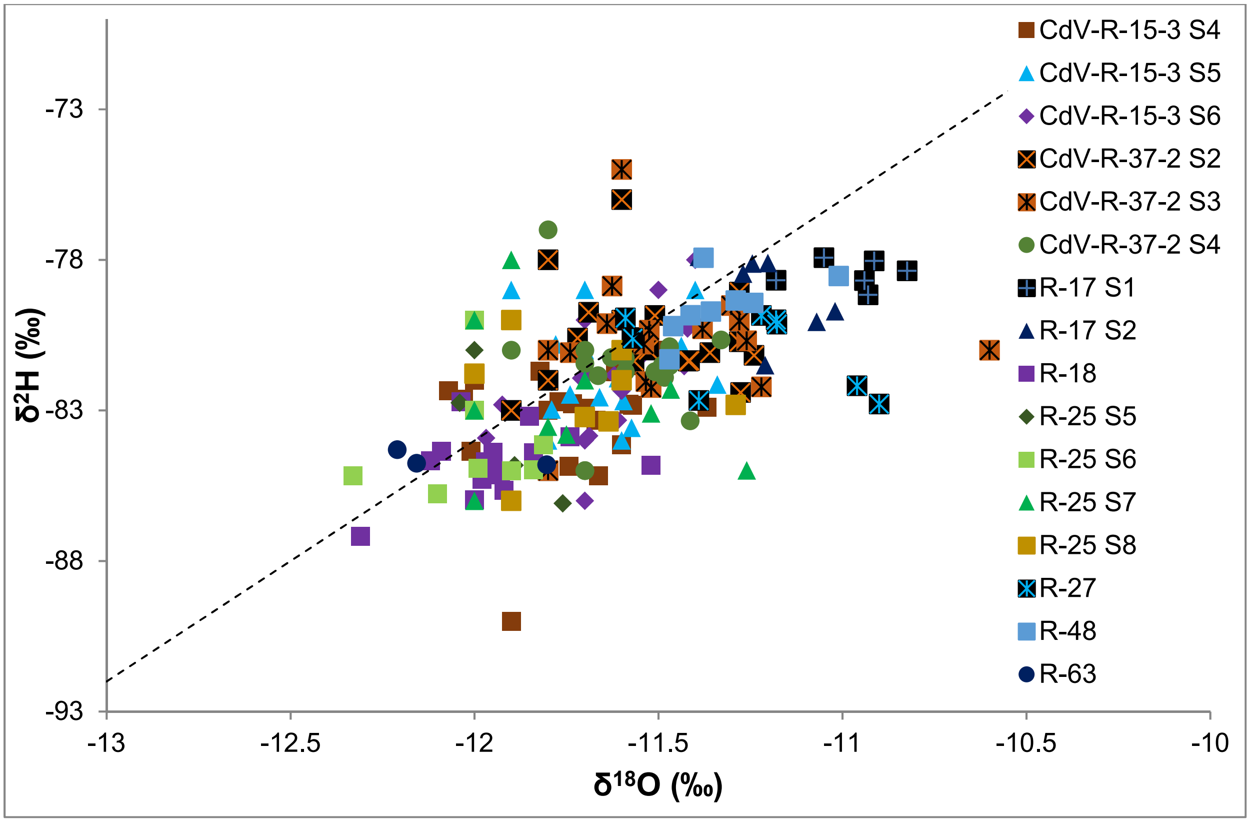

Figure 4.3-21 Regional well stable isotope ratios, grouped by well and screen

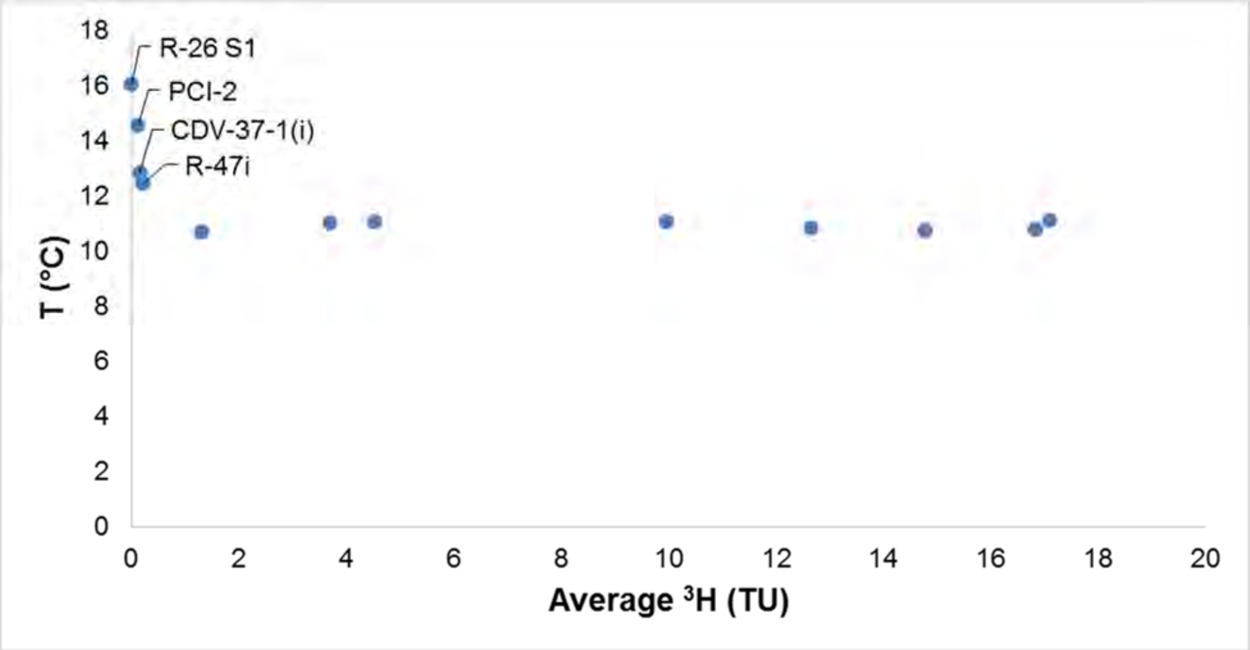

Figure 4.3-22 Temperature vs average tritium concentration for perched-intermediate wells

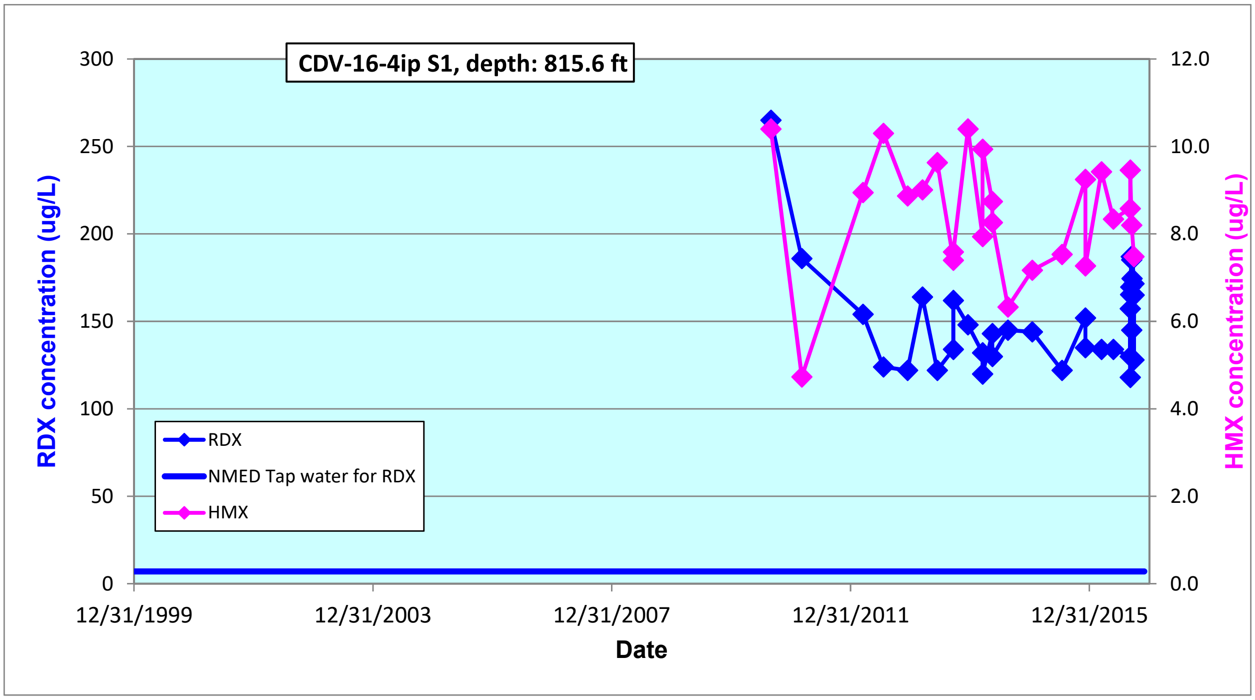

Figure 4.3-23 RDX concentration time series for CdV-16-4ip, showing variable concentrations. Data begins at the earliest sample date after well completion.

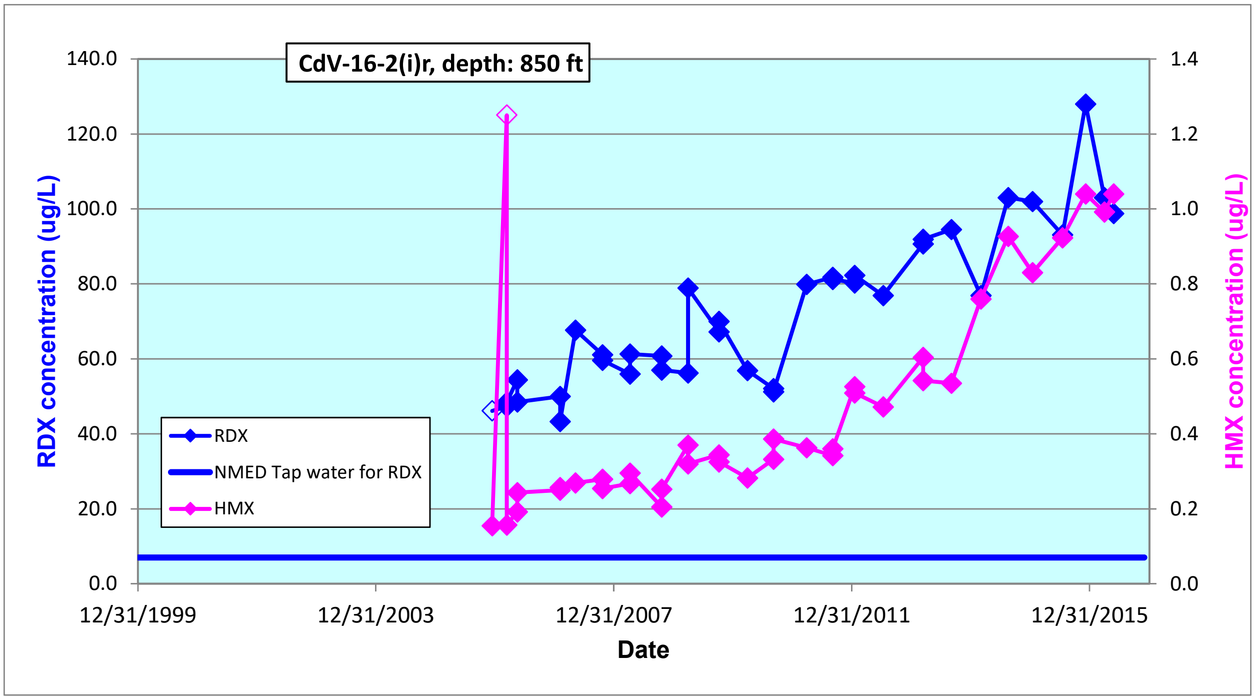

Figure 4.3-24 RDX concentration time series for CdV-16-2(i)r, showing a gradual increase. Data begins at the earliest sample date after well completion.

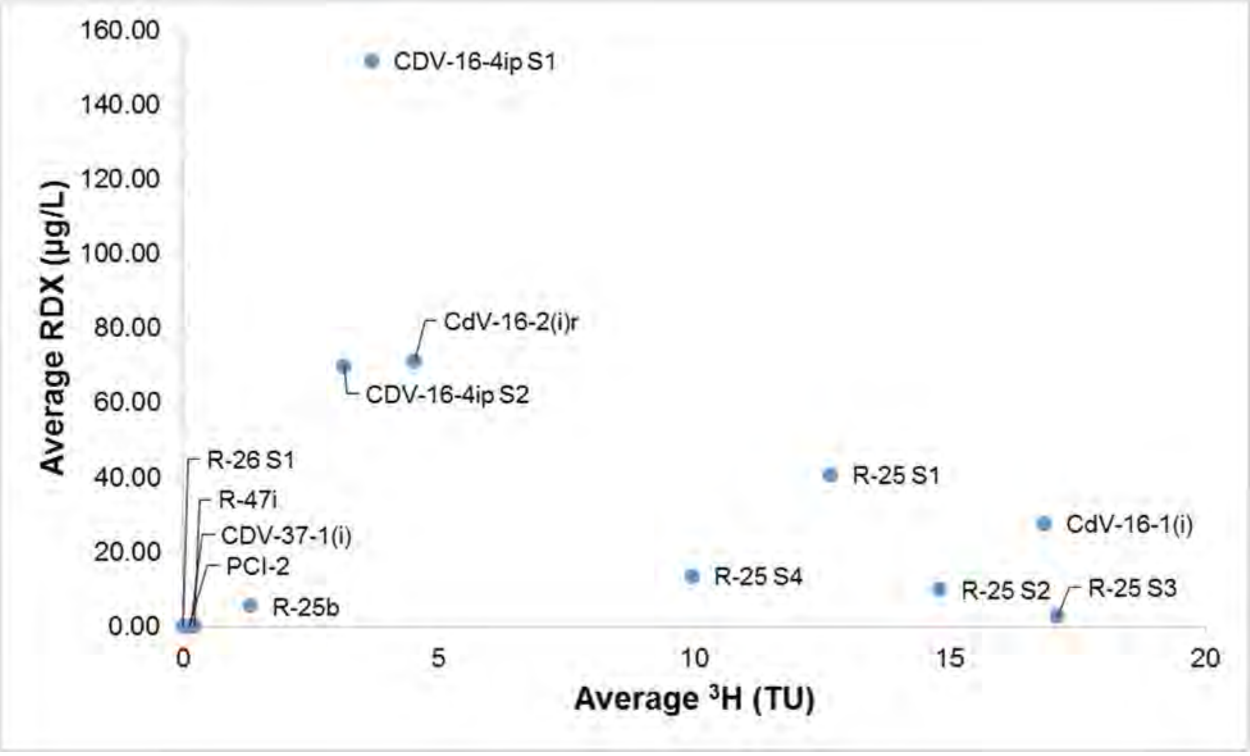

Figure 4.3-25 **RDX concentration vs average tritium concentration for perched-intermediate wells. Wells that are below the detection limit for RDX are labeled, and match high temperature wells from Figure 4.3-22 with the exception of R-25 S3.**

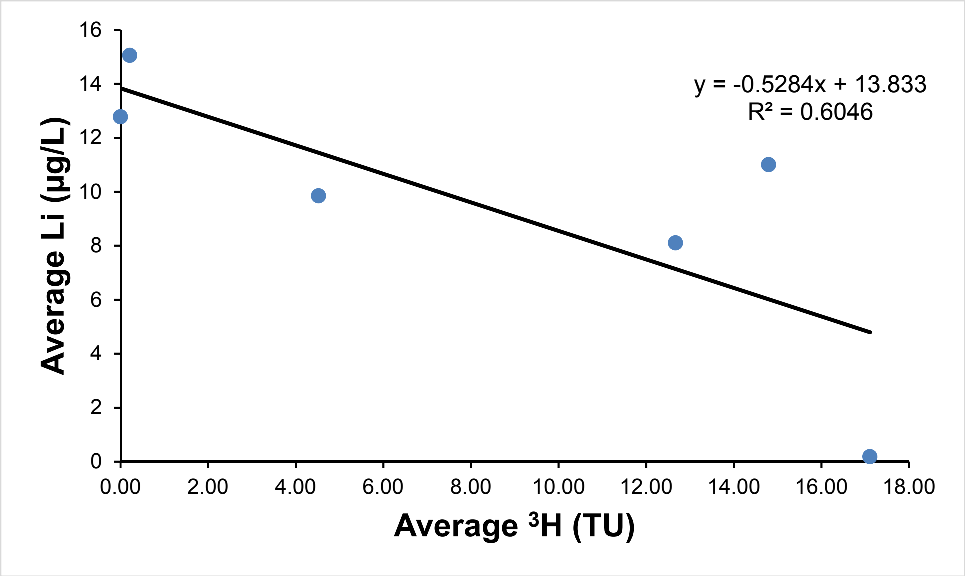

Figure 4.3-26 **Average lithium vs tritium concentration for perched-intermediate wells**

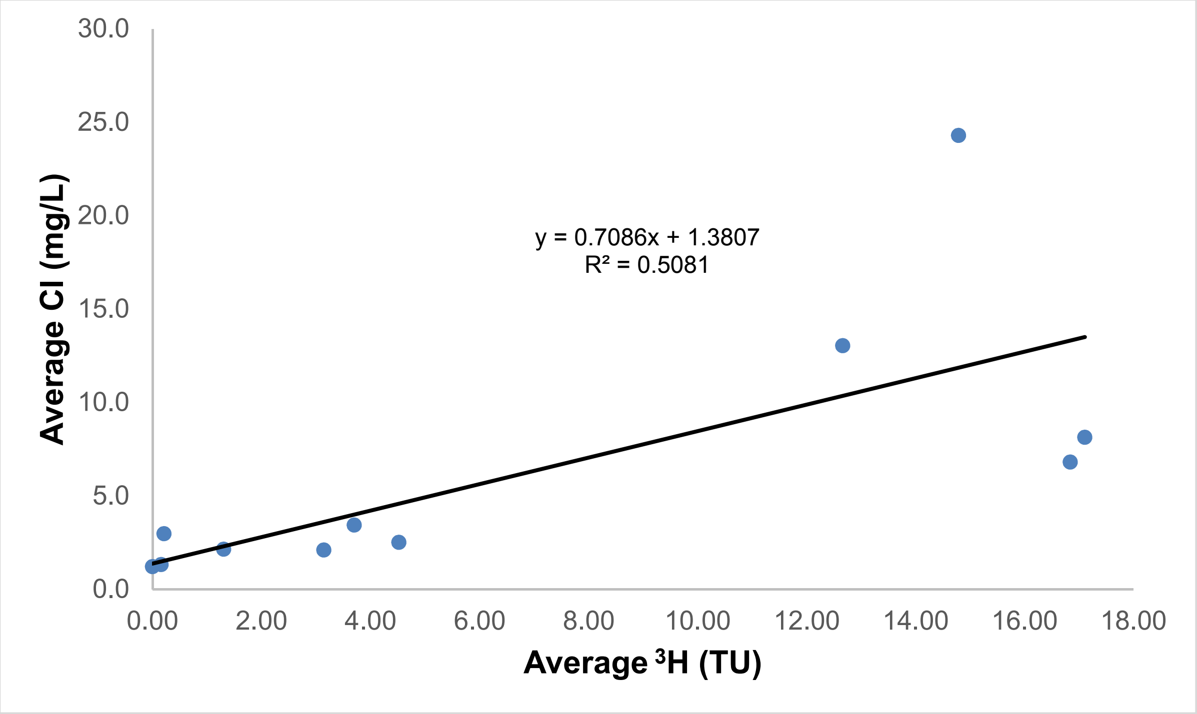

Figure 4.3-27 Average chloride vs tritium concentration for perched-intermediate wells

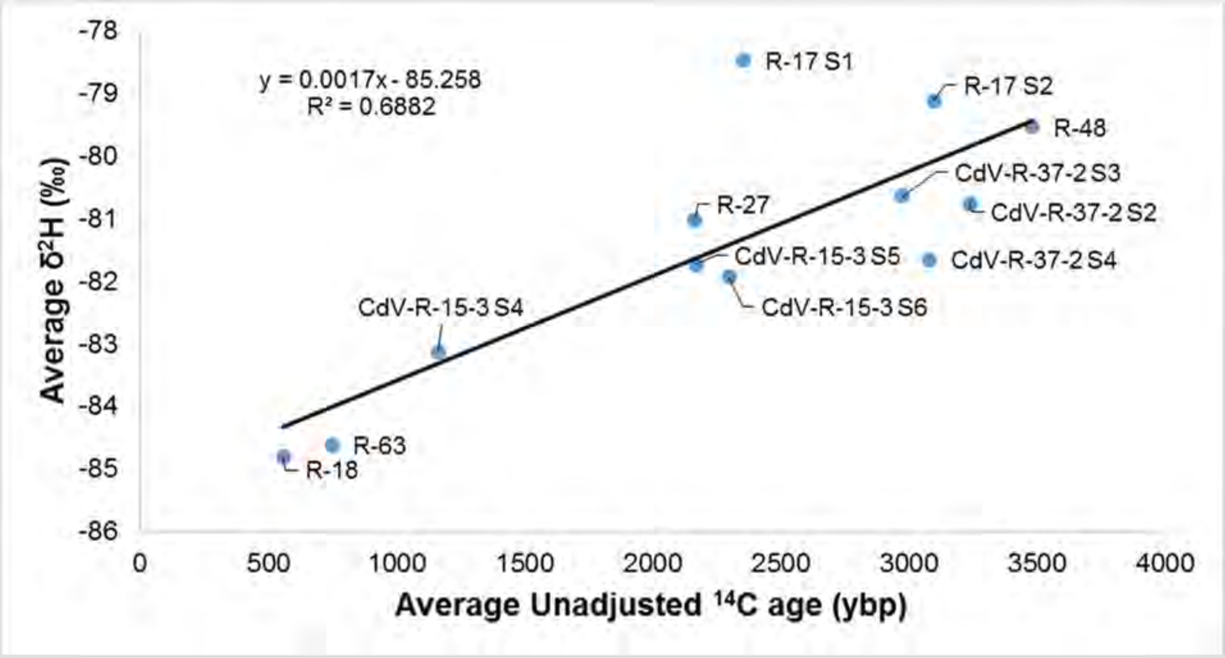

Figure 4.3-28 Average δ^2H vs unadjusted carbon-14 age for regional wells

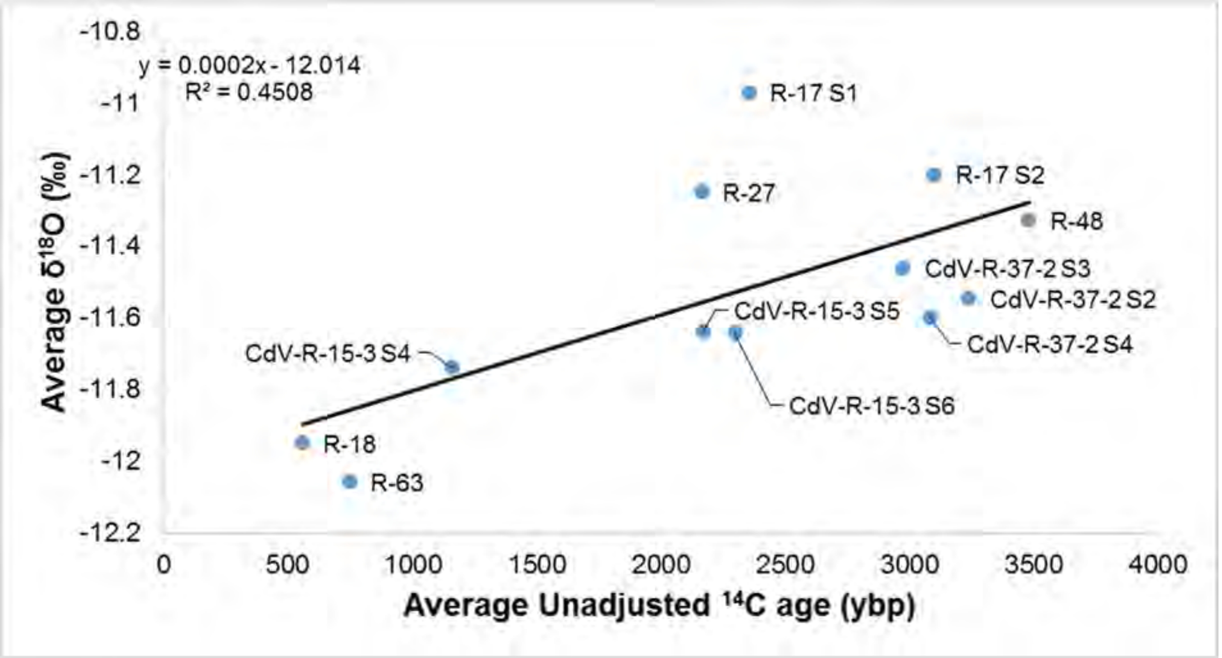

Figure 4.3-29 Average $\delta^{18}O$ vs unadjusted carbon-14 age for regional wells

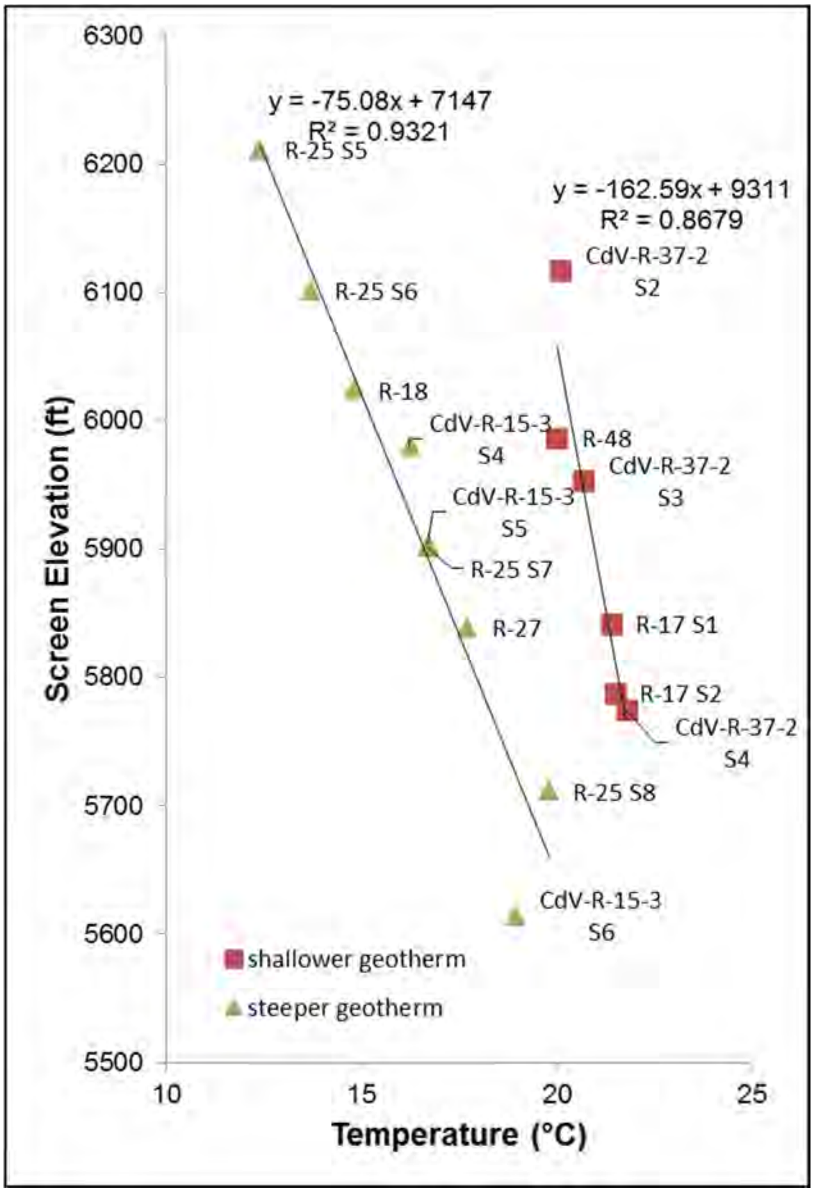

Figure 4.3-30 Screen elevation vs temperature for regional wells, split into two geothermal gradients

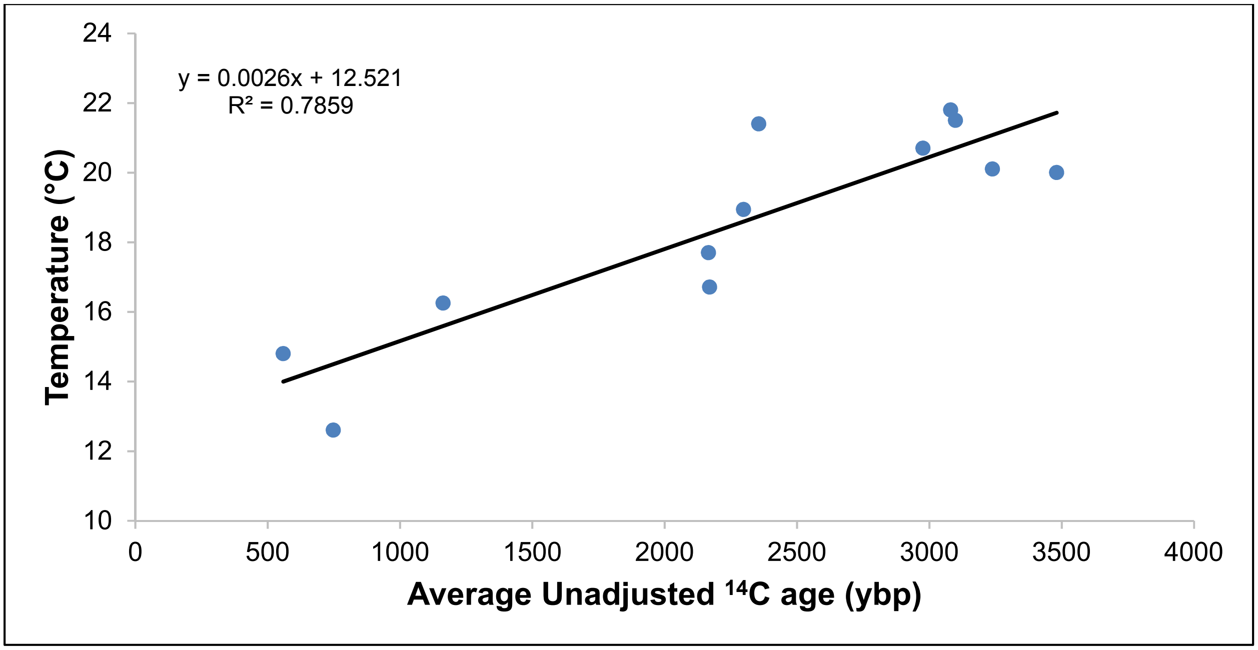

Figure 4.3-31 Temperature vs average unadjusted carbon-14 age for regional wells, with a linear regression fit to the data

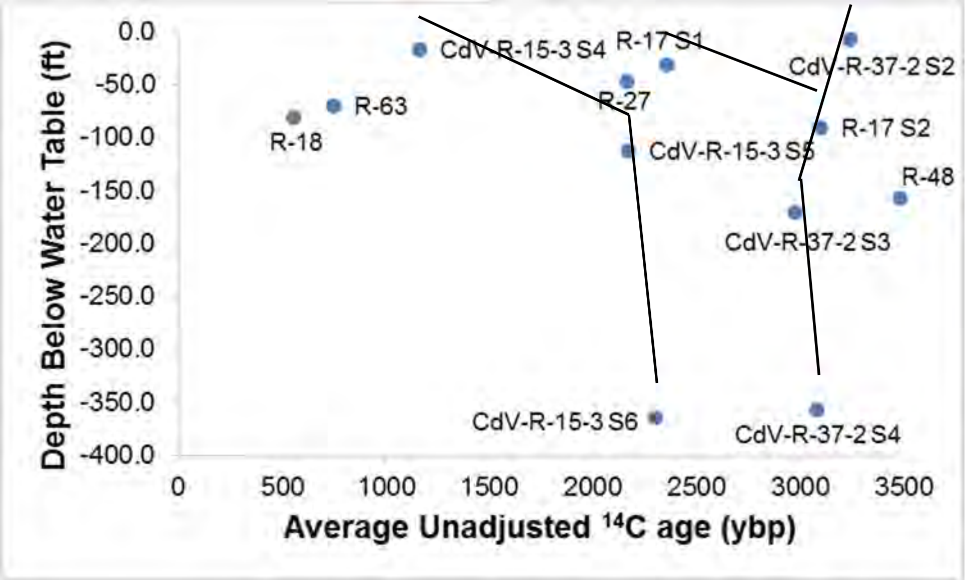

Figure 4.3-32 Carbon-14 age vs screen depth below the water table for regional aquifer wells. Multi-screen wells with unadjusted carbon-14 ages are connected by lines.

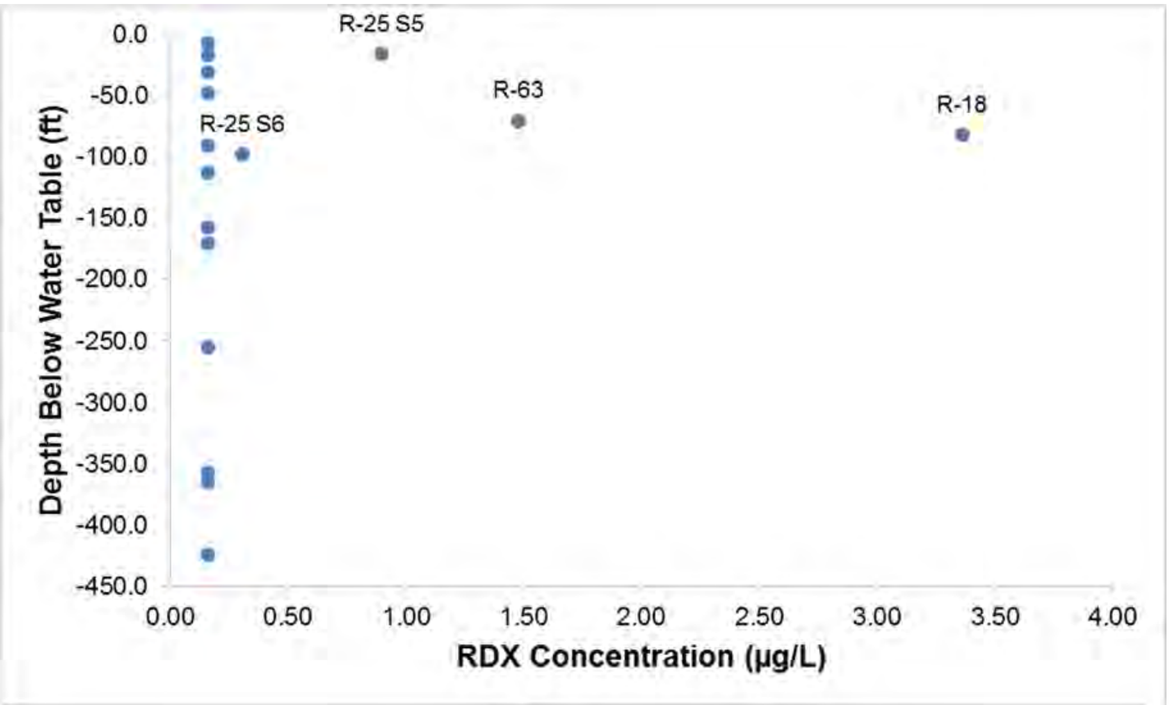

Figure 4.3-33 **RDX concentration vs average screen depth below the water table for regional wells. Well screens with detectable RDX are labeled with their well/screen designation.**

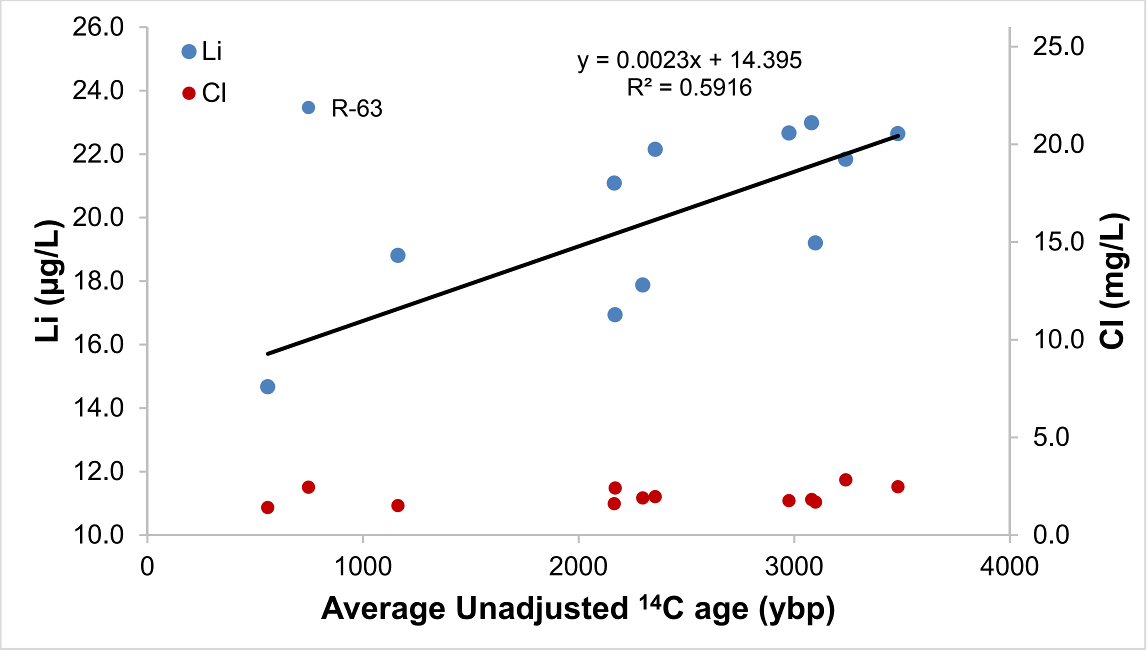

Figure 4.3-34 **Lithium and chloride concentrations vs average unadjusted carbon-14 age for regional wells. The linear relationship of lithium is much stronger if R-63 is treated as an outlier, so it is excluded from the linear regression.**

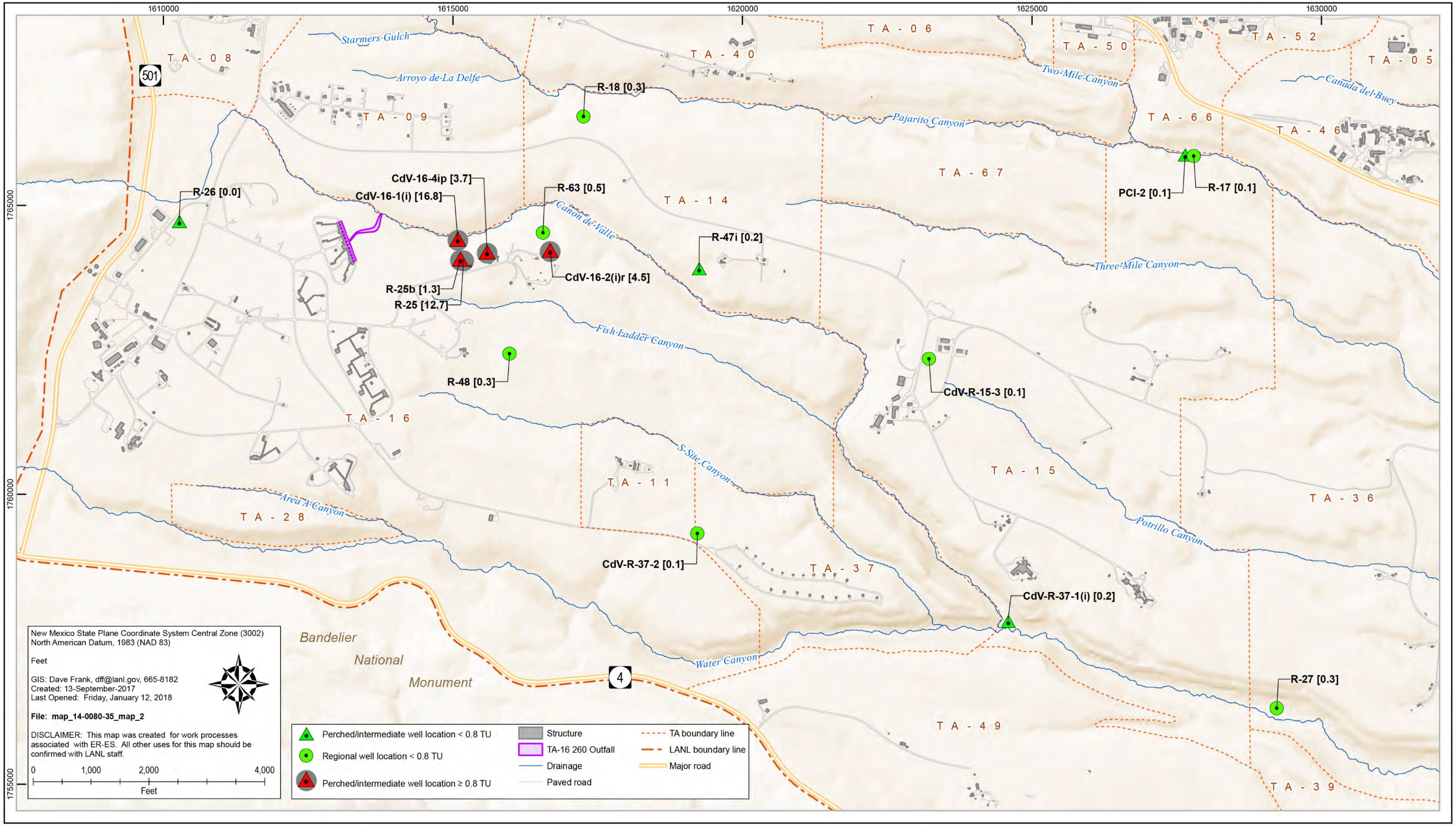

Figure 4.4-1 Intermediate and regional wells classified as "modern" (< 1950 A.D. >0.8 TU) or "submodern" (>1950 A.D. <0.8 TU) based on the average TU of each well's top screen

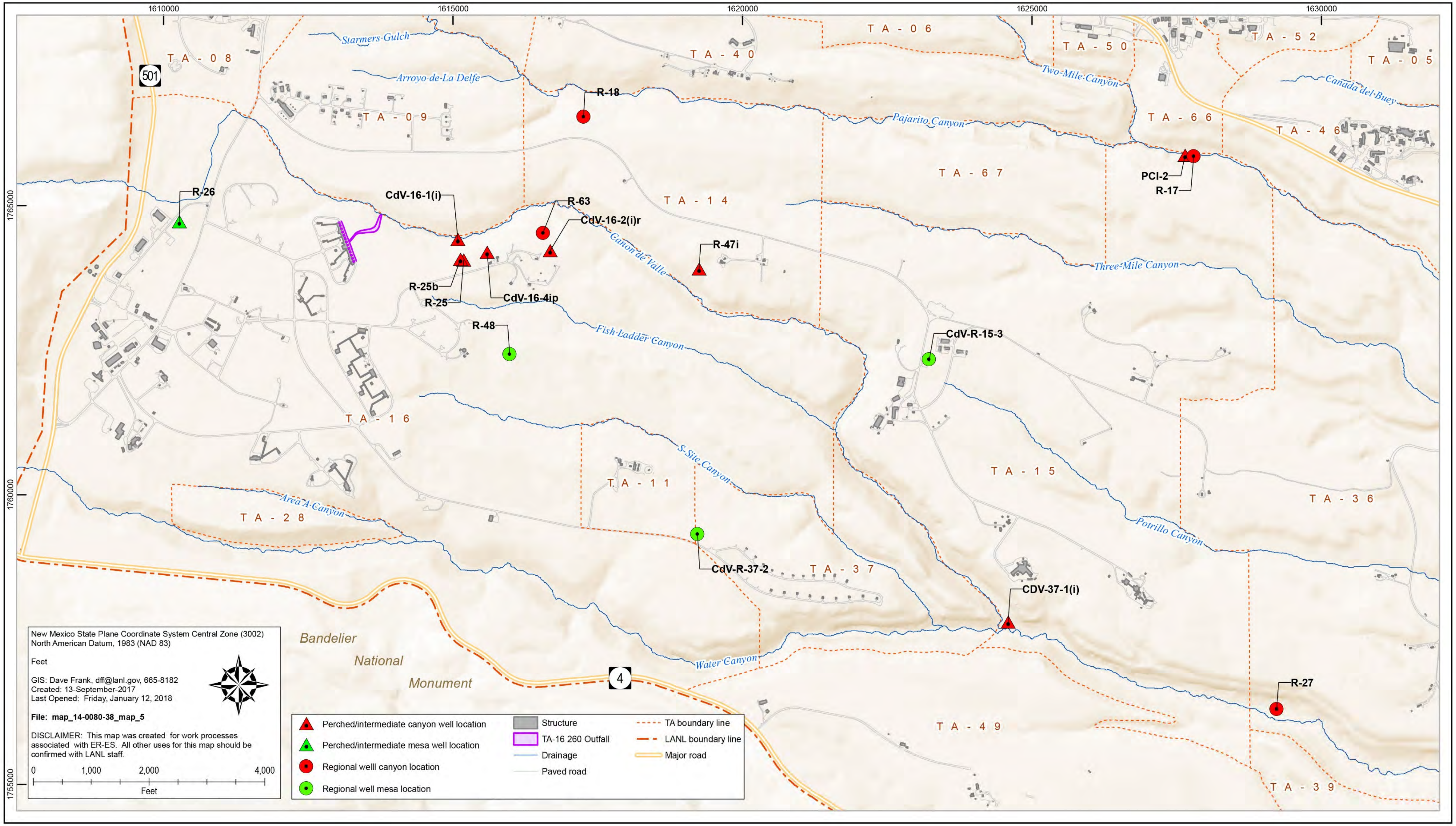

Figure 4.4-2 Intermediate and regional wells within ~1000 ft of drainages classified as "canyon" wells, whereas the remainder are classified as "mesa" wells

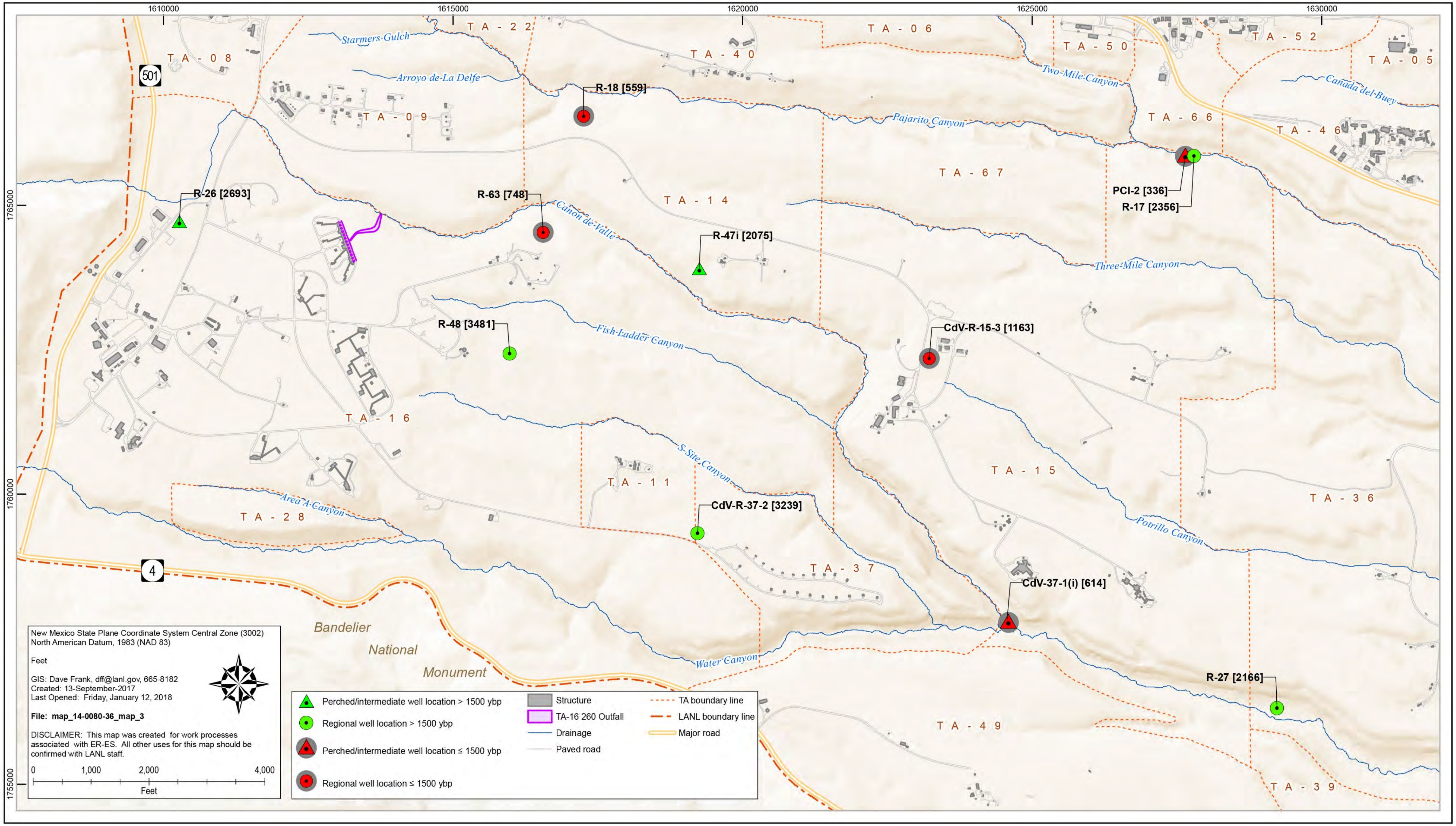

Figure 4.4-3 Intermediate and regional wells grouped by carbon-14 age at an arbitrary cutoff (1500 ybp) based on the average carbon-14 age of each well's top screen

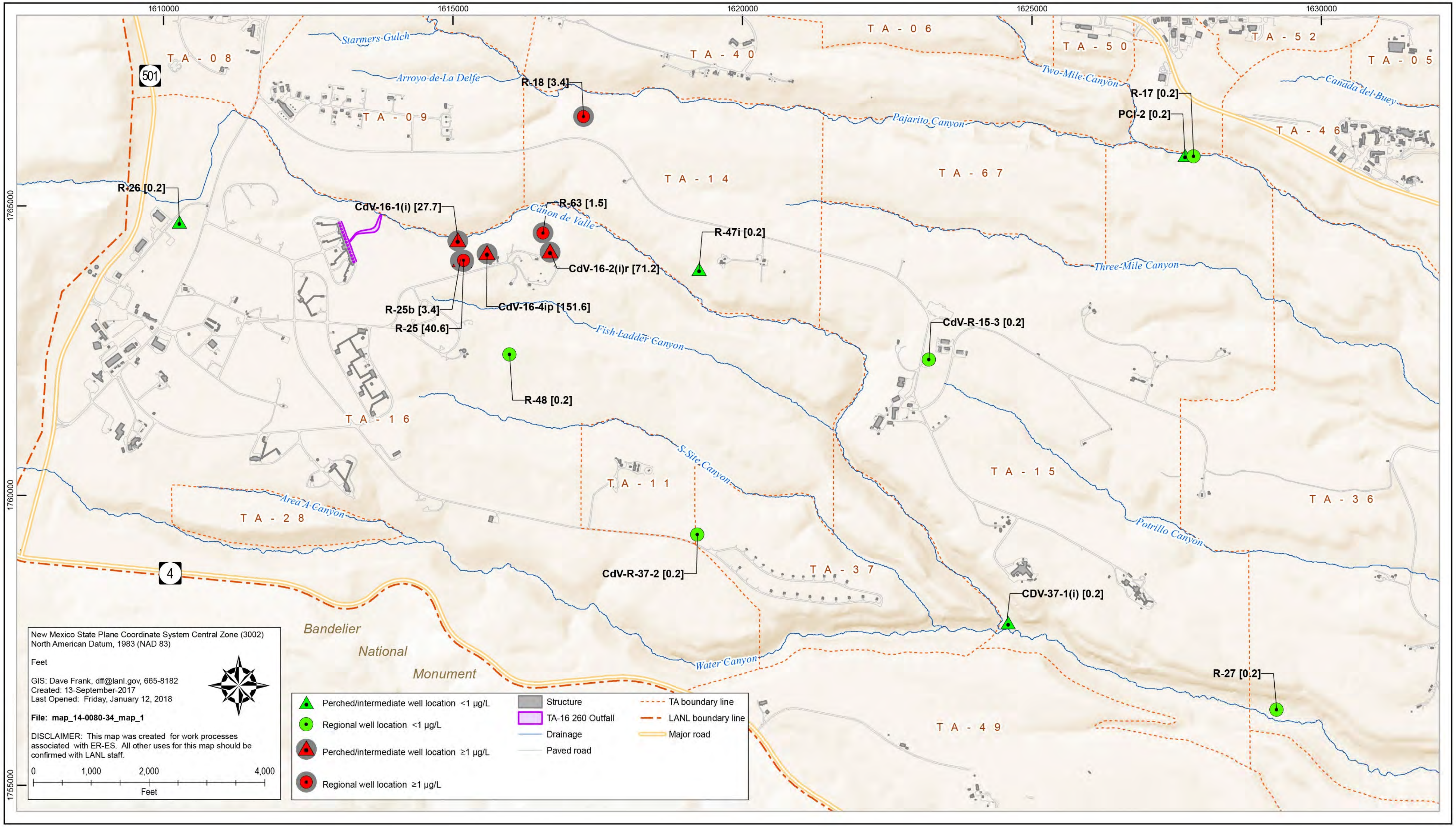

Figure 4.4-4 Intermediate and regional wells grouped by RDX concentration ≥ or < 1 µg/L, based on the most recent RDX concentration measurement of each well's top screen

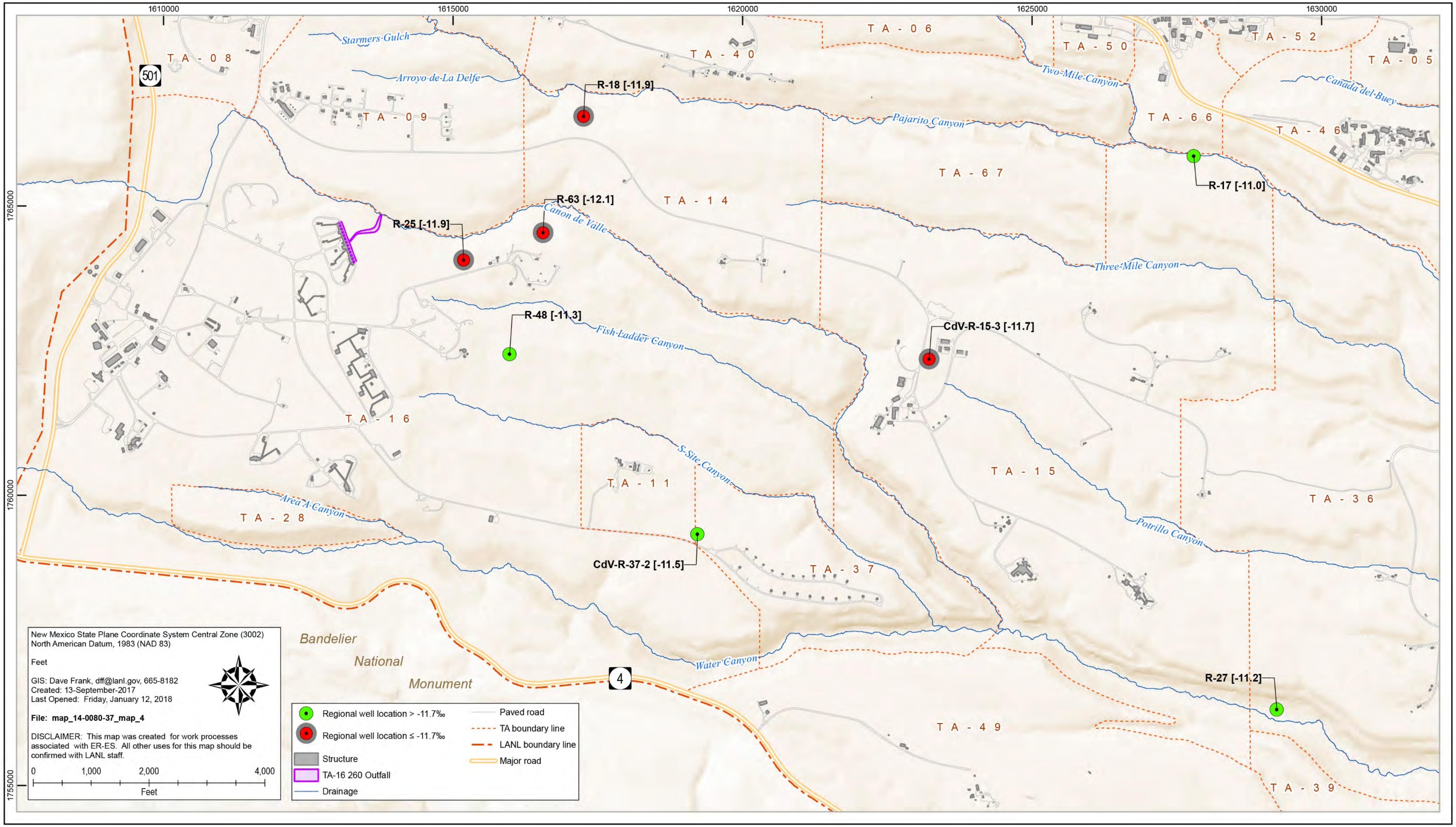

Figure 4.4-5 Regional wells grouped by $\delta^{18}O \le$ or > -11.7 ‰, based on the average $\delta^{18}O$ of each well's top screen

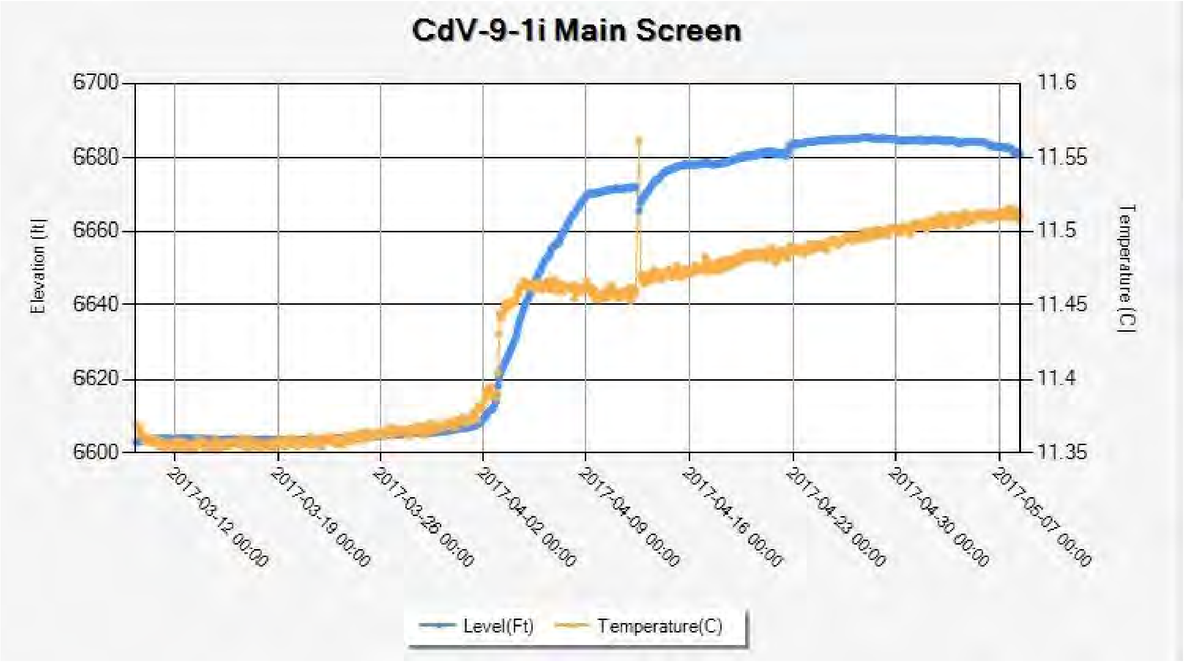

Figure 4.4-6 Spring 2017 recharge event at CdV-9-1i, showing an increase of ~85 ft in the water table and ~0.15°C in temperature

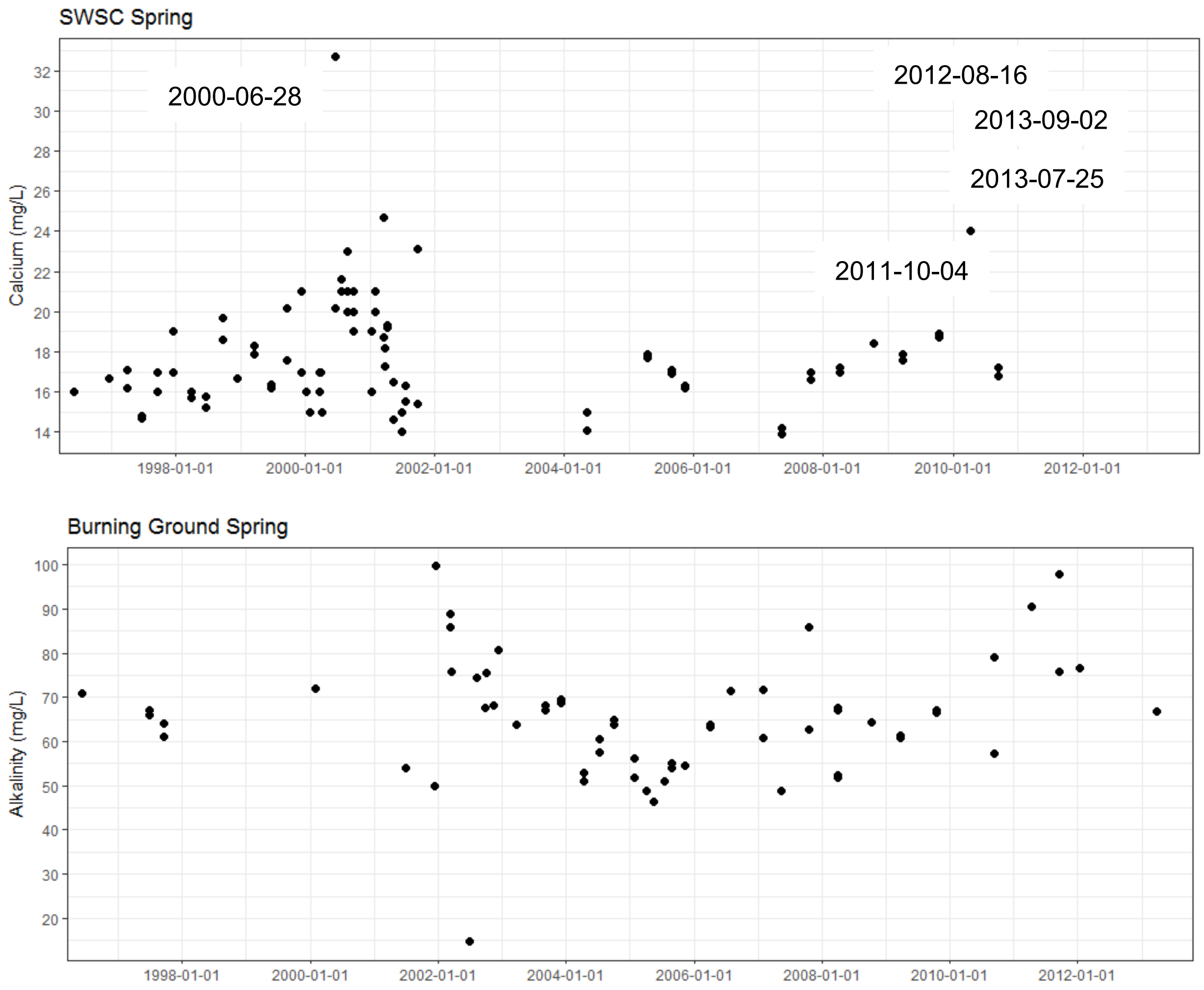

Figure 5.3-1 Alkalinity at Burning Ground Spring and calcium at SWSC Spring from 1997–2012

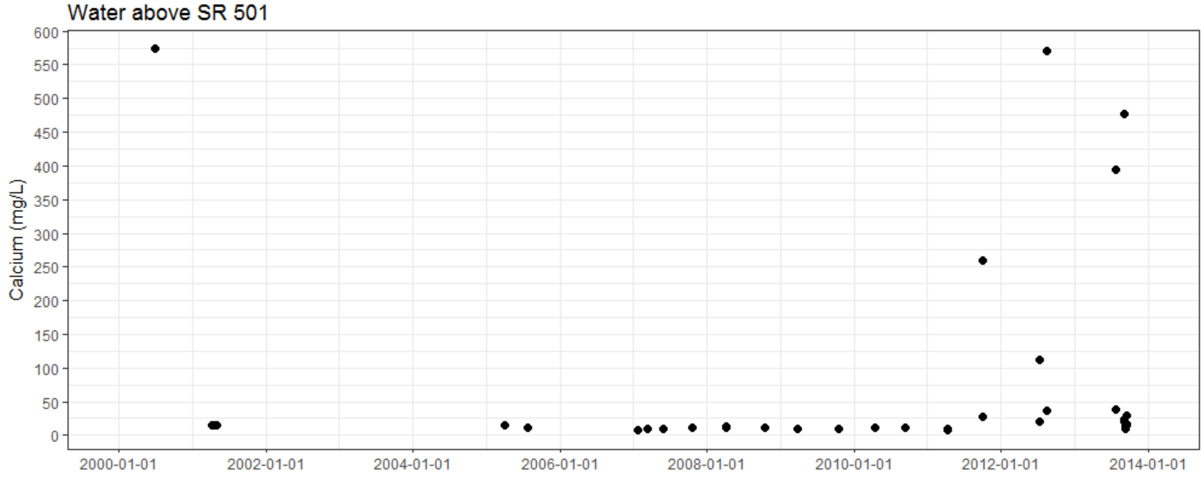

Figure 5.3-2 Calcium concentrations measured at Water Canyon above SR 501 (Gage E252; 2000–2014)

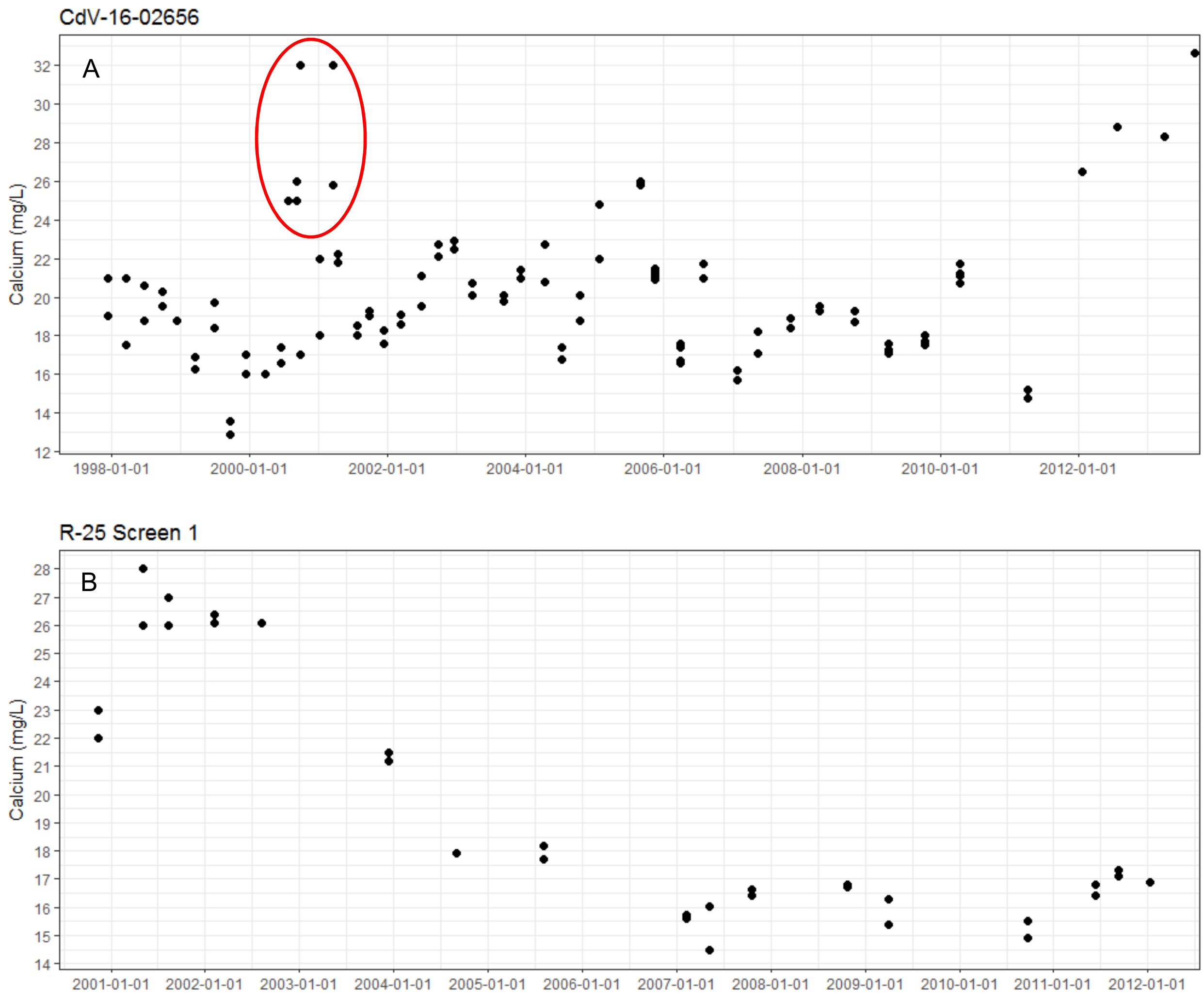

Figure 5.3-3 **A) Calcium concentration at alluvial well, CdV-16-02656. Red circle shows the period of increased calcium concentration at the end of 2000 into 2001. B) Calcium concentration at perched-intermediate/regional well, R-25 S-1.**

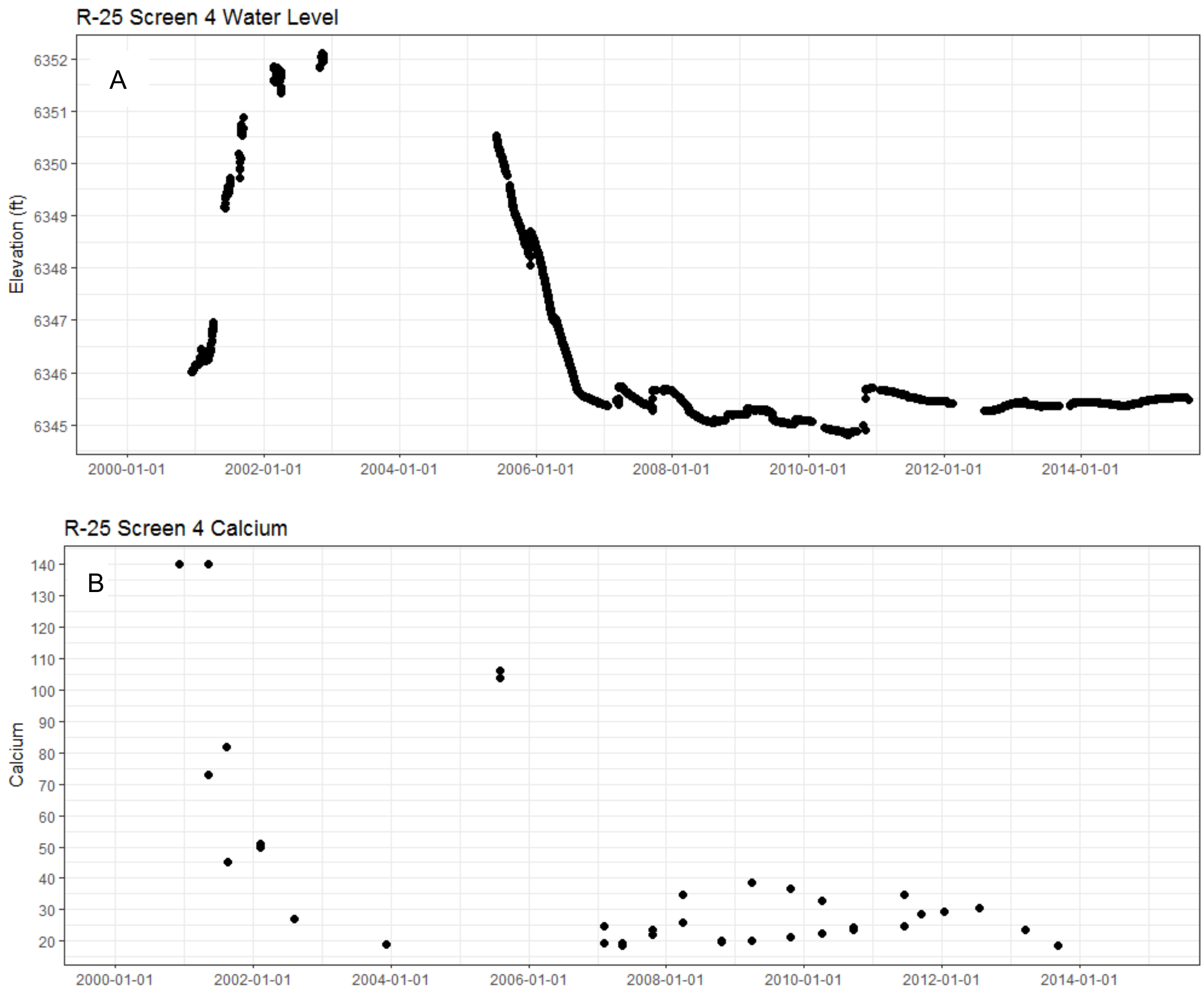

Figure 5.3-4 **Time series of calcium and water level at R-25 screen 4 compared with water level data from 2000–2015**

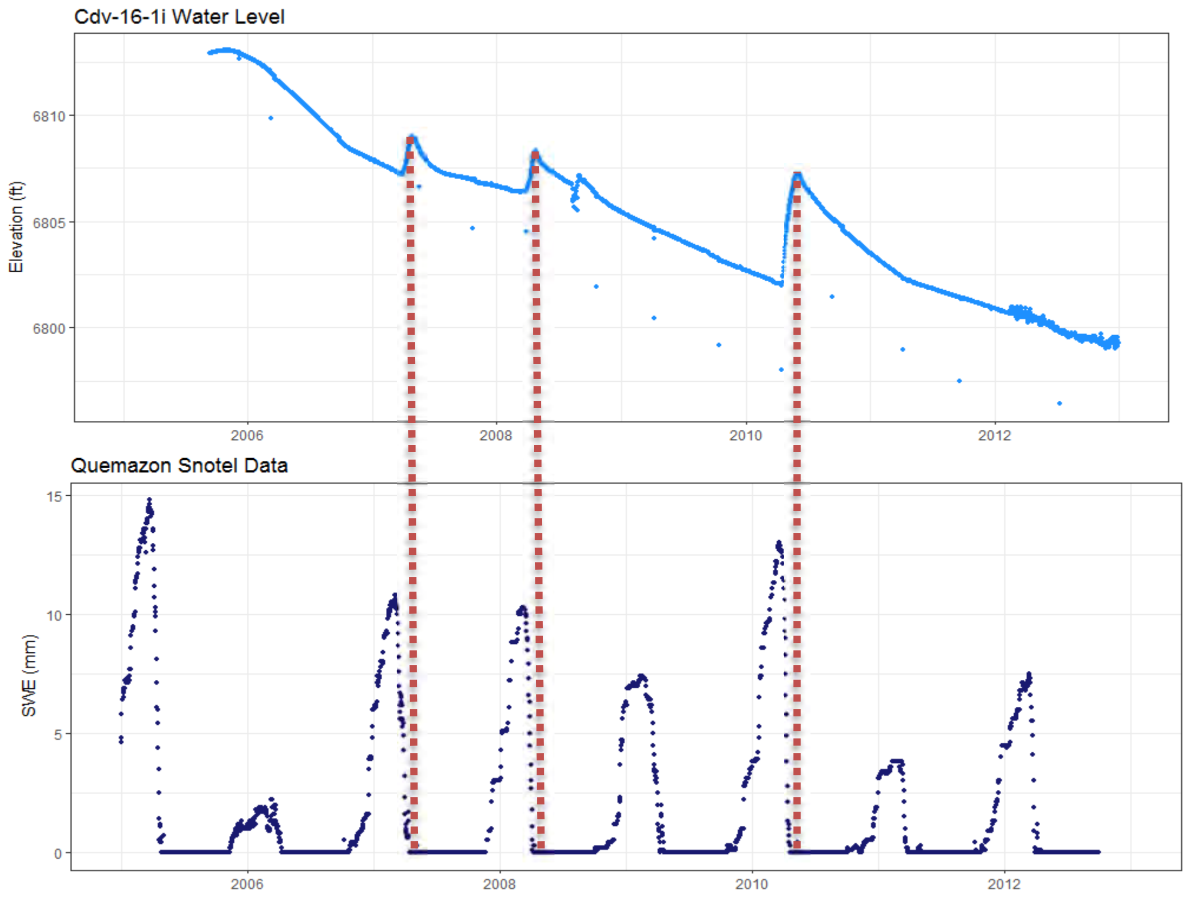

Figure 5.3-5 Time series of water level data at CdV-16-1i compared with snow water equivalent hydrograph from 2005–2012

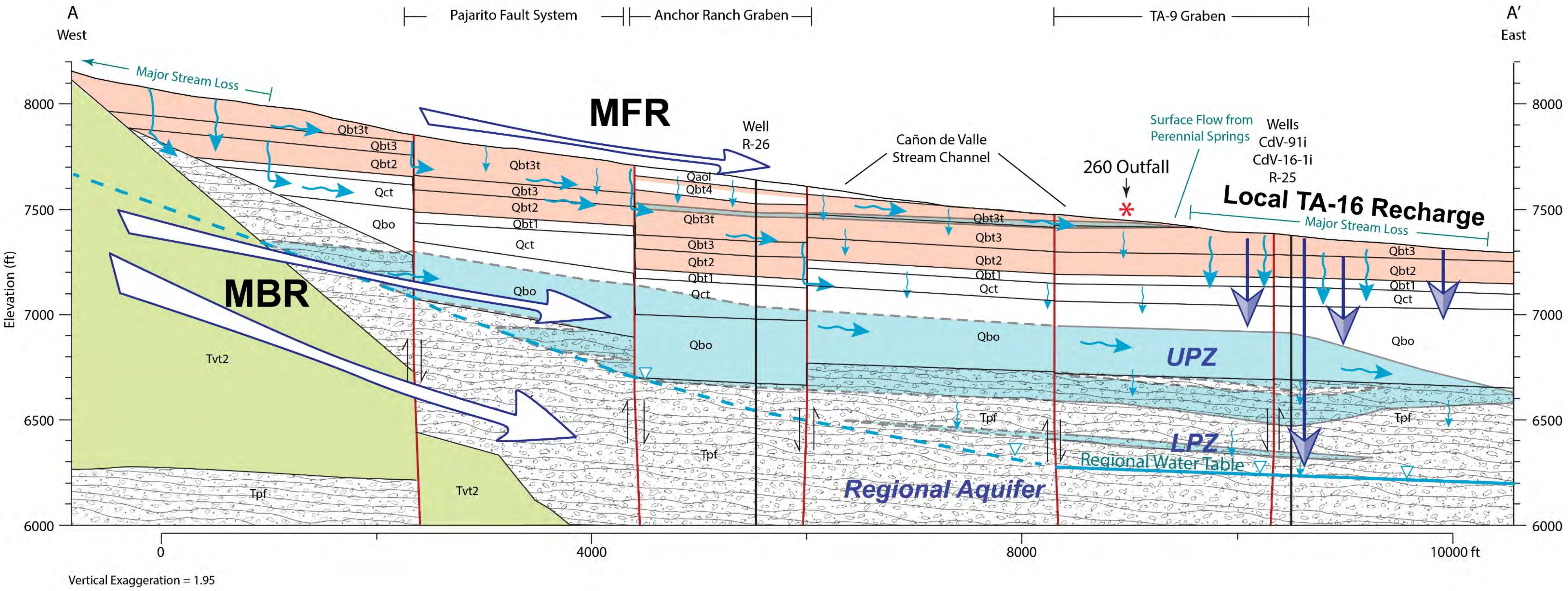

Figure 6.1-1 Modified cross-section of Cañon de Valle from Figure 7.4-1, showing mountain-block vs local TA-16 recharge pathways (dark blue arrows) to the perched-intermediate groundwater zone and regional aquifer.

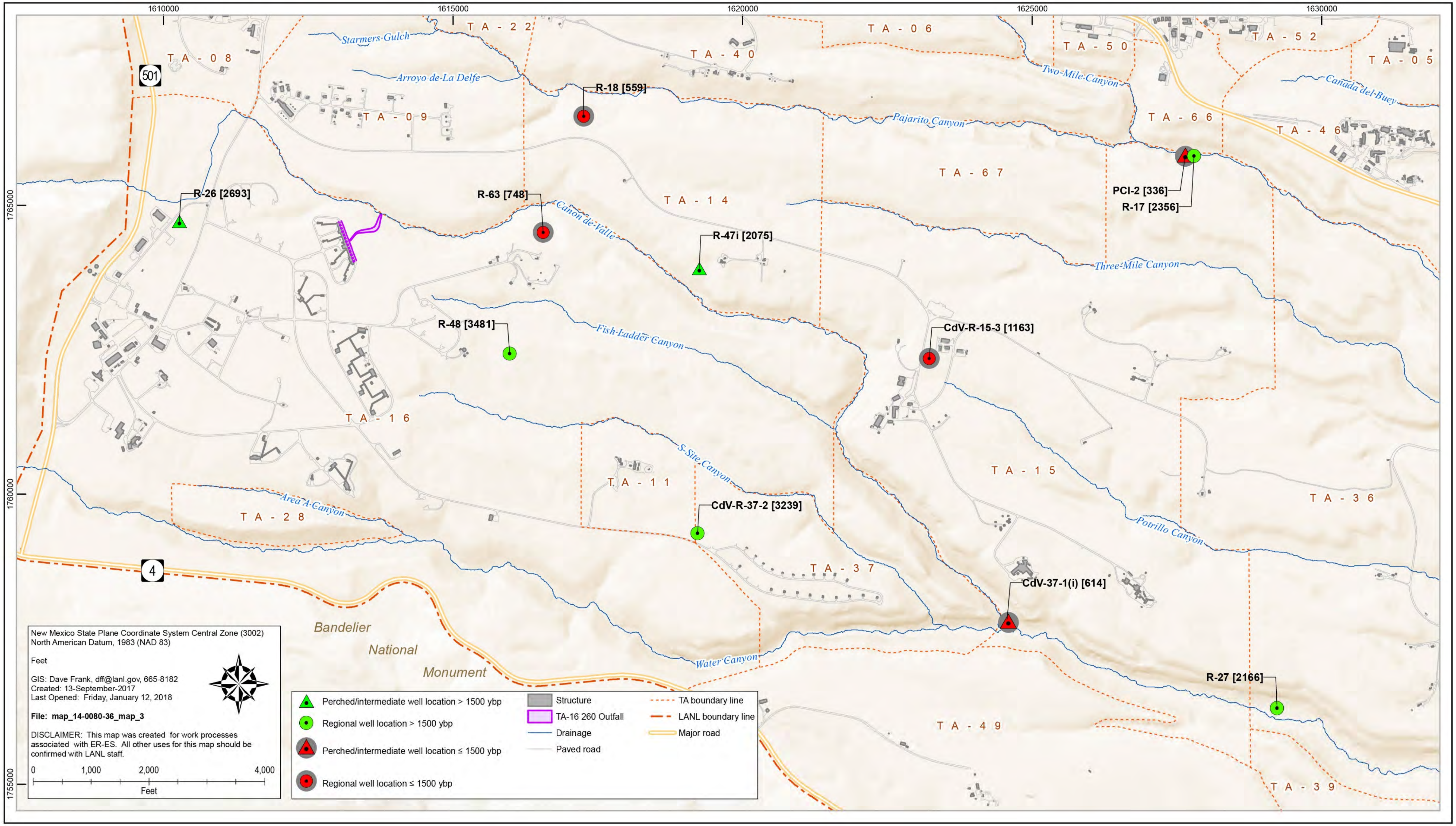

Figure 6.2-1 Map of wells with unadjusted carbon-14 age <1500 ybp or tritium activity >0.8 TU of the top-most screen in regional and intermediate wells

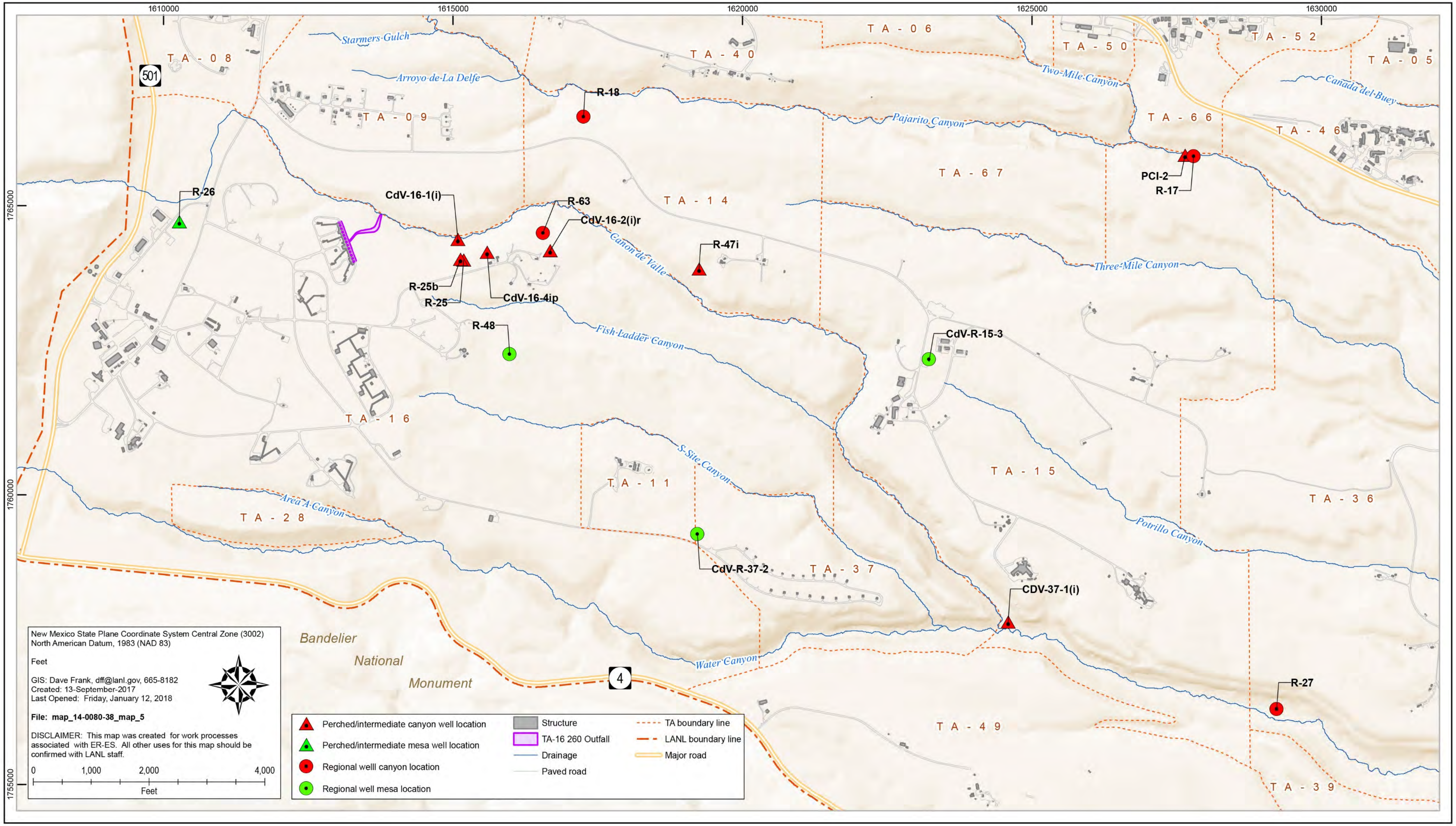

Figure 6.2-2 Map of intermediate and regional wells designated as either "canyon" (<0.25 mi from a canyon) or "mesa" wells

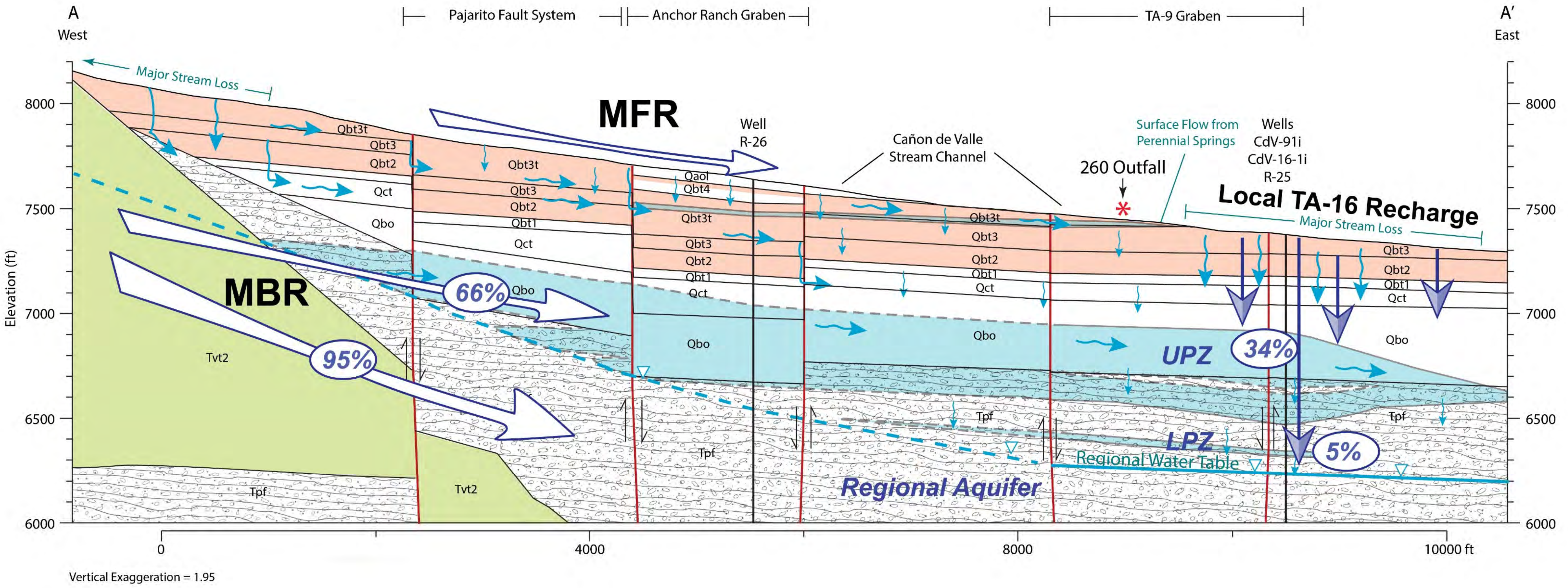

Figure 6.4-1 Modified cross-section of Cañon de Valle from Figure 7.4-1, showing mountain-block vs local TA-16 recharge pathways (dark blue arrows) to the perched-intermediate groundwater zone and regional aquifer. Percentages are averages of mean values calculated from chloride in Table 6.2-1.

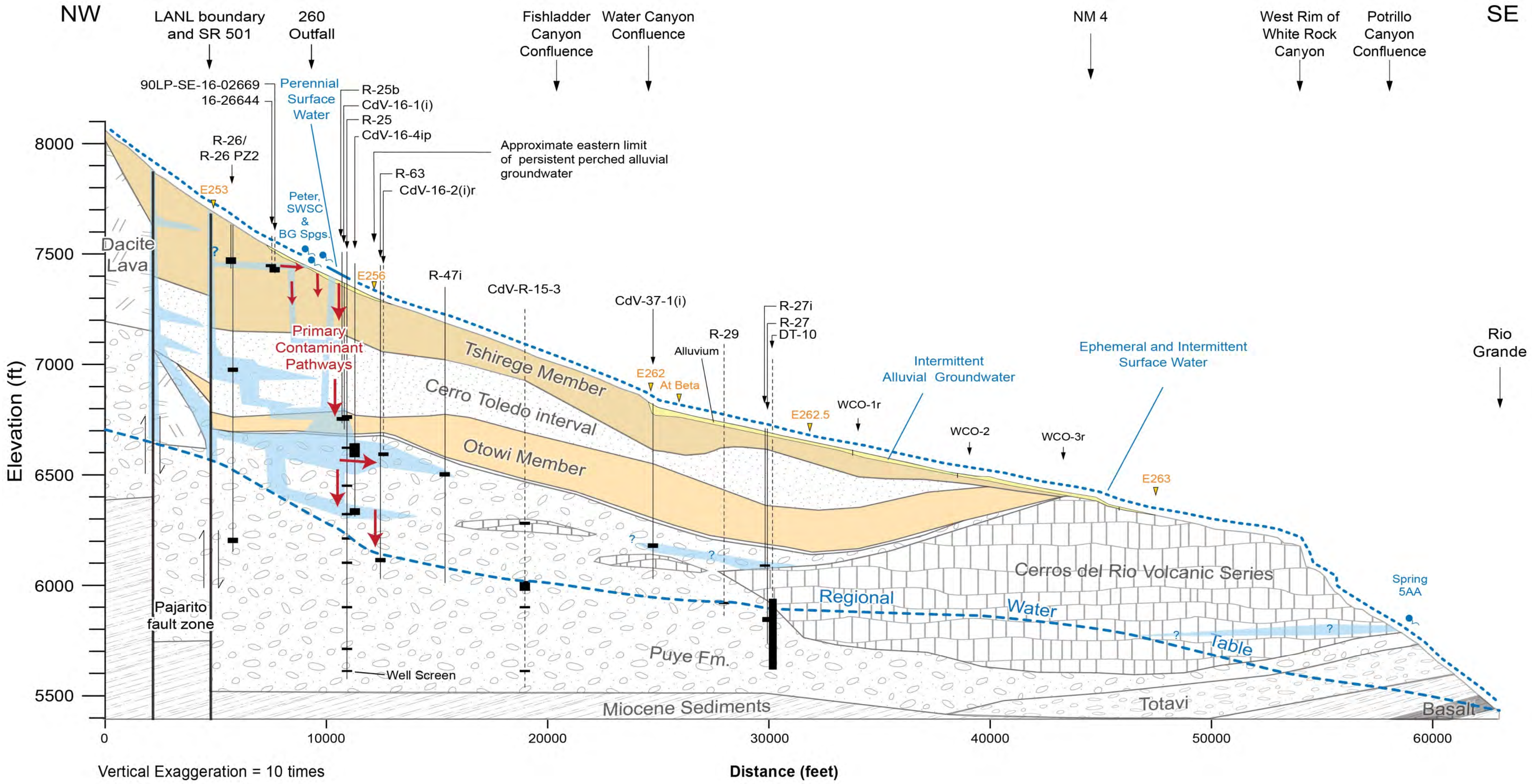

Notes: In the west the line of section follows the Cañon de Valle stream channel to the confluence with Water Canyon. From the confluence, the line of section follows the Water Canyon stream channel to the Rio Grande.

Figure 7.1-1 Conceptual hydrogeologic cross-section for Water Canyon and Cañon de Valle watershed (LANL 2011)

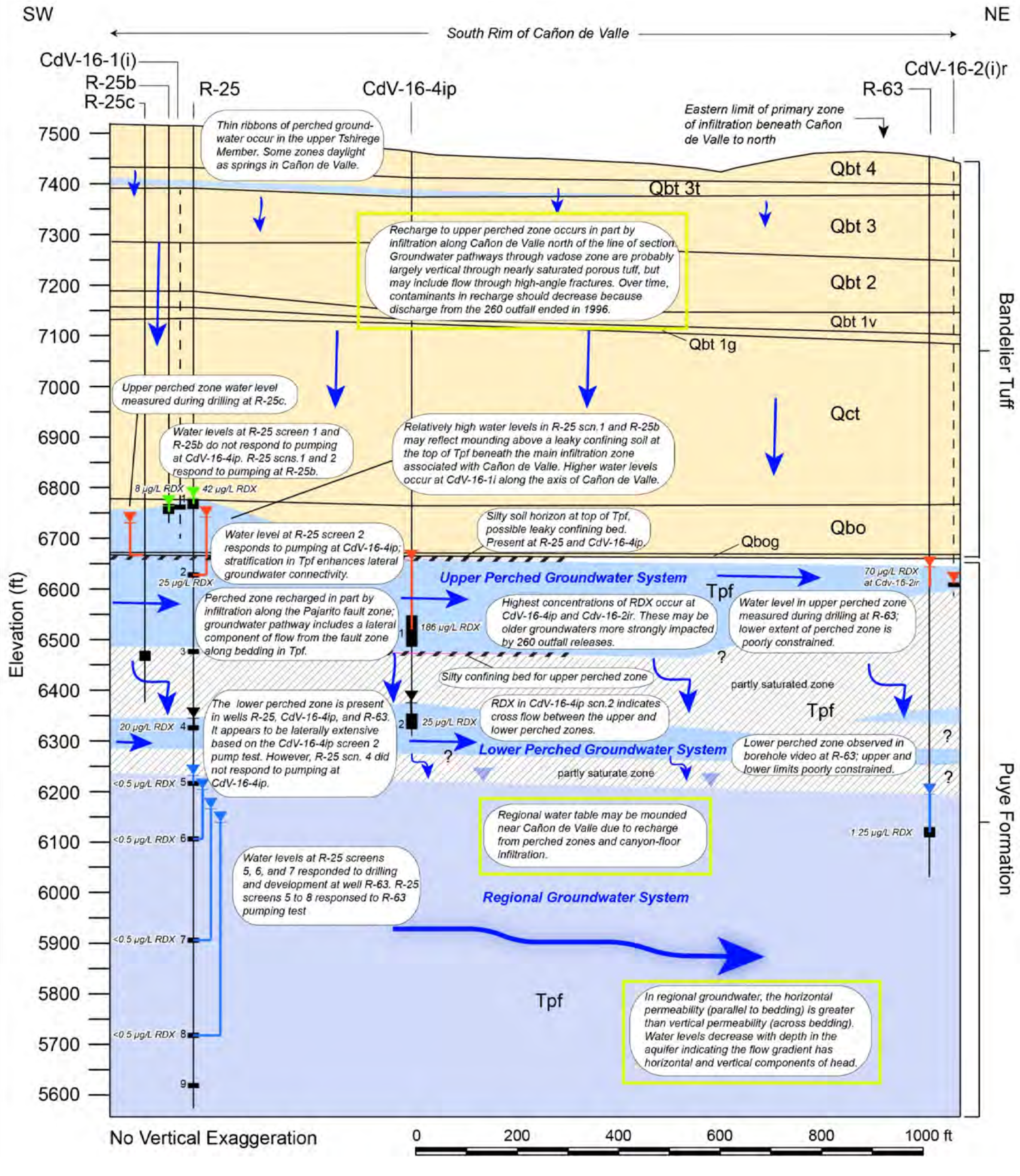

Figure 7.1-2 Conceptual cross-section showing the distribution of groundwater near and adjacent to Cañon de Valle at TA-16 (LANL 2011)

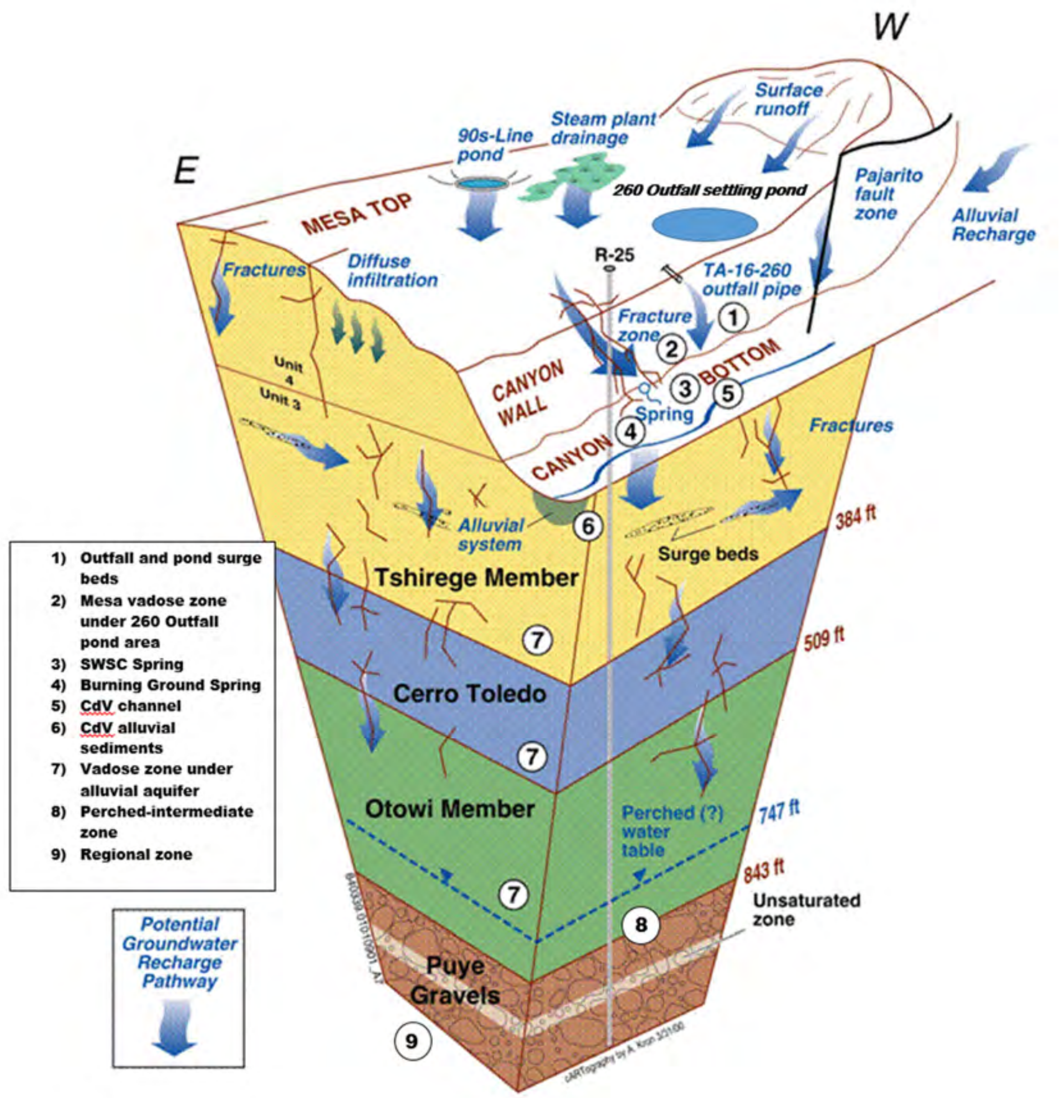

Figure 7.1-3 **Conceptual block diagram showing connections between surface water and perched-intermediate groundwater (LANL 2011)**

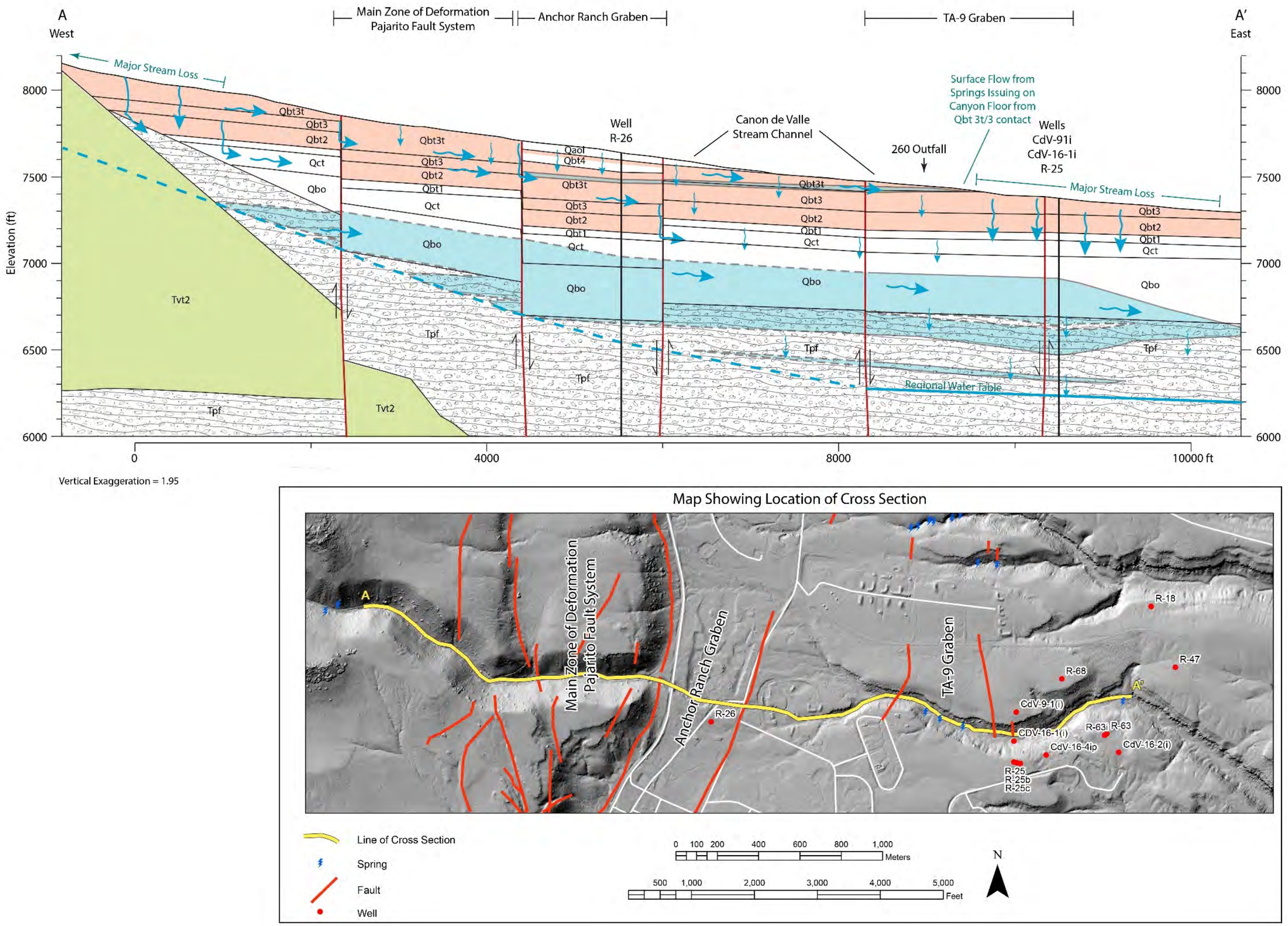

Figure 7.4-1 **West to east conceptual hydrogeologic cross-section that follows the stream channel of Cañon de Valle across the mountain front and the Pajarito fault system. Light blue indicates perched groundwater that is diverted laterally into the vadose zone where steep gradients in the regional water table intersect east-dipping geologic strata with favorable transmissive properties. The shape of the regional water table is unknown to the west, but steep gradients are expected because of proximity to the mountain front infiltration zones. Perched zones and regional water table are dashed where poorly constrained by well data. Blue arrows indicate groundwater flow in the vadose zone and along perched horizons. Geologic units in red are strongly welded tuffs with low matrix porosity and dense fracture networks; geologic units in white are non-welded tuffs with high matrix porosity and fewer penetrating fractures; geologic unit in green is dacite lava with low matrix porosity and characterized by groundwater flow in high-angle fractures and subhorizontal lava flow boundaries. Geologic units: Qaol = old alluvial deposits; Qbt1,2,3,3t,4 = Tshirege Member of the Bandelier Tuff subunits; Qct = Cerro Toledo Formation; Qbo = Otowi Member of the Bandelier Tuff including the basal Guaje Pumice Bed; Tpf = Puye Formation; and Tvt2 = Tschicoma Formation.**

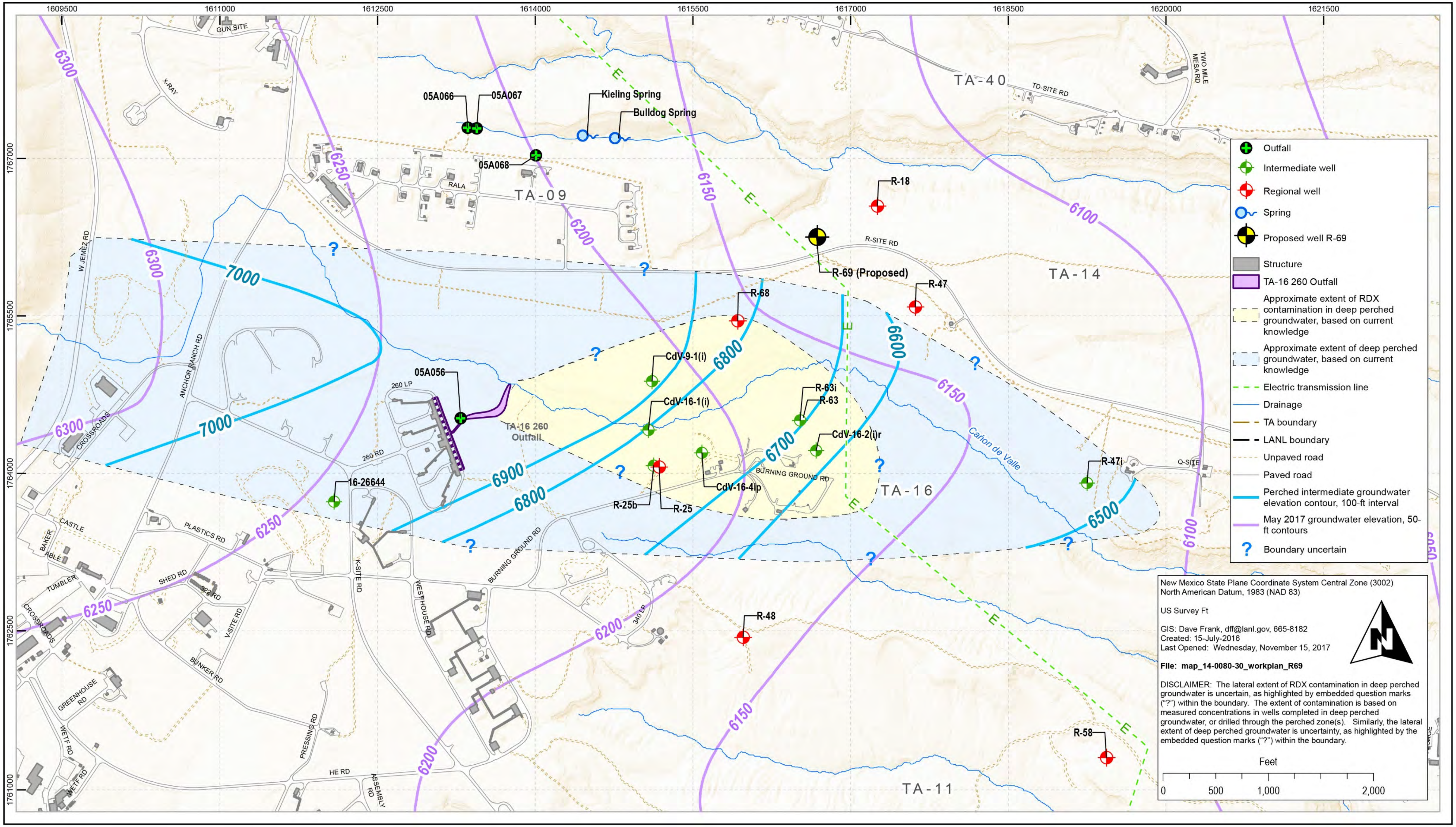

New Mexico State Plane Coordinate System Central Zone (3002)
North American Datum, 1983 (NAD 83)

US Survey Ft

GIS: Dave Frank, dff@lanl.gov, 665-8182
Created: 15-July-2016
Last Opened: Wednesday, November 15, 2017

File: map_14-0080-30_workplan_R69

DISCLAIMER: The lateral extent of RDX contamination in deep perched groundwater is uncertain, as highlighted by embedded question marks ("?") within the boundary. The extent of contamination is based on measured concentrations in wells completed in deep perched groundwater, or drilled through the perched zone(s). Similarly, the lateral extent of deep perched groundwater is uncertainty, as highlighted by the embedded question marks ("?") within the boundary.

Figure 7.4-2 Speculated extent of perched-intermediate groundwater in the TA-16 area

Table 1.3-1
Factor Analysis Results: Factor Loadings for Factors 1–4 (n=1410)

Factor 1	Loading	Factor 2	Loading	Factor 3	Loading	Factor 4	Loading
Pb	0.8914	Ca	0.8323	K	0.9607	RDX	0.8960
Ni	0.8432	Hardness	0.7776	NO3	0.9604	HMX	0.8959
Sr	0.8015	Mg	0.7064	F	0.4880	Fe	0.7716
Li	0.7988	Cl-	0.6564	Sb	0.4867	Al	0.7219
Mn	0.7910	TDS	0.6153	Cr	0.4320	Li	0.4256
Cr	0.7826	Alk (CaCO3)	0.5932	Ni	0.3546	Mn	0.4135
Zn	0.7599	SO4	0.5303	SO4	0.2137	Sb	0.3692
Sb	0.7433	Ba	0.5221	HMX	0.0872	F	0.3679
F	0.7413	TOC	0.3295	RDX	0.0870	Cr	0.3241
B	0.7334	U	0.2961	TDS	0.0856	Pb	0.3004
Al	0.2999	Na	0.1665	Li	0.0470	Ni	0.2648
Fe	0.2856	NH3	0.1325	Sr	0.0261	Cl-	0.0168
RDX	0.0888	ClO4	0.1121	TOC	0.0233	Alk (CaCO3)	0.0161
HMX	0.0882	Fe	0.0293	U	0.0185	Mg	0.0121
SO4	0.0607	Al	0.0284	Cl-	0.0029	TDS	0.0068
Cl-	0.0482	PO4	0.0282	SiO2	-0.0008	Hardness	0.0027
NO3	0.0472	Mn	0.0261	ClO4	-0.0014	Ba	0.0023
K	0.0455	Zn	0.0185	Na	-0.0042	TOC	0.0019
Alk (CaCO3)	0.0412	Sr	0.0136	PO4	-0.0082	SiO2	0.0016
Br	0.0356	Li	0.0135	Pb	-0.0088	Ca	0.0005
TDS	0.0191	B	0.0133	NH3	-0.0106	PO4	-0.0001
PO4	0.0016	F	0.0131	Ba	-0.0166	ClO4	-0.0028
ClO4	0.0013	Pb	0.0092	Hardness	-0.0209	SO4	-0.0035
Na	0.0008	Ni	0.0087	Br	-0.0230	U	-0.0036
SiO2	-0.0020	Sb	0.0073	Ca	-0.0386	Na	-0.0043
NH3	-0.0023	Cr	0.0064	Fe	-0.0691	NH3	-0.0056
Ca	-0.0098	Br	0.0063	Zn	-0.0701	Zn	-0.0178
Mg	-0.0130	NO3	0.0040	Mg	-0.0711	Br	-0.0293
Hardness	-0.0136	K	0.0013	Alk (CaCO3)	-0.0813	K	-0.0363
TOC	-0.0191	RDX	-0.0108	Al	-0.1111	NO3	-0.0363
U	-0.0211	HMX	-0.0109	pH	-0.1131	B	-0.0637
Ba	-0.0402	SiO2	-0.0208	Mn	-0.1206	pH	-0.0761
pH	-0.0640	pH	-0.2571	B	-0.1532	Sr	-0.1836

Table 1.3-2a
Permutation Comparison Results between the Deeper TA-16 Groundwater Zones

Factor	Upper vs Lower Perched		Regional vs Lower Perched		Regional vs Upper Perched		Upper & Lower vs Regional	
Pb	0.8847	ns	0.3331	ns	0.0815	ns	0.06151	ns
Ni	0.1336	ns	0.5595	ns	< 2.2e-16	***	< 2.2e-16	***
Sr	< 2.2e-16	***	0.0197	*	0.0036	**	0.1009	ns
Li	0.9764	ns	0.0739	ns	< 2.2e-16	***	< 2.2e-16	***
Mn	0.4941	ns	0.1217	ns	0.0087	**	0.0045	**
Cr	0.1466	ns	0.3339	ns	0.0594	ns	0.1304	ns
Zn	0.1532	ns	0.4120	ns	0.9563	ns	0.9324	ns
Sb	0.6377	ns	0.0820	ns	< 2.2e-16	***	< 2.2e-16	***
F	0.0215	*	0.0020	**	< 2.2e-16	***	< 2.2e-16	***
B	0.0281	*	0.9712	ns	< 2.2e-16	***	< 2.2e-16	***
Al	0.2822	ns	0.8733	ns	0.3171	ns	0.3993	ns
Fe	0.3904	ns	0.1378	ns	0.6632	ns	0.989	ns
RDX	0.1798	ns	< 2.2e-16	***	< 2.2e-16	***	< 2.2e-16	***
HMX	nd	—	nd	—	nd	—	nd	—
SO4	< 2.2e-16	***	< 2.2e-16	***	< 2.2e-16	***	< 2.2e-16	***
Cl-	0.7532	ns	< 2.2e-16	***	< 2.2e-16	***	< 2.2e-16	***
NO3	0.8712	ns	< 2.2e-16	***	< 2.2e-16	***	< 2.2e-16	***
K	< 2.2e-16	***	< 2.2e-16	***	0.0031	**	< 2.2e-16	***
Alk (CaCO3)	0.4889	ns	0.7215	ns	0.1614	ns	0.23	ns
Br	0.8576	ns	0.1323	ns	0.0344	*	0.0137	*
TDS	< 2.2e-16	***	< 2.2e-16	***	0.5999	ns	0.1033	ns
PO4	0.8326	ns	0.9993	ns	0.0100	*	0.0127	*
ClO4	0.2216	ns	0.5222	ns	0.1932	ns	0.3427	ns
Na	0.0240	*	0.2047	ns	0.5915	ns	0.4618	ns
SiO2	0.0247	*	0.2833	ns	0.0603	ns	0.08281	ns
NH3	0.0135	*	0.4093	ns	0.0460	*	0.1219	ns
Ca	< 2.2e-16	***	< 2.2e-16	***	0.0299	*	2.00E-04	***
Mg	3.00E-04	***	< 2.2e-16	***	0.0881	ns	0.0006001	***
Hardness	< 2.2e-16	***	< 2.2e-16	***	0.6108	ns	0.001	***
TOC	nd	—	nd	—	nd	—	nd	—
U	0.06561	ns	0.0046	**	0.0018	**	3.00E-04	***
Ba	< 2.2e-16	***	0.0964	ns	< 2.2e-16	***	< 2.2e-16	***
pH	0.09321	ns	< 2.2e-16	***	< 2.2e-16	***	< 2.2e-16	***

Note: Asterisks indicate level of significance: $p < 0.1$ (*); $p < 0.05$ (**); $p < 0.01$ (***); not significant (ns), and not determined (nd).

Table 1.3-2b
Permutation Comparison Results Including the Shallower TA-16 Groundwater Zones

Factor	Springs vs Alluvium		Springs vs Upper Perched		Alluvium vs Upper Perched		Springs vs Regional		Alluvium vs Regional	
Pb	0.5288	ns	0.0003	***	0.0028	**	< 2.2e-16	***	< 2.2e-16	***
Ni	0.0746	ns	< 2.2e-16	***	< 2.2e-16	***	0.5373	ns	0.0168	*
Sr	< 2.2e-16	***	< 2.2e-16	***	< 2.2e-16	***	0.0269	*	< 2.2e-16	***
Li	0.3689	ns	< 2.2e-16	***	< 2.2e-16	***	< 2.2e-16	***	< 2.2e-16	***
Mn	0.1024	ns	0.1567	ns	0.0001	***	0.06461	ns	0.0003	***
Cr	0.0009	***	< 2.2e-16	***	0.0268	*	0.0004	***	0.9144	ns
Zn	< 2.2e-16	***	0.0037	**	0.3879	ns	0.5168	ns	1.0000	ns
Sb	0.0275	*	0.0040	**	0.0103	*	< 2.2e-16	***	< 2.2e-16	***
F	< 2.2e-16	***	< 2.2e-16	***	< 2.2e-16	***	< 2.2e-16	***	0.0286	*
B	< 2.2e-16	***	0.0479	*	0.1005	ns	< 2.2e-16	***	< 2.2e-16	***
Al	0.1069	ns	0.0394	*	0.0001	***	< 2.2e-16	***	< 2.2e-16	***
Fe	0.2173	ns	0.4672	ns	0.1565	ns	0.1154	ns	0.0028	**
RDX	< 2.2e-16	***	0.0003	***	< 2.2e-16	***	< 2.2e-16	***	< 2.2e-16	***
HMX	0.0031	**	nd	-	nd	-	< 2.2e-16	***	< 2.2e-16	***
SO4	0.1382	ns	< 2.2e-16	***	< 2.2e-16	***	< 2.2e-16	***	< 2.2e-16	***
Cl-	0.3090	ns	< 2.2e-16	***	< 2.2e-16	***	< 2.2e-16	***	< 2.2e-16	***
NO3	< 2.2e-16	***	< 2.2e-16	***	< 2.2e-16	***	< 2.2e-16	***	0.1554	ns
K	< 2.2e-16	***	< 2.2e-16	***	< 2.2e-16	***	< 2.2e-16	***	< 2.2e-16	***
Alk (CaCO3)	0.8430	ns	< 2.2e-16	***	0.0003	***	< 2.2e-16	***	< 2.2e-16	***
Br	0.8451	ns	0.3682	ns	0.0004	***	< 2.2e-16	***	< 2.2e-16	***
TDS	0.0700	ns	< 2.2e-16	***	< 2.2e-16	***	< 2.2e-16	***	< 2.2e-16	***
PO4	0.2977	ns	0.1006	ns	0.3637	ns	0.6661	ns	0.9724	ns
ClO4	0.0201	*	< 2.2e-16	***	0.0071	**	< 2.2e-16	***	0.0006001	***
Na	0.1608	ns	< 2.2e-16	***	0.0001	***	0.8155	ns	0.5499	ns
SiO2	0.4637	ns	< 2.2e-16	***	< 2.2e-16	***	0.0885	ns	0.1382	ns
NH3	0.8305	ns	< 2.2e-16	***	0.0016	**	0.9537	ns	0.8413	ns
Ca	0.0001	***	< 2.2e-16	***	< 2.2e-16	***	< 2.2e-16	***	< 2.2e-16	***
Mg	0.0191	*	< 2.2e-16	***	< 2.2e-16	***	< 2.2e-16	***	< 2.2e-16	***
Hardness	0.9813	ns	< 2.2e-16	***	< 2.2e-16	***	< 2.2e-16	***	< 2.2e-16	***
TOC	0.3267	ns	nd	-	nd	-	< 2.2e-16	***	< 2.2e-16	***
U	0.4231	ns	< 2.2e-16	***	0.0021	**	< 2.2e-16	***	< 2.2e-16	***
Ba	< 2.2e-16	***	< 2.2e-16	***	< 2.2e-16	***	< 2.2e-16	***	< 2.2e-16	***
pH	< 2.2e-16	***	0.0011	**	< 2.2e-16	***	< 2.2e-16	***	< 2.2e-16	***

Note: Asterisks indicate level of significance: $p < 0.1$ (*); $p < 0.05$ (**); $p < 0.01$ (***).
ns = Not significant; nd = Not determined.

Table 2.3-1
Summary Table of Log-Log Slope Category Classifications for Each Analyte and Hydrologic System

Analyte	Burning Ground	SWSC	Martin	CdV Surface Water
SiO_2	C/D	C	C	N/A
Ca	C	C	C	C
Na	C	C	C	C
Cl-	C	C	C	C
SO_4	C	C	C	C
NO_3	C/D	C/D	C/D	U
Fe	U	U	U	C/D
RDX	C	C	U	C/D
Ba	C	C	C/D	C

Note: C = Chemostatic, D = Dilution (D), U = Unsystematic.

Table 2.3-2
CV for Each Analyte and Hydrologic System

Analyte	Burning Ground	SWSC	Martin	CdV Surface Water
SiO2	0.24	0.21	0.28	N/A
Ca	0.14	0.14	0.21	0.26
Na	0.16	0.17	0.19	1.10
Cl-	0.28	0.20	0.20	0.21
SO4	0.32	0.31	0.22	0.40
NO3	0.42	0.36	0.51	0.86
Fe	1.24	1.32	1.29	1.35
RDX	0.62	0.55	0.54	1.16
Ba	0.25	0.33	0.53	0.73

Table 3.3-1
Cañon de Valle Average Monthly Discharge, Return Flow, and MFR Estimates

		Oct	Nov	Dec	Jan	Feb	Mar	Apr	May	Jun	Jul	Aug	Sept
Total Spring Flow	gpm	7.7	6.2	5.4	5.3	6.7	10.6	14.4	12.2	32.9	24.8	6.9	8.3
E256	gpm	23.7	19	16.6	12.5	13.3	31.3	85.2	26.5	9.9	4.1	16.7	15.8
Upper Canyon Flow	gpm	15	15	5.8	5.8	16	202	636	202	35	27	27	15
Minimum Return Flow	%	52	41	94	91	42	5	2	6	94	92	26	55
Maximum Return Flow	%	160	130	290	210	83	15	13	13	28	15	62	105
Maximum MFR	%	48	59	6	9	58	95	98	94	6	8	74	45
Minimum MFR	%	—*	—	—	—	17	85	87	87	72	85	38	—

Notes: Rows 1–3, average monthly discharge estimates used to calculate MFR; rows 4 and 5 lower canyon return flow percentages; rows 6 and 7 percentages of upper canyon flow lost to MFR. Upper canyon discharges are based on measurements at station UCdV-1 (Figure 3.3-1), and 2016–2017 gauging results are used for December, April, May, and July. Other months are based on historical gauging at UCdV-1.

*— = Minimum MFR estimates represent months with non-physical results.

Table 4.3-1a
Summary Statistics of Water $\delta^{18}O$ for the Separate Hydrologic Systems

$\delta^{18}O$	Regional	Intermediate	Alluvial	Springs	Surface Water
n	191	87	198	248	75
Mean	-11.6	-11.8	-10.9	-11.2	-11.9
Median	-11.6	-11.8	-11.1	-11.3	-12.1
Max	-10.6	-11.1	-6.4	-6.0	-8.4
Min	-12.3	-12.7	-16.0	-13.6	-13.2
SD	0.30	0.29	1.34	0.98	0.73

Note: All values except n are in permil.

Table 4.3-1b
Summary Statistics of Water $\delta^{2}H$ for the Separate Hydrologic Systems

$\delta^{2}H$	Regional	Intermediate	Alluvial	Springs	Surface Water
n	191	87	198	248	75
Mean	-81.9	-83.1	-76.8	-79.3	-85.5
Median	-81.8	-83.6	-78.0	-79.4	-86.7
Max	-75.0	-78.0	-39.2	-40.5	-56.3
Min	-90.0	-85.9	-115.3	-99.8	-96.0
SD	2.30	1.79	11.26	7.44	7.23

Note: All values except n are in permil.

Table 4.3-2
Results of a Kruskal-Wallis One-Way ANOVA and Dunn's Method Test on the Sample Populations of Each Hydrologic System

Comparison Pair	$\delta^{18}O$ P-Value	Statistically Different $\delta^{18}O$ ($p<0.05$)	$\delta^{2}H$ P-Value	Statistically Different $\delta^{2}H$ ($p<0.05$)
Alluvial vs Intermediate	<0.001	yes	<0.001	yes
Alluvial vs Surface	<0.001	yes	<0.001	yes
Alluvial vs Regional	<0.001	yes	<0.001	yes
Alluvial vs Springs	0.855	no	0.293	no
Springs vs Intermediate	<0.001	yes	<0.001	yes
Springs vs Surface	<0.001	yes	<0.001	yes
Springs vs Regional	<0.001	yes	<0.001	yes
Regional vs Intermediate	0.113	no	0.127	no
Regional vs Surface	<0.001	yes	<0.001	yes
Surface vs Intermediate	0.692	no	0.495	no

Table 4.3-3
Summary Table of Tritium, Unadjusted Carbon-14 Age, Temperature, Average RDX Concentration, Lithium Concentration, and Chloride Concentration for Perched-Intermediate Well Screens

Well	Average ^{3}H (TU)	Average Unadjusted ^{14}C Age (ybp)	Temp (°C)	RDX Concentration (µg/L)	Average Li Concentration (µg/L)	Average Cl- Concentration (mg/L)
CdV-16-1(i)	16.84	–*	10.79	27.67	–	6.8
CdV-16-2(i)r	4.52	–	11.1	71.22	9.8	2.5
CDV-16-4ip S1	3.70	–	11.04	151.63	–	3.4
CDV-16-4ip S2	3.15	–	–	69.70	–	2.1
CDV-37-1(i)	0.16	614	12.82	0.16	–	1.3
PCI-2	0.12	336	14.55	0.16	–	–
R-25 S1	12.67	–	10.86	40.57	8.1	13.0
R-25 S2	14.79	–	10.73	9.87	11.0	24.3
R-25 S3	17.11	–	11.14	2.68	0.2	8.1
R-25 S4	9.97	–	11.06	13.55	–	–
R-25b	1.31	–	10.71	5.39	–	2.1
R-26 S1	0.00	2693	16.03	0.16	12.8	1.2
R-47i	0.21	2075	12.46	0.16	15.1	3.0

Note: Values of 0 for tritium data replace negative values for average tritium concentration.

* – = No data available.

Table 4.3-4a
Summary of Wells and Screens That Fit the Steeper Geothermal Trend

Steeper Geothermal Trend		
Well	**Temp (°C)**	**Average Unadjusted ^{14}C Age**
CdV-R-15-3 S4	16.25	1163
CdV-R-15-3 S5	16.71	2170
CdV-R-15-3 S6	18.94	2298
R-18	14.8	559
R-25 S5	12.4	–*
R-25 S6	13.7	–
R-25 S7	16.7	–
R-25 S8	19.8	–
R-27	17.7	2166
R-63	12.6	748

* – = No data available.

Table 4.3-4b
Summary of Wells and Screens That Fit the Shallower Geothermal Trend

Shallower Geothermal Trend		
Well	**Temp (°C)**	**Average Unadjusted ^{14}C Age**
CdV-R-37-2 S2	20.1	3239
CdV-R-37-2 S3	20.7	2976
CdV-R-37-2 S4	21.8	3081
R-17 S1	21.4	2356
R-17 S2	21.5	3099
R-48	20	3481

Table 4.3-5
Summary Table of Tritium, Unadjusted Carbon-14 Age, Temperature, Most Recent (2015–2016) RDX Concentration, Lithium Concentration, and Chloride Concentration for Regional Well Screens

Well	Average ^{3}H (TU)	Average Unadjusted ^{14}C Age (ybp)	Temp (°C)	RDX Concentration (µg/L)	Average Li Concentration (µg/L)	Average Cl- Concentration (mg/L)
CdV-R-15-3 S4	0.07	1163	16.3	0.16	18.8	1.5
CdV-R-15-3 S5	0.03	2170	16.7	0.16	16.9	2.4
CdV-R-15-3 S6	0	2298	18.9	0.16	17.9	1.9
CdV-R-37-2 S2	0.13	3239	20.1	0.16	21.8	2.8
CdV-R-37-2 S3	0	2976	20.7	0.16	22.7	1.8
CdV-R-37-2 S4	0	3081	21.8	0.16	23.0	1.8
R-17 S1	0.05	2356	21.4	0.16	22.1	2.0
R-17 S2	0	3099	21.5	0.16	19.2	1.7
R-18	0.26	559	14.8	3.36	14.7	1.4
R-25 S5	6.88	–*	12.4	0.9	14.1	3.2
R-25 S6	1.95	–	13.7	0.31	–	1.8
R-25 S7	1.47	–	16.7	0.16	–	1.8
R-25 S8	1.39	–	19.8	0.16	–	2.0
R-27	0.29	2166	17.7	0.16	21.1	1.6
R-48	0.27	3481	20.0	0.16	22.6	2.5
R-63	0.46	748	12.6	1.48	23.5	2.4

Note: Values of 0 for ^{3}H data replace negative values for average tritium concentration.
* – = No data available.

Table 4.4-1
Average (± 1 SD) Recharge Elevations of Grouped Hydrologic Zones and Noteworthy Springs Discussed in Section 4.0, Calculated from δ^{18}O after Vuataz and Goff (1986)

Hydrologic Zones and Noteworthy Springs	Average Recharge Elevation (ft)	Low	High
Springs (All)	7680	6670	8700
Burning Ground	7990	7490	8500
SWSC	7730	7190	8260
Martin	7060	5990	8130
Alluvial	7440	6060	8830
Intermediate	8330	8030	8630
Regional	8160	7850	8470

Table 4.4-2
$\delta^{18}O$ SD Ratios of the Hydrologic Systems to Precipitation from Adams et al. 1995

Hydrological Zone	Ratio of SD of Zone/SD of Precipitation
Surface Water	0.22
Springs	0.29
Alluvial	0.40
Intermediate	0.09
Regional	0.09

Note: The surface water SD ratio is likely underestimated in the TA-16 area (section 4.3.1).

Table 5.1-1
All Groundwater Wells and Springs Examined in This Study and Their Response to Flood Tracers

Well/Screen	Geologic Unit	Screen Depth (ft bgs)	Response
R-25 Screen 1	Qbof	737.6–758.4	↑ calcium 2001
R-25 Screen 2	Tpf	882.6–893.4	None
R-25 Screen 4	Tpf	1184.6–1194.6	↑ calcium 2005
R-25b	Qbof	750–770.8	None
R-26 PZ2	–*	150–180	None
R-47i	Tpf	840–860.6	None
CdV-9-1i	Tpf	937.4–992.4	None
CdV-16-1i	Qbof	624–634	Snowmelt response: ↑ alkalinity 2007, 2008, 2011
CdV-16-2ir	Tpf	850–859.7	None
CdV-16-4ip	Tpf	815.6–879.2	None
CdV-16-02656	–	~8	↑ calcium Aug. 2000; ↑ calcium July 2012
CdV-16-26644	–	130–145	None
Burning Ground Spring	N/A	N/A	↑ alkalinity 2001, 2011
SWSC Spring	N/A	N/A	↑ calcium 2000

*– = Geologic units unknown.

Table 5.3-1
Select Groundwater Wells Examined in This Study That Showed a Response to Flood Water

Well/Screen	Flood Date	Response Date	Lag Time	Comments/Assumptions
CdV-16-02656	28-Jun-2000	September 2000	~3 months	Weak calcium signal
CdV-16-02656	July 2012	July 2012	~1–4 weeks	Weak calcium signal
R-25 screen 1	28-Jun-2000	May 2001	~10 months	Weak calcium signal
R-25 screen 1	Jul–Aug 2001	August 2001	~1–4 weeks	Weak calcium signal
R-25 screen 4	May 2005	August 2005	~3 months	Strong calcium signal
CdV-16-1i	Mar–Apr 2007	April–May 2007	~1 month	Alkalinity snowmelt signal
CdV-16-1i	Mar–Apr 2008	April 2008	~2–4 weeks	Alkalinity snowmelt signal
CdV-16-1i	Mar–Apr 2010	April–June 2010	~1 month	Alkalinity snowmelt signal

Table 6.2-1
Percent of MBR vs Local Recharge for Regional and Intermediate Wells

Bulk hydrologic systems			
System	%MBR vs Surface Water	%MBR vs Alluvial Water	%MBR vs Springs
Regional – mean (µ)	95%	94%	95%
Regional – range	88%–99%	86%–99%	89%–99%
Intermediate – mean (µ)	67%	63%	70%
Intermediate – range	22%–99%	19%–99%	34%–99%

Table 6.2-2
Percent MBR vs Local Recharge
for Regional and Intermediate Wells, Split into Young/Old and Canyon/Mesa

Parsed Hydrologic Systems			
System	**%MBR vs Surface Water**	**%MBR vs Alluvial Water**	**%MBR vs Springs**
Regional Young – mean (μ)	95%	94%	95%
Regional Young – range	88%–99%	86%–99%	89%–99%
Regional Old – mean (μ)	95%	94%	95%
Regional Old – range	90%–98%	89%–97%	91%–98%
Regional Canyon – mean (μ)	95%	95%	96%
Regional Canyon – range	88%–99%	86%–99%	89%–99%
Regional Mesa – mean (μ)	95%	94%	95%
Regional Mesa – range	90%–98%	89%–98%	91%–99%
Intermediate Young – mean (μ)	65%	60%	67%
Intermediate Young – range	0%–98%	0%–99%	34%–99%
Intermediate Old (one well)	89%	88%	90%

Note: There is only one well that is intermediate “old.”

Table 6.3-1
Chemical Definitions for
End Members Used in PHREEQC Flow Path Modeling

	Mountain Block Source		**Local Recharge Source**		**Flow Path Endpoint**		
mg/L	**Spring 5.29**	**R-26 S1**	**Burning Ground Spring**	**Cañon de Valle Alluvial Wells**	**CdV 9-1i**	**CdV 16-4ip S1**	**CdV 16-4ip S2**
pH (units)	6.92	7.55	7.34	7	7.43	7.31	7.5
Al	0.9	0.0	0.7	3.5	0.19	–*	–
Ca	7.4	7.7	18.2	19.9	10.8	10.6	9.9
Cl-	1.4	1.3	19.7	23.3	11.1	3.5	2.1
Fe	0.3	0.0	0.3	0.2	0.13	0.0	0.2
Mg	2.8	2.9	5.5	5.8	3.6	3.1	3.1
K	1.5	2.2	3.3	4.1	1.3	1.0	0.7
Na	3.9	8.4	16.2	29.8	22.2	10.2	9.9
SiO2	32.7	58.7	41.3	39.3	48.1	61.2	59.1
SO4	6.1	1.4	9.4	15.0	7.3	3.7	3.6
TDS	79.0	99.8	153.3	216	134.5	117.7	119.3
HCO3-	33.1	48.2	65.4	92	64.6	47.7	48.1

* – = No data available.

Table 6.3-2
PHREEQC Mixing Model Results and Chloride Mass Balance Errors

Final Water Chemistry	Cl- Mass Balance Error (mg/L)	MBR Source (%)	Local TA-16 Recharge Source (%)
CdV 9-1i	0.66	53	47
	1.19	61	39
	1.43	62	38
CdV 16-4ip S1	0.79	87	13
	1.59	80	20
	1.83	79	21
CdV 16-4ip S2	0.08	97	3
	0.13	96	4
	0.23	98	2
R-63	1.14	95	5
	1.53	92	8
	2.58	89	11
R-18	0.09	100	0
	1.26	95	5
	1.71	91	9

Note: The three model results with the lowest chloride mass balance errors are shown for each flow path (final water chemistry well).

Appendix A

Supplementary Chemical and Stable Isotope Data

Table A-1.0a
Summary Table of Average Tritium and RDX Concentrations for Surface Water Samples

Sample Site	Average ^3H (TU)	Average RDX Concentration (µg/L)
16-05600	–*	23.17
16-05967	–	–
16-05989	–	0.29
16-05999	44.48	52.60
Between E252 and Water at Beta	12.62	0.16
Canon de Valle 10	34.86	42.38
Canon de Valle 12	33.21	32.90
Canon de Valle 13	41.08	59.17
Canon de Valle 15	34.42	47.26
Canon de Valle 16	39.32	62.60
Canon de Valle 2	49.76	9.37
Canon de Valle 5	40.28	79.65
Canon de Valle 6	37.58	105.80
Canon de Valle 7	29.12	40.56
Canon de Valle 8	28.40	39.37
Canon de Valle 9	29.09	32.11
Canon de Valle below MDA P	22.91	12.88
Martin Spring Canyon 1	48.45	57.34
Martin Spring Canyon 2	63.29	2.47
Martin Spring Canyon 3	52.42	2.44
Martin Spring Canyon 5	63.05	0.64
Martin Spring Canyon 6	74.37	0.16
Paj below S&N Anch E Basin conf	15.48	1.52
Pajarito above Twomile	16.91	0.16
TS-1W	17.01	0.16
Twomile above Pajarito	–	0.16
Water above SR-501	6.94	0.16
Water at Beta	18.67	0.18

* – = No data available.

Table A-1.0b
Summary Table of Average Tritium and RDX Concentrations for Alluvial Groundwater Samples

Sample Site	Average ^3H (TU)	Average RDX Concentration (µg/L)
CDV-16-02655	57.19	0.16
CDV-16-02656	34.32	1.35
CDV-16-02657	34.38	62.18
CDV-16-02658	26.07	5.45
CDV-16-02659	26.46	21.56
FLC-16-25278	12.99	0.19
FLC-16-25279	13.39	0.17
FLC-16-25280	22.06	5.31
MSC-16-06293	38.76	0.72
MSC-16-06294	33.38	0.20
MSC-16-06295	35.25	0.85
PCAO-5	–*	0.16
PCAO-6	–	0.16
TMO-1	11.67	0.16
WCO-2	25.98	3.09

* – = No data available.

Table A-1.0c
Summary Table of Average Tritium and RDX Concentrations for Spring Samples

Sample Site	Average ^3H (TU)	Average RDX Concentrations (µg/L)
Bulldog Spring	18.32	3.95
Burning Ground Spring	23.28	22.13
Charlies Spring	12.68	0.16
Fish Ladder Spring	40.81	1.10
Homestead Spring	13.65	0.16
Kieling Spring	19.68	0.53
Martin lower SW filt samp port	30.42	29.50
Martin Spring	27.84	108.97
Martin upper SW filt samp port	31.27	34.74
Peter Spring	36.72	8.28
Starmer Spring	12.84	0.16
SWSC Spring	25.88	50.11
Water Canyon Gallery	3.08	0.16

Table A-2.0a
Summary Table of Average Tritium and RDX Concentrations Broken Out by Location for Surface Water Samples

Canyon System	^3H (TU)	SD	RDX (µg/L)	SD
Cañon de Valle	35.73	7.38	47.43	25.93
Martin Spring Canyon	60.32	10.21	12.61	25.03
Water Canyon	12.74	5.87	0.17	0.01
Pajarito Canyon	16.2	1.01	0.84	0.96
Two Mile Canyon	17.01	na*	0.16	0
Fish Ladder Canyon	na	na	na	na

*na = Not available.

Table A-2.0b
Summary Table of Average Tritium and RDX Concentrations Broken Out by Location for Alluvial Groundwater Samples Types

Canyon System	^3H (TU)	SD	RDX (µg/L)	SD
Cañon de Valle	35.68	12.68	18.14	26.07
Martin Spring Canyon	35.8	2.73	0.59	0.34
Water Canyon	25.98	na*	3.09	na
Pajarito Canyon	na	na	0.16	0
Two Mile Canyon	11.67	na	0.16	na
Fish Ladder Canyon	16.15	5.12	1.89	2.96

*na = Not available.

Table A-2.0c
Summary Table of Average Tritium and RDX Concentrations Broken Out by Location for Spring Samples

Canyon System	^3H (TU)	SD	RDX (µg/L)	SD
Cañon de Valle	28.63	7.13	26.84	21.31
Martin Spring Canyon	29.84	1.78	57.74	44.45
Water Canyon	3.08	na*	0.16	na
Pajarito Canyon	15.43	3.31	0.99	1.66
Two Mile Canyon	na	na	na	na
Fish Ladder Canyon	40.81	na	1.1	na

*na = Not available.

Table A-2.0d
Summary Table of Average Tritium and RDX Concentrations Broken Out by Location for the Averages for Each Canyon System, Encompassing All Near-Surface Sample Types

Canyon System	^{3}H (TU)	SD	RDX (µg/L)	SD
Cañon de Valle	34.71	8.74	36.86	27.07
Martin Spring Canyon	45.32	15.98	19.86	33.74
Water Canyon	13.46	9.15	0.75	1.31
Pajarito Canyon	15.65	2.76	0.78	1.27
Two Mile Canyon	14.34	3.78	0.16	0
Fish Ladder Canyon	22.31	13.02	1.69	2.45

Table A-3.0a
Summary Table Of Δ^{18}o Statistics for Each Regional Well Screen

δ^{18}O	n	Mean	Median	Max	Min	SD	Range
CdV-R-15-3 S4	21	-11.7	-11.7	-11.4	-12.1	0.2	0.7
CdV-R-15-3 S5	19	-11.6	-11.6	-11.3	-11.9	0.1	0.6
CdV-R-15-3 S6	17	-11.6	-11.7	-11.4	-12.0	0.2	0.6
CdV-R-37-2 S2	20	-11.5	-11.6	-11.2	-11.9	0.2	0.7
CdV-R-37-2 S3	16	-11.5	-11.5	-10.6	-11.8	0.3	1.2
CdV-R-37-2 S4	17	-11.6	-11.6	-11.3	-11.9	0.1	0.6
R-17 S1	6	-11.0	-10.9	-10.8	-11.2	0.1	0.4
R-17 S2	7	-11.2	-11.2	-11.0	-11.4	0.1	0.4
R-18	17	-11.9	-12.0	-11.5	-12.3	0.2	0.8
R-25 S5	6	-11.9	-12.0	-11.8	-12.0	0.1	0.3
R-25 S6	8	-12.0	-12.0	-11.8	-12.3	0.2	0.5
R-25 S7	10	-11.7	-11.8	-11.3	-12.0	0.2	0.7
R-25 S8	8	-11.7	-11.7	-11.3	-12.0	0.2	0.7
R-27	8	-11.2	-11.2	-10.9	-11.6	0.2	0.7
R-48	8	-11.3	-11.4	-11.0	-11.5	0.1	0.5
R-63	3	-12.1	-12.2	-11.8	-12.2	0.2	0.4

Table A-3.0b
Summary Table of $\delta^{18}O$ Statistics for Each Perched-Intermediate Well Screen

$\delta^{18}O$	n	Mean	Median	Max	Min	SD	Range
CdV-16-1(i)	8	-12.0	-12.0	-11.7	-12.7	0.3	1.0
CdV-16-2(i)r	10	-11.9	-11.9	-11.7	-12.3	0.2	0.6
CDV-16-4ip S1	2	-11.7	-11.7	-11.5	-12.0	0.3	0.5
CDV-16-4ip S2	4	-12.0	-12.1	-11.9	-12.2	0.1	0.3
CDV-37-1(i)	6	-11.3	-11.3	-11.2	-11.5	0.1	0.3
PCI-2	6	-11.3	-11.3	-11.1	-11.7	0.2	0.6
R-25 S1	8	-11.8	-11.8	-11.6	-12.0	0.1	0.4
R-25 S2	9	-11.7	-11.8	-11.2	-12.1	0.2	0.9
R-25 S3	2	-11.4	-11.4	-11.1	-11.7	0.3	0.6
R-25 S4	9	-11.8	-11.9	-11.2	-12.0	0.2	0.8
R-25b	5	-11.7	-11.7	-11.6	-11.9	0.1	0.3
R-26 S1	12	-11.9	-11.9	-11.7	-12.2	0.2	0.5
R-47i	6	-11.8	-11.8	-11.7	-12.0	0.1	0.3

Attachment 4

Heerspink, B.P., S. Pandey, H. Boukhalfa, D.S. Ware, O. Marina, G. Perkins, V.V. Vesselinov, and G. WoldeGabriel, May 2, 2017. “Fate and Transport of Hexahydro-1,3,5-trinitro-1,3,5-triazine (RDX) and Its Degradation Products in Sedimentary and Volcanic Rocks, Los Alamos, New Mexico,” Chemosphere, Vol. 182, pp. 276-283.

http://dx.doi.org/10.1016/j.chemosphere.2017.04.149

Chemosphere 182 (2017) 276–283

Contents lists available at ScienceDirect

Chemosphere

journal homepage: www.elsevier.com/locate/chemosphere

Fate and transport of hexahydro-1,3,5-trinitro-1,3,5-triazine (RDX) and its degradation products in sedimentary and volcanic rocks, Los Alamos, New Mexico

Brent Porter Heerspink [a], Sachin Pandey [b], Hakim Boukhalfa [a, *], Doug S. Ware [a], Oana Marina [a], George Perkins [a], Velimir V. Vesselinov [b], Giday WoldeGabriel [a]

[a] *Earth Systems Observations (EES-14), Earth and Environmental Sciences Division, Los Alamos National Laboratory, Los Alamos, NM 87545, USA*
[b] *Computational Earth Science (EES-16), Earth and Environmental Sciences Division, Los Alamos National Laboratory, Los Alamos, NM 87545, USA*

HIGHLIGHTS

- Adsorption of RDX and its degradation products was studied in volcanic and sedimentary rock representing a deep aquifer.
- Retardation factors quantified for RDX and its degradation products for these rock types were small, ranging from 1.0 to 1.8.
- There was no measurable difference between the transport properties of RDX and its degradation products MNX, DNX, and TNX.

ARTICLE INFO

Article history:
Received 5 December 2016
Received in revised form
26 April 2017
Accepted 30 April 2017
Available online 2 May 2017

Handling Editor: Shane Snyder

Keywords:
RDX
MNX
TNX
DNX
Transport
Degradation

ABSTRACT

High-explosive compounds including hexahydro-1,3,5-trinitro-1,3,5-triazine (RDX) were used extensively in weapons research and testing at Los Alamos National Laboratory (LANL). Liquid effluents containing RDX were released to an outfall pond that flowed to Cañon de Valle at LANL's Technical Area 16 (TA-16), resulting in the contamination of the alluvial, intermediate and regional groundwater bodies. Monitoring of groundwater within Cañon de Valle has shown persistent RDX in the intermediate perched zone located between 225 and 311 m below ground surface. Monitoring data also show detectable levels of RDX putative anaerobic degradation products. Batch and column experiments were conducted to determine the extent of adsorption-desorption and transport of RDX and its degradation products (MNX, DNX, and TNX) in major rock types that are within the RDX plume. All experiments were performed in the dark using water obtained from a well located at the center of the plume, which is fairly oxic and has a neutral pH of 7.5. Retardation factors and partitioning coefficient (K_d) values for RDX were calculated from batch experiments. Additionally, retardation factors and K_d values for RDX and its degradation products were calibrated from column experiments using a one-dimensional transport model with equilibrium sorption (linear isotherm). Results from the column and batch experiments showed little to no sorption of RDX to the aquifer materials tested, with retardation factors ranging from 1.0 to 1.8 and K_d values varying from 0 to 0.70 L/kg. Results also showed no measurable differences between the transport properties of RDX and its degradation products.

1. Introduction

High explosives (HE), including TNT (2,4,6-trinitrotoluene), HMX (high melting explosive, octahydro-1,3,5,7-tetranitro-1,3,5,7-tetrazine), and RDX (hexahydro-1,3,5-trinitro-1,3,5-triazine) are common environmental contaminants at military and national laboratory research sites. These contaminants were introduced into the environment as effluents from manufacturing and testing of weapons components containing high explosives (Layton et al., 1987; Becker et al., 1987; Spalding and Fulton, 1988; Pennington and Brannon, 2002; Gard and Newman, 2005; LANL, 2011). Los Alamos National Laboratory (LANL), where weapons components containing HE material were developed and tested, released effluents from processing facilities with high-explosive compounds,

---

* Corresponding author.
E-mail address: hakim@lanl.gov (H. Boukhalfa).

http://dx.doi.org/10.1016/j.chemosphere.2017.04.149
0045-6535/

including RDX, TNT, and HMX to holding ponds (LANL, 2011). Historical records tracking effluents from machining operations at TA-16-260 show that during the period from 1951 to 1996 between 1,500 and 23,000 kg were released (LANL, 2006). This resulted in significant contamination of surface sediments as well as the alluvial, intermediate and regional groundwater bodies beneath and downstream from the 260 Outfall. Fig. 1 shows the location of TA-16 and the 260 Outfall on LANL's site. Of the compounds released from the 260 Outfall, RDX is of particular concern due to its listing as a possible human carcinogen by the USEPA (EPA, 2014). The EPA screening level for RDX in tap water is 0.61 μg/L (EPA, 2013). Remediation efforts were undertaken by LANL between 2000 and 2009 to remove RDX from the sediments directly below the 260 Outfall. This remediation process removed a significant amount of RDX from the sediments and reduced the concentration of RDX in the alluvial aquifer (LANL, 2011). However, continued sampling of a suite of monitoring wells at TA-16 shows persistent RDX contamination in the intermediate perched zone up to 170 μg/L and up to 2.8 μg/L in the regional aquifer. Concentrations are slowly increasing in the regional groundwater aquifer. The degradation products of RDX, including MNX (hexahydro-1-nitroso-3,5-dinitro-1,3,5-triazine), DNX (hexahydro-1,3-dinitroso-5-nitro-1,3,5-triazine), and TNX (hexahydro-1,3,5-trinitroso-1,3,5-triazine) are detected in these monitoring wells at a persistent concentration of about 1 μg/L with no observed accumulation.

The RDX plume at TA-16 is located within different groundwater zones. At the shallowest depth, RDX is detected within the alluvial system. RDX is also detected within the upper perched groundwater system located within the Bandelier Tuff at depths less than a hundred meters. The next RDX contamination occurs within the intermediate perched zone located at depths of 225–311 m. At this depth, the geology is dominated by volcaniclastic sediments of the Puye Formation. RDX is also detected at trace levels (2.8 μg/L or less) in the regional aquifer, encountered at depths of 350–372 m within the Puye Formation. Aspects of RDX degradation/sorption and mobility under the specific conditions of TA-16 are currently under investigation to better predict the transport of RDX to the regional aquifer and to identify proper remedial options.

Mobility of RDX and other HE compounds in sediments has been examined for a number of sites using soils and mineral separates (Purtymun et al., 1982; Becker et al., 1987; Dubois and Baytos, 1991; Selim and Iskandar, 1994; Comfort et al., 1995; Sheremata et al., 2001; Reid et al., 2005; Dontsova et al., 2006; Alavi et al., 2011; Fuller et al., 2014). Most studies examined shallow organic-rich soils and clays and found that the mobility/sorption of HE compounds, including RDX are affected by soils/clays and organic matter contents (Eriksson and Skyllberg, 2001; Singh et al., 2008, 2010; Sharma et al., 2013). In general, sorption is higher for soils with high organic matter content (Dontsova et al., 2006; Singh et al., 2008; Alavi et al., 2011; Sharma et al., 2013). Organic matter strongly influences the HE affinity of soils rich in carboxylic groups that are very effective at adsorbing these compounds (Singh et al., 2010). However, one study reported that removal of soil organic carbon in clay-rich soils increased HE compounds sorption (Charles et al., 2006). The partitioning coefficient (K_d) values reported in the literature vary significantly for different HE compounds but are mostly consistent with the influence of the soil's organic matter and clay content on their interaction with explosives. K_d values in soils for TNT range from 0.2 to 10 L/kg, 0–1.6 L/kg for RDX, and 0.7–4.5 L/kg for HMX (Selim and Iskandar, 1994; Sharma et al., 2013; Monteil-Rivera et al., 2003). Desorption is fast and reversible for RDX and HMX and much slower for TNT, which is consistent with their sorption properties.

The behavior of HE degradation products, which are often detected in soils and sediments contaminated with explosives, is less known. Generally, these derivatives are less stable and

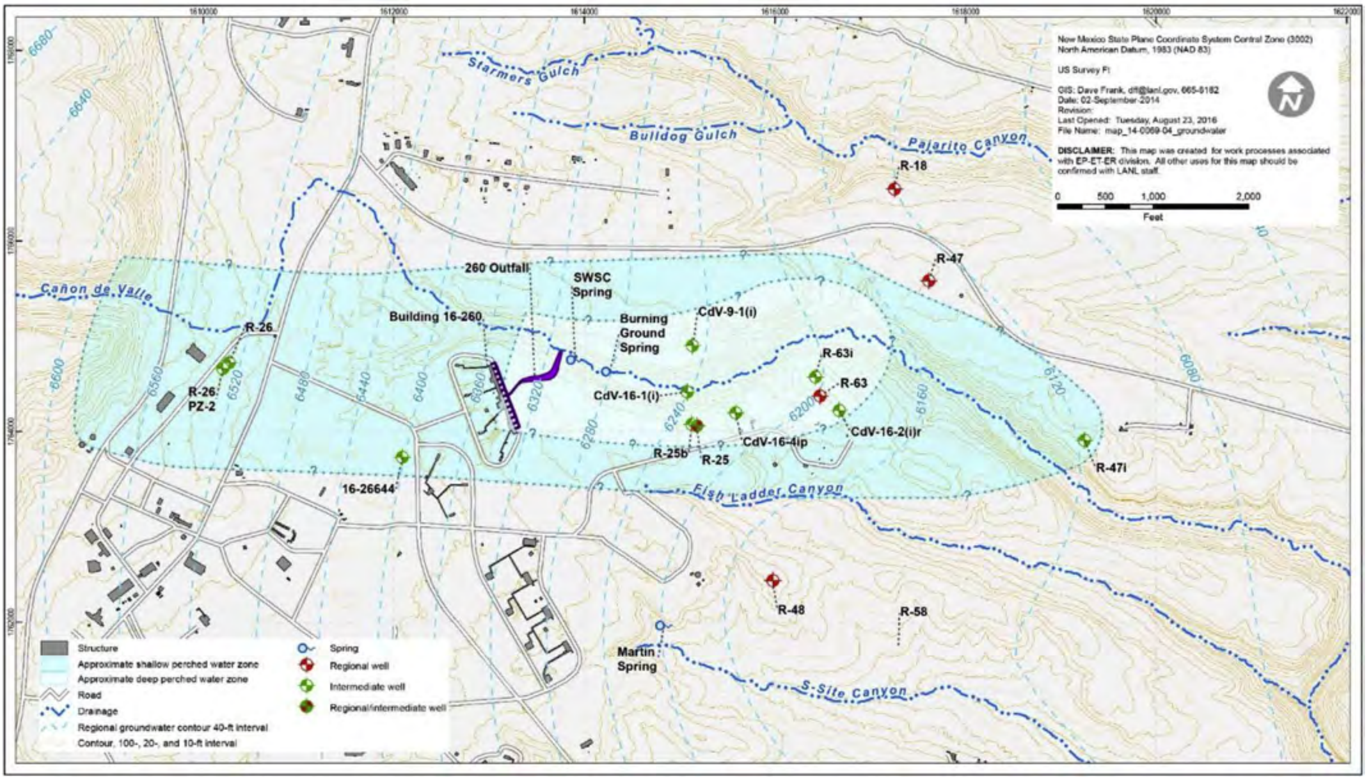

Fig. 1. Location of TA-16, 260 Outfall, and Cañon de Valle at Los Alamos National Laboratory.

methods for their detection and quantification are not well established. However, some of the derivatives are toxic and knowledge of their environmental behavior and impact is important (Smock et al., 1976; Liu et al., 1995). The anaerobic degradation products of RDX (i.e. MNX, DNX, TNX) are often observed in the environment, but their concentrations are relatively low and very little is known on their transport and rate of degradation. Under the biogeochemical conditions at TA-16, the concentrations of MNX, DNX, and TNX are often above the detection limit but there is no direct correlation with the concentration of RDX. Their detection is likely due to microbial activity, however no specific microorganisms were identified to be responsible for the observed RDX degradation in a survey of the microbial diversity in groundwater at TA-16 (Wang et al., 2017).

In this study, we used batch experiments to characterize the partitioning of RDX onto both bulk rocks and mineral separates obtained from three core samples taken from the Bandelier Tuff and sedimentary units of the Puye Formation both within and outside the RDX plume at TA-16. We also characterized the transport of both RDX and its degradation products through columns packed using the same bulk sediments and tuffs. Geochemical conditions that are representative of the subsurface conditions at TA-16 were used in all experiments, and biotic interactions of the indigenous microbes present in the groundwater were limited by using sterile water and autoclaved samples. The goal of the work performed is to better understand the physicochemical interactions that dictate transport of both RDX and its degradation products in these types of geologic units. We also explored the potential for the abiotic degradation of RDX in contact with minerals. To our knowledge, characterization of RDX transport in a deep, contaminated aquifer with low organic matter, and transport parameters for the degradation products of RDX has not been previously reported.

2. Materials and methods

2.1. Groundwater sampling and characterization

Water for the batch and column experiments were collected from the CdV-16-4ip monitoring well drilled into the intermediate perched zone within the central part of the RDX plume. The water sample was obtained from the Puye Formation screen located between 248 m and 268 m below ground surface. RDX concentration in the water was about 160 μg/L. There was also trace levels of MNX, DNX, and TNX, which were all at about 1 μg/L. The water was stored in a 20 L carboy in the dark at 4 °C. Before use in the column or batch studies, the water was treated with activated carbon to remove RDX and was purified through 0.2 μm polycarbonate filters to remove any environmental microbes. The water was degassed under vacuum for at least 24 h before use to prevent build-up of air bubbles within the columns. The water chemistry in the intermediate perched zone at TA-16 is monitored on a quarterly basis and shows very little variation with time. The concentration of dissolved oxygen varies between 5 and 7 mg/L. The major anion concentrations in the water sample consisted of Cl^- (4.69 mg/L), F^- (0.11 mg/L), NO_3^- as nitrogen (0.83 mg/L), $SO_4{}^{2-}$ (3.8 mg/L), and $PO_4{}^{2-}$ (1.1 mg/L), and the major cations consisted of Na^+ (10.2 mg/L), Ca^{2+} (7.1 mg/L), K^+ (14.0 mg/L), Mg^+ (3.0 mg/L), and Si^{4+} (30.5 mg/L). Iron and manganese were not detected. The total dissolved solids was 184.8 mg/L at a pH of 8.26 and alkalinity (CO_3^{2-}-HCO_3^-) of 50.7 mg/L. The water chemistry of the regional aquifer is also oxic and contains very little organic matter. Detailed descriptions of the hydraulic properties and water chemistry are presented elsewhere (LANL, 2011).

2.2. Rock samples for laboratory studies

Volcanic and sedimentary rocks used in the experiment were taken from cores collected at TA-16 and adjacent areas. Two of the samples were from seismic hazards core hole SHB3 drilled to a depth of 258 m about 2 km to the southwest of the RDX contamination plume. The third sample was from the 395 m deep R25 monitoring well drilled into the RDX contaminated regional aquifer. All three samples were variable in composition and contained little to no organic matter. The first sample is volcanic and was obtained from a foot-long core of the Otowi Member of the Bandelier Tuff obtained from the SHB3 core hole at a depth of 252 m below ground surface (referred to as SHB3 Otowi bulk tuff in the remainder of the paper). The sample is representative of the geology of the intermediate perched zone within the Bandelier Tuff. It is light grey, mostly non-welded, pumice-rich vitric ignimbrite and contains <10% dark grey angular to subrounded dacite lava clasts in a glassy matrix. The second foot-long core sample was from the Puye Formation also collected from the SHB3 core hole at 256 m below ground surface, underlying the Bandelier Tuff (referred to as SHB3 Puye bulk sediments). The sample is representative of the geology of the deep intermediate perched zone within the Puye Formation. The Puye Formation directly underlying the Bandelier Tuff is light brown, consolidated, matrix-supported, silty sandstone that contains minor angular dacite lava fragments up to 4 cm in size. The third sample was obtained from the R25 well at a depth of 352 m below ground surface and also belongs to the Puye Formation (referred to as R25b Puye bulk sediments). The sample is representative of the geology of the regional aquifer within the Puye Formation. The Puye Formation at this depth consists of coarse to medium gray sandstone that is poorly sorted and matrix-supported. It contains abundant dacite lava and minor pumice and other rock fragments. The matrix is tuffaceous and glassy mixed with minor quartz and feldspar crystals. The tuff and sediment samples were crushed and sieved to prepare a 75 μm to 2000 μm grain-size fraction, removing large particles which make it difficult to pack homogeneous columns. The samples were then washed with water to remove ultrafine particles, which tend to clog columns, and dried in an oven overnight.

2.3. Analytical methods

Sample analyses for water chemistry, RDX, and its degradation products were performed at the Earth and Environmental Sciences Division (EES-14) laboratory at LANL. RDX and its degradation products were analyzed by high performance liquid chromatography using USEPA Method 8330. The analysis was completed using a Dionex HPLC with a C-18 analytical column and an Ultimate 300 RS detector set at 254 nm (Pan et al., 2006). The mobile phase composition was adjusted as needed to optimize the separation of RDX and its degradation products. Increasing the methanol to water ratio achieved a better separation of the degradation products. The mobile phase was optimized at 55:45 water to methanol. A detection limit of 1.0 μg/L is obtained for RDX and its degradation products MNX, DNX, and TNX. Analytical columns were cleaned periodically by first flushing with pure methanol, then flushing with pure acetonitrile, and finally returning to the mobile phase to allow for equilibration before samples were analyzed. Anions were analyzed by a Dionex ICS-2100 system with an IonPac AS-15 hydroxide Selective Anion Exchange Column using USEPA Method 300.6. Major cations were analyzed by a Perkin Elmer Optima 2100 DV Inductively Coupled Plasma Atomic Emission Spectroscopy unit using USEPA Method 200.7. Titration for alkalinity and pH was done by a Mettler Toledo automated titration system using USEPA Method 310.1. All samples from the column and batch experiments were filtered through Millex 0.45 μm syringe filters. Bromide measurements were taken via a combination bromide probe calibrated with a set of standards prepared in house from a lithium bromide solid sample. Measurements for pH were taken via a Thermo Fisher Accumet pH probe calibrated with three commercial pH standards. Both probes were used in conjunction with an Orion 290A meter.

2.4. Batch experiments

Batch experiments were completed for individual mineral separates and the bulk samples from the tuff and sediment core samples used in this study. Individual minerals were handpicked under a binocular microscope. A sample of Tygon (R-3603) tubing, which was initially used to connect the syringes and columns, was also tested as a control, along with the vials used for the experiments. Samples were placed into two-part centrifuge tubes with built in filters. Sediments were saturated for 24 h using clean CdV-16-4ip water before addition of a standard RDX solution. The test solution was prepared using treated CdV-16-4ip water spiked with RDX to a desired concentration of ~500 μg/L. HPLC analysis of the test solution showed an actual RDX concentration of 540 μg/L. Solid to liquid ratios were kept at approximately 1:1 for all samples to maximize concentration readings. This was necessary given the very low sorption of RDX. Samples were kept covered from light on a shaker table set at 50 RPM for the duration of the experiment. Batch experiments were conducted at an ambient temperature of 23 °C. However, it should be noted that the typical aquifer temperature is about 11 °C. Once saturated, an aliquot of solution containing RDX was added to the minerals and allowed to sorb for one week before it was centrifuged and sampled. Clean CdV-16-4ip water was then added, and the system was allowed to equilibrate for two days to study desorption. Clean water was added in the exact amount that was removed from the samples to ensure the solid to liquid ratio remained the same throughout the experiment.

2.5. Column transport experiments

Column experiments were performed using Chromaflex glass columns (Kible Chase) 30 cm in length and 2.5 cm in diameter, dry packed with one of the three bulk samples (SHB3 Otowi bulk tuff, SHB3 Puye bulk sediments, and R25b Puye bulk sediments). Sediments were autoclaved to kill any environmental bacteria before packing. During packing, columns were periodically tapped to compact samples and ensure uniform porosity throughout the column. Columns were customized using Lure fittings (Value Plastics Inc.) and 3/8 in inner diameter Teflon tubing. Once packed and sealed, negative pressure from vacuum and positive pressure from compressed CO_2 were applied in alternating cycles to remove air from the system before saturation. Prior to any experimental injections, treated CdV-16-4ip water was passed through the columns for at least 24 h. Water was injected into the columns from Monoject 160 mL syringes (Medtronic) in KDS100 syringe pumps (KD Scientific) set to a rate of 2.0 mL/hr with flow oriented from the bottom upward though the column. Similar to the batch experiments, all column experiments were conducted at an ambient temperature of 23 °C. The columns were placed in a dark room to prevent photodegradation of RDX.

Two test solutions containing different amounts of explosive products and bromide as a conservative tracer were used in the columns. The first solution contained only RDX and bromide. The second solution contained RDX, its degradation products (MNX, DNX, and TNX), and bromide. Besides the addition of degradation products and a bromide tracer, the test solutions for the column experiments were prepared in the same manner as the batch experimental solution. The exact concentrations of these compounds varied between experiments, and each solution was characterized by HPLC. The concentrations in each injection are presented in Section 3.2. The concentration of degradation products in the second test solution were higher than the background concentrations of ~1 μg/L to reflect conditions that may occur during *in situ* remediation of RDX. This also allowed us to examine abiotic degradation potential of the breakdown products, although abiotic degradation may only be relevant over timescales that are longer than the duration of these experiments. Approximately 100 mL of each solution was injected over a two-day period before switching back to treated CdV-16-4ip water. Effluents from the columns were collected every two hours using Foxy Jr. fraction collectors (Teledyne Isco Inc.) housed in a humid polyurethane box to minimize evaporation.

The experimental columns were initially outfitted with Tygon tubing (R-3603). However, this tubing was found to significantly interfere with RDX transport. Interference with Tygon was previously reported for other substrates in the past (Dittrich and Reimus, 2015). The influence of Tygon on column breakthrough curves for RDX and its degradation products are illustrated in Figure S1 and Table S1 of supporting information. All Tygon parts were subsequently replaced with Teflon, which does not interfere with RDX or any of its degradation products.

2.6. Modeling the experiments

Estimates of RDX sorption in the batch experiments were achieved using a linear equilibrium sorption isotherm given below.

$$s = K_d c, \tag{1}$$

where s is the concentration of the adsorbed phase (kg/kg), c is the aqueous concentration (kg/L), and K_d is the partitioning coefficient for linear adsorption (L/kg). Sorption behavior of RDX and its degradation products was quantified in the column experiments using a one-dimensional saturated flow and transport model that also assumed equilibrium sorption following Equation (1). Under the assumption of steady-state flow in a homogeneous media, the governing equation for flow and transport reduces to the following equation:

$$\left(1 + \frac{\rho_b K_d}{\theta}\right)\frac{\partial c}{\partial t} = D\frac{\partial^2 c}{\partial x^2} - v\frac{\partial c}{\partial x}, \tag{2}$$

where v is the porewater velocity (m/hr), θ is the volumetric water content, D is the dispersion coefficient (m^2/hr), and ρ_b is the bulk density of the porous media (kg/m^3). The units for K_d in Equation (2) are m^3/kg, but these are converted to L/kg in the remainder of the paper to allow for easier comparison with previously reported values. The term $\left(1 + \frac{\rho_b K_d}{\theta}\right)$ is the retardation factor. The analytical solution of Equation (2) presented by Toride et al. (1995) for a multiple pulse input condition and first-type boundary condition was coded in Julia (a high-level, high-performance dynamic programming language for technical computing). Code verification was achieved by comparing model results with those obtained using CXTFIT 2.1 (Toride et al., 1999).

For the batch experiments, K_d was calculated for each sample by processing the experimental data using Microsoft Excel. For the column experiments, K_d and the other transport parameters were calibrated using the open-source code MADS (http://mads.lanl.gov). The model parameters were calibrated using inverse analysis (Levenberg-Marquardt optimization). Prior to calibrating sorption parameters for RDX in the columns, bromide tracer breakthrough curves were used to calibrate θ for each column using the numerical model PFLOTRAN (http://www.pflotran.org/). The unknown parameters required for the analytical solution of Equation (2) are K_d and D. Known parameters required in the solution are ρ_b, column packed length (L_{col}), specific discharge (q), and duration of injection (t_{inj}).

3. Results

3.1. Batch experiments

The results of the batch experiments are summarized in Table 1. Of the bulk samples tested, only the SHB3 Puye bulk sample had any measureable sorption, with a K_d of 0.030 ± 0.010 L/kg. The mineral separates for SHB3 Puye bulk had a range of K_d values from 0.10 to 0.70 L/kg, with the fines portion of the sample having the highest sorption. The mineral separates for SHB3 Otowi had low but measureable K_d values ranging from 0.10 to 0.34 L/kg. The mineral separates from R25 Puye also had low but measureable K_d values ranging from 0.010 to 0.20 L/kg. RDX sorption to the vials used in the experiment was found to be negligible. However, RDX sorption to Tygon tubing used in some early column experiments was very strong. The partitioning coefficient was $K_d = 16 \pm 2.0$ L/kg. As a result of this observation, Tygon was eliminated from our experimental setup and any prior experiments that used Tygon were repeated with Teflon parts.

3.2. Column experiments

Experimental RDX breakthrough curves for a representative run of each core section along with simulated breakthrough curves obtained using the calibrated one-dimensional transport model are shown in Fig. 2. The test solution for the experiments shown contained 1500 μg/L RDX, and bromide concentration ranged from 21 to 24 mg/L. In general, RDX was not strongly retained in any of the column systems. The recovery for SHB3 Otowi bulk tuff, SHB3 Puye bulk sediments, and R25b Puye bulk sediments were 96%, 100%, and 91%, respectively. For SHB3 Otowi bulk tuff (Fig. 2A), the RDX breakthrough curve is steep with no prevailing tail, and breakthrough is very close to that of the bromide tracer. The breakthrough of RDX is only slightly delayed relative to that of the bromide tracer. For SHB3 Puye bulk sediments (Fig. 2B), the breakthrough of RDX is noticeably delayed relative to that of the bromide tracer. The breakthrough curve has a shallow slope as it approaches $C/C_0 = 1$ and exhibits an elongated tail, indicating some affinity of RDX to the sediments. For the R25b Puye bulk sediments (Fig. 2C), the RDX breakthrough curve is slightly delayed compared to that of bromide. The delay in RDX breakthrough in this case is slightly greater than in the SHB3 Otowi bulk tuff but less than in the SHB3 Puye bulk sediments. The breakthrough curve has a steep slope to $C/C_0 = 1$ and exhibits a steep drop at the tail.

An additional test was conducted using the SHB3 Otowi bulk tuff column and the test solution containing RDX along with its degradation products and bromide. The test solution contained 370 μg/L RDX, 390 μg/L MNX, 370 μg/L DNX, 380 μg/L TNX, and 23 mg/L bromide. Besides the composition of the test solution, the experimental conditions were identical to the run with the RDX and bromide test solution. Fig. 3 shows the experimental breakthrough curves for MNX (Fig. 3A), DNX (Fig. 3B), and TNX (Fig. 3C). Simulated breakthrough curves for the degradation products and bromide obtained using the calibrated one-dimensional transport model are also shown in the figure. The experimental data (symbols) show almost identical results for all of the degradation products. They are also almost identical to the breakthrough curve of RDX through SHB3 Otowi bulk tuff (Fig. 2A), which indicates very little retardation. The recovery of the degradation products of MNX, DNX, and TNX was 94%, 97%, and 97% respectively. There was no indication of breakdown or retardation of the degradation products under our experimental conditions.

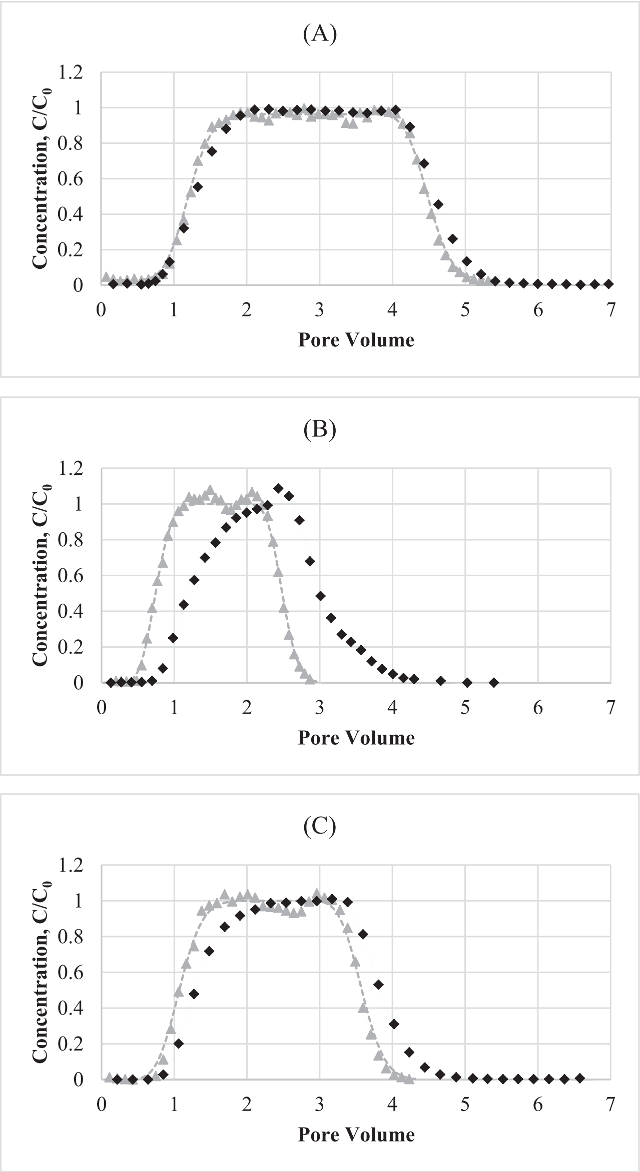

Fig. 2. RDX breakthrough curves for columns containing: (A) SHB3 Otowi bulk tuff, (B) SHB3 Puye bulk sediments, and (C) R25b Puye bulk sediments. Results for the bromide tracer are shown in gray and results for RDX are shown in black. Experimental data for bromide and RDX are shown using triangles and diamonds, respectively. Dashed lines represent the simulated curves.

During all runs with RDX, there was no apparent loss of RDX during the transport experiments. The concentrations of the known degradation products MNX, DNX, and TNX in the column effluent determined using HPLC were found to be the same as the concentrations found in the injected test solution. There was also no measurable loss of any of the degradation products run through the column containing SHB3 Otowi bulk tuff.

3.3. Modeling column breakthrough results

The bromide and RDX breakthrough curves for the column experiments were fitted using the model described in Section 2.6. The

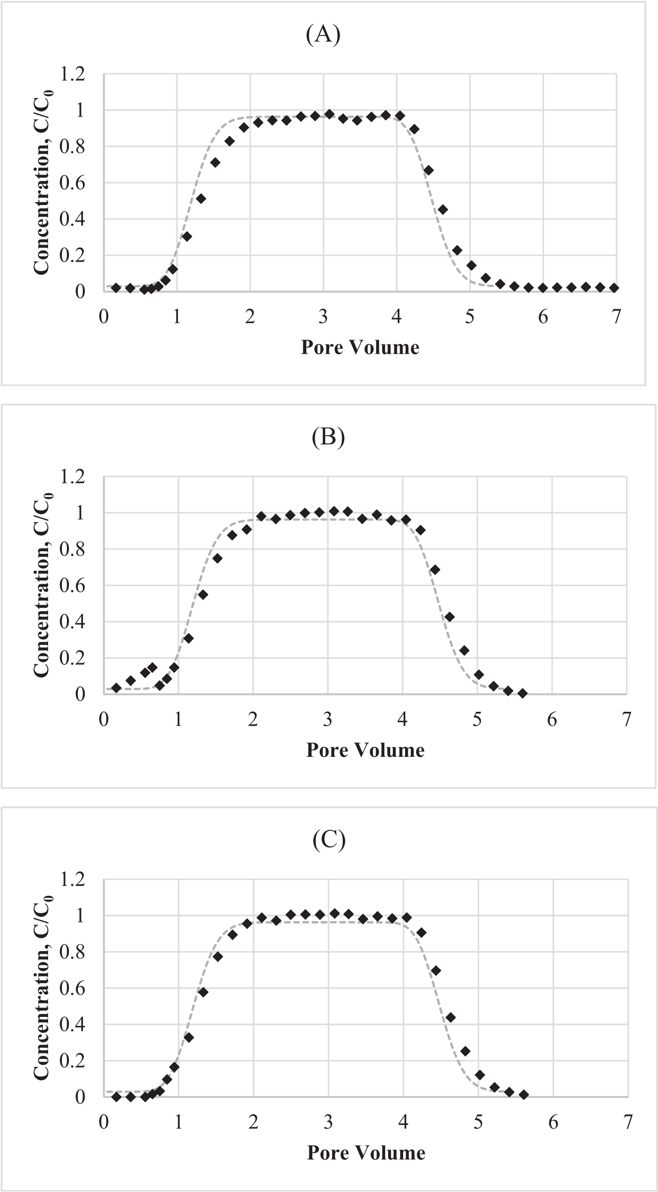

Fig. 3. Breakthrough curves for RDX degradation products in the column containing SHB3 Otowi bulk tuff. Results are shown for (A) MNX, (B) DNX, and (C) TNX. Results for the bromide tracer are shown in gray and results for degradation products are shown in black. Experimental data are shown for degradation products (diamonds) along with the simulated curves (dashed lines).

Table 1
Partitioning coefficients (K_d) values for mineral separates and bulk samples of the tuff and sediments used in this study.

Sample	K_d (L/kg)
SHB3 Otowi pumice	0.10 ± 0.080
SHB3 Otowi fines (volcanic glass)	0.34 ± 0.20
SHB3 Otowi dacite lava fragments	0.15 ± 0.010
SHB3 Otowi bulk tuff	0.00 ± 0.050
SHB3 Puye fines (sediment)	0.70 ± 0.14
SHB3 Puye dacite lava fragments	0.10 ± 0.060
SHB3 Puye bulk sediments	0.030 ± 0.010
R25b grey dacite lava fragments	0.010 ± 0.040
R25b red dacite lava fragments	0.20 ± 0.040
R25b black dacite lava fragments	0.14 ± 0.20
R25b Puye bulk sediments	0.00 ± 0.050

calibrated values of θ, K_d, and D for the RDX run for each column are shown in Table 2. The values of ρ_b, L_{col}, q, and t_{inj}, which were either measured or calculated, are also shown in the table. The calibrated values for K_d and D parameters were also determined for the degradation products using the second experiment in the column SHB3 Otowi bulk tuff and are shown in Table 3. Model fit was evaluated using R^2, which is the square of the Pearson product-moment correlation coefficient calculated using observed and simulated concentrations and are presented in Tables 2 and 3. R^2 was greater than 0.99 for all cases. In the simulated columns, θ varied (0.38–0.47), which is probably due to intrinsic sediment properties and the degree of packing. D for RDX varied slightly (5.8×10^{-5} to 8.3×10^{-5} m^2/hr) for similar reasons. D also varied slightly for degradation products (5.8×10^{-5} to 6.8×10^{-5} m^2/hr). The K_d value for RDX was the most variable parameter and was highest in SHB3 Puye bulk sediments (0.18 L/kg), moderate in R25b Puye bulk sediments (0.060 L/kg), and lowest in SHB3 Otowi bulk tuff (0.047 L/kg). The K_d values for MNX, DNX, and TNX in the SHB3 Otowi Bulk tuff were comparable to RDX and were found to be 0.055, 0.045, and 0.043 L/kg, respectively.

4. Discussion

This study focuses on the effects of the physicochemical interactions of RDX with the minerals of the different formations beneath TA-16 on RDX transport and potential degradation at Los Alamos National Laboratory. The batch experiments revealed very little to no sorption of RDX to the sediments used to pack the columns. The K_d values from the batch experiments are consistent with the column test data and corresponding one-dimensional transport model results. Of the geologic media previously studied in the context of RDX transport, these samples probably most closely resemble the shallow volcanic soils studied by Alavi et al. (2011), who also found that RDX transported nearly conservatively. Furthermore, these results agree with literature data suggesting that clays and organic matter are the two components that influence RDX transport the most (Haderlein et al., 1996; Eriksson et al., 2004; Charles et al., 2006; Dontsova et al., 2006, 2009; Singh et al., 2008, 2010; Alavi et al., 2011; Sharma et al., 2013).

In general, samples from TA-16 used in these experiments had no measurable organic matter and very little clay content. Limitation of these two adsorption pathways likely resulted in the minimal retardation observed in experiments using bulk samples of the Bandelier Tuff (SHB3 Otowi bulk tuff) and sediments of the Puye Formation that hosts the regional aquifer (R25b Puye bulk sediments). The partitioning coefficients obtained in batch experiments with bulk samples of these sediments are zero for these two materials (Table 1). There was some adsorption observed in batch experiments using their mineral separates, which could have been caused by an increased availability of clay surfaces or increased surface area. However, surface area normalized sorption was not calculated, making this is difficult to confirm. The strongest retardation occurred in the sample of the Puye Formation collected from directly beneath the Bandelier Tuff (SHB3 Puye bulk sediments, Fig. 2B and Table 1). The finest fraction of SHB3 Puye sediments was dominated by clays and had the largest partitioning coefficient measured in our experiments ($K_d = 0.70$ L/kg). Thus, the retardation of RDX observed in the column containing SHB3 Puye bulk sediments was likely a result of the clay-rich fines present in the sediments. This observation and the value of K_d calibrated using the RDX column experiment with SHB3 Puye bulk sediments are in agreement with results from both the mineral separates and bulk samples of SHB3 Puye studied in the batch experiments.

Table 2
Calibrated and calculated transport parameters of RDX for the one-dimensional transport model, which was used to simulate RDX breakthrough curves observed in the column experiments.

Parameter	Method	SHB3 Otowi bulk tuff	SHB3 Puye bulk sediments	R25b Puye bulk sediments
θ	Calibrated	0.47	0.39	0.38
D, m^2/hr	Calibrated	5.8×10^{-5}	8.3×10^{-5}	6.5×10^{-5}
K_d, L/kg	Calibrated	0.047	0.18	0.059
R^2	Calculated	0.99	0.99	0.99
ρ_b, kg/m^3	Calculated	1230	1710	1790
q, m/hr	Calculated	3.9×10^{-3}	3.7×10^{-3}	3.9×10^{-3}
L_{col}, cm	Measured	20.0	19.5	20.3
t_{inj}, hr	Measured	68	48	47

Table 3
Calibrated transport parameters for the one-dimensional transport model used to simulate RDX degradation product (MNX, DNX, and TNX) breakthrough curves observed in the column containing SHB3 Otowi bulk tuff. The values of θ, ρ_b, q, L_{col}, and t_{inj} used in these simulations are identical to those used to calibrate RDX transport parameters for SHB3 Otowi bulk tuff (Table 2).

Parameter	Method	MNX	DNX	TNX
D, m^2/hr	Calibrated	6.8×10^{-5}	6.1×10^{-5}	5.8×10^{-5}
K_d, L/kg	Calibrated	0.055	0.045	0.043
R^2	Calculated	0.99	0.99	0.99

The results from this study suggest that RDX will migrate almost conservatively through the shallow formations at TA-16 dominated by the Bandelier Tuff and that some retardation might be observed in the deep intermediate perched zone within the clay-bearing Puye Formation sediments. RDX is expected to experience minimal retardation within the regional aquifer, where the host rock consists of dark gray Puye Formation gravels dominated by dacite lava fragments that are partially coated with fine-grained tuffaceous sediments and possess minor clay contents as coatings. The transport of the degradation products was only examined for the column containing SHB3 Otowi bulk tuff. However, the results of this test indicates that transport of MNX, DNX, and TNX is very similar to RDX. Therefore, it is expected that these degradation products will also transport conservatively throughout the majority of these rock types, although some additional retardation will occur in areas of the Puye Formation with higher clay content.

Calibration of the one-dimensional transport model with linear equilibrium sorption using data from the column experiments not only helped quantify the transport parameters for RDX, MNX, DNX, and TNX in the geologic samples from TA-16 but also helped to identify the most parsimonious sorption model. In general, the linear equilibrium sorption model was successful in capturing the small degree of RDX sorption that did occur in the column experiments. Despite the subtle differences in adsorption capacities, model calibration also resulted in a nearly 1 order of magnitude difference in K_d between the calibrated value for SHB3 Puye bulk sediments and values calibrated for the other bulk samples. A more complex, non-equilibrium two-site model (Selim et al., 1976; van Genuchten and Wagenet, 1989) was used by Dontsova et al. (2006) to capture the behavior of RDX and TNT adsorption in shallow soils. This type of model was also tested in the current study but was not found to improve the overall model fit when compared to the simple equilibrium model with linear sorption. In addition, the more complex model introduced non-uniqueness of parameterization due to the higher number of parameters. This indicates that the sorption model presented by Dontsova et al. (2006) for RDX was either over-parametrized or required a higher level of complexity due to nonlinear sorption mechanisms (e.g. interactions with organic matter).

Instability of RDX, MNX, DNX, and TNX was considered as a factor that could influence transport, but our data show no significant evidence that breakdown of RDX occurred over the duration of these experiments. HPLC data were used to check if RDX degradation products are being produced *in situ* but there was no evidence that such degradation occurred. In the column experiments in which only RDX was injected (SHB3 Puye bulk and R25b Puye bulk sediments), no accumulation of any of the degradation products was observed (data not shown), and the total recovery of RDX was always close to 100%. If substantial RDX degradation occurred during transport, the cumulative percent recovery of RDX at the outflow would be much smaller than 100%. Furthermore, the occurrence of RDX degradation could potentially result in calculated percent recoveries of MNX, DNX, and TNX that exceed 100% in experiments where RDX and its degradation products were injected, which also did not occur. To further test whether or not RDX degradation was occurring, we calculated the ratio of degradation products to RDX for the experiment where RDX, MNX, DNX, and TNX were injected (SHB3 Otowi bulk tuff). The results of this calculation are shown in Figure S2 in supporting information. If RDX degradation was occurring during transport, the ratios of the degradation products to RDX would likely increase over time. In Figure S2, large spikes in DNX:RDX prior to 1 pore volume are apparent in the figure and are attributed to analytical measurement error. However, an increase in MNX:RDX after 5 pore volumes does occur. This may indicate some abiotic degradation of RDX and may suggest some natural abiotic attenuation of RDX within the contaminated plume. The residence time of the fluids injected through the column was ~25 h, and the duration of the batch experiments was ~1 week. These time scales are small relative to the residence time of RDX in the environment (i.e. years), so slow kinetics could not be captured in this study. Degradation by microbial activity under anaerobic conditions cannot be completely dismissed, especially if sterilization did not eliminate all the microbes initially present in the soil. However, we have no evidence to support or eliminate this possibility. Additional experiments with longer incubation times are needed to confirm abiotic degradation under our site-specific conditions. Experiments in which the solutions are not degassed are also required to determine if the oxidation-reduction potential influences abiotic attenuation. Finally, experiments that better characterize the influence of microbial activity are also required, since biodegradation of RDX is expected under certain conditions (Wang et al., 2017). However, microbial interactions with RDX was not the focus of this study.

5. Conclusions

The results of the batch and column experiments completed in this study show low partitioning coefficients for RDX sorption to tuff and sediment core materials obtained from the RDX plume with K_d values ranging from 0.0 to 0.70 L/kg and retardation factors varying from 1.0 to 1.8. Our results also indicate that there are no major differences between the transport of RDX and its degradation products MNX, DNX, and TNX. This suggests that the volcanic and sedimentary samples that represent the contaminated groundwater system at LANL's TA-16 have little to no capacity to delay the transport of RDX and its degradation products MNX, DNX, and TNX. Within the range of the residence times examined in our experiments (i.e. days to a week), no substantial abiotic degradation of RDX was observed in any of the core samples studied. Active remediation efforts will likely be necessary to limit RDX migration if a sizeable amount of RDX is deemed to be threatening the regional aquifer.

Acknowledgements

The authors would like to thank the Departments of Energy's Office of Environmental Management for providing funding for this project. The Environmental Programs (ADEP) department at LANL provided technical support of the experimental work. The Field Services Group (ER-FS) at LANL provided support in the gathering of monitoring data from TA-16 and facilitated access to the field sites and sampling. Michael Rearick provided support for the analysis of samples and maintenance of analytical equipment throughout the course of the experiments. Hernan Lebensohn assisted in the preparation and analysis of samples.

Appendix A. Supplementary data

Supplementary data related to this article can be found at http://dx.doi.org/10.1016/j.chemosphere.2017.04.149.

References

Alavi, G., Chung, M., Lichwa, J., D'alessio, M., Ray, C., 2011. The fate and transport of RDX, HMX, TNT and DNT in the volcanic soils of Hawaii: a laboratory and modeling study. J. Hazard. Mater. 185, 1600–1604.

Becker, N.M., Purtymun, W.D., Van Etten, D.M., 1987. Subsurface Investigations for Migration of Hazardous and Toxic Wastes in the Texas Panhandle. Los Alamos National Laboratory unpublished report.

Charles, S.M., Teppen, B.J., Li, H., Laird, D.A., Boyd, S.A., 2006. Exchangeable cationhydration properties strongly influence soil sorption of nitroaromatic compounds. Soil. Sci. Soc. Am. J. J. 70, 1470–1479.

Comfort, S.D., Shea, P.J., Horst, G., 1995. Temporal Aspects of Munitions Sorption and Transport in Contaminated Soils. U. S. Army Corps of Engineers, Cold Regions Research and Engineering Laboratory, Hanover, NH, United States. CRREL Contract Report. Report: CON 20.

Dittrich, Timothy M., Reimus, Paul William, 2015. Uranium transport in a crushed granodiorite: experiments and reactive transport modeling. J. Contam. Hydrol. 175, 44–59.

Dontsova, K., Yost, S., Simunek, J., Pennington, J., Williford, C., 2006. Dissolution and transport of TNT, RDX, and composition B in saturated soil columns. J. Environ. Qual. 35, 2043–2054.

Dontsova, K.M., Hayes, C., Pennington, J.C., Porter, B., 2009. Sorption of high explosives to water-dispersible clay: influence of organic carbon, aluminosilicate clay, and extractable iron. J. Environ. Qual. 38, 1458–1465.

DuBois, F.W., Baytos, J.F., 1991. Weathering of Explosives for Twenty Years. Los Alamos National Laboratory report LA-11931, Los Alamos, New Mexico.

EPA (Environmental Protection Agency), 2013. Regional Screening Level Summary Table. www.epa.gov/reg3hwmd/risk/human/rb-concentration_table/Generic_Tables/index.htm.

EPA (Environmental Protection Agency), 2014. Technical Fact Sheet – Hexahydro-1,3,5-trinitro- 1,3,5-triazine (RDX).

Eriksson, J., Skyllberg, U., 2001. Binding of 2,4,6-trinitrotoluene and its degradation products in a soil organic matter two-phase system. J. Environ. Qual. 30, 2053–2061.

Eriksson, J., Frankki, S., Shchukarev, A., Skyllberg, U., 2004. Binding of 2, 4, 6-trinitrotoluene, aniline, and nitrobenzene to dissolved and particulate soil organic matter. Environ. Sci. Technol. 38 (11), 3074–3080.

Fuller, M.E., Schaefer, C.E., Andaya, C., Fallis, S., 2014. Transport and dissolution of microscale Composition B detonation residues in porous media. CHEMOSPHERE 107, 400–406.

Gard, M.O., Newman, B.D., 2005. The High Explosives Source Term at TA-16. Los Alamos National Laboratory document LA-UR-05-9433, Los Alamos, New Mexico.

Haderlein, S.B., Weissmahr, K.W., Schwarzenbath, R.P., 1996. Specific adsorption of nitroaromatic explosives and pesticides to clay minerals. Environ. Sci. Technol. 30, 612–622.

LANL (Los Alamos National Laboratory), 2006. Surface Water Data at Los Alamos National Laboratory, 2005 Water Year. Los Alamos National Laboratory document LA-14239-PR, Los Alamos, New Mexico.

LANL (Los Alamos National Laboratory), 2011. Investigation Report for Water Canyon/Cañon de Valle. Los Alamos National Laboratory document LA-UR-11-5478, Los Alamos, New Mexico.

Layton, D., Mallon, B., Mitchell, W., Hall, L., Fish, R., Perry, L., Snyder, G., Bogen, K., Malloch, W., Ham, C., Dowd, P., 1987. Conventional Weapons Demilitarization: a Health and Environmental Effects Data-base Assessment Explosives and Their Co-contaminants Final Report, Phase II. Lawrence Livermore National Laboratory report UCRL-21 109, Livermore, California.

Liu, Y.Y., Yao, M., Fang, J.L., Wang, Y.W., 1995. Monitoring human risk and exposure to trinitrotoluene (TNT) using haemoglobin adducts as biomarkers. Toxicol. Lett. 77, 281–287.

Monteil-Rivera, F., Groom, C., Hawari, J., 2003. Sorption and degradation of octahydro-1,3,5,7-tetranitro-1,3,5,7-tetrazocine in soil. Environ. Sci. Technol. 37, 3878–3884.

Pan, Xiaoping, Zhang, Baohong, Cox, Stephen B., Anderson, Todd A., Cobb, George P., 2006. Determination of N-nitroso derivatives of hexahydro-1, 3, 5-trinitro-1, 3, 5-triazine (RDX) in soils by pressurized liquid extraction and liquid chromatography–electrospray ionization mass spectrometry. J. Chromatogr. A 1107, 2–8.

Pennington, Judith C., Brannon, James M., 2002. Environmental fate of explosives. Thermochim. Acta. 384, 163–172.

Purtymun, W.D., Becker, N.M., Maes, M., 1982. Supplementary Documentation for an Environmental Impact Statement Regarding the Pantex Plant Geohydrologic Investigations. Los Alamos National Laboratory report LA-9445-PNTX-H, Los Alamos, New Mexico.

Reid, Kevin D., Reneau, Steven L., Newman, Brent D., Hickmott, Donald D., 2005. Barium and high explosives in a semiarid alluvial system, Cañon de Valle, New Mexico. Vadose Zone. J. 4, 744–759.

Selim, H.M., Iskandar, I.K., 1994. Sorption-desorption and transport of TNT and RDX in soils. U. S. Army Corps of Engineers, Cold Regions Research and Engineering Laboratory, Hanover, NH, United States. CRREL Contract Report. Report: 94–7.

Selim, H.M., Davidson, J.M., Mansell, R.S., 1976. Evaluation of a two-site adsorption-desorption model for describing solute transport in soils. In: Proc. Summer Computer Simulation Conf., Washington, D.C.

Sharma, P., Mayes, M.A., Tang, G., 2013. Role of soil organic carbon and colloids in sorption and transport of TNT, RDX and HMX in training range soils. Chemosphere 92, 993–1000.

Sheremata, T.W., Halasz, A., Paquet, L., Thiboutot, S., Ampleman, G., Hawari, J., 2001. The fate of the cyclic nitramine explosive RDX in natural soil. Environ. Sci. Technol. 35, 1037–1040.

Singh, N., Hennecke, D., Hoerner, J., Koerdel, W., Schaeffer, A., 2008. Mobility and degradation of trinitrotoluene/metabolites in soil columns: effect of soil organic carbon content. J. Environ. Sci. Heal. A 43A, 682–693.

Singh, N., Berns, A.E., Hennecke, D., Hoerner, J., Koerdel, W., Schaeffer, A., 2010. Effect of soil organic matter chemistry on sorption of trinitrotoluene and 2,4-dinitrotoluene. J. Hazard. Mater. 173, 343–348.

Smock, L.A., Stoneburner, D.L., Clark, J.R., 1976. The toxic effects of trinitrotoluene (TNT) and its primary degradation products on two species of algae and the fathead minnow. Water. Res. 10, 537–543.

Spalding, Roy F., Fulton, John W., 1988. Groundwater munition residues and nitrate near Grand Island, Nebraska, USA. J. Contam. Hydrol. 2, 139–153.

Toride, N., Leij, F.J., Van Genuchten, M.T., 1995. The CXTFIT Code for Estimating Transport Parameters from Laboratory or Filed Tracer Experiments, Version 2.0. US Salinity Laboratory, Riverside, California.

Toride, N., Leij, F.J., Van Genuchten, M.T., 1999. The CXTFIT Code for Estimating Transport Parameters from Laboratory or Field Experiments, Version 2.1. US Salinity Laboratory, Riverside, California.

Van Genuchten, M. Th, Wagenet, R.J., 1989. Two-site/two-region models for pesticide transport and degradation: theoretical development and analytical solutions. Soil. Sci. Soc. Am. J. 53, 1303–1310.

Wang, Dongping, Boukhalfa, Hakim, Marina, Oana, Ware, Doug S., Goering, Tim J., Sun, Fengjie, Daligault, Hajnalk E., Lo, Chien-chi, Vuyisich, Momchilo, Starkenburg, Shawn R., 2017. Biostimulation and microbial community profiling reveal insights on RDX transformation in groundwater. Microbiol. Open 6, e00423.

Attachment 5

Heerspink, B.P., S. Pandey, H. Boukhalfa, D.S. Ware, O. Marina, G. Perkins, V.V. Vesselinov, and G. WoldeGabriel, May 2, 2017. "Fate and Transport of Hexahydro-1,3,5-trinitro-1,3,5-triazine (RDX) and Its Degradation Products in Sedimentary and Volcanic Rocks, Los Alamos, New Mexico," Chemosphere, Vol. 182, pp. 276-283.

http://dx.doi.org/10.1016/j.chemosphere.2017.04.149

Received: 3 June 2016 | Revised: 29 September 2016 | Accepted: 6 October 2016

DOI: 10.1002/mbo3.423

ORIGINAL RESEARCH

WILEY MicrobiologyOpen Open Access

Biostimulation and microbial community profiling reveal insights on RDX transformation in groundwater

Dongping Wang[1] | **Hakim Boukhalfa**[1] | **Oana Marina**[1] | **Doug S. Ware**[1] | **Tim J. Goering**[2] | **Fengjie Sun**[3] | **Hajnalka E. Daligault**[4] | **Chien-Chi Lo**[4] | **Momchilo Vuyisich**[4] | **Shawn R. Starkenburg**[4]

[1]Earth Systems Observations EES-14, Earth and Environmental Sciences Division, Los Alamos National Laboratory, Los Alamos, NM, USA

[2]Environmental Programs ADEP, Los Alamos National Laboratory, Los Alamos, NM, USA

[3]School of Science and Technology, Georgia Gwinnett College, Lawrenceville, GA, USA

[4]Bioenergy and Biome Sciences, Biology Sciences Division, Los Alamos National Laboratory, Los Alamos, NM, USA

Correspondence
Hakim Boukhalfa, Earth Systems Observations (EES-14), Earth and Environmental Sciences Division, Los Alamos National Laboratory, Los Alamos, NM, USA.
Email: hakim@lanl.gov

Funding information
Los Alamos National Laboratory.

Abstract

Hexahydro-1,3,5-trinitro-1,3,5-triazine (RDX) is a high explosive released to the environment as a result of weapons manufacturing and testing worldwide. At Los Alamos National Laboratory, the Technical Area (TA) 16 260 Outfall discharged high-explosives-bearing water from a high-explosives-machining facility to Cañon de Valle during 1951 through 1996. These discharges served as a primary source of high-explosives and inorganic-element contamination in the area. Data indicate that springs, surface water, alluvial groundwater, and perched-intermediate groundwater contain explosive compounds, including RDX (hexahydro-1,3,5-trinitro-1,3,5-triazine); HMX (octahydro-1,3,5,7-tetranitro-1,3,5,7-tetrazocine); and TNT (2,4,6-trinitrotoluene). RDX has been detected in the regional aquifer in several wells, and a corrective measures evaluation is planned to identify remedial alternatives to protect the regional aquifer. Perched-intermediate groundwater at Technical Area 16 is present at depths from 650 ft to 1200 ft bgs. In this study, we examined the microbial diversity in a monitoring well completed in perched-intermediate groundwater contaminated by RDX, and examined the response of the microbial population to biostimulation under varying geochemical conditions. Results show that the groundwater microbiome was dominated by *Actinobacteria* and *Proteobacteria*. A total of 1,605 operational taxonomic units (OTUs) in 96 bacterial genera were identified. *Rhodococcus* was the most abundant genus (30.6%) and a total of 46 OTUs were annotated as *Rhodococcus*. One OTU comprising 25.2% of total sequences was closely related to a RDX -degrading strain *R. erythropolis* HS4. A less abundant OTU from the *Pseudomonas* family closely related to RDX-degrading strain *P. putida* II-B was also present. Biostimulation significantly enriched *Proteobacteria* but decreased/eliminated the population of *Actinobacteria*. Consistent with RDX degradation, the OTU closely related to the RDX-degrading *P. putida* strain II-B was specifically enriched in the RDX-degrading samples. Analysis of the accumulation of RDX-degradation products reveals that during active RDX degradation, there is a transient increase in the concentration of the degradation products MNX, DNX, TNX, and NDAB. The accumulation of these degradation products suggests that RDX is degraded via sequential reduction of the nitro functional

---

groups followed by abiotic ring-cleavage. The results suggest that strict anaerobic conditions are needed to stimulate RDX degradation under the TA-16 site-specific conditions.

KEYWORDS

biodegradation, bioremediation, microbial structure, pseudomonas, water

1 | INTRODUCTION

Hexahydro-1,3,5-trinitro-1,3,5-triazine (RDX) was widely used in explosives formulations at Los Alamos National Laboratory (LANL), Los Alamos, New Mexico. Inadequate waste water management resulted in the release of an estimated 1464 kg to 2644 kg of RDX to the TA-16-260 outfall in Cañon de Valle in Los Alamos (LANL (Los Alamos National Laboratory), August 2006. "Investigation Report for Intermediate and Regional Groundwater, Consolidated Unit 16-021(c)-99). Other high explosives (HE), such as octahydro-1,3,5,7-tetranitro-1,3,5,7-tetrazocine (HMX), 1,3,5-triamino-2,4,6-trinitrobenzene (TATB), and 2-methyl-1,3,5-trinitrobenzene (TNT), were also released and are detected along with their degradation products in sediments and groundwater near the processing site at TA-16 in Los Alamos (Los Alamos, 2011; Figure 1). Most surface contaminations were remediated through cleanup operations performed in the last 10–15 years (LANL, 2010, 108868). In general, alluvial monitoring wells down-gradient of the outfall show long-term decreases in RDX, with concentrations currently near or below the screening level of 7.02 μg/L. The RDX concentration in the deep perched-intermediate zone underlying the upper Cañon de Valle at TA-16 varies between 20 and about 200 μg/L (LANL, 2015). RDX is also detected at low levels in several monitoring wells completed within the regional aquifer (LANL, 2011). RDX degradation products hexahydro-1-nitroso-3,5-dinitro-1,3,5-triazine (MNX), hexahydro-1,3-dinitroso-5-nitro-1,3,5-triazine (DNX), hexahydro-1,3,5-trinitroso-1,3,5-triazine (TNX), 4-nitro-2,4-diazabutanal (NDAB), and methylenedinitramine (MEDINA) are detected in groundwater, which indicates that RDX is undergoing degradation under the natural conditions of the site. The presence of these degradation products has been attributed to the activity of microorganisms capable of degrading RDX. However, the identity of the microorganisms responsible for RDX degradation in the environment remains unknown (Fuller, McClay, Higham, Hatzinger, & Steffan, 2010; Fuller, Perreault, & Hawari, 2010). Studies undertaken in the past using stable isotope labeling and high-throughput sequencing generally point to the importance of *Pseudomonas* and *Rhodococcus* in RDX degradation (Cho et al., 2013; Andeer et al., 2013). A number of studies have also associated RDX degradation to other genera such as *Comamonas*, *Clostridium*, *Enterobacter*, *Morganella*, *Acetobacterium*, *Geobacter*, *Citrobacter*, *Klebsiella*, *Rhizobium*, *Burkholderia*, *Shewanella*, and *Providencio* (Jayamani and Cupples, 2015b; Bhushan et al., 2002; Watrous et al., 2003; Adrian & Arnett, 2004; Bhushan, Halasz, Thiboutot, Ampleman, & Hawari, 2004; Cho, Lee, & Oh, 2008; Coleman, Spain, & Duxbury, 2002; Khan, Lee, & Park, 2012; Kitts, Cunningham, & Unkefer, 1994; Zhao, Halasz, Paquet, Beaulieu, & Hawari, 2002). These studies illustrate the difficulty in attributing the RDX degradation activity to a specific type of microorganism. The use of functional gene data along with microbial diversity data is starting to improve our understanding of which genes are involved in RDX degradation and help identify the specific microbes that are driving RDX degradation (Wilson & Cupples, 2016). Among the functional genes linked to RDX degradation *diaA*, *xenA*, *xenB*, *xplA*, and *xplB*, have received the most attention (Fuller, McClay, Hawari, Paquet, & Malone, 2009; Li et al., 2014; Wilson & Cupples, 2016).

The degradation of RDX through anaerobic biodegradation has been extensively investigated (Scheme 1) (Beller, 2002; Bernstein & Ronen, 2012; Fournier, Halasz, Spain, Fiurasek, & Hawari, 2002; Hawari et al., 2000; Jackson, Raylot, Fournier, Hawari, & Bruce, 2007). The main degradation pathways described involve either a sequential biotic reduction of the nitro functional groups followed by abiotic ring-cleavage (Hawari et al., 2002) or a direct denitration followed by hydration and subsequent ring-cleavage (Jackson et al., 2007). The intermediates that accumulate in solution as a result of the sequential biotic reduction pathway include MNX, DNX, TNX, NDAB, and MEDINA. In contrast, when the breakdown pathway involves denitration and ring-cleavage, the breakdown products include MEDINA, NDAB, nitrate, and formaldehyde. Stepwise denitration of RDX involves a nitrate reductase which is a ubiquitous enzyme possessed by a diverse group of bacteria, especially denitrifying bacteria (Bhushan et al., 2002). Degradation of RDX through denitration and ring-cleavage involves the microbial P450 system which was shown to be able to degrade RDX under both aerobic and anaerobic conditions (Jackson et al., 2007). The cytochrome P450 system (XplA and XplB) was originally cloned from *Rhodococcus rhodochrous* (Rylott, Jackson, Sabbadin, Seth-Smith, & Edwards, 2011; Rylott, Budarina, et al., 2011; Seth-Smith, Rosser, Basran, Travis, & Dabbs, 2002). Expression of *xplA* and *xplB* is highly induced in the presence of RDX (Indest, Hancock, Jung, Eberly, & Mohn, 2013; Indest, Jung, Chen, Hancock, & Florizone, 2010). Recent studies have shown that production of *xplA* in Arabidopsis plants confers both the ability to remove RDX from liquid culture and resistance to the toxic effects of RDX (Rylott et al., 2006; Rylott, Jackson, et al, 2011; Rylott, Budarina, et al., 2011). *xplA* and *xplB* exist in various genera including *Rhodococcus*, *Gordonia*, and *Williamsia* are commonly found in soil and groundwater (Halasz, Manno, Perreault, Sabbadin, & Bruce, 2012). The global distribution of RDX-degrading bacteria containing *xplA* and *xplB* gene homologs suggests that denitration may represent a key RDX degradation pathway in nature (Andeer, Stahl, Bruce, & Strand, 2009). Besides P450 enzymes, two flavin mononucleotide-containing oxidoreductase genes *xenA* and *xenB*, have been cloned from *Pseudomonas* (Blehert, Fox, & Chambliss, 1999). Monoculture of the *Pseudomonas* strains harboring these two enzymes demonstrated

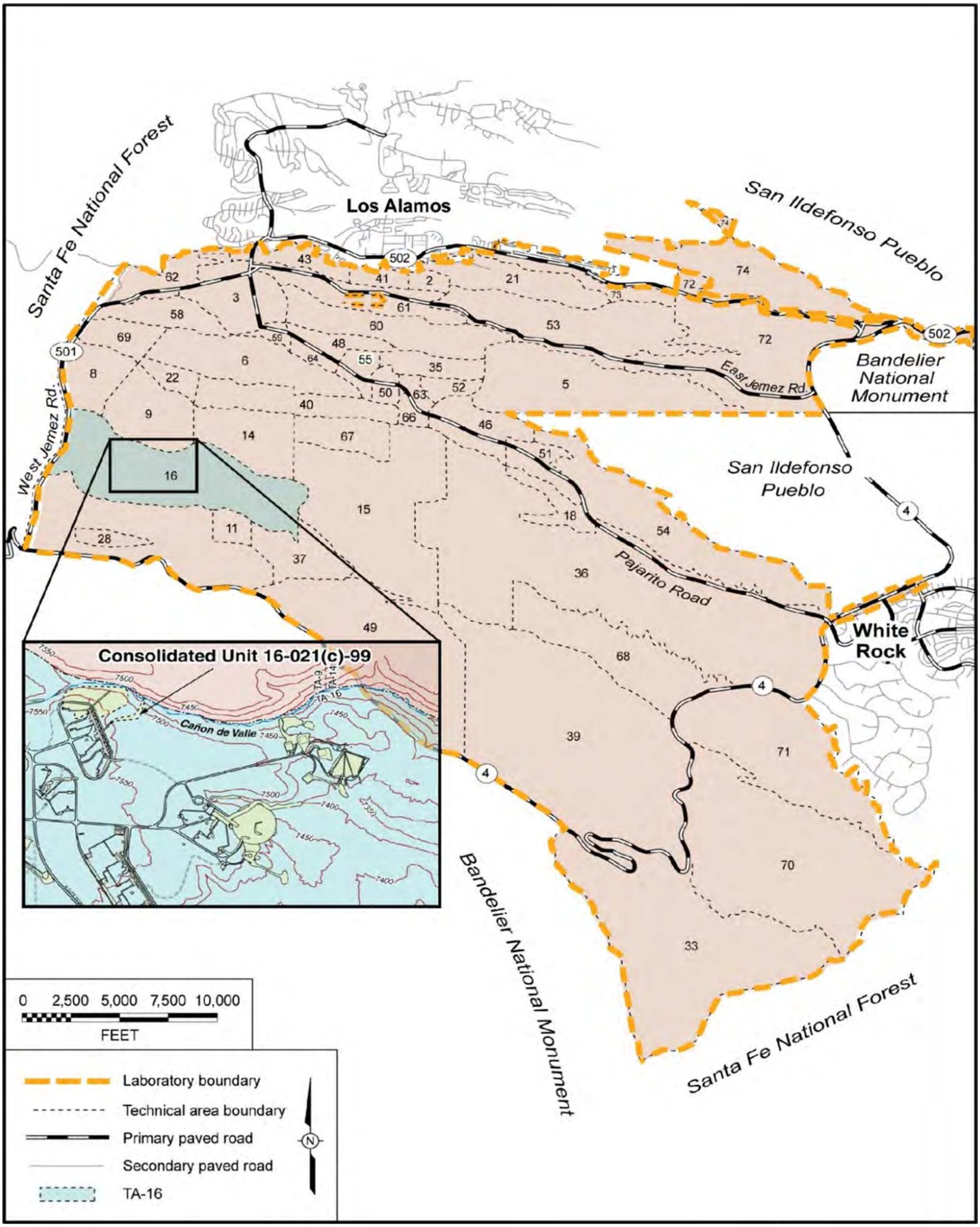

FIGURE 1 Location of TA-16 and other Laboratory technical areas at Los Alamos National Laboratory

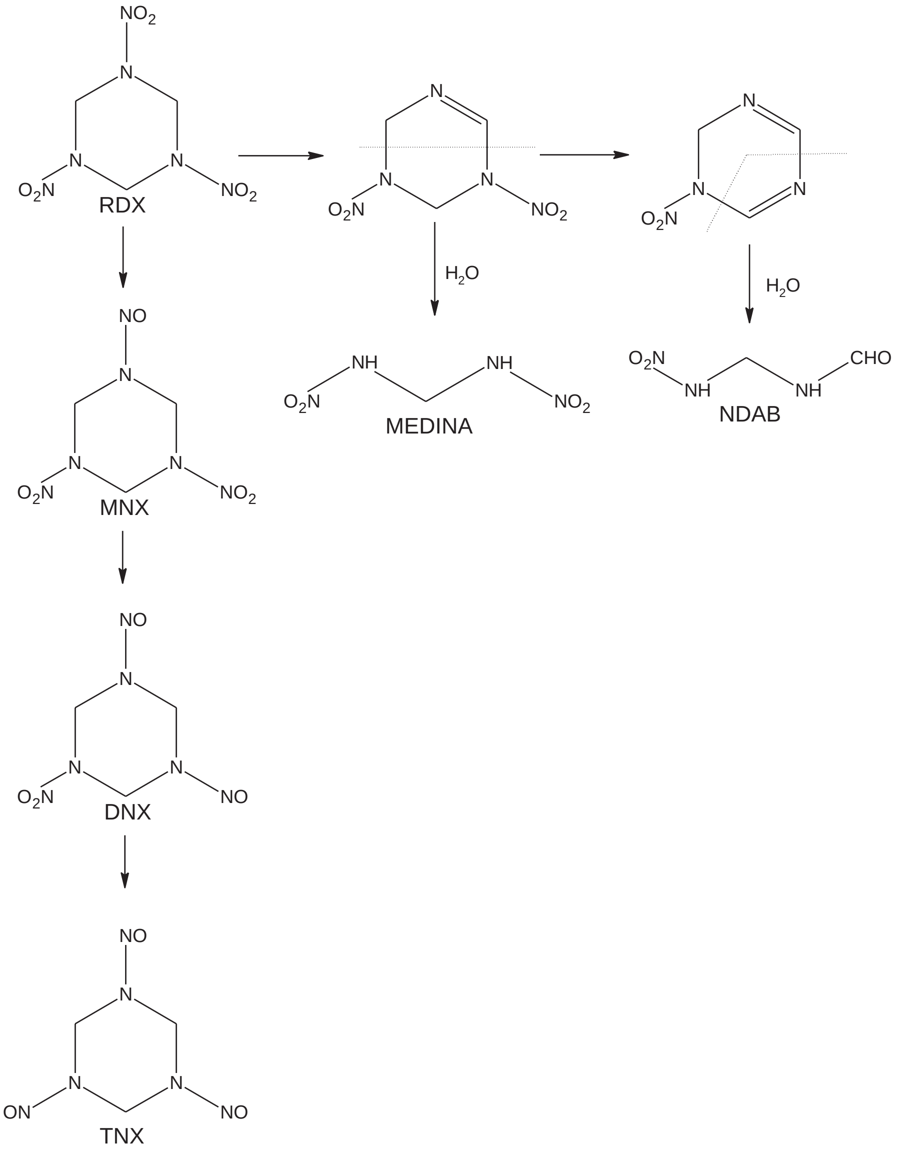

SCHEME 1 Degradation routes of RDX. Production of different transformation products depends on both biotic and abiotic factors

that both XenA and XenB were able to degrade RDX (Fuller et al., 2009). Interestingly, XenB exhibited a broader substrate specificity than XenA. The activities of both enzymes are significantly high when degrading RDX for anaerobic conditions compared with aerobic conditions.

Biostimulation has been examined as a remediation approach to treat HE contamination including RDX. Various nutrients including acetate and edible vegetable oil are known to promote bacterial growth and RDX degradation (Livermore, Oh, LePuil, Arnseth, & Mattes, 2013; Schaefer et al., 2007). Acetate is a widely applied carbon source which enriches Fe (III)-reducing bacteria such as *Pseudomonas*. Multiple studies have shown that Fe (III)-reducing bacteria degrade RDX by direct reduction or indirectly by electron shuttling (Hawari et al., 2000). On the other hand, emulsified edible oils have been successfully used to enhance biodegradation of RDX. The procedures and applications of vegetable oils for the bioremediation of RDX are applicable to numerous other biodegradable contaminants like nitrates, chlorinated solvents, and perchlorates. Biostimulation using acetate and vegetable oil is normally carried out under anaerobic conditions, when RDX can act as an electron acceptor to support microbial respiration (Beller, 2002; Bernstein & Ronen, 2012). Degradation of RDX in the presence of oxygen has also been reported and where microorganisms utilize RDX as a carbon source or a nitrogen source (Fuller, McClay, et al, 2010; Fuller, Perreault, & Hawari, 2010).

In this study, we surveyed the microbial profile of RDX-containing groundwater to determine if microorganisms are playing any active role in RDX degradation, examined the potential existence of RDX biodegradation signatures, and evaluated the response of endogenous microbes to biostimulation. This work focused on water samples collected from a well completed in deep perched-intermediate groundwater underlying Cañon de Valle at TA-16 at Los Alamos National Laboratory. We also performed a microcosm experiment to examine how environmental factors such as the availability of oxygen, sediments, and alternate sources of carbon affect RDX degradation. The microbial profile of the microcosms with the most RDX-degrading activity was also determined. Our results provide insights on microorganisms and environmental conditions that are potentially important to RDX transformation in groundwater.

2 | MATERIALS AND METHODS

2.1 | Water samples collection and processing

The CDV-16-4ip monitoring well is completed in deep perched-intermediate groundwater at Technical Area 16 (TA-16), located in the southwest corner of Los Alamos National Laboratory. The deep perched groundwater is located in several zones of saturation at depths between approximately 650 ft and 1,200 ft below ground surface (bgs). The perched groundwater is present in a variety of geologic units, including the Cerro Toledo interval, Otowi Member, and Puye Formation. These zones are potential sources of contaminated recharge to the regional aquifer. Groundwater samples were collected from CdV-16-4ip, screened between 815 and 879 feet bgs. Water samples used for DNA extraction were collected after pumping the well for a minimum of 3 casing volumes. The samples were immediately stored on ice in the field and during transportation, and then kept at 4°C in the laboratory until further analysis.

2.2 | Analytical techniques

RDX and its degradation products were analyzed on a Dionex Summit HPLC (Thermo Scientific, USA) system using the EPA method (METHOD 8330A). The HPLC was equipped with an Acclaim Explosives E1 column 25 cm × 4.6 mm E1 (Thermo Scientific, Waltham, MA). The flow rate used was 0.80 ml/min and the mobile phase composition was 52% MeOH and 48% DI Water. Absorbance detection wavelength was set at 254 nm. RDX certified standards (Ultra Scientific, North Kingstown, RI) were used for sample quantification. Degradation products TNX, DNX, and MNX were obtained from SRI International, Menlo Park, CA and were used to establish calibration curves for quantitative analysis. Major anions (SO_4^{2-}, NO_3^-, PO_4^{3-}, HCO_3^-, F^-, and Cl^-) in the groundwater were measured using ion chromatography (Dionex, USA). Trace metals were measured with an inductively coupled plasma mass spectrometer (ICP-MS) (Varian 810 ICP-MS System, California) or by atomic absorbance spectrometer (Parkin Elmer, USA).

2.3 | Microbial profiling analysis

The groundwater samples were processed immediately after reception from the field. Processing consisted of filtering 100–500 ml of the water samples using 47 mm, 0.2-μm pore size polycarbonate filters (Thermo Scientific) to concentrate the microbial biomass. Total DNA was extracted from bacterial cells collected on each filter membrane following the method of The UltraClean® Microbial DNA Isolation kit (MO BIO). DNA extracts were used to amplify the V4 region of bacterial 16S rRNA genes using bacterial barcoded primers (515F-806R [GTGCCAGCMGCCGCGGTAA and GGACTACHVGGGTWTCTAAT, respectively]) (Hugerth et al., 2014). Amplicons (equivalent to library fragments) were purified and size selected using AMPure XP beads, quantitated by picogreen assay, normalized, pooled, and sequenced on an Illumina MiSeq instrument. The sequencing run resulted in ~100,000 paired reads per sample with an average read length of 295 bp. Paired reads were combined to produce 290 bp sequences corresponding to the V4 region and filtered to retain those with an average quality score of greater than or equal to 30. Sequence data were processed using the QIIME software package v1.9.1 (Caporaso et al., 2010). Operational taxonomic units (OTUs) were clustered at the 96% similarity level. The most abundant sequence in each cluster was chosen as a representative. Alpha diversity analysis was performed using QIIME script (alpha_rarefaction.py). To determine how bacterial community compositions varied across samples, principal coordinate analysis (PCoA) was performed by comparing unweighted UniFrac profiles for each sample in QIIME. NCBI Blast was used to assign representative sequences to genus or species levels. All sequences obtained in this study were deposited at the NCBI Sequence Read Archive (SRA) and are available under the accession number PRJNA318785 (https://submit.ncbi.nlm.nih.gov/subs/bioproject/SUB1472271/overview).

2.4 | Phylogenetic analysis

A comparative analysis of nucleotide sequences was performed by Basic Local Alignment Search Tool (BLAST) at the National Center for Biotechnology Information (NCBI; http://www.ncbi.nlm.nih.gov/Blast.cgi/) to obtain sequences of 16S rDNA from species closely related to *Pseudomonas* and *Rhodococcus* for phylogenetic analysis. 16S rDNA sequences were aligned using CLUSTAL X (Jeanmougin, Thompson, Gouy, Higgins, & Gibson, 1998) and adjusted manually, as necessary. The resulting data matrix was first analyzed using equally weighted maximum parsimony in PAUP* (Swofford, 2002). Maximum parsimonious trees were sought using the heuristic search strategies of PAUP*. A neighbor-joining analysis was also performed using the uncorrected pairwise nucleotide differences ("p") in PAUP*. The confidence level of branches was evaluated by bootstrap analysis of 10,000 replicates (Felsenstein, 1985).

2.5 | Enumeration of bacterial population

Culturable microbial populations were enumerated by dilution plate count technique (Wang, Korban, Pusey, & Zhao, 2012; Wang et al., 2015). For dilution plating, groundwater samples were serially diluted in normal sterile saline (0.9%) and 100 μl of suspension from each dilution was plated on Luria-Bertani (LB) agar plate in triplicate and incubated at room temperature for 8 days. Total microbial counts were determined by direct count using a Hemocytometer plate (Cambridge Instruments, Inc) according to manufacturer's protocol.

2.6 | Biostimulation and quantification of RDX and RDX degradation products

Biostimulation experiments were performed using 200 ml sterile vials containing 100 ml groundwater from the well CdV-16-4ip. The RDX concentration in the CdV-16-4ip water is around 160 ppb. The water was spiked with RDX solution to a final concentration of 1,800 ppb. The RDX solution appeared to contain NDAB and the initial NDAB concentration is about 200 ppb. Each vial was sealed with a pair of rubber and aluminum caps. Acetate (20 mmol/L) and safflower oil (1%, v/v) were added to the sealed vial at the start of the experiment using a syringe equipped with a needle. About 100 ml air was sealed within each vial to create microoxic treatments. For strict anoxic stimulation, vials were purged with nitrogen gas for 10 min to remove oxygen. Samples were incubated in the dark at room temperature (22°C) under constant shaking at 50 rpm. Samples were prepared in triplicates for the following four conditions: AC1: CdV-16-4ip cultivated with acetate + initial oxygen; AC2: CdV-16-4ip cultivated with acetate—oxygen; OIL1: CdV-16-4ip cultivated with safflower oil—oxygen; OIL2: CdV-16-4ip cultivated with safflower oil + initial oxygen. Controls with no amendments and sterile controls were also setup in triplicates to account for RDX degradation under unstimulated biotic and abiotic conditions. For abiotic controls, the vials were autoclaved at 121°C to kill indigenous microbes present in the groundwater. Triplicate control cultures were also prepared under aerobic conditions in conical flasks and amended with acetate and safflower oil. All vials were sampled routinely every 3 to 7 days by removing a sample through the rubber stopper using a 1.0 ml syringe. The samples were analyzed for RDX degradation and production of RDX degradation products, and acetate concentration. Samples were collected from each cultivation condition after 5 weeks (i.e., AC1, AC2, OIL1, OIL2, controls) and processed for microbial profiling.

3 | RESULTS

3.1 | Physical and chemical characteristics of groundwater

The groundwater samples collected in our studies were obtained from well CDV-16-4ip which has a screened interval between 815 and 879 ft interrogating the Puye Formation. This formation is primarily made up of poorly sorted, unconsolidated, dacitic boulders, cobbles, and gravels that are either clast-supported or matrix-supported. Sand, silty sand, and silt are common matrix materials (LANL, 2011). The groundwater is well oxygenated with oxygen concentrations varying from 7.5 to 8.0 mg/L, the ORP measurements varied between 200 and 275 mV, and the pH is neutral typically varying between 7.33 and 7.67. The concentrations of the major anions in one of the CdV-16-4ip samples were: chloride = 3.5 mg/L, fluoride = 0.1 mg/L, nitrate as nitrogen = 0.89 mg/L, sulfate = 3.5 mg/L, and Na^+ = 9.7 mg/L. The alkalinity CO_3+HCO_3 = 50 mg/L and its Ca^{2+} content is 10 mg/L, Mg^{2+} = 3.1 mg/L. The total organic carbon concentration is 0.57 mg/L and total dissolved solids = 126 mg/L. The concentration of RDX is about 160 ppb and the concentrations of the degradation products TNX, MNX, and DNX are typically less than 1 ppb. Culturable cell counts as enumerated using LB agar medium were about 3.6×10^2 CFU/ml. In contrast, total bacteria counted using hemocytometer was 8.7×10^4 cells/ml.

3.2 | Bacterial community analysis

A total of 98,405 bacterial 16S rRNA gene sequences were recovered for the CdV-16-4ip sample and used for community analyses by QIIME. OTUs were assigned by clustering sequences with over 96% sequence identity. A number of 1,605 OTUs distributed in 15 phyla were identified indicating high microbial diversity in the sample. *Actinobacteria* were dominant in the sample followed by *Proteobacteria* and *Bacteroidetes* (Figure 2a). Other members with >0.1% abundance were *Verrucomicrobia*, *Chloroflexi*, *Chlamydiae*, *Cyanobacteria*, *Armatimonadetes*, *Firmicutes*, *Planctomycetes*, *Nitrospirae*, *Acidobacteria*, TM7, TM6, and others. Identification of bacterial groups at lower taxonomic level revealed the presence of 96 genera (Figure 2b). Genera *Polaromonas*, *Frateuria*, *Blastomonas* of *Proteobacteria* and *Rhodococcus*, *Nocardia* of *Actinobacteria* represented the major populations within the communities (Figure 2b). Table S1 lists dominant OTUs (>1%) and their closest relatives found in the GenBank. The two most dominant OTUs (>20%) from CdV-16-4ip are identified as *Rhodococcus erythropolis* HS4 (NR_074622) with 100% sequence identity and is known to degrade RDX (Chong, 2011) and *Nocardia ignorata* DSM 44496 also with 100% sequence identity and is a human nocardiosis pathogen isolated from respiratory specimens in Europe (Rodriguez-Nava, Couble, & Khan, 2005). Other relative abundant OTU sequences were related to

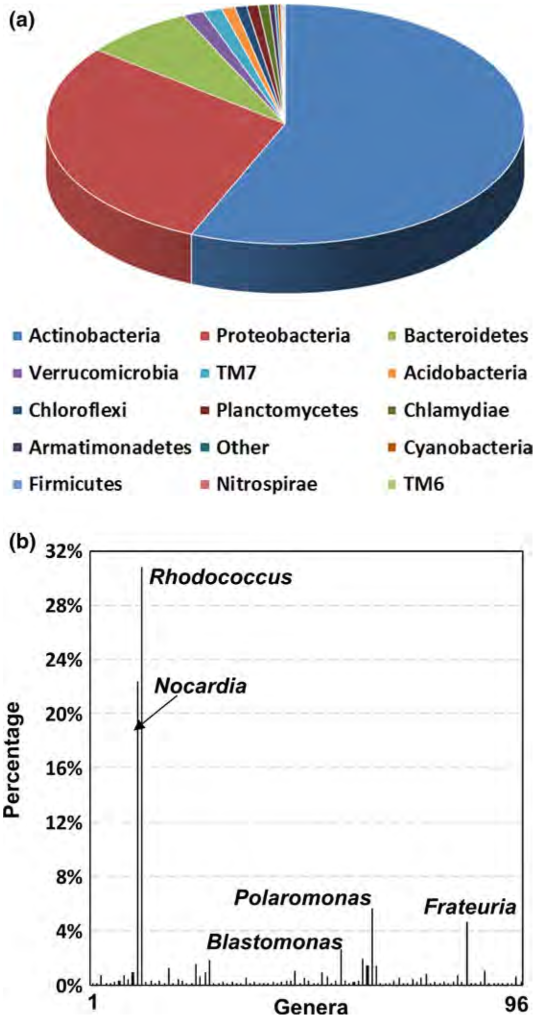

FIGURE 2 Microbial community analysis of CdV-16-4ip groundwater sample. (a) Relative abundances of major bacterial phyla. Data were analyzed using QIIME (Caporaso et al., 2010). (b) Relative abundances of bacterial genera in the groundwater sample. Dominant genera with ≥2% abundances were labeled near the column

(99% to 100% sequence identify) *Polaromonas jejuensis* NBRC 106434, *Frateuria aurantia* DSM 6220, *Rhodococcus cerastii* C5, *Sphingomonas desiccabilis* CP1D, *Flavobacterium macrobrachii* an-8, *Hydrogenophaga carboriunda* YZ2, and *Pedobacter ginsengisoli* Gsoil 104.

3.3 | *Pseudomonas and Rhodococcus*

Among known RDX-degrading genera, only *Pseudomonas* and *Rhodococcus* were detected in the CdV-16-4ip sample. Many *Rhodococcus* species are enriched by polycyclic aromatic hydrocarbon and related contaminants (Yu, Ke, Wong, & Tam, 2005). *Rhodococcus* was the most abundant genus in CdV-16-4ip (30.6%). A total of 46 OTUs were annotated as *Rhodococcus*. Phylogenetic trees of partial 16S rDNA sequences reconstructed using neighbor-joining methods revealed evolutionary positions of the 46 OTUs in relation to 27 known *Rhodococcus* species (Figure 3). Four strains in related genera *Agreia*, *Herbiconiux*, *Tessaracoccus*, and *Propionibacterium* were selected as outgroups. All of the 46 OTUs were clustered together with *Rhodococcus* strains and separated from outgroups confirming the QIIME annotation. Based on their distance to known *Rhodococcus* species, OTUs here were grouped into two categories. One comprising those distantly related to known *Rhodococcus* strains: Clade 1 (23 OTUs), Clade 2 (10 OTUs), and Clade 3 (4 OTUs); while the other constituting 36 OTUs closely related to known species. One OTU (573976 CBN. 40 73) comprising 25.2% of total sequences was closely related to a RDX-degrading strain *R. erythropolis* HS4 (Figure 3) (Chong, 2011). In contrast, *Pseudomonas* appeared to be less diverse and abundant than *Rhodococcus*. Most OTUs were closely clustered with reported strains except for two OTUs (boxed) in Clade 1 (Figure 4). An OTU (1108886 CBN. 39 944) was placed in the same clade with two RDX-degrading strains *P. putida* II-B and *P. fluorescens* I-C (Figure 4). Together, these data suggest that the CdV-16-4ip groundwater harbors a diverse group of *Rhodococcus* and *Pseudomonas* including some related to RDX-degrading strains.

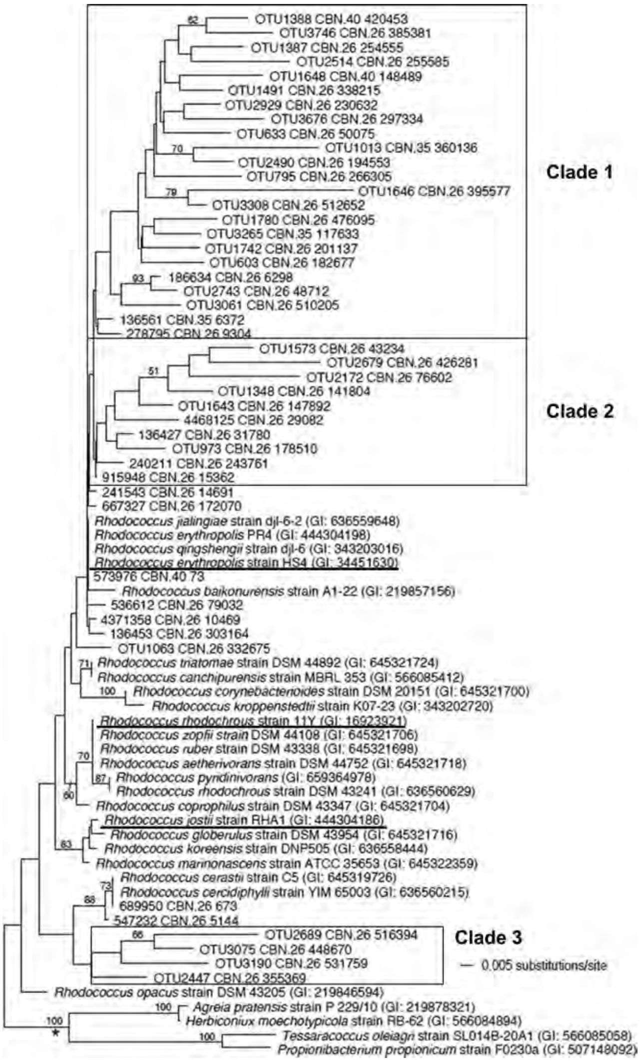

FIGURE 3 Phylogeny of *Rhodococcus* in CdV-16-4ip groundwater sample. Phylogenetic tree of 16S rRNA gene sequences showing the phylogenetic affiliation of the operational taxonomic units (OTUs) from the groundwater samples. The neighbor-joining tree was constructed from the 16S rRNA V4 hypervariable sequences of representative clones of each OTU and sequences retrieved from the GenBank database. The branch indicated by "*" contains outgroups. Numbers on branches represent bootstrap estimates from 10,000 replicate analysis; values <50% are not indicated. Strain names, if any, and GenBank accession numbers are given following the species names. Known RDX-degrading *Rhodococcus* strains were underlined

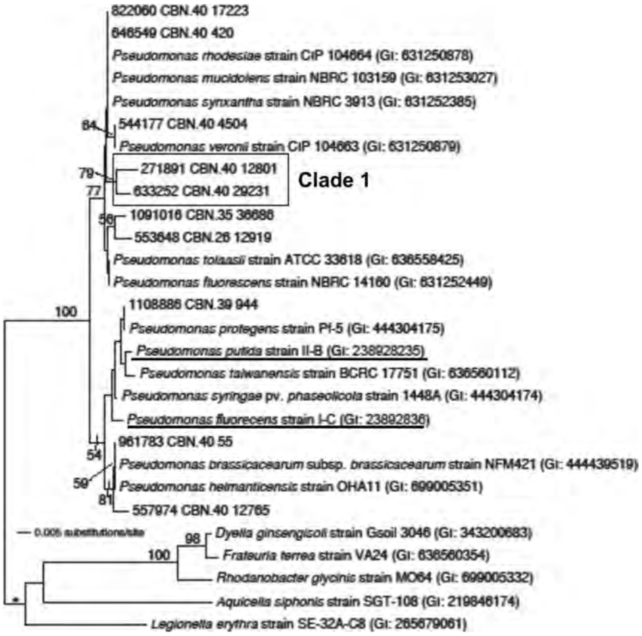

FIGURE 4 Phylogeny of *Pseudomonas* in CdV-16-4ip groundwater sample. Phylogenetic tree of 16S rRNA gene sequences showing the phylogenetic affiliation of the operational taxonomic units (OTUs) from the groundwater samples. The neighbor-joining tree was constructed from the 16S rRNA V4 hypervariable sequences of representative clones of each OTU and sequences retrieved from the GenBank database. The branch indicated by "*" contains outgroups. Numbers on branches represent bootstrap estimates from 10,000 replicate analysis; values <50% are not indicated. Strain names, if any, and GenBank accession numbers are given following the species names. Known RDX-degrading *Pseudomonas* strains were underlined

TABLE 1 Effect of acetate, safflower oil, and oxygen on microbial growth and RDX degradation. Initial groundwater bacterial population was 8.7 × 10^4 cells/ml. Final cell numbers and RDX concentrations were measured after 5 weeks

Sample ID	Treatment	Oxygen content	Bacterial cell counts after 5 weeks (cells/ml)	Culturable bacteria (cfu/ml)	Initial RDX concentration (ppm)	Final RDX concentration (ppm)
CK1	No amendments	Anoxic	1.52×10^5	2.02×10^2	2.58 ± 0.81	2.60 ± 0.35
CK2	No amendments	Microoxic	2.13×10^5	1.46×10^2	2.37 ± 0.28	2.29 ± 0.71
AC1	Acetate added	Anoxic	1.22×10^7	5.19×10^3	2.66 ± 0.72	2.08 ± 0.39
AC2	Acetate added	Microoxic	5.21×10^9	4.81×10^4	2.24 ± 0.25	1.91 ± 0.31
OIL1	Safflower oil added	Anoxic	5.83×10^9	3.90×10^4	2.09 ± 0.23	0.45 ± 0.34
OIL2	Safflower oil added	Microoxic	7.62×10^9	5.17×10^5	1.97 ± 0.15	2.24 ± 0.31

3.4 | RDX degradation in biostimulated cultures

Both acetate and vegetable oil are known to stimulate microbial activity and enhance RDX degradation. We amended groundwater samples with acetate and safflower oil and examined RDX degradation under variable geochemical conditions to determine which factors are most relevant to RDX degradation. As shown in Table 1, little bacterial growth and RDX transformation were observed in the control samples in which no amendments were added. RDX also remained unchanged in the abiotic controls (data not shown). Acetate amendment stimulated microbial growth, with a stronger effect under microoxic conditions. However, RDX concentration were not significantly reduced in these samples over 5 weeks. A similar effect was also observed for safflower oil under microoxic environment. Even though the microbes grew to densities of 7.9 × 10^9 cells/ml, no significant RDX degradation was observed. In contrast, safflower oil enhanced bacterial growth to the same level and promoted RDX degradation under more strict anaerobic conditions. Quantitative analysis of RDX and its degradation products by HPLC (Figure 5a, b) showed a transient increase in the concentrations of DNX and MNX during the active degradation of RDX, but their concentrations decrease rapidly when RDX degradation reaches a plateau. These data are consistent with the literature data which identified DNX, MNX, and TNX as intermediate products in the anaerobic degradation of RDX (Bernstein & Ronen, 2012). It also suggests that RDX degradation proceeds by the stepwise reduction of the nitroso groups followed by ring-cleavage and is consistent with the mechanisms reported in the literature (Hawari et al., 2002).

The concentration of 4-NDAB remained fairly constant throughout the experiment and TNX was barely detectible until the 5th week. The concentration of NDAB was elevated in all samples including controls with no noticeable RDX degradation and did not change over time (Fig. S2). This is likely due to the lack of separation of NDAB from other small molecular weight metabolites present in the media which are not well resolved by the HPLC method. These results show that RDX degradation is enhanced under strict anaerobic conditions, but very negligible in the presence of oxygen. The availability of oxygen seems to inhibit RDX degradation which indicates that RDX under our current experimental conditions is degraded mainly through anaerobic respiration, which is also supported by the detection of degradation products identified as intermediates of RDX anaerobic respiration. RDX remained stable in the anaerobic reactors amended with acetate under both anoxic and microoxic conditions, although the cell numbers were significantly increased. This means that the type of nutrients provided is critical for RDX degradation possibly by differentially regulating the assemblage of groundwater microbial community.

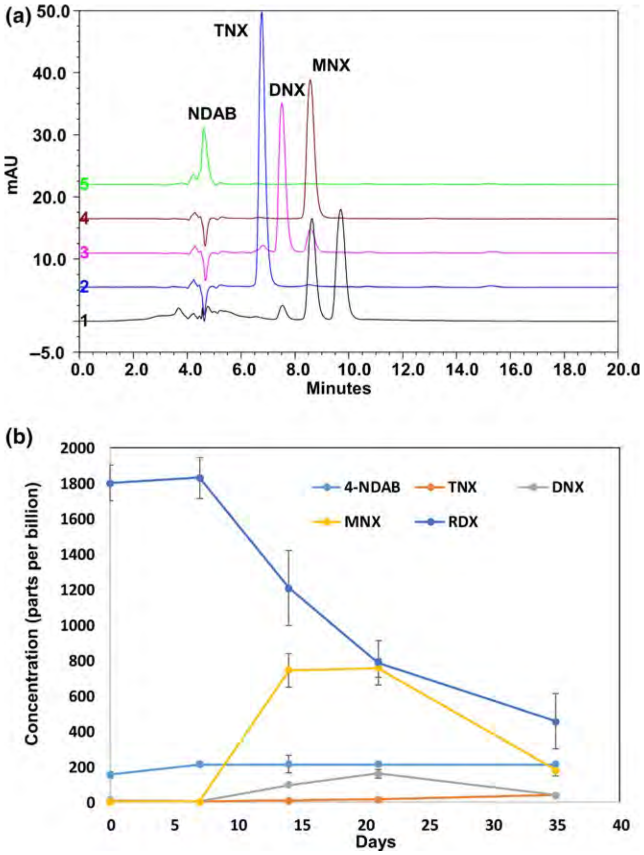

FIGURE 5 (a) HPLC chromatograms showing RDX degradation and production of RDX derivatives. 1. CdV-16-4ip with 2 ppm RDX was amended with 1% (v/v) safflower oil. The sample was incubated at anaerobic condition for 3 weeks. Samples were filtered to remove bacteria and other particles before HPLC analysis. 2. TNX standard. 3. DNX standard. 4. MNX standard. 5. NDAB standard. (b) Kinetics of RDX degradation and production of its derivatives. CdV-16-4ip (RDX ~ 2 ppm) was amended with 1% (v/v) safflower oil. The concentration of RDX, MNX, DNX, TNX, and NDAB was monitored up to 5 weeks

3.5 | Evolution of the microbial population after biostimulation

To determine how nutrients and oxygen content affect the microbial community in the stimulated groundwater, we performed a microbial profiling of the bacterial communities before and 7 weeks after the biostimulation under different conditions. In the two nonstimulated control samples, a slight increase was found in *Actinobacteria* and a decrease was observed for *Proteobacteria*. In contrast, *Proteobacteria* populations were significantly increased in all stimulated samples comprising over 90% (Figure 6a). The microbes representing the phyla *Bacteroidetes*, *Nitrospirae*, *Planctomycetes*, *Chlamydiae*, *Chloroflexi*, and *Verrucomicrobia* were decreased or completely eliminated. Rarefaction curve analysis show a significant reduction of species richness after biostimulation (Figure 6b). The original 1,605 OTUs were reduced to 440, 539, 512, and 577 in the AC1, AC2, OIL1, and OIL2, respectively. Dominant OTUs representing over 67.5% of the total population were all significantly decreased, with a stronger effect under anaerobic conditions (Table 2). Three OTUs related to *Frateuria*, *Hydrogenophaga*, and *Pedobacter* were completely eliminated suggesting that biostimulation is detrimental to these species. *Rhodococcus* are well known as aerobic bacterial species and therefore are not able to survive under anoxic conditions. As expected, they were barely detected under anaerobic growing conditions for both acetate and vegetable oil (Figure 7a). Species in *Pseudomonas* are capable of using a range of nutrients including vegetable oil (Song, Jeon, Choi, Yoon, & Park, 2008). Therefore, they are favored when cultivated with safflower oil, especially under microoxic conditions (Figure 7b).

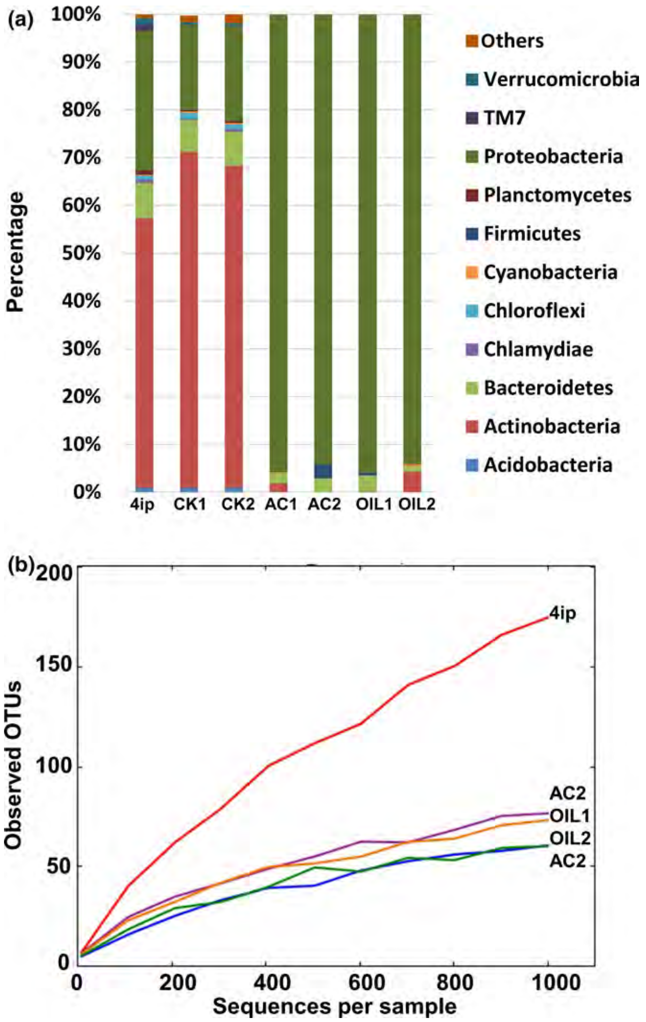

FIGURE 6 (a) Relative abundances of bacterial phyla in CdV-16-4ip before and after cultivation. Phyla with over 1% relative abundance were plotted. (b) Rarefaction curves for microbial diversity generated by QIIME (Caporaso et al., 2010). 200–1000 16S rRNA sequences were randomly selected and operational taxonomic units (OTUs) were calculated at a 97% cutoff. 4ip: CdV-16-4ip before cultivation; CK1: No amendments—oxygen; CK2: No amendments + oxygen; AC1: CdV-16-4ip cultivated with acetate + oxygen; AC2: CdV-16-4ip cultivated with acetate—oxygen; OIL1: CdV-16-4ip cultivated with safflower oil—oxygen; OIL2: CdV-16-4ip cultivated with safflower oil + oxygen

Since OIL1 was the only sample showing RDX degradation (Figure 5; Table 1), we were particularly interested in the bacterial OTUs enriched in this sample. Table 3 lists the top nine abundant OTUs (>1%) detected in OIL1. Interestingly, none of these OTUs were dominant in the original CdV-16-4ip sample and their sequence abundances were all below 1%. The OTUs exhibited 99%–100% sequence identity to six known genera (*Simplicispira*, *Aquabacterium*, *Acidovorax*, *Curvibacter*, *Sphaerotilus*, and *Hydrogenophaga)* in the family of *Comamonadaceae;* two genera *(Sediminibacterium* and *Flavobacterium) of Bacteroidetes*, and one *Pseudomonas* (OTU# 1108886 showing 99% sequence identity to the RDX-degrading strain *P. putida* II-B) of *Pseudomonadaceae*. The *Pseudomonas* OTU (1108886) comprising 3.81% in OIL1 population was much higher than those (<1%) found in the OIL2-, AC1-, and AC2-stimulated samples. Instead of OIL2 which shares the same nutrient type with OIL1, it is AC2 that showed a more similar pattern of dominant OTUs to OIL1 (Table 3). We also performed a principal coordinate analysis (PCoA) of the OTUs in the five samples (Figure S1). PC1, PC2, and PC3 accounted for 62.97%, 23.35%, and 12.53% of total variance, respectively. The score plot PC1 clearly showed that the four stimulated samples were separated from the original CdV-16-4ip sample. This indicates that biostimulation significantly shifts the composition of the microbial community. The two anaerobic samples AC2 and OIL1 were grouped together; while, AC1 and OIL2 were relatively far from each other in the plot. Altogether these results suggest that nutrient type and oxygen are interconnected and both are critical in shaping the microbiome during biostimulation.

4 | DISCUSSION

RDX degradation in groundwater is considered to be an outcome of complex interplay between the physicochemical factors and microbial activities. Although culture-independent studies have revealed

TABLE 2 Decrease of dominant OTUs in CdV-16-4ip groundwater after cultivation

OTU ID	Related bacterial strain	CdV-16-4ip	AC1	AC2	OIL1	OIL2
573976	*Rhodococcus erythropolis* HS4	25.20%	1.59%	0.01%	0.00%	4.08%
40439	*Nocardia ignorata* DSM 44496	21.90%	0.00%	0.00%	0.00%	0.00%
819037	*Polaromonas jejuensis* NBRC 106434	5.50%	0.02%	0.00%	0.01%	0.01%
707290	*Frateuria aurantia* DSM 6220	4.30%	0.00%	0.00%	0.00%	0.00%
689950	*Rhodococcus cerastii* C5	4.10%	0.08%	0.00%	0.00%	0.01%
1108960	*Sphingomonas desiccabilis* CP1D	2.50%	0.14%	0.00%	0.00%	0.10%
44265	*Flavobacterium macrobrachii* an-8	1.40%	0.01%	0.00%	0.00%	0.00%
1708706	*Hydrogenophaga carboriunda* YZ2	1.30%	0.00%	0.00%	0.00%	0.00%
4339351	*Pedobacter ginsengisoli* Gsoil 104	1.30%	0.00%	0.00%	0.00%	0.00%

OTUs, operational taxonomic units.

composition of bacterial communities at many RDX-contaminated aquifers, this study provided a better understanding of community composition and environmental factors relevant for RDX transformation in groundwater at the Los Alamos site. Physicochemical analyses of water samples were performed to better understand the link between bacterial community composition and function. Our analyses showed that the groundwater samples represented the characteristic nature of nonreducing conditions, abundant HCO_3^-, and lack of sufficient soluble carbon nutrients. These conditions are not optimal for vigorous microbial activity that would be conductive to RDX degradation either for anaerobic respiration or utilization of RDX as a nitrogen source. Also, the utilization of RDX as a carbon source seems to be very limited under our experimental conditions. Overall, the geochemical conditions of the groundwater represent a nutritionally limited medium that is not very conductive to the indigenous microorganism activity. This is consistent with the low RDX degradation activity via microbes.

Using culture-independent studies, we identified the presence of 96 genera in 15 phyla within the groundwater sample. A high abundance of OTUs was closely related to *Rhodococcus* strain HS4 (Figure 3) which exhibit low RDX biodegradation activities (Seth-Smith et al., 2008). In contrast, no OTUs are closely related to *Rhodococcus* strain 11Y (Figure 3) which contain the highly effective RDX-degrading XplA-B system (Seth-Smith et al., 2002). It seems that OTUs related to *Rhodococcus* strain HS4 are enriched by RDX at the Los Alamos site, whereas *Rhodococcus* 11Y-related strains are not present. This explains the low RDX degradation activities as indicated by little RDX degradation products in the groundwater. Our study also establishes that in spite of poor nutrient content in groundwater, the bacterial diversity in the RDX-contaminated groundwater remains significantly high.

Biostimulation has a profound impact on the microbial community. The portions of dominant OTUs were all significantly dropped after nutrient amendments (Table 2). *Polaromonas*, *Nocardia*, and *Rhodococcus* are known to use hydrocarbons; *Frateuria*, *Pedobacter*, and *Sphingomonas* include plant beneficial strains that help uptake potassium, nucleotide, and nitrogen (Subhashini, 2015; Ten et al., 2006; Videira, De Araujo, Rodrigues, Baldani, & Baldani, 2009); *Flavobacterium* and *Hydrogenophaga* are organisms that can utilize lactose and hydrogen, respectively (McCammon et al., 1998; Reinauer et al., 2014). However, none of these groups are reported to effectively utilize acetate and vegetable oil. Their suppression in the biostimulated reactors suggests their inability to grow effectively on the amendments used in this study. On the other hand, bacteria in the family of *Comamonadaceae* (*Simplicispira*, *Aquabacterium*, *Acidovorax*, *Curvibacter*, *Sphaerotilus*, *Hydrogenophaga*) and *Pseudomonadaceae* (*Pseudomonas*), which are capable of utilizing acetate and vegetable oil (Tang, Wu, Watson, & Parker, 2013), thrived and became dominant. Therefore, the shift in the microbial composition is reflective of the differential metabolic properties of the different microbial families. Moreover, bacteria in the families of *Pseudomonadaceae*, which are well known to synthesize various antimicrobial compounds such as antibiotics and bacteriocins (Loper et al., 2012), might have played a role in interspecies competition, and therefore a decrease in microbial diversity. This is supported by recent studies which have demonstrated that they possess type

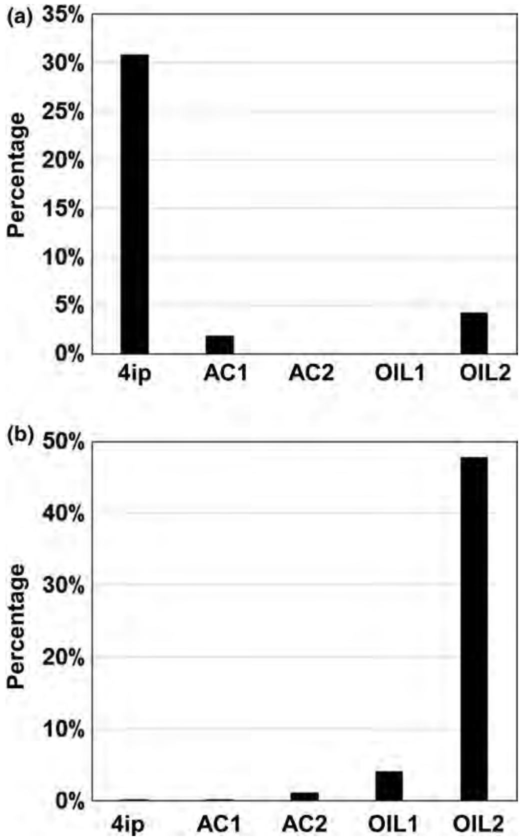

FIGURE 7 Relative abundances of *Rhodococcus* (a) and *Pseudomonas* (b) in the groundwater samples before and after cultivation. Figures were generated using numbers from QIIME analysis (Caporaso et al., 2010). 4ip: CdV-16-4ip before cultivation; AC1: CdV-16-4ip cultivated with acetate + oxygen; AC2: CdV-16-4ip cultivated with acetate—oxygen; OIL1: CdV-16-4ip cultivated with safflower oil—oxygen; OIL2: CdV-16-4ip cultivated with safflower oil + oxygen

VI secretion systems involved in interspecies competitions (Decoin et al., 2014).

Acetate and vegetable oil were used to successfully stimulate RDX degradation under anaerobic conditions in different studies (Borden et al., 2004; Livermore et al., 2013). Biostimulation at field scale of an RDX-contaminated area performed by adding acetate as a biostimulant showed a microbial population shift from a microbial community dominated by *Betaproteobacteria* to a community dominated by *Deltaproteobacteria* and *Bacteroidetes* (Livermore et al., 2013). In our study, the dominant *Actinobacteria* in CdV-16-4ip groundwater shifted to *Proteobacteria* (mostly *Betaproteobacteria*) under both anaerobic and microoxic conditions. This is likely reflective of the importance of the initial biogeochemical conditions of the site, especially the availability of oxygen and shows that amendments regulation of the microbiome assemblage in groundwater are likely to change significantly among different sites.

Amendment of CdV-16-4ip groundwater with safflower oil showed that *Gammaproteobacteria* (*Pseudomonas* in particular) were enriched in the presence of oxygen. Surprisingly, no RDX degradation is observed under aerobic conditions even under vigorous microbial activity. This is likely reflective of the inability of the microbes stimulated to utilize RDX as either a carbon or a nitrogen source or that there are abundant nitrogen and carbon in the media which are easier to utilize than RDX. Under anaerobic condition, one OTU related to RDX-degrading *Pseudomonas spp.* was enriched by safflower oil and RDX was transformed into three RDX nitroso derivatives and NDAB (Table 3). *Pseudomonas* are known to harbor XenA and XenB which convert RDX to MNX, DNX, and TNX (Hawari et al., 2002). Although denitration and ring-cleavage via *Rhodococcus* genes *xplA* and *xplB* generate MEDINA, NDAB, nitrate, and formaldehyde, production of the nitroso-derivatives suggests that RDX is degraded via XenA and XenB sequential reduction by the enriched *Pseudomonas* OTU. Since the complete set of microbial species involved in RDX degradation is not well defined, it is equally possible that other bacterial genera enriched by safflower oil rather than acetate are involved in RDX degradation in anaerobic conditions. Ongoing work is being carried out to identify genes expressed under different conditions to help identify the specific microbes involved in RDX degradation.

Our microbial profiling shows that bacterial communities in the perched-intermediate groundwater environment at TA-16 are composed of diverse taxonomic groups. Furthermore, biostimulation analysis identified environmental conditions favoring RDX degradation.

TABLE 3 OTUs enriched by safflower oil under anaerobic conditions

OTU ID	Related bacterial strain (Genbank Accession #)	CdV-16-4ip	AC1	AC2	OIL1	OIL2
576501	*Simplicispira limi* EMB325 (NR_043773.1)	0.01%	0.03%	35.10%	28.14%	0.03%
942852	*Aquabacterium commune* B8 (NR_024875.1)	0.02%	1.32%	16.84%	26.28%	4.92%
575562	*Acidovorax delafieldii* LMG 5943 (NR_116131.1)	0.01%	0.05%	7.01%	12.65%	0.20%
895220	*Curvibacter fontanus* AQ9 (NR_112221.1)	0.14%	0.19%	3.63%	8.05%	1.71%
238109	*Sphaerotilus hippei* 566 (NR_117539)	0.65%	0.12%	0.77%	3.84%	0.32%
1108886	*Pseudomonas putida II-B* (EF219419)	0.00%	0.05%	0.46%	3.81%	0.86%
647775	*Hydrogenophaga caeni* EMB71 (NR_043769)	0.39%	3.70%	0.94%	2.52%	11.39%
781203	*Sediminibacterium salmoneum* NJ-44 (NR_044197)	0.02%	0.28%	0.72%	1.40%	0.38%
662742	*Flavobacterium aquaticum* JC164 (NR_108893)	0.00%	0.04%	0.51%	1.39%	0.01%

OTUs, operational taxonomic units.

These data show that strict anaerobic conditions are required to drive biotic RDX degradation. Such conditions were also seen in remediation of contaminated aquifers that contain uranium or other radionuclides (through coffinization, etc.), which favors the immobilization of uranium (Guo et al., 2014, 2015). Our studies also show the importance of the initial availability of oxygen on the success of a bioremediation approach. Studies in an open system with continued flow are currently being carried out to specifically examine the effect of oxygen availability on microbial diversity and RDX degradation. The results will be reported in a separate paper.

ACKNOWLEDGMENT

We thank the office of environmental programs for facilitating groundwater sampling. Support for this work was provided by the DOE office of environmental management and Los Alamos National Laboratory.

CONFLICT OF INTEREST

The authors declare that they have no conflict of interest.

REFERENCES

Adrian, N. R., & Arnett, C. M. (2004). Anaerobic biodegradation of hexahydro-1,3,5-trinitro- 1,3,5-triazine (RDX) by *Acetobacterium malicum* strain HAAP-1 isolated from a methanogenic mixed culture. *Current Microbiology*, *48*, 332–340.

Andeer, P., Stahl, D. A., Bruce, N. C., & Strand, S. E. (2009). Lateral transfer of genes for hexahydro-1,3,5-trinitro-1,3,5-triazine (RDX) degradation. *Applied Environmental Microbiology*, *75*, 3258–3262.

Andeer, P., Stahl, D. A., Lillis, L., & Strand, S. E. (2013). Identification of microbial populations assimilating nitrogen from RDX in munitions contaminated military training range soils by high sensitivity stable isotope probing. *Environmental Science and Technology*, *47*, 10356–10363.

Beller, H. R. (2002). Anaerobic biotransformation of RDX (hexahydro-1,3,5-trinitro-1,3,5-triazine) by aquifer bacteria using hydrogen as the sole electron donor. *Water Research*, *36*, 2533–2540.

Bernstein, A., & Ronen, Z. (2012). Biodegradation of the Explosives TNT, RDX and HMX. In S. N. Singh (Ed.), *Microbial Degradation of Xenobiotics* (pp. 135–176). Springer: Berlin Heidelberg.

Bhushan, B., Halasz, A., Spain, J., Thiboutot, S., Ampleman, G., & Hawari, J. (2002). Biotransformation of Hexahydro-1,3,5- trinitro-1,3,5,-triazine catalyzed by a NAD(P)H: Nitrate oxidoreductase from *Aspergillus niger*. *Environmental Science Technology*, *36*, 3104–3108.

Bhushan, B., Halasz, A., Thiboutot, S., Ampleman, G., & Hawari, J. (2004). Chemotaxis-mediated biodegradation of cyclic nitramine explosives RDX, HMX, and CL-20 by *Clostridium* sp. EDB2. *Biochem Biophysics Research Communications*, *316*, 816–821.

Blehert, D. S., Fox, B. G., & Chambliss, G. H. (1999). Cloning and sequence analysis of two *Pseudomonas* flavoprotein xenobiotic reductases. *Journal of Bacteriology*, *181*, 6254–6263.

Borden, R. C., Zawtocki, C., Lee, M. D., Henry, B. M., Becvar, E. S., & Haas, P. E. (2004). *AFCEE protocol for enhanced anaerobic bioremediation using edible oils*. Remediation of Chlorinated and Recalcitrant Compounds: Battelle Press.

Caporaso, J. G., Kuczynski, J., Stombaugh, J., Bittinger, K., Bushman, F. D., Costello, E. K., Fierer, N., Pena, A. G., Goodrich, J. K., Gordon, J. I., Huttley, G. A., Kelley, S. T., Knights, D., Koenig, J. E., Ley, R. E., Lozupone, C. A., McDonald, D., Muegge, B. D., Pirrung, M., Reeder, J., Sevinsky, J. R., Tumbaugh, P. J., Walters, W. A., Widmann, J., Yatsunenko, T., Zaneveld, J., & Knight, R. (2010). QIIME allows analysis of high-throughput community sequencing data. *Nature Methods*, *7*, 335–336.

Cho, Y. S., Lee, B. U., & Oh, K. H. (2008). Simultaneous degradation of nitroaromatic compounds TNT, RDX, atrazine, and simazine by *Pseudomonas putida* HK-6 in bench-scale bioreactors. *Journal of Chemistry Technology Biotechnology*, *83*, 1211–1217.

Cho, K. C., Lee, D. G., Roh, H., Fuller, M. E., Hatzinger, P. B., & Chu, K. H. (2013). Application of ^{13}C-stable isotope probing to identify RDX-degrading microorganisms in groundwater. *Environment Pollution*, *178*, 350–360.

Chong, C.S. (2011). Biodegradation of RDX in *Rhodococcus spp*. PhD thesis, University of York.

Coleman, N. V., Spain, J. C., & Duxbury, T. (2002). Evidence that RDX biodegradation by *Rhodococcus* strain DN22 is plasmid-borne and involves a cytochrome p-450. *Journal of Applied Microbiology*, *93*, 463–472.

Decoin, V., Barbey, C., Bergeau, D., Latour, X., Feuilloley, M. G. J., Orange, N., … Merieau, A. (2014). A Type VI Secretion System Is Involved in *Pseudomonas fluorescens* Bacterial Competition. *PLoS ONE* *9*(2), e89411.

Felsenstein, J. (1985). Confidence limits on phylogenies: An approach using the bootstrap. *Evolution*, *39*, 783–791.

Fournier, D., Halasz, A., Spain, J. C., Fiurasek, P., & Hawari, J. (2002). Determination of key metabolites during biodegradation of hexahydro-1,3,5-trinitro-1,3,5-triazine with *Rhodococcus sp.* strain DN22. *Applied Environmental Microbiology*, *68*, 166–172.

Fuller, M. E., McClay, K., Hawari, J., Paquet, L., & Malone, T. E. (2009). Transformation of RDX and other energetic compounds by xenobiotic reductases XenA and XenB. *Applied Microbiology Biotechnology*, *84*, 535–544.

Fuller, M. E., McClay, K., Higham, M., Hatzinger, P. B., & Steffan, R. J. (2010). Hexahydro-1,3,5-trinitro-1,3,5-triazine (RDX) bioremediation in groundwater: Are known RDX-degrading bacteria the dominant players? *Biochemical Journal*, *14*, 121–134.

Fuller, M. E., Perreault, N., & Hawari, J. (2010). Microaerophilic degradation of hexahydro-1,3,5-trinitro-1,3,5-triazine (RDX) by three *Rhodococcus* strains. *Letter of Applied Microbiology*, *51*, 313–318.

Guo, X., Szenknect, S., Mesbah, A., Labs, S., Clavier, N., Poinssot, C., … Navrotsky, A. (2015). Thermodynamics of formation of coffinite, USiO4. *Proceedings National Academy Sciences USA*, *112*, 6551–6555.

Guo, X., Ushakov, S. V., Labs, S., Curtius, H., Bosbach, D., & Navrotsky, A. (2014). Energetics of metastudtite and implications for nuclear waste alteration. *Proceedings National Academy Sciences USA*, *111*, 17737–17742.

Halasz, A., Manno, D., Perreault, N. N., Sabbadin, F., & Bruce, N. C. (2012). Biodegradation of RDX nitroso products MNX and TNX by cytochrome P450 XplA. *Environmental Science Technology*, *46*, 7245–7251.

Hawari, J., & Halasz, A. (2002). Microbial degradation of explosives. In G. Bitton (Ed.), *The encyclopedia of environmental microbiology* (pp. 1979–1993). New York: John Wiley & Sons Ltd.

Hawari, J. A., Halasz, T., Sheremata, S., Beaudet, C., Groom, L., Paquet, C., … Thiboutot, S. (2000). Characterization of metabolites during biodegradation of hexahydro-1,3,5-trinitro-1,3,5-triazine (RDX) with municipal sludge. *Applied Environmental Microbiology*, *66*, 2652–2657.

Hugerth, L. W., Wefer, H. A., Lundin, S., Jakobsson, H. E., Lindberg, M., & Rodin, S. (2014). DegePrime, a program for degenerate primer design for broad taxonomic-range PCR in microbial ecology studies. *Applied Environmental Microbiology*, *80*, 5116–5123.

Indest, K. J., Hancock, D. E., Jung, C. M., Eberly, J. O., & Mohn, W. W. (2013). Role of nitrogen limitation in transformation of RDX (hexahydro-1,3,5-trinitro-1,3,5-triazine) by *Gordonia sp.* strain KTR9. *Applied Environmental Microbiology*, *79*, 1746–1750.

Indest, K. J., Jung, C. M., Chen, H. P., Hancock, D., & Florizone, C. (2010). Functional characterization of pGKT2, a 182-kilobase plasmid containing the *xplAB* genes, which are involved in the degradation of hexahydro-1,3,5-trinitro-1,3,5-triazine by *Gordonia* sp. strain KTR9. *Applied Environmental Microbiology*, *76*, 6329–6337.

Jackson, R. G., Raylot, E., Fournier, D., Hawari, J., & Bruce, N. C. (2007). Exploring the biochemical properties and remediation applications of the unusual explosive-degrading P450 system XplA/B. *Proceedings National Academy Sciences*, *104*, 16822.

Jeanmougin, F., Thompson, J. D., Gouy, M., Higgins, D. G., & Gibson, T. J. (1998). Multiple sequence alignment with Clustal X. *Trends Biochemical Science*, *23*, 403–405.

Khan, M. I., Lee, J., & Park, J. (2012). Microbial degradation and toxicity of hexahydro-1,3,5-trinitro-1,3,5-triazine. *Journal of Microbiology Biotechnology*, *22*, 1311–1323.

Kitts, C. L., Cunningham, D. P., & Unkefer, P. J. (1994). Isolation of three hexahydro-1,3,5-rinitro-1,3,5-triazine-degrading species of the family *Enterobacteriaceae* from nitramine explosive-contaminated soil. *Applied Environmental Microbiology*, *60*, 4608–4611.

LANL (Los Alamos National Laboratory) (2006). *The High Explosives Source Term at TA-16. Los Alamos National Laboratory document LA-UR-05-9433*. Los Alamos, New Mexico.

LANL (Los Alamos National Laboratory). (2010). Summary Report for the Corrective Measures Implementation at Consolidated Unit 16-021(c)-99, Los Alamos National Laboratory document LA-UR-10-0947, Los Alamos, New Mexico.

LANL (Los Alamos National Laboratory). (2011). Investigation Report for Water Canyon/Cañon de Valle, Los Alamos National Laboratory document LA-UR-11-5478, Los Alamos, New Mexico.

LANL (Los Alamos National Laboratory). (2015). Semiannual Progress Report for Corrective Measures Evaluation/Corrective Measures Implementation for Consolidated Unit 16-021(c)-99, Los Alamos, New Mexico.

Li, R. W., Giarrizzo, J. G., Wu, S., Li, W., Duringer, J. M., & Craig, A. M. (2014). Metagenomic insights into the RDX-degrading potential of the ovine rumen microbiome. *PLoS ONE 9*(11), e1105.

Livermore, J., Oh, J. Y., LePuil, M., Arnseth, R., & Mattes, T. E. (2013). Microbial community dynamics during acetate biostimulation of RDX-contaminated groundwater. *Environmental Science Technology*, *47*, 7672–7678.

Loper, J. E., Hassan, K. A., Mavrodi, D. V., Davis, E. W., Lim, C. K., & Shaffer, B. T. (2012). Comparative Genomics of Plant-Associated *Pseudomonas* spp.: insights into Diversity and Inheritance of Traits Involved in Multitrophic Interactions. *PLoS Genetics*, *8*(7), e1002784.

McCammon, S. A., Innes, B. H., Bowman, J. P., Franzmann, P. D., Dobson, S. J., Holloway, P. E., … Rankin, L. M. (1998). *Flavobacterium hibernum* sp. nov., a lactose-utilizing bacterium from a freshwater Antarctic lake. *International Journal of System Bacteriology*, *4*, 1405–1412.

Reinauer, K. M., Popovic, J., Weber, C. D., Millerick, K. A., Kwon, M. J., Wei, N., & Finneran, K. T. (2014). *Hydrogenophaga carboriunda* sp. nov., a tertiary butyl alcohol-oxidizing, psychrotolerant aerobe derived from granular-activated carbon (GAC). *Current Microbiology*, *68*(4), 510–517.

Rodriguez-Nava, V., Couble, A., & Khan, Z. U. (2005). *Nocardia ignorata*, a new agent of human nocardiosis isolated from respiratory specimens in Europe and soil samples from Kuwait. *Journal of Clinical. Microbiology*, *43*, 6167–6170.

Rylott, E. L., Budarina, M. V., Barker, A., Lorenz, A., Strand, S. E., & Bruce, N. C. (2011). Engineering plants for the phytoremediation of RDX in the presence of the co-contaminating explosive TNT. *New Phytologist*, *192*, 405–413.

Rylott, E. L., Jackson, R. G., Edwards, J., Womack, G. L., Seth-Smith, H. M. B., Rathbone, D. A., … Bruce, N. C. (2006). An explosive-degrading cytochrome P450 activity and its targeted application for the phytoremediation of RDX. *Nature Biotechnology*, *24*, 216–219.

Rylott, E. L., Jackson, R. G., Sabbadin, F., Seth-Smith, H. M., & Edwards, J. (2011). The explosive-degrading cytochrome P450 XplA: Biochemistry, structural features and prospects for bioremediation. *Biochimica et Biophysica Acta*, *1814*, 230–236.

Schaefer, C. E., Fuller, M. E., Condee, C. W., Lowey, J. M., & Hatzinger, P. B. (2007). Comparison of biotic and abiotic treatment approaches for co-mingled perchlorate, nitrate, and nitramine explosives in groundwater. *Journal of Contaminant Hydrology*, *89*, 231–250.

Seth-Smith, H. M. B., Edwards, J., Rosser, S. J., Rathbone, D. A., & Bruce, N. C. (2008). The explosive-degrading cytochrome P450 system is highly conserved among strains of Rhodococcus spp. *Applied and Environmental Microbiology*, *74*, 4550–4552.

Seth-Smith, H. M., Rosser, S. J., Basran, A., Travis, E. R., & Dabbs, E. R. (2002). Cloning, sequencing, and characterization of the hexahydro-1,3,5-Trinitro-1,3,5-triazine degradation gene cluster from *Rhodococcus rhodochrous*. *Applied Environmental Microbiology*, *68*, 4764–4771.

Song, J. H., Jeon, C. O., Choi, M. H., Yoon, S. C., & Park, W. (2008). Polyhydroxyalkanoate (PHA) production using waste vegetable oil by *Pseudomonas* sp. strain DR2. *Journal of Microbiology Biotechnology*, *18*, 1408–1415.

Subhashini, D. V. (2015). Growth promotion and increased potassium uptake of tobacco by potassium-mobilizing bacterium *Frateuria aurantia* grown at different potassium levels in Vertisols. *Communications in Soil Science and Plant Analysis*, *46*, 2.

Swofford, D. L. (2002). *PAUP*: Phylogenetic analysis using parsimony 455, version 4.0b10*. Sunderland, MA: Sinauer Associates.

Tang, G., Wu, W.-M., Watson, D. B., & Parker, J. C. (2013). U(VI) bioreduction with emulsified vegetable oil as the electron donor—microcosm tests and model development. *Environmental Science Technology*, *47*, 3209–3217.

Ten, L. N., Liu, Q. M., Im, W. T., Lee, M., Yang, D.-C., & Lee, S. T. (2006). *Pedobacter gingsengisoli* sp. nov., a DNase-producing bacterium isolated from soil of a ginseng field in South Korea. *International Journal System Evolution Microbiology*, *56*, 2565–2570.

Videira, S. S., De Araujo, J. L. S., Rodrigues, L. S., Baldani, V. L. D., & Baldani, J. I. (2009). Occurrence and diversity of nitrogen-fixing *Sphingomonas* bacteria associated with rice plants grown in Brazil. *FEMS Microbiology Letter*, *293*, 11–19.

Wang, D., Dorosky, R. J., Han, C. S., Lo, C., Dichosa, A. E. K., Chain, P. S., … Pierson, E. A. (2015). Adaptation genomics of a small-colony variant in a *Pseudomonas chlororaphis* 30-84 biofilm. *Applied Environmental Microbiology*, *81*, 890–899.

Wang, D., Korban, S. S., Pusey, P. L., & Zhao, Y. (2012). AmyR is a novel negative regulator of amylovoran production in *Erwinia amylovora*. *PLoS ONE*, *7*(9), e45038.

Watrous, M. M., Clark, S., Kutty, R., Huang, S., Rudolph, F. B., Hughes, J. B., & Bennett, G. N. (2003). 2,4,6-trinitrotoluene reduction by an Fe-only hydrogenase in *Clostridium acetobutylicum*. *Applied Environmental Microbiology*, *69*(3), 1542–1547.

Wilson, F. P., & Cupples, A. M. (2016). Microbial community characterization and functional gene quantification in RDX-degrading microcosms derived from sediment and groundwater at two naval sites. *Applied Microbiology Biotechnology*, *100*, 7297–7309.

Yu, S. H., Ke, L., Wong, Y. S., & Tam, N. F. Y. (2005). Degradation of polycyclic aromatic hydrocarbons (PAHs) by a bacterial consortium enriched from mangrove sediments. *Environment*, *31*, 149–154.

Zhao, J. S., Halasz, A., Paquet, L., Beaulieu, C., & Hawari, J. (2002). Biodegradation of hexahydro-1,3,5-trinitro-1,3,5-triazine and its mononitroso derivative hexahydro-1-nitroso-3,5-dinitro-1,3,5-triazine by *Klebsiella pneumoniae* strain SCZ-1 isolated from an anaerobic sludge. *Applied Environmental Microbiology*, *68*, 5336–5341.

SUPPORTING INFORMATION

Additional Supporting Information may be found online in the supporting information tab for this article.

How to cite this article: Wang, D., Boukhalfa, H., Marina, O., Ware, D. S., Goering, T. J., Sun, F., Daligault, H. E., Lo, C.-C., Vuyisich, M. and Starkenburg, S. R. Biostimulation and microbial community profiling reveal insights on RDX transformation in groundwater. *MicrobiologyOpen*. 2017;6:e423. https://doi.org/10.1002/mbo3.423

LA-UR-18-21326
March 2018
EP2018-0023

Characterization of the Microbial Population and RDX Degradation in Groundwater at Technical Area 16

Attachment 6

Prepared by the Associate Directorate for Environmental Management

EXECUTIVE SUMMARY

The high explosive RDX (hexahydro-1,3,5-trinitro-1,3,5-triazine) is commonly observed in groundwater sampled from monitoring wells that interrogate the alluvial, perched-intermediate, and regional aquifers at Technical Area 16 (TA-16) at Los Alamos National Laboratory in Los Alamos, NM. Degradation products MNX (hexahydro-1-nitroso-3,5-dinitro-1,3,5-triazine), DNX (hexahydro-1,3-dinitro-5-nitro-1,3,5-triazine), and TNX (2,4,6-trinitroxylene) are also observed, indicating active RDX degradation. Microbial diversity analysis of the different groundwater zones at TA-16 reveals a rich microbial diversity in the groundwater system. *Proteobacteria* were ubiquitously present in all the wells sampled, followed by *Bacteroidetes* and *Actinobacteria*. Members of *Verrucomicrobia*, *Actinobacteria*, *Planctomycetes*, *Nitrospirae*, *Acidobacteria*, TM7 (*Candidatus Saccharibacteria*), OP3 (*Omnitrophica*), and OD1 (*Parcubacteria*) were also detected. The survey also reveals the presence of *Rhodococcus* species in the perched-intermediate zone that has the highest RDX concentrations, suggesting that perhaps these species were enriched by the RDX contamination. However, the study does not identify specific microorganisms that can be directly linked to RDX degradation in any of the aquifers. The alluvial aquifer, which is situated in a dynamic environment and undergoes frequents transition between aerobic and anaerobic conditions, is likely to support the activity of anaerobic bacteria at least intermittently. By comparison, the perched-intermediate zones are stable and aerobic and are unlikely to support the activity of anaerobic bacteria. The increase in the ratios of MNX/RDX, DNX/RDX, and TNX/RDX observed in the alluvial aquifer is a good indication that anaerobic degradation occurs in the alluvial aquifer. In general, this study found that the perched-intermediate aquifer harbors a diverse population of microbes that have the ability to degrade RDX; however, there are no indications that these microbes are actually degrading RDX. The degradation products MNX, DNX, and TNX found at tracer levels in the perched-intermediate aquifer have likely formed in the alluvial aquifer and migrated to the deeper aquifers along with RDX.

CONTENTS

Figures

Tables

1.0 INTRODUCTION

The high explosive RDX (hexahydro-1,3,5-trinitro-1,3,5-triazine) is present as a low-level contaminant at several locations near facilities used for explosives manufacturing and testing at Los Alamos National Laboratory (LANL or the Laboratory) in Los Alamos, NM. An estimate of 1500–2700 kg of RDX has been discharged to the 260 Outfall in Cañon de Valle at Technical Area 16 (TA-16) (Gard and Newman, 2005; LANL 2018). Concerns about the release of RDX into the environment arise from its apparent resistance to decay and low soil sorption properties, which increase its potential to migrate to groundwater (ATSDR 2012; EPA 2005; Heerspink et al., 2017). RDX is classified by the U.S. Environmental Protection Agency (EPA) as a possible human carcinogen (EPA 2014). The EPA regional screening level for RDX in drinking water is 0.71 µg/L (EPA 2014) for a target cancer risk (TR) of 10^{-6} and a target hazard quotient of 1.0. The New Mexico Environment Department (NMED) drinking water screening level for RDX is 7.02 µg/L (NMED 2017).

RDX persists at low levels in the alluvial wells downstream of the 260 Outfall discharge point at TA-16 to depths of about 3 to 5 m, with maximum concentrations historically on the order of 48 µg/L (LANL 2011) (Figure 1.0-1). Current concentrations in alluvial wells are considerably lower and are at or near the NMED drinking water screening level of 7.02 µg/L. RDX is also found in the perched-intermediate zone underlying the upper Cañon de Valle at TA-16 located at depths of 179 to 361 m at concentrations varying between 20 and about 200 µg/L (LANL 2011). RDX is also detected in several monitoring wells completed in the regional aquifer at concentrations ranging from a few µg/L up to ~9 µg/L. The regional aquifer in the study area is present at depths of 337 to 413 m below ground surface within the Puye Formation (LANL 2011). RDX environmental transformation products MNX (hexahydro-1-nitroso-3,5-dinitro-1,3,5-triazine), DNX (hexahydro-1,3-dinitroso-5-nitro-1,3,5-triazine), and TNX (hexahydro-1,3,5-trinitroso-1,3,5-triazine) are also detected in groundwater.

The detection of these breakdown products indicates that RDX is undergoing degradation under natural conditions at TA-16. However, the extent of the breakdown and the location where it occurs remain unknown. Identification of RDX degradation mechanisms under site-specific conditions is important for evaluating potential corrective actions. Signatures of RDX degradation mechanisms can be identified by careful examination of the groundwater for specific degradation products. The main pathway for RDX degradation in surficial soils and water is through photo-degradation. However, this process is only significant in aqueous solutions; it is generally insignificant in soils (ATSDR 2012; CRREL 2006; HSDB 2013). Photo-decomposition of RDX produces small fragments such as formaldehyde, acetate, nitrous oxide, and ammonia. In aqueous systems, RDX also degrades by hydrolysis fairly quickly (~7 d half-life) under alkaline conditions of pH> 10. Degradation also occurs by denitration, ring cleavage, and breakdown to smaller fragments such as nitrite, nitrous oxide, ammonia, formate, and formaldehyde (Table 1.0-1). In soils, RDX can also be mineralized by reduced minerals under anaerobic conditions by sequential reduction of the nitroso groups and ring cleavage. Nitroso products DNX, MNX, and TNX are produced as degradation-product intermediates (Table 1.0-1).

RDX can be degraded by a wide range of microorganisms within the phyla *Firmicutes Actinobacteria*, *Proteobacteria*, and *Fusobacteria*. These include *Acetobacterium malicum sp*. HAAP-1 in the Firmicutes *phylum*, *Rhodococcus*. *Rhodochrous* 11Y, and *Rhodococcus* sp. Strain DN22, *Citrobacter*, *Clostridium* in the *Actinobacteria* phylum. RDX-degrading isolates in the phylum *Proteobacteria* include *Morganella*, *Klebsiella, Pseudomonas, Providencio*, *Desulfovibrio*, *Geobacter*, and *Shewanella*. RDX biodegradation occurs most effectively under anaerobic conditions (U.S. Army 1980a; Hawari et al., 2002; Walker and Kaplan, 1992). The process is relatively fast, with half-lives ranging from a few days to a few weeks depending on the microbes involved. However, the availability of oxygen and other electron acceptors can inhibit RDX degradation (Halasz et al., 2010; Indest et al., 2013). Degradation occurs by either a sequential reduction of the nitro groups to nitroso groups followed by ring cleavage, or by the denitration and ring cleavage and formation of methylenedinitramine (MEDINA) followed by abiotic breakdown to smaller fragments such as methanol, nitrous oxide and carbon dioxide (Table 1.0-1).

Degradation under aerobic conditions is not as widely prevalent but has been reported for a number of organisms such as *Stenotrophomonas maltophilia* PB1, *Rhodococcus* sp. strain DN22, *Rhodococcus Rhodochrous* strain 11Y (Seth-Smith et al., 2002; Zhu et al., 2014). Degradation is attributed to cytochrome P450 XplA and XplB reductases activity, which mediates RDX transformation under aerobic conditions. The degradation proceeds by denitration, and ring cleavage generates degradation products MEDINA, 4-nitro-2,4-diazabutanal (NDAB), nitrate, formaldehyde, and formate. RDX is also used as a carbon or nitrogen source by *Williamsia* sp. KTR4, and *Gordonia* sp. KTR9 under nitrogen-limited conditions (Thompson et al., 2005; Zhu et al., 2014). Degradation products include nitrite, formaldehyde, and NDAB (Thompson et al., 2005).

The goal of this research is to characterize the mechanisms, location, and factors important for the natural degradation of RDX observed under TA-16 site-specific conditions. Specifically, in this study we examine (1) the occurrence of RDX degradation products in water sampled from the different groundwater zones at TA-16, (2) the microbial profile of the different groundwater zones at TA-16, and (3) the abiotic and biotic factors that affect RDX degradation in TA-16 groundwater. The results from these examinations are used to discuss the potential mechanisms responsible for the observed degradation of RDX under TA-16 biogeochemical conditions. An understanding of the active mechanisms of RDX degradation will help guide the evaluation of potential remedial alternatives for RDX contamination at the Los Alamos site.

2.0 MATERIALS AND METHODS

2.1 Description of Groundwater Conditions at TA-16

TA-16 is located in the southwestern portion of the Laboratory and occupies portions of Water Canyon, Cañon de Valle, and S-Site Canyon watersheds (Figure 1.0-1). This site was established for the development, engineering design, prototype manufacture, and environmental testing of nuclear-weapons components. Developing, processing, and testing using tritium, high explosives (HE), and plastics; and conducting research on process development for manufacture of items using these and other materials, were conducted in extensive facilities. As a result of these activities, effluents released to Cañon de Valle contained HE compounds including RDX, TNT, and HMX and many other contaminants. The release of these eluents affected the different aquifers beneath and downstream from TA-16. Groundwater at TA-16 is present at different depths within the alluvial aquifer, the upper and lower perched aquifers, and the regional aquifer. The alluvial aquifer is found at depths of less than 5 m, and perched groundwater zones situated in the upper 30 m aliment the springs (LANL 2011). There are also two deep perched aquifers observed at depths of 179 to 361 m. The regional aquifer is present beneath the TA-16 area at depths of 337 to 413 m. The water chemistry and biogeochemical parameters characterizing each aquifer have been thoroughly characterized and are monitored quarterly. The data for wells intercepting the different aquifers is available through the NMED website http://intellusnm.com/.

The alluvial aquifer is usually well oxygenated, but intermittent occurrences of low dissolved oxygen concentration are frequent (Figure 2.1-1). The dissolved oxygen concentration varies between 0.4 and 9 mg/L. The alkalinity ($CO_3^{2-}HCO_3^-$) is 86 mg/L and the pH varies between 4.65 and 6.81. Total organic carbon is approximately 2.6 mg/L. The major anion concentrations in the water samples consist of Cl^- (25 mg/L), F^- (0.2 mg/L), NO_3^- as nitrogen (1.0 mg/L), SO_4^{2-} (13 mg/L), and PO_4^{2-} (0.03 mg/L), and the major cations consist of Na^+ (20 mg/L), Ca^{2+} (22 mg/L), K^+ (3.5 mg/L), Mg^{2+} (6 mg/L), and Si^{4+} (33 mg/L).

Iron concentrations fluctuate significantly, ranging from a few tens to a few hundreds of µg/L, and manganese concentrations are usually low (7.5 µg/L) (Figure 2.1-2). The water chemistry suggests the alluvial aquifer undergoes some intermittent anoxic events that are likely driven by microbial activity, reflected in the decreases in oxygen level and an apparent increase in dissolved iron concentrations. The water chemistry in the two perched-intermediate aquifers [wells Cdv-16-4(i)p and Cdv-9-1(i)] is consistently oxic, with the dissolved oxygen concentration varying between 5 and 7 mg/L and a total organic carbon concentration of 0.7 mg/L. The alkalinity ($CO_3^{2-}HCO_3^-$) is 51 mg/L and pH ranges from 6.5 to 7.4. The major anions in the water consist of Cl^- (9.6 mg/L), F^- (0.1 mg/L), NO_3^- as nitrogen (1.0 mg/L), SO_4^{2-} (5.7 mg/L), and PO_4^{2-} (0.08 mg/L), and the major cations consist of Na^+ (17 mg/L), Ca^{2+} (9.6 mg/L), K^+ (1.2 mg/L), Mg^{2+} (3.2 mg/L), and Si^{4+} (48 mg/L). Iron is <40 µg/L and manganese is 2 µg/L. The water chemistry in the lower perched aquifer is very similar to that of the upper perched aquifer. The groundwater in the regional aquifer is also oxic, with average dissolved oxygen concentration ranging between 5 and 6 mg/L. The pH varies slightly between 7.40 and 8.10 and the alkalinity ($CO_3^{2-}HCO_3^-$) is 52 mg/L. The total organic carbon is 0.6 mg/L. The major anion concentrations in the water sample consist of Cl^- (1.4 mg/L), F^- (0.08 mg/L), NO_3^- as nitrogen (0.6 mg/L), SO_4^{2-} (2.0 mg/L), and PO_4^{2-} (0.04 mg/L), and the major cations are Na^+ (8.87 mg/L), Ca^{2+} (10.7 mg/L), K^+ (1.23 mg/L), Mg^+ (3.0 mg/L), and Si^{4+} (58 mg/L). Iron (<10 µg/L) and manganese (<2 µg/L) are very low.

2.2 Water Sample Collection and Processing

Groundwater samples used in this study were obtained from nine monitoring wells located within or near the RDX contamination area at TA-16, in the southwest corner of the Laboratory (Figure 1.0-1). Water samples used for diribonucleic acid (DNA) extraction were collected after pumping the well for a minimum of three casing volumes. The samples were collected without filtration in polycarbonate containers and immediately stored on ice in the field and during transportation, then kept at 4°C in the dark in the laboratory until further analysis. Samples were processed for DNA extraction within 24 h of sampling. Table 2.2-1 summarizes the different wells used for groundwater sampling showing the depth of the well screens and the RDX concentration in the wells at the time of sampling. The wells interrogate the main three groundwater aquifers beneath TA-16 that show the presence of RDX and additional wells, used as controls, with no RDX contamination. Wells CdV-16-02659 and CdV-16-02656 were sampled as representatives of the alluvial aquifer. Before the corrective measure implemented in 2009–2010, RDX concentrations frequently exceeded the NMED drinking water screening level of 7.02 µg/L. RDX concentrations in most alluvial wells currently are near or below the NMED drinking water screening level. Wells Cdv-16-1(i), CdV-16-4ip, CdV-9-1(i) and CdV-16-2(i)r were sampled as representatives of the deep intermediate aquifer. The concentration of RDX in these wells is the highest among all wells monitored. Wells R-47, R-63, R-18, and R-68 were sampled as representatives of the regional aquifer groundwater system. Regional monitoring well R-18 has RDX at concentrations on the order of 3 µg/L. Well R-68 has RDX at approximately 14 µg/L. Groundwater used for the batch experiment was obtained from sampling wells CdV-16-4(i)p and CdV-9-1(i). A 10-gal. sample was obtained from each well during aquifer test pumping and stored in the dark at 4°C.

2.3 Analytical Methods

RDX and its degradation products within groundwater samples were analyzed by high-performance liquid chromatography (HPLC) using EPA Method 8330. The analysis was performed with a Dionex HPLC system equipped with a C-18 analytical column and an Ultimate 300 RS detector set at 254 nm (Pan et al., 2006). The mobile phase composition was fixed at a 55:45 water to methanol ratio. This method achieved a detection limit of about 1.0 µg/L for RDX and its degradation products MNX, DNX, and TNX. RDX certified standards (Ultra Scientific, North Kingstown, RI) were used to establish calibration curves for sample quantification. Samples of TNX, DNX, and MNX were purchased from SRI International, Menlo

Park, CA, and used without any further processing to establish calibration curves. The samples were assumed to be 100% pure. All water samples were filtered through Millex 0.45-µm syringe filters, which did not adsorb any RDX or any of its degradation products. Measurements for pH were taken using a Thermo Fisher Accumet pH probe calibrated with three commercial pH standards and connected to an Orion 290A meter.

2.4 Microbial Profiling Analysis

To isolate DNA, 100- to 500-mL water samples were filtered through 47-mm, 0.2-µm pore-size polycarbonate filters (Thermo Scientific). The material retained on the filters was processed using the UltraClean® Microbial DNA Isolation kit (MO BIO) according to the manufacturer's protocol. DNA extracts were used to amplify 16S ribosomal ribonucleic acid (rRNA) genes using bacterial 16S rRNA specific primers (515F-806R [GTGCCAGCMGCCGCGGTAA and GGACTACHVGGGTWTCTAAT, respectively]) (Hugerth et al., 2014). Amplicons were purified using a solid-phase reversible immobilization (SPRI) bead cleanup step, quantitated by picogreen assay, normalized, pooled, and then sequenced on an Illumina MiSeq instrument. The sequencing run resulted in approximately 1 million reads per sample with an average read length of 295 bp. The samples were filtered retaining those longer than 250 bp with an average quality score of greater than or equal to 30. Sequence data was processed by using the QIIME (Quantitative Insights into Microbial Ecology) software package v1.6.0 (Caporaso et al., 2012). Operational taxonomic units (OTUs) were clustered at the 97% similarity level. The most abundant sequence in each cluster was chosen as a representative. Alpha diversity analysis was performed using QIIME script (alpha_rarefaction.py). Principal Coordinates Analysis (PCoA) was implemented using QIIME based on the Jaccard distance. The National Center for Biotechnology Information (NCBI) Basic Local Alignment Search Tool (BLAST) was used to assign representative sequences to genus or species levels.

3.0 RDX DEGRADATION UNDER BIOTIC AND ABIOTIC CONDITIONS

3.1 RDX Degradation under Unstimulated Conditions

RDX degradation under unstimulated conditions was studied by monitoring the decrease in RDX concentration in a series of 27 (100-mL) serum bottles prepared to simulate different geochemical conditions. The availability of oxygen, the presence of sediments, sterile conditions, and exposure to daylight were varied. All the sterile vials received 50 mL of Cdv-9-1(i) groundwater, which contained about 100 µg/L RDX and trace levels of degradation products MNX, DNX, and TNX. The vials were wrapped in aluminum foil to prevent light exposure. The following conditions were examined: (1) no sediments plus oxygen, (2) no sediments minus oxygen, (3) no sediments plus oxygen, sterile filtered, (4) no sediments, no oxygen, sterile filtered. The same four series were also set up in the presence of 1.0 g of sterile cuttings obtained from archived R-25 well drill cuttings. The cuttings obtained from archived R-25 were sterilized by autoclaving for 30 min. Three sterile controls without sediments, maintained in the light for the duration of the experiment, were also set up to account for RDX photo-degradation. The no-oxygen conditions were set up by degassing the water with argon for 20 min. Sterile conditions were set up by sterile-filtering the groundwater using 0.2-µm polycarbonate filters. The vials were sealed with thick rubber stoppers and an aluminum cap crimped to limit gas exchange with the atmosphere and were placed on a benchtop shaker at room temperature (23.5°C) in the dark for the entire duration of the experiments. Sampling was performed with syringes equipped with a needle. All samples were filtered immediately after removal and analyzed by HPLC the same day.

3.2 RDX Degradation under Biostimulated Conditions

Sterile glass serum bottles (100 mL) and Corning® cell culture flasks (100 cm^2) were filled with 50 mL of unfiltered groundwater from monitoring well Cdv-16-4(i)p. The vials were amended with an aliquot of RDX dissolved in acetonitrile to bring the concentration of RDX to 1.0 mg/L. Sediments (1.0 g) were added to select vials to test the effect of sediments. The samples were amended with either 10-mM sodium acetate or safflower oil (1 volume/volume percent [v/v%]) and incubated either under aerobic or anaerobic conditions in the dark under constant shaking at 50 revolutions per minute (rpm). The aerobic studies were performed in Corning® cell culture flasks with a cap that allowed free exchange with the atmosphere. The initial anaerobic conditions in the serum vials used for the anaerobic cultivation were created by degassing the water with argon for 20 min. Each vial was sealed with a rubber stopper/aluminum cap pair crimped to limit gas exchange with the atmosphere. Controls were also set up without nutrient amendments. Aliquots were removed at selected time intervals using syringes equipped with needles. Microbial growth by direct cell counts and RDX degradation quantification by HPLC were performed at each time point. The concentrations of degradation products MNX, DNX, TNX, NDAB, and MEDINA were also monitored by HPLC analysis. Other known degradation products such as formaldehyde and nitrosamines were not examined in this study. Microbial diversity was examined for select conditions at the end of the experiment. The samples were processed as described in the microbial profiling and analysis section.

4.0 RESULTS

4.1 Distribution of RDX and Degradation Products DNX, MNX, and TNX in Groundwater at TA-16

RDX concentration in the alluvial wells, which is expected to reflect the concentration of RDX in the alluvial aquifer, deceased significantly over the years (Figure 4.1-1 A). The long-term decline in RDX concentrations in the alluvial aquifer may in part be due to Laboratory cleanup efforts undertaken between 2000 and 2009 in the vicinity of the 260 Outfall. The remediation efforts removed a significant amount of RDX from the sediments (LANL 2011) (Figure 4.1-1 A). The biodegradation of RDX as evidenced by the elevated concentration of degradation products MNX, DNX, and TNX, which are established signatures of microbial degradation of RDX under anaerobic conditions, has also contributed to the removal of RDX from the alluvial aquifer. The concentration of RDX is consistently less than 10 µg/L, and the concentration of the degradation products MNX, DNX, and TNX varies between 0.5 and 2.0 µg/L. No other degradation products were identified. The concentration of RDX in the perched-intermediate aquifer is steady and varies from 30 to 160 µg/L, with the highest concentrations currently measured at the location of monitoring well Cdv-16-4(i)p (Figure 4.1-1, B). RDX concentrations are steady and not trending down. The concentrations of degradation products MNX, DNX, and TNX are also detected but remain very consistent and at trace levels. RDX is also detected in the regional aquifer at the location of monitoring wells R-18, R-63, and R-68. The concentration of RDX at the R-18 location has been steadily increasing but is still below any regulatory screening levels (Figure 4.1-1 C). However, at monitoring locations R-68 the RDX concentration is on the order of 14 µg/L. It is worth noting that in the alluvial aquifer, which has RDX concentrations of approximately 10 µg/L, degradation products MNX, DNX, and TNX are always present; however, they are barely detected in the perched-intermediate aquifer, which has steady RDX concentrations of 30 to 160 µg/L, and are not detected in any of the regional aquifer samples that exhibit RDX concentrations on the order of 14 µg/L.

4.2 Bacterial Community Analysis in Groundwater at TA-16

Nine libraries were constructed using the 16S rRNA gene amplified from the DNA extracted from the different groundwater samples. Figure 1.0-1 shows the location of the individual sampling wells along with a visualization of the contamination area. A range of 20,549 to 143,844 bacterial 16S rRNA sequences were recovered from individual samples and used for community analyses by QIIME. OTUs were assigned by clustering sequences with over 97% sequence identity. A total of 23,815 OTUs were identified with relative low numbers (1000-4600) in the deeper aquifers R-18, R-47, R-63, CdV-16-4(i)p, CdV-16-2(i)r, and CdV-9-1(i), and high numbers (>10,000) for the alluvial aquifer at locations CdV-16-02659, CdV-16-02656, and the upper perched-intermediate aquifer at location CdV-16-1(i). Rarefaction curves were generated at 3% cutoff to make a comparison of species abundances among the nine samples (Figure 4.2-1, B). Only one of the curves, [CdV-9-1(i)], approached a plateau, suggesting that further sequencing would have resulted in more OTUs in the remaining eight samples. The nine samples can be grouped into different levels of species abundance: low level [R-47, R-63, CdV-16-4ip, CdV-16-2(i)r and CdV-9-1(i)], medium level [R-18 and CdV-16-1(i)], and high level (CdV-16-02659 and CdV-16-02656). These results are consistent and show that the alluvial wells have high microbial diversity compared with deeper groundwater samples.

A total of 58 bacteria phyla were identified indicating high microbial diversities in the TA-16 groundwater system. The high abundance and common existence of *Proteobacteria* in samples obtained from all nine groundwater sampling wells used in this study suggests that these microbes are members of the natural microbiome of the Los Alamos groundwater. *Proteobacteria* were ubiquitously present within the samples followed by *Bacteroidetes* and *Actinobacteria*. Members of *Verrucomicrobia*, *Actinobacteria*, *Planctomycetes*, *Nitrospirae*, *Acidobacteria*, TM7 (*Candidatus Saccharibacteria*), OP3 (*Omnitrophica*), and OD1 (*Parcubacteria*) also were detected as common populations shared by the nine samples (Figure 4.2-2). Identification of bacterial groups at lower taxonomic level revealed the presence of 997 genera. Genera *Pseudomonas*, *Rhodococcus*, *Sphingomonas*, *Methylotenera*, *Limnohabitans*, *Polaromonas*, *Perlucidibaca* of *Proteobacteria*, *Nodularia*, *Nocardia* of *Actinobacteria* and *Flavobacterium* of *Bacteroidetes* represented the major populations within the communities (Table 4.2-1). Species of *Rhodococcus* and *Pseudomonas,* which harbor effective RDX-degrading genes, and their abundances are shown in Figure 4.2-3. These two genera were present in all groundwater samples. The highest number of reads mapped to *Rhodococcus* was detected in CdV-16-4(i)p followed by CdV-16-2(i)r and R-18. In contrast, *Pseudomonas* reads were high in R-18, CdV-9-1(i) and R-47.

Other important species identified include two *sphingomonad*-related OTUs composing 26% of the total microbial population detected in CdV-16-2(i)r. The *sphingomonads* are known degraders of aromatic hydrocarbons in contaminated soils. They are found in a wide variety of environments, including marine sediments, deep subsurface sediments, plant rhizospheres, and in clinical samples. They are able to survive under low nutrient conditions and capable of metabolizing a wide variety of carbon sources. A number of strains have been isolated from contaminated environments, where they display bioremediation capabilities. *Limnohabitans* are abundant in a number of wells, including CdV-9-1(i), R-63, and CdV-16-02659. Species from this genus were isolated from freshwater lakes, reservoirs, and streams. *Polaromonas* were detected in CdV-16-4(i)p and R-47 at >5% of the total microbial population. Members of this genus are aquatic gram-negative, non-spore forming, non-motile coccus. Some strains are capable of growth with naphthalene as its sole carbon and energy source. *Nocardia ignorata*, a new agent of human nocardiosis isolated from respiratory specimens in Europe and soil samples from Kuwait, is abundant in CdV-16-2(i)r and CdV-16-4(i)p with abundances of 9.4 % and 22.3% respectively.

The two water samples from the alluvial wells CdV-16-02656 and CdV-16-02659 share a dominant OTU similar to *Nodularia spumigena* PCC 73104 (Table 4.2-1). *Nodularia* is a genus of filamentous nitrogen-fixing cyanobacteria and they occur mainly in brackish or saline waters. Some species produce toxins and are found in groundwater. Members of the genus *Simplicispira* are highly abundant in CdV-9-(1)i. They are gram-staining-negative rod-shaped bacteria that contain ubiquinone-8 (Q-8) as a major quinone. R-18 was found to contain *Perlucidibaca*, a genus of gram-negative motile bacteria with a polar flagellum, which belong to the class *Gamma-proteobacteria*. So far, this genus contains only a single freshwater living species. *Echloromonas* found in R-63 have rod-shaped cells and are found in aquatic habitats. They can degrade aromatic compounds such as toluene, benzoate, and chlorobenzoate. *Methylotenera* found in CdV-16-1(i) at 11.6% abundance include microbes capable of using single C1 compounds as sole sources of energy and carbon. Based on metagenomics surveys, *Methylotenera* species are ubiquitously detected in marine, freshwater, acid mine drainage, polluted soil, sedimentary rock, and glacier environments consistent with their important roles in global nutrient cycling. The *Flavobacterium* genus, also abundant in Cdv-16-1(i), includes about 130 nonpathogenic species and several species that cause fish diseases. *Flavobacteria* are found in soil and fresh water in a variety of environments including arsenic-contaminated groundwater. Strains of *Fluviimonas* abundant in Cdv-16-1(i) are aerobic, contain poly-β-hydroxybutyrate, are nonmotile, and consist of long rods. They represent a new family of *Cytophagaceae*. The genus *Albidiferax* also detected in Cdv-16-1(i) contains a single species, *A. ferrireducens,* which reduces iron.

4.3 Geochemical Factors Affecting RDX Degradation under Abiotic Conditions and Degradation Signatures

RDX degradation was examined in sealed vials by varying the presence of sediments and availability of oxygen. The data in Figure 4.3-1 show that RDX degradation under abiotic conditions is slow. There is no visible degradation when RDX is incubated in sealed reactors in the presence of oxygen and sediments in the dark. The data also show a slight decrease in RDX concentration in all vials labeled -oxygen and in the controls exposed to light. Sediments do not appear to affect RDX degradation. RDX degradation under -oxygen conditions is likely because of hydrolysis. Effectively, the -oxygen conditions were created by degassing the vials with argon gas for 20 min. The pH in the degassed vials was 8.6 and remained stable throughout the experiment, whereas the pH in the non-degassed vials remained near neutral. Analysis of the water samples by HPLC for degradation signatures indicates that for all the samples, the concentration of the degradation products MNX, DNX, and TNX is barely detectable. The HPLC data indicate the presence of unidentified compounds that are eluted early in the column.

4.4 Microbial Degradation of RDX under Aerobic and Anaerobic Conditions

Groundwater samples collected from the upper perched aquifer well Cdv-16-4(i)p were supplied with safflower oil and incubated under various conditions of oxygen availability. Controls without any nutrients were also set up under various oxygen availability. The data in Figure 4.4-1 show that RDX is most actively degraded under complete anaerobic conditions in the vials amended with safflower oil. The vials exhibited measurable microbial growth that was visible by the increase of the solution’s turbidity. Microscopic examination and cell counting confirmed the cell density increase. The sterile controls and the controls without safflower oil did not show any significant growth, and RDX degradation was not measurable. Microbial growth was strongest in vials amended with safflower oil and continually aerated. However, in the presence of oxygen, RDX degradation was inhibited. At week 5 of the incubation, RDX concentrations had decreased by about 80% under anaerobic conditions but had decreased by less than 20% in all other controls. HPLC analysis shows a significant variation of the ratio of the degradation products to RDX over time for the reactors under anaerobic conditions (Figure 4.4-1), which is consistent with the successive production of MNX, DNX, and TNX from RDX transformation. The ratios of MNX/RDX and DNX/RDX increased by the end of the first week and peaked (0.96 and 0.44 for MNX/RDX and DNX/RDX, respectively) in the third week. The decrease of MNX and DNX concentrations was then accompanied by an increase in TNX concentration. A steady increase was observed for NDAB over the incubating period. In the abiotic controls, RDX remained stable and no nitroso derivatives were produced. The ratios between RDX and its degradation products remain unchanged over five weeks (Figure 4.4-2).

5.0 DISCUSSION

Degradation products MNX, DNX, and TNX are commonly observed in groundwater. These products are known to be signatures of RDX degradation under strict anaerobic conditions (Table 1.0-1). They were also reported to be produced under reducing conditions by reduced iron minerals. Degradation products MNX, DNX, and TNX have been shown to be fairly stable under oxic conditions, and their transport properties are very similar to that of RDX (Heerspink et al., 2017). However, their detection in groundwater might not necessarily indicate that RDX is produced at the location of their detection. Effectively, in the absence of favorable degradation conditions, the degradation products MNX, DNX, and TNX can be transported long distances from the location where they formed, making it hard to assess RDX natural attenuation. However, as the experimental data show (Figure 4.4-1 and Figure 4.4-2), under active degradation conditions the ratios of MNX/RDX, DNX/RDX, and TNX/RDX increase significantly compared with the ratios observed when no degradation is occurring (Figure 4.4-2). When RDX is stable the concentrations of the degradation products remain low and no accumulation of the degradation products is observed. Figure 5.0-1 shows plots of the ratio of DNX/RDX using data from waters representative of the springs, the alluvial aquifer, and the perched-intermediate and regional aquifers. There is a slight and consistent increase in the ratios of DNX, MNX, and TNX to RDX in the alluvial aquifer compared with all other aquifers. The alluvial aquifer is only a few meters deep but has the highest variability in dissolved oxygen concentrations varying from 0.4 to 10 mg/L (Figure 2.1-1 A). By comparison groundwater from the deeper aquifers have a more consistent dissolved oxygen concentrations (Figure 2.1-1 B and C). Furthermore, the alluvial aquifer has a higher dissolved organic content on average (i.e., 2.7 mg/L) relative to that of the deeper aquifers, which varies from 5.0 to 0.7 mg/L.

Collectively the degradation products data, dissolved oxygen concentration, and availability of organic carbon suggest the alluvial aquifer might experience transient anaerobic conditions that could be conducive to RDX degradation. The deeper aquifers do not show any indication that anaerobic conditions might exist. However, the potential existence of micro-environments in which anaerobic conditions exist cannot be either excluded or supported. The data presented here suggest that an increase in the DNX, MNX, and TNX to RDX ratios could be used as a good indication of active RDX degradation. The data also indicate that the detection of low levels of degradation products cannot be considered an indication of active natural attenuation. More importantly, our data suggest that RDX is most likely degraded in the alluvial aquifer, which undergoes frequent transient, episodic geochemical conditions (c.f. Attachment 3, this compendium).

Microbial diversity data shows that groundwater at TA-16 harbors a diverse population of microbes. The alluvial aquifer showed the highest microbial diversity compared with the deeper aquifers. Uncultivable bacteria in TM7, OP3, and OD1 were also more abundant in the shallow aquifer compared with deeper aquifers. However, microbial data did not identify microbes that are known to degrade RDX under anaerobic conditions to account for the relatively elevated concentrations of the degradation products observed in the alluvial aquifer. Microbial diversity data were similar in the groundwater obtained from alluvial wells CdV-16-02659 and CdV-16-02656 (Figure 5.0-2). Table 4.2-1 lists the dominant OTUs (>5%) and their closest relatives found in the GenBank. The most dominant OTU (650048) shared by CdV-16-02659 and CdV-16-02656 showed a sequence identity of 76% to *Nodularia spumigena* PCC 73104. These data do not shed any light on the potential for RDX degradation by microorganisms present in the alluvial aquifer.

The deeper wells CdV-16-4(i)p and CdV-16-2(i)r, which are both screened in the upper perched aquifer at similar depth, were grouped together (Figure 5.0-2). These two wells also have very similar RDX concentrations of about 100 to 144 µg/L. Two dominant OTUs from CdV-16-4(i)p and CdV-16-1(i) that exhibit the highest RDX levels were most closely related to *Rhodococcus erythropolis* PR4 (NR_074622) and *Nocardia ignorata* DSM 44496, both with a sequence similarity of 100%. Since *Rhodococcus* are well-known RDX degraders and can use RDX as a nitrogen source, RDX in these two wells may have specifically enriched these species. However, the possibility cannot be ruled out that the abundance of this group is caused by other chemical components that might be enriching *Rhodococcus* in the groundwater. The degradation proceeds by denitration and ring cleavage and generates degradation products MEDINA, NDAB, nitrate, and formaldehyde. There are some indications from the HPLC analysis that NDAB and MEDINA compounds might be present in the groundwater samples obtained from the perched aquifer. However, their identification was inferred only from the retention time on the HPLC analysis and could not be confirmed by mass spectrometry analysis.

Studies of the factors that affect RDX degradation under abiotic conditions indicate that light exposure contributed to RDX degradation. Degradation was slow and only 15% of the RDX was degraded after 35 days (Figure 4.3-1). HPLC analysis did not show the appearance of any of the known degradation products: MNX, DNX, TNX, NDAB, and MEDINA. This is consistent with the scientific literature that indicates that RDX photo-decomposition by sunlight varies significantly based on the water composition (Felt et al., 2009). Very rapid RDX decomposition with a half-life of 9 to13 h was reported for clear water, and a decomposition of several years was reported for shallow but dark water (U.S. Army, 1980a, b). The main products of photo-degradation reported in the literature are formaldehyde and nitrosamines (Table 1.0-1). Degradation under abiotic conditions was also significant in samples that were purged with argon to remove dissolved oxygen. Degradation of about 30% of the initial RDX was observed in 35 d in the no-oxygen samples. The pH in these samples increased to about 8.6 as a result of the degassing process. The observed degradation is likely due to RDX hydrolysis, which is known to occur at a high pH. In fact RDX hydrolysis at a high pH is well documented in the literature, and the rate of RDX hydrolysis is much faster at pH values higher than 10 (Balakrishnan et al., 2003). Under the conditions used in this study, the increased pH to about pH 8.6 resulted in a slow but measurable RDX degradation. HPLC analysis of the solution over time did not show the accumulation of any of the known degradation products. This is consistent with the literature reports that describe the breakdown products to be ring cleavage products including 4-nitro-2,4-diazabutanal, NO2-, N2O, formaldehyde, and formic acid (Balakrishnan et al., 2003).

Degradation of RDX under biostimulated conditions in groundwater obtained from the perched aquifer is only important under strict anaerobic conditions. Degradation products that result from anaerobic degradation include MNX, DNX, TNX, and MEDINA. In the presence of oxygen, no measurable degradation was observed. This is consistent with the data from the scientific literature that shows that oxygen competes with RDX for electrons and hence inhibits RDX anaerobic degradation (Halasz et al., 2010; Indest et al., 2013). RDX degradation under oxic conditions was minimal in all our tests, indicating that the microbes present in the groundwater from Cdv-16-4(i)p are not using RDX as a nitrogen or a carbon source. This is consistent with the literature that shows that under biotic conditions oxygen is the most critical factor in RDX degradation. Biotransformation of RDX can be achieved under varied oxygen levels depending on the presence of specific microbes and abiotic factors. For instance, *Rhodococcus* strains effectively degrade RDX under aerobic conditions only, as they are not able to grow in the absence of oxygen. In contrast, *Pseudomonas* are facultative anaerobes that can degrade RDX under both conditions. Under abiotic conditions, iron promotes RDX degradation under anoxic conditions. The results of this study show that oxygen negatively impacts RDX degradation under biotic conditions at the Los Alamos site.

5.1 Additional studies and data gaps

The current study has demonstrated that (1) groundwaters at TA-16 contain a diverse population of microbes, some of which are known to possess the ability to degrade RDX, and that (2) biostimulation can create favorable conditions for RDX degradation. However, it is not clear if the native microbes are currently playing any role in RDX degradation. We believe that additional studies that specifically identify and quantify the occurrence of genes known to be involved in RDX degradation would be beneficial for determining if in situ biodegradation is occurring under ambient biogeochemical conditions at TA-16. We also suggest that a more detailed analysis and identification of small RDX degradation products (i.e., nitrite, nitrous oxide, ammonia, formate, formaldehyde) should be conducted to identify additional processes that could drive RDX degradation under biotic and abiotic conditions. The use of stable isotopes suggested in the U.S. Department of Energy review might be a valid approach. The current study did not attempt to compare the overall rate of RDX decay in the groundwater with the observed rates of RDX degradation from the laboratory studies. This approach is difficult because of the large differences in the time scales involved, days at most for the laboratory studies, and up to decades for groundwater flow. However, it would be beneficial to perform a study in which the evolution of the RDX concentrations in groundwater is analyzed by a flow and transport model that would include contributions from biotic and abiotic degradation processes including sorption/desorption processes. Rate constants for the different processes would have to be gathered from the literature and interpolated from the data provided in this report.

6.0 CONCLUSION

Microbial surveys of the different aquifers at TA-16 in Los Alamos (i.e., alluvial, perched-intermediate and regional aquifers) show a very diverse microbial population in all the wells tested. *Proteobacteria* were ubiquitously present in all the aquifers sampled, followed by *Bacteroidetes* and *Actinobacteria*. Members of *Verrucomicrobia*, *Actinobacteria*, *Planctomycetes*, *Nitrospirae*, *Acidobacteria*, TM7, OP3, and OD1 were also detected. The surveys also detected the presence of *Rhodococcus* and *Pseudomonas*, which harbor effective RDX degrading genes. The highest number of reads mapped to *Rhodococcus* was in CdV-16-4(i)p, followed by CdV-16-2(i)r. These two wells have the highest RDX concentration, suggesting these populations might have been enriched by RDX. *Pseudomonas* reads were high in R-18, CdV-9-(1)i, and R-47. The microbial diversity data is in good agreement with the groundwater chemistry that shows that the deeper aquifers are fairly oxic and are unlikely to support the activity of anaerobic bacteria. The alluvial wells, on the other hand, exhibit more variable dissolved oxygen concentrations, suggesting that these wells might undergo transient events with low oxygen content, which could be conducive to anaerobic microbial activity. Data from groundwater monitoring seem to indicate that at least qualitatively, the alluvial aquifer might have a much higher activity of microbially induced degradation of RDX than that of the deeper wells. The increase in the ratios of MNX/RDX, DNX/RDX, and TNX/RDX is a good measure of active microbial degradation of RDX overall. Taking into account the limitations of laboratory observations, which are usually of short duration and fail to capture processes that occur at much longer time scales in the subsurface, the results of this study seem to suggest that (1) RDX is primarily degraded by microbes in the alluvial aquifer, and (2) the detection of the RDX degradation products MNX, DNX, and TNX in the deeper aquifers is likely due to the transport of these compounds from the alluvial wells.

7.0 REFERENCES AND MAP DATA SOURCES

7.1 References

The following reference list includes documents cited in this report.

ATSDR (Agency for Toxic Substances and Disease Registry). "Toxicological Profile for RDX," www.atsdr.cdc.gov/toxprofiles/tp78.pdf (2012).

Balakrishnan, V.K., A. Halasz, and J. Hawari. "Alkaline Hydrolysis of the Cyclic Nitramine Explosives RDX, HMX and CL-20: New Insights into Degradation Pathways Obtained by the Observation of Novel Intermediates," *Environmental Science and Technology*, Vol. 37, No. 9, pp.1838–1843 (2003).

Caporaso, J.G., C.L. Lauber, W.A. Walters, D. Berg-Lyons, J. Huntley, N. Fierer, S.M. Owens, J. Betley, L. Fraser, M. Bauer, N. Gormley, J.A. Gilbert, G. Smith, and R. Knight. "Ultra-High-Throughput Microbial Community Analysis on the Illumina HiSeq and MiSeq Platforms," *The ISME Journal*, Vol. 6, pp. 1621–1624 (2012).

CRREL (Cold Regions Research and Engineering Laboratory). "Conceptual Model for the Transport of Energetic Residues from Surface Soil to Groundwater by Range Activities," ERDC/CRREL TR-06-18. www.dtic.mil/cgi bin/GetTRDoc?Location=U2&doc=GetTRDoc.pdf&AD=ADA472270 (2006).

EPA (Environmental Protection Agency). "EPA Handbook on the Management of Munitions Response Actions," EPA 505-B-01-001 http://nepis.epa.gov/Exe/ZyPURL.cgi?Dockey=P100304J.txt (2005).

EPA (Environmental Protection Agency). "Technical Fact Sheet–Hexahydro-1,3,5-trinitro-1,3,5-triazine (RDX)," https://www.epa.gov/sites/production/files/2014-03/documents/ffrrofactsheet_contaminant_rdx_january2014_final.pdf (2014).

Felt, D.R.; A. Bednar, C. Arnett, and R. Kirgan. "Bio-Geochemical Factors That Affect RDX Degradation," *Proceedings of the Annual International Conference on Soils, Sediments, Water and Energy*, Vol. 14, Article 17 (2009).

Gard, M.O., and B.D. Newman. "The High Explosives Source Term at TA-16," Los Alamos National Laboratory document LA-UR-05-9433, Los Alamos, New Mexico (2005).

Halasz, A., D. Manno, S. Strand, N.C. Bruce, and J.A. Hawari. "Biodegradation of RDX and MNX with Rhodococcus sp. Strain Biodegradation of RDX and MNX with Rhodococcus sp. Strain DN22: New Insights into the Degradation Pathway," *Environmental Science and Technology*, Vol. 44, pp. 9330–9336 (2010).

Hawari, J.A., T. Halasz, L. Groom, S. Deschamps, C. Paquet, C. Beaulieu, and A. Corriveau. "Photodegradation of RDX in Aqueous Solution: A Mechanistic Probe for Biodegradation with Rhodococcus sp.," *Environmental Science and Technology*, Vol. 36, pp. 5117–5123 (2002).

Heerspink B.P., S. Pandey, H. Boukhalfa, D.S. Ware, O. Marina, G. Perkins, V.V. Vesselinov, and G. WoldeGabriel. "Fate and Transport of Hexahydro-1,3,5-trinitro-1,3,5-triazine (RDX) and its Degradation Products in Sedimentary and Volcanic Rocks, Los Alamos, New Mexico," *Chemosphere*, Vol. 182, pp. 276–283 (2017).

HSDB (Hazardous Substance Data Bank). Cyclonite, https://www.toxnet.nlm.nih.gov/cgi-bin/sis/search2/f?./temp/~C8Ns37:1 (2013).

Hugerth L.W., H.A. Wefer, S. Lundin, H.E. Jakobsson, M. Lindberg, S. Rodin, L. Engstrand, and A.F. Andersson. "DegePrime, a Program for Degenerate Primer Design for Broad-Taxonomic-Range PCR in Microbial Ecology Studies" *Applied and Environmental Microbiology*, Vol. 80, pp. 5116–5123 (2014).

Indest, K.J., D.E. Hancock, C.M. Jung, J.O. Eberly, and W.W. Mohn. "Role of Nitrogen Limitation in Transformation of RDX (Hexahydro-1,3,5-trinitro-1,3,5-triazine) by Gordonia sp. Strain KTR9," *Applied and Environmental Microbiology,* 79, pp. 1746–1750 (2013).

LANL (Los Alamos National Laboratory). "Investigation Report for Water Canyon/Cañon de Valle," Los Alamos National Laboratory document LA-UR-11-5478, Los Alamos, New Mexico (2011).

LANL (Los Alamos National Laboratory). "2017 Update of the RDX Inventory Report," Los Alamos National Laboratory document LA-UR-18-21326, Los Alamos, New Mexico (2018).

NMED (New Mexico Environment Department). "Risk Assessment Guidance for Site Investigations and Remediation, Volume 1, Soil Screening Guidance for Human Health Risk Assessments," Hazardous Waste Bureau and Ground Water Quality Bureau, Santa Fe, New Mexico. (2017.)

Seth-Smith, H.M.B., S.J. Rosser, A. Basran, E.R. Travis, E.R. Dabbs, S. Nicklin, and N.C. Bruce. "Cloning, Sequencing, and Characterization of the Hexahydro-1,3,5-trinitro-1,3,5-triazine Degradation Gene Cluster from Rhodococcus rhodochrous," *Applied and Environmental Microbiology*, Vol. 68, No. 10, pp. 4764–4771 (2002).

Thompson, K.T., F.H. Crocker, and H.L. Fredrickson. "Mineralization of the Cyclic Nitramine Explosive Hexahydro-1,3,5- trinitro-1,3,5-triazine by Gordonia and Williamsia spp.," *Applied and Environmental Microbiology*, Vol. 71, pp. 8265−8272 (2005).

U.S. Army. "Environmental fate of RDX and TNT," U.S. Army Medical Research and Development Command document TR 81-538, Frederick, MD (author: H.C. Sikka et al.) (1980a).

U.S. Army. "Environmental Fate Studies on Certain Munition Wastewater Constituents: Phase II–Laboratory Studies," U.S. Army Medical Research and Development Command document ADA099256, Frederick, MD (author: Spanggord et al.) (1980b).

Walker, J.E., and D.L. Kaplan. "Biological Degradation of Explosives and Chemical Agents," *Biodegradation,* Vol. 3, Nos. 2–3, pp. 369–385 (1992).

Zhu S.H., J. Reuther, J. Liu, F.H. Crocker, K.J. Indest, L.D. Eltis, and W.W. Mohn. "The Essential Role of Nitrogen Limitation in Expression of xplA and Degradation of Hexahydro-1,3,5-trinitro-1,3,5-triazine (RDX) in Gordonia sp. Strain KTR9," *Applied Microbiology and Biotechnology,* Vol. 99, No. 1, pp. 459–467 (2014).

7.2 Map Data Sources

Hillshade; Los Alamos National Laboratory, ER-ES, As published; \\slip\gis\Data\HYP\LiDAR\2014\Bare_Earth\BareEarth_DEM_Mosaic.gdb; 2014

Structures; Los Alamos National Laboratory, KSL Site Support Services, Planning, Locating and Mapping Section; 06 January 2004; as published 29 November 2010.

Unpaved road;; Los Alamos National Laboratory, ER-ES, As published, GIS projects folder; \\slip\gis\GIS\Projects\14-Projects\14-0062\project_data.gdb; digitized_site_features; digitized_road; 2017

Paved Road Arcs; Los Alamos National Laboratory, FWO Site Support Services, Planning, Locating and Mapping Section; 06 January 2004; as published 29 November 2010.

Drainage channel; Los Alamos National Laboratory, ER-ES, As published, GIS projects folder; \\slip\gis\GIS\Projects\11-Projects\11-0108\gdb\gdb_11-0108_generic.mdb; drainage; 2017

Approximate extent of RDX contamination in deep perched groundwater, based on current knowledge; Los Alamos National Laboratory, ER-ES, As published, GIS projects folder; \\slip\gis\GIS\Projects\15-Projects\15-0041\shp\perched_aquifer.shp; 2016

Approximate extent of deep perched groundwater, based on current knowledgePerched intermediate groundwater elevation contour, 100-ft interval

Primary Electric Grid; Los Alamos National Laboratory, KSL Site Support Services, Planning, Locating and Mapping Section; 06 January 2004; as published 29 November 2010.

Perched intermediate groundwater elevation contour, 100-ft interval; Los Alamos National Laboratory, ER-ES, As published, GIS projects folder; \\slip\gis\GIS\Projects\15-Projects\15-0041\shp\sketch_contour.shp; 2016

May 2017 groundwater elevation, 50-ft contours; Los Alamos National Laboratory, ER-ES, As published, GIS projects folder; \\slip\gis\GIS\Projects\16-Projects\16-0027\project_data.gdb\contour_wl2017may_2ft; 2017

wqh_npdes_outfalls_pnt; WQH NPDES Outfalls; Los Alamos National Laboratory, ENV Water Quality and Hydrology Group; Edition 2002.01; 01 September 2003.

.

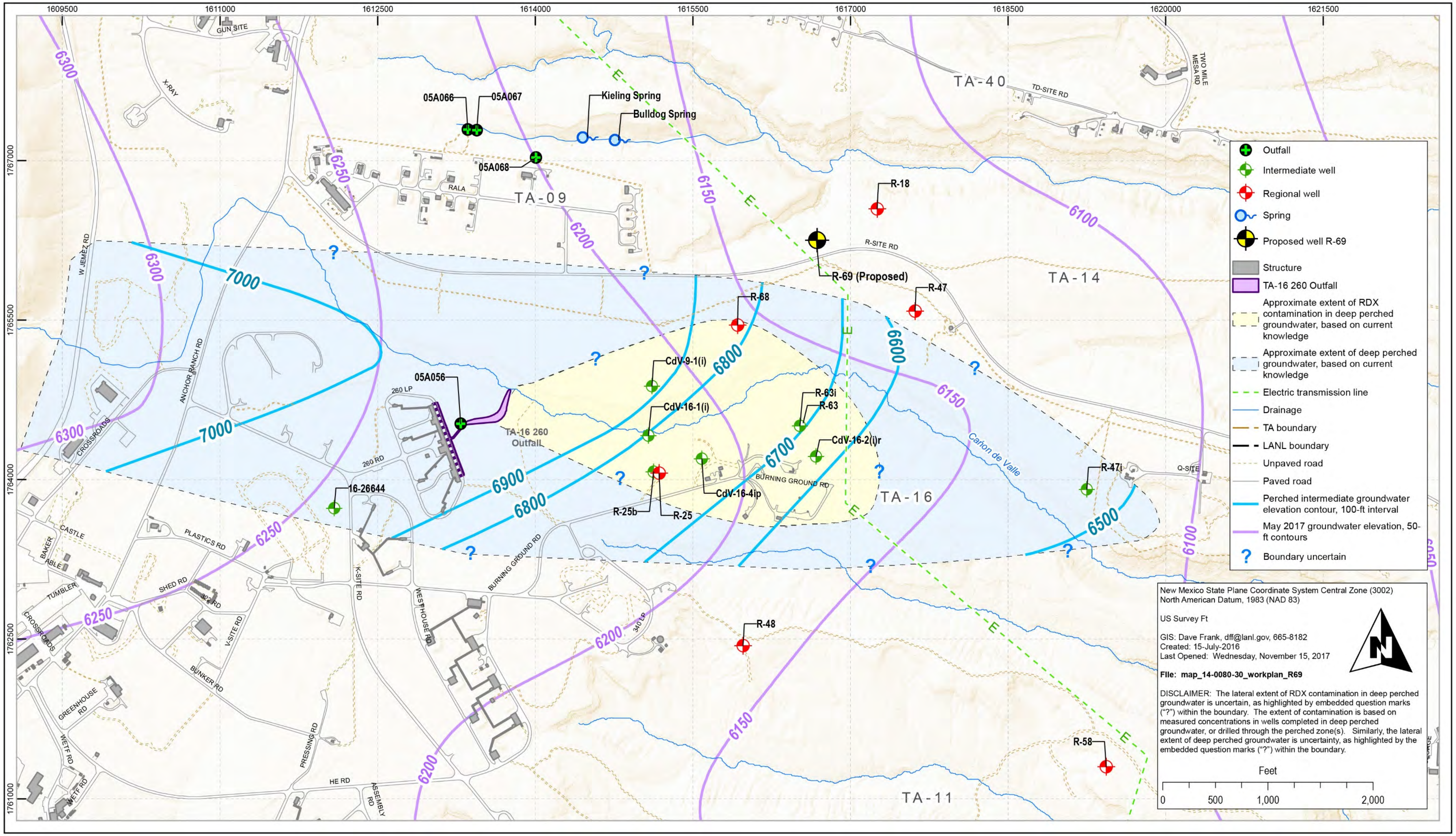

Figure 1.0-1 Location map of the 260 Outfall and the TA-16 study area. Monitoring wells are shown, along with the footprint representing the extent of the RDX contamination in the perched-intermediate and regional groundwater aquifers in the vicinity (shown in cyan).

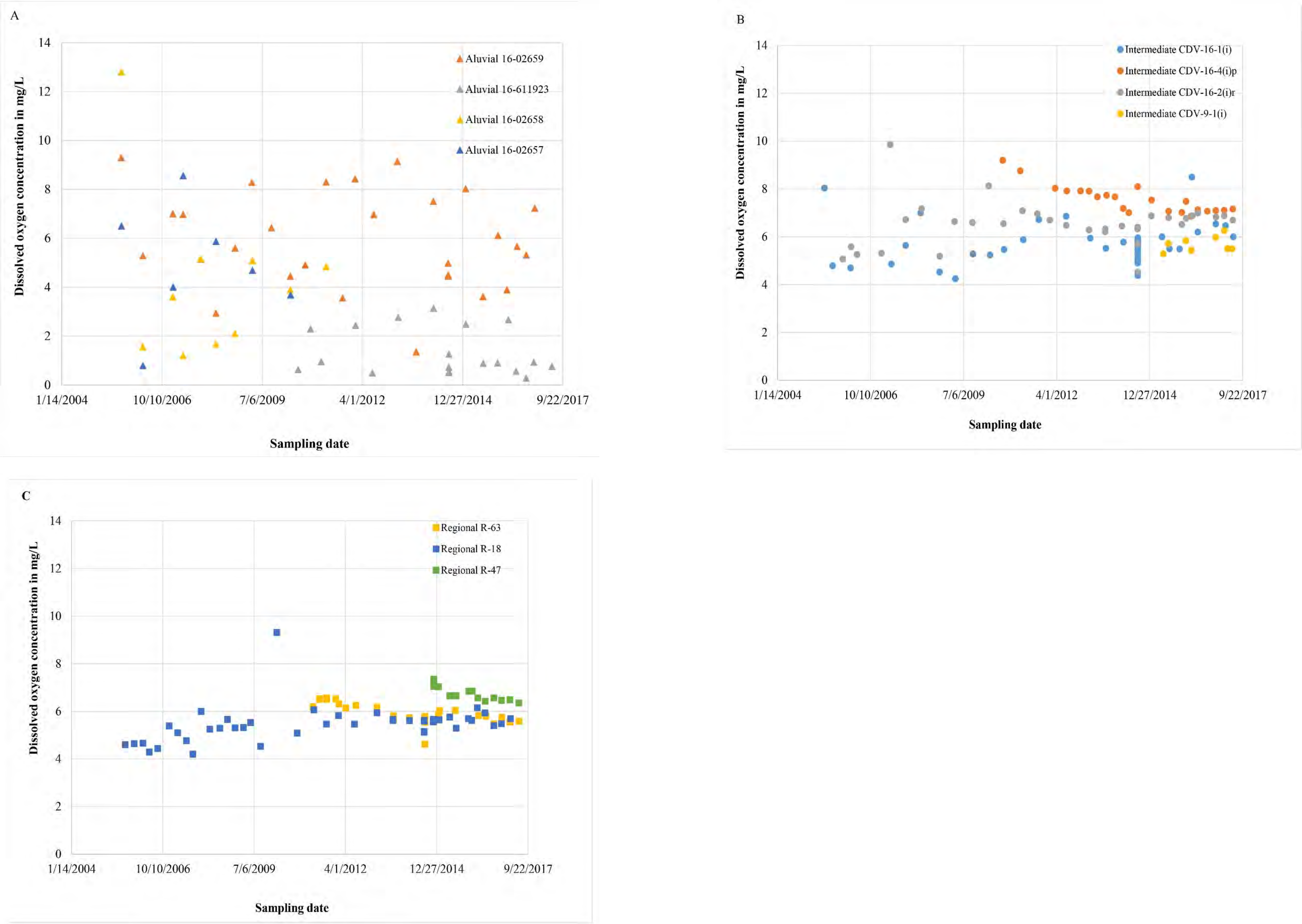

Figure 2.1-1 Dissolved oxygen concentrations in the different aquifers at TA-16 (A) alluvial aquifer Cdv-16-611923, Cdv-16-02659, Cdv-16-02658, and Cdv-16-02657; (B) intermediate perched aquifer Cdv-16-1(i), Cdv-16-4(i)p, Cdv-16-2(i)r, Cdv-9-1(i); and the regional aquifer (C) R-63, R-18, R-47

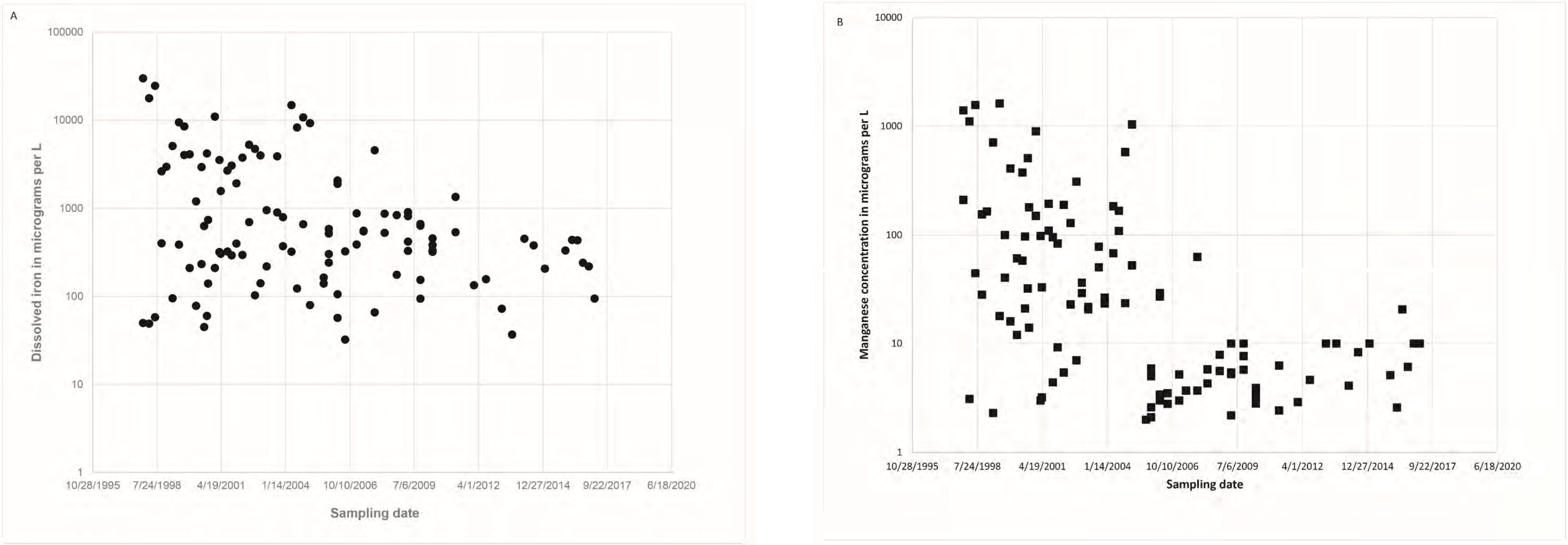

Figure 2.1-2 Plots showing the concentrations of iron and manganese in alluvial well Cdv-16-02656: (A) iron concentrations, (B) manganese concentrations. The location of the well is shown in Figure 1.0-1.

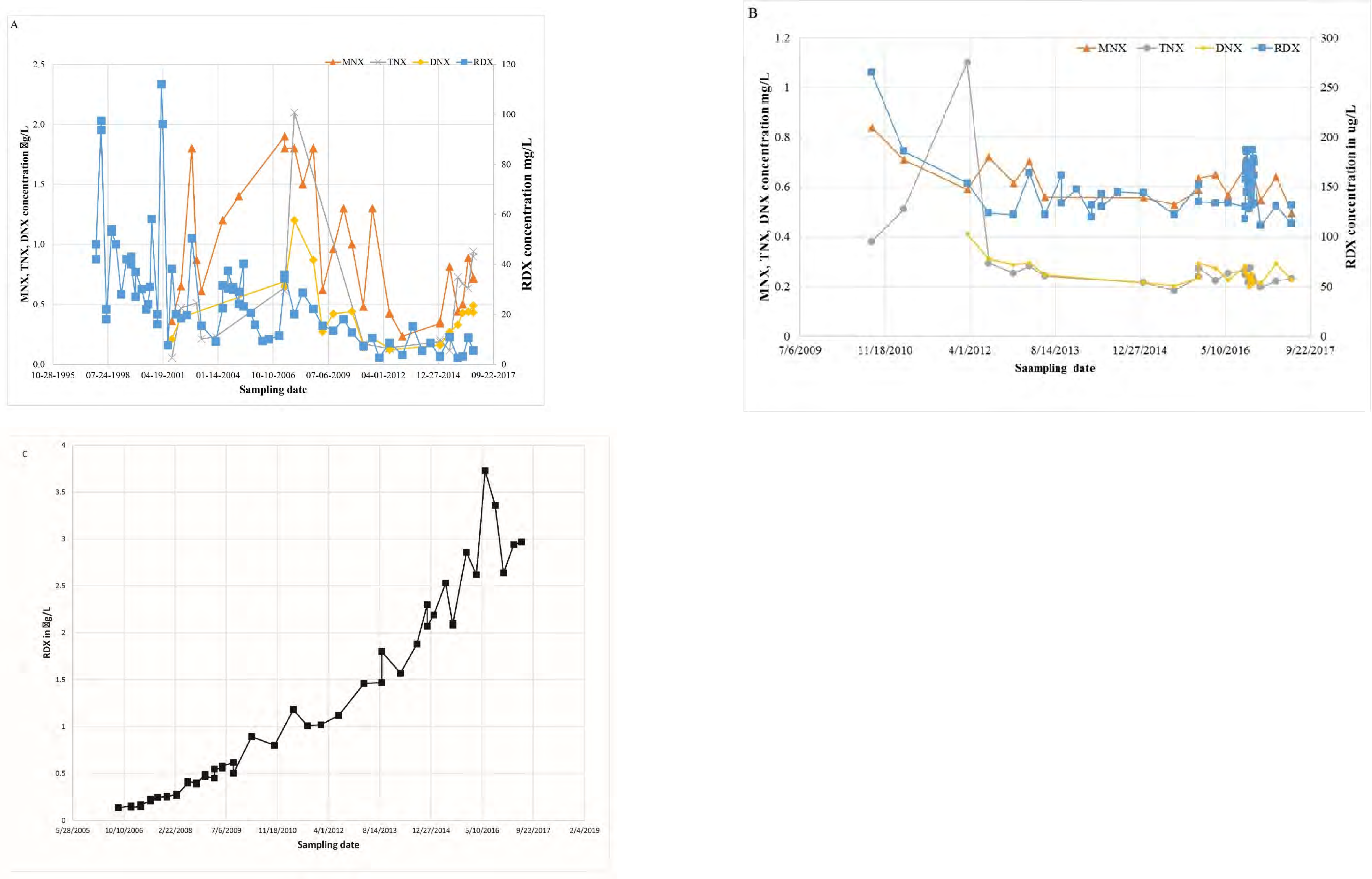

Figure 4.1-1 Plot showing RDX concentrations over time at location CdV-16-026559 (A) as a representative for the alluvial aquifer, location CdV-16-4(i)p (B) as a representative for the deep intermediate aquifer, and location R-18 (C) as a representative for the regional aquifer. The locations of CdV-16-026559, CdV-16-4(i)p, and R-18 relative to the RDX contamination are shown in Figure 1.0-1.

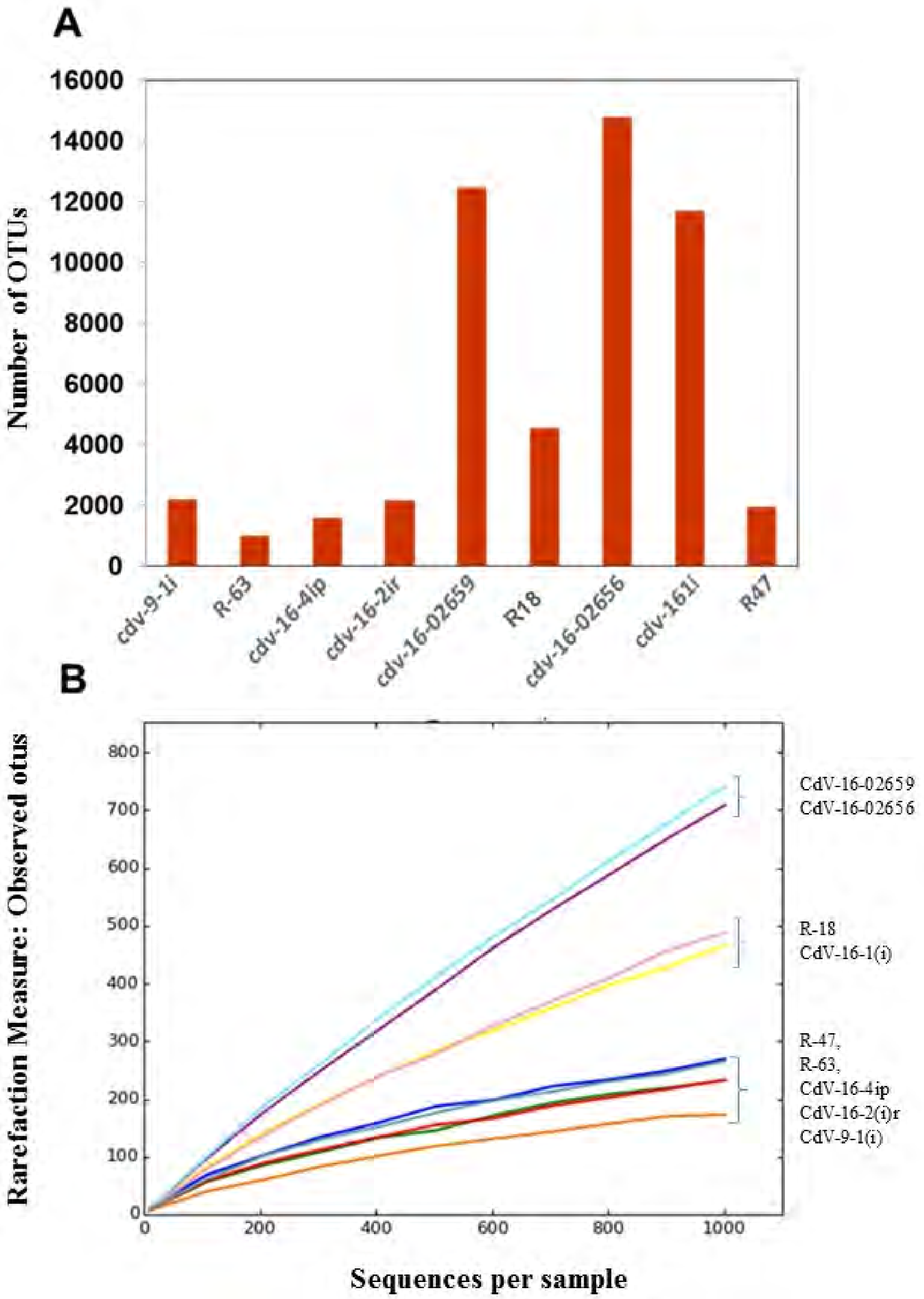

Figure 4.2-1 **Plot of curves for microbial diversity generated by QIIME for nine different locations within the alluvial aquifer (CdV-16-02659, CdV-16-022656), the deep intermediate aquifer [CdV-16-1(i), cdv-16-4(i)p, CdV-16-2(i)r, and CdV-9-1(i)], and the regional aquifer (R-18, R-47, R63). (A) Representation of number of OTUs per sampling location (200 to 1000 16S rRNA sequences were randomly selected and OTUs were calculated at a 97% cutoff). (B) Plot of the rarefaction curves of species richness.**

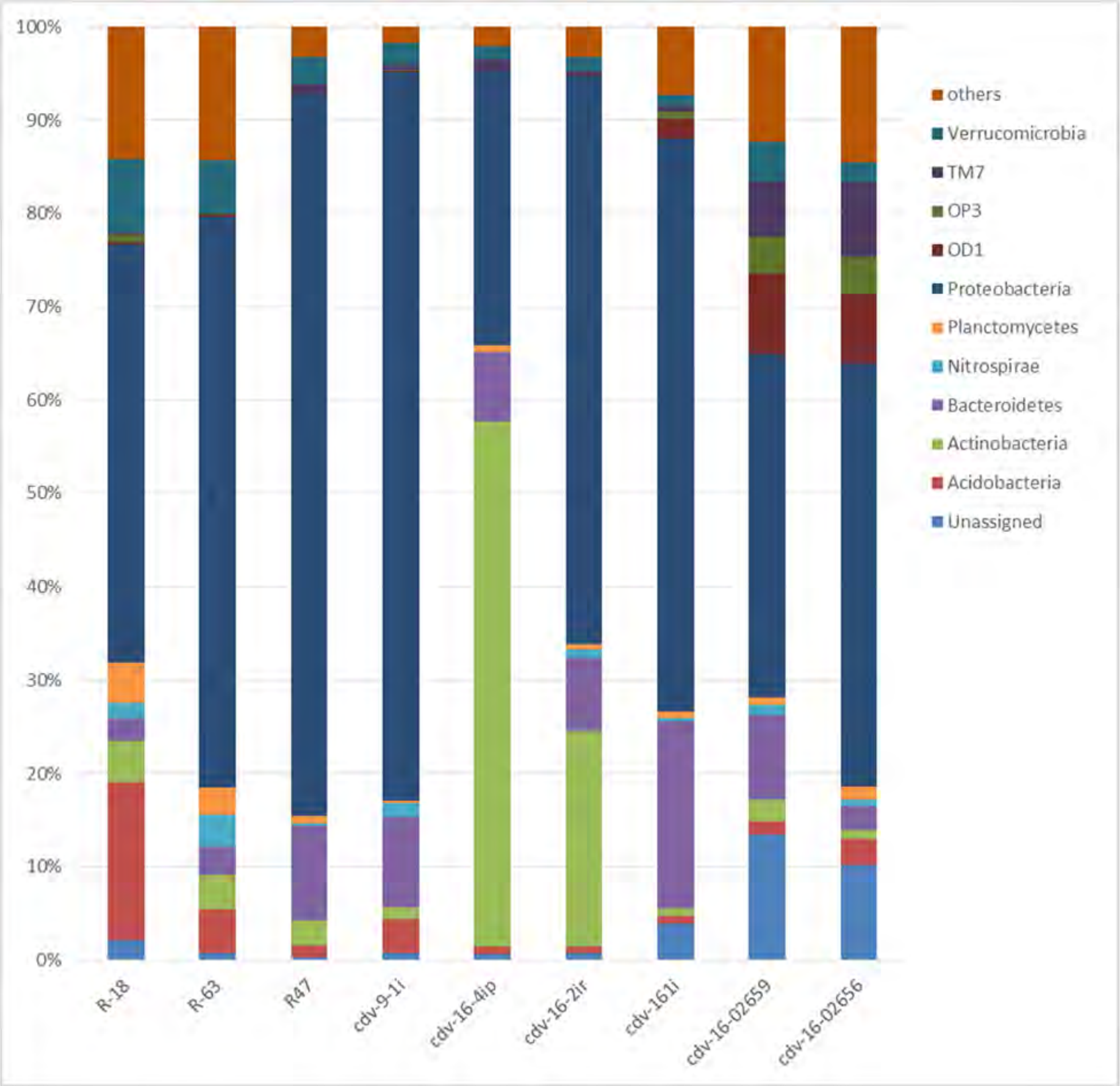

Figure 4.2-2 **Relative abundances of major bacterial phyla in TA-16 aquifer water samples. Data were analyzed using QIIME (Caporaso et al., 2012) and phyla numbers ≥ 1% were plotted.**

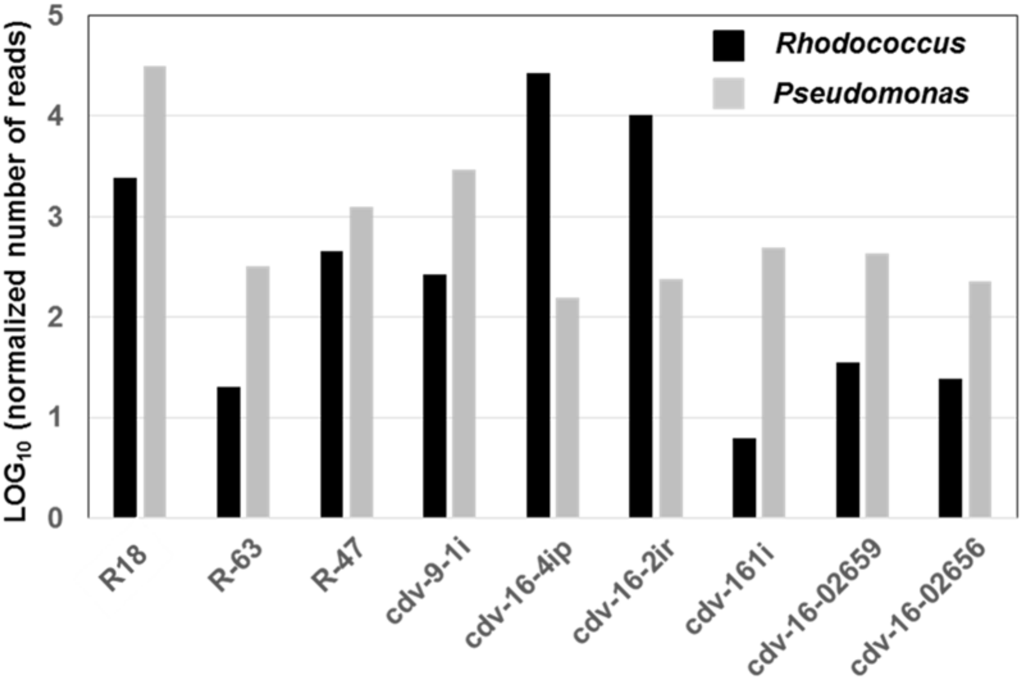

Figure 4.2-3 Relative abundances of Pseudomonas and Rhodococcus. Read numbers were normalized to 100,000 total reads for each sample.

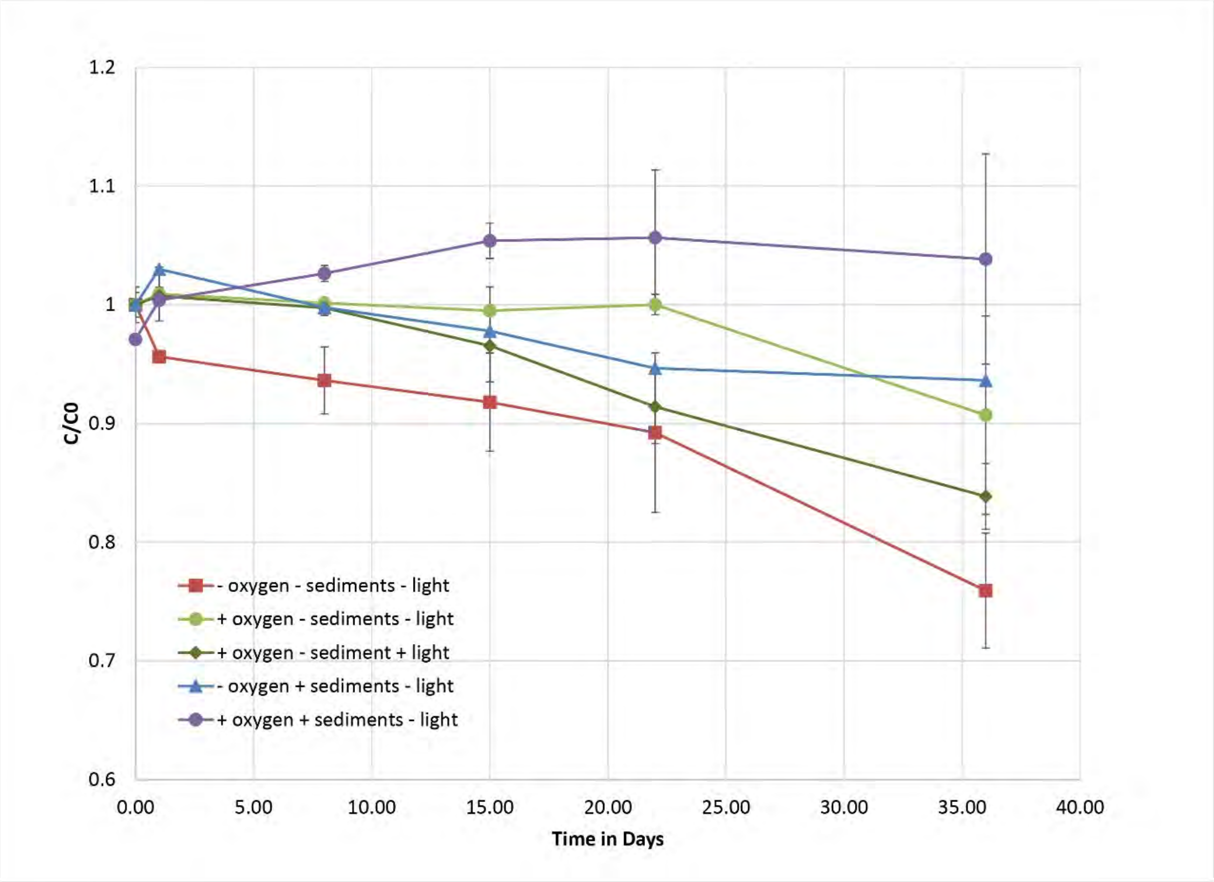

Figure 4.3-1 **Decomposition of RDX under abiotic conditions. The concentration is represented as C/C0 for all samples. The pH varied slightly between samples. The +Oxygen samples were not degassed and the pH remained at pH = 7.5. The pH in -Oxygen was pH = 8.4. + sediment samples received 1.0 g of sterilized sediments.**

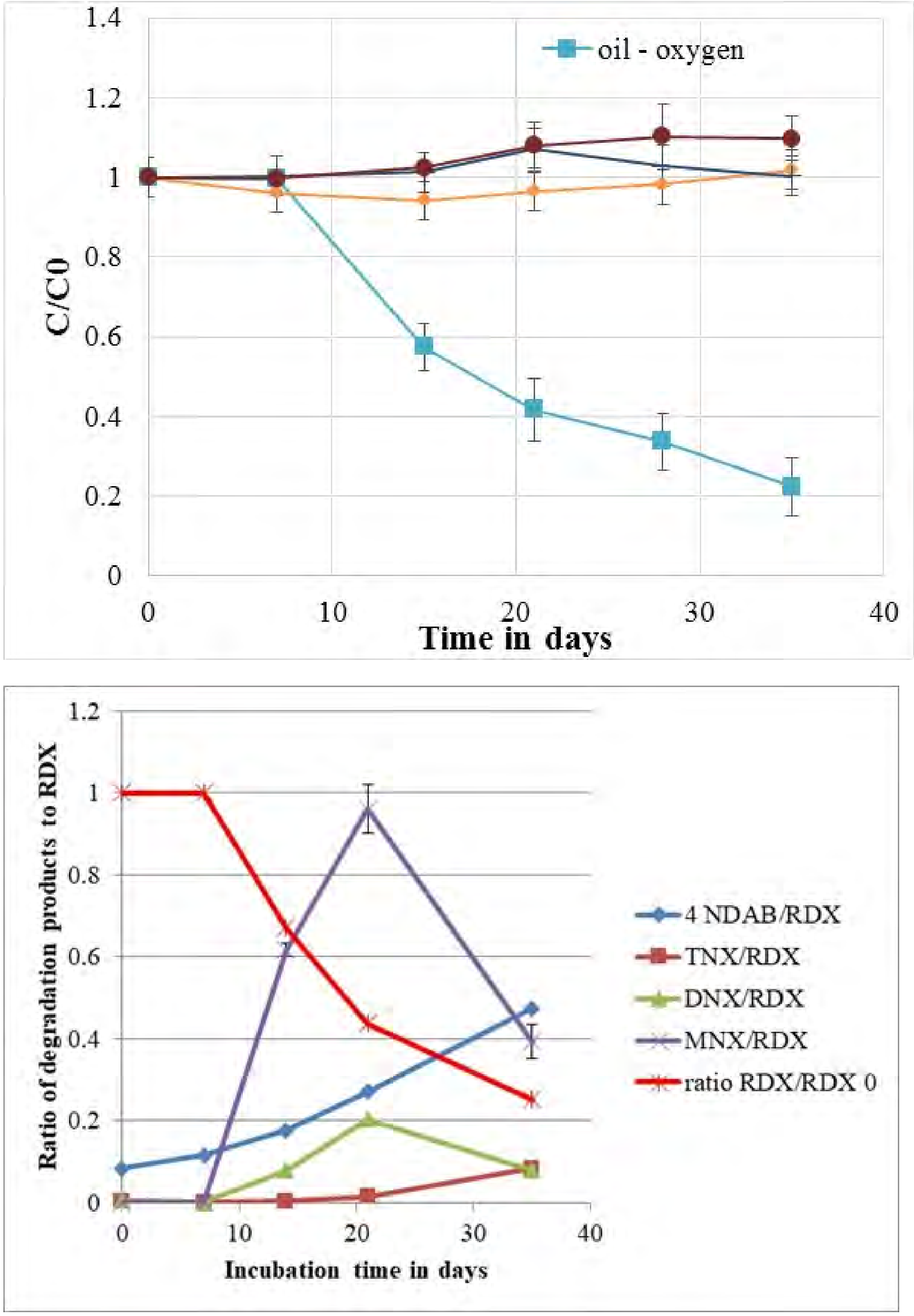

Figure 4.4-1 Rate of RDX degradation under stimulated conditions (aerobic and anaerobic) (left) and the ratio between the different degradation products and RDX as a function of time for reactors amended with 1 vol% safflower oil and incubated under strict anaerobic conditions (right). Error bars represent the standard deviation calculated by averaging values from three triplicates. Concentrations for each sample were normalized to the initial concentration C0 obtained from sampling the vials immediately after setting up the experiment. The initial pH was pH = 7.5 in the aerobic reactors and pH = 8.4 in the strict anaerobic reactors.

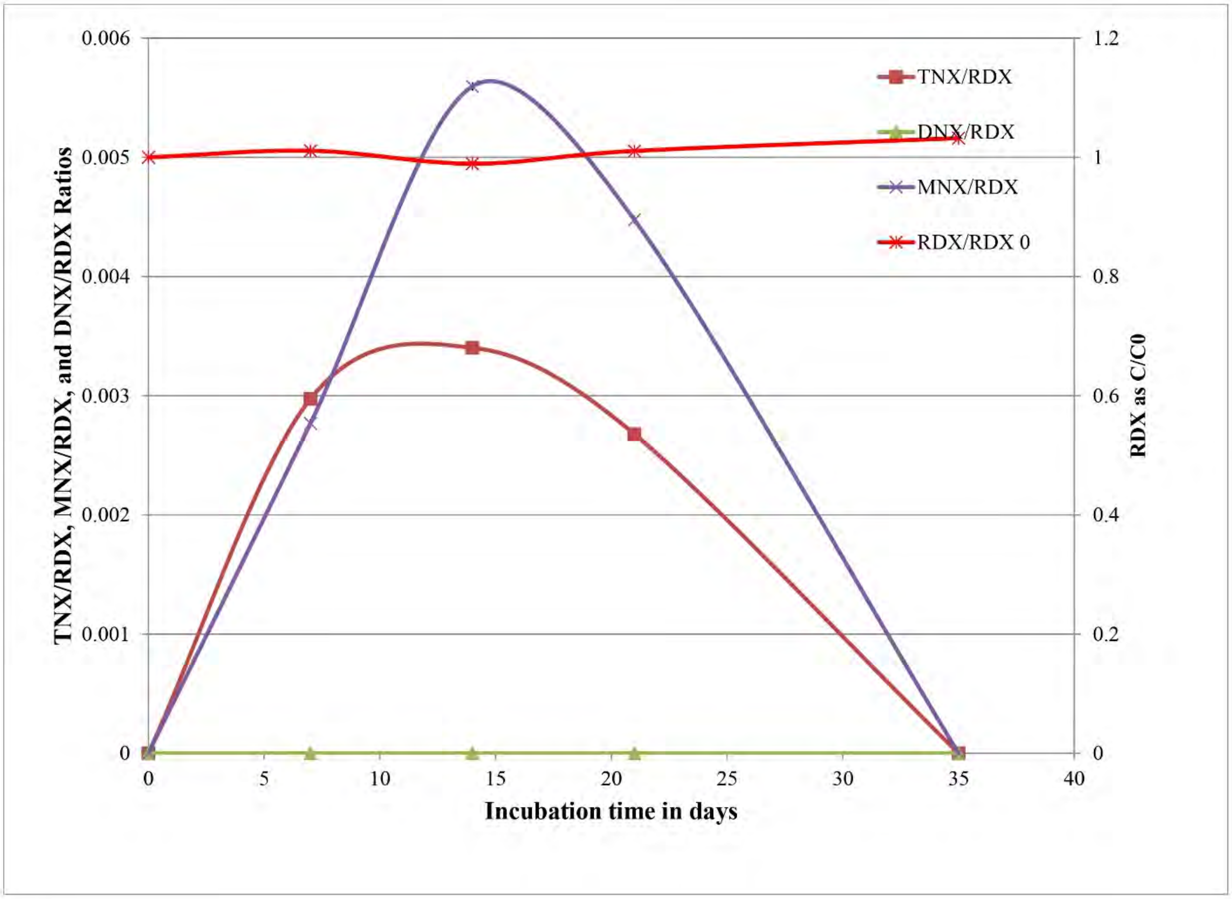

Figure 4.4-2 **Plot showing the evolution of the ratios between the different degradation products and RDX for the abiotic controls. Degradation products are represented as ratios of their concentration at the sampling time to the initial RDX concentration, and RDX is represented C/C0.**

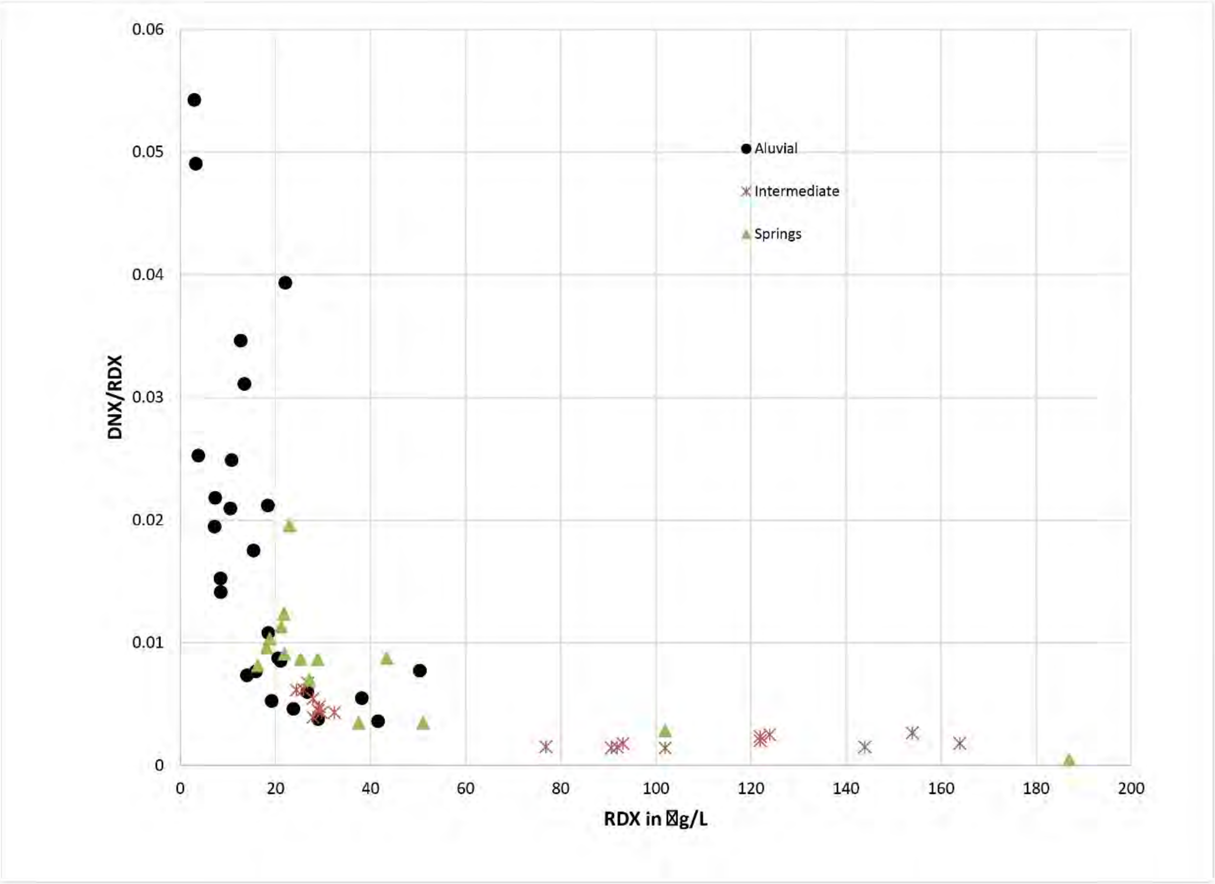

Figure 5.0-1 **Plot of the ratio of DNX/RDX as a function of the RDX concentration for springs, alluvial aquifer, intermediate aquifer, and the regional aquifer. The data were obtained by interrogating the database at www.intellusnm.com.**

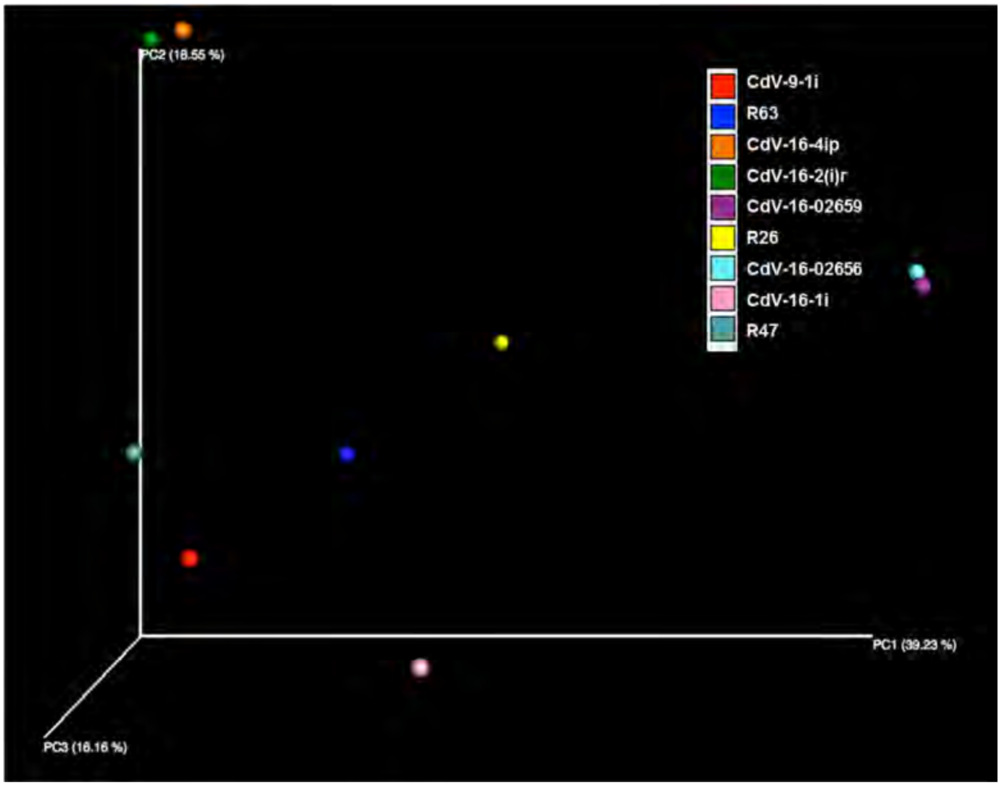

Figure 5.0-2 PCoA of the OTUs in the nine groundwater samples

Table 1.0-1
Summary of the RDX Degradation Pathways and Signatures of Degradation

Degradation Mode	Biotic				Abiotic		
	Aerobic		Anaerobic		Photo-degradation	Hydrolysis	Reduced iron and other minerals
Mechanism	Use as a carbon source	Denitration Ring cleavage	Nitro groups to reduction	Denitration Ring cleavage		Denitration and ring cleavage	Nitro groups reduction
Degradation Products	nitrite, formaldehyde, NDAB	MEDINA, NDAB, nitrate, formaldehyde, formate	MNX, DNX, TNX Ring cleavage	MEDINA methanol, nitrous oxide, carbon dioxide	formaldehyde, acetate, nitrous oxide, ammonia	nitrite, nitrous oxide, ammonia, formate, formaldehyde	DNX, MNX, and TNX

Table 2.2-1
Summary of Monitoring Wells Sampled for Microbial Profiling

Monitoring well	RDX (µg/L)	Ratios DNX/RDX, MNX/RDX, TNX/RDX	Screen depth in meters
Cdv-16-02659	0	0.05, 0.10, 0.054	2.3
Cdv-16-02656	0	Not detected	3.2
CdV-16-1(i)	25	0.006, 0.012, 0.009	190
CdV-16-4(i)p	130	0.002, 0.005, 0.002	338
CdV-16-2(i)r	52	0.004, 0.01, 0.007	259
cdv-9-1(i)	20	0.013, 0.006, 0.013	285
R-18	3.2	Not detected	413
R-63	0	Not detected	410
R-47	0	Not detected	409

Notes: The concentration of RDX and the ratios of RDX/degradation products are shown.
Data from sampling on 03/08/2017.

Table 4.2-1
Sequence Identity of the Dominant OTUs (>5%) Obtained from QIIME Analysis from the Bacterial Communities of the TA-16 Groundwater Samples

Sample ID (OTU number)	Relative Abundances	Related Bacterial Strain	Sequence Identify	Accession Number
CdV-16-4ip (573976)	30.6%	Rhodococcus erythropolis PR4	100%	NR_074622
CdV-16-4ip (40439)	22.3%	Nocardia ignorata DSM 44496	100%	NR_115832
CdV-16-4ip (819037)	5.6%	Polaromonas jejuensis NBRC 106434	100%	NR_114301
CdV-9-1(i) (846104)	9.7%	Limnohabitans australis MWH-BRAZ-DAM2D	99%	NR_125544
CdV-9-1(i) (576501)	12.1%	Simplicispira psychrophila NBRC 13611	99%	NR_113622
CdV-9-1(i) (617766)	8.0%	Limnohabitans parvus II-B4	100%	NR_125542
CdV-16-2(i)r (1108960)	17.2%	Sphingomonas alpina S8-3	100%	NR_117230
CdV-16-2(i)r (573976)	11.5%	Rhodococcus erythropolis PR4	100%	NR_074622
CdV-16-2(i)r (40439)	9.4%	Nocardia ignorata DSM 44496	100%	NR_115832
CdV-16-2(i)r (4336568)	8.8%	Sphingobium xenophagum BN6	100%	NR_026304
R18 (646549)	10.1%	Pseudomonas mohnii IpA-2	100%	NR_042543
R18 (524618)	6.4%	Perlucidibaca piscinae IMCC1704	97%	NR_043919
R47 (4478803)	21.6%	Algiphilus aromaticivorans DG1253	93%	NR_115808
R47 (819037)	9.2%	Polaromonas jejuensis NBRC 106434	100%	NR_114301
R63 (463546)	8.0%	Limnohabitans planktonicus II-D5	99%	NR_125541
R63 (591986)	6.0%	Dechloromonas aromatica RCB	99%	NR_074748
CdV-16-1(i) (802011)	11.6%	Methylotenera versatilis 301	100%	NR_074693
CdV-16-1(i) (960076)	9.3%	Flavobacterium succinicans DSM 4002	100%	NR_118478
CdV-16-1(i) (OTU448)	6.8%	Fluviimonas pallidilutea TQQ6	96%	NR_117642
CdV-16-1(i) (578572)	6.7%	Albidiferax ferrireducens T118	100%	NR_074760
CdV-16-02656 (650048)	5.4%	Nodularia spumigena PCC 73104	76%	NR_115707
CdV-16-02659 (650048)	6.1%	Nodularia spumigena PCC 73104	76%	NR_115707
CdV-16-02659 (617766)	5.6%	Limnohabitans parvus II-B4	100%	NR_125542

LA-UR-18-21326
March 2018
EP2018-0024

RDX Degradation in Sediments Treated Both Chemically and with Biostimulant Amendments

Attachment 7

Los Alamos
NATIONAL LABORATORY
EST. 1943

Prepared by the Associate Directorate for Environmental Management

EXECUTIVE SUMMARY

The high explosive RDX (hexahydro-1,3,5-trinitro-1,3,5-triazine) has previously been demonstrated to undergo very little to no attenuation when it has migrated to the deep intermediate aquifer and regional aquifer. This study involved examining alternative treatment options to enhance in situ RDX degradation. Batch and column experiments were performed to examine RDX degradation by sediments treated chemically using sodium dithionite, potassium permanganate, and sodium bicarbonate. RDX degradation was also examined in columns packed with sediments and biostimulated by the addition of molasses and safflower oil. The experiments were conducted using representative sediments from the Puye Formation, a thick heterogeneous formation underlying the Bandelier Tuff. Groundwater from the perched-intermediate aquifer at Technical Area 16 at Los Alamos National Laboratory was used as the source water for the experiments. RDX degraded within a few hours in all sediment samples treated chemically in batch testing. However, under continuous flow conditions in columns pretreated with the same chemicals, the sediments treated with sodium dithionite were the only sediments that had a complete RDX degradation. RDX reached the injection concentration after 2 and 4 pore volumes in the potassium permanganate and alkaline treatments, respectively, and over 50 pore volumes in the sodium dithionite treatment. All chemical treatments resulted in a transient pulse of elevated dissolved metals and anions, which was attributed to either partial dissolution of the mineral species in the sediments or desorption of adsorbed metals caused by the excessive concentrations of sodium and potassium present in the pretreatment solutions. No known degradation products could be identified in the column effluents. RDX attenuation capacity in the biostimulated columns was not very high. RDX reached the injection concentration after 6 pore volumes in the molasses column. The column biostimulated by safflower oil clogged after 4 pore volumes. Degradation products MNX (hexahydro-1-nitroso-3,5-dinitro-1,3,5-triazine), DNX (hexahydro-1,3-dinitro-5-nitro-1,3,5-triazine), and TNX (2,4,6-trinitroxylene) were visible in the biostimulated column effluents. Low attenuation capacity in the biostimulated columns is attributed to the rapid oxygenation of the columns' sediments in the absence of a carbon substrate.

CONTENTS

Figures

Tables

1.0 INTRODUCTION

High explosives (HE), including TNT (2,4,6-trinitrotoluene), HMX (high melting explosive, octahydro-1,3,5,7-tetranitro-1,3,5,7-tetrazocine), and RDX (hexahydro-1,3,5-trinitro-1,3,5-triazine) are common environmental contaminants at military testing facilities and national laboratory research sites. These contaminants were introduced into the environment as effluents from manufacturing and testing of weapons components containing HE (Clark and Boopathy, 2007; Dong, 2006; Brannon and Pennington, 2002; Newman et al. 2007; LANL 2011). Los Alamos National Laboratory (LANL or the Laboratory), which developed and tested weapons components containing HE materials, released effluents contaminated with HE compounds including RDX, TNT, and HMX from processing facilities to holding ponds and Cañon de Valle at Technical Area 16 (TA-16) (LANL 2011). Historical records tracking effluents from machining operations at TA-16 Building 260 and inventory evaluation efforts have estimated that between ~1500 and 3600 kg of RDX are still present in the environment at TA-16 (see Attachment 1 of this compendium, "2017 Update of the RDX Inventory Report"). The RDX contamination is present in surface sediments in the alluvium within Cañon de Valle, as well as in the perched-intermediate aquifer and the regional aquifer in the vicinity of the Building 260 Outfall. Figure 1.0-1 shows the location of the Building 260 Outfall and the study area in TA-16 and the estimated lateral extent of RDX contamination in the perched-intermediate aquifer. The figure also shows the monitoring wells used to monitor the RDX contamination.

Of the compounds released from the 260 Outfall, RDX is of particular concern because of its mobility in groundwater and because it exceeds the New Mexico Environment Department (NMED) drinking water screening level of 7.02 µg/L in the perched-intermediate and regional aquifers. Remediation efforts were undertaken by the Laboratory between 2000 and 2009 to remove sediments contaminated with RDX directly below the 260 Outfall. This remediation process removed a significant amount of RDX and reduced the concentration of RDX in the alluvial aquifer (LANL 2011). However, RDX contamination above the NMED screening level persists in the perched-intermediate aquifer at concentrations ranging from 20 to 170 µg/L. RDX is also detected in the regional aquifer at concentrations ranging from trace levels to ~17 µg/L.

Natural attenuation studies have found indications of active biological degradation of RDX as indicated by the detection of degradation products MNX, DNX, and TNX (see Attachment 6 of this compendium, "Characterization of the Microbial Population and RDX Degradation in Groundwater at Technical Area 16"). However, these studies have determined that for RDX and its degradation products—MNX, DNX, and TNX—degradation occurs only in the alluvium system. These studies suggest that RDX remains stable in the deep aquifers. In addition, RDX transport studies (Heerspink et al. 2017) showed that RDX and its degradation products transport conservatively in sediments representative of the contaminated aquifers at TA-16. These findings are consistent with the literature and emphasize the persistence and mobility of HE compounds, especially RDX, in the environment. Often, in situ remediation options using chemical or biological amendments may be considered as potential corrective actions for RDX remediation in groundwater.

The effectiveness of in situ remediation technologies for RDX has been extensively researched by laboratory and field-scale deployments of both chemical and biological treatments (Kalderis, 2011). Bench-scale studies have shown that sodium dithionite (Szecsody et al. 2001), potassium permanganate (Adam et al. 2004, Chokejaroenrat et al. 2011), and to a lesser extent alkaline hydrolysis (Heilmann et al. 1996) were effective at degrading RDX. The majority of these studies focused on batch or slurry type reactor tests, but few have also used treatments in continuous flow systems. Pilot field treatments are rare but have been conducted to test in situ RDX remediation. A pilot field test of the permanganate treatment was demonstrated at the Nebraska Ordnance Plant, where a curtain of permanganate was created between wells in an extraction/injection system. While in situ distribution of the treatment was not uniform, permanganate was shown to degrade 70% to 80% of RDX in monitoring wells near the extraction/injection system (Albano et al. 2010). No studies are known to have examined the efficiency of sodium dithionite treatments or alkaline hydrolysis at a large scale. Bioremediation of RDX has been studied at both the laboratory and field scales. Wani et al. (2002) demonstrated that biostimulation with carbon sources, including acetate and ethanol, could promote RDX biodegradation in column studies. In the system demonstrated, the addition of a carbon source promotes anaerobic metabolic processes and RDX is used as a terminal electron acceptor to support microbial respiration (Kalderis et al. 2011, Livermore et al. 2013). Bioremediation of RDX via biostimulation has also been shown to be effective at the field scale using molasses and acetate (Payne et al. 2013). At the field scale this process has been shown to shift the population of the microbial community towards groups of microbes capable of metabolizing RDX (Livermore et al. 2013). While both biological and chemical remediation schemes have been shown to be effective, the effectiveness of the treatment is significantly influenced by the site-specific hydrologic, geochemical, and microbial conditions.

The focus of this study was to test the viability of potential chemical and biological treatments for the in situ remediation of RDX under the conditions of the deep perched groundwater system at TA-16. Three potential chemical in situ treatments were tested in sealed batch reactors and under continuous flow in columns packed with sediments selected as representative materials of the deep-perched aquifer below TA-16. These treatments consisted of a chemical reduction treatment using sodium dithionite, an oxidative treatment using potassium permanganate, and an alkaline hydrolysis treatment by carbonate/bicarbonate solution buffered at a pH of 9.9. In addition, RDX biodegradation was studied under continuous flow in columns packed with sediments representative of the TA-16 area. The data for the batch and column studies will be presented along with a discussion of the effect of the different treatments on the biogeochemical conditions of groundwater.

2.0 MATERIALS AND METHODS

2.1 RDX Contamination Location

The TA-16 study area is located near the western edge of the Pajarito Plateau on a mesa where alluvial fan deposits overlie a thick, mostly unsaturated interval of the Bandelier Tuff (Figure 2.1-1). RDX is located in both saturated and unsaturated environments and depths ranging from a few meters in the alluvial sediments down to 400 m reaching the regional aquifer (Figure 2.1-2). The “2017 Update of the RDX Inventory Report” (Attachment 1 of this compendium) found that the most significant RDX mass persists in the upper perched groundwater aquifer at depths from 150 to 200 m and in the regional aquifer groundwater at depths of 300 to 400 m, with an estimated 1500 to 2600 kg of RDX in perched-intermediate groundwater, and 35 to 400 kg of RDX in the regional aquifer. RDX is also present in the shallow alluvial sediments and in the unsaturated Bandelier Tuff beneath the surface at concentrations ranging from tens to hundreds of kilograms (Attachment 1 of this compendium).

2.2 Geochemical Conditions at the Contamination Area at TA-16

The Puye Formation, which sits directly beneath the Bandelier Tuff at depths from 150 to 400 m, is light-brown, consolidated, matrix-supported, silty sandstone that contains minor angular dacite fragments up to 4 cm in size. At the regional aquifer depths of 300 to 400 m, the Puye Formation consists of coarse to medium-gray sandstone, poorly sorted, and matrix supported. It contains dacite, pumice, and other rock fragments. The matrix is tuffaceous and glassy, mixed with minor quartz and feldspar crystals. The groundwater chemistry in the perched-intermediate aquifer and regional aquifer are very similar. The groundwater is well oxygenated with dissolved oxygen concentration varying between 5 and 7 mg/L, and the oxidation-reduction potential (ORP) varies between 118 and 180 mV. Total organic carbon is very low and varies between 0.50 and 0.69 mg/L. The pH varies between 6.50 and 8.10 and the alkalinity CO_3^{2-}+HCO_3^-) is 52 mg/L. Recent analysis of groundwater from monitoring well CdV-164ip showed the following results: Cl^- (9.58 mg/L), F^- (0.10 mg/L), NO_3^- as nitrogen (1.01 mg/L), SO_4^{2-} (5.76 mg/L), and PO_4^{-} (0.09 mg/L), and the major cations consisted of Na^+ (17.09 mg/L), Ca^{2+} (9.61 mg/L), K^+ (1.2 mg/L), Mg^{2+} (3.17 mg/L), and Si^{4+} (48 mg/L). Iron (100 µg/L) and manganese (7.54 µg/L) concentrations are relatively low. The major anion concentrations in the regional aquifer are slightly different as indicated by a recent analysis of groundwater from R-18, with the following results: Cl^- (1.37 mg/L), F^- (0.08 mg/L), NO_3^- as nitrogen (0.59 mg/L), SO_4^{2-} (2.0 mg/L), and PO_4^{2-} (0.04 mg/L), and the major cations consisted of Na^+ (8.87 mg/L), Ca^{2+} (10.7 mg/L), K^+ (1.23 mg/L), Mg^{2+} (3.0 mg/L), and Si^{4+} (58 mg/L), Fe (100 µg/L), and Mn (10 µg/L).

2.3 Groundwater Sampling and Sample Preservation

All treatment experiments described in this report used groundwater samples obtained from TA-16 groundwater monitoring well CdV-16-4ip, which is completed within the perched-intermediate aquifer (Figure 1.0-1). The water samples were obtained from the Puye Formation screen located between 248 and 268 m below ground surface (bgs) (Figure 2.1-2). This well has been monitored for groundwater parameters since its completion in August of 2010 (LANL 2011). RDX concentration in the water was 160 µg/L at the time the water samples were obtained. There were also trace levels of MNX, DNX, and TNX, which were all at about 1 µg/L. The water samples were stored in 20-L plastic carboys at 4°C in the dark. Water used in the pretreatments of the batch and columns was sterilized by filtration though 0.2-µm filters and treated with activated carbon to remove residual RDX and its degradation products. Water used in the batch experiments was sterilized by filtration and treated with activated carbon to remove any organic compounds and spiked with RDX to the desired concentrations. Water used in the pretreatment of the column sediments was also sterilized by filtration and treated with activated carbon, while water used in the evaluation of the attenuation capacity of the columns used untreated water spiked with RDX to the desired concentration. All water was left aerated to accurately represent the oxic environment observed in the deep perched-intermediate aquifer.

2.4 RDX Degradation by Chemical Treatments in Batch Reactors

Bench-scale batch experiments were conducted to test the ability of sediments treated chemically to degrade RDX. Approximately 25 g of sediments from the Puye Formation were placed in two-part centrifuge tubes with built-in filters. Five sets of triplicate tubes were prepared to test different chemical treatments. Two triplicate tubes were equilibrated with 0.20 M $NaHCO_3/Na_2CO_3$ adjusted to pH 9.5 and then treated with a 1.0-mM sodium dithionite solution and 5.0-mM potassium permanganate solution respectively. An additional three triplicate tubes were equilibrated with 0.20 M $NaHCO_3/Na_2CO_3$ adjusted to pH 9.5, pH 10.0, and pH 11.25 respectively. The sediments were saturated with 8.0 mL of the treatment solution and equilibrated for 24 h. After 24 h, the pore water in equilibrium with the sediments was removed by centrifugation. The sediments were then washed with 8 mL of clean CdV-16-4ip water to remove any excess chemicals from the treatment. The wash water was removed via centrifugation, and 8 mL of a groundwater from the CdV-16-4ip solution containing RDX at 1000 µg/L was added to each centrifuge tube. The alkaline tubes received solutions of groundwater from CdV-16-4ip with 1000 µg/L RDX in 0.10 M $NaHCO_3/Na_2CO_3$ adjusted to either pH = 9.5, pH = 10, or pH = 11.25. The initial liquid:solid ratio was maintained constant for all samples.

The tubes were sampled periodically by removing water via centrifugation. Excess centrifuged water was pipetted back on the sediments. Permanganate- and dithionite-treated sediments were sampled every hour for 6 h, then daily for three days. The alkaline treated sediments were sampled once daily for one week. The preparation of dithionite solutions, as well as sampling of the dithionite reactors, was completed in a glove bag purged under vacuum and filled with argon. Throughout the duration of the experiment, reactors were kept at room temperature (23.5°C), in the dark on a shaker table set at 50 revolutions per minute (rpm). Along with the experimental reactors (15), 5 control tubes were prepared by treating empty centrifuge tubes with the 5 treatment solutions and then washed once with clean CdV-16-4ip water. These centrifuge tubes were filled with groundwater from CdV-16-4ip and used as controls to account for RDX degradation by the centrifuge tubes' walls in the absence of sediments. An additional control experiment was performed by adding 1000 µg/L of RDX to a 2-morpholin-4-methylethanesulfonic acid– (MES-) buffered acidic solution, adjusted to pH 4.38. Samples from the batch experiments, as well as the controls, were frozen upon sampling to preserve them from further degradation.

2.5 RDX Attenuation Degradation in Columns Filled with Aquifer Sediments Treated Chemically

A set of column experiments was performed to study the degradation of RDX in sediments treated by sodium dithionite, potassium permanganate, and carbonate/bicarbonate solutions. Chromaflex glass columns (Kible Chase), 30 cm in length and 1cm in diameter, were dry-packed with the Puye Formation sediments described above. Sediments were sieved to select grain sizes between 75 and 2000 µm before being washed to remove a majority of the ultrafine clay fraction. Sediments were loosely packed to avoid clogging in the small-diameter columns. The top of the column was packed with glass wool, and the column, as well as the top and bottom fittings, were sealed with silicone caulk. The columns were saturated using standard procedures, which consist of filling the pore space with CO_2 followed by flooding the column with the desired solution. However, the injection solutions were not degassed, in order to mimic the oxic environment present in the deep perched-intermediate aquifer observed at TA-16. Sediments for all three columns were saturated with sterile filtered CdV-16-4ip water pretreated with activated carbon to remove any residual RDX and buffered to pH 10 with 0.2 M carbonate/bicarbonate. Buffering to this pH was done to slow the rate of dithionite decompositions. The columns were weighed empty, after dry-packing and after saturation, and the pore volume of the columns was calculated from these values. The pore volumes were 18.9, 19.3, and 18.5 mL for the columns used for the sodium dithionite, potassium permanganate, and carbonate/bicarbonate treatments respectively.

Once saturated, the sediments were treated with approximately 3 to 6 pore volumes of one of three test solutions containing a chemical compound and a conservative bromide tracer. The chemical treatment solution did not contain any RDX. After treatment, a test solution of RDX and a second conservative tracer (iodine) were injected in the column. Table 2.5-1 contains the data on the specific concentrations of the different chemicals and test solutions. During treatments and testing of the columns, the solutions were injected via Monoject 160-mL syringes (Medtronic) in KDS100 syringe pumps (KD Scientific) set to a rate of 1.0 mL/h with flow oriented from the bottom upward though the column. The linear velocity was calculated to be approximately 0.30 cm/h for all columns used in this study. Fractions of the effluents were collected every hour in glass test tubes by a fraction collector. These samples were analyzed for concentration breakthrough of tracers, for RDX, and for changes in anion and cation concentrations throughout the course of the experiment.

A fourth column was prepared the same way as described above and pretreated with a 0.2-M carbonate/bicarbonate solution buffered to pH 10. The column was treated with 2.73 pore volumes of a 0.005-M dithionite solution prepared in CdV-16-4ip water (pretreated by activated carbon to remove RDX) before being flushed with CdV-16-4ip water for 3.5 additional pore volumes. A bromide tracer was used as a conservative tracer. This column was used to collect high-resolution water chemistry data to study changes in the geochemical conditions following a sodium dithionite treatment of the sediments. These detailed geochemical determinations were performed to evaluate how chemical treatments affect the water chemistry, which is important in evaluating the potential adverse effects of chemical treatments on the quality of groundwater. Specifically, the mobilization of toxic metals is a concern for sodium dithionate treatments. Upon completion of treatment, the column was frozen to preserve the treated sediments. Once frozen, the column was transferred to a glove bag filled with argon, and four samples along the length of the column were epoxied to create thin sections for petrographic and scanning electron microscope (SEM) analyses. A control sample of untreated Puye Formation sediments was also prepared as a thin section for petrographic and SEM analyses.

2.6 Biostimulation of Columns Filled with Aquifer Sediments and Evaluation of RDX Degradation Capacity

Two parallel Chromaflex glass columns (Kible Chase) 30 cm in length and 2.5 cm in diameter, dry-packed with sterile sediments representative of the regional aquifer sediments, were prepared and biostimulated using two different amendments. The columns were packed with tuff and sediment samples obtained from a depth of 352 m bgs (archived sediments were obtained during drilling of well R25b, Figure 1.0-1). The sediment samples were crushed and sieved to prepare a 75- to 2000-µm grain-size fraction. The samples were washed with water to remove ultrafine particles and autoclaved to kill or minimize the activity of any environmental bacteria before packing. The columns were saturated using sterile filtered groundwater from TA-16 groundwater monitoring well CdV-16-4ip. Before any experimental injections, fresh filtered groundwater was passed through the columns for at least 24 h to equilibrate the sediments with the groundwater. Water was injected into the columns with Monojet 160-mL syringes (Medtronic) in KDS100 syringe pumps (KD Scientific) set to a flow rate of 2.0 mL/h with flow oriented from the bottom upward though the column. As in the batch experiments, all column experiments were conducted at room temperature 23.5 ± 2°C. The pore volumes of the two columns were 39 and 52 mL.

A series of experiments was performed to test for the existence of any attenuation capacity inherent to the sediments and any microbes that might have resisted autoclaving before biostimulating the columns. These experiments were performed by injecting solutions containing RDX and a tracer through the columns and monitoring concentration breakthrough. The results from this initial testing were published in a separate report (Heerspink et al. 2017). The studies showed that RDX transported conservatively without any degradation in these columns. At the completion of the initial testing, the columns were inoculated by the injection of a water sample containing microbes native to the Puye Formation obtained from a core sample obtained using sonic drilling, which preserves the composition of the microbial population. The fresh sediment core used to collect the inoculum was obtained for another study focused on chromium contamination. The samples were collected from a depth that intercepted the Puye Formation. The inoculum sample was prepared by suspending about 10 g of sediments in 50 mL of sterile filtered groundwater from monitoring well CdV-16-4ip. The mixture was vortexed and then centrifuged at 2000 rpm for 1 min to separate the larger particles. A 5.0-mL water sample containing the microbes was sampled above the sediments and was diluted in 200 mL of a sterile filtered groundwater sample, resulting in a diluted water sample containing approximately 1×10^4 cells/mL. The cell numbers in the water samples injected in the columns were determined using direct cell counting on a hemocytometer plate. The bacterial suspension was injected at a flow rate of 2.0 mL/h into the columns. The flow was stopped twice for 2 h during the injection to stimulate microbial attachment to the sediments. At the completion of the inoculation phase, the columns were biostimulated by injection of nutrient amendments. The first column was biostimulated by the injection of a molasses solution, and the second column was biostimulated by the injection of safflower oil. The target molasses concentration in the injection solution was 3.6 g/L and the target safflower oil concentration was 1.84 g/L. The target concentrations were fixed by adjustment of the flow rate of a dual syringe system that mixed the nutrients with fresh groundwater (treated by activated carbon to remove RDX) at the inlet of the column. Mixing groundwater with the nutrients at the inlet of the column was selected to avoid microbial growth in the syringes. This was necessary, especially for molasses, which rapidly developed bubbles and made the injection difficult when it was premixed with groundwater in the syringe. The columns were biostimulated for 3 wk by the injection of approximately 360 mL of amended groundwater at a flow rate of 1.0 mL/min. To assess the RDX degradation properties of the biostimulated columns, CdV-16-4ip water spiked with RDX to a concentration of 1200 µg/L and 26 µg/L of a tracer (Br^-) was injected into the columns at a rate of 2.0 mL/h. Effluents from the columns were collected every 2 h in glass test tubes using Foxy Jr. fraction collectors (Teledyne Isco, Inc.) housed in a humid polyurethane box to minimize evaporation. The samples were stored in a refrigerator set at 4°C until analyzed. Analyses were performed using high-performance liquid chromatography (HPLC) to determine the concentration of RDX and related degradation products. The samples were also analyzed by a bromide selective ion probe to determine the concentration of bromide.

2.7 Analytical Methods

Analyses of measurable RDX and its degradation products were performed by HPLC using U.S. Environmental Protection Agency (EPA) Method 8330. The analysis was performed with a Dionex HPLC system equipped with a C-18 analytical column and an Ultimate 300 RS detector set at 254 nm (Pan et al. 2006). The mobile phase composition was fixed at a 55:45 water to methanol ratio. This method achieved a detection limit of about 1.0 µg/L for RDX and its degradation products MNX, DNX, and TNX. RDX-certified standards (Ultra Scientific, North Kingstown, RI) were used to establish calibration curves for sample quantification. Samples of TNX, DNX, and MNX were purchased from SRI International, Menlo Park, CA and used without any further processing to establish calibration curves. The samples were assumed to be 100% pure. All water samples were filtered through Millex 0.45-µm syringe filters, which did not adsorb any RDX or any of its degradation products.

Anions were analyzed by a Dionex ICS-2100 system with an IonPac AS-15 hydroxide selective anion exchange column using EPA Method 300.6. Bromide measurements were taken via a Thomas bromide combination ion-selective electrode (ISE) probe (Thomas Scientific) calibrated with a set of standards prepared in-house from a lithium bromide solid sample. Iodine was measured with an Orion 9635 ion-selective combination probe (Thermo Fisher) calibrated with in-house iodine standards prepared from a solid sodium iodine sample. All probes were used in conjunction with an Orion 290A meter (Thermo Scientific). Major cations were analyzed by a Perkin Elmer Optima 2100 DV inductively coupled plasma optical emission spectroscopy unit using EPA Method 200.7. Minor cations and trace metals were analyzed on a Perkin Elmer NexION 300S inductively coupled plasma mass spectrometry (ICPMS) system following EPA method 200.8. Titration for alkalinity and pH was done by a Mettler Toledo automated titration system using EPA Method 310.1. Before cation analysis, samples were preserved with nitric acid to a final concentration of 2%. Measurements for pH were taken via an Accumet pH probe (Thermo Fisher) calibrated with three commercial pH standards. ORP measurements were taken with an Electorder GOR-A00B glass-body platinum-band combination electrode (Erlich Industrial Development Corp.). The ORP electrode was calibrated with standards made by saturating commercial pH 4 and pH 7 standards with Quinhydrone (Sigma-Aldrich).

2.8 Analysis of Leachable Ferrous Iron

Sediments were analyzed for leachable ferrous iron by a modification of procedures described in the literature for ferrous iron analysis in the presence of ferric iron (Lee and Stumm, 1960). Dry samples of the sediments, typically 0.5 to 1.0 g, were treated with 10 mL of 6 M HCl in 150-mL Erlenmeyer flasks maintained under CO_2 atmosphere for the entire treatment. The flasks containing the acidified sediments were incubated at 60ºC overnight. The leachates and sediments were diluted to 100 mL using 0.02 M sulfuric acid to bring the concentration of leached ferrous iron to tens of µg/L levels. The leachates were analyzed for Fe(II) by the bathophenanthroline method. A 0.1-mL aliquot of the solution was mixed with 0.9 mL of a 0.1-M solution of an MES buffer and 1.0 mL of a solution containing 0.01% 1,10-Phenanthroline

(Ricca Chemical Company). The solutions turn orange immediately in the presence of Fe(II), which forms a strong complex with 1,10-Phenanthroline. The pH of the solutions analyzed was between 2.5 and 4. The solutions were analyzed by ultraviolet-visible spectroscopy at 554 nm. All solutions were analyzed 10 to 15 min after mixing to ensure complete ferrous iron complexation by 10-Phenanthroline. The concentration of Fe(II) was determined by comparing the readings of the unknown solution with a calibration curve established using known Fe(II) standards treated under the exact same conditions.

3.0 RESULTS

3.1 RDX Degradation Batch Studies

3.1.1 RDX Degradation Sediments Treated Using Sodium Dithionite

The profile of RDX concentration in sediments treated with sodium dithionite, along with controls without sediments, is shown in Figure 3.1-1. The samples extracted at each time point were analyzed for RDX, MNX, DNX, and TNX concentrations and pH. The data show that sediments treated with sodium dithionite degraded RDX rapidly. More than 90 % of RDX was completely degraded within 2 h. The observed rate constant for RDX degradation was determined by fitting the concentration profile with a mono-exponential decay curve. The observed degradation rate constant was determined to be $k_{obs\text{-}dithionite} = 0.86 \pm 0.08\ h^{-1}$ (Table 3.1-1). RDX degradation progressed more slowly at longer reaction times and residual RDX was observed after 1 wk of reaction time, with final RDX concentration averaging approximately 100 µg/L. The pH of the pore water re-equilibrated to approximately 8.56 in all samples. HPLC data indicate that the breakdown products resulting from the reaction of RDX with the treated sediments are not well separated using the C-18 column. No known breakdown products could be identified (Figure 3.1-2), and efforts to identify the degradation products by mass spectrometry were unsuccessful. The control centrifuge vials, without sediments treated with sodium dithionite and sodium permanganate and washed once with groundwater, show some degradation of RDX in the first hour after RDX addition but little degradation thereafter.

3.1.2 RDX Degradation Sediments Treated Using Potassium Permanganate

RDX degradation in sediments treated by potassium permanganate, along with controls without sediments, is shown in Figure 3.1-3. RDX concentrations decreased rapidly in the pore water of all the sediments. Most of the reduction in RDX concentration occurred in the initial hours following the potassium permanganate treatment. The observed rate constant for RDX degradation was determined by fitting the concentration profile with a mono-exponential decay curve. The observed rate constant $k_{obs\text{-}permanganate} = 0.56 \pm 0.13\ h^{-1}$ was determined (Table 3.1-1). A residual concentration of about 100 mg/L remained in the pore water even at a longer incubation time. The control vials with no sediments had some visible loss of RDX initially, but the concentrations remained stable after the initial decrease. The pH of the pore water re-equilibrated to approximately 8.56 in all samples. HPLC analysis of the pore water does not show the presence of any of the known degradation products MNX, DNX, and TNX, and no other breakdown products could be identified (Figure 3.1-2).

3.1.3 RDX Degradation under Alkaline Conditions

Three alkaline treatments were set up with sediments with target pHs of 9.5, 10.5, and 11.25, along with three solution-only controls with the same target pHs. The pH of the pore water in all three sample sets containing sediments converged to pH = 8.41 ± 0.2 by the end of the experiment. The data in Figure 3.1-4 show RDX concentration profiles for all three controls, as well the RDX concentration profile for the sediments. The observed rate constant for RDX degradation in the sediments was determined by fitting the concentration profile with a mono-exponential decay curve. The observed rate constant $k_{obs\text{-}alkaline\text{-}ph8.41} = 0.021 \pm 0.006\ h^{-1}$ was determined. All nine independent sediment samples were averaged since their pH was the same. The observed degradation rate constants determined for each pH control following the same analytical treatment were $k_{obs\text{-}alkaline\text{-}ph9.5} = 0.014 \pm 0.009\ h^{-1}$, $k_{obs\text{-}alkaline\text{-}ph10} = 0.037 \pm 0.02\ h^{-1}$, and $k_{obs\text{-}alkaline\text{-}ph11.25} = 0.044 \pm 0.03\ h^{-1}$ (Table 3.1-1). The data show that RDX degraded slowly in the alkaline solution without sediments, with faster degradation occurring in the highest pH solutions. RDX degradation was also slow in the sediments, though the pH was only slightly higher than the groundwater pH. No known degradation products were identified in the samples from the batch experiment. Complete RDX breakdown was not observed in any of the samples tested. After 4 d, all three sediment treatments converged to similar RDX levels of approximately 77 to 140 µg/L.

3.1.4 RDX Degradation in Sealed Biostimulated Reactor Batch Studies

Biostimulation of groundwater from CdV-16-4ip and CDV-9-1(i) under strict anaerobic conditions has been demonstrated to result in RDX degradation (Dongping et al. 2017). The presence of oxygen has also been found to significantly inhibit RDX degradation. In the presence of oxygen and added biostimulant, the microbial cell numbers increased to more than 10^8 cells/mL but RDX remained stable in solution. This is consistent with literature data that consistently show that RDX is most effectively degraded under strict anaerobic conditions. Under strict anaerobic conditions, degradation products MNX, DNX, and TNX are produced as intermediates of RDX degradation (see Attachment 6 of this compendium). At longer incubation times, degradation products methylenedinitramine (MEDINA), 4-nitro-2,4-diazabutanal (NDAB), nitrate, formaldehyde, and formate are formed.

3.2 RDX Degradation Column Studies

3.2.1 Treatment Using Sodium Dithionite

The sediments were treated in situ to induce strong reducing conditions by the injection of a 0.05-M sodium dithionite solution. The sediments were pretreated with a 0.2-M carbonate/bicarbonate solution to buffer the pore water at pH 9.9 and were then treated by 3.2 pore volumes of a sodium dithionite solution (see section 2.5 for more details). The sediments progressively changed color from red-brown to gray through the course of the solution injection, indicating reduction of the sediments as the solution migrated through the column. The front of this color change began at the inlet of the column and progressed approximately 15 cm upward, following the direction of the flow. The color change stopped after the water injected in the column was switched to groundwater from CdV-16-4ip containing RDX and the iodine tracer. The profiles of RDX concentration breakthrough, along with the profile of the iodine tracer, are shown in Figure 3.2-1. These data represent the start of the injection of CdV-16-4ip groundwater containing RDX and the iodine. The initial pretreatment with sodium dithionite was not represented. The data show that RDX is completely degraded, with no RDX concentration breakthrough occurring at any point during the course of the injection. The RDX solution was injected through the column for approximately 46 pore volumes before the column began to clog, with flow stopping at 52 pore volumes (Figure 3.2-2). Late during the injection of the CdV-16-4ip water, a second color change was observed in the sediments at the bottom of the column. The sediments' color changed from grey to light yellow; however, this front progressed only 1 cm up the column before complete plugging occurred.

The geochemical parameters of the column effluents were monitored during the sediment treatments (sodium dithionite injection) and during the period of performance (injection of groundwater from CdV-16-4ip) by monitoring the concentration of anions and metals in the effluents. These characterizations were performed to evaluate how the sodium dithionate treatment could affect the quality of the groundwater. Redox readings were also performed by a platinum electrode and used as a qualitative indicator of the redox conditions in the column. The redox readings (Figure 3.2-3) indicate that the redox potential decreased immediately after the injection of sodium dithionate indicating the establishment of reducing conditions immediately after the start of the dithionite injection. The measured redox potential dropped to between 0 and –100 mV initially and slowly increased to read about 0 mV. The readings increased even before the completion of the dithionate injection (pore volume 2.5). This is an indication of the malfunction of the electrode and is related to the poisoning of the platinum electrode by sulfur compounds. This is consistent with the literature, as it is known that sulfur compounds bind to and affect the performance of platinum electrodes. Anion concentration analysis showed no significant changes in the concentrations of nitrate and phosphate, which both remained under 5 mg/L. This is not surprising, as abiotic nitrate reduction rates are known to be very slow. However, sulfate concentrations started to significantly increase after approximately 0.6 pore volume of sodium dithionite injection (Figure 3.2-4). The data in Figure 3.2-4 show the concentration profile of the sulfate anion throughout the experiment. Sulfate anion concentrations increased to upwards of 5000 mg/L but started to decrease after the injection of sodium dithionite was switched to groundwater from CdV-16-4ip (3.2 pore volumes). The increase in sulfate concentration was expected, as it is the product of dithionate oxidation. Sulfate concentration breakthrough mirrored the concentration breakthrough of the conservative tracer bromide, which indicates that dithionate oxidizes very rapidly. A total of 0.62 g of sodium dithionate was injected through the column, from which, if it is all converted to sulfate, we would expect the production of 0.284 g of sulfate. This is very close to the 0.274 mg of sulfate obtained by integrating the concentration breakthrough of sulfate, which indicates that sodium dithionite is completely transformed in the column to sulfate. Chloride concentrations varied between 10 and 87 mg/L until approximately 2.3 pore volumes of the sodium dithionite injection, where the chloride concentration leveled off to between 6 and 10 mg/L (Figure 3.2-4). This indicates that chloride was present in the column and flushed out by the dithionate treatment and following wash with CdV-16-4ip groundwater. The final chloride concentration is consistent with the concentration of chloride in groundwater.

Metal concentrations in the effluents are represented in Figure 3.2-5. The concentration breakthrough behavior is divided into three groups. The first group of metals, which includes silicon dioxide, barium, lithium, manganese, strontium, cadmium, cobalt, nickel, calcium, magnesium, and copper, has slightly elevated concentrations at the start of the sodium dithionite injection and concentrations decrease slowly until approximately 1 pore volume and stabilize until approximately 2 pore volumes, when the concentrations start to increase significantly. A pulse with elevated metal concentrations is visible between approximately 2 and 4 pore volumes. The concentrations and magnitude of concentration changes, however, vary between species. The second group of metals, which includes zinc, iron, aluminum, chromium, and uranium, shows no trend in concentration changes, and all concentrations remain below 1 mg/L in the water samples through 5 pore volumes. Concentrations for the third group of metals, which includes vanadium, arsenic, beryllium, silver, cesium, and titanium, remain very low for the duration of the experiment. Sodium, a component of the sodium dithionite solution and also present in the sediments, increases significantly in concentration, reaching a maximum of 5000 mg/L after 1 pore volume and then decreases progressively. The concentration of the bromide tracer is also shown in the plot and is consistent with the behavior of a non-reactive tracer. The bromide tracer concentration breakthrough indicates that the profile of the metals is not directly correlated with the solution injection, except for sodium. These data indicate that the treatment solution used to pretreat the sediments and create strong reducing conditions promoted the dissolution of the silicate minerals in the sediments and the release of the trace metals associated with them.

3.2.2 Treatment Using Potassium Permanganate

For the potassium permanganate treatment, the sediments were pretreated with a solution of carbonate/bicarbonate adjusted to pH 9.91 to buffer the pH of the pore water, and then a pulse of potassium permanganate was injected through the column. The concentration breakthrough curves representing the treatment phase (injection of potassium permanganate) and the injection of CdV-16-4ip groundwater spiked with up to 1.2 mg/L RDX are shown in Figure 3.2-6. Two different tracers were used to identify the initial treatment phase and the attenuation phase. The data show that the potassium permanganate treatment was not very effective at creating conditions favorable for RDX degradation. The concentration breakthrough of RDX is slightly delayed relative to the bromide tracer but starts to elute from the column at about 1.5 pore volumes after introduction of CDV-16-4ip groundwater spiked with RDX and reaches injection concentration after about 2.2 pore volumes. There is no buildup of any of the known RDX degradation products (Figure 3.1-2). Anion concentrations in the effluents fluctuated but remained stable (Figure 3.2-7). Sulfate and chloride concentrations varied between 3.5 and 6 mg/L; nitrate concentrations varied between 0 and 3 mg/L. Fluoride and phosphate concentrations remained below 0.2 mg/L for all samples monitored. Nitrite concentrations showed a distinct variation in the experiment, steadily increasing from 0.4 to 3.5 mg/L between 0 and 4.5 pore volumes before falling back to 1 mg/L at the end of the experiment. Generally, metal concentrations remained stable throughout the experiment. Slight increases in the concentrations of arsenic, barium, calcium, cesium, magnesium, manganese, silicon and strontium occur, coinciding with the period of pretreatment with potassium permanganate, and the concentrations return to baseline at the end of the treatment (Figure 3.2-8). Lithium is the only species to break through differently. It is low during the pretreatment phase and increases when groundwater is injected. All other species are near the detection limit.

3.2.3 Alkaline Treatment Using Carbonate Bicarbonate Solutions

Sediments from the Puye Formation were treated with 4.3 pore volumes of a carbonate/bicarbonate solution adjusted to pH 9.91 to establish alkaline conditions in the sediment pore water. The pretreatment of the sediments was followed by the injection of groundwater from well CdV-16-4ip spiked with 1.25 mg/L RDX. The data in Figure 3.2-9 show the concentration breakthrough of RDX and the iodine conservative tracer. RDX concentration breakthrough is slightly delayed relative to the conservative tracer. It starts to elute from the column at approximately 5.5 pore volumes and reaches complete concentration breakthrough after approximately 8.6 pore volumes. This indicates retardation or breakdown of RDX. The pH of the effluent samples remained between 9.8 and 10.5 for the duration of the RDX injection. The pH of the RDX injection solution was approximately 8.24. There are no known degradation products in the column effluents (Figure 3.1-2). The chemistry of the water changed consistently during the treatment. The data in Figure 3.2-10 show a very elevated concentration of sodium during the pretreatment phase, which is consistent with the injection of sodium bicarbonate. The concentration of most metals did not change during the pretreatment phase (Figure 3.2-10). The concentrations of calcium, potassium, magnesium, and strontium are all highest at the beginning of the experiment and decrease continuously over the course of the experiment. Concentrations of other trace metals such as arsenic, barium, copper, strontium, uranium, and vanadium all show a decreasing trend over the course of the experiment. The concentrations of iron, chromium, and aluminum were unaffected initially but increased slightly between 1 and 2 pore volumes after the start of the injection of CdV-16-4ip groundwater spiked with RDX. The concentration of silicon dioxide seems to be inversely correlated with the concentration of sodium in solution, which could suggest that elevated sodium inhibits the dissolution of silicate minerals. At high sodium concentrations, the concentration of silicon dioxide is stable at approximately 55 mg/L and increases to approximately 130 mg/L as the concentration of sodium decreases to background.

The anion concentrations are relatively stable, with bromide, sulfate, nitrate, and phosphate concentrations all remaining below 8 parts per million (ppm) for the duration of the experiment, while nitrite is never detected (Figure 3.2-11). The only anion showing a significant change in concentration is chloride, which drops sequentially from 280 ppm to 5 ppm thought the course of the experiment. Its initial presence in solution is due to the use of HCl for adjusting the pH of the carbonate/bicarbonate solutions.

3.2.4 RDX Degradation in Biostimulated Columns Packed with Puye Formation Sediments

Microbial diversity analysis was performed for several monitoring wells that interrogate the different groundwater bodies encountered at TA-16. Details of the experimental procedures and results were presented elsewhere (Dongping et al. 2017). Briefly, the survey data suggest the existence of a highly diverse microbial population in the groundwater. The survey found that bacteria related to *Rhodococcus* are more abundant in wells within the deep intermediate aquifer, which has the highest concentration of RDX. The survey also found that *Pseudomonas* are abundant in the regional aquifer, which has very low to no detectable RDX. However, there was no direct evidence that the microbes identified played an active role in RDX degradation. The response of the microbes, collected from monitoring well CdV-16-4ip and present in the groundwater, to biostimulation and the kinetics and mechanism of RDX biodegradation, is published elsewhere (Dongping et al. 2017; Attachment 6 of this compendium). The study shows that biostimulation can effectively create conditions favorable for RDX degradation but only under strict anaerobic conditions. The presence of oxygen completely inhibits RDX degradation. Degradation products MNX, DNX, and TNX are produced during anaerobic RDX degradation.

This study reports on the performance of columns packed with sterile sediments from the Puye Formation and inoculated by the injection of extract from sediments collected from a core drilled into the same formation. The columns were biostimulated by the injection of either molasses (3.6 g/L) or safflower oil (10 g/L) for 3 wk. At the completion of the biostimulation phase, groundwater from well CdV-16-4ip was spiked with 1.0 mg/L RDX and injected into the column to evaluate the column’s capacity to attenuate RDX. Dissolved oxygen content in the water injected in the columns was not adjusted and varied between 5 to 7 mg/L. The data in Figure 3.2-12 A and B, show the profiles of RDX concentration breakthrough from the columns biostimulated with molasses (A) or safflower oil (B) respectively. The column biostimulated with molasses operated without any significant clogging for the entire duration of the experiment. The data in Figure 3.2-12 show that RDX is transformed to its degradation products DNX, MNX, and TNX in both columns. The ratio of RDX to the sum of all degradation products shown in Figure 3.2-13 A, indicates that complete degradation of RDX in the molasses column was achieved for the initial 4 pore volumes. Progressive increase of the ratio after 4 pore volumes indicates incomplete RDX degradation. The HPLC chromatogram of effluent samples (Figure 3.2-14) shows that degradation products DNX, MNX, and TNX are the main breakdown products of RDX degradation. The column biostimulated with safflower oil was also very effective at degrading RDX (Figure 3.2-13 B). However, the column clogged very rapidly and flow was interrupted several times, requiring manual intervention to resume flow. Clogging was due to biofouling, which was visible in the tubing exiting the column. Flow completely stopped, and the column was abandoned after flowing for about 4 pore volumes.

4.0 DISCUSSION

4.1 RDX Degradation in Sediments Treated Chemically

Sodium dithionite was shown to be the most effective treatment in the batch experiments, with the highest decomposition rate constant, $k_{obs\text{-}dithionate}$ = 0.86 h^{-1}. Dithionite has been previously shown to be effective at reducing RDX in batch systems in the presence of aquifer sediments. Szecsody et al. (2001) reported rapid degradation of RDX in aquifer sediments treated with dithionite, reporting a half-life of less than 3 min. The significantly shorter half-life observed is because of the higher-concentration dithionite used in that study (up to 1 M) compared with the concentrations used in the present study (0.001 M). Szecsody et al. also observed the known anaerobic RDX degradation products (MNX, DNX, and TNX) in their samples, which were not observed in the current study (Figure 3.1-2), possibly indicating a difference in the degradation mechanism.

In the column experiments, sodium dithionite also proved to be the most efficient treatment. RDX was completely degraded for 52 pore volumes before plugging occurred and the flow stopped. The plugging is attributed to the oxidation of ferrous iron and precipitation of ferric oxides in the pore space. This was not directly documented in the present study's columns, but dithionate treatment of sediments is known to produce large amounts of ferrous iron, which oxidize and precipitate when they react with oxygen. The plugging of pore space due to treatment with dithionite is one potential complication of deploying this treatment in the field. Column studies by Szecsody et al. (2001) achieved RDX complete degradation for 260 pore volumes with a 15 cm-long column. There are no known pilot field-scale deployments of sodium dithionite for the in situ treatment of RDX.

The high-resolution water chemistry data obtained from the dithionite column provide considerable information about the effect of dithionite treatment on aquifer geochemistry. While dithionite was not measured in the column samples, sodium and sulfate measurements were used as indicators of dithionite breakthrough as shown in Figure 3.2-4. The amount of sulfate produced in the column (0.274 mg) is very close to the theoretical value of 0.284 mg predicted from the amount of dithionate injected into the column. This is a good indication of the complete transformation of the dithionate to sulfate. The coincidence of the sulfate concentration breakthrough with the concentration breakthrough of the bromide conservative tracer is interpreted as an indication of the rapid and complete transformation of sodium dithionate within the column. Sulfate breakthrough precedes the breakthrough of metals by approximately 1.3 pore volumes. The observed mobilization of metal species from the sediments is likely because of the solubilization of amorphous silica under alkaline conditions and reduction of available mineral phases by dithionite. Figure 4.1-1 shows an SEM image obtained for sediment samples collected from the inlet of the column taken at the completion of the experiment. The image shows extensive weathering and clear indication of extensive dissolution of the silicate matrix of the sediments. The high concentrations of sodium and sulfate in the system are attributed to the decomposition of sodium dithionite.

Iron is expected to be the main species transformed in the sediments treated by dithionite; however, no mobilization of iron was observed in effluent samples. Effectively, under the alkaline conditions maintained in the column throughout the treatment, ferrous iron is expected to form insoluble ferrous hydroxide species. It is also possible that iron in the sediments is within the matrix of minerals, and therefore the amount of iron available for transformation is limited. The study by Szecsody et al. (2001) of the treatment of sediments with sodium dithionite for RDX reduction showed that after transformation, the total amount of extracted iron could not explain the observed reduction capacity. They attributed this difference to either the presence of manganese oxides or structural iron(II). This study performed experiments at a pH below 7 and noted that Fe(II) will not partition into the aqueous phase above a pH of approximately 7.5, but rather precipitates as iron hydroxides. The concentration breakthrough data show extensive dissolution of silicate as indicated by the concentration of SiO_2. However, the concentration of silicate in the effluents is inversely correlated with the concentration of sodium. High sodium concentrations reduce the concentration of soluble SiO_2. At the start of the column run, the concentration of sodium is low and the concentration of SiO_2 is high, but as the treatment with sodium dithionite progresses, elevated sodium concentrations coincide with silicate dissolution. Two clear domains of elevated metals are observed at the start of the column run and after the injection of the sodium dithionite pulse. These elevated metal intervals are correlated with the elevated concentration of SiO_2, which suggest that the metals released were associated with a silicate phase. The enhanced dissolution of silicate phases is not surprising. In fact, under alkaline conditions, silicate minerals dissolve to form silicic acid compounds H_2SiO_3, HSO_3^-, and SiO_3^{2-}. The concentrations of arsenic, lead, beryllium, chromium, and uranium remained low, which is consistent with their relatively low abundance in the sediments.

The batch experiment indicated that potassium permanganate treatment of the sediments was effective at degrading RDX. The observed decomposition rate, $k_{obs\text{-}permanganate}$= 0.56 h^{-1}, is slightly slower but equivalent to that of dithionite, $k_{obs\text{-}dithionate}$= 0.86 h^{-1}. Sediments treated with potassium permanganate degraded RDX over the course of 24 h. This is consistent with previous studies showing that permanganate can be effective at degrading RDX in batch systems. Adam et al. (2004) and Albano et al. (2010) both showed RDX to be effectively degraded by potassium permanganate in the presence of sediment slurries. In both experiments, the permanganate solution was allowed to directly contact RDX, while in the present study's system, sediments were treated with potassium permanganate and then washed once to remove excess potassium permanganate before the introduction of RDX.

In comparison to the batch experiment, the permanganate treatment proved ineffective in the column system. Only a short delay of 0.8 pore volumes in RDX concentration breakthrough relative to the tracer is observed. This is the shortest delay observed in the three treatments examined in this study. It is not clear if RDX degraded to any significant degree in these columns. It is possible that some of the delay in RDX concentration breakthrough could be attributed to sorption of RDX onto the fines and clay materials in the column. However, previous studies have determined that RDX sorption to Puye sediment is negligible (Heerspink et al. 2017). Previous investigations determined that only 0.2 pore volume delay is observed because of RDX sorption onto the column sediments. In the present study, none of the RDX degradation products that had standards (MNX, TNX, and DNX) were observed in HPCL analysis of the effluents from the permanganate column samples (Figure 3.1-2). As noted above, the previous lab studies on permanganate allowed the oxidant to directly contact RDX. In the present study's column system RDX, did not contact RDX directly. The results of the present study indicate that potassium permanganate did not transform the sediments to create conditions favorable to RDX degradation. The results from the batch studies, which showed a rapid and complete degradation of RDX, contrast with the column results, which show very little degradation of RDX. This is likely due to the presence of residual potassium permanganate in the batch sediments that acted to directly degrade RDX. Effectively, the sediments were centrifuged to remove the excess pore water, and some residual permanganate has likely remained in the sediments. In addition, in the batch experiment, sediments were buffered with pH 9.5 carbonate/bicarbonate solution before permanganate treatment. Observed RDX degradation in the permanganate batch samples could also be attributed to alkaline hydrolysis rather than permanganate oxidation. However, the rates of RDX alkaline degradation is slow ($k_{obs\text{-}alkaline\text{-}ph8.41}$ = 0.021 h^{-1}), and is unlikely to have contributed significantly to the observed RDX degradation. Furthermore, when permanganate oxidizes an organic compound, the reduced permanganate species precipitates and can cause clogging of pore space. Clogging of the sediments was observed in the batch experiment with permanganate but not in the column experiment. This is another indication that RDX was degraded by direct oxidation by permanganate in the batch experiment but not in the column experiments. While the column experiments showed the potassium permanganate to be ineffective, a pilot test on the treatment showed it to be effective at the field scale. Albano et al. (2010) executed a pilot field test where a curtain of permanganate was introduced into RDX-contaminated water though an injection/extraction system.

This system was proven to be effective, with RDX concentration decreasing by 70% to 80% in monitoring wells downstream of the treatment system. In this case, potassium permanganate likely came in direct contact with RDX and operated as an oxidant. Data from the present study suggest that direct contact between organic contaminants and potassium permanganate is necessary to achieve breakdown of the organics. It seems that batch and slurry-type experiments in which potassium permanganate is in direct contact with the contaminant is more appropriate than are column studies for the evaluation of the rate of the potassium permanganate. However, the column studies have demonstrated that potassium permanganate does not transform the sediments to create an indirect decomposition mechanism.

Based on inductively coupled plasma mass spectrometry analysis, the permanganate treatment did not significantly alter the geochemical conditions of the sediments. Slight increases in some major and trace metal species occurred during treatment but rapidly returned to background during the course of the experiment.

All three alkaline test solutions, set up at pHs 9.5, 10.5, and 11.2 and in the absence of sediments, proved to be conducive to RDX degradation in the batch experiments. Observed rate constants increased with increasing pH but were in general much slower than the rates observed for dithionite and potassium permanganate. In the presence of sediments, the rate of RDX degradation was also slow relative to the rate of RDX degradation in sediments treated with sodium dithionate and potassium permanganate. Overall, the rate of RDX degradation in alkaline media is slow. This is consistent with previous studies of the kinetics of alkaline hydrolysis of RDX, which are slow and dependent on pH and temperature. Heilmann et al. (1996), Balakrishnan (2003), Hwang (2006), and Oh (2015) studied the effects of pH and temperature on RDX-hydrolysis-contaminated marine waters at a range of pH from 10 to 12 and temperature from 30^{o}C to 50^{o}C. Based on these experiments, they estimated that RDX hydrolysis at 20^{o}C would require adding enough strong base to achieve pH between 10 and 11 and would likely cause calcium carbonate precipitation. They also estimated that at 10^{o}C and similar pH, RDX would take roughly 112 y to fully hydrolyze. A study by Heilmann et al. (1996) of alkaline hydroids of RDX by strong base also suggested that elevated temperatures were required for the reaction to progress at a significant rate. In the presence of sediments, all three sets of experimental reactors buffered to a similar pH within 24 h, despite being treated with solutions of significantly different pHs. This indicates that the sediments have a strong buffering capacity that outweighed that of the solutions introduced. Data from the present study show that even though the pH in sediments was relatively lower than in the controls with no sediments, RDX degradation was observed.

The alkaline treatment in the column system, however, showed limited RDX degradation capacity. RDX was delayed by only 1.2 pore volumes relative to the conservative tracer. The batch study results indicated that RDX concentration breakthrough would be further delayed. The transport of RDX in the tested sediment is known and untreated RDX should break through approximately 0.2 pore volumes after the conservative tracer (Heerspink et al. 2017). This is significantly sooner than the 1.0 pore volume delay observed in the alkaline column. The reduced treatment effectiveness in the column system could be because of the short residence time of RDX in the columns. This is supported by the slow decomposition rate $k_{obs\text{-}pH9.5}$= 0.014 ±0. 009 h^{-1} observed at pH 9.5. The approximately 19-h residence time in the column is too short for the hydrolysis to progress significantly in this system. Column runs with variable residence times and longer residence times are needed in order to confirm that the lack of effectiveness observed in the column experiments was effectively due to the short residence time. Unfortunately, these experiments were not performed in the time frame of this project.

The trends observed in metals concentrations over the course of the experiment suggest that the alkaline treatment induced desorption of divalent cations and other trace metals that were likely sorbed onto the sediments. This is likely because of a cation exchange process in which the very high concentration of sodium injected in the column (sodium bicarbonate) enhances the desorption of trace metals, which partition to the pore water and are transported through the column. This behavior was not observed for aluminum, iron, and chromium, whose concentrations did not significantly change. The concentration of SiO_2 follows a trend that suggests elevated sodium concentrations suppress the solubilization of SiO_2, which is favored under alkaline conditions.

4.2 RDX Degradation in Biostimulated Sediments

Previous investigations of RDX biodegradation in CdV-16-4ip groundwater revealed that both molasses and vegetable oil substrates can stimulate the microbes present in the groundwater (Dongping et al. 2017). However, these studies also determined that strict anaerobic conditions were necessary to drive RDX degradation to completion. Under strict anaerobic conditions, complete RDX degradation takes more than 3 mo.; additionally when the concentrations of RDX are very low (about 100 mg/L), microbes do not appear to use it as a terminal electron acceptor. Under the specific experimental conditions of the present study, no degradation was observed. The presence of sediments did not significantly affect the rate of RDX biodegradation. This is likely because of the low levels of iron phases in the sediments used in this study or the inability of reduced iron phases to degrade RDX.

Column data from the present study show that biostimulation is likely effective at reducing RDX. The molasses column operated without any significant stop-flow issues. RDX underwent complete degradation within approximately 4 pore volumes. It is important to compare the residence time in the columns (approximately 40 h) with the time required to completely reduce RDX in the batch studies, which was about 3 mo. Reduction is significantly more effective in the column than in a reactor system. This is likely because of elevated cell numbers/volume in the confined pore space of the sediment in the column relative to the sealed reactors. The cell numbers in the sediments in the molasses column were determined to be 1.2×10^8 cells/g determined after the completion of the experiment. Sediments were harvested from the bottom (influent) and top (effluent) of the column and characterized to determine the sediments' cells content by direct cell counts. The cell numbers in the anaerobic reactors cultivated in liquid cultures were $5x10^6$ cells/mL (Dongping et al. 2017). Detection of degradation products MNX, DNX, and TNX indicates that RDX is degraded by anaerobic degradation (Figure 3.2-14). The microbes responsible for RDX degradation were not determined. The column stimulated by safflower oil was also effective at degrading RDX but clogged several times and required manual forced injections at high flow rates to resume flow. No RDX exited the column during the column operation, but complete clogging occurred at about 4 pore volumes. This is likely because of biofouling, which was visible in the tubing exiting the column. However, it was not clear if biofouling in the sediments also occurred and contributed to the clogging. Cell counts were similar to the molasses column. However, cell counts were performed on limited samples at the inlet and outlet of the column.

The relatively short attenuation capacity of the biostimulated column is likely because of the oxygenation of the column. The groundwater injected into the biostimulated column contains on average 5 to 7 mg/L of dissolved oxygen. In the absence of carbon substrates that would support rapid consumption of available dissolved oxygen and microbial activity, the environment in the column is expected to slowly shift back to being oxidizing. As has been demonstrated in the batch experiment, RDX is not degraded under aerobic conditions in the system of the present study. These data show that complete anaerobic conditions are required from RDX degradation under the present study's specific conditions.

4.3 Additional Studies and Data Gaps

The current study has demonstrated that the rates of RDX degradation in sediments treated chemically or biostimulated by the addition of carbon amendments are all fast (Table 3.1-1). Kinetic limitations are unlikely to be important. We believe additional studies on the alkaline treatment should be performed at different residence times, which can be achieved by reducing the flow rate. Flow-through data for the column experiment were not modeled in this study. All the raw column data, including tracer breakthrough, were saved and should be treated with an appropriate reactive transport model to determine the different flow parameters, RDX mass balance, and rates of degradation. This exercise would be especially beneficial for the alkaline treatment in which RDX degradation rates were more than an order of magnitude slower than the rates of degradation determined for the other treatments examined in this report. We also believe that if the risk assessment studies determine that active remedial treatments are needed to protect the regional aquifer, aquifer test studies should be considered to examine the feasibility of injecting amendments in the aquifer and assessing the overall impact of the amendments on the long-term quality of the groundwater.

5.0 CONCLUSIONS

The present study demonstrates that RDX can be degraded very rapidly by sediments treated with sodium dithionite in both batch and column tests packed with sterile sediments. Sediments treated by sodium dithionite in batch tests and in the columns performed under continuous flow conditions degraded RDX completely. The sodium dithionite treatment of the sediments resulted in transient periods of high dissolved metal concentrations and anions such as sulfate. Complete clogging of the columns is also observed after an extended time and is attributed to the formation of insoluble iron hydroxides that reduced the permeability of the column. Potassium permanganate also degraded RDX very rapidly in batch testing but failed to induce any degrading ability to the sediment under continuous flow conditions. Direct contact between potassium permanganate and RDX is required to achieve RDX degradation. Alkaline hydrolysis is slow relative to the dithionite and permanganate treatments (Table 3.1-1). RDX degradation is limited in the columns treated to establish alkaline conditions. The low degradation of RDX is attributed to the significantly reduced residence time of RDX in the columns and is consistent with the slow kinetics of alkaline hydrolysis (Table 3.1-1). However, alkaline hydrolysis remains promising and needs to be investigated further to examine if the effectiveness of RDX degradation could be enhanced by longer residence times. Treatment of the sediments to establish alkaline conditions in the sediments alters the geochemical conditions of the pore water and can lead to the mobilization of unwanted metals. RDX degradation in biostimulated columns is relatively fast, but frequent additions of amendments may be required to sustain strict anaerobic conditions for RDX degradation. Degradation products MNX, DNX, and TNX were present in all column effluents.

6.0 REFERENCES AND MAP DATA SOURCES

6.1 References

The following reference list includes documents cited in this report.

Adam, M.L., S.D. Comfort, M.C. Morley, and D.D. Snow. "Remediating RDX-Contaminated Ground Water with Permanganate," *Journal of Environmental Quality*, Vol. 33, No. 6, pp. 2165–2173 (2004).

Albano, J., S.D. Comfort, V. Zlotnik, T. Halihan, M. Burbach, C. Chokejaroenrat, S. Onanong, and W. Clayton. "In Situ chemical Oxidation of RDX-Contaminated Groundwater with Permanganate at the Nebraska Ordnance Plant," *Groundwater Monitoring & Remediation*, Vol. 30, No. 3, pp.96–106 (2010).

Balakrishnan V.K., A. Halasz, and J. Hawari. "Alkaline Hydrolysis of the Cyclic Nitramine Explosives RDX, HMX, and CL-20: New Insights into Degradation Pathways Obtained by the Observation of Novel Intermediates," *Environmental Science & Technology* 37 (9), 1838-1843 (2003).

Brannon J.M., and J.C. Pennington. "Environmental Fate and Transport Process Descriptors for Explosives," Engineer Research and Development Center Vicksburg MS Environmental Lab document ADA403162 (2002).

Chokejaroenrat, C., S.D. Comfort, C.E. Harris, D.D Snow, D. Cassada, C. Sakulthaew, and T Satapanajaru. "Transformation of Hexahydro-1, 3, 5-trinitro-1, 3, 5-triazine (RDX) by Permanganate," *Environmental Science & Technology*, Vol. 45, No. 8, pp.3643–3649 (2011).

Clark B., and R.J. Boopathy. "Evaluation of Bioremediation Methods for the Treatment of Soil Contaminated with Explosives in Louisiana Army Ammunition Plant, Minden, Louisiana," *Journal of Hazardous Materials,* Vol. 143, No. 3, pp. 643–648 (2007).

Dong, W., G. Xie, M.P. Franklin, T. Palmateer Oxenberg, T.R. Miller, E.J. Bouwer, W.P. Ball, and R.U. Halden. "Sorption and Bioreduction of Hexavalent Uranium at a Military Facility by the Chesapeake Bay," *Environmental Pollution*, Vol. 142, No. 1, pp. 132–142 (2006).

Dongping W., H. Boukhalfa, O. Marina, D.S. Ware, T.J. Goering, F. Sun, H.E. Daligault, C.C. Lo, and M. Vuyicish. "Biostimulation and Microbial Community Profiling Reveal Insights on RDX Transformation in Groundwater," *MicrobiologyOpen*, Vol. 6, No. 2, e00423 https://doi.org/10.1002/mbo3.423 (2017).

Heilmann, H.M., U. Wiesmann, and M.K. Stenstrom. "Kinetics of the Alkaline Hydrolysis of High Explosives RDX and HMX in Aqueous Solution and Adsorbed to Activated Carbon," *Environmental Science & Technology*, Vol. 30, No. 5, pp.1485–1492 (1996).

Heerspink B.P., S. Pandey, H. Boukhalfa, D.S. Ware, O. Marina, G. Perkins, V.V. Vesselinov, and G. WoldeGabriel. "Fate and Transport of Hexahydro-1,3,5-trinitro-1,3,5-triazine (RDX) and Its Degradation Products in Sedimentary and Volcanic Rocks, Los Alamos, New Mexico," *Chemosphere*, Vol. 182, pp. 276–283 (2017).

Hwang S., D.R. Felt, E.J. Bouwer, M.C. Brooks, S.L. Larson, and J.L. Davis. "Remediation of RDX-Contaminated Water Using Alkaline Hydrolysis," *Journal of Environmental Engineering,* Vol. 132, No. 2 (2006).

Kalderis D., A.L. Juhasz, R. Boopathy, and S. Comfort. “Soils Contaminated with Explosives: Environmental Fate and Evaluation of State-of-the-Art Remediation Processes” (IUPAC Technical Report), *Pure and Applied Chemistry,* Vol. 83, No. 7, pp. 1407–84 (2011).

LANL (Los Alamos National Laboratory). “Investigation Report for Water Canyon/Cañon de Valle,” Los Alamos National Laboratory document LA-UR-11-5478, Los Alamos, New Mexico (2011).

Lee, G.F., and W. Stumm. “Determination of Ferrous Iron in the Presence of Ferric Iron with Bathophenanthroline,” *Journal American Water Works Association*, Vol. 52, No. 12, pp. 1567–1574 (1960).

Livermore J.A., Y.O. Jin, R.W. Arnseth, M. LePuil, and T.E. Mattes. “Microbial Community Dynamics During Acetate Biostimulation of RDX-Contaminated Groundwater,” *Environmental Science & Technology,* Vol. 47, pp. 7672–7678 (2013).

Newman B.D., D.D. Hickmott, and P. Gram. “Flow and High Explosives Transport in a Semiarid Mesa in New Mexico, USA*,” Vadose Zone Journal*, Vol. 6, No. 4, pp. 774–785 (2007).

Oh, S-Y, and D-S Shin. “Remediation of Explosive-Contaminated Soils: Alkaline Hydrolysis and Subcritical Water Degradation,” *Soil and Sediment Contamination: An International Journal*, Vol. 24, No. 2, pp. 157–171 (2015).

Payne, D., R. Darlington, J. Gilette, and A. Bodour. “Enhanced In Situ Biogeochemical Pilot Study of a Chlorinated Ethene Plume,” Second International Symposium on Bioremediation and Sustainable Environmental Technologies, Jacksonville, Florida. (2013).

Szecsody, J.E., C.T. Resch, J.S. Fruchter, T.J. Gilmore, and M.A. McKinley. “Feasibility of In Situ Redox Manipulation of Subsurface Sediments for RDX Remediation at Pantex,” Pacific Northwest National Laboratory report PNNL-13746, Richland, Washington (2001).

Wani, A.H., B.R. O'Neal, J.L. Davis, and L.D. Hansen. “Environmental Security Technology Certification Program: Treatability Study for Biologically Active Zone Enhancement (BAZE) for In Situ RDX Degradation in Groundwater,” US Army Corps of Engineers, Engineer Research and Development Center document ERDC/ELTR-02-35, Vicksburg, MS (2002).

6.2 Map Data Sources

Hillshade; Los Alamos National Laboratory, ER-ES, As published; \\slip\gis\Data\HYP\LiDAR\2014\Bare_Earth\BareEarth_DEM_Mosaic.gdb; 2014

Structures; Los Alamos National Laboratory, KSL Site Support Services, Planning, Locating and Mapping Section; 06 January 2004; as published 29 November 2010.

Unpaved road;; Los Alamos National Laboratory, ER-ES, As published, GIS projects folder; \\slip\gis\GIS\Projects\14-Projects\14-0062\project_data.gdb; digitized_site_features; digitized_road; 2017

Paved Road Arcs; Los Alamos National Laboratory, FWO Site Support Services, Planning, Locating and Mapping Section; 06 January 2004; as published 29 November 2010.

Drainage channel; Los Alamos National Laboratory, ER-ES, As published, GIS projects folder; \\slip\gis\GIS\Projects\11-Projects\11-0108\gdb\gdb_11-0108_generic.mdb; drainage; 2017

Approximate extent of RDX contamination in deep perched groundwater, based on current knowledge; Los Alamos National Laboratory, ER-ES, As published, GIS projects folder; \\slip\gis\GIS\Projects\15-Projects\15-0041\shp\perched_aquifer.shp; 2016

Approximate extent of deep perched groundwater, based on current knowledgePerched intermediate groundwater elevation contour, 100-ft interval

Primary Electric Grid; Los Alamos National Laboratory, KSL Site Support Services, Planning, Locating and Mapping Section; 06 January 2004; as published 29 November 2010.

Perched intermediate groundwater elevation contour, 100-ft interval; Los Alamos National Laboratory, ER-ES, As published, GIS projects folder; \\slip\gis\GIS\Projects\15-Projects\15-0041\shp\sketch_contour.shp; 2016

May 2017 groundwater elevation, 50-ft contours; Los Alamos National Laboratory, ER-ES, As published, GIS projects folder; \\slip\gis\GIS\Projects\16-Projects\16-0027\project_data.gdb\contour_wl2017may_2ft; 2017

wqh_npdes_outfalls_pnt; WQH NPDES Outfalls; Los Alamos National Laboratory, ENV Water Quality and Hydrology Group; Edition 2002.01; 01 September 2003.

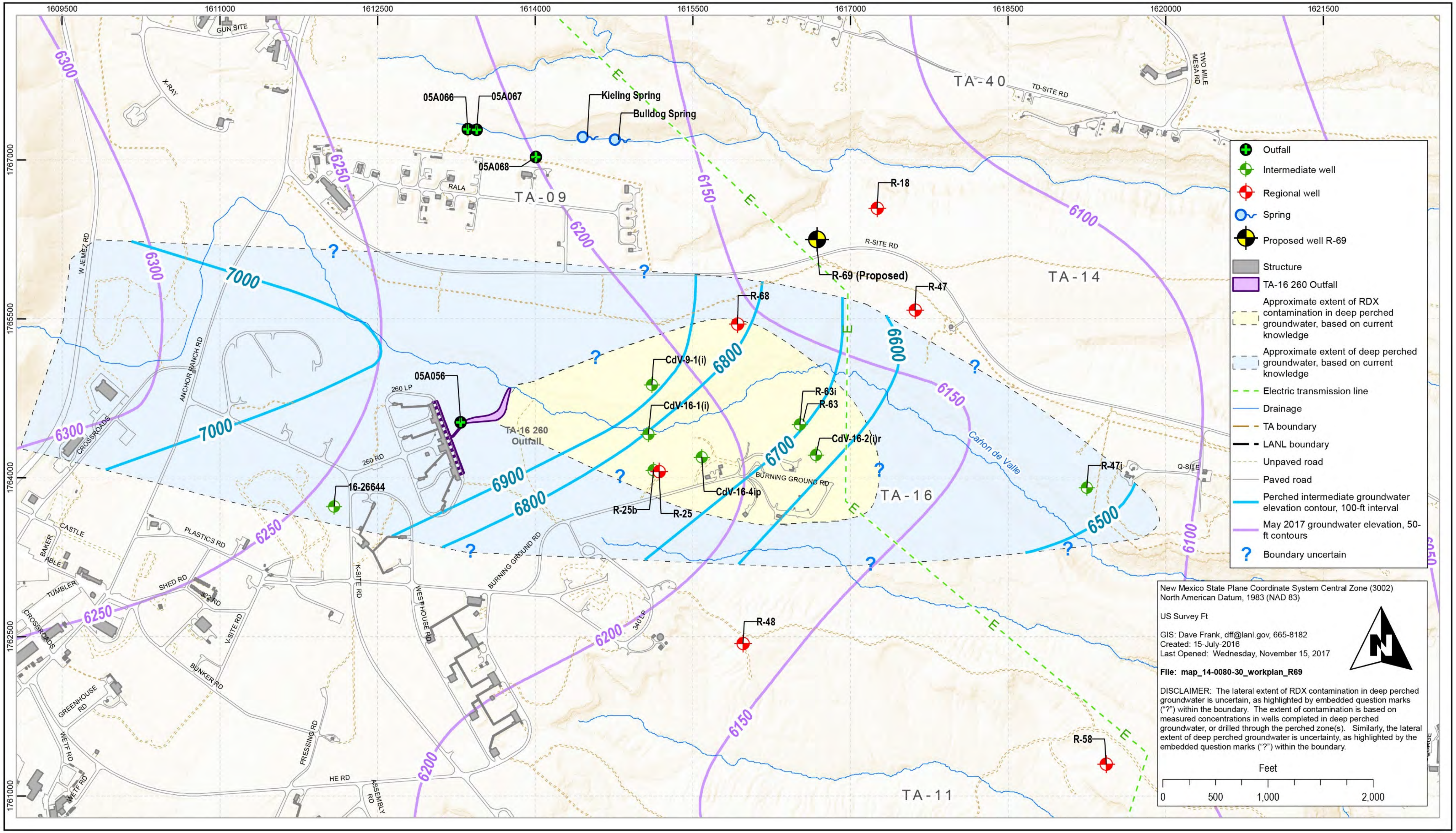

New Mexico State Plane Coordinate System Central Zone (3002)
North American Datum, 1983 (NAD 83)

US Survey Ft

GIS: Dave Frank, dff@lanl.gov, 665-8182
Created: 15-July-2016
Last Opened: Wednesday, November 15, 2017

File: map_14-0080-30_workplan_R69

DISCLAIMER: The lateral extent of RDX contamination in deep perched groundwater is uncertain, as highlighted by embedded question marks ("?") within the boundary. The extent of contamination is based on measured concentrations in wells completed in deep perched groundwater, or drilled through the perched zone(s). Similarly, the lateral extent of deep perched groundwater is uncertainty, as highlighted by the embedded question marks ("?") within the boundary.

Figure 1.0-1 Location of the 260 Outfall and the TA-16 study area. The yellow area shows the estimated extent of RDX contamination in the perched-intermediate aquifer. The blue area shows the estimated lateral extent of the perched-intermediate aquifer. Also shown are monitoring wells completed in the perched-intermediate aquifer (shown in green) and in the regional aquifer (shown in red).

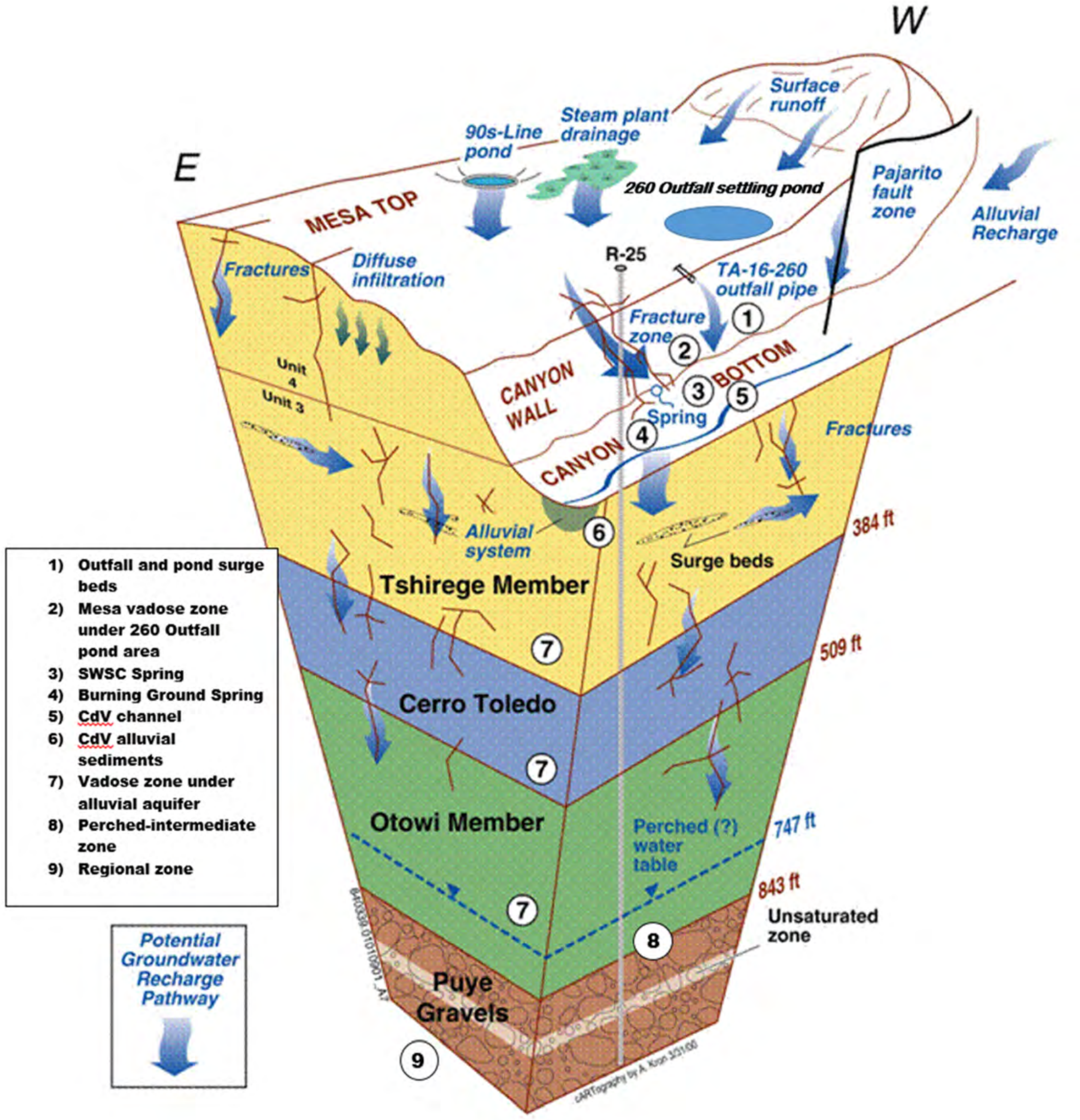

Figure 2.1-1 Conceptual model of RDX source areas and transport pathways through the subsurface at TA-16

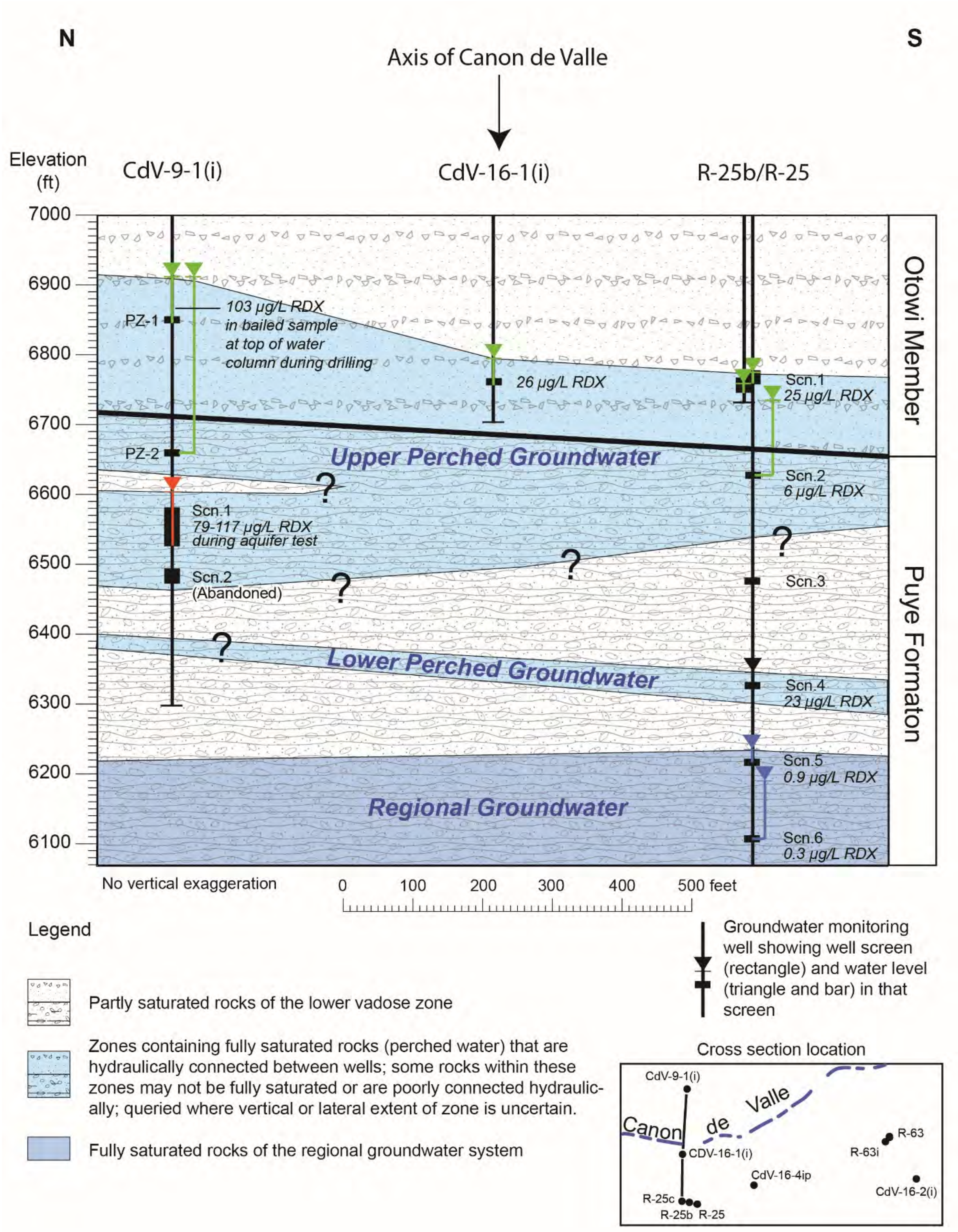

Figure 2.1-2 North-south geologic cross-section for the lower part of the vadose zone showing geologic contacts and RDX groundwater concentrations in wells CdV-9-1(i), CdV-16-1(i), R-25b, and R-25

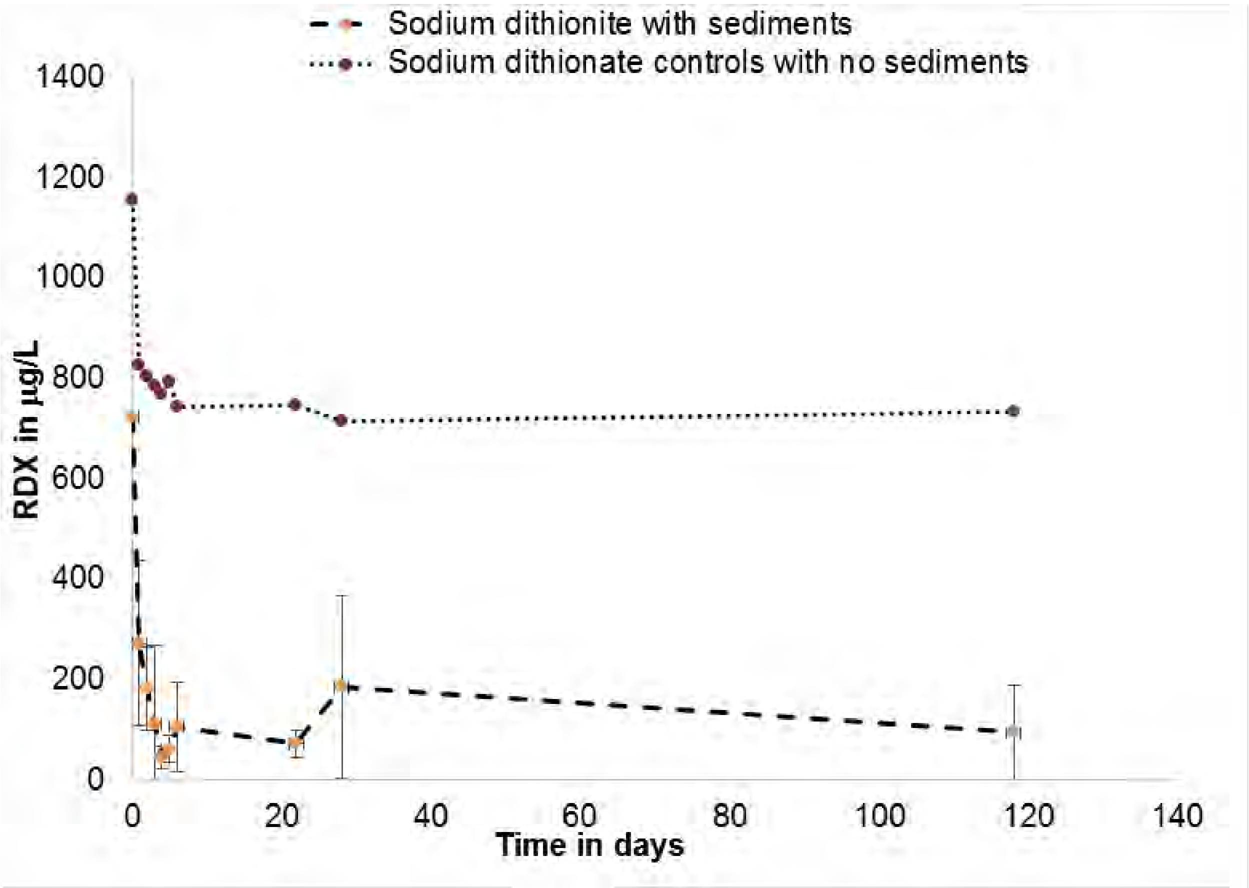

Figure 3.1-1 **Plots showing RDX degradation in sediments treated with sodium dithionite. The sediments were buffered with a pH 9.5 solution of $NaHCO_3/Na_2CO_3$ before the experiment. All experiments were conducted at an ambient temperature of 23.5°C.**

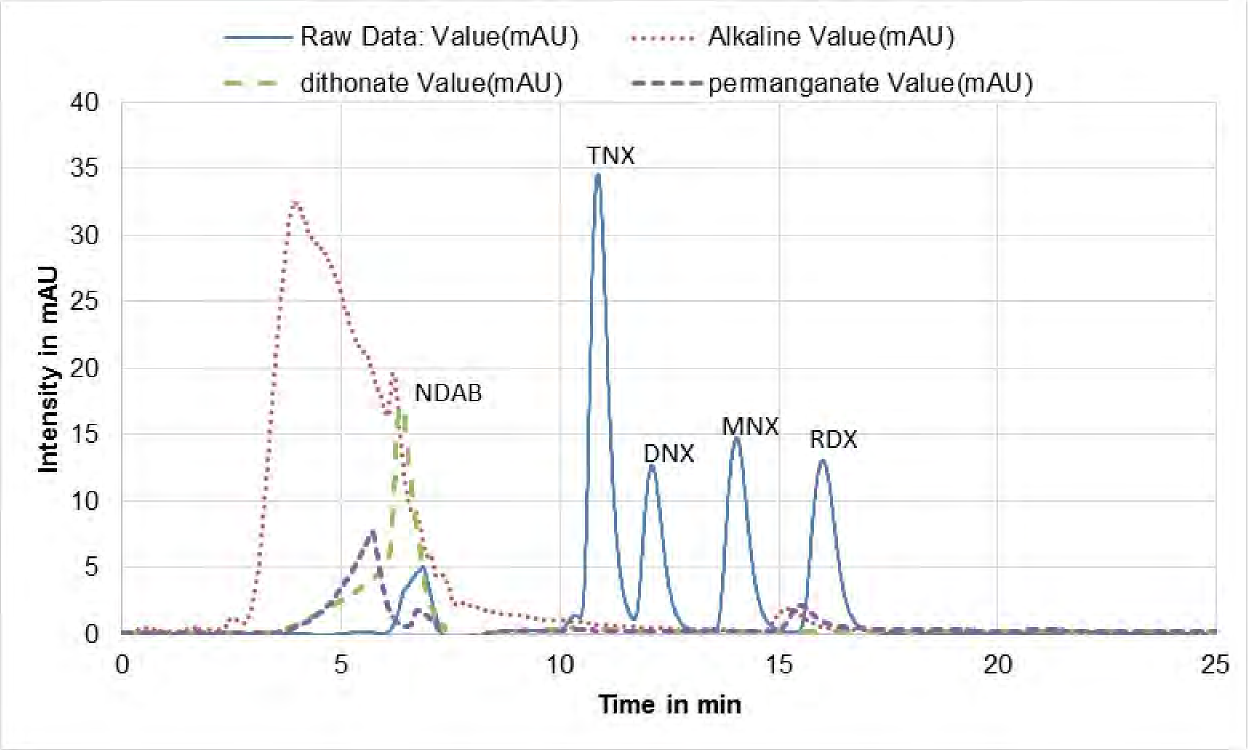

Figure 3.1-2 **HPLC analysis showing chromatograms of water samples from each treatment, as well as a set of 1 mg/L standards of RDX and its known degradation products: TNX, DNX, and MNX. The standards elute from left to right as TNX, DNX, MNX, and RDX.**

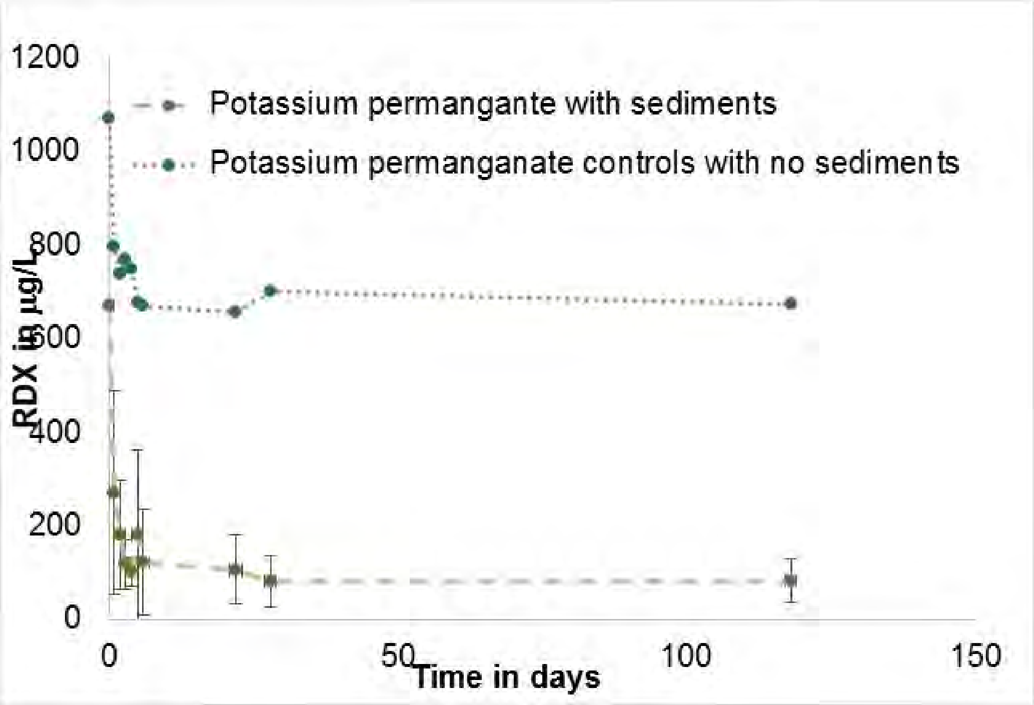

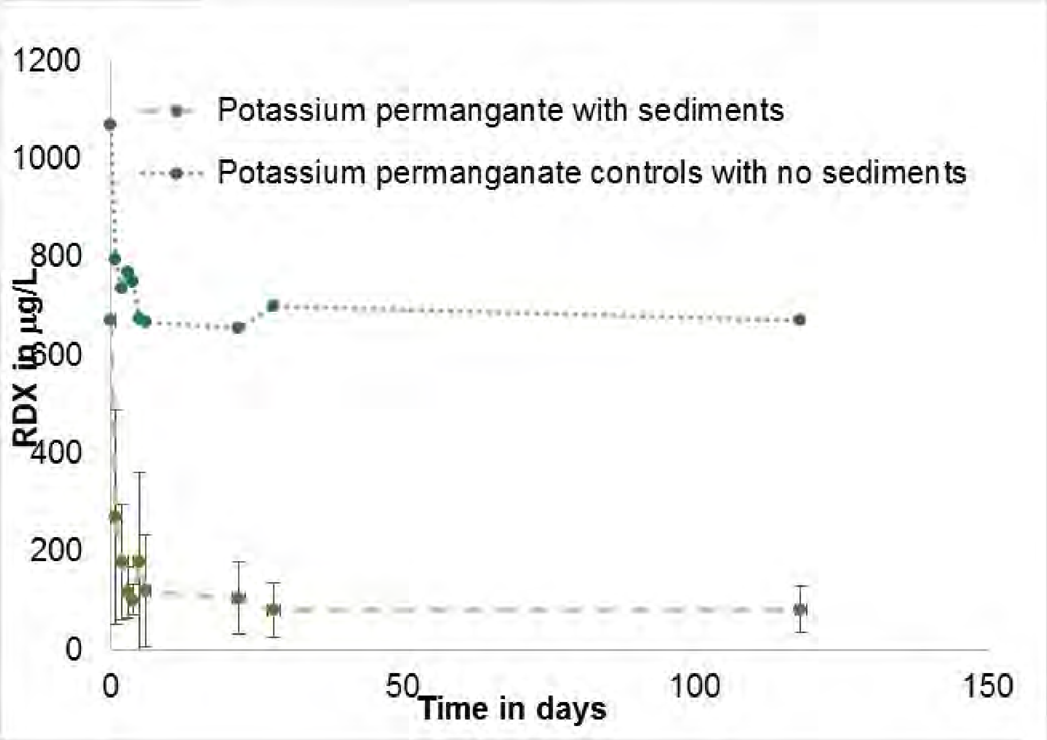

Figure 3.1-3 **Plots showing RDX degradation in sediments treated with potassium permanganate. The sediments were buffered with a pH 9.5 solution before the experiment. All experiments were conducted at an ambient temperature of 23.5ºC.**

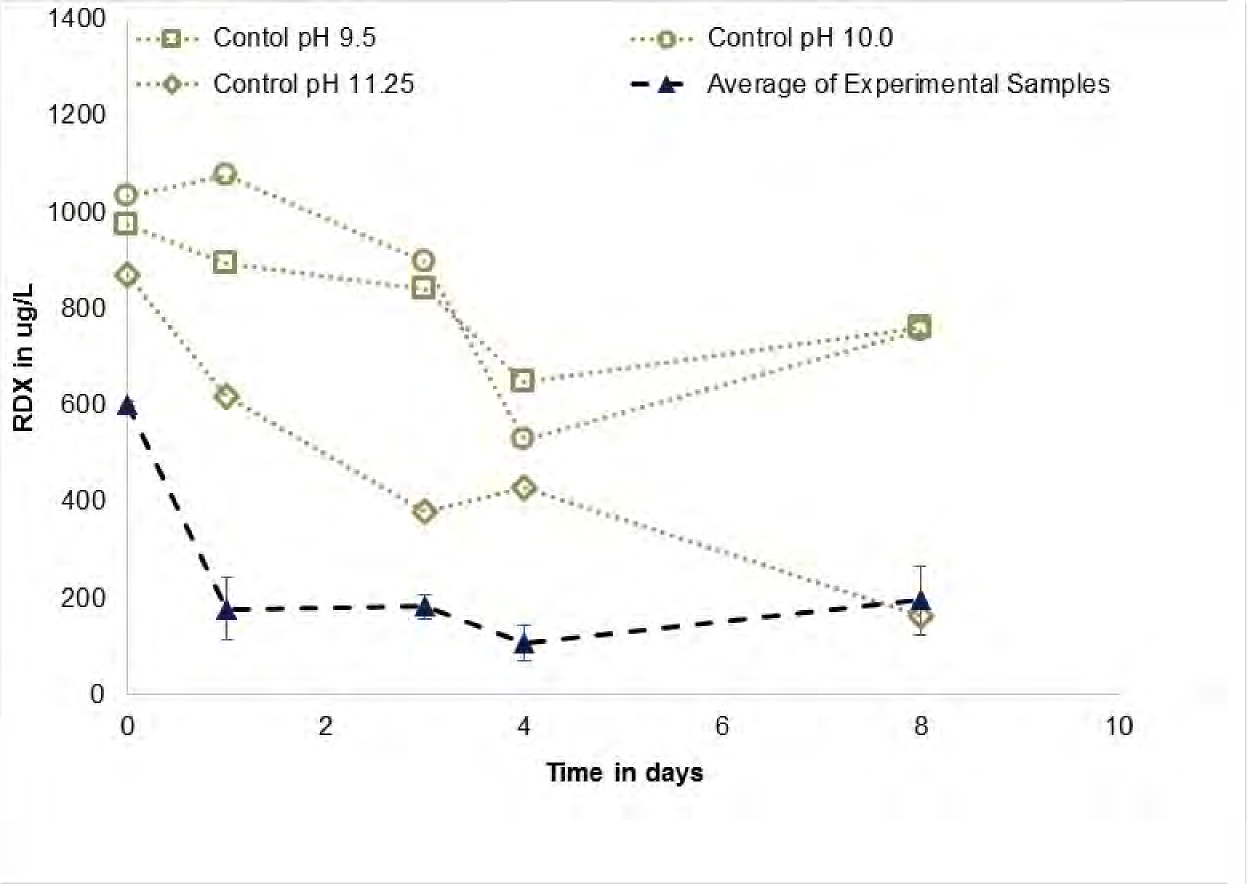

Figure 3.1-4 Plots showing RDX degradation in sediments buffered at pH 8.41 along with controls of solutions buffered at pH 9.5, 10.5, and 11.25 respectively. All experiments were conducted at an ambient temperature of 23.5°C.

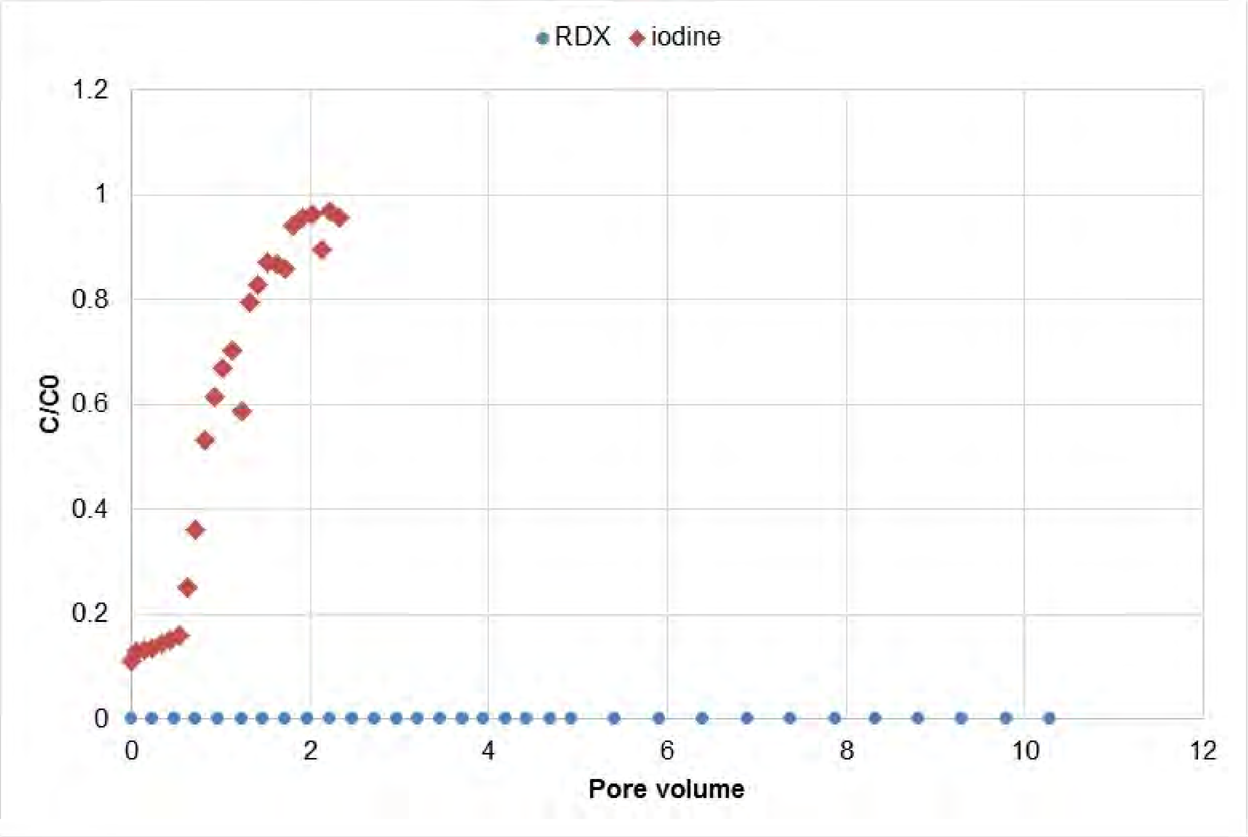

Figure 3.2-1 Concentration breakthrough curves showing RDX transport through columns treated with sodium dithionite along with the iodine tracer used as a conservative tracer. The flow rate was fixed at 1.0 mL/h. pH was initially adjusted to pH = 9.25.

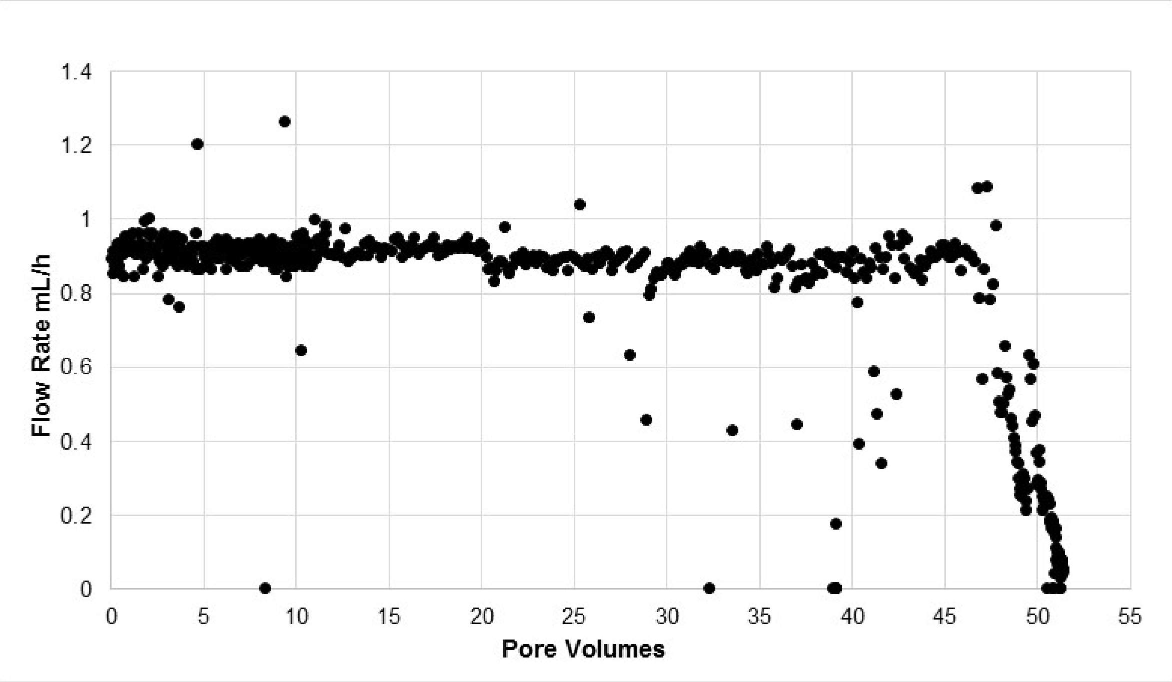

Figure 3.2-2 A plot of the actual flow rate as a function of pore volume for the column treated with sodium dithionite. Plugging of the column occurs rapidly between 46 pore volumes and the end of the experiment at 51.4 pore volumes.

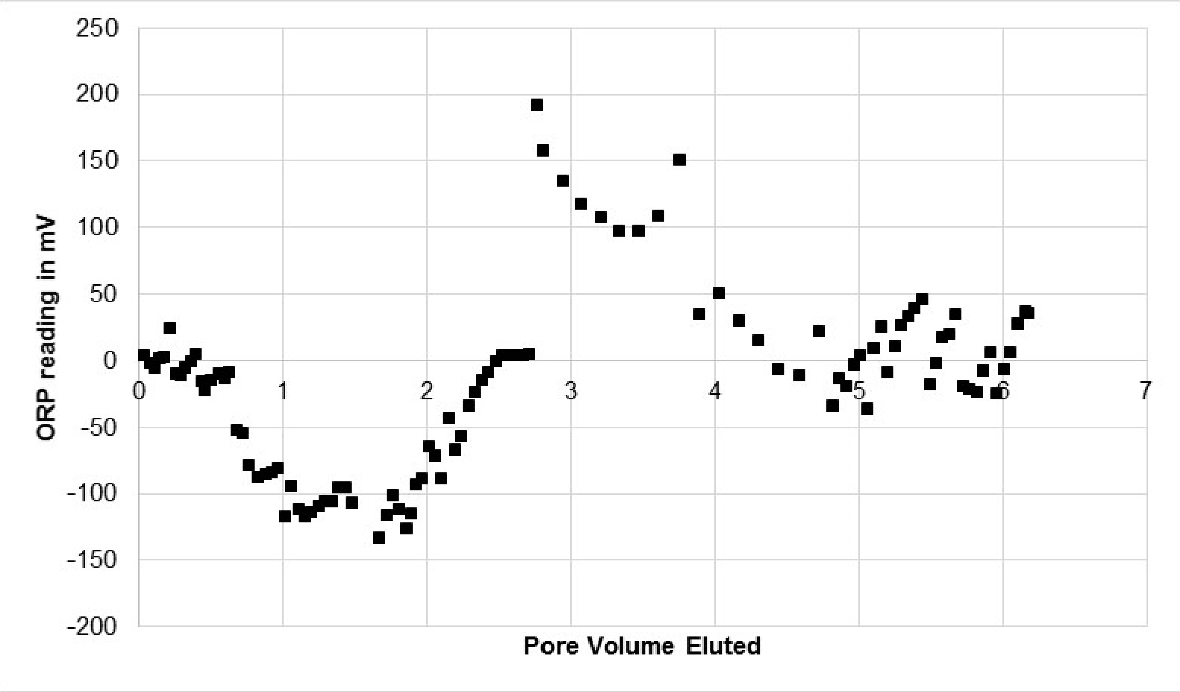

Figure 3.2-3 Redox potential readings for effluents from the column treated using sodium dithionite. The measurements were performed for the period of injection of the sodium dithionite solution and for a few pore volumes after.

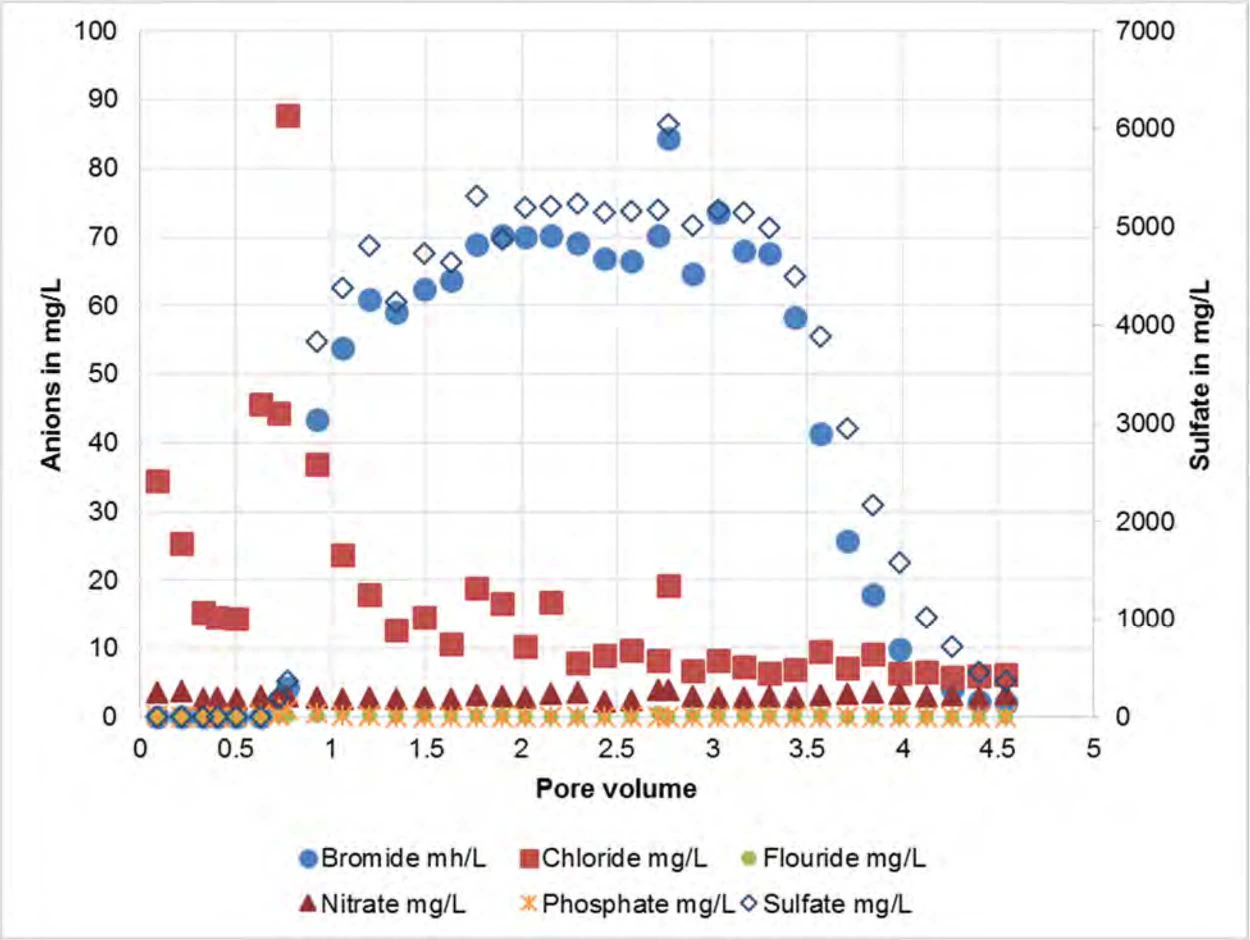

Figure 3.2-4 Concentration breakthrough of various anions relative to the bromide tracer from the column treated with sodium dithionite. The volume of the dithionite pulse is 3.2 pore volumes. The groundwater used was from CdV-16-4ip.

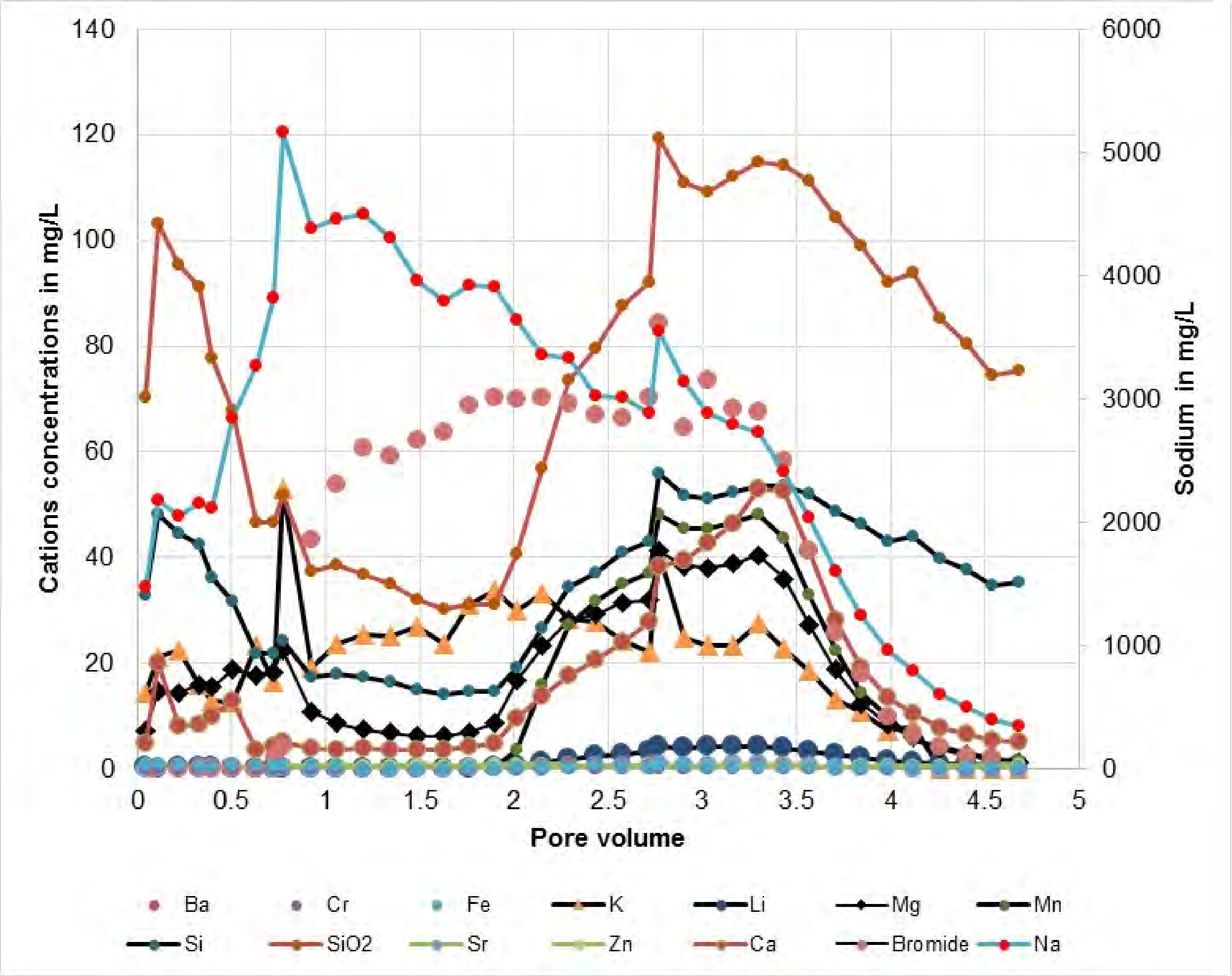

Figure 3.2-5 Concentration breakthrough curves showing cation transport through a column pretreated with a sodium carbonate/sodium bicarbonate solution and treated with a 3.2 pulse of a 1-mM sodium dithionite solution adjusted to pH 9.9.

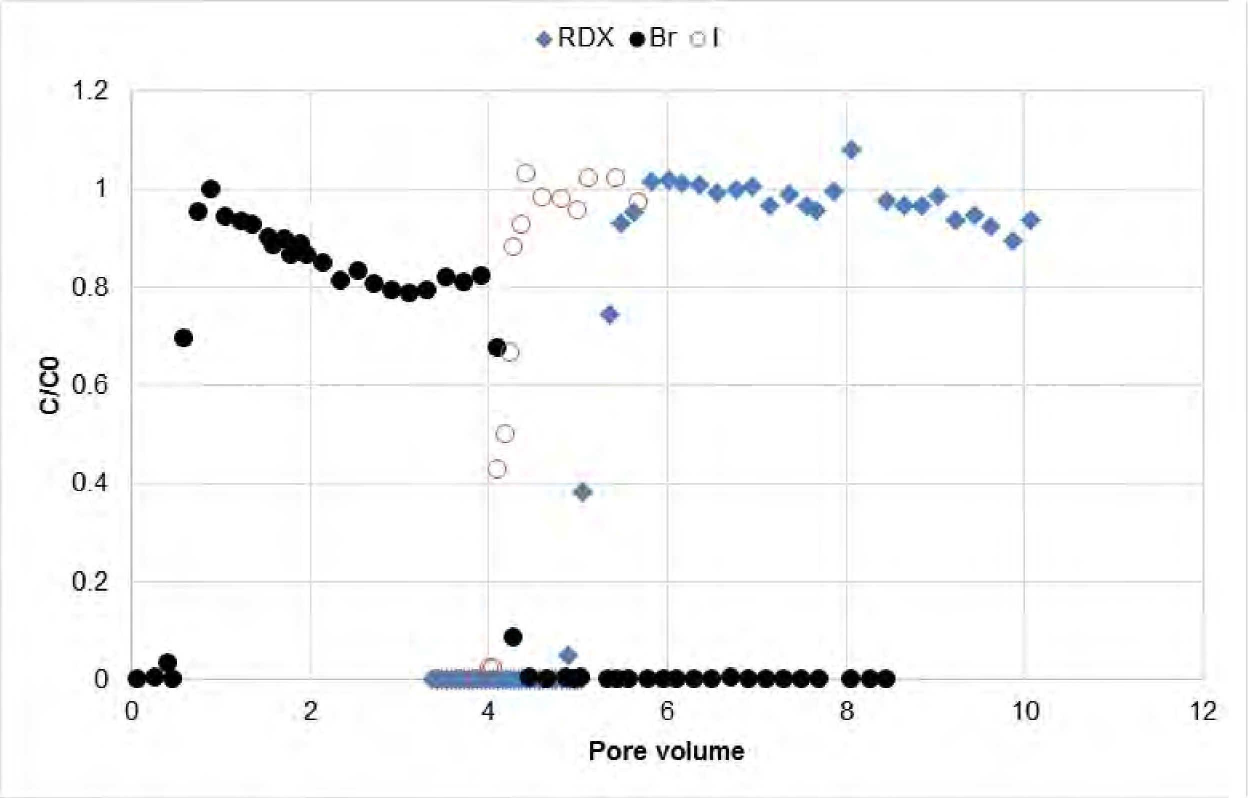

Figure 3.2-6 **Breakthrough curves showing RDX transport through columns pretreated with potassium permanganate. A bromide conservative tracer was added to the pretreatment solution. Injection of a solution containing RDX started at pore volume = 3.4. An iodine tracer was added to the CDV-16-4(i) groundwater solution. The flow rate was fixed at 1.0 mL/h for all columns. pH was adjusted to 9.9.**

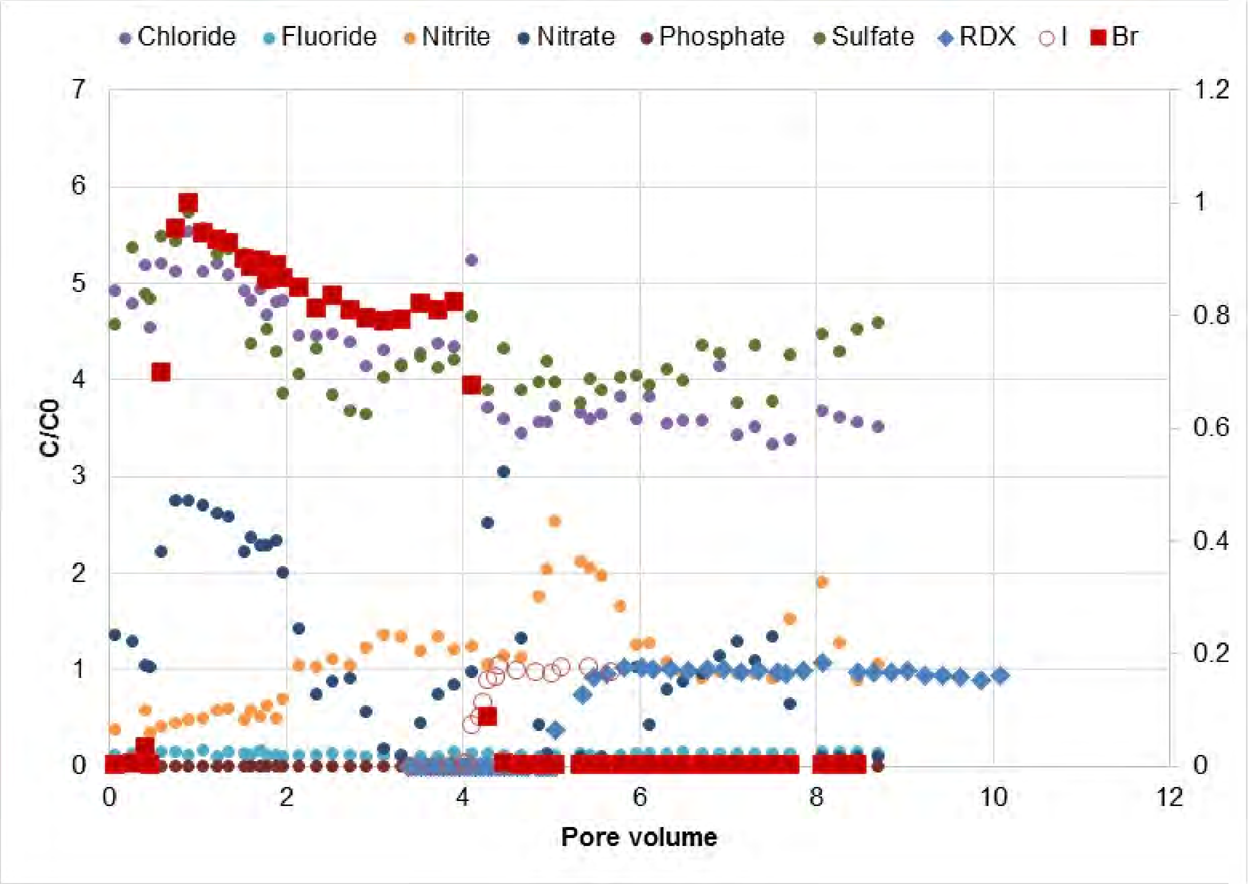

Figure 3.2-7 **Concentration breakthrough curves showing the concentration of anions in the effluent transport through columns pretreated with potassium permanganate. Bromide, a conservative tracer, was added to the pretreatment solution. Injection of a solution containing RDX strated at pore volume = 3.4. An iodine tracer was added to the CDV-16-4(i) groundwater solution.**

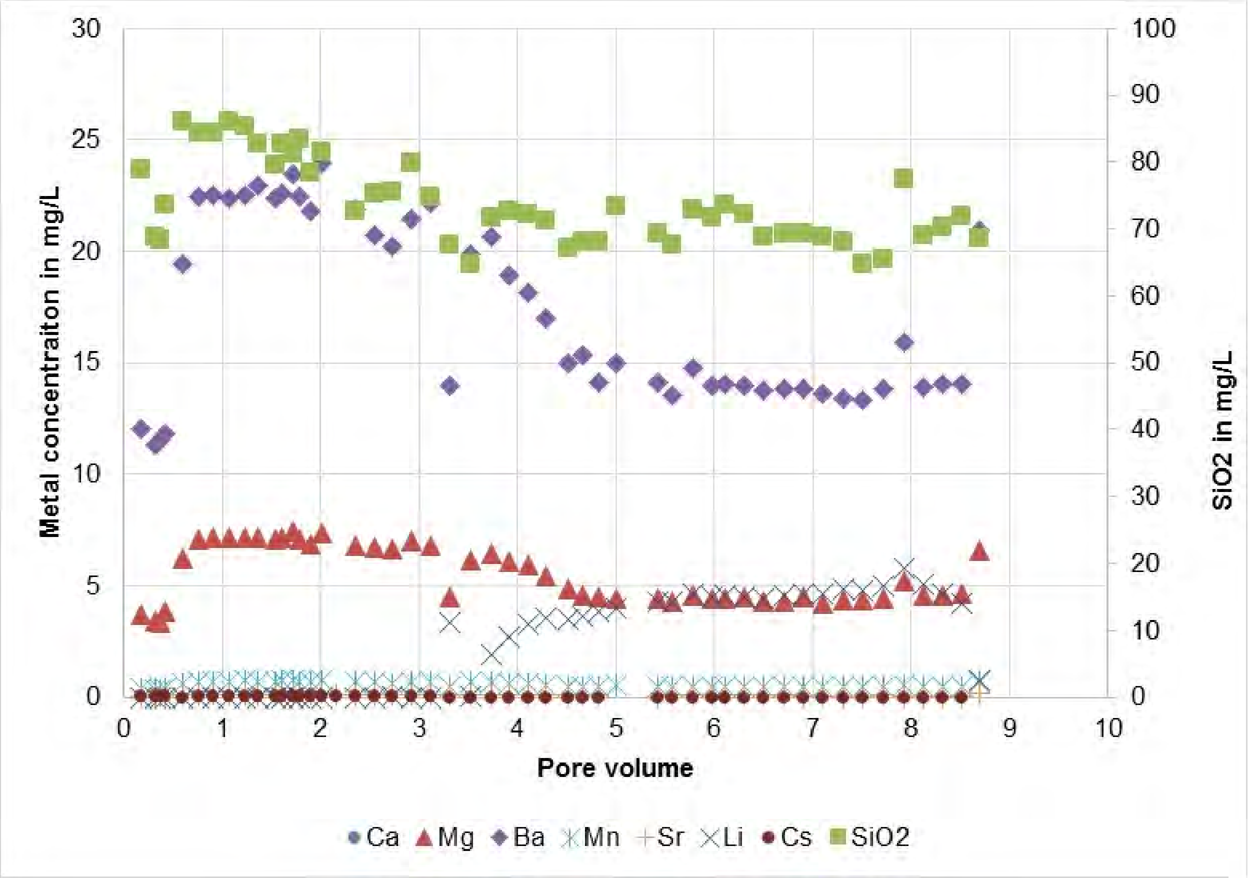

Figure 3.2-8 **Metal concentrations in the effluents from a column filled with Puye Formation sediments and treated with 3.4 pore volumes of potassium permanganate.**

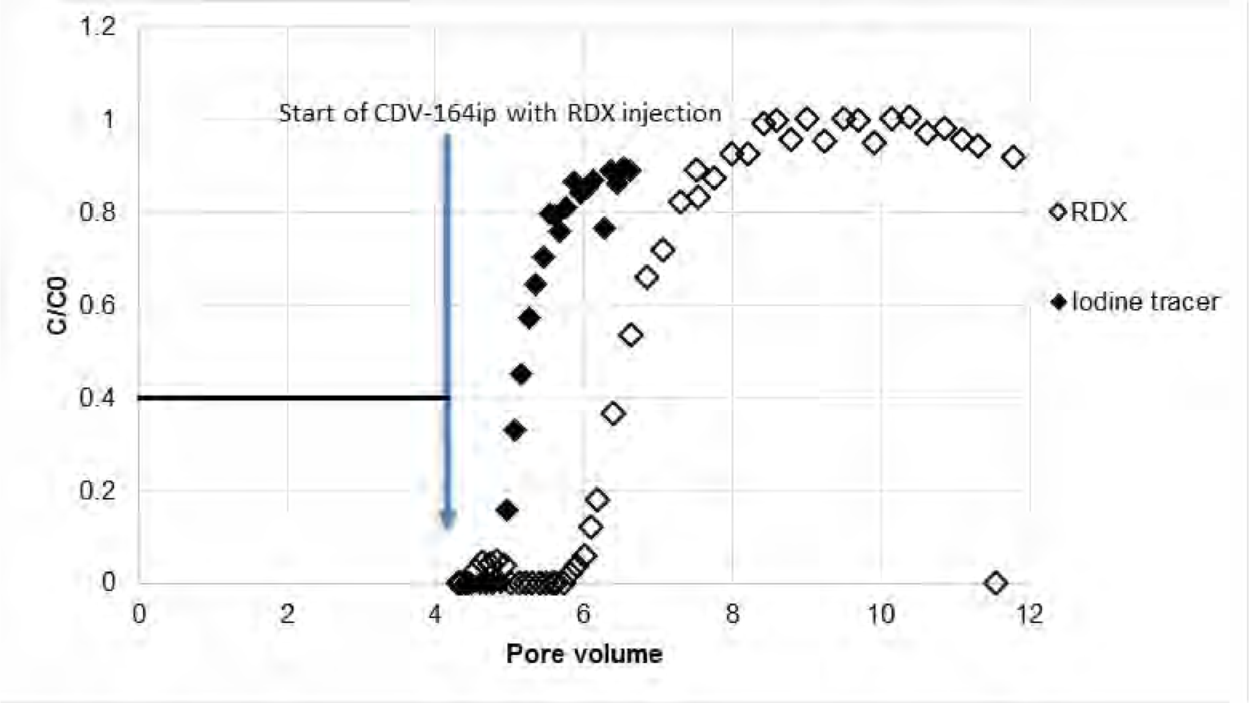

Figure 3.2-9 **Concentration breakthrough curves showing iodine tracer along with RDX transport through a column pretreated with sodium carbonate/sodium bicarbonate solution adjusted to pH 9.9. Injection of a solution containing RDX started at pore volume = 4.3. The flow rate was fixed at 1.0 mL/h for all columns. pH was adjusted to 9.94.**

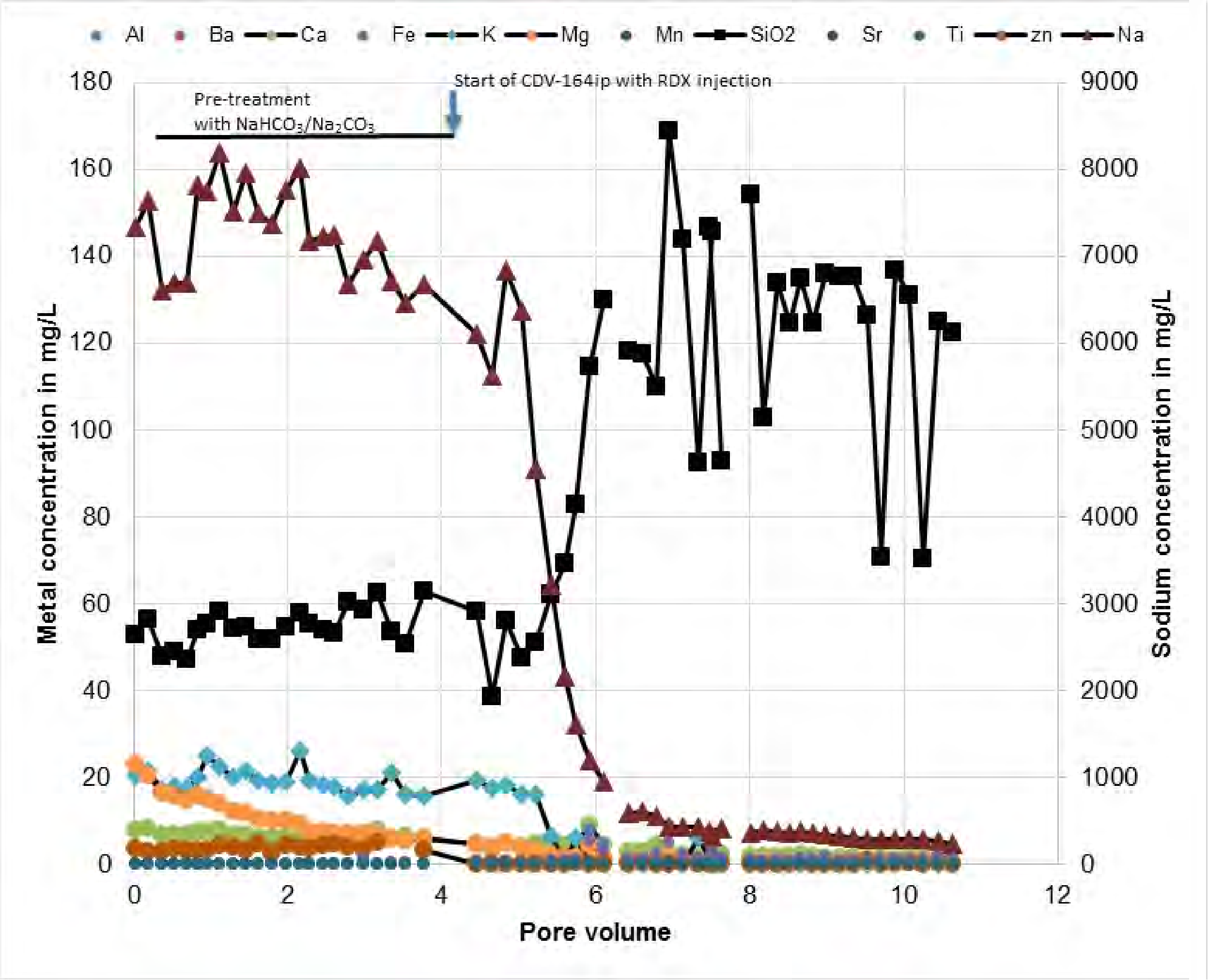

Figure 3.2-10 Concentration breakthrough curves showing metals transport through a column pretreated with sodium carbonate/sodium bicarbonate solution adjusted to pH 9.9. Injection of a solution containing RDX started at pore volume = 4.3. The flow rate was fixed at 1.0 mL/h for all columns. pH was adjusted to 9.94.

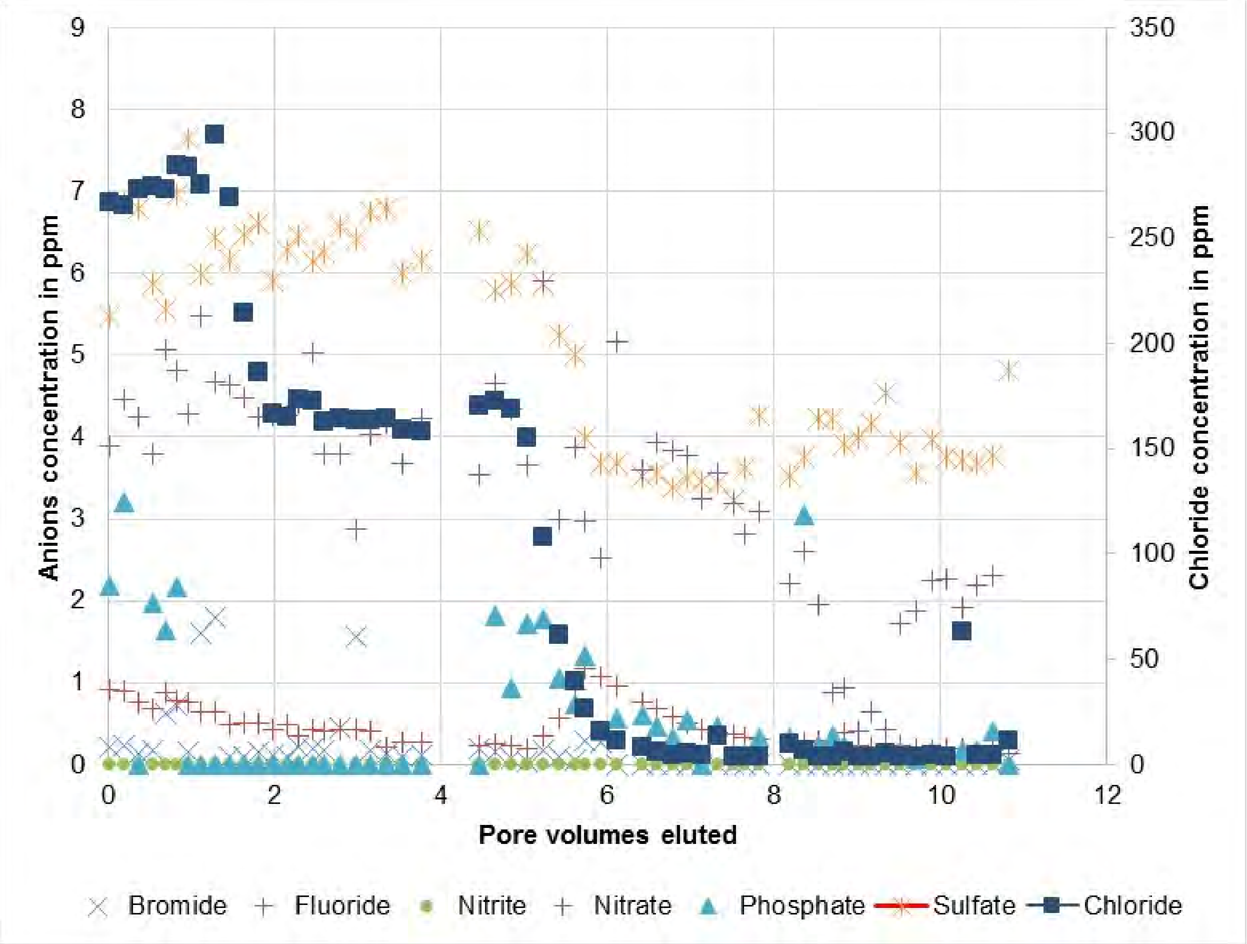

Figure 3.2-11 **Concentration breakthrough curves showing anion transport through a column pretreated with sodium carbonate/bicarbonate solution adjusted to pH 9.9. Injection of a solution containing RDX started at pore volume = 4.3. The flow rate was fixed at 1.0 mL/h for all columns. pH was adjusted to 9.94.**

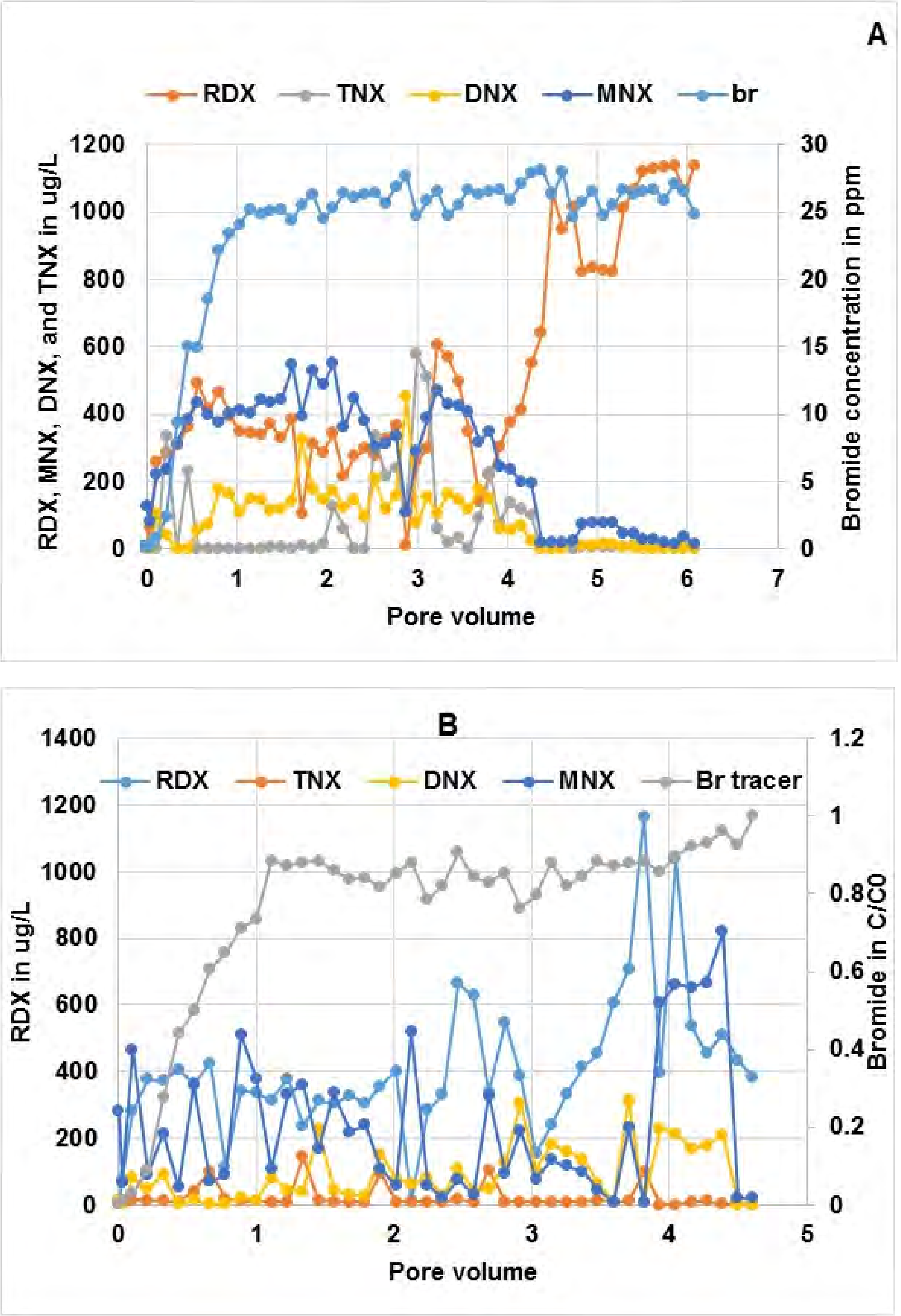

Figure 3.2-12 Concentration breakthrough showing RDX and bromide tracer breakthrough curves for columns biostimulated with molasses (3.6 g/L mM) and safflower oil (10 g/L %). The plots also show the concentration breakthrough of the degradation products MNX, DNX, and TNX. The initial concentration of RDX was 1161 µg/L and the concentration of the degradation products was less than 1 µg/L. The flow rate was fixed at 2.0 mL/L.

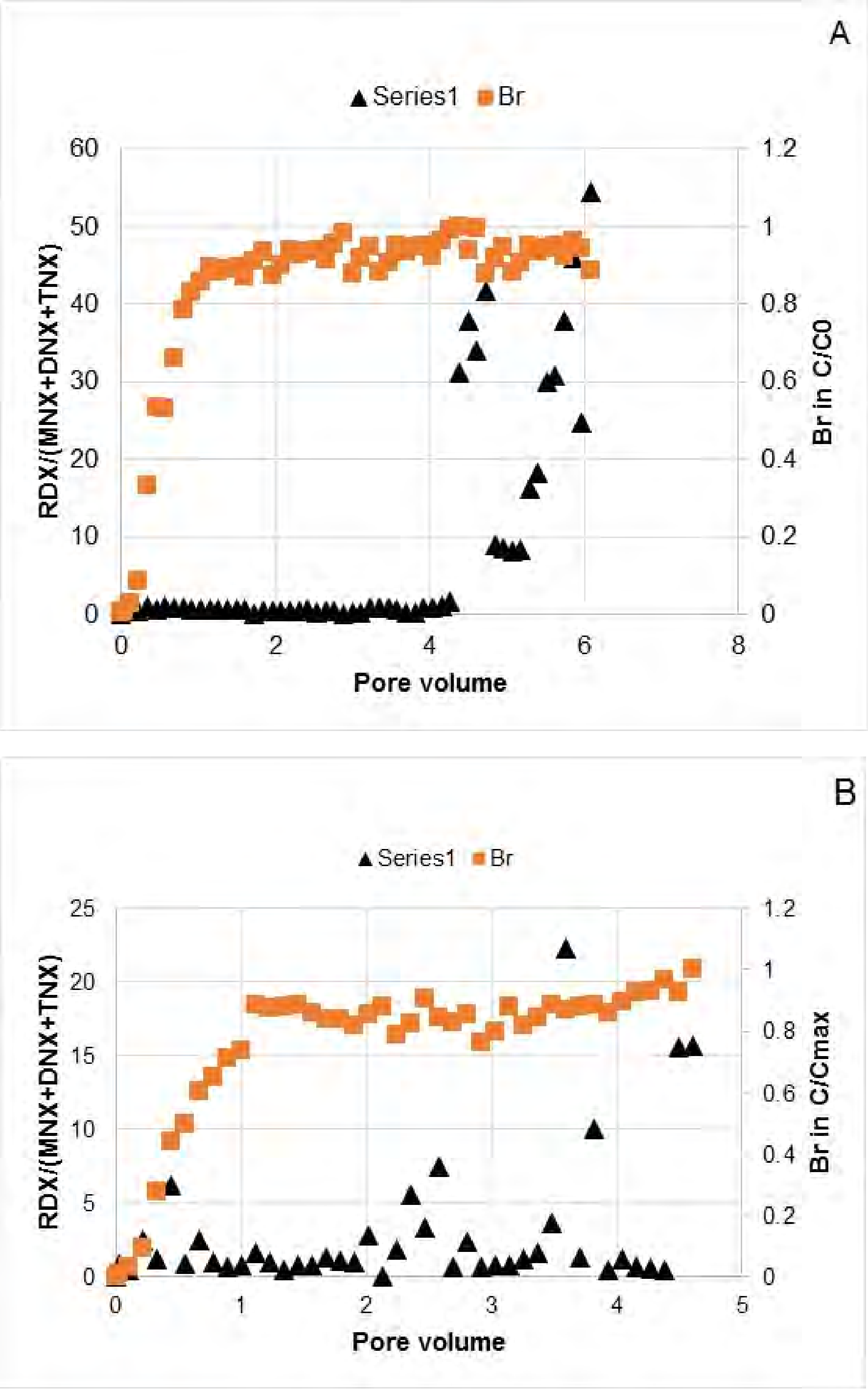

Figure 3.2-13 Molar ratios of RDX to degradation products MNX +DNX+ TNX (Series 1) during the breakthrough of the column stimulated with molasses (A) and the column stimulated with safflower oil (B), along with the breakthrough of the bromide tracer. The initial concentration of the RDX was fixed at 1161 µg/L and concentration of degradation products were less than 1 µg/L. The pH of the column effluents increased from 4.5 to 8.4 in the molasses column and remained stable at pH = 8.4 in the safflower oil column.

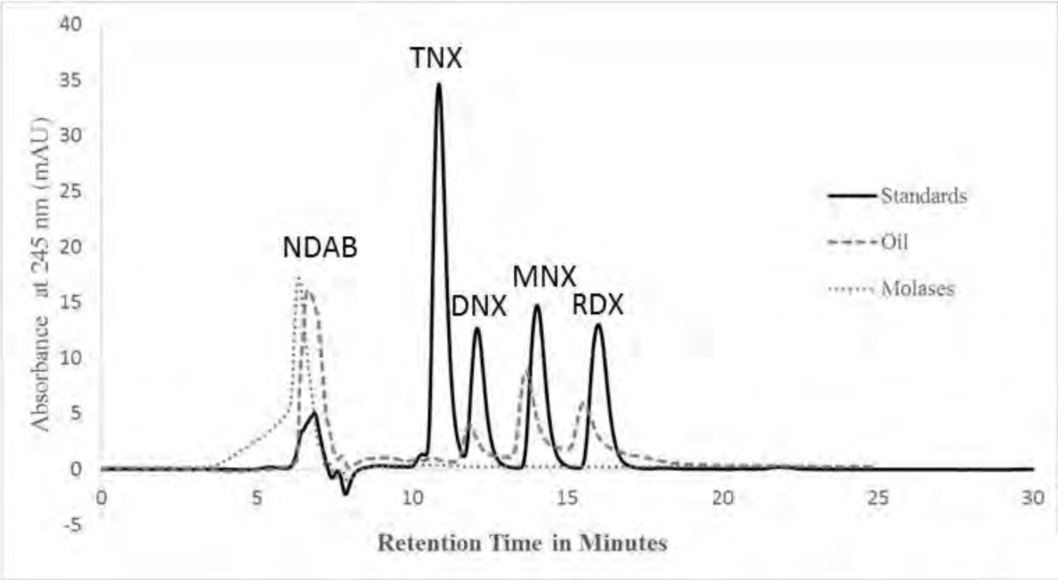

Figure 3.2-14 HPLC analysis showing chromatograms of water samples from the biostimulated column as well as a set of 1-mg/L standards of RDX and its known degradation products TNX, DNX, and MNX. The standards elute from left to right as TNX, DNX, MNX, and RDX.

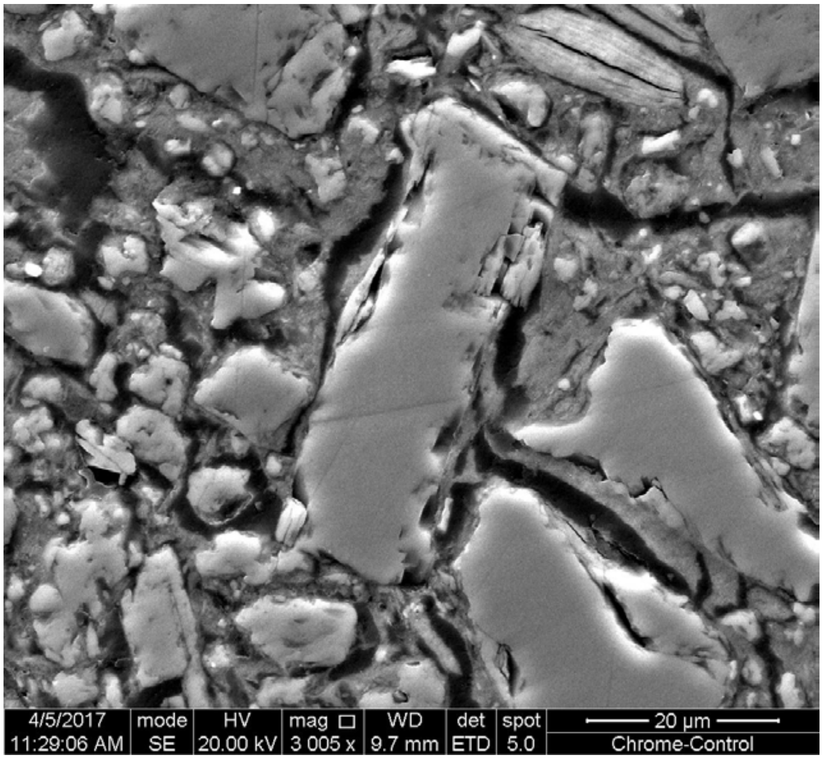

Figure 4.1-1 SEM image of sediments post-treatment with sodium dithionite and flow of 52 pore volumes of groundwater from CdV-16-4ip. The SEM image was obtained for a sample taken from the inlet of the column (1 cm). The sample was preserved in an epoxy resin under an argon atmosphere.

Table 2.5-1
Specific Parameters for Treatment and Test Injections in the Four Experimental Columns

	Alkaline	**Dithionite**	**Dithionite 2**	**Permanganate**
Treatment concentration (mM)	200.00	50.00	50.00	5.00
Iodine/bromide tracer concentration (mg/L)	91.69	108.07	n/a*	100.41
Treatment duration in pore volume	4.50	5.78	2.73	3.37
RDX concentration (μg/L)	1249.37	1249.37	n/a	908.50

* n/a = Not applicable.

Table 3.1-1
Specific Parameters for Treatment and Test Injections in the Four Experimental Columns

	Dithionite	**Alkaline**		**Permanganate**	**Biostimulation**
	$k_{obs\text{-}dithionate}$	$k_{obs\text{-}alkaline}$	**pH**	$k_{obs\text{-}permanganate}$	
Observed rate constants in h^{-1}	0.86 ± 0.08	0.021 ± 0.006*	8.41	0.56 ± 0.13	Not applicable.
		0.014±0.009	9.50		
		0.037±0.02	10.0		
		0.044±0.03	11.25		

*In the presence of sediments.

LA-UR-18-21326
March 2018
EP2018-0025

Hydrogeology and Model Calibration for Contaminant Fate and Transport at Technical Area 16

Attachment 8

Prepared by the Associate Directorate for Environmental Management

CONTENTS

Figures

Tables

Appendixes

1.0 MODEL DESCRIPTION

1.1 Continuous Three-Dimensional Vadose Zone/Saturated Zone Model

A three-dimensional (3-D) flow and transport model of the vadose zone (VZ) and upper saturated zone (SZ) in the vicinity of the Cañon de Valle (CdV) area is being developed to serve as a platform for (1) the integration of Technical Area 16 (TA-16) site information and models developed over the past several years, and (2) quantitative predictions for the fate and transport of RDX (hexahydro-1,3,5-trinitro-1,3,5-triazine) at TA-16. The model must honor the key hydrologic and hydrogeochemical data collected at the site and provide the ability to predict RDX concentrations, transport rates, and long-term contaminant mass flux to the regional aquifer beneath the contaminated source. Ultimately, this model is critical to the system model that simulates the behavior of RDX in the regional aquifer out into the future, and quantifies uncertainties of key parameters such as RDX concentrations at hypothetical compliance locations downstream of TA-16. The model must also predict the rates of attenuation of high explosives (HE) contaminant concentrations by dispersion and the fate of a limited contaminated VZ source that dissipates with time.

The VZ is the pathway through which RDX must travel to supply contaminant to the regional aquifer. Therefore, proper representation of flow and transport parameters and the operative subsurface processes is essential to the completion of this model, or future model(s), at a more mature stage of development, in order to provide the RDX flux, time frame(s) and arrival location(s) at the regional aquifer water table. Important criteria that must be satisfied in order to use this model in quantitative predictions include the following:

- The model must capture the main elements of subsurface VZ flow, including the time-averaged local TA-16 recharge and mountain front recharge (MFR) rates of fluid flow from the surface and the deeper lateral flow entering the deeper aquifers via mountain block recharge (MBR).
- In the model, the perched water zones, considered to be important pathways in the VZ, must reproduce the observed geologic, hydrologic, and hydrochemical data collected from wells drilled in the vicinity.
- The model must reproduce the observed RDX time-dependent concentration data in the VZ, via transient flow and transport simulations that model the impact in the VZ of the substantial flux of RDX-contaminated water from the 260 Outfall to the system from the year 1951 to the present day.
- The model must be generally consistent with field observations, the geologic framework model (Attachment 2), and the hydrogeochemical conceptual model (HGCM, Attachment 3), developed during the course of the many years of data collection and study of the system and presented in this compendium.

With these requirements in mind, the assumptions related to the development of the TA-16 VZ flow and transport model are described and justified below, by reference to the specific findings in several of the individual chapters of this compendium.

Flow Model Features: Flow processes important to the prediction of RDX travel times and concentrations include infiltration, anthropogenic inputs, surface local recharge and MFR, and deeper MBR sources. The flow model must capture background infiltration from mesas and canyons, anthropogenic inputs of water from the 260 Outfall from 1951 to 1996, and water supplying the perched VZ groundwater and the regional aquifer. This is accomplished using various flow inputs for water sources with a specified flux at different locations. According to the TA-16 HGCM update (Attachment 3, "A Refined Hydrogeochemical Conceptual Model for the RDX Project"), the perched zones in the VZ are likely fed by a substantial MBR component (>40%). These perched zones are sustained due to barriers to vertical downward percolation associated with hydro-lithologic contacts (i.e., Attachment 2, "Geology of Technical Area 16 and Vicinity, Los Alamos National Laboratory"). The barriers are in part controlled by the lithostratigraphy, represented in the model as interface zones of low permeability that divert flow in the perched zones towards the east and southeast. These barriers are controlled by the dip of bedding and contact surfaces within major stratigraphic units. Although there is substantial seasonal variability in measurements at some locations as well as transients induced by wildfire impacts (e.g., Attachment 3), this model assumes that to a first approximation, such short-term transients can be averaged in a long-term model in which only the flow transient associated with the 260 Outfall perturbation is considered. Isothermal flow is also assumed, as thermal effects on flow should be negligible.

Transport Processes and Properties: RDX transport through the deep subsurface is primarily affected by the processes of advection-dispersion, light exposure at the surface and potentially by retardation due to sorption, and degradation from biologic processes at depth. Advection and dispersion are accounted for in the model using standard assumptions, with flow represented by the flow model above. The experimental laboratory batch and column test results on RDX and its degradation products suggest that the volcanic and sedimentary lithologies that represent the contaminated VZ in the vicinity of TA-16 have little to no capacity to delay RDX or its derivatives (Attachment 4, "Fate and Transport of Hexahydro-1,3,5-trinitro-1,3,5-triazine [RDX] and Its Degradation Products in Sedimentary and Volcanic Rocks, Los Alamos New Mexico").

By contrast, in this preliminary version of the model, a sorption term is allowed, using effective equilibrium constants (Kd's) that are estimated by inverse modeling used in the model calibrations. This deviation from the updated HGCM is because of parallel development of the model and experiments at this preliminary stage. The model will be adjusted in the near future to reflect recent geochemical findings, by eliminating or severely reducing the sorption coefficient values. Additionally, no substantial abiotic degradation of RDX was observed in the laboratory experiments, even though field measurements often detect RDX degradation products. This is explained in the HGCM update (i.e., Attachments 3 and 4, as caused by the surface degradation of RDX produced predominantly under transient anoxic conditions in the shallow alluvial groundwaters (c.f. Attachment 6, "Characterization of the Microbial Population and RDX Degradation in Groundwater at Technical Area 16"). In the model, the alluvial system is not explicitly represented in the flow and transport calculation: rather, the water and RDX are represented as a direct input term from the 260 Outfall to the deeper subsurface. Therefore, this model assumes no degradation occurs and the RDX is tracked in the deep system as a nonreactive species in an oxic environment.

Model parameters identified as uncertain are estimated by calibration using observed field data described in a subsequent section. Inverse analyses are carried out using the model analysis and decision support (MADS) code (http://mads.lanl.gov) (Vesselinov and O'Malley, 2016; Vesselinov et al., 2016), which involves a number of forward flow and transport model simulations using the finite element heat and mass (FEHM) code (http://fehm.lanl.gov).

2.0 MODEL SETUP

The VZ model domain includes both SZs represented by perched-intermediate groundwaters and the top of the regional water table, and unsaturated zones (UZs). In the UZ, a van Genuchten water-retention model is used to describe the constitutive relationship between the water pressure and water content. An extension of the van Genuchten model based on Mualem-Mualem theory is applied to describe the constitutive relationship between the water content and relative unsaturated permeability. The subsections below lay out the remainder of the model setup, including the development of the computational grid, boundary and initial conditions.

Numerical Grid

The computational grid for the RDX model is designed with the Los Alamos National Laboratory (LANL or the Laboratory) LaGrit mesh generator. This facilitates the tasks of calibration and validation of the VZ model in order to (1) reproduce observed geological, hydrologic, and geochemical data, (2) capture principal geologic structures and lithologies, (3) incorporate geometries and locations of perched zones and boreholes, and (4) use measured transient, temporally variable RDX concentrations from various borehole locations at TA-16.

The geologic framework model (GFM) used for this model is identified as version WC15c, and is constructed by Dan Strobridge of Weston Solutions, Inc., using geologic data and maps from Broxton and Vaniman (2016), and the EarthVision modeling software from Dynamic Graphics, Inc. There are 13 hydrogeologic units in the model domain, including Puye Formation below Cerros del Rio Basalt (Tpf2), Younger Tschicoma Dacites (Tvt2), Puye Formation on top of Cerros del Rio Basalt (Tpf3), Otowi Member, ash flow (Qbof), Cerro Toledo Formation (Qct), Otowi Member, Guaje Pumice bed (Qbog), Tshirege Unit 1g – glassy (Qbt1g), Tshirege Unit 1v – upper vitric (Qbt1vu), Tshirege Unit 2, Bandelier (Qbt2), Tshirege Unit 3, Bandelier (Qbt3), Tshirege Unit 3t, Bandelier Tuff (Qbt3t), Tshirege Unit 4, Bandelier (Qbt4), Otowi Member, ash flow (Qbof_G2), and Otowi Member, ash flow (Qbof_G3). The fixed hydraulic properties for these units are listed in Table 2.0-1. Other properties such as a permeability and a sorption coefficient for each unit are estimated parameters from the inverse model (not listed here). In general, uncertain model parameters selected for inverse modeling determinations have significant effects on the water balance, flow velocities, occurrences of perched water in the VZ, and/or RDX transport processes. Finally, this site model includes supplemental Otowi sub-layers that are present in the EarthVision model input file, TA16.seq.

The goal of the modeling is to capture the heterogeneity in the portion of the system characterized both horizontally and vertically by the four wells R-25, CDV-9-1(i), CDV-16-4ip, and R-63i, where sampling data from perched water zones indicates significant elevated RDX concentrations. The domain of this mesh is the shape of a polygon that encompasses perched water zones that extend eastwards from the Pajarito fault zone past the estimated edge of the alluvial aquifer. While this is an appropriate choice for a VZ model, a larger model domain would be required to model RDX transport of mass within the regional aquifer. Alternatively, separate VZ and SZ models could be developed in which the RDX flux from the VZ model is mapped onto the SZ model. Because this preliminary model is focused on VZ flow and transport, the more restricted lateral boundaries of the model chosen are adequate.

The mesh strategy is optimized to both minimize numerical dispersion and accommodate data input via the construction of a partially unstructured mesh with orthogonal elements at variable elevations stacked into a 3-D mesh. This allows the selection of a smaller area-fitting domain and a grid resolution choice that does not depend on high resolution (more nodes) to capture important interfaces. The stacked mesh is made up of selected surfaces extracted from GFM, and individual grid layers divided proportionally in between layer pairs for the vertical spacing. The layers in this mesh that conform to GFM surfaces are the top surface, the top of Qbof (Otowi), Tpf3 (Puye), and the water table surface. The bottom is flat at an elevation equal to 1700 meters, which is significantly below the water table elevation at all locations in the model domain. The GFM materials are interpolated onto the grid nodes and the nodes above the ground surface are removed.

The grid nodes are connected into tetrahedral elements based on the Delaunay criteria. After constructing and verifying the grid, attributes are assigned to grid nodes and model setup files are written for input into FEHM simulations. As a verification of grid quality, LaGriT reported a successful matrix for this mesh with positive Voronoi volumes and zero negative coefficients on the interior of the grid. The final mesh consists of 60,516 nodes and 345,050 elements. The grid mesh is illustrated in Figure 2.0-1, where the vertical lines represent the locations of wells present within the model domain. The spatial distribution of all 13 hydrostratigraphic units is shown in Figure 2.0-2.

Initial and Boundary Conditions for Flow Simulations

Because the goal is to build a model that accurately represents the observed perched zones and measured RDX concentrations at various locations, it is important to set initial and boundary conditions for flow simulations in such a way that observed perched zones are honored.

To establish the boundary condition representing the regional aquifer, nodes at the regional water table are assigned to fixed full saturation and atmospheric pressure (0.1 MPa) values, consistent with the natural hydrogeological conditions. All nodes below the water table are assigned to full saturation and fixed constant hydrostatic pressure (reference to the water table). Potential water table changes for the regional aquifer because of recharge from canyons or the mountain front are not represented in the model. For the perched zones located above the regional water table, all nodes are initially assigned to full saturation, and the pressure at these nodes is calculated from the hydrostatic condition with a pressure of 0.1 MPa at the top node in each vertical column of nodes. Broxton and Vaniman (2016) developed a 3-D depiction of the perched zones based on available well data; this rendering of the perched water bodies is used to establish an initial condition for the model runs. To maintain the perched zones, pressure and saturation at those perched nodes along model boundaries are fixed (enabling flux to exit the model at those locations if needed), except for the western boundary, where the total water flux into the model domain through these perched nodes is a parameter to be estimated. Pressure and saturation at the rest of perched nodes are allowed to drain or fill up during the course of the simulations.

The flow properties used to create and maintain the perched zones include a permeability reduction factor at the bottom of the perched zones to simulate the presence of a thin perching layer at that location. This permeability reduction is implemented in FEHM, and is typically applied to the interfaces between pairs of materials. In this case, since the bottoms of the perched zones run across several material interfaces, new FEHM zones are created in such a way that the interface between a pair of zones is consistent with the bottom of the perched zones. Permeability reduction is also allowed between zones that are part of Tfp3 and were created to allow water drainage in Tfp3, because otherwise the water in the perched zone will move along the bottom of the upper perched zone indefinitely.

Groundwater flux is specified at the top boundary. This flux varies spatially and, in the case of the 260 Outfall, temporally. The background infiltration is applied to all top nodes except for the canyons. The total recharge from canyons (not including CdV) is also a parameter to be estimated. This recharge is distributed as a uniform flux applied to all nodes in the canyons. The CdV area has an additional water source from the 260 Outfall, which was active from 1951 to 1996. The annual flow rate of this water source was estimated from the production conditions (the number of shifts per day, production hours per shift, and gallons of water per minute, etc.).

Initial and Boundary Conditions for Transport Simulations

Zero initial RDX concentration is assumed in the entire domain at the beginning of the simulation (1/1/1950). The 260 Outfall is assumed to be the only source of the RDX mass input, and the time-dependent rate of RDX mass input is assumed to be equal to the product of the 260 Outfall water flow rate and the maximum solubility (44 mg/L) of the RDX. This assumption is appropriate at this initial stage of model development, but in future versions of the model variations of this approach that include uncertainties and variations in mass input should also be considered.

2.1 Discrete 3-D VZ/SZ (Pipe-and-Disk) Model

Recently we developed a discrete 3-D VZ/SZ model that represents the medium as a series of discrete zones. This model is also called a *pipe-and-disk* transport model because the SZ paths are represented as 3-D disks and the vadose (unsaturated) zone paths are represented as vertical pipes. The model is developed and coded as a Julia-language module (http://julialang.org). This model includes a set of analytical solutions that can link together an arbitrary number of UZs with an arbitrary number of SZs. Here, the SZs can be either perched SZs within the VZ or the regional aquifer. A model is built by defining a number of “pathways” where each pathway can have stacked UZs/SZs. Pathways are summed by superposition to represent multiple ways for contaminants to travel from the ground surface through the VZ (“pipes”) to common perched SZs (“disks”).

The UZ(s) are simulated as 1-D vertical conduits (“pipes”) with advection and diffusion of contaminants. SZs are collapsed to horizontal “disks” with uniform vertical thickness; the contaminant flux through the “disk” can be simulated as 2-D or 3-D starting from the areas of contaminant arrival (“SZ1Origin” and “SZ2Origin”; Figure 2.1-1), to the location of contaminant exit (“SZ1DP”; Figure 2.1-1). Typically, “SZ1Origin” and “SZ2Origin” are located along the disk surfaces “SZ1” and “SZ2”, and “SZ1DP” is located along the bottom of the disk surface “SZ1.” The location of “SZ2OP” is defined by the location of a respective monitoring well or point of compliance, depending on the type of solved problem. For the case presented in Figure 2.1-1, a single pathway defined by two UZ “pipes” and two SZ “disks,” concentration (*C*) at several key points versus time is shown in Figure 2.1-2.

The solution in the pipe-and-disk model was tested against an appropriate analytical solution for the case of advection and dispersion through the first pipe, measured at the point “SZ1Origin” (Figure 2.1-3). The analytical solution for 1-D advection with longitudinal dispersion in a homogeneous medium with unidirectional flow is given by Ogata and Banks (1961):

$$\frac{C}{C_0} = \frac{1}{2}\left\{\operatorname{erfc}\left(\frac{z-vt}{2\sqrt{Dt}}\right) + e^{vz/D}\operatorname{erfc}\left(\frac{z+vt}{2\sqrt{Dt}}\right)\right\}, \qquad \textbf{Equation 1}$$

where C is concentration,

C_0 is initial concentration (equal to Cmax; Figure 2.1-3),

z is position along the 1-D coordinate axis,

v is velocity parallel to z,

t is time, and

D is the dispersion coefficient.

Appendix A discusses in detail how the input parameters for the pipe-and-disk module are defined. Results from this model will be presented in a future groundwater investigation report.

2.2 Pajarito Scale Aquifer Model

The Laboratory’s Pajarito scale aquifer model represents the regional aquifer flow under the Pajarito Plateau and extends from the Valles Caldera to the Rio Grande River. The model accounts for the water-level transients caused by the municipal water-supply pumping and various pumping tests conducted at the Laboratory. The groundwater flow and contaminant transport in these models is currently calibrated against the transient data for the hydraulic pressures and chromium contaminant concentrations observed in the regional aquifer. The groundwater flow and contaminant transport in these models is calibrated by modifying (1) aquifer heterogeneity, (2) contaminant source properties (location, size, and contaminant concentration) from multiple point sources that represent contaminant "drips" from the bottom VZ into the top of the regional aquifer, and (3) properties of groundwater flow and contaminant transport in the regional aquifer, including aquifer dispersivity. While this model has focused more on the chromium plume, the model can be readily adapted to assimilate information on the RDX plume. We plan to extend the applicability of the model for the RDX site by adding calibration data in the model related to the RDX contaminant concentrations observed from new wells in the regional aquifer. We also envision adding the water-level transients observed during the regional aquifer pumping test at the RDX site, and machine-learning results on blind source separation (BSS) analyses presented in section 7.0.

2.3 Biochemical Remediation Model

There exists a large body of experimental work illustrating the biodegradability of RDX and other explosives (Hawari et al., 2000a; Fuller et al., 2010; Michalsen et al., 2016; Wang et al., 2017), prompting a series of Los Alamos exploratory studies presented in this compendium. RDX can be biodegraded both aerobically and anaerobically, although some studies indicate RDX transformation rates are faster under anaerobic conditions (Autenrieth et al., 1999; Attachments 6 and 7, this compendium). A variety of microbial communities and redox-dependent degradation pathways have been identified (Hawari 2000; Cho et al., 2013; Cho et al., 2015; Attachment 6), although the exact mechanisms are strongly dependent on local geochemical environmental conditions. In general, attack of the RDX molecule by microbial enzymes can result in the formation of the nitroso derivatives MNX (hexahydro-1-nitroso-3,5-dinitro-1,3,5-triazine), DNX (hexahydro-1,3-dinitroso-5-nitro-1,3,5-triazine), and TNX (hexahydro-1,3,5-trinitroso-1,3,5-triazine), or simpler molecules such as nitrite, ammonia, nitrous oxide, formaldehyde, and formic acid (Fournier et al., 2002 Hawari et al., 2000b). Large amounts of measurable nitrous oxide and carbon dioxide in some experiments indicate that RDX could quickly destabilize after the initial enzymatic attack (Hawari et al., 2000a). The apparent biodegradability of RDX has prompted a number of column and field scale studies, which have treated RDX-contaminated groundwater through biostimulation (Davis et al., 2004; Michalsen et al., 2013; Michalsen et al., 2016; Attachment 6).

2.4 CHROTRAN Model

The parametric flexibility of Chromium Transport Code (CHROTRAN) version 2.0 allows for its utilization as a comprehensive modeling tool used to evaluate bioremediation of RDX-contaminated groundwater at TA-16. The full capabilities of CHROTRAN version 2.0 are described in Appendix B and Hansen et al. (2017). This section describes a numerical model that has the potential to capture the primary elements of RDX biodegradation at the field scale, along with model sensitivity and uncertainty analysis for decision support. Processes related to biostimulation and biodegradation include biomass growth and natural decay, degradation of RDX by biomass and their associated extracellular material, biomass crowding, and bio-inhibition by amendment additives. For a more detailed description of these features, refer to Appendix B and Hansen et al., 2017.

Simulating bioremediation of RDX requires consideration of the following species:

- **RDX:** The contaminant to be remediated.
- **The amendment:** Fructose or other electron donor that serves as the biostimulant.
- **Biomass**: A collection of microbial consortia and their associated extracellular material.
- **Ethanol:** A biomass-growth inhibitor represented as a conservative species that decreases microbial growth.

These biochemical species interact through the following reactions:

- **Biomass growth:** This represents the irreversible consumption of fructose to increase biomass. It is assumed to be linear in biomass and Monod in fructose (Monod, 1949). The potential for reduction in the growth rate because of biomass crowding, which causes cell stress, is included using a Monod inhibition term in the growth rate equation.
- **Bio-reduction:** This represents the degradation of RDX by biomass. Since CHROTRAN does not assume that reduction of the contaminant is directly tied to any particular cell metabolic process, it provides a general approximation of the complex metabolic pathways of RDX biodegradation. The process is assumed to be linear in biomass and Monod in RDX.
- **Biomass natural decay:** This represents the death of microorganisms. If left unstimulated, the amount of living cell and associated extracellular material in the aquifer will ultimately return to background levels. It is modeled as a first-order process. Since RDX degradation is irreversible, biomass decay does not release previously degraded contaminant back into the aquifer.
- **Nonlethal biomass-growth inhibition:** The addition of ethanol in the treatment solution prevents excessive growth and biofouling near the injection well. This allows for further dispersal of fructose, thereby increasing the spatial extent of the treatment zone. The biomass growth rate is scaled by ethanol concentration in a manner similar to biomass crowding.

3.0 MODEL RESULTS AND UNCERTAINTY ANALYSES

3.1 Continuous 3-D VZ/SZ Model

Observation Data Available

The purpose of this modeling work is to build a calibrated VZ model that can reproduce observed data, including geometries and locations of perched zones and measured transient RDX concentrations at various borehole locations at TA-16.

The geometries and locations of perched zones are represented by the thickness field of each perched zone defined on the 2-D mesh that is a projection of the 3-D mesh discussed above, onto the horizontal plane. This 2-D mesh has 1476 nodes. For the calibration target, the perched zone is predefined as a set of nodes in a 3-D grid, and for each location in this 2-D mesh, the thickness of the perched zone is determined by cumulatively adding the average thickness of the two vertical elements associated with each perched node in the column, if it exists. Similarly, for each location in this 2-D mesh, the thickness of the simulated perched zone is determined by counting the number of fully saturated nodes and multiplying the average thickness of the two vertical elements associated with the saturated node.

The RDX concentrations have been measured at various wells/screens and surface locations (ponds/springs). These original measurements have been post-processed to fit the spatial and temporal resolutions. If the locations of two or more measurements are mapped to the same grid node, the average of these measurements is used as one measurement at this node. Similarly, to facilitate transport simulations, we limited the time resolution of measurements to one day. In other words, if two or more measurements were made in the same day at the same location, their average was used as the measurement for the day at that location. After post-processing we eliminated the RDX concentration surface measurements and only used measurements made at 17 wells/screens, represented by 281 values from R-47i, CdV-16-1(i), CdV-16-2(i)r, CDV-16-4ip_S1, CDV-16-4ip_S2, R-25-S1, R-25-S8, R-63, R25b, R-26_S1, and R-26_PZ-2.

Calibrated Parameters

The following is a list of flow/transport parameters to be estimated in the inverse modeling:

- Anisotropic permeability values (in the horizontal and vertical directions) for 13 hydro-stratigraphic units
- Permeability reduction factors along the bottoms of the perched zones (three parameters)
- Background infiltration rate at the ground surface. To achieve a uniform areal flux, this total rate is distributed to all surface nodes (except for canyon nodes), weighted by the nodal area.
- CdV infiltration flux. This rate is added to the time-dependent water flux from the 260 Outfall, and the total amount at any timeflux is distributed to all CdV nodes.
- Infiltration flux at other canyons. The reason this infiltration is separated from that in CdV is that CdV has an additional water source from the 260 Outfall and needs to be defined as a separate zone. This infiltration is distributed over all nodes in the canyon zone, excluding CdV.
- Local TA-16 recharge and MFR to the perched nodes on the western boundary. This does not include the deep MBR recharge to the lower perched-intermediate and regional aquifers in the lower part of the model domain.
- Sorption coefficient (Kd) for 10 hydro-stratigraphic units.
- Matrix diffusion coefficient, assumed to be the same for all hydro-stratigraphic units.
- Dispersivity in three directions, assumed the same for all units.

4.0 MODEL CALIBRATION RESULTS AND DISCUSSIONS

Calibrated Model Parameters

The calibrated model parameter values for the 3-D VZ model are listed in Tables 4.0-1 and 4.0-2.

Note that these results from the inverse model are preliminary and non-unique; therefore, the estimated parameter values present one possible solution to the problem. Other combinations of parameter values significantly different than these might yield a fit that is as good or almost as good as our final calibrated model. In future work, uncertainty and sensitivity analyses will be performed to evaluate the non-uniqueness issue.

Using the calibrated model parameters, flow and transport simulations were performed and the simulation results were post-processed to display the spatial distributions of perched zones and RDX concentration at observed times and locations. The comparisons between the observed and simulated perched zones and RDX concentrations are discussed below as an illustration of the ability of the calibrated model to represent the observations.

Distribution of Perched Zones

Figure 4.0-1 shows the simulated, fully saturated regions (the unsaturated regions have been filtered) in the entire model domain viewed from two angles (front and back), where the bottom SZ is the regional aquifer, while the regions embedded in the UZ represent the perched zones. The upper perched zone is visible in the left-hand side, and the thin lower perched zone is also shown in the right-hand side of Figure 4.0-1.

To better illustrate the ability of the inverse model to represent perched zones, we compared the thickness of the "true" upper perched zone, based on the model developed by Broxton and Vaniman (2016). The simulated upper perched-intermediate zone is represented by contour maps (Figures 4.0-2 and 4.0-3). In these figures, the "true" perched zone thickness map is on the left-hand side, and the model results are on the right. These comparisons demonstrate that the simulated perched zone generally matches the true one, confirming that the modeling approach and calibration methodology are capable of representing the perched horizons.

RDX Concentrations

The performance of the inverse modeling is assessed further by comparing the measured RDX concentrations at various locations against the simulated concentrations from the calibrated flow and transport model. Figure 4.0-4 illustrates such comparisons at most of the observation locations used in the model calibration process. Each point in the figure stands for one data point, and different symbol colors represent different observation locations. In a perfect model, all points should be aligned with the 45^o reference line. While this is an unrealistic expectation of any model, the comparison indicates good agreement between the data and model.

4.1 Model Predictions

Transient data are also available at several monitoring locations. Figures 4.1-1, 4.1-2, and 4.1-3 compare the observed and simulated RDX concentration over time at several selected wells. In general, temporal trends are well represented by the model at these three locations.

Finally, Figure 4.1-4 illustrates the comparison of model and data for the various screen depths at R-25. The figure employs a similar comparison technique as was used in Figure 4.0-4 but displays the data on a log scale to allow for better visualization of the results. The trend of decreasing concentrations with depth at this location is well represented by the model. As with the perched zone comparisons, these RDX concentration results indicate that the model is capable of reproducing the available transport data.

Having demonstrated that the model is capable of providing good agreement with available information on perched-zone thicknesses and RDX concentrations in the VZ, we now present representative calculations to illustrate the use of the model to predict the evolution of RDX mass in the VZ over time. These simulations proceed from the time RDX was first discharged to the environment (1951) to the present day and into the future (2050 was chosen as simulation end-date for illustrative purposes).

RDX Mass Distribution

This section presents the temporal distribution of RDX in different domains (e.g. perched zones, the regional aquifer, etc.). Figure 4.1-5 illustrates the predicted time-dependent RDX mass distribution in different parts of the domain out to the year 2050. Starting in about 1960, a very small portion of the RDX reaches the upper perched zone (PZ1) and increases until 2011, when it reaches a maximum and, in this version of the model, remains roughly constant thereafter. On the other hand, the RDX mass is predicted to reach the lower perched zone much later (1984), and plateaus at a much lower level. RDX is predicted to reach the regional groundwater by about 1990.

As expected, at early times when RDX was first discharged, most of RDX mass resides in the UZ, as indicated by the visual consistency of the curves representing UZ and the total mass in the system throughout the period of RDX discharge. However, this version of the model predicts that by 2050, RDX mass will be distributed throughout the UZ, the perched zones, and the regional aquifer.

Recalling that the previous simulation included RDX sorption, which recent studies (Attachment 4) indicate is probably minimal in the deep subsurface, a set of calculations was performed with no sorption to examine the differences. In principle, the inverse simulation should be rerun without sorption since RDX data are used in the calibration. In this preliminary model, the flow parameters from the calibrated model are used and sorption is eliminated to provide a qualitative look at the influence of sorption. As shown in Figure 4.1-6, without sorption, the cumulative mass input and the mass in the system is nearly identical at early times. However, treating RDX as a nonsorbing species results in more rapid flushing of contaminant through the VZ, which ultimately will affect the source term and concentrations in the regional aquifer. As the modeling effort matures, the finding of minimal sorption will be incorporated into the inverse model, resulting in a more realistic representation of RDX migration through the VZ.

Model Predictions of RDX Concentration at R-18 and R-68

Because this preliminary version of the model focuses on VZ processes rather than regional aquifer flow and transport, it is difficult to test the model's ability to match data collected from the regional aquifer. For example, well R-18, one of the regional aquifer well screens experiencing rising RDX concentrations (spatial coordinates x = 492939.1 m, y = - 538443.1 m), has a relatively deep well screen (1358 to 1381 m below ground surface). This location is outside the model domain, and the model representation of the regional aquifer does not currently include boundary conditions corresponding to natural flow recharge and discharge flows, given the limited extent of the current model. This suggests that lateral and vertical transport of RDX is unlikely to be well captured. Therefore, to provide a preliminary look at the regional aquifer, we selected a node in the grid mesh that is closest to R-18. The comparison indicates that the model fails to predict the rise in RDX concentrations at this location, suggesting that a better representation of the regional aquifer is required in order to match the observations.

R-68 is a more recently drilled and completed monitoring well for which initial sampling indicates RDX concentrations on the order of 14 to 17 ppb. The well of coordinates (x=492532.9 and y=538110.5) are within the model domain. At the time this version of the model was being calibrated, a preliminary dataset was available and used as a calibration target. The simulated RDX concentrations at the model locations associated with the sampling locations all indicated negligible contamination, as opposed to the initial field observations of higher concentrations. More recent RDX measurements at R-68 have stabilized, and are now considered to be more reliable. The reason that the model is not yet able to predict appreciable RDX concentrations is that, as with R-18, the representation of the regional aquifer needs to be enhanced by expanding the model domain and tuning the model with flow boundary conditions representing the natural flow processes in the aquifer.

In summary, additional work is needed to reproduce the regional aquifer observations by the TA-16 model. The model was designed to address the flow and transport in the VZ. Adequate representation of the regional aquifer flow and transport will require extension of the model domain and the development of appropriate boundary conditions. Flow gradients and RDX concentrations in the regional aquifer will then be used to tune the model to reproduce observed behavior, which will provide a better platform for simulating contaminant transport through the deep subsurface.

5.0 SUMMARY

A preliminary 3-D VZ model was built and calibrated to hydraulic and transport data at the TA-16 site. The model reproduces observed site data (contaminant concentrations, hydraulic heads, etc.) as well as geometries and locations of perched zones in the VZ at TA-16. However, at this preliminary stage, the model has limited capability to represent the flow and transport in the regional aquifer because of limited spatial extent, which in turn prevents the establishment of natural boundary conditions, namely pressures and/or fluxes that can be estimated based on observations and hydrologic studies.

Despite the limitations that need to be addressed as model development matures, this preliminary version produces predictions of the contaminant mass distribution in the VZ that are generally consistent with the site conceptual model. Therefore, the representation of RDX migration through the VZ is considered reliable, although future work is necessary to quantify the uncertainty of this prediction. The model illustrates that since the 1950s and the subsequent course of operations, RDX discharges to the system and transport through the VZ, have resulted in the emerging arrival of a relatively small portion of the total RDX mass to the regional aquifer. The majority of the contaminant mass is predicted to still remain in the VZ, and in the absence of immobilization or other attenuation mechanisms, should continue to feed the regional aquifer for decades. The rate of arrival and subsequent transport in the regional aquifer will ultimately control the downstream concentration at potential points of compliance. As the modeling effort matures, this model should be an important tool for quantifying the RDX concentrations, their distribution and uncertainties.

5.1 Discrete 3-D VZ/SZ Model

Predictions of the Contaminant Mass near R-18/R-68

Pipe-and-disk models for the RDX site (section 2.1) have been applied as a screening tool for addressing (1) plausible contaminant regional plume source areas, (2) the timing and flux of the contaminant arrivals at the top of the regional aquifer, and (3) contaminant mass distributions in the perched-intermediate and regional aquifers. Site data collected in the perched and regional aquifer wells will be used as calibration targets in MADS.

Here we focus only on data collected from the regional aquifer monitoring wells R-18 and R-68. The next stages of this analysis will include data collected at all regional and intermediate monitoring wells from the RDX-contaminated site.

RDX concentrations measured in the regional aquifer at well R-18 are shown in Figure 5.1-1. In an attempt to match data from two separate locations, an early data point from well R-68, collected in 2017 (8 µg/L), was also used in this analysis. The focus is to identify plausible contaminant source locations and geometries required to match the data at both wells, and narrow the possible timing of source arrival to the regional aquifer. We also attempt to address whether one or two separate contaminant source arrivals or “drip points” from the VZ to the regional aquifer are needed to reproduce the R-18 and R-68 observations.

This preliminary analysis did not use multiple pipes and disks in our discrete vadose/saturated transport model described in section 2.1, but a single point source from the SZ only. A simulation with one mass influx rate from a point source at the top of the regional aquifer was performed and calibrated using random initial guesses and Markov chain Monte Carlo (MCMC) analyses in MADS.

Hydrogeology data from nearby boreholes, tracer tests, and pumping tests were used to parameterize the model. Tables 5.1-1 and 5.1-2 list the fixed parameters used in most runs and sensitivity analyses, although in certain cases described below, aquifer parameters were also allowed to vary.

With these aquifer parameters and the contaminant mass flow rate (f) fixed, the possible locations for the centers of two ellipsoidal drip areas were allowed to vary along with their size and aspect ratios, from start time (*t0*) to the end (*t1*) of the contaminant mass arrival to the regional aquifer. The ellipsoidal drip areas are defined by Gaussian distributions, with source centers located at point (x, y, z) and Gaussian spread defined by inputs dx, dy, dz. In a case where source centers were allowed to range across the limits shown in Figure 5.1-2, 500 allowable solutions matched the data at R-18 and R-68, spanning the entire range allowed, with a slightly greater density for source 1 locations (pink) in between the two wells.

For the case above, the timing of the plume arrival and mass rate (f) matching the solutions (Figure 5.1-2) are shown in Figure 5.1-3. Source 1 (a) has the strongest preferred arrival time around the late 1980s, while source 2 (b) has a wider range of possible source arrival times beginning from the earliest allowed time (1960) to the latest (2010). Because source 2 generally affects the concentrations in R-68, the wide range is likely the result of the paucity of data (a single point). The timing of mass shut-off is not expected to be well constrained in our analysis because the data at R-18 still exhibit rising concentrations today, indicating that calibration would be insensitive to end time *t1* after the present day. However, some solutions with mass arrival cut-off at the regional aquifer before the present day are allowed in the optimized solutions.

The question of whether a single source could be responsible for both concentrations was also tested. The resulting Gaussian source ellipses (Figure 5.1-4) show a strong preference for a region partway between the two wells. If the RDX concentration of the single measurement from R-68 is correct, this result may be explained by back-diffusion from a single contaminant source. The timing and mass rates for this case are shown in Figure 5.1-5.

Given the limited data and the heterogeneity of the aquifer system, current estimates of groundwater velocity (Table 5.1-1) are highly uncertain. When significantly higher aquifer velocities are used, and based on R-18 hydraulic conductivities reported in the “Corrective Measures Evaluation Report, Intermediate and Regional Groundwater, Consolidated Unit 16-021(c)-99” (LANL 2007), the likelihood that source 2 is caused by back-diffusion is much smaller. Higher aquifer velocities imply much later start times to the sources and smaller contaminant mass rates. For example, a case with a higher velocity (v = 108 m/yr) results in a range of arrival times (Figure 5.1-6), with most estimates after the year 2000.

Based on the analyses presented, the following preliminary observations can be made:

- Measured RDX concentration data from regional wells R-18 and R-68 can be explained by a single contaminant source at the top of the regional aquifer (drip area) if a low groundwater flow velocity is assumed.
- For high and low groundwater flow velocities, two contaminant sources located at the top of the regional aquifer can also represent the R-18 and R-68 data:
    - In the case of high groundwater flow velocities, the contaminant may have arrived at the top of the regional aquifer in 2000 or later.
    - In the case of low groundwater flow velocities, the contaminant may have arrived at the top of the regional aquifer in the 1960s and 1980s.

Additional questions will be studied in the near future using similar methods, but with the full UZ/SZ pipe-and-disk model, including:

- How many VZ “pipes” are needed to match the data observed at existing monitoring wells screened in the regional aquifer and in the vadose perched horizons, and what are their locations?
- How much contaminant mass remains in the VZ?

- Has the peak contaminant flux already reached the regional aquifer or will it peak sometime in the future?
- Does the contaminant mass migrate laterally along the perched horizons or along the top of the regional aquifer?
- Do we observe RDX contaminant impacts at R-18 from contaminant sources other than from TA-16 (e.g., 260 Outfall/CdV) such as from TA-9/Pajarito Canyon?
- Does the contaminant mass migrate laterally along the perched horizons or along the regional aquifer?

6.0 COMPUTATION FRAMEWORK CAPABILITIES (MADS)

MADS is a Laboratory-developed, open-source, high-performance computational framework for model analysis and decision support. MADS can be coupled with existing simulators and has been extensively tested and verified on an array of example and real-world problems. MADS contains a number of computational capabilities including sensitivity analysis, parameter estimation, model inversion/calibration, uncertainty quantification, model selection/averaging, model reduction, surrogate modeling, machine learning (ML), blind source separation (BSS), and decision analyses. MADS provides the basis for the groundwater risk assessment that will be presented in a future groundwater investigation report.

In this study we focus on the MADS capability for uncertainty quantification, and, in particular, the MCMC method. MCMC methods are designed to handle large parameter spaces since, unlike probability distributions, they do not require the computation of a normalizing constant. We also note that MCMC techniques can readily handle large amounts of data. This is because they reduce the data to a single number via a likelihood function.

There are a wide variety of MCMC methods. MADS uses a version called “affine invariant” MCMC. The basic concept of the affine invariant MCMC method (Goodman and Weare, 2010) is that if a distribution is highly skewed (i.e., much more sensitive to some parameters than others) and the skew is not known a priori, then it would be beneficial to have a sampler whose samples would remain unchanged if the model parameters undergo an affine transformation. An affine transformation is of the form $y = Ax + b$ where x is a vector of parameters, A is a matrix that transforms the parameters, b is a vector that shifts the parameters, and y represents the parameters that result from the affine transformation.

Probability distributions arising from subsurface flow and transport models often have a high degree of skewness. This is simply caused by some parameters (e.g., permeability in a region with large amounts of contaminant and/or pumping activity) being far more important than others (e.g., boundary conditions far from the region of interest). This ability to handle skewness in a robust fashion also enables the model to have a large number of parameters, since higher-dimensional spaces typically have greater skewness.

A major challenge in applying MCMC methods to problems with computationally expensive models is that a large number of model runs must be performed to obtain a sufficiently long MCMC chain. Most MCMC methods operate in a serial fashion where one model run must finish before the next one can start, because the next model run depends on the results of the previous run. The affine invariant MCMC method employs an ensemble of walkers so that many model runs can be performed simultaneously (e.g., the number of model runs can be equal to the number of central processing units [CPUs] available). This ensemble works collectively to determine the next steps in the chain. The number of CPU hours that are required to obtain a useful MCMC chain is not necessarily reduced by the ensemble, but the number of wall hours is greatly reduced.

Another difficulty with many MCMC methods is that they require tuning before they can efficiently provide samples from a distribution. The number of variables that must be tuned is often equal to or greater than the number of parameters in the model. The affine invariant MCMC method has only one tunable variable and experience indicates that using a default value often works well (Foreman-Mackey et al., 2013). The small number of tuning variables needed for the affine invariant approach should not be surprising because tuning variables are usually needed to describe the skewness of the distribution. Since the affine invariant MCMC method circumvents the skewness (with the affine invariance property), these tuning variables are not needed.

These MCMC capabilities can be leveraged to capture uncertainties in the RDX plume. The outcome of a MADS MCMC analysis is a collection of samples where each sample is a set of model parameters. These samples arise assimilating observational data about the plume and hydrologic conditions, so each sample is a plausible scenario that respects the observational data.

By considering the full collection of samples, this type of analysis enables the computation of probabilities for various scenarios, enabling an MCMC analysis to be used to perform a probabilistic risk assessment. For example, each sample is used to perform a model run that in turn highlights if contaminant concentrations exceed the maximum contaminant level (MCL). The fraction of model runs that indicate exceedance of the MCL provides the probability that the MCL is exceeded. Similarly, each model run indicates when and where contaminant concentrations exceed the MCL. This information can be used to obtain a time-varying map of the probability of exceeding the MCL at each point on the map. This probability is obtained by finding the fraction of model runs that indicate the contaminant exceeds the MCL at a given point in space and time. These capabilities provide a robust framework for assessing the risk.

7.0 EVALUATION OF POTENTIAL RDX SOURCES USING ML DATA ANALYSES OF GEOCHEMICAL DATA

7.1 Objective

The objective of this analysis is to utilize a novel approach for evaluating geochemical variability within the RDX-contaminated groundwater for the purpose of identifying spatially or temporally-unique source areas. Different originating sources of contamination and/or groundwater geochemical signatures that have been modified through water-rock interaction can mix in the VZ or within the regional aquifer. The method attempts to deconvolve data from individual wells to identify potential contaminant source areas and potential breakthrough locations in the regional aquifer. Identification of source areas may provide insight into plume dynamics, plume evolution, and support optimization of remediation strategies.

7.2 Methodology

Unsupervised ML methods are powerful tools for objective and robust analysis of monitoring data. Recently, we have developed a novel unsupervised ML method for BSS, specifically designed for the interpretation of geochemical data (Vesselinov et al., 2017). In addition to existing statistical and modeling techniques, BSS analysis provides an important approach for interpreting site groundwater geochemical data. Numerous statistical techniques exist to interpret datasets of interest, including principle component analysis (PCA), factor analysis (FA), and independent component analysis (ICA). In general, these statistical methods are widely used and powerful techniques for geochemical data interpretation, but all of them lack the capability of the ML BSS techniques to robustly and objectively identify mixed groundwater types represented in a dataset of groundwater samples (Alexandrov and Vesselinov, 2014). It is important to note that the ML BSS analysis makes no assumptions about the statistical properties of the processed data. Whereas modeling analyses of site geochemical data require development, calibration and interpretation of complex geochemical models, the ML BSS analyses are nearly assumption-free, objective, robust, and fast. BSS results can also be applied in a complimentary manner as a starting point in a complex model analysis, which can substantially reduce the modeling effort.

The monitoring of contaminant plume migration typically relies on sensors or sampling points (typically located at monitoring wells) that record spatiotemporal geochemical characteristics of the contaminated groundwater flowing through the aquifer. These records are then used to infer flow and transport properties of the aquifer and contaminant source characteristics (e.g., location, loading transients, etc.) that are essential for reliable assessment of the contamination hazards and risks.

When the sensors are recording a single source, the inverse problem to identify the aquifer and contaminant source properties is challenging. The problem becomes even more challenging when there are multiple contaminant sources. In this case, the sensors typically measure mixtures where the mixing ratios are unknown. To overcome this difficulty, we have developed a new ML methodology and computational framework, called rNMF, for inverse analysis and source identification based on non-negative matrix factorization (NMF) techniques. The rNMF framework is based on our work for the assumption-free inverse analysis of water-level (pressure) data (Alexandrov and Vesslinov, 2014) and includes three different BSS algorithms: (a) NMFk, (b) ShiftNMFk, and (c) GreenNMFk.

NMFk is developed to decouple the observational data of mixtures, and to find the number of unknown contamination sources, based simply on the robustness of the reconstructed solutions, without additional information about the sources, aquifer properties, or the physical/biogeochemical processes of contaminant transport in the aquifer.

ShiftNMFk takes into account transients in the observations and the velocity of signal propagation (in this case, representative of advective transport), which result in delays (time shifts) in the recorded signals; the unknown time shift is identified based on the transient observations only. ShiftNMFk identifies (1) the number of contaminant sources, (2) the source locations, (3) the signal delays, and (4) the velocity of signal propagation (advective transport velocity).

Similar to ShiftNMFk, GreenNMFk performs NMF decomposition of the observed transient signals, but accounts for the physics of the contaminant transport process using Green functions of advection-diffusion equation (O'Malley and Vesselinov, 2014). GreenNMFk identifies (1) the number of contaminant sources; (2) the source locations, (3) the transients in the source releases, (4) advective transport velocity, and (v) transport dispersivities (assuming a Fickian dispersion model). Note that in this case, though relatively minimal, there are assumptions associated with the Fickian dispersion model (i.e., advective velocities and transport dispersivities).

The work related to developments of the rNMF theory, methods, and computational frameworks resulted in a Laboratory-filed U.S. Patent Application, titled: "*Source Identification by Non-Negative Matrix Factorization Combined with Semi-Supervised Clustering*," Inventors: B.S. Alexandrov, V.V. Vesselinov *et al.*, LANS Ref. No: S-133, 364, KS Ref. No. 8472-97415-01 U.S. Provisional App. No. 62/381, 486. The patent application is pending (submitted, August 2017).

In addition to the matrix techniques in the rNMF framework, we have recently developed a novel unsupervised ML based on non-negative tensor factorization (NTF) that allows one to analyze multi-dimensional data called NTFk. Though limited to matrix 2-D datasets, the NTFk can be applied to perform analyses of the spatial and temporal behavior of the observed geochemical data. At this time, the paucity of RDX site data does not allow for robust and scientifically defensible NTFk analyses.

7.3 Results and Discussion

The NMFk methods and tools are used to explore the geochemical data from the Laboratory groundwater contamination sites. The analyses are performed for the RDX site using different data sets and different sets of well data for the TA-16 site and its vicinity.

The ML NMFk analysis presented here (Table 7.3-1) is principally based on perched-intermediate and regional aquifer data from 14 site monitoring wells: CdV-16-2(i)r, CDV-16-4ip_S1, CdV-R-15-3_S4, R-26 S1, CdV-R-37-2_S2, R-25b, R-18, R-47i, R-48, R-63, CDV-37-1(i), R-27, CDV-9-1(i), and R-68. No alluvial well data are included in this analysis. The data includes recent representative measurements for 25 different geochemical species: pH, Alkalinity (CO_3, HCO_3), NH_3, Cl, F, NO_3, ClO_4, SO_4, TDS, HMX, RDX, Ba, B, Ca, Fe, Li, Mg, Mn, Mo, K, SiO_2, Na, Sr, U, and Zn.

This dataset is analyzed to define the potential groundwater source types that are represented as geochemical mixtures in the monitoring wells. The NMFk analysis accounts for the mixing of different groundwaters where some of them may be associated with background groundwater types and others with contamination sources. The analysis does not account for actual groundwater flow and transport, as the data are insufficient to characterize the temporal behavior of the measured groundwater concentrations. With more extensive data in the future, ShiftNMFk and GreenNMFk ML methods can account for temporal changes in groundwater chemistry and provide estimates on groundwater flow and transport properties.

7.3.1 Sources

For the given input data and based on the methodology outlined in Vesselinov et al. (2017), the NMFk analysis identifies four groundwater types or mixed component sources 1 through 4, using the site monitoring wells investigated (Table 7.3-2). The same data are presented in graphical form (Figure 7.3-1), where the relative concentrations of the species observed at the monitoring wells are scaled from 0 (lowest) to 1 (highest). Groundwater chemistries for the near-surface MFR (column 5) and the deeper MBR (column 6) are also shown in Table 7.3-2 for comparison to the BSS results.

Based on the HGCM (Attachment 3), MFR and MBR represent the two noncontaminated end-member sources proposed for the TA-16 site. Local TA-16 recharge represents a mixed surface source that feeds the alluvial aquifer system at TA-16 and includes surface waters from springs, outfall, snowmelt, postfire-contaminated runoff, and episodic flooding events originating from the MFR. Together, these shallow alluvial and deeper regional groundwater source end-members are respectively represented in Table 7.3-2 by the aqueous chemistries from alluvial aquifer wells (i.e., CdV-16-02656) and regional aquifer wells (i.e., R-26-S1).

Analyzing the BSS results presented in Table 7.3-2, BSS source 1 (column 1) is identical to the uncontaminated deep MBR source (column 6), proposed in the HGCM (Attachment 3), and typical of deeper regional well compositions. In contrast, source 3 (column 3) is not identical to the local TA-16 recharge end-member source water chemistry (column 5) typically found in noncontaminated alluvial aquifers at TA-16. BSS source 3 has higher values for lithium, manganese, silica, and lower barium, calcium, and strontium concentrations compared with alluvial groundwater. BSS source 3 can be explained as an uncontaminated perched-intermediate composition represented by a mixture of local TA-16 recharge and MBR sources, modified by water-rock interactions along subsurface pathways (Attachment 3). The overall mixing ratio between deep MBR and local infiltration can be estimated as approximately 4:1 using the analytes Fe, Mg, Na, Ca, and Sr, and assuming the high SiO_2 and Mn values are due to susbsurface pathway rock-water interaction reactions. The high SiO_2 values from BSS source 3 are readily explained by water-rock interactions during infiltration of local recharge waters through the subsurface and leaching of the glass phase in rhyolitic Bandelier tuffs (75% SiO_2;

Attachment 2, Appendix A, Tables A-1.0-1 and A-1.0-2). Further iterations of this work are necessary, nevertheless this interpretation is consistent with the HGCM that suggests that regardless of the geochemical composition or contaminant concentrations of the local recharge end-member(s), MBR is a major component in both the perched-intermediate (>40%) and regional (>90%) aquifers**.**

BSS sources 2 and 4 are clearly contaminated sources where the groundwater chemistries have been modified by HE contamination (i.e., high RDX concentrations). Source 4 in particular shows very pronounced differences in analyte concentrations with elevated values for Cl, F, NO_3, ClO_4, SO_4, TDS, HMX, RDX, Ba, B, Fe, Mg, Mo, Na, Sr, U, and Zn and the lowest alkalinity, and very high Fe and B values. Further analysis is required to explain these differences.

How the four groundwater types are mixed at each site monitoring well is represented in Table 7.3-3. Figure 7.3-2 shows the same information in graphic form. Note that the mixing ratios for each well add up to 1 (along each table and graph row). Source 1 (MBR) is dominantly represented at most of the wells except for perched-intermediate wells CdV-16-2(i)r, CDV-16-4ip_S1, CdV-R-37-2_S2, and CDV-9-1(i). Contaminated source 2 is dominant at CdV-16-2(i)r, CDV-16-4ip_S1, CDV-9-1(i), and to a lesser extent in R-68. Source 3 is dominant in CdV-R-37-2_S2. The most RDX-contaminated source 4 is represented in well CDV-9-1(i) located at the center of the contaminant plume within the perched-intermediate aquifer.

Figure 7.3-3 presents how the four groundwater source types are manifested at each monitoring well included in this BSS analysis (Table 7.3-3). Concentrations of the species observed at each monitoring well are scaled from 0 (lowest) to 1 (highest) as in previous figures, representing the contributions of the four groundwater types (sources) to generate the geochemical concentrations observed at these wells.

Clearly some of the wells are very similar in their groundwater mixing composition. For example, regional aquifer wells R-26 S1, R-25b, R-18, R-63, CdV-R-15-3_S4, R-47i, R-48, and R-27 can be grouped together based on their mixing similarities where their geochemistry is dominated by deep MBR infiltration, with some slightly impacted by TA-16 site MFR infiltration. In contrast, the remaining wells CdV-16-2(i)r, CdV-16-4ip_S1, CdV-R-37-2_S2, CdV-37-1(i), and R-68 are highly mixed and with unique groundwater compositions. Well CdV-9-1(i) is representative of the geochemical compositions prevalent in the central portion of the RDX plume and clearly associated with sources 2 and 4 mixtures.

It is important to note the differences between R-18 and R-68 results based on the presented ML BSS analyses. Though both are RDX-contaminated, the groundwater mixtures at these two wells are distinct. Both wells are dominantly MBR-sourced; however, well R-68 has a greater local recharge component or near-surface influx of RDX contaminant. Based on our analysis we suggest that both wells are located along the same contaminant flow pathway. Well R-68 shows higher concentrations of contaminants because it is closer to the local surface source, and contamination in R-18 is more diluted by pristine uncontaminated MBR groundwater. Based on the mixing ratios for sources 2 and 4 presented in Table 7.3-2, contaminants have been diluted by an approximate factor of 3 when comparing mixing ratios for R-68 and R-18. On the other hand, the relative influence of source 3 (MBR + local TA-16 recharge mix) has been reduced by an order of magnitude between R-68 and R-18, so that the influence of source 1 (MBR) remains dominant.

7.3.2 Key Observations

- The performed ML BSS analysis can provide critical insights related to the conceptual understanding of site groundwater flow and transport conditions, and preliminary results are consistent with the TA-16 HGCM (c.f. Attachment 3).
- Based on the preliminary ML BSS analysis, there are four mixed groundwater source types that represent the aqueous geochemistries of all the monitoring wells investigated within the RDX site. Further work is needed to further refine these conclusions; however, the MBR source and the local TA-16 recharge source represent the two primary “uncontaminated” end-member components.
- The overall mixing ratio between deep MBR infiltration and local TA-16 infiltration is approximately 4:1 for the perched-intermediate end-member source 3, consistent with site geochemical constraints (c.f. Attachments 2 and 3).
- There are no indications that additional groundwater source types are required to explain R-18 concentration measurements; suggesting that a separate TA-9 source (groundwater type) is not necessary to explain the data.
- R-68 and R-18 have different mixing signatures and contaminant concentrations; however, these wells are probably located along the same regional-aquifer groundwater flow pathway. The higher RDX concentrations in well R-68 are because of higher local recharge/MBR mixing ratios. Differences in the mixing ratios between the two wells will result in either greater RDX contamination in R-68 from local recharge sources and/or contaminant dilution in R-18 because of MBR.

8.0 REFERENCES

The following reference list includes documents cited in this attachment.

Alexandrov, B.S., and V.V. Vesselinov, “Blind Source Separation for Groundwater Pressure Analysis Based on Nonnegative Matrix Factorization,” *Water Resources Research,* Vol. 50, pp. 7332–7347 (2014).

Autenrieth, R.L., M.D. Jankowski, J.S. Bonner, and M. Kodikanti. “Optimizing the Biotransformation of RDX and HMX,” *In Situ and On-Site Bioremediation*, Vol. 5, No. 7, pp. 21–26 (1999).

Broxton, D.E., and D.T. Vaniman. “Geologic Framework of a Groundwater System on the Margin of a Rift Basin, Pajarito Plateau, North-Central New Mexico,” *Vadose Zone Journal*, Vol. 4, pp. 522–550 (2005).

Cho, K.C., D.G. Lee, H. Roh, M.E. Fuller, P.B. Hatzinger, and K.H. Chu. “Application of 13 C-stable Isotope Probing to Identify RDX-degrading Microorganisms in Groundwater,” *Environmental Pollution*, Vol. 178, pp.350–360 (2013).

Cho, K.C., D.G. Lee, M.E. Fuller, P.B. Hatzinger, C.W. Condee, and K.H. Chu. “Application of 13 C and 15 N Stable Isotope Probing to Characterize RDX Degrading Microbial Communities under Different Electron-accepting Conditions,” *Journal of Hazardous Materials*, Vol. 297, pp.42–51 (2015).

Davis, J.L., A.H. Wani, B.R. O'Neal, and L.D. Hansen. "RDX Biodegradation Column Study: Comparison of Electron Donors for Biologically Induced Reductive Transformation in Groundwater," *Journal of Hazardous Materials*, Vol. 112, Number 1, pp.45–54 (2004).

Foreman-Mackey, D., D.W. Hogg, D. Lang, and J. Goodman. "emcee: the MCMC hammer" *Publications of the Astronomical Society of the Pacific,* Vol.125, No. 925 (2013): 306.

Fournier, D., A. Halasz, J. Spain, P. Fiurasek, and J. Hawari. "Determination of Key Metabolites during Biodegradation of Hexahydro-1, 3, 5-trinitro-1, 3, 5-triazine with Rhodococcus sp. Strain DN22," *Applied and Environmental Microbiology*, Vol. 68, No. 1, pp.166–172 (2002).

Fuller, M.E., K. McClay, M. Higham, P.B. Hatzinger, and R.J. Steffan. "Hexahydro-1, 3, 5-trinitro-1, 3, 5-triazine (RDX) Bioremediation in Groundwater: Are Known RDX-degrading Bacteria the Dominant Players?" *Bioremediation Journal*, Vol. 14, No. 3, pp.121–134 (2010).

Goodman, J., and J. Weare. "Ensemble Samplers with Affine Invariance," *Communications in Applied Mathematics and Computational Science*, Vol. 5, No. 1, pp.65–80 (2010).

Hansen, S., S. Pandey, S. Karra, and V.V. Vesselinov. "ChroTran: A Massively Parallel Numerical Simulator for In Situ Biogeochemical Remediation of Heavy Metals in Heterogeneous Aquifers," available at: https://chrotran.github.io (2017).

Hawari, J. "Biodegradation of RDX and HMX: From Basic Research to Field Application," *Biodegradation of Nitroaromatic Compounds and Explosives,* pp. 277–310 (2000).

Hawari, J., S. Beaudet, A. Halasz, S. Thiboutot, and G. Ampleman. "Microbial Degradation of Explosives: Biotransformation versus Mineralization," *Applied Microbiology and Biotechnology*, Vol. 54, No. 5, pp.605–618 (2000a).

Hawari, J., A. Halasz, T. Sheremata, S. Beaudet, C. Groom, L. Paquet, C. Rhofir, G. Ampleman, and S. Thiboutot. "Characterization of Metabolites during Biodegradation of Hexahydro-1, 3, 5-trinitro-1, 3, 5-triazine (RDX) with Municipal Anaerobic Sludge," *Applied and Environmental Microbiology*, Vol. 66, No. 6, pp.2652–2657 (2000b).

LANL (Los Alamos National Laboratory). "Corrective Measures Evaluation Report, Intermediate and Regional Groundwater, Consolidated Unit 16-021(c)-99," Los Alamos National Laboratory document LA-UR-07-5426, Los Alamos, New Mexico (2007).

Michalsen, M.M., A.S. King, R.A. Rule, M.E. Fuller, P.B. Hatzinger, C.W. Condee, F.H. Crocker, K.J. Indest, C.M. Jung, and J.D. Istok. "Evaluation of Biostimulation and Bioaugmentation to Stimulate Hexahydro-1, 3, 5-trinitro-1, 3, 5,-triazine Degradation in an Aerobic Groundwater Aquifer," *Environmental Science & Technology* Vol. 50, No. 14, pp. 7625–7632 (2016).

Monod, J. "The Growth of Bacterial Cultures," *Annual Review of Microbiology*, Vol. 3, pp. 371–394, https://doi.org/10.1146/annurev.mi3, 100149.002103 (1949).

Ogata, A., and R.B. Banks, "A Solution of the Differential Equation of Longitudinal Dispersion in Porous Media," Geological Survey Professional Paper 411-A, Washington, D.C., pp. A1–A7 (1961.)

O’Malley, D., and V.V. Vesselinov. “Analytical Solutions for Anomalous Dispersion Transport,” *Advances in Water Resources,* Vol. 68, pp. 13–23 (2014).

Vesselinov, V.V, and D. O’Malley. “Model Analysis of Complex Systems Behavior Using MADS,” AGU Fall Meeting, San Francisco, CA (2016).

Vesselinov, V.V., D. O'Malley, Y. Lin, and S. Hansen, “MADS.jl: Model Analyses and Decision Support in Julia,” (2016).

Vesselinov, V.V., B.S. Alexandrov, and D. O’Malley. “Contaminant Source Identification Using Semi-supervised Machine Learning,” *Journal of Contaminant Hydrology,* (submitted 2017) doi:10.1016/j.jconhyd.2017.11.002.

Wang, D., H. Boukhalfa, O. Marina, D.S. Ware, T.J. Goering, F. Sun, H.E. Daligault, C.C. Lo, M. Vuyisich, and S.R. Starkenburg. “Biostimulation and Microbial Community Profiling Reveal Insights on RDX Transformation in Groundwater,” *MicrobiologyOpen*, Vol. 6, No. 2 (2017).

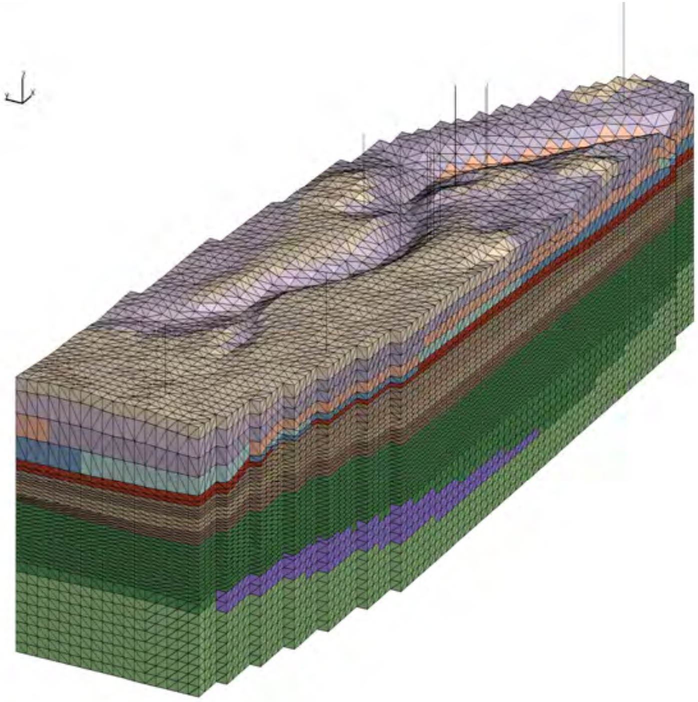

Figure 2.0-1 **RDX full 3-D model domain: TA-16 computational grid with 3X vertical exaggeration. Well locations indicated by vertical lines extending above grid surface for visualization purposes.**

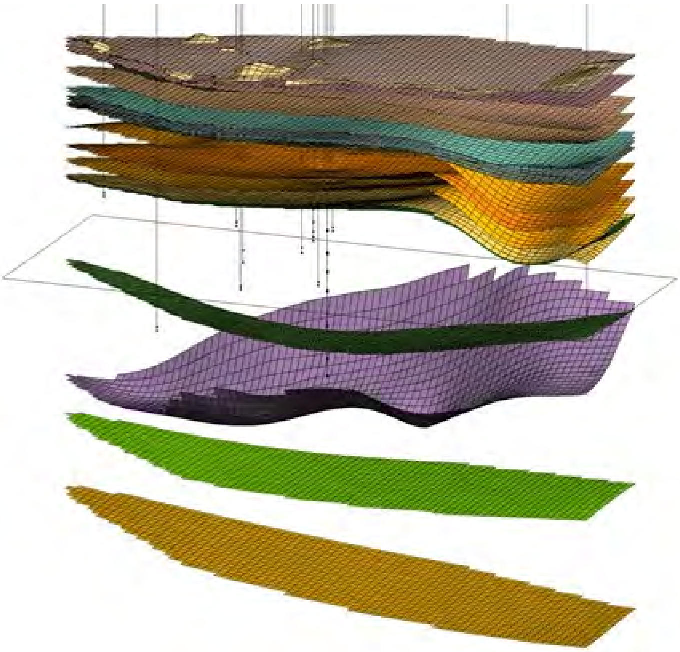

Figure 2.0-2 **Spatial distribution of geologic units for the 3-D VZ model. These include the WC15c EarthVision surfaces and supplemental Otowi surfaces. Well locations indicated by vertical lines; the locations of the well screens are shown along the wells as thicker black lines.**

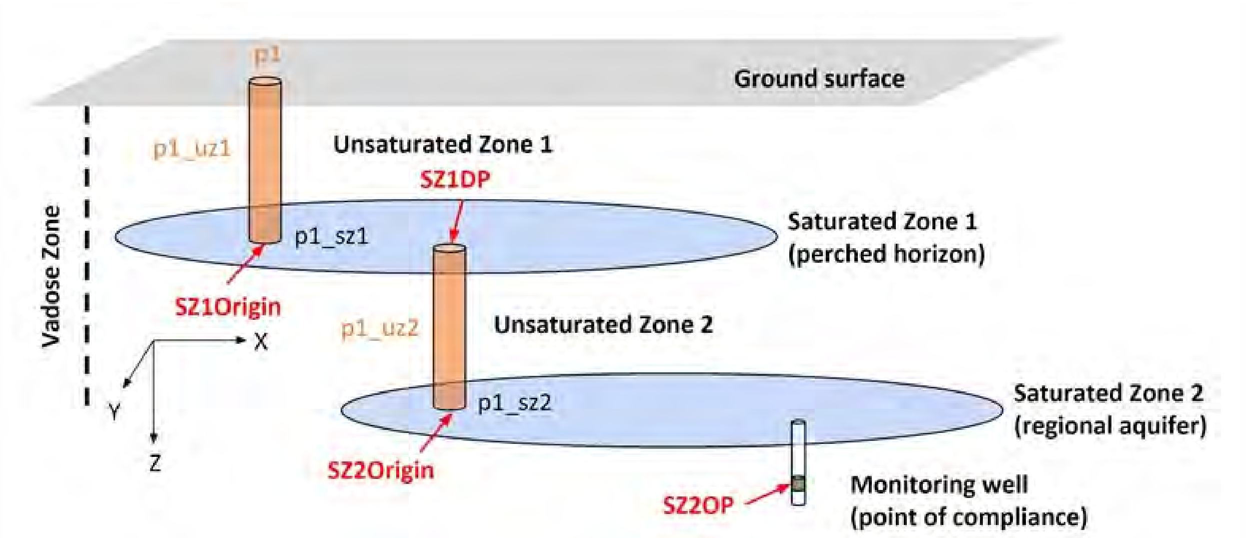

Figure 2.1-1 **Schematic of a pipe-and-disk model case with a single pathway (p1), two UZs (uz1 and uz2), two SZs (sz1 and sz2), a drip area location in sz1 (SZ1_DP) and an observation point (OP) in SZ2**

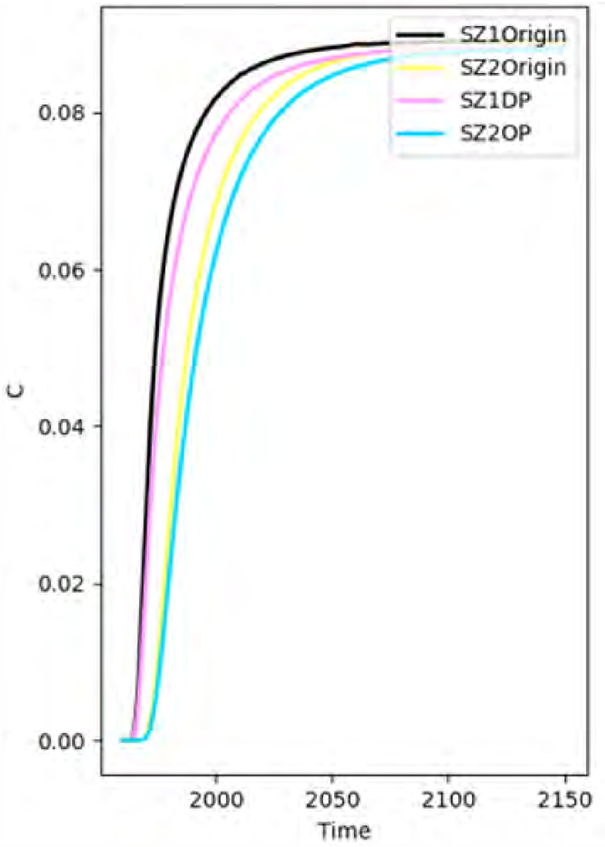

Figure 2.1-2 **Example model-predictions of concentration (*C*) at the points identified in Figure 2.1-1 for a pipe-and-disk transport model case with one pathway, two VZs, and two SZs**

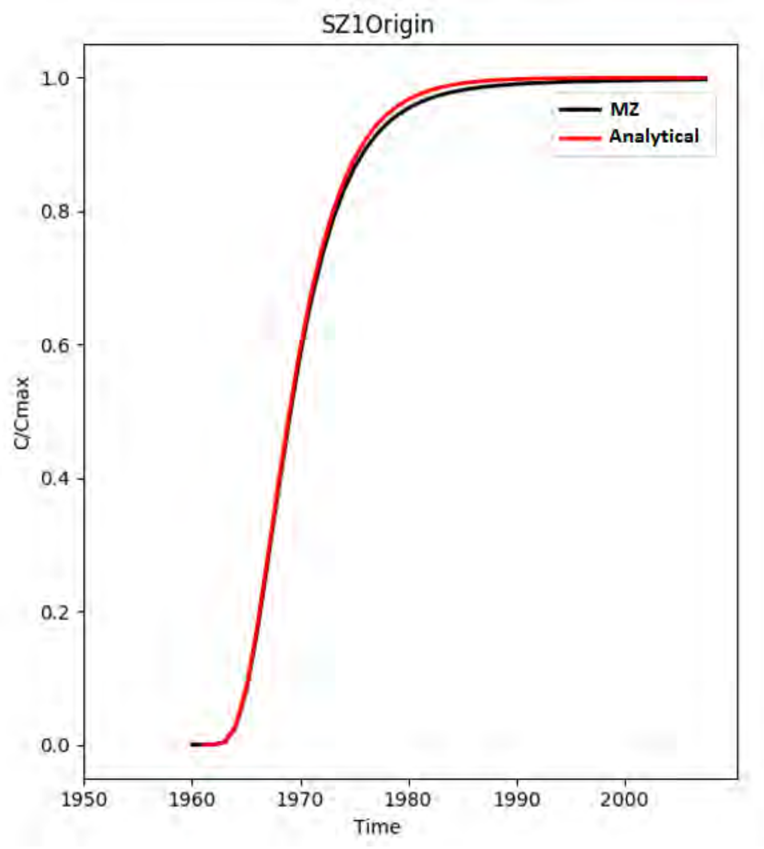

Figure 2.1-3 Comparison of the pipe-and-disk model result against the analytical solution of Ogata and Banks (1961)

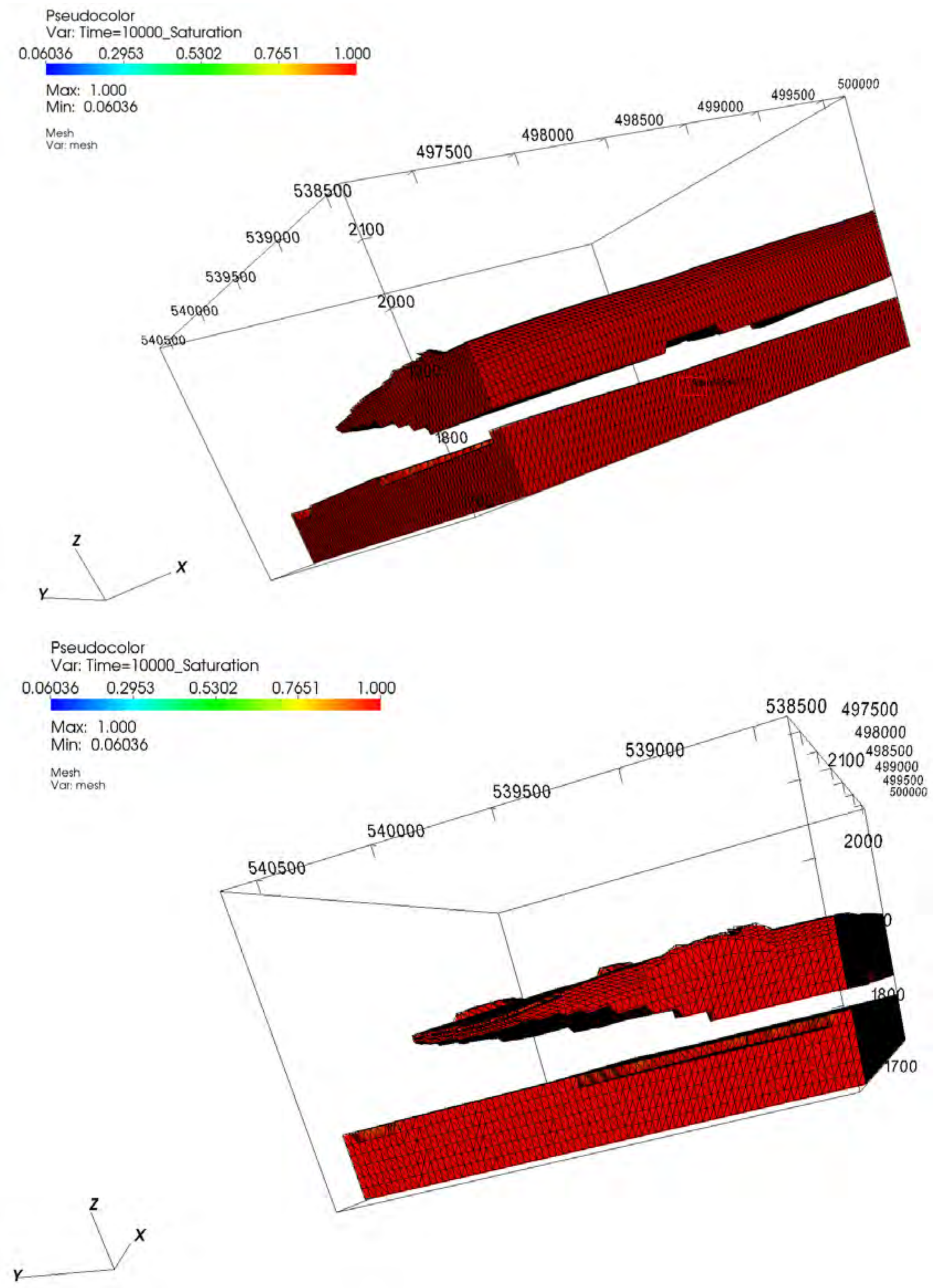

Figure 4.0-1 **Calibrated saturated perched water zones viewed from two different angles. Orthogonal directions X, Y, Z represent cardinal directions west-east and south-north, and elevation respectively.**

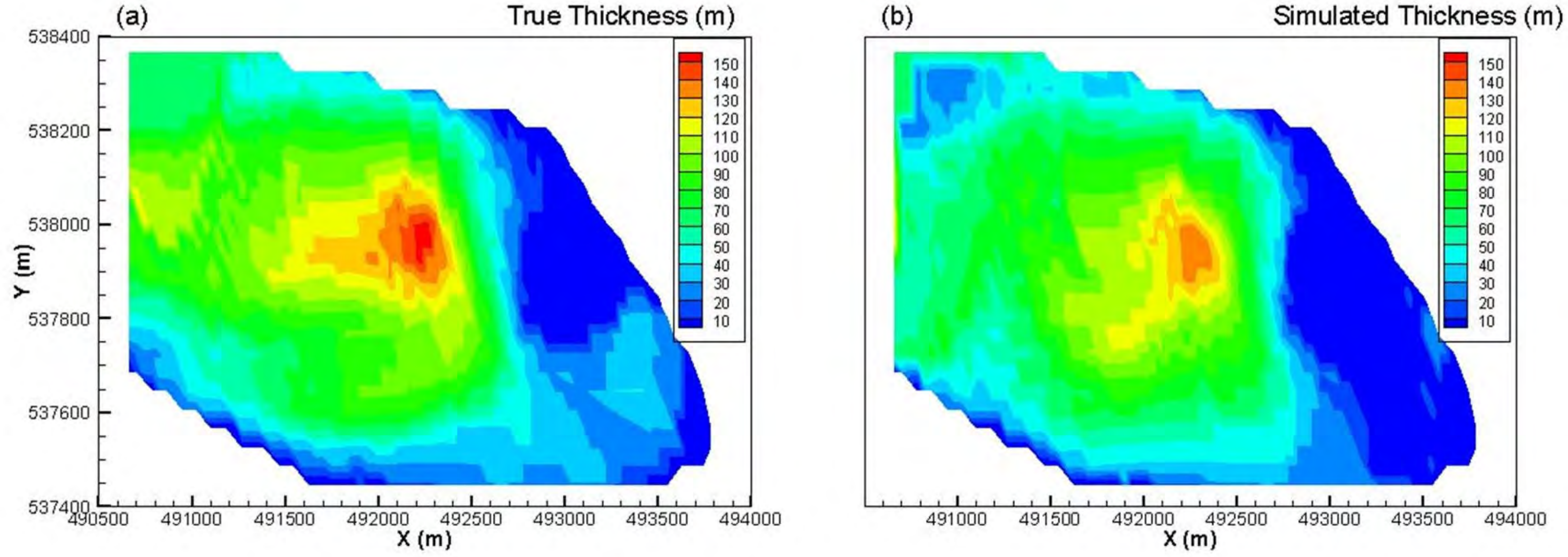

Figure 4.0-2 Comparison of “true” and simulated upper perched zone

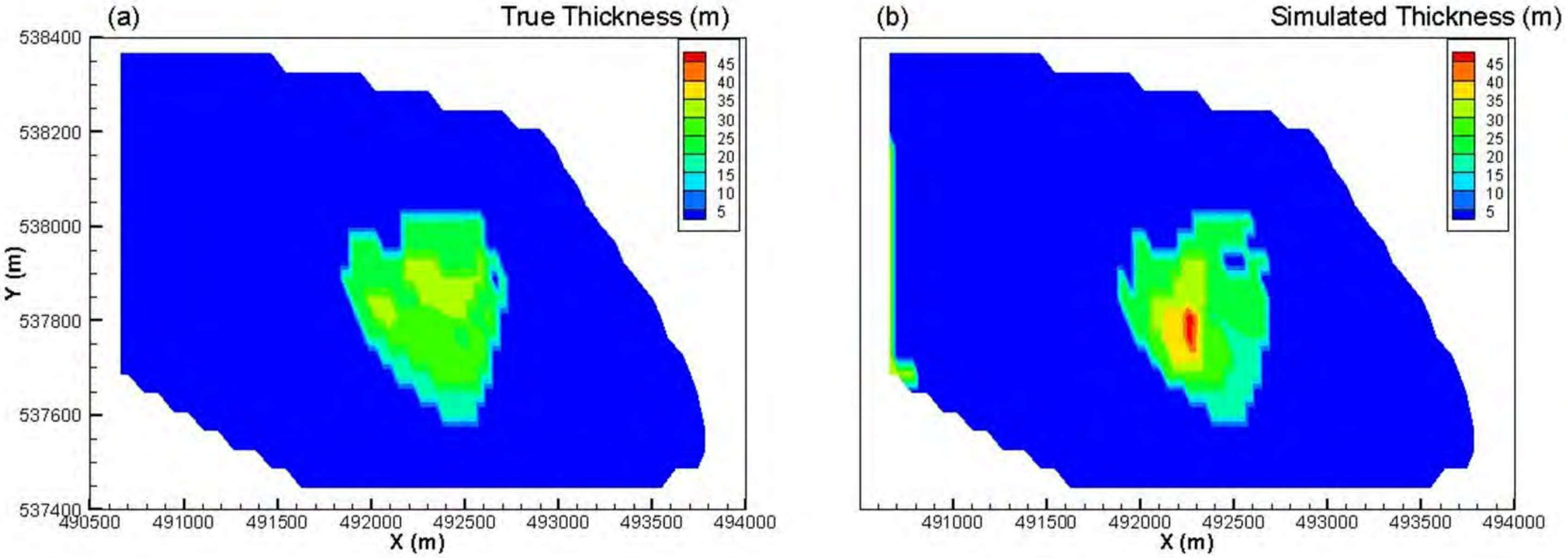

Figure 4.0-3 Comparison of “true” and simulated lower perched zone

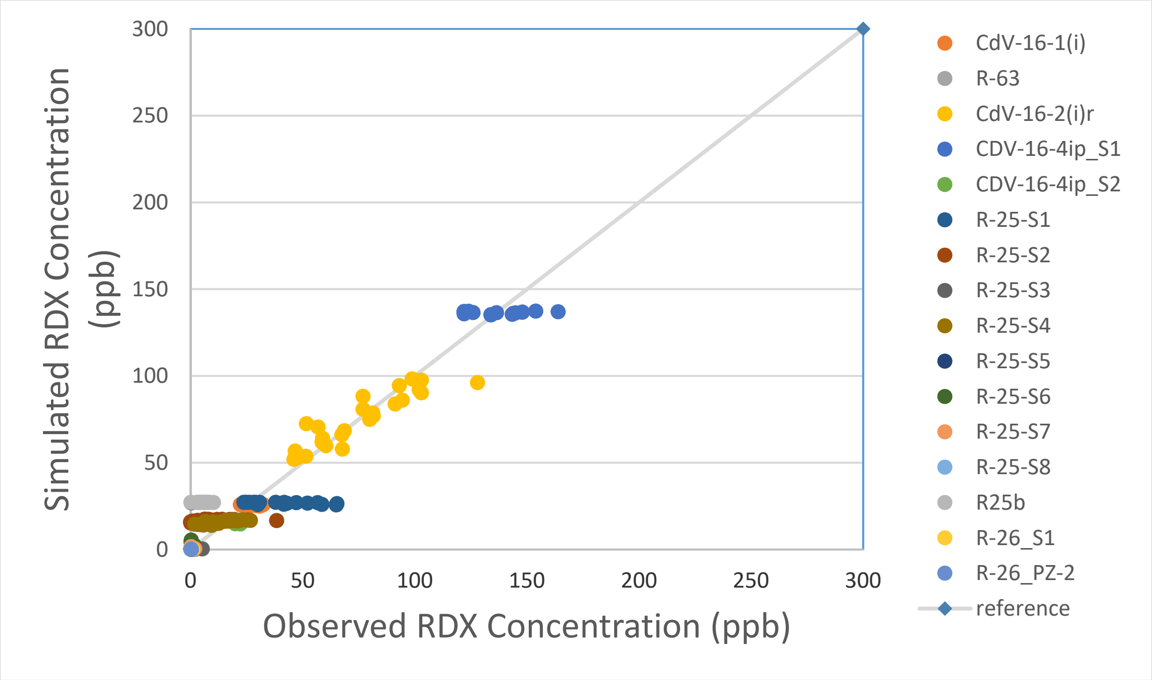

Figure 4.0-4 A scatter-plot of observed and simulated RDX concentrations for all wells

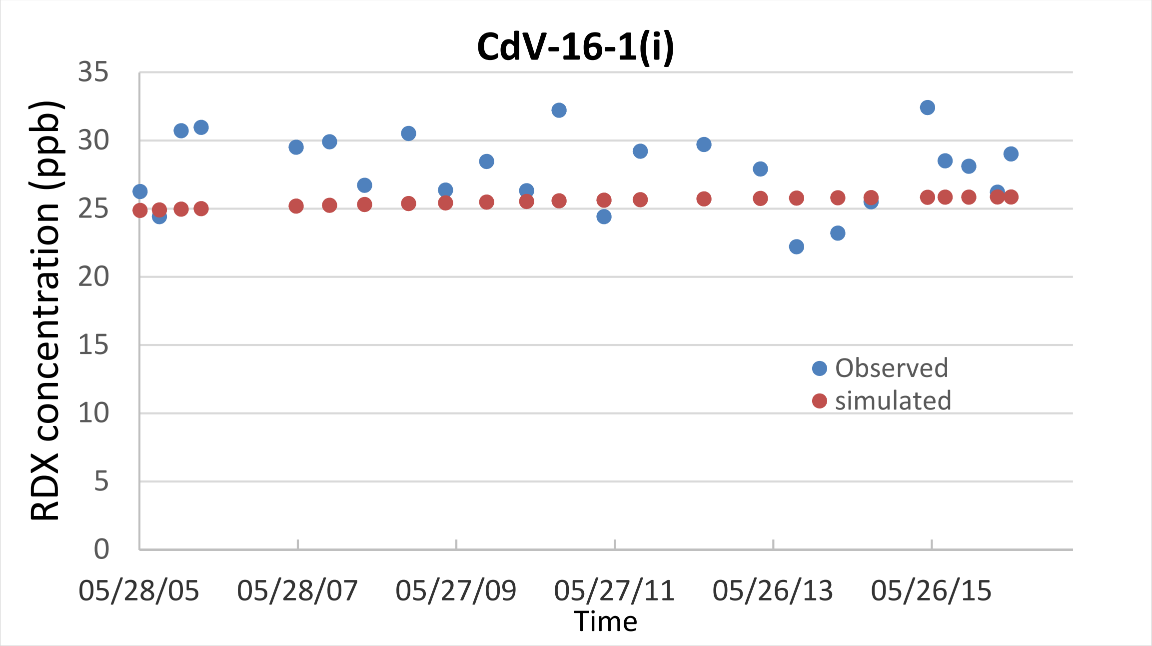

Figure 4.1-1 Comparison of observed and simulated RDX concentrations over time at CdV-16-1(i)

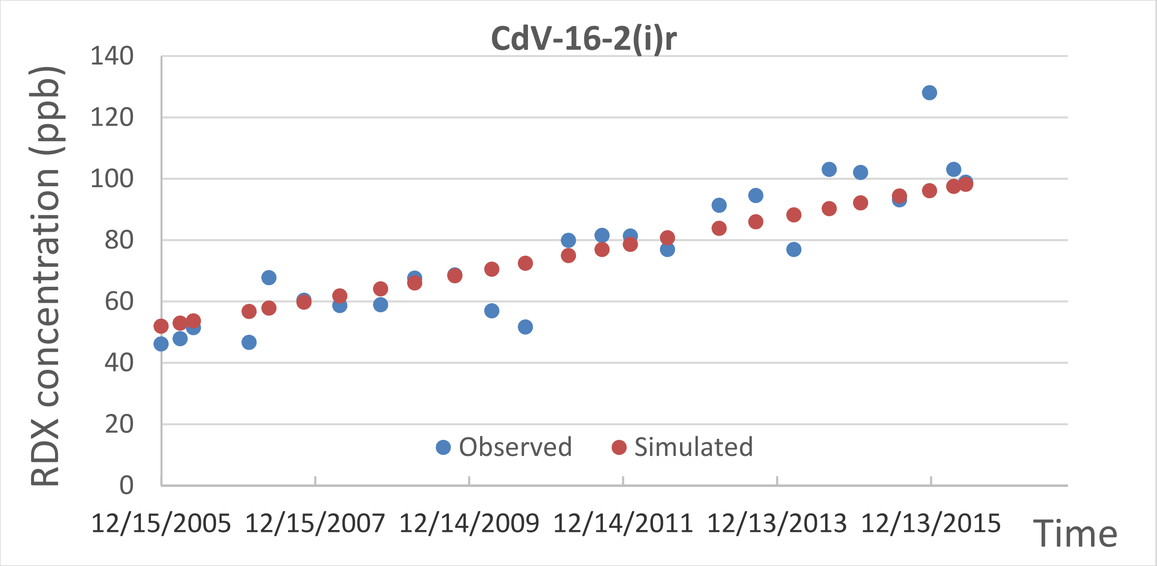

Figure 4.1-2 Comparison of observed and simulated RDX concentration over time at CdV-16-2(i)r

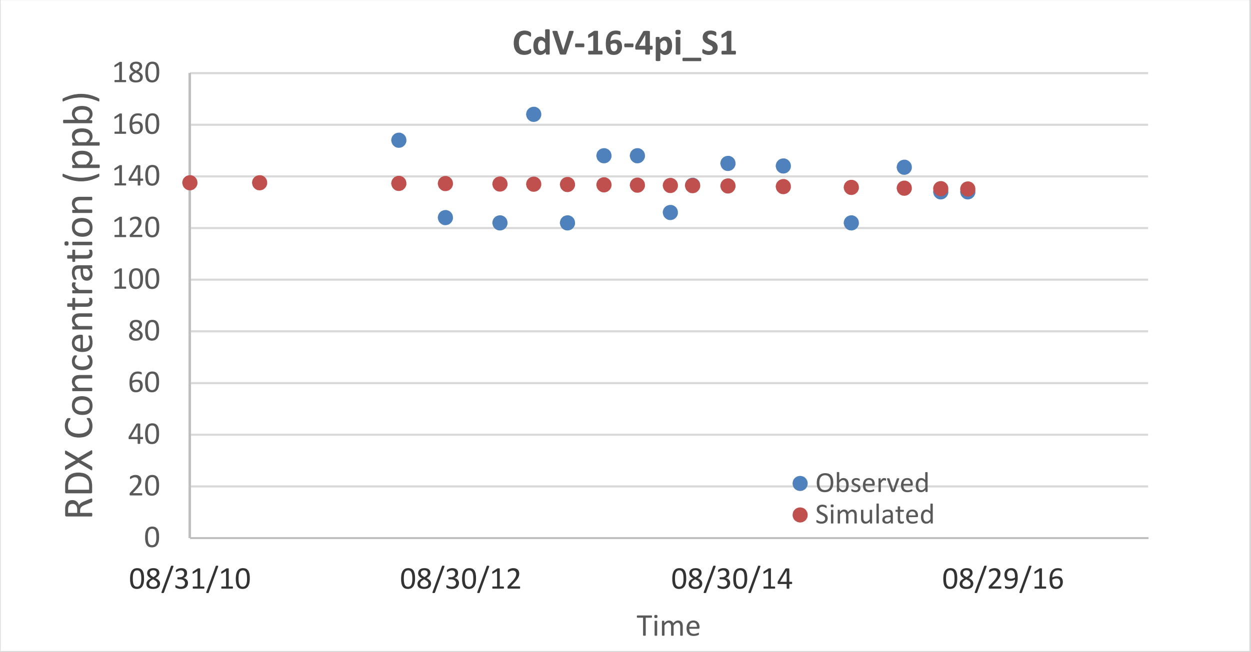

Figure 4.1-3 Comparison of observed and simulated RDX concentration over time at CdV-16-4pi_S1

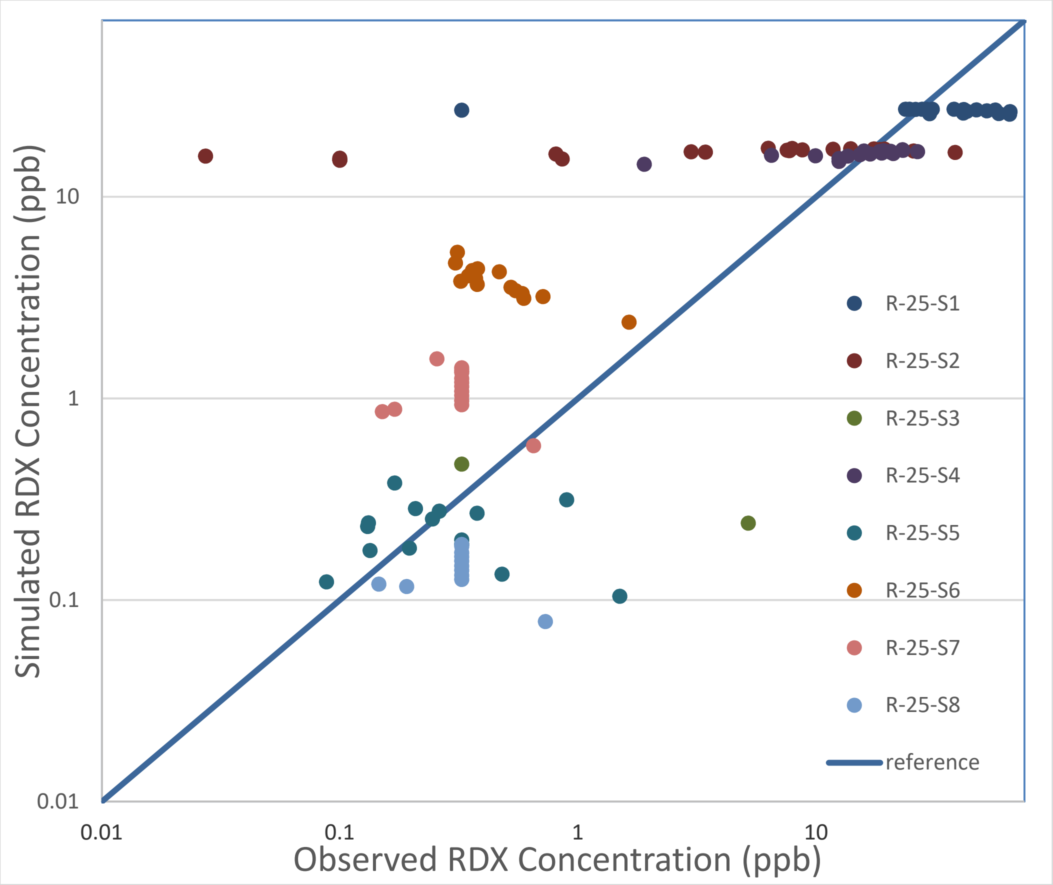

Figure 4.1-4 **Comparison of observed and calibrated RDX concentrations for various depths in well R-25**

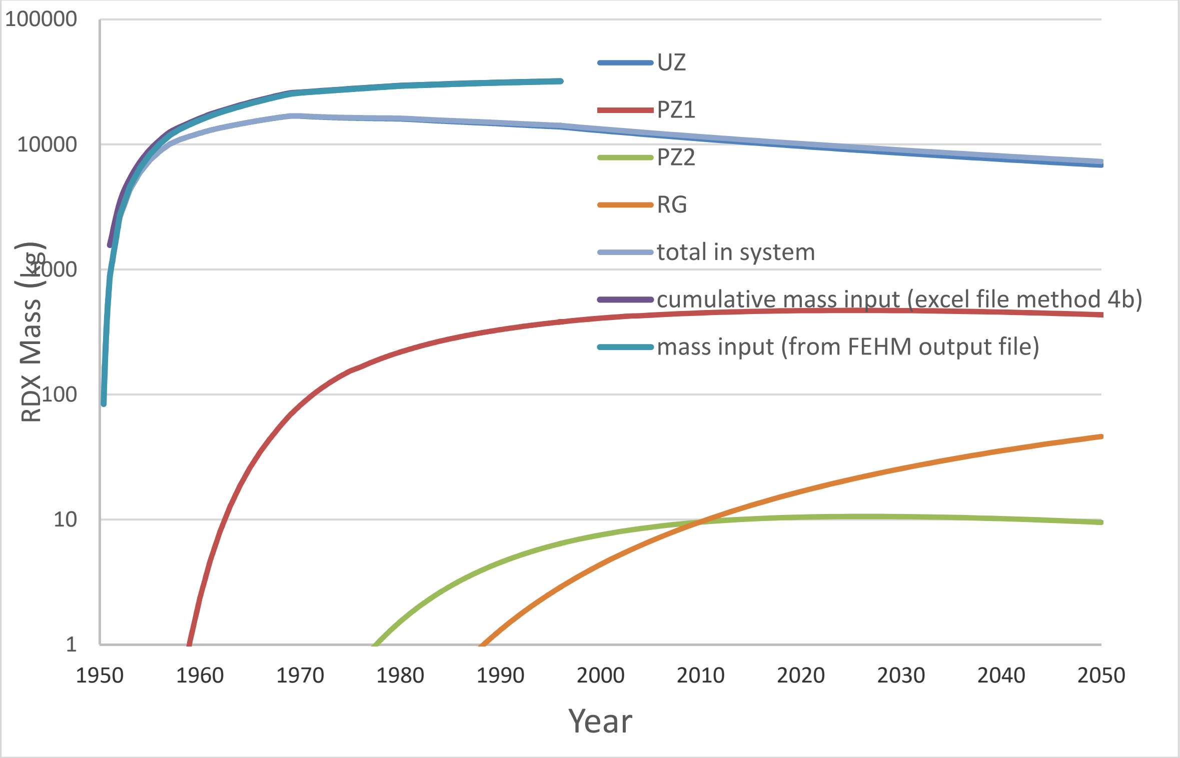

Figure 4.1-5 Time-dependent mass distribution in the simulation domain with sorption

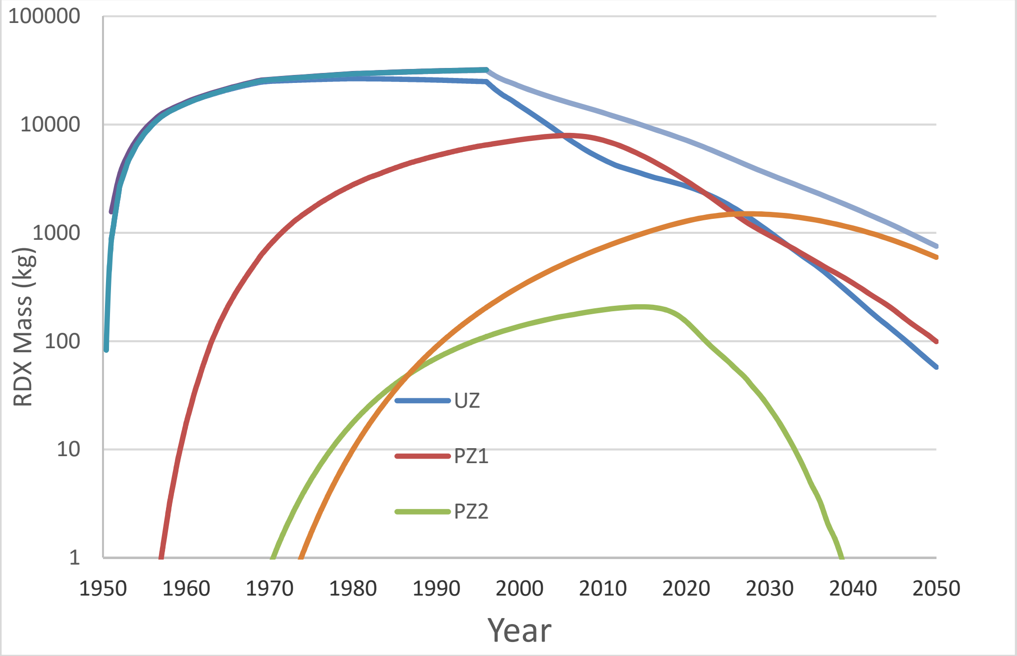

Figure 4.1-6 Time-dependent mass distribution in the simulation domain without sorption. Note that the overall decline in RDX mass is a function of the mass leaving the model domain, which is of limited extent. This mass resides in the regional aquifer but outside the model domain.

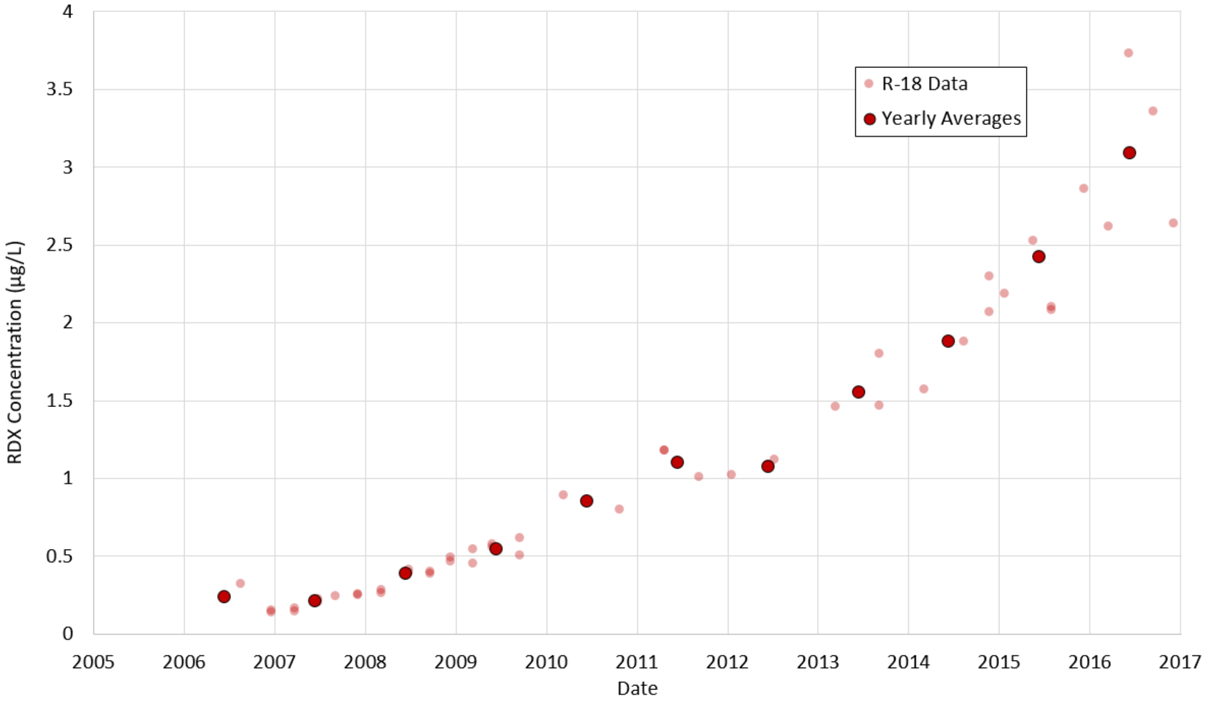

Figure 5.1-1 RDX concentrations observed in the regional aquifer at monitoring well R-18; the figure also presents the yearly averages applied in the model analyses

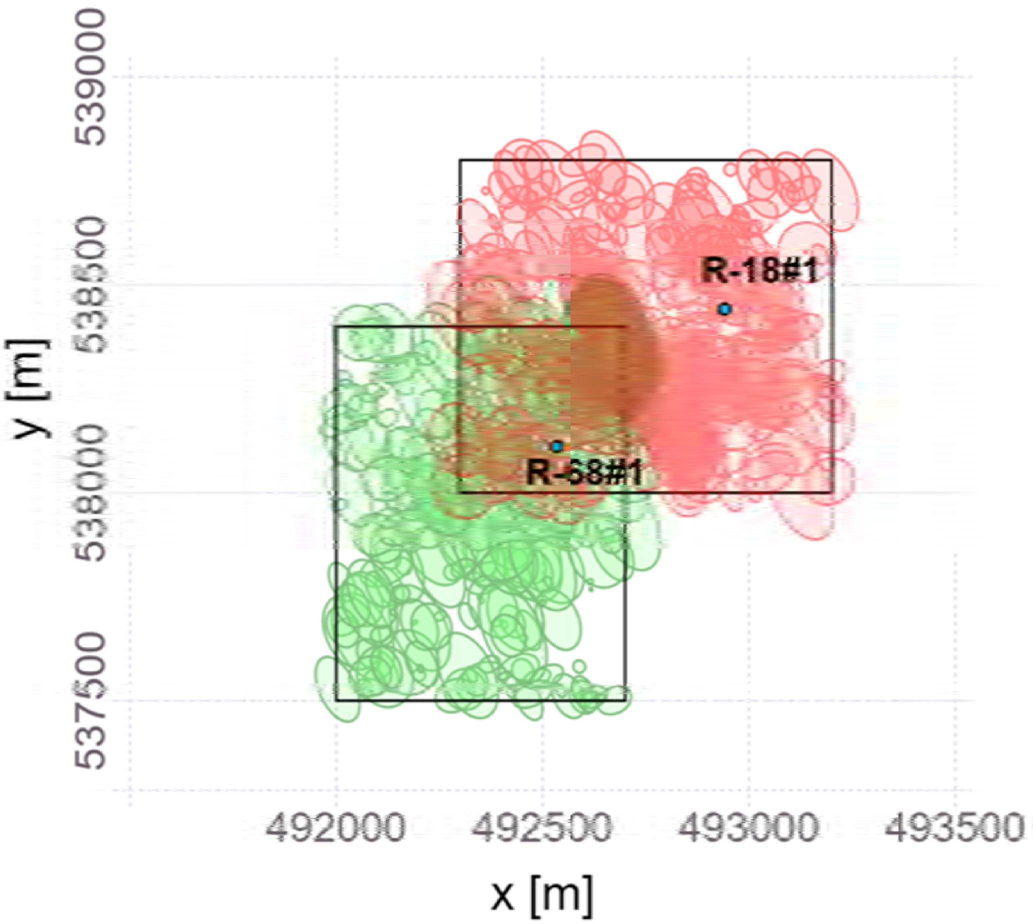

Figure 5.1-2 500 alternative solutions for size and locations of source ellipses for source 1 (pink) and source 2 (green) matching the RDX concentration data for wells R-18 and R-68. Allowed ranges for the centroids of the source locations are shown as black rectangles.

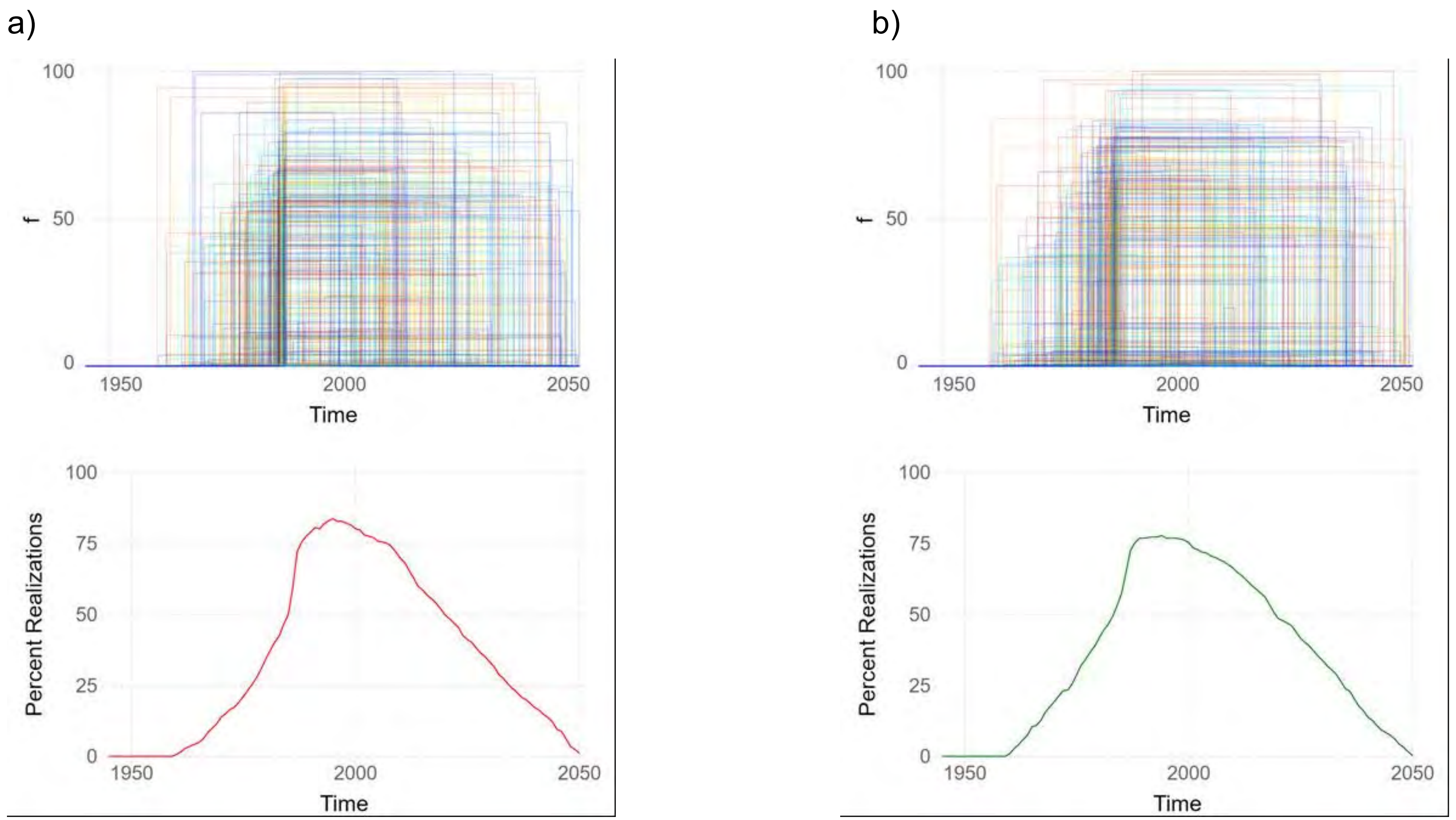

Figure 5.1-3 **500 alternative solutions for the timing of pulse arrival and mass flow rate (*f*) for the two contaminant sources shown in Figure 5.1-2. The graphs on the left (a) and the right (b) represent sources 1 and 2, respectively. The two top graphs show step functions of the contaminant mass flux *f* over time which also show the start (*t0*) and end (*t1*) time of plume arrival. The bottom two graphs plot percent of realizations having contaminant mass arrival to the regional aquifer over time.**

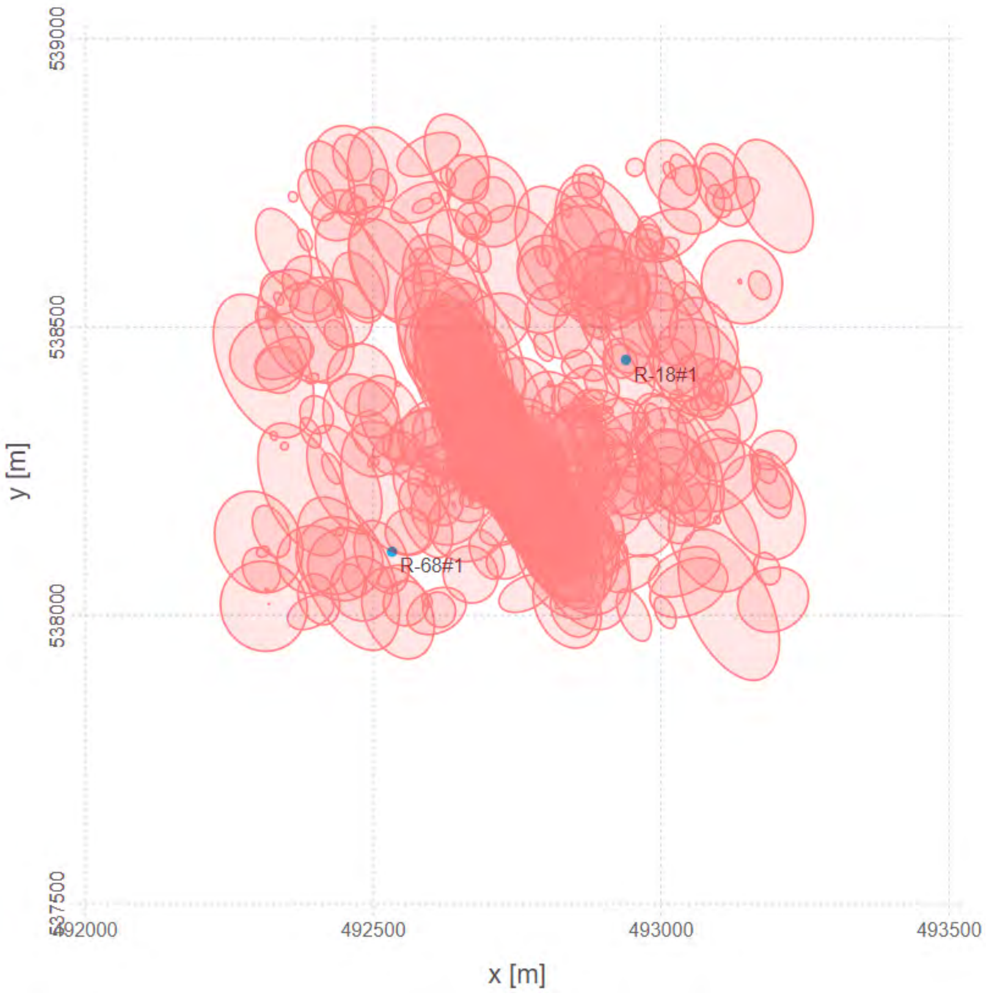

Figure 5.1-4 **1000 alternative solutions for size and location of source ellipse for a single source resulting in good matches to the RDX concentration data for wells R-18 and R-68**

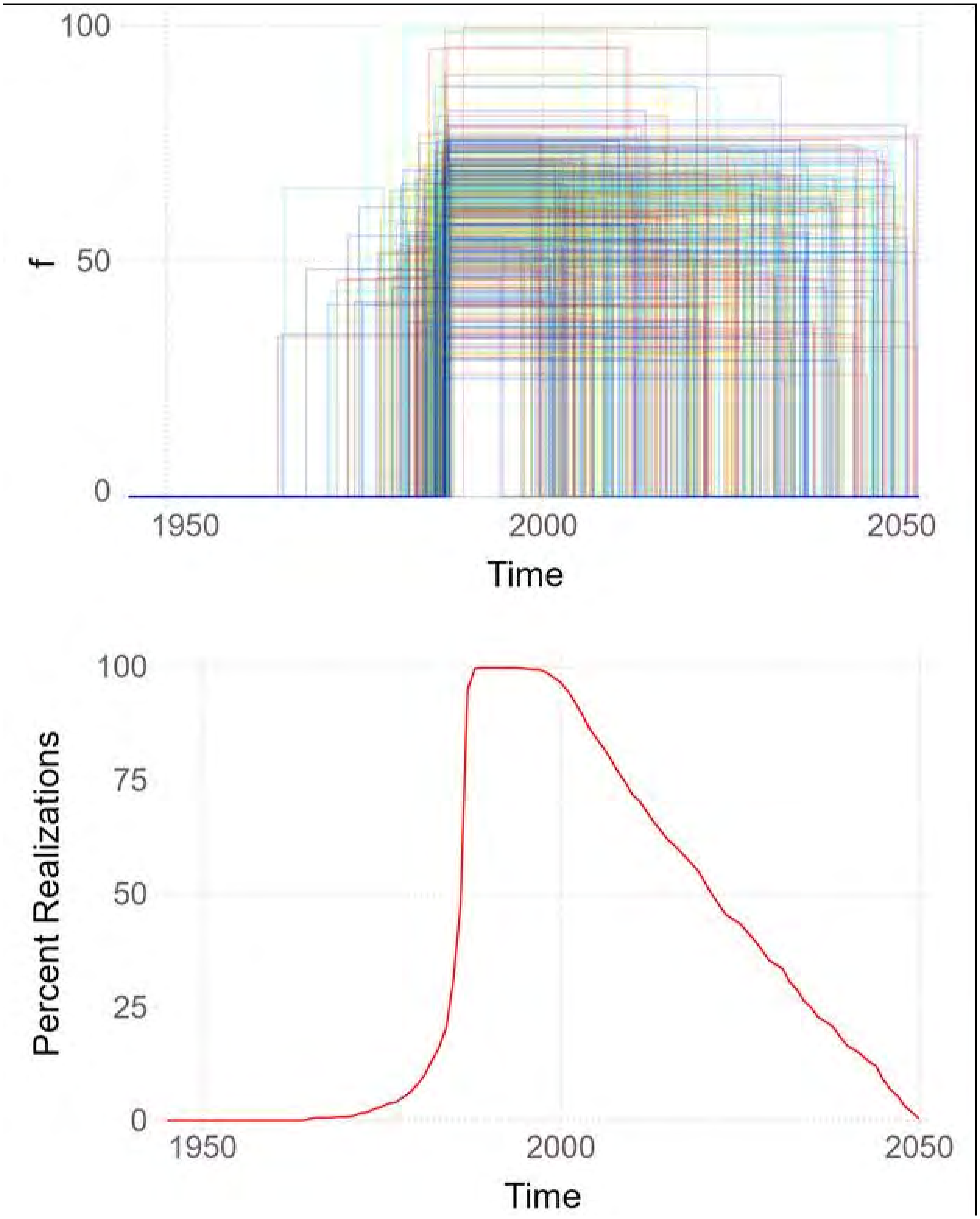

Figure 5.1-5 **1000 alternative solutions for the timing of pulse arrival and mass flow rate (*f*) for the single source shown in Figure 5.1-4. The top graph shows step functions of the contaminant mass flux *f* over time that also shows the start (*t0*) and end (*t1*) time of plume arrival. The bottom graph is a plot of the percent of realizations with contaminant mass arrival to the regional aquifer versus time.**

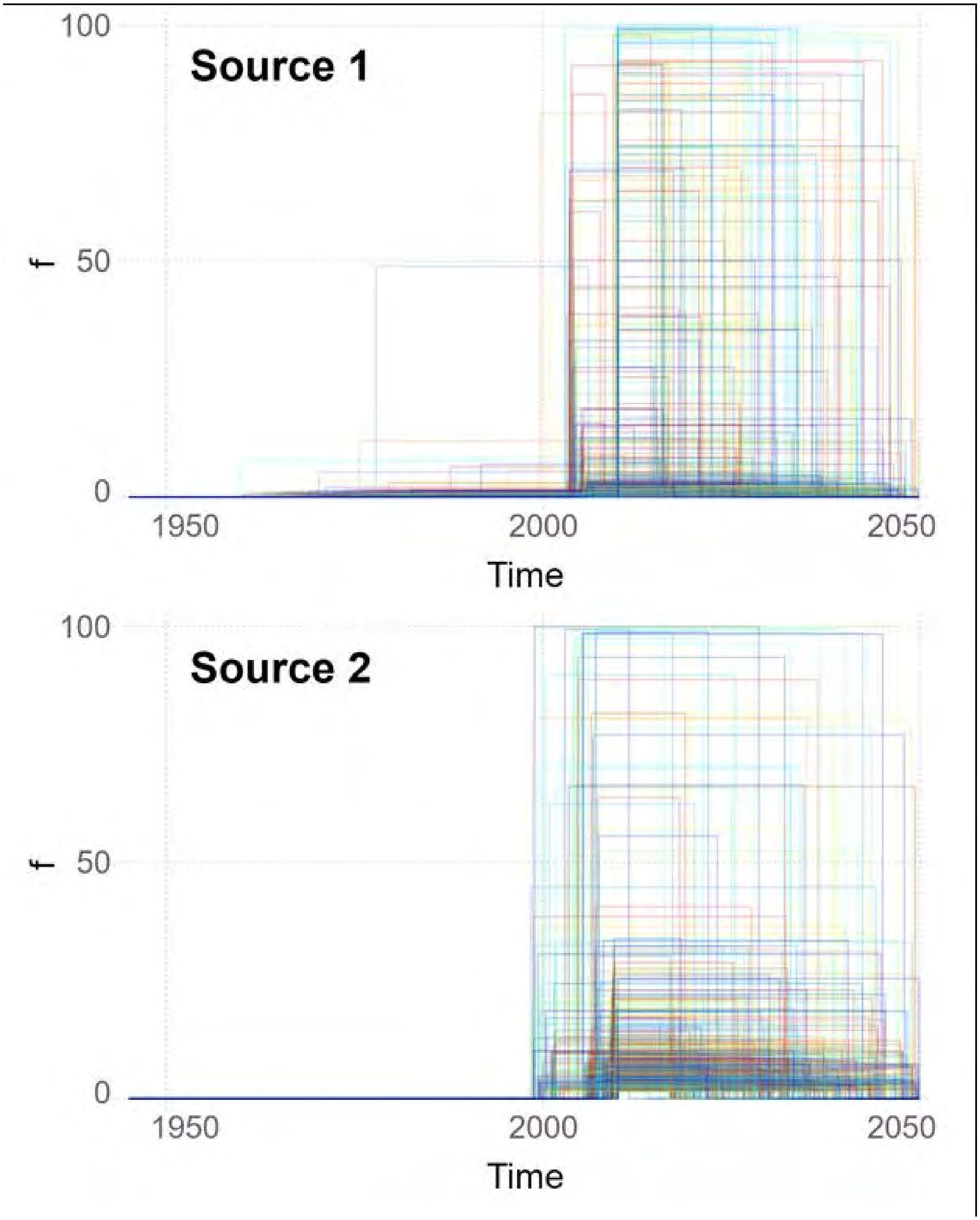

Figure 5.1-6 500 alternative solutions for the timing of pulse arrival and mass flow rate (*f*) for two sources, with the same parameters as before but with *v* = 108 m/yr

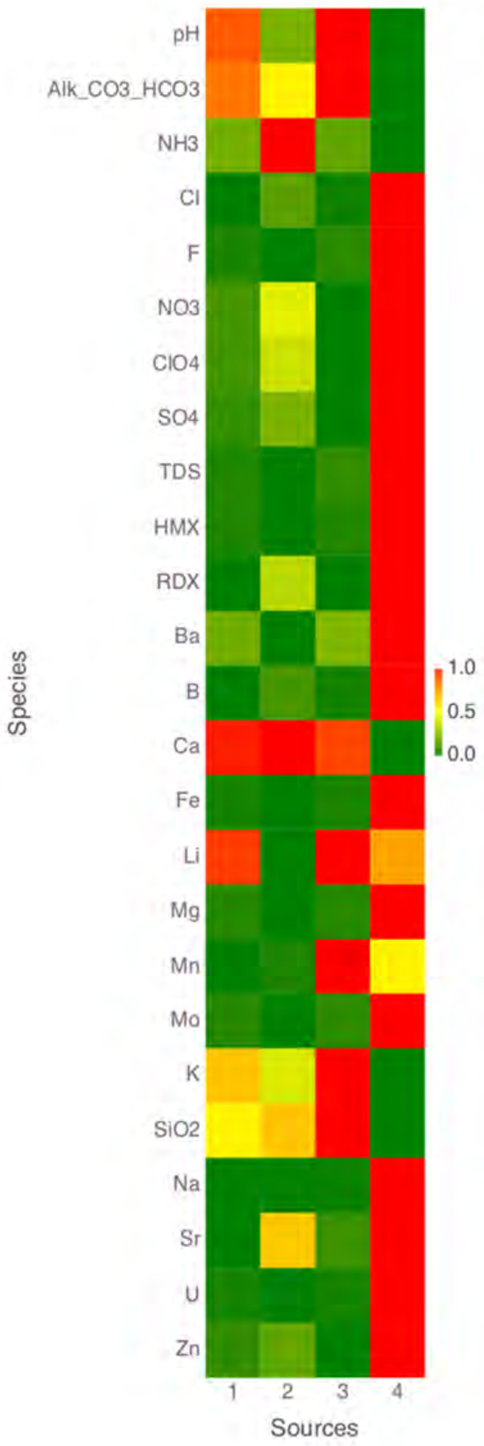

Figure 7.3-1 Geochemical concentrations associated with the four mixed groundwater source types identified by BSS for the RDX monitoring wells. The species concentrations along each row are scaled between 0 and 1. The original (unscaled) data is presented in Table 7.3-1. The figure represents how the four groundwater source types are differentiated by different geochemical species.

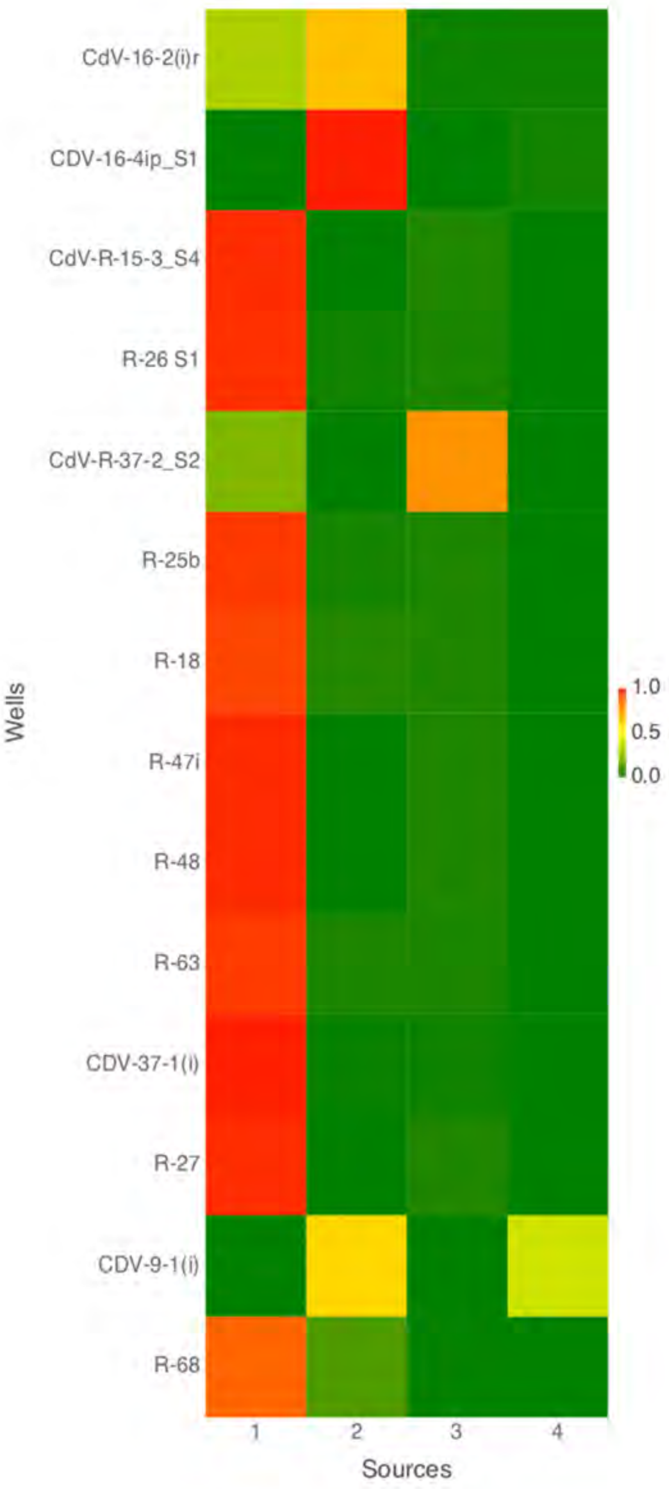

Figure 7.3-2 Mixing ratios of the four groundwater source types identified for site monitoring wells. The mixing ratios add up to 1 for each row.

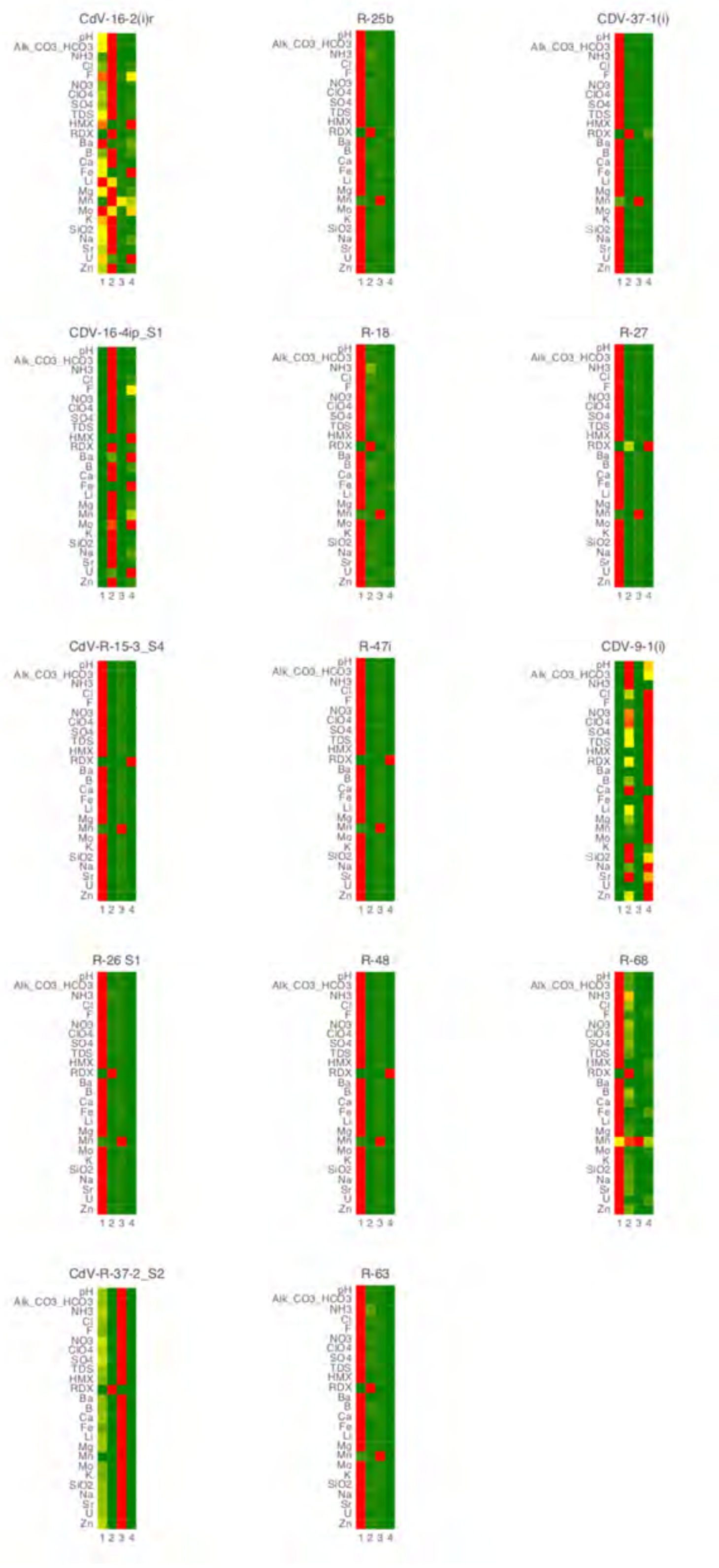

Figure 7.3-3 Graphical representation of BSS groundwater source type distributions for RDX monitoring wells. Each monitoring well is represented by four source types determined by ML BSS; the mixing ratios add up to 1 for each row.

Table 2.0-1
Fixed Hydraulic Properties for Stratigraphic Units in the Model Domain

Unit ID	Lithology	Porosity	Residual Saturation Sr	van Genuchten α (1/m)	van Genuchten n
10	Tpf2	0.35	0.01	5	2.68
11	Tvt2 Younger Tschicoma	0.05	0.066	0.1	2
14	Tpf3	0.35	0.01	5	2.68
16	Qbof Otowi Member, ash flow	0.44	0.043	0.59	1.76
17	Qct Cerro Toledo	0.45	0.007	1.3	1.5
19	Qbt1g Tshirege Unit 1 - glassy	0.46	0.022	0.5	1.75
21	Qbt1vu Tshirege Unit 1 - vitric	0.49	0.006	0.36	1.74
22	Qbt2 Tshirege Unit 2	0.41	0.024	0.47	2.06
23	Qbt3 Tshirege Unit 3	0.469	0.045	0.29	1.884
24	Qbt3t Tshirege Unit 3, transition zone	0.466	0	2.57	1.332
25	Qbt4 Tshirege Unit 4	0.478	0.000377	0.667	1.685
27	Qbof G2 Otowi Member, ash flow	0.44	0	0.081	4.03
28	Qbof G3 Otowi Member, ash flow	0.44	0	0.081	4.03
140, 141,142	Tpf3	0.35	0.01	5	2.68

Table 4.0-1
Calibrated Parameter Values for All Stratigraphic Units

Unit ID	Units	Kxy (m^2)	Kz (m^2)	Kd (kg/kg)	D (m^2/s)	λx (m)	λy (m)	λz (m)
10	Tpf2	3.105E-12	6.394E-12	3.61e-4	3.88E-10	0.102	0.288	15.00
11	Tvt2	9.164E-12	3.433E-13	0.5				
14	Tpf3	3.107E-12	9.995E-13	3.99				
16	Qbof	9.988E-12	9.158E-11	2.3e-6				
17	Qct	3.080E-14	9.696E-11	0.407				
19	Qbt1g	6.139E-12	1.515E-15	1.636				
21	Qbt1vu	2.807E-12	4.295E-14	1.11e-5				
22	Qbt2	6.663E-13	6.031E-12	9.47e-5				
23	Qbt3	4.229E-11	1.582E-14	4.405				
24	Qbt3t	4.350E-12	8.804E-12					
25	Qbt4	1.771E-12	2.270E-12	0.567				
27	Qbof G2	1.786E-14	7.321E-13	2.3e-6				
28	Qbof G3	2.310E-13	5.860E-12					
140	Tpf3	7.553E-13	2.595E-13	3.99				
141	Tpf3	9.283E-11	5.386E-14					
142	Tpf3	8.758E-13	1.556E-13					

Table 4.0-2
Calibrated Flux and Permeability Reduction Parameters

Parameters	Estimated Values
Background infiltration (kg/s)	0.0332
Flux into CdV (kg/s)	1.75E-04
Flux to other canyons (kg/s)	5.71011
Flux from mountain front to upper perched zone (kg/s)	9.99312
Permeability reduction factor between zones 60 and 61	1.13e-5
Permeability reduction factor between zones 70 and 71	4.83e-4
Permeability reduction factor between zones 141 and 142	4.49e-5

Table 5.1-1
Fixed Aquifer Parameters in the Regional Aquifer Analysis of RDX Plume Arrival

Parameter	Value
Groundwater Flow Velocity, v	2 m/yr
Flow angle, θ	25°
Porosity, n	0.2
Longitudinal dispersivity, α_x	50 m
Transverse dispersivity, α_y	5 m
Transverse dispersivity, α_z	0.5 m

Table 5.1-2
Description of Model Parameters Used for Sensitivity Analysis

Symbol	Description	Role
λ_{B_1}	Biomass growth rate constant	Controls biomass growth rate
K_D	Fructose Monod constant	Controls biomass growth rate
K_B	Biomass Monod Inhibition constant	Controls biomass growth rate
K_I	Ethanol Monod Inhibition constant	Controls biomass growth rate
λ_{B_2}	Biomass natural decay rate constant	Controls biomass death rate
λ_C	RDX bio-reduction rate constant	Controls RDX degradation rate
K_C	RDX bio-reduction Monod constant	Controls RDX degradation rate

Table 7.3-1
Geochemical Concentrations at the Site Monitoring Wells

Species	Unit	Wells													
		CdV-16-2(i)r	CdV-16-4ip_S1	CdV-R-15-3_S4	R-26 S1	CdV-R-37-2_S2	R-25b	R-18	R-47i	R-48	R-63	CdV-37-1(i)	R-27	CdV-9-1(i)	R-68
pH	n/a[a]	7.67	7.67	8.03	7.8	7.87	7.86	7.89	7.765	8.06	7.82	7.67	7.9	7.61	7.7
Alk_CO_3−HCO_3	mg/L	78	72.5	88.4	71.6	83.6	90	79.7	82.8	87.7	72.5	84.4	92.6	66.2	52.9
NH_3	mg/L	0.122	0.235	0.030	0.030	0.030	0.030	0.030	0.096	0.083	0.030	0.030	0.030	0.114	0.020
Cl	mg/L	3.06	3.37	1.53	1.16	1.65	1.81	1.34	2.26	2.46	1.1	1.2	1.52	7.92	1.41
F	mg/L	0.105	0.067	0.080	0.064	0.123	0.055	0.051	0.117	0.129	0.055	0.138	0.192	0.817	0.043
NO_3	mg/L	2.89	4.03	1.33	1.67	1.32	2.64	2.62	1.65	1.23	2.05	0.66	1.26	5.24	3.2
ClO_4	µg/L	0.323	0.342	0.243	0.221	0.202	0.28	0.237	0.254	0.297	0.238	0.127	0.197	0.441	0.244
SO_4	mg/L	4.31	3.61	2.4	1.11	1.63	2.3	2.06	4.205	2.34	2.2	1.66	1.29	7.83	2.75
TDS	mg/L	104	77.1	98.6	78.6	94.3	90	95.7	104.45	97.1	62.9	90	82.9	154	98.6
HMX	µg/L	ND[b]	ND	0.136	ND	0.138	ND	0.132	ND	0.136	0.131	ND	0.13	1.96	0.042
RDX	µg/L	102	144	0.136	0.136	0.138	3.12	2.19	0.132	0.136	1.660	0.132	0.130	249.35	17.1
Ba	µg/L	2.66	3	22.1	7.67	15.4	19.9	9.12	6.275	9.16	12.6	7.2	26.7	28.739	10.3
B	µg/L	27.9	62.8	25	25	25	25	25	19.1	25	25	25	25	154.44	7.5
Ca	mg/L	9.75	9.87	10.6	7.62	9.44	9.89	11.7	9.71	9.7	9.19	9.65	10.3	6.09	10.3
Fe	µg/L	50	50	50	50	78.4	50	50	50	50	50	50	50	1489.9	50
Li	µg/L	9.43	ND	18.25	11.88	16.59	ND	ND	14.93	23.12	13.61	ND	20.23	8.16	9.73
Mg	mg/L	2.53	2.98	3.22	2.89	3.07	3.42	3.95	2.41	3.24	2.85	2.41	3.05	7.66	3.16
Mn	µg/L	5	5	5	5	157	5	5	5	5	5	2.17	5	38.68	2
Mo	µg/L	0.869	0.637	1.06	1.01	1.35	0.62	0.844	1.68	2.43	0.511	1.03	1.03	9.88	0.77
K	mg/L	0.298	1.08	1.51	2.21	1.5	1.18	1.25	0.41	1.24	0.748	0.332	1.21	0.478	0.774
SiO_2	mg/L	61.8	60.4	64.4	58.3	63.4	60.3	59.2	61.4	55.5	58.4	60.5	64.5	58.74	57.1
Na	mg/L	12.1	10.5	10.8	7.91	10.2	8.71	8.69	12.5	11	8.35	10.4	9.76	44.93	9.21
Sr	µg/L	64.5	65.8	54.2	43.3	52.8	50.8	69.9	48.8	47.3	49.9	49.4	47.7	71.192	54.7
U	µg/L	0.286	0.426	0.655	0.31	0.439	0.461	0.403	0.321	0.514	0.359	0.407	0.511	9.6	0.474
Zn	µg/L	15.4	5	5	14.9	5	5	9.46	5	5	5	6.14	5	18.31	1.65

[a] n/a = Not applicable.

[b] ND = Not detected.

Table 7.3-2
Geochemical Concentrations Associated with the Four BSS-Determined Groundwater Source Types and Measured Noncontaminated Local TA-16 Recharge (Alluvial Aquifer) and MBR (Regional Aquifer) Well Data

Species	BSS Source 1	BSS Source 2	BSS Source 3	BSS Source 4	Local TA-16 Recharge	MBR
pH	7.9	7.6	7.9	7.6	7.6	7.6
Alk_CO_3−HCO_3 (mg/L)	80.7	71.9	84.8	57.3	118.56	76.65
NH_3 (mg/L)	0.0	0.2	0.0	0.0	0.10	0.05
Cl (mg/L)	1.5	3.3	1.7	15.1	19.1	1.21
F (mg/L)	0.1	0.0	0.1	2.0	0.2	0.13
NO_3 (mg/L)	1.8	3.9	1.3	7.3	1.38	1.53
ClO_4 (µg/L)	0.2	0.3	0.2	0.6	0.4	0.3
SO_4 (mg/L)	2.2	4.0	1.6	13.8	10.3	1.19
TDS (mg/L)	90.3	85.6	94.7	261.1	152	96
HMX (µg/L)	0.1	0.0	0.1	5.0	0.3	0
RDX (µg/L)	0.0	142.3	0.0	416.6	3	0.2
Ba (µg/L)	13.2	0.2	15.9	73.4	3007	8
B (µg/L)	21.7	48.0	25.7	320.9	21.8	20
Ca (mg/L)	9.9	10.0	9.4	0.0	19.74	7.61
Fe (µg/L)	49.3	0.0	81.5	3819.0	235	30.0
Li (µg/L)	16.3	4.6	16.8	13.8	0.4	10
Mg (mg/L)	3.0	2.6	3.1	15.5	5.12	2.93
Mn (µg/L)	0.3	3.8	173.5	93.1	8.4	2.0
Mo (µg/L)	1.1	0.3	1.4	24.8	1	1.0
K (mg/L)	1.1	0.7	1.6	0.1	3.09	2.22
SiO_2 (mg/L)	59.9	60.9	63.9	55.4	38.9	57.9
Na (mg/L)	9.8	10.1	10.3	99.5	17.3	8.48
Sr (µg/L)	51.2	67.7	53.0	76.7	152	50
U (µg/L)	0.4	0.0	0.4	24.5	0.1	0.3
Zn (µg/L)	6.4	9.0	5.0	32.8	8.0	7.0

Notes: Local TA-16 Recharge (column 6)—Surface infiltration source component (well CdV-16-02656; alluvial aquifer chemistry). MBR (column 7)—Deep source component (well R-26-S1; regional well chemistry). Compositions for Local TA-16 recharge and MBR sources each based on screened averages from EMS well database spanning from 2005–2015.

Table 7.3-3
Mixing Ratios of the Four Groundwater Source Types Identified by BSS for Site Monitoring Wells

Well	Source 1	Source 2	Source 3	Source 4
CdV-16-2(i)r	0.3123	0.6707	0.0082	0.0089
CdV-16-4ip_S1	0.0000	0.9869	0.0000	0.0131
CdV-R-15-3_S4	0.9730	0.0000	0.0268	0.0001
R-26 S1	0.9690	0.0106	0.0204	0.0000
CdV-R-37-2_S2	0.2127	0.0010	0.7863	0.0000
R-25b	0.9583	0.0164	0.0251	0.0002
R-18	0.9416	0.0338	0.0241	0.0004
R-47i	0.9752	0.0000	0.0247	0.0000
R-48	0.9754	0.0000	0.0246	0.0001
R-63	0.9576	0.0224	0.0199	0.0000
CdV-37-1(i)	0.9850	0.0051	0.0097	0.0002
R-27	0.9741	0.0000	0.0259	0.0000
CdV-9-1(i)	0.0000	0.6099	0.0000	0.3901
R-68	0.8898	0.1063	0.0025	0.0014

Appendix A

Pipe-and-Disk Transport Module Input Parameters

Input to the pipe-and-disk transport module is in a MADS file in a format typical of other MADS input files (format of the MADS input files is described at http://mads.lanl.gov). The user needs to ensure consistent units for the inputs.

The first part of an example input file to pipe-and-disk transport module is shown below, followed by descriptions of the entries.

```
MADS model: "mzmads.jl"

Pathways: 1

Time samples: 5000

p1_sz1_anasolfunc: Anasol.long_bbb_ddd_aii_cf

p1_sz2_anasolfunc: Anasol.long_bbb_ddd_iii_cf
```

Each input-file entry is defined as follows:

MADS model: Fill in the forward model desired while running MADS. mzmads.jl calls pipe-and-disk model.

Pathways: Define the number of drip areas within each UZ. For example, in this case we intend to have one drip area in each of 2 UZs that separate 2 SZs, so the number of pathways is 1. The drip areas may be staggered horizontally or directly atop one another.

Time samples: Number of time steps

The next two lines of text indicate the solution method and boundary conditions for the SZs. In this example, the analytical solver (anasol; https://github.com/madsjulia/Anasol.jl) recognizes three dimensions. In SZ1, dispersion is Brownian (bbb), the source is dispersed (ddd), the boundary along the *x* axis is absorbing (a) and along the *y* and *z* axes is infinite (ii), and source strength is provided as a flux function (cf). SZ2 is the same except all three dimensions (*x, y* and *z*) have infinite boundaries. The dispersed or distributed source may be Gaussian or other Levy alpha stable distribution. The source is defined by center location and spread σ_0 in three dimensions, as described below.

The next block in the input file includes parameters that define the pathways. A minimum/maximum range is specified if the parameter will be optimized. For single forward solution, the initial ("init") value is used.

```
Parameters:

- p1_t0: {init: 1960, min: 1950, max: 1980, type: opt}

- p1_t1: {init: 2700, min: 1980, max: 2700, type: opt}

- p1_massrate: {init: 10000, min: 100, max: 100000, type: opt, log: yes}

- p1_maxtime: {init: 2000, type: null}
```

p1_t0: Defines the origin time of contaminant release in the simulation.

p1_t1: Defines the final time of contaminant release.

p1_massrate: Mass rate of contaminant release at the top of this pathway.

p1_maxtime: Maximum time of simulation.

The next block of the input file defines UZ parameters and will be repeated for each UZ in the pathway, with the number incremented as necessary.

```
- p1_uz1_v: {init: 25, min: 5, max: 500, type: opt, log: yes}

- p1_uz1_dispersivity: {init: 10, min: 1, max: 300, type: opt, log: yes}

- p1_uz1_drippoint: {init: 100, type: null}
```

v: advective groundwater velocity (e.g., infiltration rate) in the vadose zone.

dispersivity: Dispersivity in consistent units.

drippoint: The vertical depth of the UZ.

The next block defines SZ parameters and is repeated for each SZ in the pathway, with the numbers in the parameter names incremented as necessary:

```
- p1_sz1_x0_1: {init: 492306.38, type: null}

- p1_sz1_x0_2: {init: 537685.64, type: null}

- p1_sz1_x0_3: {init: 100, type: null}

- p1_sz1_sigma0_1: {init: 1, min: 0, max: 500, type: opt}

- p1_sz1_sigma0_2: {init: 1, min: 0, max: 500, type: opt}

- p1_sz1_sigma0_3: {init: 0.001, type: null}

- theta1: {init: 0, min: -90, max: 90, type: opt, log: no}

- xyspeed1: {init: 10, min: 1, max: 500, type: opt, log: yes}

- p1_sz1_v_1: {exp: "cosd(theta1) * xyspeed1"}

- p1_sz1_v_2: {exp: "sind(theta1) * xyspeed1"}

- p1_sz1_v_3: {init: 0, min: -0.1, max: 0.1, type: opt}

- p1_sz1_dispersivity_1: {init: 100, min: 10, max: 300, type: opt, log: yes}

- p1_sz1_dispersivity_2: {init: 10, min: 1, max: 10, type: opt, log: yes}

- p1_sz1_dispersivity_3: {init: 1, min: 0.1, max: 10, type: opt, log: yes}

- p1_sz1_drippoint: {init: 100, min: 50, max: 500, type: opt}
```

x0_1, x0_2, x0_3: coordinates of the SZ contaminant source center

sigma0_1, sigma0_2, sigma0_3: source spatial standard deviations as the UZ plume hits the saturated zone SZ

theta: Angle of groundwater flow in the SZ, relative to *x* axis

xyspeed1: Velocity of the groundwater flow

v_1, v_2, v_3: Values or expression for velocity vector components in *x, y, z*

dispersivity_1, 2, 3: SZ dispersivities in the *x*, *y*, and *z* directions

drippoint: Location of the center of the drip area relative to the specified coordinates.

The input file next contains keyword Wells and is followed by location and time series information from observation points at which concentrations will be computed and/or calibrated against.

Appendix B

CHROTRAN: A Massively Parallel Numerical Simulator for In Situ Biogeochemical Reduction of Heavy Metals in Heterogeneous Aquifers

B-1.0 INTRODUCTION

CHROTRAN (Chromium Transport Bio-Chemical Remediation Code) is a novel biogeochemical simulator capable of modeling the governing processes of in situ remediation of chromium, hexahydro-1,3,5-trinitro-1,3,5-triazine (RDX), and other contaminants in heterogeneous aquifers. CHROTRAN features full coupling between groundwater flow and reactive transport, allowing for three-dimensional simulation of the complex interactions of hydrology and biogeochemistry that occur during contaminant transport and remediation. CHROTRAN is based upon the existing PFLOTRAN code framework (Lichtner et al. 2017a, b), leveraging existing capabilities to model multi-component flow and reactive transport using highly parallelized computational solvers. CHROTRAN provides a framework for modeling biostimulation, biodegradation, abiotic degradation, growth inhibitors, and biocides, which can be used to evaluate remediation of chromium along with a variety of other contaminants. The CHROTRAN framework also considers specific processes related to chromium remediation by sodium dithionite, a strong chemical reductant with unique oxidation-reduction behavior. These key features allow CHROTRAN to simulate sophisticated, multiscale biogeochemical remediation processes and aid in the design of field pilot studies and long-term deployments at the Los Alamos National Laboratory (LANL) contamination sites.

CHROTRAN is open-source software that can be redistributed and/or modified under the terms of the GNU Lesser General Public License as published by the Free Software Foundation. The Fortran source code files for CHROTRAN, along with input files for the examples are freely available at https://github.com/chrotran/release. Additional information regarding CHROTRAN is available at http://chrotran.lanl.gov. Please refer to Hansen et al. (2017a) for a more detailed description of model development and implementation. CHROTRAN allows for simulations employing complex models with a large number of computational cells and unknown variables. Because of the abstraction of the model and its parametric flexibility, CHROTRAN can also be used to model the in situ remediation of groundwater contaminated with heavy metals besides chromium, along with a wide range of organic contaminants. These include but are not limited to explosives (e.g., RDX), hydrocarbons, chlorinated solvents, pesticides, and volatile organic compounds.

B-2.0 USING CHROTRAN TO MODEL BIOCHEMICAL REMEDIATION

CHROTRAN biochemical remediation simulations account for spatial and temporal transients of (1) the heavy metal to be remediated, (2) introduced amendments (e.g., through well injection), and (3) biomass growth and decay. The introduced amendments can include (1) an electron donor (e.g., molasses), (2) a nontoxic conservative bio-inhibitor (e.g., ethanol), and (3) a biocide (e.g., dithionite). In addition, direct abiotic reduction by donor-metal interaction, as well as donor-driven biomass growth and bioreduction, are explicitly modeled in CHROTRAN. Other critical governing processes, such as donor sorption, bio-fouling and biomass death, are also modeled.

B-2.0-1 Key Features

The following summarizes the key processes involved in CHROTRAN bioremediation simulations.

- **Direct abiotic reaction between introduced electron donor and contaminant:** Experimental results (Chen et al. 2015; Hansen et al. 2017b) have established a rapid direct redox reaction of hexavalent chromium [Cr(VI)] to trivalent chromium [Cr(III)] when molasses is used as an electron donor.

- **Indirect Monod kinetics:** CHROTRAN models Cr(VI) biotic degradation based upon Monod kinetics of microorganism growth (Monod 1949; Wang and Xiao 1995; Okeke 2008; Hansen et al. 2017b).
- **Biofouling/Bioclogging:** CHROTRAN adjusts flow parameters such as porosity and hydraulic conductivity to account for biomass growth. This feature can be used to represent buildup of biological material near the amendment injection wells, which interferes with amendment injection and may rapidly consume electron donors.
- **Biomass crowding:** CHROTRAN accounts for changes in the biomass growth if biomass becomes overly dense. This causes cell stress, which reduces the rate of further growth.
- **Amendment additives:** CHROTRAN simulates the impact of bio-inhibitors and biocides injected to control biomass density near the amendment injection wells. This helps the spread of injected electron donors farther from the well before they are consumed by microorganisms.
- **Multiple donor consumption pathways:** CHROTRAN accounts for different biogeochemical models of electron donor consumption.

B-2.0-2 Relevant Species

CHROTRAN bioremediation simulations model five species whose dynamics are governed by physical and biogeochemical aquifer processes:

- **Aqueous contaminant(s)** to be remediated.
- **Immobile and mobile electron donors**, with mass exchange between the two states.
- **Biomass**, a collection of microbial consortia and their associated extracellular material.
- **Biomass-growth inhibitor**, represented as a conservative species, whose increasing concentration decreases microbial growth.
- **Biocide**, which reacts directly with biomass and is consumed.

These species interact in the following manner:

- **Biomass growth**: the biomass growth reaction irreversibly consumes the donor to produce biomass. The process rate is linearly proportional to the biomass concentration and controlled by the contaminant concentration through Monod kinetics. Two inhibition effects are accounted for: (1) biomass crowding attenuates growth rate as the biomass concentration rises, (2) biomass growth rate is reduced as the concentration of nonlethal inhibitor increases.
- **Bioreduction**: removal of the contaminant by the biomass; the process rate is linearly proportional to the biomass concentration and controlled by the contaminant concentration through Monod kinetics. The contaminant reduction is not directly tied to any particular biological process.
- **Biocide reaction**: an interphase bimolecular reaction between the biocide and the biomass based on a second-order mass action rate law, with the added condition that the biomass concentration cannot fall below a specified minimum.
- **Biomass natural decay**: If left unstimulated (without electron donor), the biomass decays based on a first-order process and returns to its natural background level represented by a specified minimum biomass concentration.
- **Biomass respiration**: consumption of the electron donor by biomass for purposes of life maintenance, unrelated to growth.

- **Abiotic reduction:** an aqueous-phase reaction between the electron donor and the contaminant based on a second-order mass action rate law.
- **Mobile-immobile mass transfer:** a process with first-order kinetics representing sorptive retardation of the electron donor.

B-3.0 USING CHROTRAN TO MODEL SODIUM DITHIONITE TREATMENT (GEOCHEMICAL REMEDIATION)

In situ geochemical remediation of aquifers contaminated with chromium involves the injection of a strong chemical reductant into sediments containing redox-sensitive elements. In the case of iron-bearing sediments, this results in the reduction of ferric iron [Fe(III)] to ferrous iron [Fe(II)], which binds to mineral surfaces and becomes a long-term, stationary source of reductant capable of transforming dissolved Cr(VI) to Cr(III). This process is referred to as in situ redox manipulation (ISRM). In the past, simple numerical models have been used by others (Amonette et al. 1994; Istok et al. 1999; Williams et al. 2000; Chilakapati et al. 2000) to help quantify certain steps of this process. However, a unified predictive model that combines all of the important steps that occur throughout the remediation process has not previously been developed. Such a model is critical to quantitatively evaluate remediation design strategies for field deployment. CHROTRAN is capable of modeling the entire process of ISRM using sodium dithionite from laboratory to field scale. Along with simulation of in situ reduction of Cr(VI), it is also capable of modeling other important processes that may influence remediation, such as mineral precipitation/dissolution, aqueous speciation, and pH.

B-3.0-1 Key Features

The following reactions are included to accurately model in situ remediation of Cr(VI) through the injection of a sodium dithionite amendment. These reactions are assumed to be kinetically limited, and rate laws were formulated after an extensive literature review (Morello et al. 1964; Creutz and Sutin 1974; Eary and Rai 1989; Rubio et al. 1992; Amonette et al. 1994; Buerge and Hug 1997, 1999; Istok et al. 1999; Williams et al. 2000; Chilakapati et al. 2000; Williams and Scherer 2001; Bond and Fendorf 2003).

- **Reduction of Fe(III) sediments by dithionite:** CHROTRAN accounts for Fe(III) and its reduction to Fe(II) by dithionite, which results in the formation of an ISRM zone (Istok et al. 1999; Williams et al. 2000).
- **Reduction of Cr(VI) by reduced iron sediments:** CHROTRAN models the reduction of and subsequent immobilization of Cr(VI) as it passes through the ISRM zone and reacts with Fe(II). This results in decreased Cr(VI) concentrations downstream of the ISRM zone but also decreases the concentration of Fe(II) within the ISRM zone.
- **Loss of dithionite through disproportionation:** Dissolved dithionite is known to be unstable and is prone to degradation through disproportionation reactions, which are accelerated in the presence of sediments (Amonette et al. 1994). This reaction is included in CHROTRAN and decreases the overall availability of dithionite, causing less reduction of Fe(III).
- **Loss of dithionite through reactions with oxygen:** In an aerobic aquifer, dissolved oxygen will also react with dithionite through redox reactions. This will also decrease the amount of injected dithionite available to reduce Fe(III) and is an important limiting factor of ISRM accounted for in CHROTRAN.
- **Oxidation of Fe(II) sediments by oxygen:** Surface-bound Fe(II) is capable of reducing other dissolved oxidants, which reduces the overall capacity of the ISRM zone to reduce Cr(VI). In an aerobic aquifer, dissolved oxygen will most likely be the dominant oxidant. The oxidation of Fe(II) sediments by dissolved oxygen is included in CHROTRAN.

B-3.0-2 Relevant Species

CHROTRAN geochemical remediation simulations model the following species whose dynamics are governed by physical and geochemical aquifer processes:

- **Oxidants:** CHROTRAN accounts for dissolved oxygen, Cr(VI), and Fe(III). Oxygen and Cr(VI) exist in the aqueous phase and Fe(III) is represented in the solid phase as a mineral precipitate.
- **Injected reductant and its reaction products:** The injected reductant is sodium dithionite, which dissociates to sodium and dithionite. The reaction products of the different reactions involving dithionite are sulfate, sulfite, and thiosulfate.
- **Reduced species:** Dithionite reduces Fe(III) precipitates to Fe(II) bound to mineral surfaces. Surface-complexed Fe(II) is subsequently capable of reducing Cr(VI) to Cr(III) in the aqueous phase.
- **pH and pH buffers:** The degradation of dithionite is strongly pH dependent, as the kinetics of the reaction is greatly accelerated at high pH. CHROTRAN simulates pH changes that result from the redox reactions outlined above. In addition, the model accounts for injectant pH buffering (e.g., potassium bicarbonate, calcium carbonate).
- **Other aqueous species:** Equilibrium speciation is also included in CHROTRAN to estimate the concentrations of secondary aqueous species (e.g., OH^-, CO_3^{-2}, $H_2CO_3(aq)$, $HCrO_4^-$). These species influence the ionic strength, charge balance, and pH of the groundwater.
- **Mineral species and their dissolved constituents:** Both Cr(III) and Fe(III) are highly insoluble and readily precipitate in neutral to alkaline pH groundwater. For this reason, mineral precipitation is included in CHROTRAN to account for the fate of Cr(III) as chromium hydroxide and Fe(III) as ferric hydroxide. CHROTRAN considers the potential release of carbonates through the dissolution of minerals such as calcite, which will influence pH.

B-4.0 REFERENCES

The following reference list includes documents cited in this report.

Amonette, J.E., J.E. Szecsody, H.T. Schaef, Y.A. Gorby, J.S. Fruchter, and J.C. Templeton. “Abiotic Reduction of Aquifer Materials by Dithionite: A Promising In-Situ Remediation Technology,” Pacific Northwest Laboratory technical report PNL-SA-24505 (1994).

Bond, D.L., and S. Fendorf. “Kinetics and Structural Constraints of Chromate Reduction by Green Rusts,” *Environmental Science & Technology*, Vol. 37, No. 12, pp. 2750–2757 (2003).

Buerge, I.J., and S.J. Hug. “Kinetics and pH Dependence of Chromium (VI) Reduction by Iron (II),” *Environmental Science & Technology,* Vol. 31, No. 5, pp. 1426–1432 (1997).

Buerge, I.J., and S.J. Hug. “Influence of mineral Surfaces on chromium (VI) Reduction by Iron (II),” *Environmental Science & Technology*, Vol. 33, No. 23, pp. 4285-4291 (1999).

Chen, Z.F., Y.S. Zhao, J.W. Zhang, and J. Bai. “Mechanism and Kinetics of Hexavalent Chromium Chemical Reduction with Sugarcane Molasses,” *Water, Air, & Soil Pollution*, Vol. 226, pp. 1–9, https://doi.org/10.1007/s11270-015-2629-6 (2015).

Chilakapati, A., M. Williams, S. Yabusaki, C. Cole, and J. Szecsody. “Optimal Design of an In Situ Fe (II) Barrier: Transport Limited Reoxidation,” *Environmental Science & Technology*, Vol. 34, No. 24, pp. 5215–5221 (2000).

Creutz, Carol and Norman Sutin. Kinetics of the reactions of sodium dithionite with dioxygen and hydrogen peroxide. Inorganic Chemistry, 13(8):2041–2043, 1974.

Eary, L.E., and D. Rai. “Kinetics of Chromate Reduction by Ferrous Ions Derived from Hematite and Biotite at 25 Degrees C,” American Journal of Science, Vol. 289, No. 2, pp. 180–213 (1989).

Hansen, S.K., H. Boukhalfa, S. Karra, D. Wang, and V.V. Vesselinov. “Chromium (VI) Reduction in Acetate- and Molasses Amended Natural Media: Empirical Model Development,” Los Alamos National Laboratory document LA-UR-17-30690, Los Alamos, New Mexico (2017a).

Hansen, S.K., S. Pandey, S. Karra, and V.V. Vesselinov. “CHROTRAN 1.0: A Mathematical and Computational Model for In Situ Heavy Metal Remediation in Heterogeneous Aquifers,” *Geoscientific Model Development*, Vol. 10, pp. 4525-4538 (2017b).

Istok, J.D., J.E. Amonette, C.R. Cole, J.S. Fruchter, M.D. Humphrey, J.E. Szecsody, S.S. Teel, V.R. Vermeul, M.D. Williams, and S.B. Yabusaki. “In Situ Redox Manipulation by Dithionite Injection: Intermediate-scale Laboratory Experiments,” *Ground Water*, Vol. 37, No. 6, pp. 884–889 (1999).

Lichtner, P.C., G.E. Hammond, C. Lu, S. Karra, G. Bisht, B. Andre, R.T. Mills, J. Kumar, and J.M. Frederick. *PFLOTRAN User Manual*, available at: http://www.documentation.pflotran.org, last access: 12 December (2017a).

Lichtner, P.C., G.E. Hammond, C. Lu, S. Karra, G. Bisht, B. Andre, R.T. Mills, J. Kumar, and J.M. Frederick. PFLOTRAN web page, available at: http://www.pflotran.org, last access: 12 December (2017b).

Monod, J. “The Growth of Bacterial Cultures,” *Annual Review of Microbiology*, Vol. 3, pp. 371–394, https://doi.org/10.1146/annurev.mi.03.100149.002103, (1949).

Morello, J.A., M.R. Craw, H.P. Constantine, and R.E. Forster. “Rate of Reaction of Dithionite Ion with Oxygen in Aqueous Solution,” *Journal of Applied Physiology*, Vol. 19, No. 3, pp. 522–525, (1964).

Okeke, B.C. “Bioremoval of Hexavalent Chromium from Water by a Salt Tolerant Bacterium, Exiguobacterium sp. GS1,” *Journal of Industrial Microbiology & Biotechnology*, Vol. 35, pp. 1571–1579, https://doi.org/10.1007/s10295-008-0399-5 (2008).

Rubio, F.C., M.P. Paez Dueñas, G. Blazquez Garcia, and J.M. Garrido Martin. “Oxygen Absorption in Alkaline Sodium Dithionite Solutions,” Chemical Engineering Science, Vol. 47, Nos. 17–18, pp. 4309–4314, (1992).

Wang, Y.T., and C. Xiao. “Factors Affecting Hexavalent Chromium Reduction in Pure Cultures of Bacteria,” *Water Research*, Vol. 29, pp. 2467–2474, https://doi.org/10.1016/0043-1354(95)00093-Z, (1995).

Williams, M.D., V.R. Vermeul, J.E. Szecsody, and J.S. Fruchter. “100-D area In Situ Redox Treatability Test for Chromate Contaminated Groundwater,” Pacific Northwest National Laboratory technical report PNNL-13349 (2000).

Williams, A.G.B., and M.M. Scherer. “Kinetics of Cr(VI) Reduction by Carbonate Green Rust,” *Environmental Science & Technology*, Vol. 35, No. 17, pp. 3488–3494 (2001).

LA-UR-18-21326
March 2018
EP2018-0050

2017 Status Report: Tracer Tests at Consolidated Unit 16-021(c)-99, Technical Area 16

Attachment 9

Los Alamos
NATIONAL LABORATORY
EST. 1943

Prepared by the Associate Directorate for Environmental Management

CONTENTS

Figures

Table

Appendix

1.0 INTRODUCTION

This report provides information on a series of large-scale, multi-year, groundwater tracer tests being conducted in the vicinity of Technical Area 16 (TA-16) at Los Alamos National Laboratory (LANL or the Laboratory). Deployments were made in October and November 2015 (LANL 2017), and tracer monitoring results from perched-intermediate and regional groundwater wells through December 2017 are discussed here. The TA-16 tracer study is being conducted to test connectivity of various parts of the TA-16 hydrological system (see Figure 1.0-1) and will support activities related to understanding of the long-term fate of high explosives in groundwater, and potential remedial alternatives.

The tracer study will improve understanding of (1) groundwater flow paths, (2) lateral travel times and associated hydrologic parameters within the Otowi Member of the Bandelier Tuff Formation and the Puye Formation, and (3) vertical travel times between perched-intermediate groundwater and the regional aquifer. The hydrogeologic framework (Figure 1.0-1) for the contaminated deep perched-intermediate zone and regional aquifer is complex (LANL 2011). A wide range of hydrologic, geochemical, and geophysical data suggest these groundwater zones are quite heterogeneous. The perched-intermediate zone is divided into an upper and a lower zone, with the upper zone consistently more contaminated than the lower. Conservative geochemical signatures vary both spatially and, to a lesser degree, temporally (LANL 2011). Hydrologic data, including water levels, pump-test results, and drilling observations, demonstrate that deep perched-intermediate zones are hydrogeologically complex with localized hydrogeologic regimes (LANL 2011). Implementation of the tracer study was based on a work plan (LANL 2015) that was approved by the New Mexico Environment Department (NMED) on August 3, 2015 (NMED 2015).

2.0 METHODS

A detailed discussion of the TA-16 tracer plans and the deployment details for the small dilution tests and large-scale tests is provided in the previous tracer status report (LANL 2017). For reference, a summary of all the deployments is presented in Table 2.0-1. The table includes information on the various tracers deployed and their locations, tracer masses and water volumes, and start and completion dates of deployment. The deployment and monitoring well locations are shown in Figure 2.0-1. Deployed tracers are abbreviated as, for example, 1 NS, 1,6 NDS, and 1,3,6 NTS, representing single sulfonate (NS), disulfonate (NDS) and trisulfonate (NTS) versions of the sodium-naphthalene sulfonate tracers, respectively.

2.1 Dilution Tests

No additional dilution tests have been run or are planned beyond those described in the previous tracer status report (LANL 2017) and summarized in Table 2.0-1.

2.2 Large Tracer Tests

Details of the large tracer test deployments for each well screen and piezometer are provided in LANL 2017. The large tracer deployments began at CdV-9-1(i) screen 1 starting on October 29, 2015, and injection was completed on November 6, 2015. Injection of tracer at CdV-9-1(i) piezometer 1 began on November 9, 2015, and was completed on November 10, 2015. Injection of tracer at CdV-9-1(i) piezometer 2 began on November 10, 2015, and was completed on November 16, 2015. Injection of tracer at R-25b began on November 18, 2015, and was completed on November 20, 2015. Injection of tracer at CdV-16-1(i) began on November 20, 2015, and was completed on November 21, 2015.

All investigation-derived waste (IDW) generated during sampling was managed in accordance with EP-DIR-SOP-10021, “Characterization and Management of Environmental Programs Waste.” This procedure incorporates the requirements of all applicable U.S. Environmental Protection Agency and NMED regulations, U.S. Department of Energy orders, and Laboratory implementation requirements, policies, and/or procedures. IDW was also managed in accordance with the approved waste characterization strategy form.

3.0 RESULTS AND DISCUSSION

3.1 Dilution Tests

Details of the dilution test results can be found in the previous tracer status report (LANL 2017).

3.2 Large Tests

The tracers used in the large tests in wells R-25b, CdV-9-1(i), and CdV-16-1(i) have been deployed just over two years (Table 2.0-1), so the results presented here still represent the early phase of the multi-year tests. Results from each of the three tracer deployment wells will be discussed individually, after which results from the other monitoring wells in the TA-16 area will be discussed.

The tracer 1,6 NDS was injected into R-25b and the time series shows a dilution trend through December, 2017 (Figure 3.2-1). Even though a clear dilution trend was evident, tracer concentrations were still over 500 mg/L during the December 2017 sampling round, and concentrations were substantially higher than the deployed tracers in CdV-9-1(i), and CdV-16-1(i) for the same sampling dates (the results from these two wells are discussed below). The high R-25b concentrations suggest a relatively low rate of transport, which is consistent with the dilution test results where local flow velocities at R-25b were substantially lower than at CdV-9-1(i) screen 1 (LANL 2017). Both 1,5 NDS and 2,6 NDS were also detected in the March and June 2016 sampling rounds from R-25b at the level of about 1 mg/L or less (Appendix A). These detections are probably related to impurities in the 1,6 NDS tracer and not from transport from other wells. Because the 1,6 NDS concentrations were still quite high, it seems reasonable that tracer impurities could be detectible. Laboratory analyses of stock solutions also showed the presence of NS impurities. 1,5 NDS and 2,6 NDS concentrations are now below the detection limit. Bromide was also detected but was not above background. No other deployed tracers have been detected in R-25b since the June 2016 sampling event.

Four tracers were deployed in well CdV-9-1(i): 1,3,6 NTS in piezometer 1; 1,3,5 NTS in piezometer 2; and 2,6 NDS and bromide in screen 1. Because of the small-diameter configuration, the two piezometers could not be sampled after tracer deployment, and only screen 1 was monitored. As with R-25b, the deployed 2,6 NDS tracer in CdV-9-1(i) screen 1 shows a clear dilution trend (Figure 3.2-2). However, unlike R-25b, screen 1 shows rapid dilution, and 2,6 NDS was below detection by March 2016. It has remained below detection even during the July 2016 CdV-9-1(i) pump test period. This result suggests the tracer moved relatively rapidly downgradient beyond the point where it could be recovered during the pump test. Bromide showed a similar dilution behavior, but remained elevated for a longer period than 2,6 NDS. As of December 2017, bromide concentrations are similar to background concentrations at TA-16. Some bromide tracer was removed during the July 2016 pump test (< 0.5 kg). The differences in bromide and 2,6 NDS transport were expected, and this is why both tracers were included in the tracer work plan (LANL 2015). Bromide has different diffusion properties than the much-larger 2,6 NDS molecule, and the dual-tracer approach should help clarify transport characteristics in the TA-16 area in the future.

Both of the tracers from the two CdV-9-1(i) piezometers have been detected in screen 1 (Figure 3.2-3). The piezometer 2 tracer, 1,3,5 NTS, was detected in the first sampling round in December 2015 in CdV-9-1(i) screen 1 about 1 month after the tracer was deployed in the piezometer (piezometer 2 is the deepest piezometer and closest to screen 1). The concentration then dropped below the detection limit in January 2016, after which it rose to about 0.1 mg/L by the March 2016 sampling round. Repeated higher detections occurred during the July 2016 pump test period. The first detection in December 2015 may be related to impurities in the tracer introduced into screen 1, and detection of 1,6 NDS during this sampling round supports this interpretation (Appendix A). However, by March 2016, there is clear indication of transport from piezometer 2 to screen 1, and it appears that the July pump test temporarily induced additional transport. Starting in December 2016 there was a large increase in the concentrations of 1,3,5 NTS through May 2017. Increases in Cdv-91i water levels prompted a special series of samples in April and May which captured the pulse of 1,3,5 NTS very well. The implications of this tracer pulse are discussed later in this section. There was also a large and rapid decline in tracer concentrations after the May 2017 peak, and by August 2017 concentrations had dropped to a similar range as the prepulse concentration (December 2016).

The piezometer 1 tracer, 1,3,6 NTS, was first detected in March 2016 and increased in concentration once the pump test was initiated in May 2016 (Figure 3.2-3). Concentrations of 1,3,6 NTS were about an order of magnitude lower than the 1,3,5 NTS from piezometer 2, which is consistent with the fact that piezometer 1 is farther above screen 1 than piezometer 2. This concentration difference has been maintained throughout the current monitoring period. 1,3,6 NTS concentrations fluctuated during and just after the pump test in May 2016 (which is likely related to pumping and recovery periods). However, like the piezometer 2 tracer, a large relative increase in concentrations was observed after December 2016. The 1,3,6 NTS concentrations peaked in April 2017, but remained elevated in May 2017 when the piezometer 2 tracer peaked. Similar to the piezometer 2 tracer, there was a rapid decrease in 1,3,6 NTS, and by August 2017 concentrations had dropped to near prepulse concentrations.

The relatively large concentration increases of the two piezometer tracers in spring of 2017 is clearly linked to increases in water levels observed in multiple wells in the TA-16 area, including the CdV-9-1(i) piezometers. The implication is that snowmelt/springtime recharge to the shallower piezometer zones facilitated a downward transport pulse to screen 1. This behavior is consistent with discussions in Attachment 3 of this compendium that show the importance of springtime recharge at TA-16. Concentrations of both tracers peaked and declined rather rapidly. It is interesting to note that although piezometers 1 and 2 are separated by about 200 feet, the two piezometer tracers arrive in screen 1 almost simultaneously and concentrations increase and fall off again at the same time. The observations of 1,3,5 NTS and 1,3,6 NTS through December 2017 demonstrate flow path connections from the shallower parts of the perched-intermediate zone to screen 1. The March 2016 initial detections imply about a 3- to 4-month transport time to screen 1. Detections in 2016 may have been due to relatively low-volume, fast, vertical pathways connecting CdV-9-1(i) piezometers 1 and 2 to screen 1. However, this transport time does not represent rates under natural hydraulic gradients because the tracer deployments in piezometers 1 and 2 increased heads substantially during addition of the tracers, and the pump test at screen 1 appeared to have increased gradients that would also promote faster transport. The spring 2017 pulses dramatically demonstrate the vertical connection to screen 1. However, it is unclear whether the connections between the piezometers and screen 1 represent natural flow paths or if the detections of tracers in the piezometer are related to short-circuiting along the well bore or through potentially damaged regions adjacent to the well bore.

The tracer 1,5 NDS was injected into well CdV-16-1(i). Because of adverse winter conditions in the canyon bottom, well monitoring did not begin until March 2016. By that time, concentrations of 1,5 NDS had dropped to about 50 mg/L (Figure 3.2-4). Concentrations declined slowly through early August 2016 and then increased sharply during the August 2016 pump test period. Approximately 11.4 kg of 1,5 NDS was removed during the pump test (about 29% of the original mass). After the pump test was completed, a fairly symmetrical reduction in concentrations occurred during the rebound period. During the last sampling round in December 2017, 1,5 NDS could still be detected in the well at about 0.6 mg/L.

In addition to the deployed 1,5 NDS tracer, multiple detections of 1,3,5 NTS were observed in well CdV-16-1(i) into September 2016 (Figure 3.2-4). Concentrations peaked at about 1 mg/L during the August 2016 CdV-16-1(i) pump test and then declined to below-detection levels by the end of September. In piezometer 2 of CdV-9-1(i), 1,3,5 NTS was deployed; however, it is likely that the detections are related to impurities in the 1,5 NDS tracer used at CdV-16-1(i). During the first two sampling rounds, 1,3,5 NTS was detected and the general shape of the tracer time series is similar to 1,5 NDS during both the early dilution phase and the pump test (Figure 3.2-4). A few early detections of 2,6 NDS and 1,3,6 NTS were also observed, and as with 1,3,5 NTS, are likely the result of impurities.

Perched-intermediate wells CdV-16-2(i)r, CdV-16-4ip, and R-47i and regional aquifer wells R-18, R-25 (one-time sampling of screens 1, 2, 4, and 5), R-47, R-48, R-58, and R-63 were also monitored for tracers. No tracer detections were observed for CdV-16-2(i)r, R-18, R-25, R-47, R-58, and R-63. Wells CdV-16-4ip, R-47i, and R-48 each had single detections of 1,6 NDS that were just above the detection limit. These detections are likely false positives. Apparently,1,6 NDS is sometimes prone to an interference that can result in concentrations just above the 0.002-mg/L detection limit. No tracer detections were observed in R-25 screens, including of 1,6 NDS, which had been deployed in nearby well R-25b. The lack of detection of 1,6 NDS is consistent with the slow movement of the tracer away from R-25b.

4.0 SUMMARY AND RECOMMENDATIONS

Although this report describes results from what is still the early phase of the large tracer tests, useful results have been obtained that are increasing understanding of subsurface flow and transport in the TA-16 subsurface. The large tracer tests showed clear dilution effects in all three deployment wells, but implied rates based on concentration differences suggest the groundwater flow velocity at R-25b is much lower than the flow velocity at CdV-16-1(i), and flow velocity in CdV-9-1(i) is greater than the flow velocity at CdV-16-1(i). The spatially variable flow conditions implied by the large tracer results support the idea of a heterogeneous flow system as described by the TA-16 conceptual model (LANL 2011).

Another key result is that tracers from both CdV-9-1(i) piezometers have been detected in CdV-9-1(i) screen 1, and the large pulses of piezometer tracers observed in screen 1 in the spring of 2017 clearly demonstrate vertical flow path connections. It is unclear whether these detections represent naturally occurring flow conditions or if they are the result of short-circuiting along the well bore or in the adjacent damaged zone (from drilling). Even if the flowpath connections are artificial, the tracer pulses in the spring of 2017 demonstrate the importance of seasonally transient recharge events at TA-16. Further analysis of the TA-16 water level data and CdV-9-1(i) geochemical samples from the spring 2017 period could provide valuable information regarding these transient recharge events and the site conceptual model.

The pump tests in CdV-9-1(i) and CdV-16-1(i) affected the deployed tracers in these wells. The effects in CdV-9-1(i) were minor and only affected bromide (and the piezometer tracers). The test in CdV-16-1(i) had a much more substantial effect (Figure 3.2-6), showing clear pumpback of a significant quantity (29%) of the introduced tracer. This result is useful from a qualitative perspective but could also provide an opportunity to quantify flow conditions around the well using numerical modeling. Because it was not possible to conduct a small-scale dilution test in CdV-16-1(i), the pumpback tracer data could potentially be used instead to understand more about the subsurface near the well screen.

Another important result thus far is that no credible cross-well detections have been observed. It has taken some time for the tracers to move beyond the vicinity of the deployment screens. Only 2,6 NDS and bromide in CdV-9-1(i) are no longer detectible (or above background in the case of bromide) in the screened zone where they had been deployed. Although it appears that 1,5 NDS in CdV-16-1(i) is also approaching the limit of detection. Over time it is expected all the tracers should reach below detection limits in the screens where they were deployed. However, in the case of R-25b this period may be especially protracted.

The fact that most of the tracers have not yet fully moved beyond the vicinity of the screens where they were deployed and no cross-well detections have occurred is not surprising. However, these two observations demonstrate the need for continued monitoring to quantify the complete dispersal behavior of tracers from the wells where they were deployed and to observe any potential transport to downgradient monitoring wells. Long-term tracer breakthrough monitoring is recommended to realize the full benefits of the TA-16 tracer study. Monitoring for tracers can be conducted at minimal additional cost during routine groundwater monitoring activities at TA-16.

5.0 REFERENCES

The following reference list includes documents cited in this report.

LANL (Los Alamos National Laboratory). “Investigation Report for Water Canyon/Cañon de Valle,” Los Alamos National Laboratory document LA-UR-11-5478, Los Alamos, New Mexico (2011).

LANL (Los Alamos National Laboratory). “Work Plan for a Tracer Test at Consolidated Unit 16-021(c)-99, Technical Area 16, Revision 1,” Los Alamos National Laboratory document LA-UR-15-24089, Los Alamos, New Mexico (2015).

LANL (Los Alamos National Laboratory). Status Report for the Tracer Tests at Consolidated Unit 16 021(c)-99, EP2017-0009 (2017).

NMED (New Mexico Environment Department). “Approval with Comment, Work Plan for a Tracer Test at Consolidated Unit 16-021(c)-99, Technical Area 16, Revision 1,” New Mexico Environment Department letter to C. Gelles (DOE-NA-LA) and M.T. Brandt (LANL) from J.E. Kieling (NMED-HWB), Santa Fe, New Mexico (2015).

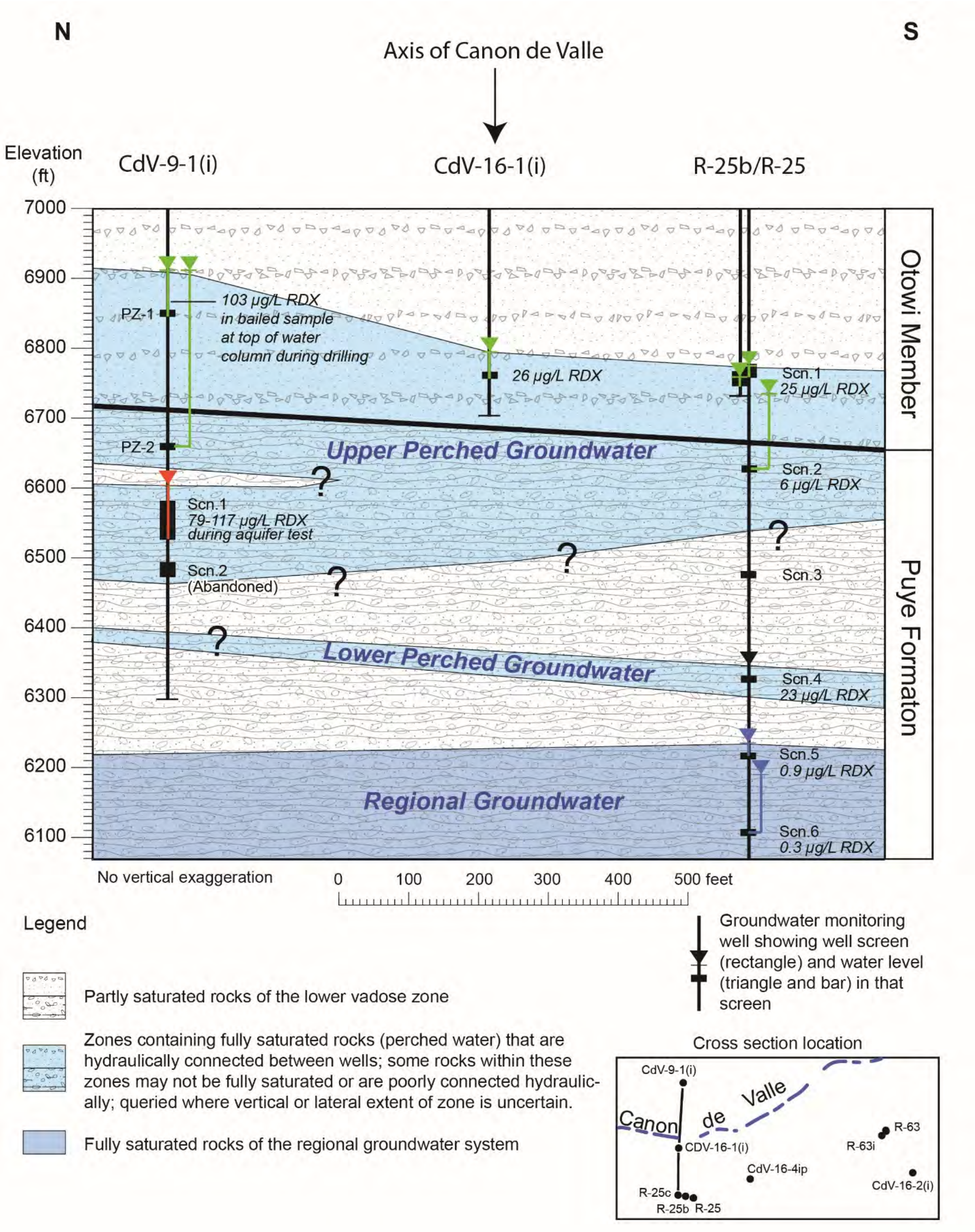

Figure 1.0-1 **Hydrogeological conceptual model of the vicinity of TA-16. Screen and piezometer locations in wells CdV-9-1(i), CdV-16-1(i), R-25b, and R-25 are also shown.**

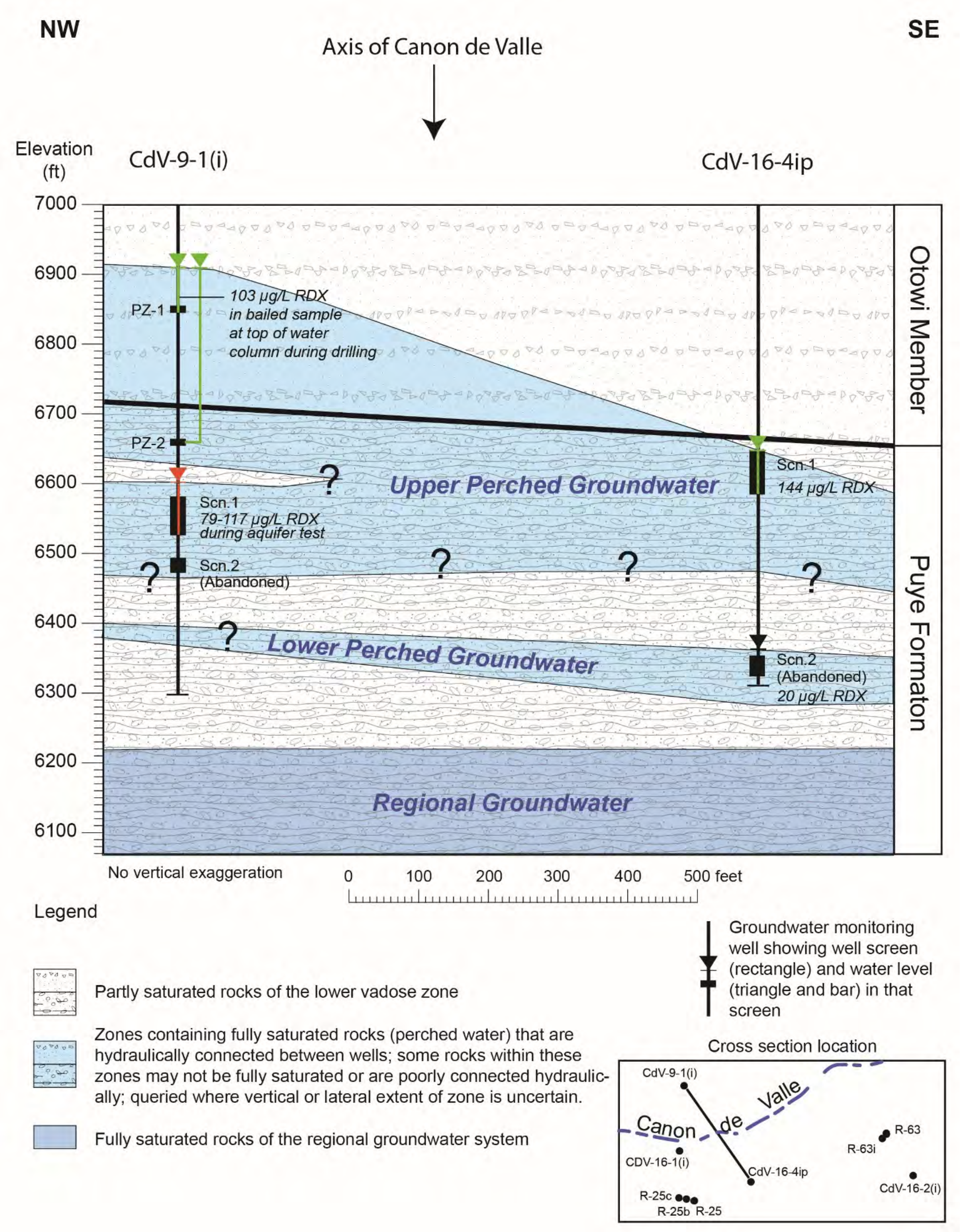

Figure 1.0-1 (continued) **Hydrogeological conceptual model of the vicinity of TA-16. Screen and piezometer locations in wells CdV-9-1(i) and CdV-16-4ip are also shown.**

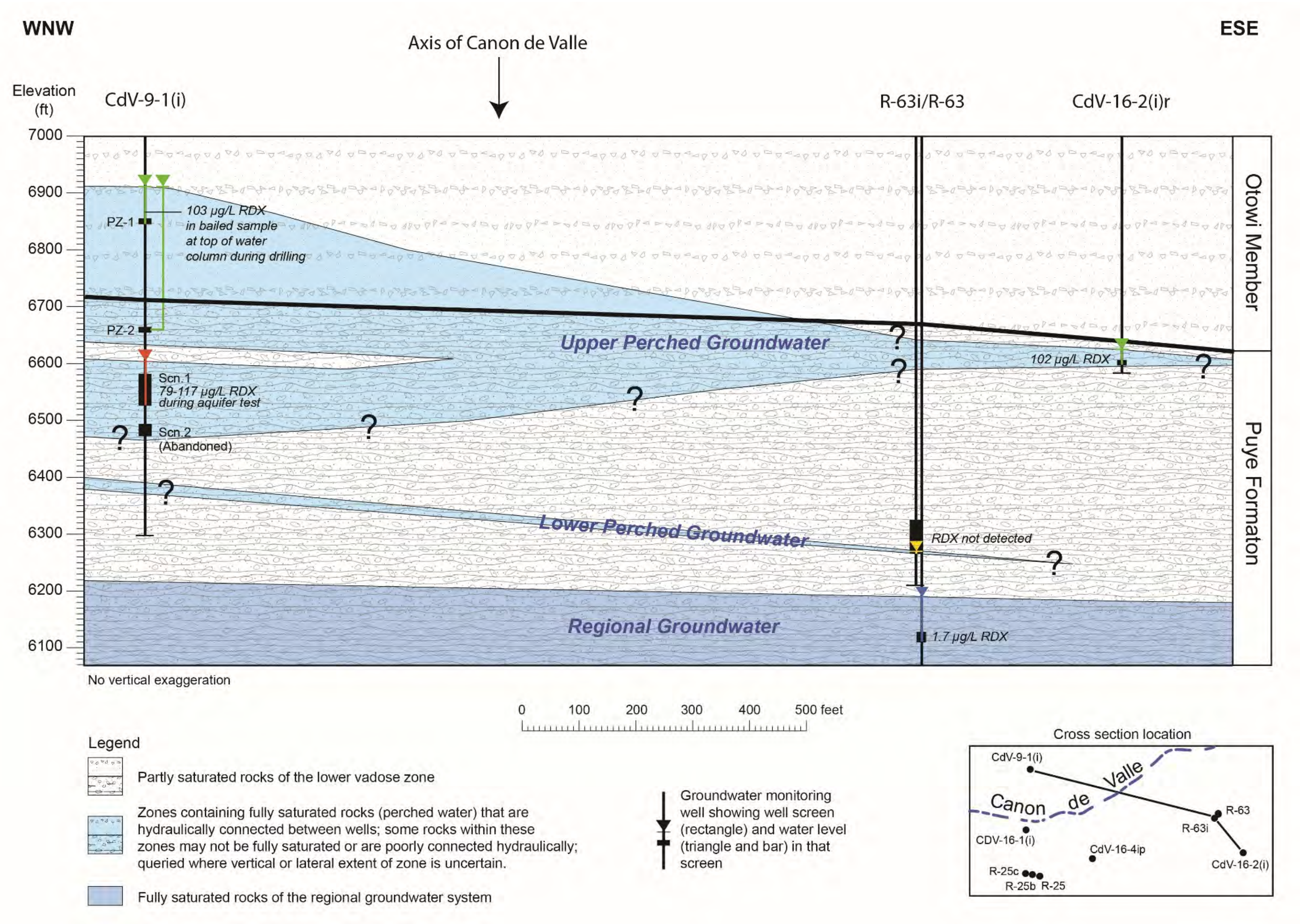

Figure 1.0-1 (continued) **Hydrogeological conceptual model of the vicinity of TA-16. Screen and piezometer locations in wells CdV-9-1(i), R-63, R-63i and CdV-16-2(i)r are also shown.**

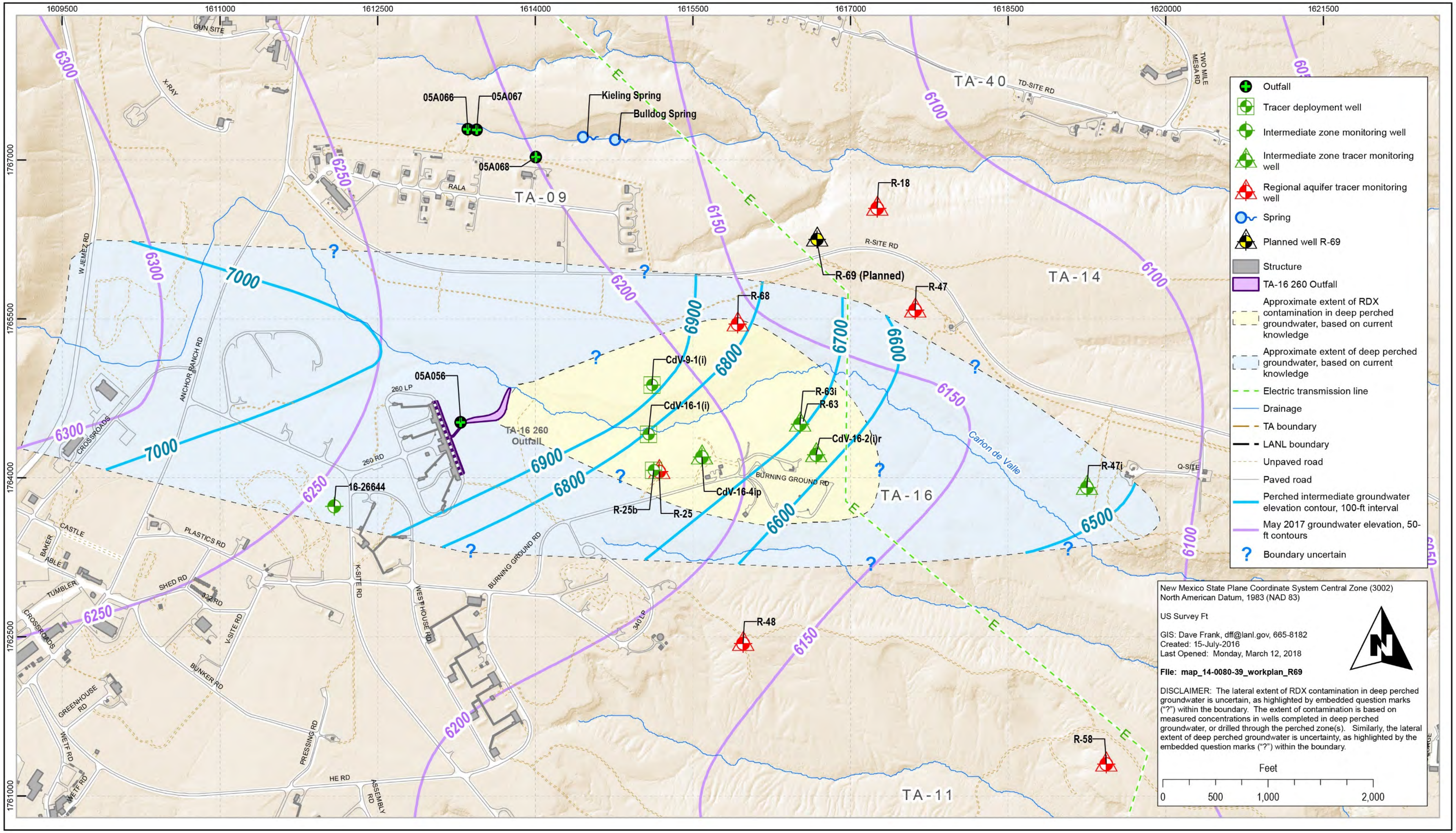

New Mexico State Plane Coordinate System Central Zone (3002)
North American Datum, 1983 (NAD 83)

US Survey Ft

GIS: Dave Frank, dff@lanl.gov, 665-8182
Created: 15-July-2016
Last Opened: Monday, March 12, 2018

File: map_14-0080-39_workplan_R69

DISCLAIMER: The lateral extent of RDX contamination in deep perched groundwater is uncertain, as highlighted by embedded question marks ("?") within the boundary. The extent of contamination is based on measured concentrations in wells completed in deep perched groundwater, or drilled through the perched zone(s). Similarly, the lateral extent of deep perched groundwater is uncertainty, as highlighted by the embedded question marks ("?") within the boundary.

Figure 2.0-1 Location of tracer deployment wells, monitoring wells, and other hydrologic features in the vicinity of TA-16. The extent of the upper perched zone (with water-elevation contour lines) and the extent of RDX contamination in this zone are shown as an example of the subsurface conditions at TA-16.

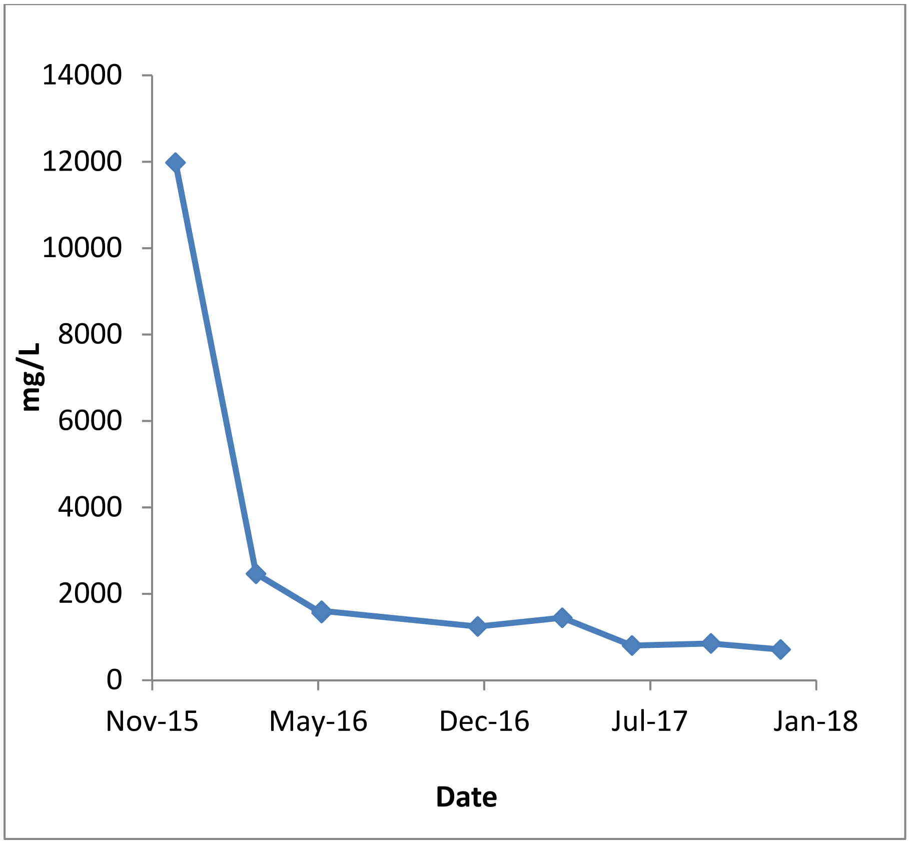

Figure 3.2-1 Time series of deployed tracer 1,6 NDS in well R-25b

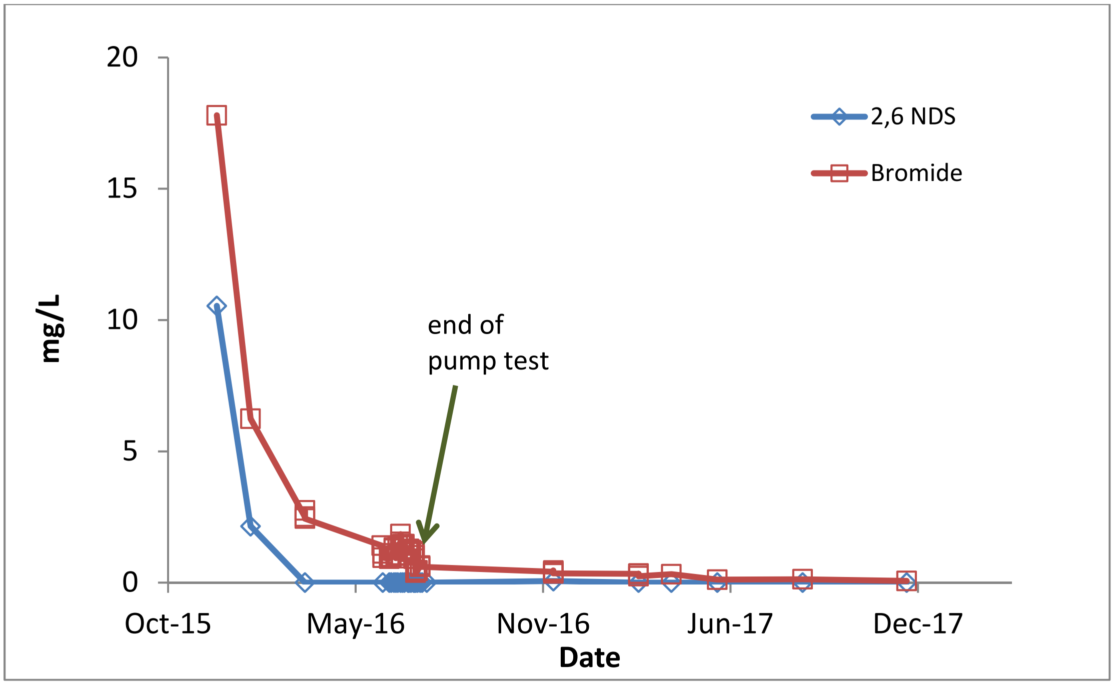

Figure 3.2-2 Time series of deployed tracers 2,6 NDS and bromide in screen 1 well CdV-9-1(i)

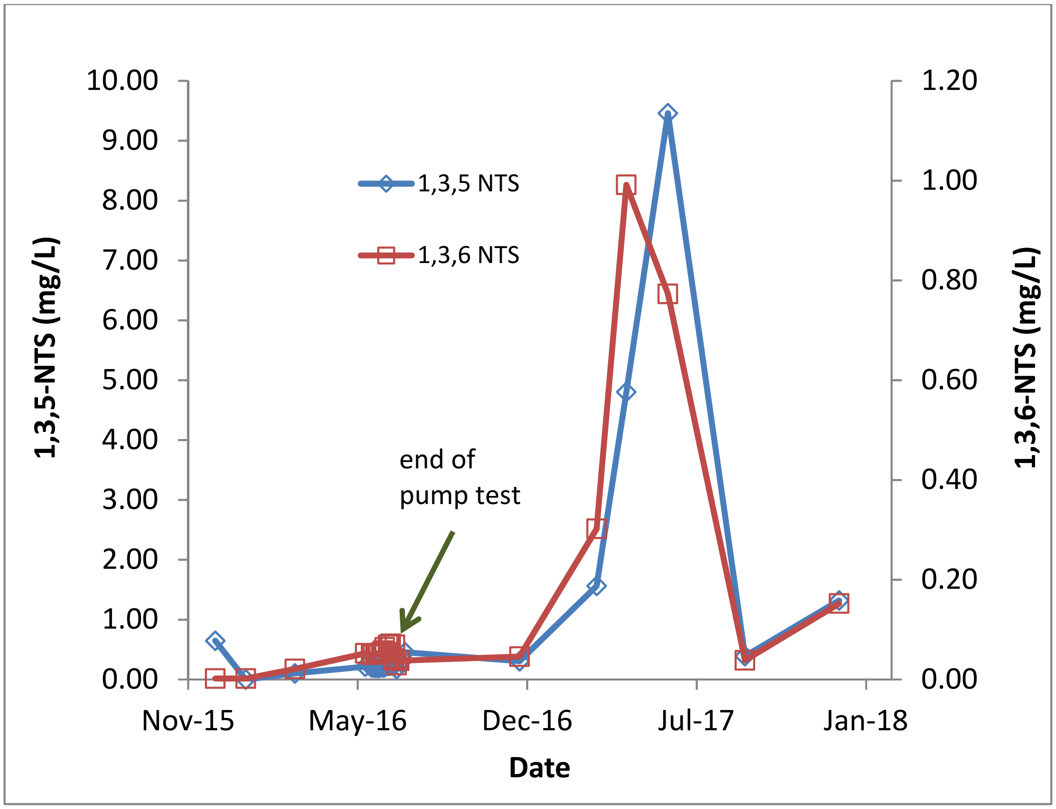

Figure 3.2-3 Time series of piezometer 1 tracer (1,3,6 NTS, in red, right axis) and piezometer 2 tracer (1,3,5 NTS, in blue, left axis) in screen 1 well CdV-9-1(i)

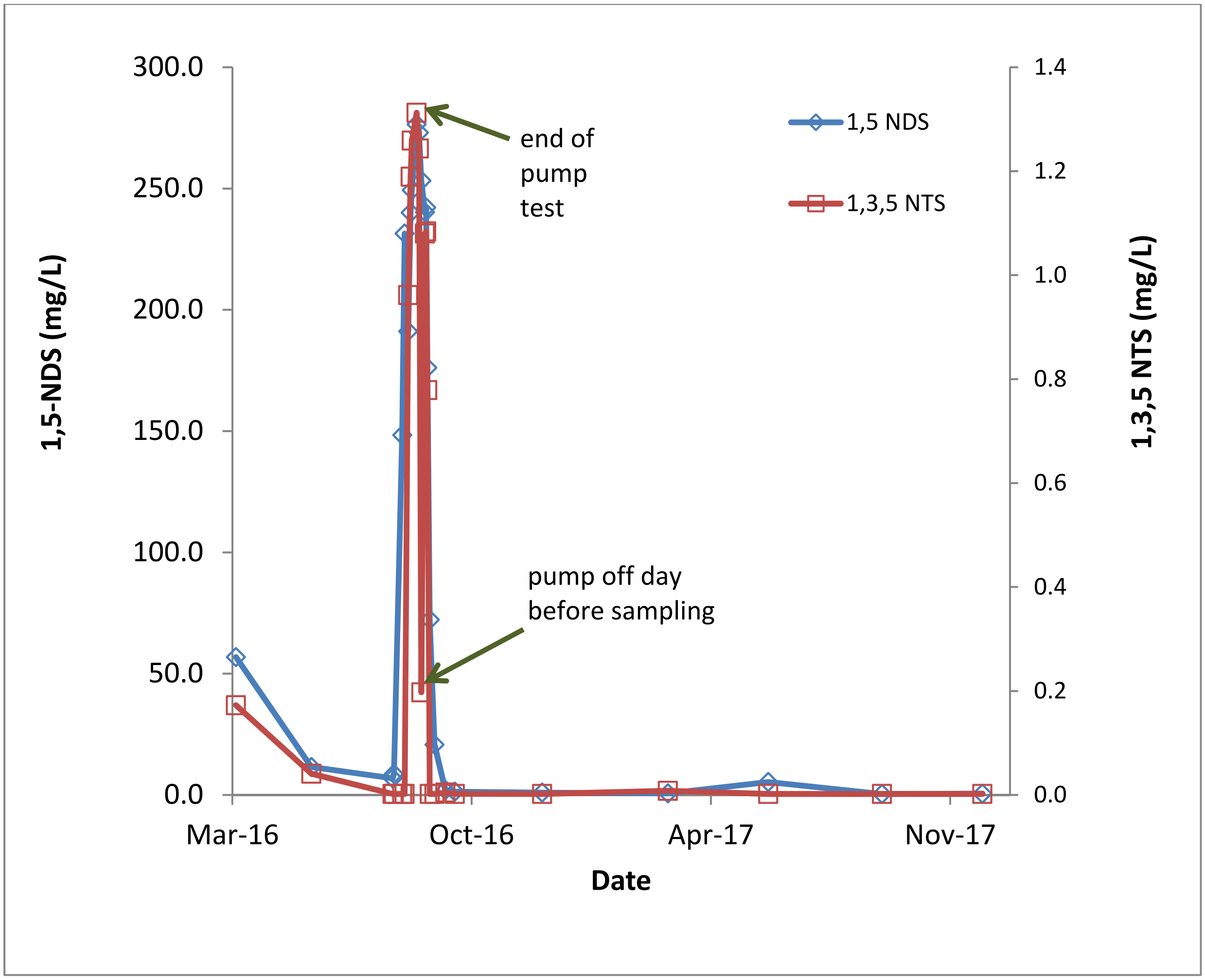

Figure 3.2-4 Time series of deployed tracer 1,5 NDS (in blue, left axis) and probable impurity 1,3,5 NTS (in red, right axis) in well CdV-16-1(i)

Table 2.0-1
Summary of TA-16 Tracer Deployment Details

Well Name	Tracer Test Type	Tracer(s) Added	Quantity Injected (g or kg)	Tracer Added Start	Tracer Added Finish	Volume of Tracer Solution Injected (gal.)	Chase Water Volume (gal.)
R-25b	Dilution	1 NS	2 g	10/5/2015	10/05/2015	40	N/A[a]
CdV-9-1(i)	Dilution	1 NS	2 g	10/15/2015	10/15/2015	270	N/A
CdV-9-1(i)	Injection	2,6-NDS	40 kg	10/29/2015	11/06/2015	10,550 (2,6-NDS	82
Screen 1	Injection	NaBr	150 kg	10/29/2015	11/06/2015	plus NaBr)	N/A
CdV-9-1(i)	Injection	1,3,6-NTS	25 kg	11/09/2015	11/10/2015	2900	50
Piezometer 1	N/A	N/A	N/A	N/A	N/A	N/A	N/A
CdV-9-1(i)	Injection	1,3,5-NTS	25 kg	11/10/2015	11/16/2015[b]	200	55
Piezometer 2	N/A	N/A	N/A	N/A	N/A	N/A	N/A
R-25b	Injection	1,6-NDS	40 kg	11/18/2015	11/20/2015	6000	30
CdV-16-1(i)	Injection	1,5-NDS	40 kg	11/20/2015	11/21/2015	6000	60

[a] N/A = Not applicable.

[b] Injections occurred during the day on 11/10/2015, 11/12/2015 and 11/16/2015

Appendix A

Analytical Results for Tracer Tests
(on CD included with this document)